

Next-Generation High-Fidelity Image and Video Transmission Using Quantum Communication Techniques

Udara Jayasinghe Mudalige

Registration No.: 20235149

A thesis submitted in partial fulfilment of the requirements for the degree of Doctor of Philosophy (PhD)

Department of Computer and Information Sciences

University of Strathclyde, Glasgow

1 August 2026

Declaration

This thesis is the result of the author's original research. It has been composed by the author and has not been previously submitted for examination which has led to the award of a degree.

The copyright of this thesis belongs to the author under the terms of the United Kingdom Copyright Acts as qualified by University of Strathclyde Regulation 3.50. Due acknowledgement must always be made of the use of any material contained in, or derived from, this thesis.

Signed: Udara Jayasinghe Mudalige

Date: 1 August 2026

Acknowledgements

I would like to express my sincere gratitude to all those who have supported and guided me throughout this research journey. First and foremost, I would like to express my deepest gratitude to my primary supervisor, Prof. Anil Fernando, for his invaluable guidance, continuous support, constructive feedback, and encouragement throughout every stage of this research. His expertise, patience, and insightful discussions have played a fundamental role in shaping the direction and quality of this work. I am especially grateful for the trust and academic freedom he provided, which allowed me to explore innovative research ideas while maintaining strong scientific rigour. I would also like to sincerely thank my second supervisor, Dr. Robert Atkey, for his valuable advice, encouragement, and thoughtful feedback throughout this study. His support and academic insights greatly contributed to the successful completion of this research. I would like to thank the University of Strathclyde and the Department of Computer and Information Sciences for providing an excellent research environment, access to computational resources, and opportunities for academic and professional development. In addition, I would like to express my sincere appreciation to the University of Castilla–La Mancha, Spain, for their valuable collaboration, academic support, and financial assistance throughout this research. I am grateful to my colleagues and fellow researchers for the many stimulating discussions, shared insights, and collaborative spirit that made this experience both productive and enjoyable. In particular, I would like to acknowledge the members of my research group for their feedback during presentations and for their willingness to share ideas and expertise. Finally, I owe an immeasurable debt of gratitude to my family for their unwavering love, patience, and encouragement throughout this journey. Their belief in me, particularly during the most challenging periods, has been a constant source of strength and motivation. This thesis is dedicated to them.

Previously Published Material

This thesis incorporates material that has been previously published in peer-reviewed journals and conference proceedings. The candidate was the first author of all publications arising from this doctoral research and conducted the research under the guidance of the supervisory panel. The candidate was primarily responsible for the conception of the research, development of the methodology, system design, simulation implementation, experimental evaluation, analysis and interpretation of results, and preparation of the manuscripts. Where publications involved collaboration with co-authors, their contributions were limited to supervision, technical guidance, manuscript review, and editorial feedback. The candidate's specific contributions are clearly identified in the respective publications. All previously published material included in this thesis has been appropriately cited and reproduced or adapted in accordance with university regulations and publisher copyright requirements. Rather than providing a consolidated list of publications in this section, each chapter or section containing previously published material includes a publication statement identifying the relevant source publication, full bibliographic details, the candidate's contribution as first author, and a statement regarding copyright permission where applicable. A complete list of publications arising from this doctoral research is provided in Section 1.5.

Candidate Declaration

I confirm that the above statement accurately reflects my contribution to the previously published work included in this thesis.

Name: Udara Jayasinghe Mudalige

Date: 1 August 2026

Abstract

The rapid growth of image and video applications has exposed fundamental limitations in existing communication systems. Unlike conventional data, multimedia content consists of large data volumes and requires the reliable preservation of perceptual quality under stringent bandwidth constraints and in the presence of channel noise. Existing communication systems rely on binary representations that are highly susceptible to channel impairments, where even minor transmission errors can significantly degrade reconstructed quality. Although quantum communication has the potential to overcome these limitations by exploiting the principles of quantum mechanics, existing research has primarily focused on secure information exchange, while its application to end-to-end high-fidelity communication remains unexplored. Motivated by these gaps, this thesis proposes a new multimedia-oriented quantum communication paradigm for image and video transmission that rethinks how multimedia information is represented, protected, compressed, transmitted, and reconstructed over noisy communication channels. The proposed paradigm is progressively developed through a series of interconnected contributions. First, an end-to-end quantum communication framework based on Hadamard superposition encoding is established with and without quantum error correction. Second, multi-qubit encoding strategies map multimedia data into higher-dimensional Hilbert spaces to improve transmission robustness and bandwidth efficiency. Third, the framework is extended through quantum frequency-domain transformations, enabling frequency-domain multimedia transmission and high-ratio compression. Fourth, a novel complex-valued orthogonal unitary superposition (COUS) encoding framework jointly exploits amplitude and phase diversity to enhance robustness while maintaining linear gate complexity. Finally, the proposed paradigm is integrated with multiple-input multiple-output (MIMO), orthogonal frequency-division multiplexing (OFDM),

hybrid MIMO-OFDM, multiple description coding (MDC), and semantic communication systems, demonstrating its applicability to practical multimedia communication systems. Extensive simulation results demonstrate that the proposed paradigm consistently outperforms conventional communication systems by improving transmission robustness, reconstruction quality, compression efficiency, and semantic reliability under noisy channel conditions. Collectively, these findings establish a scalable foundation for next-generation multimedia communication systems.

Contents

Declaration i

Acknowledgements ii

Previously Published Material iii

Abstract iv

List of Figures xiv

List of Tables xxvi

List of Abbreviations xxix

1 Introduction 1

1.1 Background and Motivation 1

1.1.1 Limitations of Classical Communication Systems for Image and Video Transmission 2

1.1.2 Challenges in Image and Video Compression 3

1.1.3 Emerging Application Requirements 4

1.1.4 Quantum Communication as an Alternative Paradigm 5

1.1.5 From Quantum Key Distribution to Quantum Image and Video Transmission 6

1.1.6 Research Motivation and Scope 8

1.2 Problem Statement 10

1.3 Research Aim and Objectives 11

1.3.1 Research Aim 11
1.3.2 Objectives 11
1.4 Research Contributions 12
1.4.1 Design of a Single-Qubit Encoding Quantum Communication Framework for Image and Video Transmission 13
1.4.2 Design and Analysis of Multi-Qubit Quantum Encoding Techniques for Image and Video Transmission 13
1.4.3 Design and Analysis of Quantum Frequency-Domain Techniques for Quantum Communication 14
1.4.4 Introduction of Novel Quantum Encoding Techniques for Noise Resilience and Computational Efficiency 14
1.4.5 Design of an Integrated Quantum Communication Framework with Existing Image and Video Transmission Systems 15
1.5 Research Dissemination and Scholarly Contributions 15
1.5.1 Journal Publications 16
1.5.2 Conference Publications 19
1.5.3 Under Review Manuscripts 20
1.5.4 Collaborative Research Contributions 21
1.5.5 International Conference Presentations 21
1.6 Thesis Outline 22

2 Literature Review **25**
2.1 System Model of Classical Communication 26
2.1.1 Source Encoder 27
2.1.2 Channel Encoder 28
2.1.3 Modulation Techniques 29
2.2 Classical OFDM System 30
2.3 Classical MIMO System 32
2.4 Classical MIMO-OFDM System 33
2.5 Multiple Description Coding (MDC) 34
2.6 Semantic Communication Systems 35

2.7 Prior Works on Classical Communication Systems for Multimedia Transmission . . . 36
2.8 Quantum Mechanics . . . 40
2.8.1 Qubits . . . 40
2.8.2 Quantum Superposition . . . 41
2.8.3 Entanglement . . . 42
2.8.4 No-Cloning Theorem . . . 43
2.8.5 Quantum Gates . . . 44
2.9 Quantum Computing . . . 45
2.9.1 Current Quantum Computing Technologies and NISQ Challenges 46
2.10 Quantum Communication . . . 47
2.11 Quantum Noise Models in Quantum Communication Systems . . . 49
2.11.1 Bit-Flip Noise . . . 49
2.11.2 Phase-Flip Noise . . . 49
2.11.3 Depolarising Noise . . . 50
2.11.4 Amplitude Damping Noise . . . 50
2.11.5 Phase Damping Noise . . . 51
2.11.6 Summary . . . 51
2.12 Quantum Error Correction (QEC) . . . 51
2.13 Quantum Network Simulators . . . 53
2.14 Prior Works on Quantum Computing and Communication . . . 54
2.14.1 Prior Works on Quantum Communication for Secure Transmission 56
2.14.2 Prior Works Using Quantum Superposition for Communication Tasks . . . 56
2.14.3 Prior Works on Transform-Domain Analysis in Quantum Systems 58
2.14.4 Prior Works on Quantum Error Correction . . . 59
2.14.5 Prior Works on Quantum Image Representation and Compression 61
2.14.6 Prior Works on Quantum Communication Applications . . . 62
2.14.7 Prior Works on Quantum Multimedia Transmission . . . 64
2.14.8 Limitations of Existing Quantum Communication Research and Motivation . . . 66

2.15 Chapter Summary 68

3 Design of a Single-Qubit Encoding Quantum Communication Framework for Image and Video Transmission 70

3.1 Quantum Communications for Image Transmission over Error-Prone Channels 71

3.1.1 System Model 73

3.1.2 Results 79

3.1.3 Section Summary 85

3.2 A Three-Qubit Quantum Error Correction Framework for Image Transmission 86

3.2.1 System Model 88

3.2.2 Results 93

3.2.3 Section Summary 97

3.3 An Adaptive Quantum Error Correction Framework for Reliable Quantum Image Transmission 99

3.3.1 System Model 101

3.3.2 Results 106

3.3.3 Section Summary 114

3.4 Quantum Video Transmission over Noisy Communication Channels . . . 115

3.4.1 System Model 117

3.4.2 Results 119

3.4.3 Section Summary 128

3.5 Chapter Summary 129

4 Design and Analysis of Multi-Qubit Quantum Encoding Techniques for Image and Video Transmission 132

4.1 Error-Resistant Quantum Image Communication Based on Multi-Qubit Encoding 134

4.1.1 System Model 136

4.1.2 Results 141

4.1.3 Section Summary 151

4.2 An Adaptive Multi-Qubit Encoding Framework for Robust Video Transmission over Noisy Quantum Channels . . . 152
4.2.1 System Model . . . 154
4.2.2 Results . . . 155
4.2.3 Section Summary . . . 160
4.3 Chapter Summary . . . 161

5 Design and Analysis of Quantum Frequency-Domain Techniques for Quantum Communication 163

5.1 A Quantum Multi-Qubit Frequency-Domain Approach for Reliable Image Transmission . . . 165
5.1.1 System Model . . . 167
5.1.2 Results . . . 177
5.1.3 Section Summary . . . 190
5.2 A Quantum Multi-Qubit Frequency-Domain Approach for Reliable Video Transmission . . . 191
5.2.1 System Model . . . 192
5.2.2 Results . . . 194
5.2.3 Section Summary . . . 200
5.3 Quantum Fourier Transform for Image Compression and Transmission over Error-Prone Channels . . . 201
5.3.1 System Model . . . 202
5.3.2 Results . . . 207
5.3.3 Section Summary . . . 220
5.4 Quantum Fourier Transform for Video Compression and Transmission over Error-Prone Channels . . . 221
5.4.1 System Model . . . 222
5.4.2 Results . . . 225
5.4.3 Section Summary . . . 240
5.5 Semantic-Aware Quantum Frequency-Domain Image Transmission with Channel-Aware Denoising . . . 241
5.5.1 System Model . . . 243

5.5.2 Results . . . 251
5.5.3 Section Summary . . . 259
5.6 Semantic-Aware Quantum Frequency-Domain Video Transmission with Post-Channel Noise Reduction . . . 260
5.6.1 System Model . . . 261
5.6.2 Results . . . 266
5.6.3 Section Summary . . . 271
5.7 Chapter Summary . . . 271

6 Introduction of Novel Quantum Encoding Techniques for Noise Resilience and Computational Efficiency 275
6.1 A Complex-Valued Orthogonal Unitary Superposition Encoding-Based Multi-Qubit System for Quantum Image Transmission . . . 278
6.1.1 System Model . . . 280
6.1.2 Results . . . 287
6.1.3 Section Summary . . . 301
6.2 A Complex-Valued Orthogonal Unitary Superposition Encoding-Based Multi-Qubit System for Quantum Video Transmission . . . 302
6.2.1 System Model . . . 304
6.2.2 Results . . . 306
6.2.3 Section Summary . . . 324
6.3 Chapter Summary . . . 325

7 Design of an Integrated Quantum Communication Framework with Existing Image and Video Transmission Systems 328
7.1 Quantum Communication Techniques for Image Transmission in Diversity-Assisted MIMO Systems . . . 332
7.1.1 System Model . . . 334
7.1.2 Results . . . 338
7.1.3 Section Summary . . . 345
7.2 Quantum Communication Techniques for Video Transmission in Diversity-Assisted MIMO Systems . . . 346

7.2.1 System Model . . . 348
7.2.2 Results . . . 350
7.2.3 Section Summary . . . 358
7.3 Quantum OFDM-Based Image Transmission for Noise-Impaired Communication Channels . . . 358
7.3.1 System Model . . . 360
7.3.2 Results . . . 368
7.3.3 Section Summary . . . 379
7.4 Quantum OFDM-Based Video Transmission for Noise-Impaired Communication Channels . . . 380
7.4.1 System Model . . . 381
7.4.2 Results . . . 383
7.4.3 Section Summary . . . 396
7.5 Enhanced Quantum Image Transmission Using MIMO-OFDM with Transmit and Receive Diversity . . . 396
7.5.1 System Model . . . 398
7.5.2 Results . . . 405
7.5.3 Section Summary . . . 420
7.6 A Quantum Multiple Description Coding Framework for Robust Image Transmission . . . 420
7.6.1 System Model . . . 423
7.6.2 Results . . . 430
7.6.3 Section Summary . . . 438
7.7 Quantum Communication for Semantic Communication-Based Image Transmission . . . 440
7.7.1 System Model . . . 442
7.7.2 Results . . . 449
7.7.3 Section Summary . . . 455
7.8 Chapter Summary . . . 455

8 Conclusions and Future Work 458

8.1 Summary of Contributions . . . 458

8.2 Overall Conclusion 461
8.3 Key Scientific Insights 464
8.4 Limitations 467
8.5 Future Work 469
8.6 Closing Remarks 472

A Analysis of COUS Encoding with Three-Qubit QEC **474**

B Derivation of the COUS Gate Decomposition **479**

References **481**

List of Figures

2.1 The end-to-end classical communication system. 26
2.2 The end-to-end classical OFDM communication system. 30
2.3 The end-to-end classical MIMO communication system. 32

3.1 End-to-end information transmission system using quantum communications. 73
3.2 Rate-distortion performance measured by averaged PSNR and averaged SSIM of the test images for different QP values (QP = 25, 50, 75, 100). 81
3.3 Sample decoded images (JPEG) for QP100 and SNR = 10.45 dB. 82
3.4 BER vs. SNR performance of JPEG-format images for quantum and classical communication systems. 82
3.5 End-to-end quantum communication system with three-qubit QEC. . . 88
3.6 Encoding and decoding circuit of the three-qubit error correction method. 89
3.7 Rate-distortion performance measured by averaged PSNR and averaged SSIM of the test images for quantum three-qubit QEC, quantum polar-coded, and classical polar-coded systems across different QP values (QP = 25, 50, 75, 100) using JPEG and HEIF image formats: (a) QP25 - PSNR, (b) QP25 - SSIM, (c) QP50 - PSNR, (d) QP50 - SSIM, (e) QP75 - PSNR, (f) QP75 - SSIM, (g) QP100 - PSNR, (h) QP100 – SSIM. . . . 94
3.8 Sample decoded images (JPEG) for QP25 and SNR = 6 dB. 96
3.9 Proposed adaptive QEC-based quantum image communication system. . 102
3.10 Quantum three-qubit encoder and decoder circuit. 103
3.11 PSNR variation with channel SNR for different multi-qubit QEC configurations applied to HEIF-compressed images. 107

3.12 Input JPEG images for different QEC schemes: (a) Q3, (b) Q5, (c) Q7, and (d) Q9. 108
3.13 Decoded JPEG images at an SNR of 0 dB for different QEC schemes: (a) Q3, (b) Q5, (c) Q7, and (d) Q9. 109
3.14 Decoded JPEG images at an SNR of −5 dB for different QEC schemes: (a) Q3, (b) Q5, (c) Q7, and (d) Q9. 110
3.15 Performance of adaptive QEC applied to JPEG-compressed images. . . 111
3.16 Performance of adaptive QEC applied to HEIF-compressed images. . . . 112
3.17 PSNR and SSIM comparison of quantum three-qubit QEC, quantum polar-coded, and classical polar-coded systems under identical bandwidth conditions. 113
3.18 Proposed quantum communication frameworks for video transmission with: (a) quantum error correction, and (b) classical error correction. . . 117
3.19 Three-qubit encoder and decoder circuit. 119
3.20 PSNR, SSIM, and VMAF variation for VVC videos with GOP = 8 for Q-S, Q-F, Q-T, Q-P, and C-P systems. 121
3.21 PSNR, SSIM, and VMAF variation for VVC videos with GOP = 16 for Q-S, Q-F, Q-T, Q-P, and C-P systems. 122
3.22 PSNR, SSIM, and VMAF variation for VVC videos with GOP = 32 for Q-S, Q-F, Q-T, Q-P, and C-P systems. 123
3.23 Subjective experiment results for VVC videos with different GOP values over Q-S, Q-F, Q-T, Q-P, and C-P systems. 127

4.1 Proposed adaptive multi-qubit encoding based end-to-end quantum communication system for image transmission. 136
4.2 Performance of all qubit configurations (k = 1–8) for JPEG image transmission without channel coding: (a) PSNR, (b) SSIM, (c) UQI. . . 143
4.3 Performance of JPEG image transmission using adaptive (Ad) qubit encoding. 145
4.4 Performance of HEIF image transmission using adaptive (Ad) qubit encoding. 146

4.5 Input JPEG images for different multi-qubit configurations: (a) 1, (b) 2, (c) 3, (d) 4, (e) 5, (f) 6, (g) 7, and (h) 8. 148
4.6 Decoded JPEG images (uncoded) for different multi-qubit configurations at an SNR of 11 dB: (a) 1, (b) 2, (c) 3, (d) 4, (e) 5, (f) 6, (g) 7, and (h) 8. 149
4.7 Decoded JPEG images (uncoded) for different multi-qubit configurations at an SNR of 9 dB: (a) 1, (b) 2, (c) 3, (d) 4, (e) 5, (f) 6, (g) 7, and (h) 8. 149
4.8 PSNR comparison of three-qubit QEC, multi-qubit superposition encoding, and classical polar-coded systems for JPEG image transmission. . . 151
4.9 Proposed variable-qubit encoding system for video transmission. 154
4.10 PSNR performance variation with qubit size and GOP size in quantum and classical video communication systems at 320×180 resolution. . . . 156
4.11 SSIM performance variation with qubit size and GOP size in quantum and classical video communication systems at 320×180 resolution. . . . 157
4.12 VMAF performance variation with qubit size and GOP size in quantum and classical video communication systems at 320×180 resolution. . . . 158

5.1 Complete block architecture of the proposed frequency-domain multi-qubit quantum communication pipeline. 168
5.2 Schematic design of the introduced frequency-domain multi-qubit quantum encoding unit. 169
5.3 Operational architecture of the proposed frequency-domain quantum decoding system. 173
5.4 Hardware circuit layout for a three-qubit QFT processing system. 175
5.5 Performance evaluation of BER, PSNR, SSIM, and UQI for JPEG images transmitted using frequency-domain encoding across varying SNR levels, under both uncoded and channel-coded conditions. 178
5.6 Performance evaluation of BER, PSNR, SSIM, and UQI for JPEG images transmitted using time-domain encoding across varying SNR levels, under both uncoded and channel-coded conditions. 180
5.7 Comparative analysis of BER, PSNR, SSIM, and UQI for JPEG image transmission using time-domain and frequency-domain encoding schemes over varying SNR levels, under both uncoded and channel-coded conditions. 181

5.8 Performance evaluation of BER, PSNR, SSIM, and UQI for HEIF images transmitted using frequency-domain encoding across varying SNR levels, under both uncoded and channel-coded conditions. 183
5.9 Performance evaluation of BER, PSNR, SSIM, and UQI for HEIF images transmitted using time-domain encoding across varying SNR levels, under both uncoded and channel-coded conditions. 184
5.10 Comparative analysis of BER, PSNR, SSIM, and UQI for HEIF image transmission using time-domain and frequency-domain encoding schemes over varying SNR levels, under both uncoded and channel-coded conditions. 185
5.11 Performance comparison between time-domain single-qubit quantum system and classical system at the same bandwidth. 186
5.12 Subjective quality assessment results for JPEG image transmission using frequency-domain and time-domain multi-qubit systems under uncoded and channel-coded conditions. 187
5.13 Proposed end-to-end video transmission system. 193
5.14 Performance comparison of quantum video communication systems for GOP8 using PSNR, SSIM, and VMAF metrics. 196
5.15 Performance comparison of quantum video communication systems for GOP16 using PSNR, SSIM, and VMAF metrics. 197
5.16 Performance comparison of quantum video communication systems for GOP32 using PSNR, SSIM, and VMAF metrics. 198
5.17 Decoded video frames at –12 dB channel SNR for GOP 8 and qubit size 8: (a) frequency-domain, (b) time-domain. 200
5.18 Proposed framework of quantum Fourier transform-based image compression and transmission. 202
5.19 Proposed quantum encoder. 203
5.20 Proposed quantum decoder. 205
5.21 Performance of the proposed system for different qubit sizes in a non-channel coding scenario for uncompressed image inputs. 209
5.22 Performance of the proposed system for different qubit sizes in a non-channel coding scenario for JPEG images. 210

5.23 Performance of JPEG image transmission for different qubit sizes in a non-channel coding scenario across two different communication systems: time-domain without compression (dash lines), frequency-domain without compression (solid lines). 212
5.24 Performance of the proposed system for different qubit sizes with channel coding for uncompressed image inputs. 213
5.25 Performance of JPEG image transmission for different qubit sizes with channel coding across two different communication systems: time-domain without compression (dash lines), frequency-domain without compression (solid lines). 215
5.26 Comparison of the proposed system with classical communication systems: (a) Peak Signal-to-Noise Ratio (PSNR), (b) Structural Similarity Index Measure (SSIM), and (c) Subjective Quality Score. 217
5.27 Histogram comparison between the original image and the reconstructed images at different SNR levels using eight-qubit encoding. 218
5.28 Proposed quantum communication pipeline for joint video compression and transmission. 223
5.29 Objective quality results for raw video processed through the proposed QFT pipeline without channel coding. 226
5.30 Objective quality results for raw video processed through the proposed QFT pipeline with polar channel coding. 228
5.31 Quality metrics for VVC-encoded input video (GOP8) transmitted through the proposed QFT pipeline without channel coding. 230
5.32 Quality metrics for VVC-encoded input video (GOP32) transmitted through the proposed QFT pipeline without channel coding. 232
5.33 Quality metrics for VVC-encoded input video (GOP8) processed by the QFT pipeline with polar channel coding. 233
5.34 Reconstructed video frames at SNR values from 38 dB down to -10 dB using the 8-qubit configuration ($F8$) at $256:1$ compression on raw input. 235
5.35 Performance comparison between the proposed two-qubit configuration and classical communication baselines. 236

5.36 Proposed framework for quantum Fourier transform-based image compression, transmission, and semantic-aware image reconstruction. 243
5.37 Multi-stage denoising diffusion probabilistic model (DDPM) architecture for quantum image reconstruction. 245
5.38 DDPM reconstruction performance on uncompressed images without channel coding. 252
5.39 DDPM reconstruction performance on uncompressed images with channel coding. 253
5.40 Sample reconstructed images from the uncompressed and uncoded COCO dataset at SNR = −4 dB, comparing QFT-based and DDPM-based reconstructions. 255
5.41 Performance of the proposed channel-aware adaptive reconstruction mechanism on the uncoded dataset. 256
5.42 Proposed end-to-end framework for video compression, transmission, reconstruction, and denoising. 261
5.43 Three-stage U-Net architecture for video denoising. 262
5.44 Performance evaluation of the U-Net-based video reconstruction framework for uncompressed and uncoded video inputs using eight-qubit encoding. 267
5.45 Performance evaluation of the U-Net-based video reconstruction framework for uncompressed and channel-coded video inputs using eight-qubit encoding. 269
5.46 Sample reconstructed video frames at SNR = −4 dB for uncompressed and uncoded inputs using eight-qubit encoding, comparing the original frame, QFT-reconstructed frame (V_{rec}), and the U-Net-enhanced frame (V_{final}). 270

6.1 Architecture of the proposed COUS-based multi-qubit quantum communication system for high-fidelity image transmission. 280
6.2 Performance comparison of the proposed COUS-based quantum transmission system (CS1–CS8), the Hadamard-based encoding framework (H1–H8), and the classical BPSK system (C) for JPEG uncoded images. 289

6.3 Performance comparison of the proposed COUS-based quantum transmission system (CS1–CS8), the Hadamard-based encoding framework (H1–H8), and the classical BPSK system (C) for HEIF uncoded images. 290
6.4 Performance comparison of the proposed COUS-based quantum transmission system (CS1–CS8), the Hadamard-based encoding framework (H1–H8), and the classical BPSK system (C) for JPEG images with rate-1/2 polar channel coding. 292
6.5 Performance comparison of the proposed COUS-based quantum transmission system (CS1–CS8), the Hadamard-based encoding framework (H1–H8), and the classical BPSK system (C) for HEIF images with rate-1/2 polar channel coding. 293
6.6 Block diagram illustrating the proposed COUS-driven multi-qubit framework optimised for quantum video delivery. 304
6.7 Analytical evaluation of video reconstruction fidelity across the classical (C), Hadamard (H1–H8), and COUS (CS1–CS8) setups utilising a GOP8 framework. 307
6.8 Analytical evaluation of video reconstruction fidelity across the classical (C), Hadamard (H1–H8), and COUS (CS1–CS8) setups utilising a GOP16 framework. 309
6.9 Analytical evaluation of video reconstruction fidelity across the classical (C), Hadamard (H1–H8), and COUS (CS1–CS8) setups utilising a GOP32 framework. 311
6.10 Subjective perceptual-quality scores comparing the classical communication baseline (C) with the proposed COUS-based multi-qubit configurations (CS1–CS8) under the GOP 8 transmission setting. 318
6.11 Representative reconstructed video frames produced by the Hadamard-based (H1) and COUS-based (CS1) transmission frameworks at an SNR of 6 dB. 319

7.1 Organisation of Chapter 7. 331
7.2 Block diagram of the proposed quantum-enabled MIMO image transmission framework. 334

7.3 Antenna configurations adopted in the simulation study: (a) a single-antenna baseline without diversity, (b) a transmit-diversity arrangement, and (c) a receive-diversity arrangement. 336
7.4 Average PSNR (left column) and SSIM (right column) achieved by the classical (C) and quantum (Q) pipelines for JPEG-coded images at QP = 25 (lossy) and QP = 100 (near-lossless), across (a), (b) the SISO baseline, (c), (d) the 2×1 MISO configuration, and (e), (f) the 1×2 SIMO configuration. 340
7.5 Reconstructed lossy JPEG images for the classical and quantum pipelines under each configuration: (a), (b) SISO at 10 dB channel SNR; (c), (d) 2×1 MISO at 7 dB channel SNR; (e), (f) 1×2 SIMO at 7 dB channel SNR. 341
7.6 Average PSNR (left column) and SSIM (right column) for classical (C) and quantum (Q) pipelines applied to HEIF-coded images at QP = 25 (lossy) and QP = 100 (near-lossless), under (a), (b) SISO, (c), (d) 2×1 MISO, and (e), (f) 1×2 SIMO. 342
7.7 BER as a function of channel SNR for JPEG-coded (left column) and HEIF-coded (right column) images at QP = 25 under the classical (C) and quantum (Q) pipelines, with (a), (b) SISO, (c), (d) 2×1 MISO, and (e), (f) 1×2 SIMO. 343
7.8 Average PSNR (left column) and SSIM (right column) for the classical (C) and quantum (Q) pipelines applied to JPEG-coded images at QP = 25 and QP = 100, under (a), (b) the 2×2 configuration and (c), (d) the 4×1 configuration. 345
7.9 Block diagram of the proposed quantum-enabled MIMO link for video transmission. 348
7.10 Average PSNR (left column), SSIM (centre column), and VMAF (right column) obtained with the classical (C) and quantum (Q) pipelines for GOP size 8 under three antenna configurations: (a–c) 1×1 SISO, (d–f) 2×1 MISO, and (g–i) 1×2 SIMO. 351

7.11 Average PSNR (left column), SSIM (centre column), and VMAF (right column) obtained with the classical (C) and quantum (Q) pipelines for GOP size 16 under three antenna configurations: (a–c) 1 × 1 SISO, (d–f) 2 × 1 MISO, and (g–i) 1 × 2 SIMO. 352
7.12 Average PSNR (left column), SSIM (centre column), and VMAF (right column) obtained with the classical (C) and quantum (Q) pipelines for GOP size 32 under three antenna configurations: (a–c) 1 × 1 SISO, (d–f) 2 × 1 MISO, and (g–i) 1 × 2 SIMO. 353
7.13 Representative reconstructed video frames for classical (top row) and quantum (bottom row) transmission under different antenna configurations: 1×1 SISO at 10.0 dB SNR, and 2×1 MISO and 1×2 SIMO at 7.5 dB SNR. 356
7.14 Block diagram of the proposed QOFDM pipeline for image transmission. 361
7.15 Behaviour of the proposed QOFDM pipeline without channel coding under urban Rayleigh fading for the different qubit widths considered: (a) BER, (b) PSNR, and (c) SSIM. 371
7.16 Behaviour of the proposed QOFDM pipeline with channel coding under urban Rayleigh fading for the different qubit widths considered: (a) BER, (b) PSNR, and (c) SSIM. 372
7.17 Behaviour of the proposed QOFDM pipeline without channel coding under indoor Rayleigh fading for the different qubit widths considered: (a) BER, (b) PSNR, and (c) SSIM. 373
7.18 Behaviour of the proposed QOFDM pipeline with channel coding under indoor Rayleigh fading for the different qubit widths considered: (a) BER, (b) PSNR, and (c) SSIM. 374
7.19 Block diagram of the proposed QOFDM pipeline for video transmission. 382
7.20 Behaviour of the proposed QOFDM pipeline at GOP8 under an indoor Rayleigh fading channel: (a) PSNR, (b) SSIM, and (c) VMAF. 385
7.21 Behaviour of the proposed QOFDM pipeline at GOP16 under an indoor Rayleigh fading channel: (a) PSNR, (b) SSIM, and (c) VMAF. 388

7.22 Behaviour of the proposed QOFDM pipeline at GOP32 under an indoor Rayleigh fading channel: (a) PSNR, (b) SSIM, and (c) VMAF. 389
7.23 Behaviour of the proposed QOFDM pipeline at GOP8 under an urban Rayleigh fading channel: (a) PSNR, (b) SSIM, and (c) VMAF. 391
7.24 Representative reconstructed video frames for GOP8 sequences under an urban Rayleigh fading channel at an SNR of 13 dB. 393
7.25 Block diagram of the proposed quantum MIMO-OFDM framework for high-fidelity image transmission. 398
7.26 Architecture of the proposed quantum MIMO-OFDM transmitter. . . . 401
7.27 Block diagram of the proposed quantum MIMO-OFDM receiver. 404
7.28 PSNR, SSIM, and UQI curves for JPEG image transmission using the proposed quantum MIMO-OFDM and the classical MIMO-OFDM benchmark, 1×1 (SISO). 407
7.29 PSNR, SSIM, and UQI curves for JPEG image transmission using the proposed quantum MIMO-OFDM and the classical MIMO-OFDM benchmark, 2×1 (MISO). 408
7.30 PSNR, SSIM, and UQI curves for JPEG image transmission using the proposed quantum MIMO-OFDM and the classical MIMO-OFDM benchmark, 1×2 (SIMO). 409
7.31 PSNR, SSIM, and UQI curves for HEIF image transmission using the proposed quantum MIMO-OFDM and the classical MIMO-OFDM benchmark, 1×1 (SISO). 411
7.32 PSNR, SSIM, and UQI curves for HEIF image transmission using the proposed quantum MIMO-OFDM and the classical MIMO-OFDM benchmark, 2×1 (MISO). 412
7.33 PSNR, SSIM, and UQI curves for HEIF image transmission using the proposed quantum MIMO-OFDM and the classical MIMO-OFDM benchmark, 1×2 (SIMO). 413
7.34 System architecture of the proposed Q-MDC framework for image transmission. 423

7.35 PER and BER comparison for the Q-MDC system before and after applying the proposed recovery mechanism. 430
7.36 PSNR, SSIM, and UQI comparison for JPEG, JPEG2000, and HEIF images transmitted using uncoded Q-MDC and single-stream configurations over different SNR conditions. 432
7.37 PSNR, SSIM, and UQI comparison for uncompressed images transmitted using uncoded Q-MDC and single-stream configurations under different SNR conditions. 432
7.38 PSNR, SSIM, and UQI comparison for JPEG images transmitted using channel-coded Q-MDC and single-stream configurations under different SNR conditions. 433
7.39 Comparison of reconstructed PSNR, SSIM, and UQI for JPEG and JPEG2000 images using Q-MDC, classical MDC, and channel-coded single-stream transmission under equal bandwidth constraints and varying SNR conditions. 435
7.40 BER comparison of alternative correlated-description generation approaches, namely CNOT, Pauli-X with CNOT, and interleaved CNOT, for D1 and D2 over different SNR levels. 437
7.41 Proposed end-to-end quantum communication system for semantic communication based image transmission. 443
7.42 Proposed semantic encoder. 445
7.43 Proposed semantic decoder. 446
7.44 Proposed CNN for machine-based perception. 448
7.45 Comparison of different communication schemes under varying channel SNR levels. Columns represent performance evaluation metrics (PSNR, SSIM, UQI), and rows represent comparisons: (Row 1) Q-JPEG vs. C-JPEG, (Row 2) C-SEMANTIC vs. C-JPEG, (Row 3) Q-SEMANTIC vs. C-SEMANTIC. 450
7.46 Ability of image classification using CNN model. 453

A.1 The proposed COUS encoding based three-qubit QEC scheme. 474

A.2 Performance of JPEG QP=25 compressed image transmission evaluated using (a) PSNR, (b) SSIM, and (c) UQI, under the proposed COUS encoding-based three-qubit QEC system (Q COUS), the conventional Hadamard encoding-based three-qubit QEC system (Q HADAMARD), and the classical polar-coded system (C POLAR). 475

A.3 Performance of JPEG QP=100 compressed image transmission evaluated using (a) PSNR, (b) SSIM, and (c) UQI, under the proposed COUS encoding-based three-qubit QEC system (Q COUS), the conventional Hadamard encoding-based three-qubit QEC system (Q HADAMARD), and the classical polar-coded system (C POLAR). 476

A.4 Performance of HEIF QP=25 compressed image transmission evaluated using (a) PSNR, (b) SSIM, and (c) UQI, under the proposed COUS encoding-based three-qubit QEC system (Q COUS), the conventional Hadamard encoding-based three-qubit QEC system (Q HADAMARD), and the classical polar-coded system (C POLAR). 477

A.5 Performance of HEIF QP=100 compressed image transmission evaluated using (a) PSNR, (b) SSIM, and (c) UQI, under the proposed COUS encoding-based three-qubit QEC system (Q COUS), the conventional Hadamard encoding-based three-qubit QEC system (Q HADAMARD), and the classical polar-coded system (C POLAR). 478

List of Tables

2.1 Truth table for the CNOT gate. 44
2.2 Evolution of Existing Quantum Multimedia Transmission Approaches. . 66

3.1 Comparison of classical and quantum encoding schemes. 75
3.2 Received states, error positions, and ancilla measurement outcomes for the three-qubit QEC code. 90
3.3 Syndrome measurement outcomes and corresponding correction actions. 90
3.4 Possible received states and corresponding eight-dimensional state vectors. 92
3.5 Rate–distortion performance of JPEG compression at different QP settings. 108
3.6 Maximum SNR gain (dB) for each quantum system compared to the classical system across different resolutions and frame rates (GOP = 8). 125

4.1 Rate–distortion performance of JPEG compression for different multi-qubit configurations. 148
4.2 Relative SNR advantage of adaptive variable-qubit quantum communication compared with the classical reference, across spatial resolutions and frame rates (GOP = 8). 160

5.1 Comparison of encoding complexity and error resilience (based on BER at an SNR of -8 dB) for JPEG uncoded images across time-domain and frequency-domain systems (Q1–Q8). 189
5.2 Maximum SNR gain compared to classical communication systems across different resolutions and frame rates for frequency (F1–F8) and time (T1–T8) domain quantum systems. 199

5.3 Maximum SNR gains (in dB) achieved by each qubit system compared to the 8-qubit configuration. 214
5.4 Experimental environment parameters. 225
5.5 Maximum SNR gain (dB) achieved by each qubit configuration relative to the 8-qubit baseline, across resolutions and frame rates. 234
5.6 Effective channel capacity for QFT-based compression at SNR = 10 dB and $B = 1$ Hz. 239
5.7 Estimated hardware resource requirements for different QFT register sizes. 240
5.8 Classification accuracy (%) vs. SNR under identical compression settings. 254

6.1 Statistical summary of performance metrics for JPEG-based uncoded transmission for CS1. 294
6.2 Maximum SNR gains of COUS (CS1–CS8) and Hadamard (H1–H8) encoding schemes over the classical communication (C) system for JPEG images. 296
6.3 Comparison of SNR gains (dB) under identical system conditions compared with classical baseline. 297
6.4 Complexity and runtime comparison between COUS and Hadamard encoding. 298
6.5 Comparison between COUS and Hadamard encoding schemes. 299
6.6 Simulation parameters adopted for evaluating the proposed COUS-based multi-qubit video-transmission framework. 305
6.7 Maximum channel SNR gains achieved by the Hadamard-based (H1–H8) and COUS-based (CS1–CS8) multi-qubit frameworks relative to the classical communication baseline across different video resolutions. . . . 314
6.8 Channel SNR gains (dB) together with the corresponding standard deviations across different video resolutions for representative transmission configurations. 315
6.9 Maximum channel SNR gains (dB) achieved by the proposed COUS-based framework relative to the classical communication baseline for different motion categories and spatial resolutions at 30 fps. 316

6.10 Contrast of SNR improvements (dB) achieved at a 1280 × 720 resolution (30 fps) against the classical system under standardised testing variables. 320

7.1 Comparison of the highest channel SNR reduction achieved by the proposed quantum transmission framework relative to the equivalent classical system for different antenna diversity configurations under varying spatial resolutions and frame rates. 355

7.2 Observed channel SNR advantages of the proposed QOFDM framework compared with conventional BPSK modulation-based OFDM under different fading environments and coding conditions for varying qubit dimensions. 375

7.3 Estimated quantum computational resources required for QFT processing under different qubit dimensions in the proposed image transmission framework. 378

7.4 Simulation setup used for the classical OFDM baseline and the proposed QOFDM scheme. 384

7.5 Highest channel SNR improvements achieved by the proposed QOFDM framework relative to classical BPSK modulation-OFDM under urban Rayleigh fading conditions for different qubit dimensions, video resolutions, and motion categories (dB). 394

7.6 Highest channel SNR improvements achieved by the proposed multi-qubit quantum MIMO-OFDM framework relative to the classical BPSK-based MIMO-OFDM benchmark for different image formats (dB). 417

7.7 QFT gate count and circuit depth as a function of qubit width. 418

7.8 State-vector size, memory, FLOP count, and estimated CPU runtime for QFT simulation. 418

List of Abbreviations

AI	Artificial Intelligence
AR	Augmented Reality
ARQ	Automatic Repeat Request
AWGN	Additive White Gaussian Noise
BER	Bit Error Rate
BPSK	Binary Phase Shift Keying
CNN	Convolutional Neural Network
CNOT	Controlled-NOT
COCO	Common Objects in Context
COUS	Complex-Valued Orthogonal Unitary Superposition
CP	Cyclic Prefix
CPTP	Completely Positive Trace-Preserving
CSI	Channel State Information
DDPM	Denoising Diffusion Probabilistic Model
FEC	Forward Error Correction
FFT	Fast Fourier Transform
FID	Frechet Inception Distance
FLOP	Floating-Point Operation
FRQI	Flexible Representation of Quantum Images
GOP	Group of Pictures
GQIR	General Quantum Image Representation
HD	High Definition
HEIF	High Efficiency Image File Format

HEVC	High Efficiency Video Coding
ICI	Inter-Carrier Interference
IFFT	Inverse Fast Fourier Transform
IQFT	Inverse Quantum Fourier Transform
ISI	Inter-Symbol Interference
IoT	Internet of Things
JPEG	Joint Photographic Experts Group
LDPC	Low-Density Parity-Check
LPIPS	Learned Perceptual Image Patch Similarity
MDC	Multiple Description Coding
MIMO	Multiple-Input Multiple-Output
MISO	Multiple-Input Single-Output
ML	Maximum Likelihood
MMSE	Minimum Mean Square Error
MOS	Mean Opinion Score
MRC	Maximal-Ratio Combining
MRI	Magnetic Resonance Imaging
NEQR	Novel Enhanced Quantum Representation
NISQ	Noisy Intermediate-Scale Quantum
NN	Nearest Neighbour
OFDM	Orthogonal Frequency-Division Multiplexing
PAPR	Peak-to-Average Power Ratio
PER	Packet Error Rate
PNG	Portable Network Graphics
PSNR	Peak Signal-to-Noise Ratio
QAM	Quadrature Amplitude Modulation
QDCT	Quantum Discrete Cosine Transform
QEC	Quantum Error Correction
QFT	Quantum Fourier Transform
QHWT	Quantum Haar Wavelet Transform
QKD	Quantum Key Distribution

QOFDM	Quantum Orthogonal Frequency-Division Multiplexing
QP	Quantisation Parameter
QPSK	Quadrature Phase Shift Keying
QWT	Quantum Wavelet Transform
SC	Successive Cancellation
SCL	Successive Cancellation List
SI	Spatial Information
SIMO	Single-Input Multiple-Output
SISO	Single-Input Single-Output
SNR	Signal-to-Noise Ratio
SSIM	Structural Similarity Index Measure
STBC	Space–Time Block Coding
TI	Temporal Information
UHD	Ultra-High Definition
UQI	Universal Quality Index
V2X	Vehicle-to-Everything
VMAF	Video Multimethod Assessment Fusion
VR	Virtual Reality
VVC	Versatile Video Coding
ZF	Zero-Forcing

Chapter 1

Introduction

1.1 Background and Motivation

The rapid evolution of digital technologies has fundamentally transformed the generation, processing, and transmission of visual information across modern communication networks. Over the past two decades, advancements in imaging sensors, display technologies, and video capture systems have enabled the widespread adoption of high-resolution images and high-definition (HD) video in numerous applications. Visual content is no longer limited to traditional broadcasting and entertainment; it now plays a vital role in healthcare diagnostics through medical imaging, remote sensing through satellite imagery, autonomous driving through real-time video analysis, and virtual collaboration through video conferencing systems.

Alongside these developments, the volume of visual data transmitted over communication networks has increased dramatically. High-resolution images and HD, Full HD, and ultra-high-definition (UHD) video formats require substantially higher bandwidth, lower latency, and improved transmission reliability compared to conventional multimedia applications. Consequently, modern communication systems are increasingly challenged by the growing demand for efficient and reliable visual data transmission. Recent industry reports indicate that video traffic accounts for more than 80% of all global IP traffic [1] and around 70% of global mobile network traffic [2], with this share projected to continue increasing as visual applications become more widespread.

This rapid increase in visual data traffic is further accelerated by the widespread

use of internet-connected devices, including smartphones, tablets, smart televisions, drones, and Internet of Things (IoT) devices equipped with imaging capabilities. These devices continuously generate, transmit, and consume large volumes of image and video data, placing significant pressure on existing communication infrastructures. Many conventional communication systems were originally designed for comparatively lower data rates and less demanding multimedia services, making it increasingly difficult to support modern high-fidelity visual communication requirements efficiently and reliably.

1.1.1 Limitations of Classical Communication Systems for Image and Video Transmission

Despite significant advances in classical communication and compression technologies over several decades, a number of fundamental challenges continue to affect the reliable and efficient transmission of high-quality images and videos over practical communication channels. These challenges arise at multiple stages of the transmission pipeline, including source encoding, channel coding, modulation, transmission, and reconstruction.

At the physical layer, communication channels are inherently impaired by noise, interference, multipath fading, and signal attenuation. In wireless communication systems, these impairments are particularly severe due to the unpredictable nature of the propagation environment. Additive white Gaussian noise (AWGN), Rayleigh fading [3], and co-channel interference can introduce bit errors into the transmitted signal, which in turn cause visible degradation in the reconstructed image or video at the receiver [4]. Even in wired communication systems, thermal noise and crosstalk can affect transmission quality, particularly over long distances or at high data rates.

To combat these channel impairments, classical communication systems employ a range of error protection mechanisms, including channel coding [5], forward error correction (FEC) [6], automatic repeat request (ARQ) protocols [7], [8], and hybrid ARQ schemes. While these techniques improve transmission reliability, they come at the cost of increased redundancy, reduced effective throughput, and additional processing latency. In particular, retransmission-based schemes such as ARQ introduce variable delays that are incompatible with the strict latency requirements of real-time image and video applications, including live broadcasting, video conferencing, telemedicine,

and remote vehicle control.

Adaptive transmission techniques [9], [10] offer partial solutions by dynamically adjusting modulation schemes, coding rates, and transmission power in response to changing channel conditions. However, the effectiveness of these approaches is limited by the speed at which channel state information can be estimated and fed back to the transmitter, and by the inherent trade-off between adaptability and system complexity. In rapidly varying channel environments, such as those encountered in high-mobility scenarios, the channel conditions may change faster than the system can adapt, leading to mismatched transmission parameters and degraded performance.

1.1.2 Challenges in Image and Video Compression

Modern image and video compression standards have achieved remarkable reductions in data size, enabling the practical transmission of high-resolution visual content over bandwidth-constrained channels. The Joint Photographic Experts Group (JPEG) standard [11] remains widely used for still image compression, while more recent formats such as the High Efficiency Image File Format (HEIF) [12] offer improved compression efficiency through advanced prediction and transform coding techniques. For video, the High Efficiency Video Coding (HEVC/H.265) standard [13] and the more recent Versatile Video Coding (VVC/H.266) standard [14] have progressively improved coding efficiency by exploiting spatial, temporal, and statistical redundancies within video sequences.

However, the relationship between compression efficiency and reconstruction quality is fundamentally governed by a rate-distortion trade-off. Higher compression ratios reduce the amount of data that must be transmitted, but they also discard finer details and introduce compression artefacts such as blocking, ringing, blurring, and colour distortion. These artefacts are perceptually noticeable and can significantly reduce the subjective quality of the reconstructed content, particularly in regions with fine textures, sharp edges, or complex motion.

Furthermore, the degradation introduced by compression is often exacerbated by channel errors during transmission. When compressed image or video bitstreams are transmitted over noisy communication channels, even a small number of bit errors

can produce severe distortion in the reconstructed output due to the high sensitivity of compressed data to transmission errors [4]. In compressed image transmission, corrupted bits may affect entropy-coded segments, transform coefficients, or prediction information, leading to visible artefacts and partial image degradation. In video transmission, the impact can be even more severe because modern video codecs employ predictive coding structures, such as inter-frame prediction, where each frame depends on previously decoded frames. Consequently, errors introduced in one frame may propagate to subsequent frames, causing cascading degradation that is disproportionate to the number of transmission errors.

1.1.3 Emerging Application Requirements

The limitations described above are further amplified by the requirements of emerging image and video applications. Immersive virtual reality (VR) [15] and augmented reality (AR) [16] systems require the delivery of high-resolution stereoscopic or omnidirectional video with extremely low latency, typically below 20 milliseconds [17], to avoid motion sickness and maintain user immersion. Real-time high-fidelity streaming applications, such as cloud gaming and live event broadcasting in 4K or 8K resolution, demand sustained high throughput with minimal quality fluctuation. Medical imaging applications, including remote radiology and telesurgery, require lossless or near-lossless transmission of diagnostic images where any quality degradation could affect clinical decision-making.

These applications require communication systems that can simultaneously deliver robustness against channel impairments, scalability across different data resolutions and network conditions, efficient use of available bandwidth, and high perceptual reconstruction quality at the receiver. Meeting all of these requirements simultaneously within the constraints of classical communication frameworks represents a significant and ongoing challenge.

Collectively, these limitations suggest that incremental improvements within conventional classical communication paradigms alone may be insufficient to meet the demands of next-generation image and video transmission systems. Therefore, there is a growing need for fundamentally new communication frameworks that can overcome the inherent limitations of classical approaches while supporting reliable, scalable, and high-quality

image and video transmission under dynamic and noisy communication environments.

1.1.4 Quantum Communication as an Alternative Paradigm

Quantum communication [18] offers a fundamentally different approach to information representation and transmission, grounded in the principles of quantum mechanics [19]. The key distinction between quantum and classical communication lies in the nature of the information carrier. In classical communication, information is represented using bits that take definite binary values, either 0 or 1. Each bit exists in one of these two states at any given time, and all classical encoding, processing, and transmission operations are performed on these binary representations.

In contrast, quantum communication represents information using quantum bits, or qubits, which can exist in superposition states [20], [21]. A qubit in superposition is described as a weighted combination of the basis states $|0\rangle$ and $|1\rangle$, expressed mathematically as $|\psi\rangle = \alpha|0\rangle + \beta|1\rangle$, where α and β are complex-valued probability amplitudes satisfying $|\alpha|^2 + |\beta|^2 = 1$ [22]. This means that a single qubit can represent a richer state space than a single classical bit, as both the amplitudes and the relative phase between the two basis states contribute to the quantum state. When multiple qubits are considered together, a system of k qubits can represent 2^k basis states simultaneously through superposition, enabling a fundamentally richer encoding space compared to k classical bits.

This property of superposition gives rise to several characteristics that are directly relevant to image and video transmission. First, the encoding density offered by multi-qubit systems means that image and video data can potentially be mapped into more compact quantum representations than equivalent classical binary encodings, improving bandwidth utilisation. Second, quantum error correction (QEC) codes, such as the three-qubit bit-flip code and the three-qubit phase-flip code, exploit redundancy across entangled qubits to detect and correct channel-induced errors without requiring classical retransmission, thereby reducing latency overhead. Third, the unitary nature of quantum operations ensures that encoding and decoding transformations are reversible and norm-preserving, which provides inherent structural robustness during signal processing. Fourth, quantum entanglement enables non-local correlations between qubits that can

be exploited for distributed encoding and error detection across spatially separated components of the communication system.

It is important to note that these advantages are realised under specific conditions and system designs; they are not universal properties of any quantum system. The extent to which each benefit translates into practical performance gains depends on factors such as qubit fidelity, decoherence rates, channel noise models, and the encoding strategy employed. A central aim of this thesis is to investigate these factors systematically in the context of image and video transmission.

1.1.5 From Quantum Key Distribution to Quantum Image and Video Transmission

The most mature application of quantum communication to date is quantum key distribution (QKD) [23], where quantum mechanical principles, particularly the no-cloning theorem [24] and the disturbance caused by measurement, enable theoretically secure key exchange [25], [26]. The no-cloning theorem guarantees that an unknown quantum state cannot be perfectly copied, which means that any attempt by an eavesdropper to intercept and duplicate quantum-encoded information will necessarily introduce detectable disturbances. This property has been successfully exploited in QKD protocols to achieve information-theoretic security, and practical QKD systems have been demonstrated in both fibre-optic and free-space channels [27].

While QKD focuses on transmitting a small number of random bits with security guarantees, the underlying physical and engineering infrastructure (qubit state preparation, quantum channel transmission, and quantum measurement) is equally applicable to other communication tasks. The critical difference for image and video transmission is the nature of the payload: rather than random key bits, the system must convey structured, high-volume visual data where reconstruction fidelity, not secrecy, is the primary objective. This shift from security-oriented to fidelity-oriented quantum communication introduces several distinct challenges, including the need for efficient encoding techniques for pixel-level image and video data, quantum-domain processing methods for perceptual quality enhancement, effective decoding algorithms for accurate data reconstruction, and seamless integration with classical communication architectures

to ensure practical scalability and real-world deployment.

Building on the foundations established by QKD research, increasing interest has been shown in the application of quantum communication principles to image and video transmission. Early research in this area has mainly focused on quantum image representation models, such as the Flexible Representation of Quantum Images (FRQI) [28] and the Novel Enhanced Quantum Representation (NEQR) [29], through which pixel information is encoded in quantum states. Although important theoretical foundations for quantum visual data representation have been established by these approaches, they have mainly been designed for quantum computing and image processing applications rather than practical communication systems.

Subsequently, various research directions have been explored, including quantum image processing [30], quantum image compression [31], quantum watermarking [32], and quantum encryption techniques [33]. Although the potential of quantum technologies for visual data applications has been demonstrated in these studies, most existing work remains focused on isolated functionalities and specific research objectives. Consequently, comparatively limited attention has been given to the development of complete end-to-end communication frameworks in which source encoding, quantum-domain encoding, noisy channel transmission, error mitigation, decoding, and high-fidelity reconstruction are jointly considered within a unified communication architecture.

Furthermore, fully integrated quantum communication systems specifically designed for end-to-end image and video transmission have not yet been comprehensively established in the existing literature. Most existing studies focus on theoretical image representations, standalone quantum processing techniques, or isolated communication components rather than unified transmission systems capable of supporting reliable, efficient, and high-fidelity multimedia communication under realistic channel conditions. Consequently, a significant gap remains between the theoretical potential of quantum communication and its practical application to multimedia transmission. Although this gap is gradually narrowing due to continuing advances in quantum hardware, including improvements in qubit counts, gate fidelities, coherence times, quantum error correction, and quantum networking technologies, these developments have not yet enabled practical end-to-end multimedia communication systems. Addressing the remaining challenges

requires a unified multimedia-oriented quantum communication paradigm that integrates quantum information representation, transmission, error resilience, compression, and reconstruction within a single end-to-end communication framework. This thesis is motivated by this evolving research landscape and seeks to establish such a paradigm for reliable image and video transmission over noisy communication channels, providing a foundation for future quantum-enabled multimedia communication systems as quantum technologies continue to mature.

1.1.6 Research Motivation and Scope

While continual advances in classical communication technologies will undoubtedly improve future multimedia transmission systems, they remain constrained by the fundamental principles of classical information representation. Improvements in source coding, channel coding, modulation, and network protocols primarily optimise existing transmission pipelines rather than fundamentally changing how multimedia information is represented and communicated. As image and video applications continue to evolve towards immersive, intelligent, and data-intensive services, these incremental improvements alone may become insufficient to satisfy future communication requirements.

Furthermore, future communication systems are expected to support not only higher data rates but also intelligent processing, semantic understanding, adaptive reliability, distributed computing, and seamless integration with artificial intelligence. Meeting these demands requires communication frameworks that move beyond the conventional bit-centric paradigm towards richer information representations and more flexible processing mechanisms.

Quantum communication provides a fundamentally different information processing model based on the principles of quantum mechanics. The high-dimensional state spaces enabled by quantum superposition, together with quantum transformations and quantum error correction, provide new opportunities to rethink how multimedia information is represented, protected, compressed, transmitted, and reconstructed. Although large-scale quantum communication systems are still emerging, investigating multimedia-oriented quantum communication architectures is essential to understand their long-term potential for future intelligent communication networks.

Motivated by these challenges and opportunities, this thesis develops a new multimedia-oriented quantum communication paradigm for reliable and high-fidelity image and video transmission over noisy communication channels. Rather than proposing a collection of independent transmission techniques, the research establishes a unified end-to-end paradigm in which each contribution addresses a fundamental capability required for practical quantum multimedia communication.

The proposed paradigm is systematically developed by integrating a sequence of interconnected contributions. It first establishes an end-to-end quantum communication framework based on quantum superposition and quantum error correction for reliable multimedia transmission over noisy channels. Building upon this foundation, scalable multi-qubit encoding strategies are introduced to improve transmission robustness and bandwidth efficiency through higher-dimensional quantum representations. The paradigm is subsequently extended through quantum-domain transformation techniques that enable simultaneous multimedia transmission and compression, followed by the development of novel quantum encoding mechanisms that further enhance robustness while reducing computational complexity. Finally, the proposed paradigm is integrated with existing communication architectures, demonstrating its applicability to practical next-generation multimedia communication systems.

Accordingly, the principal contribution of this thesis is the establishment of a unified multimedia-oriented quantum communication paradigm that integrates quantum information processing, adaptive error resilience, compression, reconstruction, and advanced communication architectures within a single end-to-end framework. By addressing the challenges of transmission reliability, bandwidth efficiency, scalability, and semantic awareness, the proposed paradigm provides a foundation for future quantum-enabled multimedia communication systems capable of supporting reliable, efficient, and high-fidelity image and video transmission.

Furthermore, this research focuses on the theoretical development and simulation-based evaluation of multimedia-oriented quantum communication architectures, which is the standard practice for the investigation of emerging communication systems at an early stage. Although current Noisy Intermediate-Scale Quantum (NISQ) devices are constrained by limited qubit counts, gate errors, and decoherence, the proposed frame-

works are intended to investigate the long-term potential of quantum communication for multimedia transmission. The practical implementation and optimisation of these techniques on NISQ hardware are beyond the scope of this thesis and remain important directions for future research.

1.2 Problem Statement

Despite major advancements in image and video compression and communication technologies, existing systems remain limited in their ability to provide reliable, scalable, low-latency, low-complexity, and high-fidelity image and video transmission under noisy and dynamically varying channel environments. The major research challenges are as follows:

- **Transmission Reliability:** Classical image and video communication systems remain vulnerable to channel impairments, resulting in transmission errors and reconstruction quality degradation, particularly in high-noise environments where error correction alone is insufficient.
- **Communication Latency:** Retransmission-based error recovery and iterative decoding mechanisms introduce processing delays that limit real-time image and video transmission performance.
- **Limited Adaptability:** Most transmission frameworks rely on fixed or semi-static configurations that cannot respond dynamically to time-varying channel conditions.
- **Binary Representation Constraints:** Classical binary encoding limits the representational flexibility available for image and video data, restricting the design space for efficient transmission strategies.
- **Compression–Reconstruction Trade-off:** Aggressive compression improves bandwidth efficiency but degrades perceptual quality, and this degradation is amplified by channel noise during transmission.
- **Computational Complexity:** Many advanced image and video transmission techniques rely on computationally intensive processing, iterative optimisation, and

complex error correction mechanisms, making real-time and scalable deployment challenging, particularly for high-resolution visual data applications.

To address these limitations, quantum communication introduces new possibilities through quantum state representation, superposition-based encoding, quantum frequency-domain processing, and hybrid quantum–classical architectures. However, existing research remains fragmented, focusing primarily on isolated theoretical models or security-oriented systems. Comprehensive frameworks that jointly address reliability, adaptability, scalability, reconstruction quality, and computational efficiency for image and video transmission remain largely unexplored.

The central research question addressed in this thesis is therefore:

How can quantum communication techniques be effectively designed and integrated with classical communication pipelines to improve reliability, reduce complexity, enhance adaptability, and preserve reconstruction quality in image and video transmission over noisy and bandwidth-constrained channels?

1.3 Research Aim and Objectives

1.3.1 Research Aim

The aim of this research is to develop a quantum communication-based multimedia transmission framework that leverages quantum mechanical principles to enhance transmission reliability, communication efficiency, and reconstruction quality for high-fidelity image and video transmission under noisy and dynamically varying communication environments.

1.3.2 Objectives

1. To develop a quantum communication-based framework for reliable and high-fidelity image and video transmission over noisy communication channels.

2. To investigate the integration of quantum and classical error correction techniques for improving transmission robustness and reconstruction quality under adverse channel conditions.

3. To develop efficient and scalable strategies for image and video transmission with improved communication performance and low computational complexity.

4. To analyse the potential advantages of different quantum encoding techniques in terms of transmission efficiency, robustness, scalability, and complexity.

5. To investigate quantum-based signal processing approaches for enhancing image and video reconstruction quality under noisy transmission environments.

6. To evaluate adaptive encoding and various quantum state representations for improving transmission fidelity, efficiency, and overall system performance.

7. To assess the integration of quantum communication techniques with existing image and video transmission frameworks for scalable and efficient communication system design.

1.4 Research Contributions

This thesis provides multiple interrelated contributions in order to address the problem formulated in Section 1.2 and to achieve the overall aim of the research. These contributions are directly aligned with the objectives defined in Section 1.3 and collectively address the challenges of reliability, latency, adaptability, and perceptual quality in multimedia transmission over noisy and bandwidth-constrained channels. In this context, the contributions delivered in this thesis are:

1. Design of a Single-Qubit Encoding Quantum Communication Framework for Image and Video Transmission

2. Design and Analysis of Multi-Qubit Quantum Encoding Techniques for Image and Video Transmission

3. Design and Analysis of Quantum Frequency-Domain Techniques for Quantum Communication

4. Introduction of Novel Quantum Encoding Techniques for Noise Resilience and Computational Efficiency

5. Design of an Integrated Quantum Communication Framework with Existing Image and Video Transmission Systems

1.4.1 Design of a Single-Qubit Encoding Quantum Communication Framework for Image and Video Transmission

In support of **Objectives 1 and 2**, a novel quantum communication framework is developed for image and video transmission over noisy and bandwidth-constrained communication channels. The proposed framework establishes a complete end-to-end image and video transmission pipeline incorporating classical image and video representation, channel coding, quantum encoding, noisy channel transmission, quantum decoding, channel decoding, and reconstruction at the receiver side. The framework further investigates the role of QEC in improving transmission reliability and reconstruction performance under noisy channel conditions. Unlike conventional classical communication systems, the proposed framework incorporates quantum state representation to improve robustness and transmission efficiency for multimedia delivery.

Summary of Achievements

- An end-to-end quantum communication framework is developed.
- The structured encoding–transmission-reconstruction pipeline is established.
- The impact of QEC on image and video transmission is systematically analysed.
- Improved robustness under noisy channels is demonstrated.

1.4.2 Design and Analysis of Multi-Qubit Quantum Encoding Techniques for Image and Video Transmission

In support of **Objectives 3, 4, and 6**, a multi-qubit quantum encoding strategy is introduced for efficient and scalable representation of image and video data. The proposed approach maps classical image and video bitstreams into multi-qubit quantum states using quantum superposition principles, thereby increasing encoding efficiency and representational flexibility. Furthermore, adaptive qubit allocation mechanisms are developed to dynamically adjust encoding structures according to system complexity and channel conditions, enabling improved scalability and transmission adaptability.

Summary of Achievements

- The multi-qubit encoding scheme for image and video representation is developed.
- Efficient mapping between classical data and quantum states is achieved.
- Adaptive encoding flexibility is introduced.
- The scalability of the system across different qubit configurations is analysed.

1.4.3 Design and Analysis of Quantum Frequency-Domain Techniques for Quantum Communication

In support of **Objectives 4, 5, and 6**, quantum frequency-domain transformation techniques are investigated to improve reconstruction quality in image and video transmission systems. The proposed approach transforms image and video data into a quantum frequency-domain representation while selectively preserving significant spectral components. This enables improved robustness against channel noise and enhances reconstruction accuracy at the receiver. The study further demonstrates the effectiveness of quantum frequency-domain encoding for improving perceptual quality in image and video transmission systems.

Summary of Achievements

- Quantum frequency-domain transformation techniques are developed.
- A novel quantum-based compression mechanism is introduced.
- Improved reconstruction quality through spectral-domain representation is achieved.
- Enhanced preservation of significant signal components is demonstrated.

1.4.4 Introduction of Novel Quantum Encoding Techniques for Noise Resilience and Computational Efficiency

In support of **Objectives 3, 4, 5, and 6**, novel quantum encoding techniques are proposed to improve noise resilience while reducing computational complexity in image and video transmission systems. The proposed methods address limitations of existing classical and quantum approaches by enhancing transmission robustness under noisy

channel conditions while maintaining computational feasibility and reconstruction quality. The overall design focuses on achieving efficient encoding performance without sacrificing transmission reliability or perceptual reconstruction quality.

Summary of Achievements

- Novel low-complexity quantum encoding techniques are introduced.
- Improved resilience to noise is achieved.
- Reduced computational complexity is achieved.

1.4.5 Design of an Integrated Quantum Communication Framework with Existing Image and Video Transmission Systems

In support of **Objectives 3, 4, 5, and 7**, an integrated quantum–classical communication architecture is developed for scalable multimedia transmission. The proposed framework combines quantum communication principles with advanced classical communication architectures and analyses robustness across multiple communication layers, including the physical layer through MIMO, OFDM, and MIMO-OFDM techniques, the source layer through MDC, and the content layer through semantic communication. This integration improves scalability, adaptability, transmission reliability, and overall multimedia communication performance under dynamic channel conditions while maintaining computational feasibility.

Summary of Achievements

- Hybrid quantum–classical communication architecture is developed.
- Integration with advanced communication frameworks is achieved.
- Improved scalability and transmission performance are demonstrated.

1.5 Research Dissemination and Scholarly Contributions

The following scholarly contributions are associated with the research presented in this thesis. The candidate was the primary researcher and lead author on all listed publications, responsible for the development of the research methodology, system

design, simulation implementation, experimental analysis, result interpretation, and manuscript preparation.

1.5.1 Journal Publications

Chapter 3: Design of a Single-Qubit Encoding Quantum Communication Framework for Image and Video Transmission

1. U. Jayasinghe, P. Samarathunga, Y. Ganearachchi, T. Fernando, and A. Fernando, "Quantum communications for image transmission over error-prone channels," *Electronics Letters*, vol. 60, no. 15, e13300, 2024, doi: 10.1049/ell2.13300.

2. U. Jayasinghe, P. Samarathunga, N. Pollwaththage, Y. Ganearachchi, T. Fernando, and A. Fernando, "Quantum communication for video transmission over error-prone channels," *IEEE Transactions on Consumer Electronics*, vol. 71, no. 1, pp. 1148–1155, 2025, doi: 10.1109/TCE.2025.3552930.

3. U. Jayasinghe, P. Samarathunga, T. Fernando, Y. Ganearachchi, and A. Fernando, "Image transmission over quantum communication systems with three-qubit error correction," *Electronics Letters*, vol. 61, no. 1, e70205, 2025, doi: 10.1049/ell2.70205.

4. U. Jayasinghe, P. Samarathunga, Y. Ganearachchi, T. Fernando, and A. Fernando, "Adaptive coding-based quantum communication system for image transmission," *Electronics Letters*, vol. 61, no. 1, e70299, 2025, doi: 10.1049/ell2.70299.

Chapter 4: Design and Analysis of Multi-Qubit Quantum Encoding Techniques for Image and Video Transmission

5. U. Jayasinghe, N. Kushantha, T. Fernando, and A. Fernando, "A robust multi-qubit quantum communication system for image transmission over error-prone channels," *IEEE Transactions on Consumer Electronics*, vol. 71, no. 3, pp. 7551–7558, 2025, doi: 10.1109/TCE.2025.3594368.

6. U. Jayasinghe, T. Fernando, and A. Fernando, "A multi-qubit phase shift keying paradigm for quantum image transmission over error-prone channels," *Multimedia*, vol. 1, no. 2, art. no. 5, 2025, doi: 10.3390/multimedia1020005.

Chapter 5: Design and Analysis of Quantum Frequency-Domain Techniques for Quantum Communication

7. U. Jayasinghe, T. Fernando, and A. Fernando, "High-fidelity image transmission in quantum communication with frequency domain multi-qubit techniques," *Algorithms*, vol. 18, no. 8, p. 501, 2025, doi: 10.3390/a18080501.

8. U. Jayasinghe and A. Fernando, "Rethinking video transmission: A quantum Fourier transform-based approach for error-prone channels," *Electronics*, vol. 15, no. 6, art. no. 1323, 2026, doi: 10.3390/electronics15061323.

9. U. Jayasinghe, T. Fernando, and A. Fernando, "Quantum Fourier transform-based adaptive image compression and transmission system," *Electronics Letters*, vol. 61, no. 1, e70430, 2025, doi: 10.1049/ell2.70430.

10. U. Jayasinghe, T. Fernando, and A. Fernando, "A comparative study of quantum Haar wavelet and quantum Fourier transforms for quantum image transmission," *Information*, vol. 16, no. 11, p. 962, 2025, doi: 10.3390/info16110962.

11. U. Jayasinghe, T. Fernando, and A. Fernando, "A quantum frequency-domain framework for image transmission with three-qubit error correction," *Algorithms*, vol. 18, no. 9, p. 574, 2025, doi: 10.3390/a18090574.

Chapter 6: Introduction of Novel Quantum Encoding Techniques for Noise Resilience and Computational Efficiency

12. U. Jayasinghe and A. Fernando, "Complex-valued unitary superposition-driven multi-qubit encoding for quantum video transmission," *Electronics*, vol. 15, no. 9, art. no. 1906, 2025, doi: 10.3390/electronics15091906.

13. U. Jayasinghe and A. Fernando, "Complex-valued orthogonal unitary superposition encoding for robust three-qubit quantum-error-correction-based image transmission," *Algorithms*, vol. 19, no. 4, p. 304, 2026, doi: 10.3390/a19040304.

14. U. Jayasinghe and A. Fernando, "Circular polarization-based quantum encoding for image transmission over error-prone channels," *Signals*, vol. 7, no. 2, p. 37, 2026, doi: 10.3390/signals7020037.

Chapter 7: Design of an Integrated Quantum Communication Framework with Existing Image and Video Transmission Systems

15. U. Jayasinghe, T. Fernando, Y. Ganearachchi, P. Samarathunga, and A. Fernando, "Quantum communication based image transmission with transmit and receive diversity in MIMO communication systems," *IEEE Transactions on Consumer Electronics*, vol. 71, no. 2, pp. 2500–2507, 2025, doi: 10.1109/TCE.2025.3559634.

16. U. Jayasinghe and A. Fernando, "A quantum OFDM framework for high-fidelity image transmission," *IEEE Transactions on Consumer Electronics*, vol. 71, no. 4, pp. 9628–9636, 2025, doi: 10.1109/TCE.2025.3619569.

17. U. Jayasinghe, P. Samarathunga, T. Fernando, and A. Fernando, "Transmit and receive diversity in MIMO quantum communication for high-fidelity video transmission," *Algorithms*, vol. 18, no. 7, p. 436, 2025, doi: 10.3390/a18070436.

18. U. Jayasinghe, T. Fernando, and A. Fernando, "A quantum MIMO-OFDM framework with transmit and receive diversity for high-fidelity image transmission," *Telecom*, vol. 6, no. 4, art. no. 96, 2025, doi: 10.3390/telecom6040096.

19. U. Jayasinghe and A. Fernando, "A quantum OFDM framework for next-generation video transmission over noisy channels," *Electronics*, vol. 15, no. 2, art. no. 284, 2026, doi: 10.3390/electronics15020284.

20. U. Jayasinghe, P. Cuenca, and A. Fernando, "Exploiting quantum-domain correlations for robust image transmission: a novel quantum multiple description coding framework," *IEEE Open Journal of Vehicular Technology*, 2026, pp. 1–16, doi: 10.1109/OJVT.2026.3711773.

21. U. Jayasinghe, P. Samarathunga, N. Pollwaththage, T. Fernando, and A. Fernando, "Quantum communication for semantic communication based image transmission," *IEEE Transactions on Vehicular Technology*, early access, 2026, doi: 10.1109/TVT.2026.3663843.

1.5.2 Conference Publications

Chapter 3

22. U. Jayasinghe, T. Fernando, and A. Fernando, "Optimizing quantum image transmission through an adaptive quantum error correction framework," in *Proc. IEEE ICCE*, 2026, doi: 10.1109/ICCE67443.2026.11449609.

23. U. Jayasinghe, N. Pollwaththage, Y. Ganearachchi, P. Samarathunga, T. Fernando, and A. Fernando, "Quantum communication based image transmission over error-prone channels with three-qubit stabilizer code," in *Proc. IEEE ICCE*, 2025, doi: 10.1109/ICCE63647.2025.10930032.

Chapter 5

24. U. Jayasinghe, T. N. Atulugama, and A. Fernando, "A quantum frequency-domain multi-qubit encoding framework for robust video transmission," in *Proc. IEEE International Conference on Consumer Electronics (ICCE)*, Dubai, United Arab Emirates, 2026, pp. 1–6, doi: 10.1109/ICCE67443.2026.11449606.

25. U. Jayasinghe and A. Fernando, "A channel-adaptive quantum transform-domain variable-qubit encoding for quantum image transmission," in *Proc. IEEE ICC*, 2026 (in press).

Chapter 6

26. U. Jayasinghe, T. N. Atulugama, and A. Fernando, "Complex-valued orthogonal superposition encoding for quantum image transmission," in *Proc. IEEE International Conference on Consumer Electronics (ICCE)*, Dubai, United Arab Emirates, 2026, pp. 1–6, doi: 10.1109/ICCE67443.2026.11449899.

Chapter 7

27. U. Jayasinghe, T. Fernando, P. Samarathunga, and A. Fernando, "A semantic-aware multiple description coding framework for robust quantum image transmission," in *Proc. IEEE International Conference on Consumer Electronics (ICCE)*, 2026 (in press).

1.5.3 Under Review Manuscripts

Chapter 4

28. U. Jayasinghe, T. Fernando, and A. Fernando, "Circular polarization-based adaptive variable qubit framework for quantum image transmission," *IEEE Transactions on Consumer Electronics* (under review).

Chapter 5

29. U. Jayasinghe and A. Fernando, "Quantum Fourier transform for image transmission over error-prone channels," *IEEE Transactions on Consumer Electronics* (under review).

30. U. Jayasinghe, V. Gowrisetty, and A. Fernando, "Semantic-aware quantum frequency-domain image transmission with channel-aware denoising," *IEEE Transactions on Communications* (under review).

31. U. Jayasinghe, V. Gowrisetty, and A. Fernando, "Semantic-aware quantum frequency-domain video transmission with post-channel noise reduction," *IEEE Transactions on Vehicular Technology* (under review).

Chapter 6

32. U. Jayasinghe, T. Fernando, and A. Fernando, "A novel complex-valued orthogonal unitary superposition encoding-based multi-qubit system for quantum image transmission," *IEEE Transactions on Communications* (under review).

33. U. Jayasinghe, P. Cuenca, and A. Fernando, "Quantum chirp transform for image compression and transmission with multi-stage UNet-based image reconstruction," *IEEE Open Journal of the Communications Society* (under review).

34. U. Jayasinghe, P. Cuenca, and A. Fernando, "A quantum chirp transform-based multi-qubit encoding framework for quantum-inspired image transmission over error-prone channels," *IEEE Open Journal of the Communications Society* (under review).

1.5.4 Collaborative Research Contributions

1. P. Samarathunga, N. Pollwaththage, T. Fernando, U. Jayasinghe, N. Ihalagamage, Y. Ganearachchi, and A. Fernando, "Semantic and technical noise modeling in semantic image communication over wireless channels," *IEEE Access*, vol. 13, pp. 150872–150900, 2025.

2. P. Samarathunga, U. Jayasinghe, Y. Ganearachchi, T. Fernando, N. Senanayake, and A. Fernando, "Semantic communication based lossless distributed video coding for error prone channels," in *Proc. IEEE International Conference on Consumer Electronics (ICCE)*, 2025, pp. 1–4, doi: 10.1109/ICCE63647.2025.10929820.

3. T. Fernando, N. Pollwaththage, U. Jayasinghe, P. Samarathunga, J. El Gemayel, and A. Fernando, "Beyond disparity: A semantic communication framework for stereoscopic video coding," in Proc. *IEEE 19th International Conference on Industrial and Information Systems (ICIIS)*, Peradeniya, Sri Lanka, 2026, pp. 85-90, doi: 10.1109/ICIIS69028.2026.11450610.

4. T. Fernando, N. Pollwaththage, P. Samarathunga, U. Jayasinghe, J. El Gemayel, and A. Fernando, "A hybrid semantic-syntactic video codec with CNN-transformer encoding and VVC residual coding," in *IEEE 19th International Conference on Industrial and Information Systems (ICIIS)*, Peradeniya, Sri Lanka, 2026, pp. 79-84, doi: 10.1109/ICIIS69028.2026.11450731.

1.5.5 International Conference Presentations

- **IEEE International Conference on Consumer Electronics (ICCE), Dubai, 2026**

  Presented the following research papers:

  - Complex-Valued Orthogonal Superposition Encoding for Quantum Image Transmission
  - A Quantum Frequency-Domain Multi-Qubit Encoding Framework for Robust Video Transmission

– Optimising Quantum Image Transmission through an Adaptive Quantum Error Correction Framework

1.6 Thesis Outline

The remainder of this thesis is organised as follows.

- **Chapter 2: Literature Review**

  This chapter provides a comprehensive overview of classical image and video transmission systems and emerging quantum communication principles. It reviews the classical communication pipeline, examines existing quantum communication approaches and their limitations, and identifies the research gaps that motivate quantum-based methods for image and video transmission. The chapter establishes the theoretical foundations upon which subsequent chapters build.

- **Chapter 3: Design of a Single-Qubit Encoding Quantum Communication Framework for Image and Video Transmission**

  This chapter presents the design and implementation of the end-to-end quantum communication framework for image and video transmission. It details the system architecture, encoding and decoding procedures, and transmission modelling over noisy quantum channels, together with a systematic analysis of QEC within the pipeline. The simulation results evaluate the performance of the framework under varying channel conditions in terms of reconstruction fidelity, noise resilience, and robustness. This chapter addresses Objectives 1 and 2.

- **Chapter 4: Design and Analysis of Multi-Qubit Quantum Encoding Techniques for Image and Video Transmission**

  This chapter formulates a multi-qubit encoding strategy for efficient representation and transmission of image and video data. It details the mapping of classical bitstreams into quantum states, introduces adaptive qubit allocation mechanisms, and evaluates encoding efficiency, transmission accuracy, and computational overhead across varying data resolutions. This chapter addresses Objectives 3, 4, and 6.

- **Chapter 5: Design and Analysis of Quantum Frequency-Domain Techniques for Quantum Communication**

  This chapter develops quantum frequency-domain transformation techniques, based on QFT, to enhance image and video reconstruction quality. It analyses signal representation in the quantum frequency domain, examines the relationship between transformation parameters and reconstruction accuracy, and demonstrates the effectiveness of spectral-domain processing across image and video transmission scenarios. This chapter addresses Objectives 4, 5, and 6.

- **Chapter 6: Introduction of Novel Quantum Encoding Techniques for Noise Resilience and Computational Efficiency**

  This chapter introduces novel quantum encoding techniques, including complex-valued orthogonal unitary superposition (COUS) encoding, designed to simultaneously improve noise resilience and reduce computational complexity. It presents the theoretical formulation, validates the effectiveness through experimental results under varying channel noise conditions, and assesses the practical viability within the wider framework. This chapter addresses Objectives 3, 4, 5, and 6.

- **Chapter 7: Design of an Integrated Quantum Communication Framework with Existing Image and Video Transmission Systems**

  This chapter presents the integrated quantum–classical communication architecture that combines quantum processing with classical frameworks. It describes the hybrid encoding and decoding procedures and evaluates the proposed architecture across the physical layer, the source layer, and the content layer. The architecture is assessed under dynamic channel conditions in terms of scalability, adaptability, transmission efficiency, and multimedia quality, demonstrating its effectiveness for practical image and video transmission. This chapter addresses Objectives 3, 4, 5, and 7.

- **Chapter 8: Conclusions and Future Work**

  This chapter summarises key contributions, reflects on the extent to which the stated objectives have been achieved, discusses the theoretical and practical

implications of the findings, and proposes directions for future research including extensions to real-world quantum hardware, adaptive hybrid architectures, and broader image and video application domains.

Chapter 2

Literature Review

This chapter presents a comprehensive review of existing literature related to classical multimedia communication systems and emerging quantum communication technologies. It begins with an overview of conventional multimedia transmission frameworks, including source coding, channel coding, and modulation techniques. Furthermore, advanced communication techniques such as orthogonal frequency division multiplexing (OFDM), multiple-input multiple-output (MIMO) systems, MIMO-OFDM communication frameworks, multiple description coding (MDC), and semantic communication techniques are discussed, as they form the foundation for the quantum communication frameworks proposed in Chapter 7. Particular emphasis is placed on their performance under noisy and error-prone communication environments. The limitations of existing classical approaches in terms of reliability, latency, adaptability, bandwidth efficiency, and reconstruction quality are also discussed.

The chapter subsequently reviews the fundamental principles and recent advancements in quantum communication, including quantum information representation, quantum encoding techniques, quantum signal processing, and quantum communication architectures. Existing research on quantum-based image and video transmission is critically analysed to evaluate current capabilities, practical limitations, and unresolved challenges. Based on the reviewed literature, key research gaps are identified, particularly in relation to scalable multimedia-oriented quantum communication frameworks, adaptive transmission mechanisms, reconstruction-oriented processing, and hybrid quantum–classical communication architectures. Finally, the chapter positions the

proposed research within the broader context of existing studies and establishes the theoretical and technical foundation for the subsequent chapters of this thesis.

2.1 System Model of Classical Communication

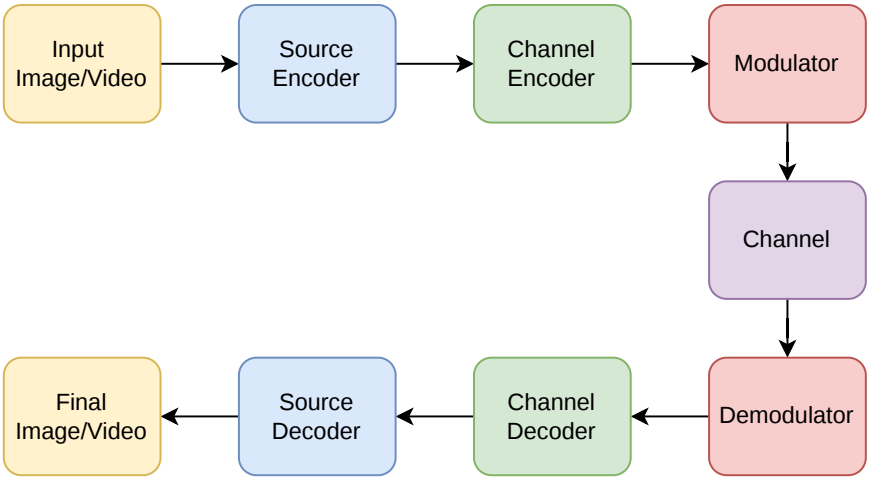


Figure 2.1: The end-to-end classical communication system.

The classical communication system is designed to transmit information from a source to a destination reliably over a communication channel, as shown in Figure 2.1. In the context of multimedia transmission, this process involves several sequential stages, each performing a specific function to ensure efficient and accurate delivery of image or video data. The system begins with the input multimedia source, such as an image or video sequence. This data is first processed by the source encoder, which compresses the information by removing redundant and perceptually less significant components. The primary objective of source encoding is to reduce the data rate while maintaining acceptable visual quality. The compressed bitstream is then passed to the channel encoder, where controlled redundancy is introduced to enable error detection and correction. This step improves the robustness of the transmission against channel impairments such as noise and interference. Following channel encoding, the signal undergoes modulation, where the digital data is mapped onto a suitable waveform for transmission over the physical channel. The communication channel represents the medium through which the signal propagates and may introduce various distortions, including additive noise,

fading, and interference. At the receiver, the reverse operations are performed. The received signal is first demodulated to recover the transmitted symbols, followed by channel decoding to correct any errors introduced during transmission. Finally, the source decoder reconstructs the original image or video from the decoded bitstream. This end-to-end system model highlights the fundamental trade-off between compression efficiency and transmission reliability. While higher compression reduces bandwidth requirements, it also increases vulnerability to transmission errors, making the design of robust communication systems essential for maintaining multimedia quality. The following subsections explain in detail each block of the classical communication system, which is important for building the quantum communication pipeline.

2.1.1 Source Encoder

The source encoder is the first processing block in a classical communication system and is responsible for efficiently representing multimedia data before transmission. In image and video communication systems, the primary objective of source encoding is to reduce the amount of data required to represent the original signal while preserving perceptual quality [34]. This process is achieved through two main operations: redundancy reduction and irrelevancy reduction. Redundancy reduction eliminates statistical redundancy present in the data, while irrelevancy reduction removes information that is less perceptually significant to the human visual system. In practical multimedia systems, source encoding is typically performed using compression standards such as Joint Photographic Experts Group (JPEG) [11], High Efficiency Image File Format (HEIF) [12] for images, and H.264/H.265 High Efficiency Video Coding (HEVC) [13] and Versatile Video Coding (VVC) [14] for video sequences. These standards apply a combination of transform coding, quantisation, and entropy coding. Transform coding converts spatial-domain data into a frequency-domain representation, where most of the signal energy is concentrated in a few coefficients. Quantisation then reduces precision to achieve compression, and entropy coding further compresses the resulting symbols based on their statistical occurrence. The output of the source encoder is a compressed bitstream that significantly reduces bandwidth requirements. However, this compression introduces a trade-off between compression efficiency and reconstruction quality, since

higher compression ratios typically lead to greater information loss. This compressed representation is then forwarded to the channel encoder for reliability enhancement prior to transmission.

2.1.2 Channel Encoder

The channel encoder is responsible for improving the reliability of the transmitted bitstream by introducing controlled redundancy [35]. This redundancy enables the detection and correction of errors that may occur due to channel impairments such as noise, fading, and interference. Different channel coding techniques employ different encoding structures and decoding algorithms depending on the communication requirements. Common channel coding techniques include convolutional codes [36], turbo codes [37], and block codes such as low-density parity-check (LDPC) codes [38] and polar codes [39]. Among common channel coding techniques, LDPC and polar codes are widely used in modern communication systems due to their near-capacity error-correction performance. In particular, polar codes have been adopted in fifth-generation (5G) communication standards because of their capacity-achieving properties and efficient decoding performance. Overall, channel encoding significantly improves transmission reliability by enabling error detection and correction, thereby ensuring that the received data closely approximates the original transmitted information even in the presence of channel impairments.

Polar Codes

Polar codes are a class of error-correcting codes introduced by Erdal Arıkan in [39]. They are widely used in modern communication systems, including 5G standards, due to their strong error-correction capability and capacity-achieving properties for symmetric binary-input memoryless channels. The fundamental principle of polar coding is known as *channel polarisation*, in which a set of identical communication channels is transformed into synthesised channels with different reliability levels. During this process, some channels become highly reliable for data transmission, while others become unreliable. Information bits are transmitted through the reliable channels, whereas the unreliable channels are assigned predetermined values called frozen bits.

At the receiver, decoding is typically performed using Successive Cancellation (SC) decoding or improved variants such as Successive Cancellation List (SCL) decoding. These decoding techniques estimate the transmitted information bits by utilising channel reliability information and previously decoded bits. In this work, polar codes are employed as the channel coding scheme to improve robustness against channel noise and transmission errors, thereby enabling reliable recovery of the transmitted image and video bitstreams.

2.1.3 Modulation Techniques

Modulation is the process of converting digital information into waveforms suitable for transmission through a communication channel [40]. It acts as the interface between digital baseband data and the physical transmission medium. The primary objective of modulation is to transmit information efficiently while maintaining reliability in the presence of noise, interference, and channel impairments.

In digital communication systems, binary information is grouped into symbols and mapped onto specific signal states. Different modulation schemes determine how the carrier signal properties such as phase, amplitude, or frequency are varied to represent data. Common digital modulation techniques include binary phase shift keying (BPSK) [41], quadrature phase shift keying (QPSK) [42], and quadrature amplitude modulation (QAM) [43].

BPSK is one of the simplest and most robust modulation schemes, where each symbol represents one bit using two distinct phase states. Due to its high noise tolerance, BPSK is widely used in low signal-to-noise ratio (SNR) communication environments. QPSK improves spectral efficiency by allowing each symbol to represent two bits through four different phase states. This enables higher data rates while maintaining reasonable robustness against noise and interference. Higher-order modulation techniques such as 16-QAM and 64-QAM further increase spectral efficiency by combining both amplitude and phase variations in the transmitted signal. These schemes can transmit multiple bits per symbol, significantly improving data throughput. However, as the modulation order increases, the constellation points become more closely spaced, making the system more sensitive to noise, fading, and synchronisation errors. Consequently, higher-order

modulation schemes require higher SNRs for reliable communication. The selection of an appropriate modulation scheme involves a trade-off between transmission reliability and spectral efficiency. Lower-order modulation schemes provide improved robustness under challenging channel conditions, whereas higher-order modulation schemes achieve greater data rates at the expense of reduced noise immunity.

While modulation techniques define how information is mapped onto carrier signals, modern wireless communication systems require additional strategies to combat the challenges of wireless channels, such as frequency-selective fading and limited spectral resources. To address these challenges, multicarrier transmission schemes and multi-antenna architectures have been developed.

2.2 Classical OFDM System

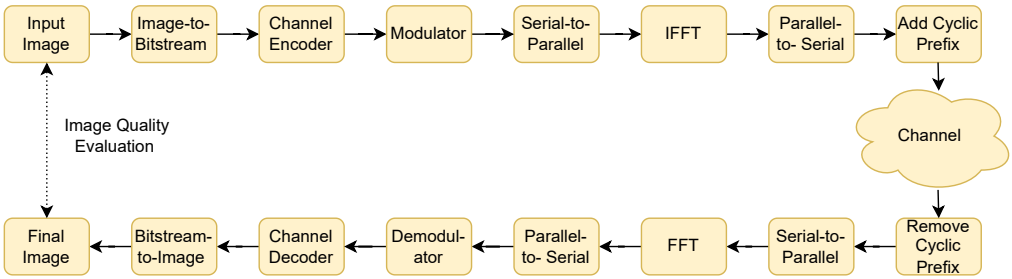


Figure 2.2: The end-to-end classical OFDM communication system.

OFDM is a multicarrier transmission technique widely used in modern wireless communication systems due to its high spectral efficiency and robustness against frequency-selective fading [44], [45]. In OFDM, the available transmission bandwidth is divided into multiple orthogonal subcarriers, allowing parallel transmission of data over narrowband subchannels. This significantly reduces the effects of inter-symbol interference (ISI) caused by multipath propagation and simplifies equalisation at the receiver.

In a typical OFDM system, as shown in Figure 2.2, the input bitstream is channel encoded and digitally modulated using schemes such as BPSK, QPSK, or QAM. The modulated symbols are grouped into parallel streams corresponding to individual sub-carriers. OFDM modulation is then performed using the inverse fast Fourier transform

(IFFT), which converts frequency-domain symbols into a composite time-domain OFDM signal as expressed in (2.1).

$$x[n] = \frac{1}{\sqrt{N}} \sum_{k=0}^{N-1} X[k] e^{j2\pi kn/N}, \quad n = 0, 1, ..., N-1 \tag{2.1}$$

where $x[n]$ represents the time-domain OFDM signal sample at time index n, $X[k]$ denotes the modulated symbol transmitted on the kth subcarrier, N represents the total number of subcarriers, and $e^{j2\pi kn/N}$ denotes the orthogonal complex exponential basis function.

The subcarrier spacing is determined according to (2.2).

$$\Delta f = \frac{B}{N} \tag{2.2}$$

where B represents the total transmission bandwidth, N denotes the number of subcarriers, and Δf represents the frequency spacing between adjacent subcarriers. Proper selection of the subcarrier spacing ensures orthogonality among subcarriers and minimises inter-carrier interference (ICI).

To reduce ISI caused by multipath propagation, a cyclic prefix (CP) is inserted before transmission. The CP extends the OFDM symbol duration as shown in (2.3).

$$T_{\text{symbol}} = N + L_{\text{CP}} \tag{2.3}$$

where T_{symbol} represents the total OFDM symbol duration, N denotes the useful OFDM symbol length, and L_{CP} represents the CP length.

At the receiver, the cyclic prefix is removed and fast Fourier transform (FFT) processing is performed to recover the transmitted frequency-domain symbols as expressed in (2.4).

$$X[k] = \frac{1}{\sqrt{N}} \sum_{n=0}^{N-1} x[n] e^{-j2\pi kn/N}, \quad k = 0, 1, ..., N-1 \tag{2.4}$$

where $X[k]$ represents the recovered symbol corresponding to the kth subcarrier, $x[n]$ denotes the received time-domain OFDM signal, and $e^{-j2\pi kn/N}$ represents the orthogonal basis function used during FFT demodulation.

By converting a frequency-selective fading channel into multiple orthogonal flat-fading subchannels, OFDM significantly improves transmission robustness and spectral efficiency. Due to these advantages, OFDM has become a fundamental transmission technique in modern broadband wireless communication and multimedia transmission systems.

2.3 Classical MIMO System

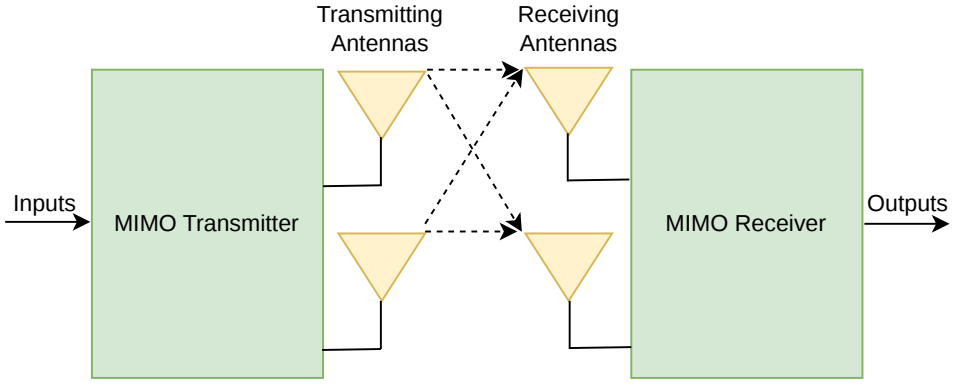


Figure 2.3: The end-to-end classical MIMO communication system.

Multiple-input multiple-output (MIMO) [46], [47] is a wireless communication technique that employs multiple transmitting and receiving antennas to improve communication reliability, spectral efficiency, and system capacity, as illustrated in Figure 2.3. Unlike conventional single-antenna systems, MIMO exploits the spatial dimension of the wireless channel in addition to time and frequency dimensions, enabling significant performance improvements without requiring additional bandwidth or transmission power.

One of the key advantages of MIMO systems is spatial diversity. Spatial diversity refers to the use of multiple antennas to provide independently faded replicas of the transmitted signal. In wireless communication environments, transmitted signals often experience fading due to multipath propagation. Since different antenna paths experience independent fading conditions, the probability that all signal paths simultaneously undergo deep fading is significantly reduced. This improves transmission robustness, enhances signal quality, and reduces communication errors under noisy and fading

channel conditions.

MIMO systems can provide both transmit diversity and receive diversity. In transmit diversity, multiple transmitting antennas are used to transmit encoded versions of the same signal, improving reliability at the receiver. In receive diversity, multiple receiving antennas are employed to capture independently faded versions of the transmitted signal, which are then combined to improve detection performance. These diversity techniques significantly improve communication reliability in practical wireless communication systems. In addition to diversity gain, MIMO systems can also support spatial multiplexing, where multiple independent data streams are transmitted simultaneously through different antennas. This increases data throughput and improves spectral efficiency in modern wireless communication systems. Overall, MIMO systems significantly improve transmission reliability, spectral efficiency, and communication capacity by exploiting spatial diversity and spatial multiplexing, making them a fundamental component of modern wireless multimedia communication systems.

2.4 Classical MIMO-OFDM System

MIMO-OFDM is a communication framework that integrates MIMO and OFDM technologies to improve transmission reliability, spectral efficiency, and communication capacity in wireless communication systems [48], [49]. By combining the spatial diversity and multiplexing capabilities of MIMO with the multicarrier transmission characteristics of OFDM, MIMO-OFDM systems provide robust communication performance under multipath fading environments. In MIMO-OFDM systems, OFDM is employed to divide the available bandwidth into multiple orthogonal subcarriers, while MIMO utilises multiple transmit and receive antennas to improve communication reliability and throughput. This integration enables efficient high-speed multimedia transmission while reducing the effects of frequency-selective fading and ISI.

In practical wireless communication systems, MIMO-OFDM significantly improves spectral efficiency, transmission robustness, and communication capacity compared to conventional single-antenna OFDM systems. Due to these advantages, MIMO-OFDM has become a core transmission framework in modern broadband wireless communication standards, including long-term evolution (LTE), Wi-Fi, and 5G communication systems.

Although MIMO-OFDM provides strong transmission-layer robustness, it does not address vulnerabilities at the source-coding level, where the loss of compressed bitstream segments can cause severe reconstruction degradation. Source-level error-resilience techniques are therefore required to complement transmission-layer methods. Multiple description coding (MDC), discussed next, addresses this requirement by introducing controlled redundancy at the source-coding stage.

2.5 Multiple Description Coding (MDC)

MDC [50], [51] is a source coding technique designed to improve robustness and reliability in multimedia transmission over unreliable or error-prone communication channels. Unlike conventional source coding methods that generate a single compressed bitstream, MDC produces multiple independently decodable bitstreams, referred to as descriptions. Each description contains partial information about the original multimedia content and can independently reconstruct the signal with acceptable quality. When multiple descriptions are successfully received, the reconstruction quality is significantly improved.

The primary objective of MDC is to reduce the impact of packet loss, transmission errors, and channel failures in multimedia communication systems. Since each description is transmitted independently, the loss of one description does not completely prevent multimedia reconstruction. This makes MDC highly suitable for image and video transmission over wireless, packet-switched, and unreliable communication networks.

In a typical MDC framework, the original multimedia signal is partitioned or transformed into multiple correlated descriptions using techniques such as spatial splitting, transform-domain decomposition, subband coding, or redundant encoding. These descriptions are transmitted through separate communication paths or independently over the same channel to improve transmission robustness. At the receiver, the reconstruction quality depends on the number of correctly received descriptions. If all descriptions are successfully received, high-fidelity reconstruction can be achieved. However, even partial reception allows acceptable multimedia reconstruction with reduced quality degradation.

MDC and other conventional error-resilience techniques operate at the bit level, focusing on accurate reconstruction of the transmitted bitstream. A complementary paradigm shifts the goal of communication from exact bit recovery to the delivery of

task-relevant meaning, significantly reducing transmission overhead. This emerging approach, known as semantic communication, is reviewed in the following section.

2.6 Semantic Communication Systems

Semantic communication [52], [53] is an emerging communication paradigm that focuses on transmitting the meaning or semantic content of information rather than ensuring exact bit-level reconstruction of transmitted data. Unlike conventional communication systems, which primarily aim to accurately recover every transmitted bit, semantic communication seeks to preserve the importance of underlying information while reducing communication redundancy and transmission overhead.

The fundamental concept of semantic communication originates from semantic information theory [54], where the objective is to transmit task-relevant or meaningful information efficiently under constrained communication resources. In multimedia communication systems, semantic communication commonly employs artificial intelligence (AI) and deep learning techniques to extract high-level semantic features from images, videos, speech, or textual data prior to transmission.

In a typical semantic communication framework, the input multimedia content is first processed using feature extraction or latent representation learning models to generate compact semantic representations. These semantic features are then transmitted through the communication channel instead of conventional raw bitstreams. At the receiver side, reconstruction or inference models utilise the received semantic information to recover the multimedia content or accomplish a specific downstream task.

Semantic communication systems have demonstrated significant potential for improving bandwidth efficiency, reducing transmission redundancy, and enabling task-oriented communication in multimedia applications. Recent studies have investigated semantic-aware image transmission, semantic video streaming, intelligent edge communication, and deep learning-based joint source-channel coding frameworks.

The preceding sections have introduced the building blocks of classical multimedia communication systems, including source coding, channel coding, modulation, OFDM, MIMO, MIMO-OFDM, MDC, and semantic communication. Building on this foundation, the next section critically reviews the prior research that has applied these techniques

to image and video transmission, identifying both the achievements and the limitations of existing classical approaches.

2.7 Prior Works on Classical Communication Systems for Multimedia Transmission

Classical communication systems have been extensively studied for reliable image and video transmission over wireless and wired communication channels. Over the past several decades, significant research efforts have focused on improving transmission reliability, spectral efficiency, bandwidth utilisation, and reconstruction quality for multimedia communication applications [55], [56], [57]. Conventional multimedia transmission systems commonly integrate source coding, channel coding, and modulation techniques to improve overall communication performance [58]. Early multimedia communication systems primarily relied on single-carrier transmission techniques combined with conventional modulation and channel coding schemes. Although these approaches provided reliable communication under moderate channel conditions, their performance significantly degraded in multipath fading environments due to ISI, limited spectral efficiency, and poor robustness against channel impairments [59].

To address these limitations, OFDM was introduced as an effective multicarrier communication technique for high-speed multimedia transmission [44], [45]. OFDM divides the available transmission bandwidth into multiple orthogonal subcarriers, allowing parallel transmission of multimedia data streams while reducing the effects of frequency-selective fading and ISI. Due to its high spectral efficiency and robustness against multipath propagation, OFDM has been widely adopted in broadband wireless communication systems, including Wi-Fi, LTE, and multimedia streaming applications [60], [61], [62], [63]. Several studies have investigated OFDM-based multimedia transmission systems under noisy and fading communication environments [64], [65]. These studies demonstrated that OFDM significantly improves transmission robustness and bandwidth efficiency compared to conventional single-carrier systems. However, OFDM systems remain sensitive to synchronisation errors, high peak-to-average power ratio (PAPR), ICI, and channel estimation inaccuracies, which can degrade multimedia

reconstruction quality under adverse channel conditions [66].

In parallel with OFDM development, MIMO communication systems emerged as an important technology for improving wireless communication capacity and reliability [46], [47], [67]. MIMO systems employ multiple transmitting and receiving antennas to exploit spatial diversity and spatial multiplexing gains. Spatial diversity improves robustness against fading by transmitting independently faded replicas of the signal through multiple antenna paths, while spatial multiplexing increases transmission throughput by enabling simultaneous transmission of multiple independent data streams. Numerous studies have demonstrated that MIMO systems significantly improve spectral efficiency, transmission reliability, and channel capacity compared to conventional single-antenna communication systems [68], [69], [70]. Techniques such as space-time block coding (STBC) [71], Alamouti coding [72], zero-forcing (ZF) detection [73], minimum mean square error (MMSE) detection [74], and maximum likelihood (ML) detection have been extensively investigated to improve MIMO system performance under fading communication environments. Despite these advantages, standalone MIMO systems remain limited by channel estimation complexity, inter-antenna interference, computational overhead, and reduced performance under highly dynamic wireless environments. Furthermore, implementing large-scale MIMO systems introduces additional hardware complexity and increased power consumption.

To further improve communication performance, MIMO and OFDM technologies were later integrated to form MIMO-OFDM communication systems. MIMO-OFDM combines the spectral efficiency and multipath robustness of OFDM with the spatial diversity and multiplexing gains of MIMO [75]. As a result, MIMO-OFDM has become a fundamental transmission framework in modern broadband wireless communication systems and multimedia transmission applications [48], [49], [76], [77]. A large body of research has investigated MIMO-OFDM systems for high-speed image and video transmission under noisy wireless communication channels. These studies demonstrated improved throughput, robustness, and spectral efficiency compared to conventional OFDM and single-antenna communication systems. In particular, MIMO-OFDM systems have been widely adopted in 4G, 5G, wireless local area networks (WLANs), and real-time multimedia streaming systems [78], [79], [80]. Despite these advantages,

MIMO-OFDM systems continue to face several challenges, including channel estimation complexity, synchronisation sensitivity, ICI, computational overhead, and increased hardware complexity in large-scale antenna configurations. Furthermore, multimedia transmission over MIMO-OFDM systems remains vulnerable to channel impairments under highly noisy communication environments.

Several studies have also explored adaptive transmission techniques in classical multimedia communication systems. Adaptive modulation, adaptive coding, power allocation, and adaptive resource management approaches have been proposed to dynamically improve communication performance under varying channel conditions. These adaptive techniques aim to improve reliability and bandwidth utilisation while reducing transmission errors and communication latency [81], [82], [83], [84].

In addition, MDC has been widely investigated for robust image and video transmission in wireless multimedia communication systems due to its resilience against packet loss and transmission errors [50], [51], [85], [86]. Several studies have integrated MDC with adaptive transmission frameworks to improve multimedia reliability under fading and noisy channel environments. Despite its advantages, MDC systems also introduce several limitations, including increased redundancy, higher bandwidth requirements, synchronisation complexity, and additional encoding and decoding overhead. Furthermore, designing optimal description generation and reconstruction mechanisms for dynamically varying communication environments remains a significant research challenge.

Recent research has also explored semantic communication systems as an alternative approach for improving communication efficiency in multimedia transmission [87], [88]. Unlike conventional communication frameworks that focus primarily on accurate bit-level transmission, semantic communication aims to transmit the underlying meaning or semantic information of multimedia content. By leveraging artificial intelligence and deep learning techniques, semantic communication systems attempt to reduce transmission redundancy while preserving perceptually important information. Several studies have investigated semantic-aware image and video transmission frameworks for improving bandwidth efficiency and reducing communication overhead under constrained network environments [89], [90], [91], [92], [93], [94], [95]. These approaches

commonly employ feature extraction, latent representation learning, and task-oriented communication strategies to improve transmission efficiency. Semantic communication has demonstrated promising performance in applications such as intelligent multimedia streaming, edge communication, and low-bandwidth visual communication systems. However, despite recent progress, semantic communication systems still face several important challenges, including semantic representation accuracy, robustness against channel impairments, generalisation capability across varying multimedia content, computational complexity of deep learning models, and difficulties in preserving high-fidelity reconstruction quality under noisy communication environments. Furthermore, most existing semantic communication frameworks remain heavily dependent on classical communication architectures and data-driven learning models.

Despite substantial progress in classical multimedia communication systems, several important limitations remain unresolved. Existing systems continue to experience challenges related to transmission reliability, communication latency, adaptability under dynamically varying channel conditions, computational complexity, and reconstruction quality under noisy communication environments. Furthermore, compressed multimedia streams remain highly sensitive to channel impairments, where even small transmission errors can significantly degrade perceptual reconstruction quality. Although adaptive communication techniques partially improve system performance, they remain fundamentally constrained by classical binary-based information representation and associated communication overhead. Consequently, further improvements within purely classical communication paradigms may be insufficient to fully satisfy the increasing demands of next-generation multimedia transmission systems.

These limitations motivate the exploration of fundamentally different communication paradigms. Quantum communication, grounded in the principles of quantum mechanics, offers new mechanisms for information representation, transmission, and reconstruction that may overcome several of these classical constraints. The following sections introduce the relevant quantum-mechanical principles before reviewing their application to communication systems.

2.8 Quantum Mechanics

Quantum mechanics [19] has become one of the fundamental theories driving the advancement of modern computing and communication technologies. Since its inception, quantum mechanics has undergone rigorous testing and validation, establishing itself as the cornerstone of many modern technologies [96], [97]. Applications such as semiconductors, lasers, and magnetic resonance imaging (MRI) exemplify how quantum principles are harnessed in practical ways [98]. In recent years, quantum mechanics has laid the groundwork for emerging fields such as quantum computing and quantum communication [99], which promise to revolutionise information processing and security by utilising unique quantum phenomena.

Unlike classical systems that rely on binary bits for information processing, quantum systems utilise quantum bits (qubits), which can exist in multiple states simultaneously through the principle of superposition [21]. This capability enables more efficient information representation, parallel processing, and advanced computational operations compared to conventional computing approaches. In addition, quantum mechanics introduces unique properties such as entanglement [22] and the no-cloning theorem [100] that enable new computational and communication models beyond the capabilities of classical systems.

The rapid growth of data-intensive applications and modern communication networks has increased the demand for advanced processing and transmission techniques. In this context, quantum-based computational models and algorithm design approaches have emerged as promising solutions for addressing the limitations of conventional communication systems. The following subsections discuss the fundamental quantum mechanical principles that contribute directly to the development of modern quantum computing and communication technologies.

2.8.1 Qubits

Qubits, or quantum bits, are the fundamental units of information in quantum information processing. Unlike classical bits, which can exist in one of two distinct states (0 or 1), qubits can exist in a state of superposition, enabling them to represent both states simultaneously. This unique characteristic allows quantum systems to perform complex

calculations and process information in ways that classical systems cannot [101].

In quantum information processing, qubits are represented mathematically using vector notation and matrices. The standard basis states for a single qubit are denoted as $|0\rangle$ and $|1\rangle$. These states can be expressed in matrix form as in (2.5) and (2.6).

The basis state $|0\rangle$ is represented as in (2.5).

$$|0\rangle = \begin{pmatrix} 1 \\ 0 \end{pmatrix} \tag{2.5}$$

The basis state $|1\rangle$ is represented as in (2.6).

$$|1\rangle = \begin{pmatrix} 0 \\ 1 \end{pmatrix} \tag{2.6}$$

These two basis states serve as the building blocks for more complex quantum states.

2.8.2 Quantum Superposition

Quantum superposition [20], [102] is one of the most fundamental concepts in quantum mechanics. It refers to the ability of quantum systems, such as qubits, to exist in multiple possible states simultaneously, rather than being restricted to a single, well-defined state as in classical systems. This principle is especially important in quantum communication, where qubits can exist not just in the classical binary states of 0 or 1, but in a superposition of both. The ability to manipulate quantum states in superposition enables efficient and secure methods of transmitting information, supporting technologies such as quantum cryptography and quantum teleportation.

In quantum mechanics, superposition allows a quantum system to be in a combination of different states at the same time. For a qubit, this means that it can be in a state represented as in (2.7).

$$|\psi\rangle = \alpha|0\rangle + \beta|1\rangle \tag{2.7}$$

where $|\psi\rangle$ represents the quantum state of a single qubit, $|0\rangle$ and $|1\rangle$ are the computational basis states, and α and β are complex probability amplitudes. The amplitudes must

satisfy the normalisation condition as in (2.8).

$$|\alpha|^2 + |\beta|^2 = 1 \tag{2.8}$$

where $|\alpha|^2$ and $|\beta|^2$ represent the probabilities of measuring the qubit in the $|0\rangle$ and $|1\rangle$ states, respectively.

The principle of superposition enables parallel processing in quantum computing, where a quantum computer can evaluate multiple solutions simultaneously. This parallelism forms the basis of quantum algorithms such as Grover's search algorithm [103] and Shor's factoring algorithm [104], which achieve significant speedup over their classical counterparts. In quantum communication, superposition can be utilised to encode information in a way that is less susceptible to noise and interference, leading to more reliable data transmission over quantum channels. Superposition has been experimentally verified in numerous quantum systems, including photon polarisation states and electron spin states, confirming its validity as a practical resource for quantum information processing.

2.8.3 Entanglement

Entanglement [105], [106] is one of the most important and unique phenomena in quantum mechanics, where two or more quantum particles become strongly correlated in such a way that the quantum state of one particle cannot be described independently from the others. Once particles become entangled, the measurement or observation of one particle instantly influences the state of the other entangled particles, regardless of the physical distance between them. This behaviour is fundamentally different from classical systems, where information and state changes are typically limited by direct physical interactions.

For example, consider two entangled qubits prepared in a shared quantum state. If one qubit is measured and collapses into a specific state, the second qubit will also immediately collapse into a corresponding state determined by the entangled relationship. This correlation exists even if the particles are separated by very large distances. Due to this property, entanglement has become a fundamental resource in quantum computing and quantum communication systems.

In quantum computing, entanglement enables coordinated operations between multiple qubits, allowing quantum systems to perform complex computations more efficiently than classical systems. In quantum communication, entanglement supports advanced communication mechanisms and distributed quantum processing frameworks by enabling highly correlated quantum state transmission and processing. As a result, entanglement plays a critical role in the development of modern quantum computational models, communication architectures, and next-generation quantum technologies [107].

Although the fundamental principles of quantum entanglement are well established, several aspects of its physical behaviour, large-scale implementation, and practical utilisation remain active areas of research. In particular, the efficient generation, distribution, verification, and long-term preservation of high-fidelity entangled states over realistic quantum channels continue to present significant scientific and engineering challenges due to decoherence, environmental interactions, photon loss, and hardware imperfections. Consequently, many current quantum communication studies adopt mathematical models of quantum channels and quantum states to investigate communication-system performance without relying on the physical realisation of large-scale entanglement distribution. This simulation-based approach enables the investigation of the long-term potential of quantum communication while remaining independent of the current limitations and continuing developments in quantum hardware and networking technologies.

2.8.4 No-Cloning Theorem

The no-cloning theorem [100] is a key principle in quantum mechanics, stating that it is impossible to create an exact copy of an arbitrary unknown quantum state. This differs from classical information, where data such as bits can be copied without any restrictions. In quantum communication, this theorem plays a crucial role in ensuring the integrity of quantum information as it cannot be duplicated without disruption. Quantum systems exist in superposition, meaning they can simultaneously represent multiple states. Attempting to clone a quantum state would require complete knowledge of its properties, but due to the probabilistic nature of quantum mechanics, measuring the state collapses it to a definite value. As a result, any attempt to copy an unknown quantum state would disturb its original configuration, making perfect cloning impossible.

2.8.5 Quantum Gates

Quantum gates are the basic building blocks of quantum circuits, functioning similarly to classical logic gates but with unique capabilities due to the principles of quantum mechanics. These gates perform unitary transformations on qubits and are essential for constructing quantum algorithms and quantum communication protocols. The most commonly used quantum gates are described below.

Hadamard Gate

The Hadamard gate [108] creates superposition states from basis states. It transforms a qubit as shown in (2.9) and (2.10).

$$H|0\rangle = \frac{1}{\sqrt{2}}(|0\rangle + |1\rangle) \tag{2.9}$$

$$H|1\rangle = \frac{1}{\sqrt{2}}(|0\rangle - |1\rangle) \tag{2.10}$$

The matrix representation of the Hadamard gate is given in (2.11).

$$H = \frac{1}{\sqrt{2}} \begin{pmatrix} 1 & 1 \\ 1 & -1 \end{pmatrix} \tag{2.11}$$

CNOT Gate

The CNOT (Controlled-NOT) gate [109] is a fundamental two-qubit quantum gate used particularly for creating entanglement between qubits. It operates on a control qubit and a target qubit: if the control qubit is $|0\rangle$, the target qubit remains unchanged, and if the control qubit is $|1\rangle$, the target qubit is flipped. The operation of the CNOT gate is summarised in Table 2.1.

Table 2.1: Truth table for the CNOT gate.

Control Qubit	**Target Qubit**	**Output (Control, Target)**
0	0	$(0, 0)$
0	1	$(0, 1)$
1	0	$(1, 1)$
1	1	$(1, 0)$

Pauli Gates

The three Pauli gates [110] are single-qubit gates that represent fundamental quantum operations corresponding to bit-flip, phase-flip, and combined bit-flip and phase-flip transformations.

The Pauli-X gate acts as a quantum NOT gate, flipping the state of a qubit as shown in (2.12). Its matrix representation is given in (2.13).

$$X|0\rangle = |1\rangle \quad \text{and} \quad X|1\rangle = |0\rangle \tag{2.12}$$

$$X = \begin{pmatrix} 0 & 1 \\ 1 & 0 \end{pmatrix} \tag{2.13}$$

The Pauli-Y gate introduces a phase flip in addition to flipping the state of the qubit as shown in (2.14). Its matrix representation is given in (2.15).

$$Y|0\rangle = i|1\rangle \quad \text{and} \quad Y|1\rangle = -i|0\rangle \tag{2.14}$$

$$Y = \begin{pmatrix} 0 & -i \\ i & 0 \end{pmatrix} \tag{2.15}$$

The Pauli-Z gate applies a phase flip to the $|1\rangle$ state while leaving the $|0\rangle$ state unchanged, as shown in (2.16). Its matrix representation is given in (2.17).

$$Z|0\rangle = |0\rangle \quad \text{and} \quad Z|1\rangle = -|1\rangle \tag{2.16}$$

$$Z = \begin{pmatrix} 1 & 0 \\ 0 & -1 \end{pmatrix} \tag{2.17}$$

2.9 Quantum Computing

Quantum computing [111], [112] is a computational paradigm that leverages the principles of quantum mechanics to perform computations. Unlike classical computers, which use bits as their basic unit of information, quantum computers utilise qubits, which can exist in multiple states simultaneously due to the phenomenon of superposition. A quantum computer operates on the principles of superposition and entanglement, allowing it

to process information in fundamentally different ways than classical computers. This unique capability enables quantum computers to solve certain problems more efficiently than their classical counterparts, with applications in cryptography, materials science, optimisation, and artificial intelligence.

2.9.1 Current Quantum Computing Technologies and NISQ Challenges

Recent advances in quantum computing have resulted in several physical implementations of quantum processors, each with distinct advantages and technological challenges. Among the most mature approaches are superconducting qubits [113], trapped-ion systems [114], photonic quantum computing [115], neutral-atom quantum processors [116], and semiconductor spin qubits [117]. Superconducting quantum processors, adopted by companies such as IBM and Google, currently provide the largest publicly accessible quantum computers and support cloud-based quantum computation through software platforms such as Qiskit [118]. Trapped-ion systems [114], developed by organisations including IonQ and Quantinuum, offer high gate fidelities and long coherence times, while photonic and neutral-atom technologies provide promising alternatives for achieving scalable quantum information processing. Although these technologies continue to advance rapidly, existing quantum computers remain in the NISQ era [99], where hardware limitations restrict the execution of large-scale fault-tolerant quantum applications.

NISQ devices are affected by several practical limitations that influence the implementation of quantum communication systems. Physical qubits possess finite coherence times and are susceptible to decoherence arising from interactions with the surrounding environment. Furthermore, quantum gate operations introduce operational errors, measurement processes are imperfect, and limited qubit connectivity often requires additional routing operations that increase circuit depth and error accumulation. As the number of qubits and quantum operations increases, these hardware imperfections progressively reduce computational reliability, making the execution of large and complex quantum circuits particularly challenging on current quantum processors [99], [113], [119].

These limitations are especially significant for multimedia communication applications. Practical image and video transmission involves processing long compressed

bitstreams, encoding large numbers of qubits, performing repeated quantum operations, and supporting reliable communication under noisy channel conditions. Such computational and communication requirements currently exceed the capabilities of available NISQ hardware, where limited qubit resources, accumulated gate errors, and short coherence times restrict the implementation of complete end-to-end multimedia communication systems.

To mitigate these challenges, significant research efforts are directed towards fault-tolerant quantum computing through the development of scalable quantum error correction, logical qubit encoding, improved gate fidelities, longer coherence times, hardware-aware circuit optimisation, and scalable quantum memory technologies [120]. These developments are expected to enable progressively larger and more reliable quantum computing and communication systems as quantum hardware continues to mature.

Owing to the limitations of current NISQ hardware, this thesis focuses on the algorithmic design and simulation-based evaluation of the proposed quantum multimedia communication frameworks rather than deployment on physical quantum processors. The presented models assume ideal quantum operations except where quantum noise is explicitly introduced to investigate communication channel impairments. Consequently, hardware-specific issues such as finite coherence times, limited qubit connectivity, gate calibration errors, and quantum processor scheduling are considered outside the scope of this work. As quantum hardware continues to mature, future research will investigate the implementation and optimisation of the proposed frameworks on fault-tolerant quantum computing platforms.

2.10 Quantum Communication

Quantum communication [112] is a field of study that leverages the principles of quantum mechanics to transmit information efficiently and securely [121], [122]. Unlike classical communication, which relies on electromagnetic signals, quantum communication utilises quantum states of particles (such as photons) to encode and transmit data. The key advantages of quantum communication include efficient data transmission, enhanced error resilience, and increased bandwidth capacity. Quantum communication enables more efficient transmission of data compared to classical communication systems. This

efficiency arises from the unique properties of qubits that can exist in multiple states simultaneously due to superposition. While a classical bit is restricted to either 0 or 1, a qubit can represent both states at the same time, enabling more information to be encoded in fewer qubits. Error resilience is another important advantage of quantum communication. Classical systems rely on error correction codes to detect and correct errors during data transmission, whereas quantum communication introduces new approaches to enhance error resilience through intrinsic quantum properties such as entanglement and quantum error correction techniques.

Quantum communication also offers the potential for increased bandwidth efficiency by allowing more data to be transmitted using fewer resources. Through quantum parallelism, where multiple qubits can represent different combinations of states simultaneously, a single quantum channel can carry multiple streams of information at the same time. In quantum superdense coding [123], for instance, one qubit can effectively transmit the equivalent of two classical bits, doubling the bandwidth of the communication channel.

Quantum communication has advanced significantly with entanglement-based protocols [121], [122], while the direct use of superposition for communication remains a largely unexplored area with significant potential for developing new communication methods. In addition to fully quantum communication systems, hybrid quantum-classical frameworks have recently attracted considerable attention [99]. These approaches combine classical computing and communication infrastructures with quantum technologies to exploit the strengths of both paradigms [124]. Classical systems are typically responsible for tasks such as control, data preprocessing, optimisation, and error management, while quantum components perform state preparation, information processing, or secure information exchange. A similar hybrid philosophy underlies quantum computing, where classical optimisers are combined with parameterised quantum circuits to overcome near-term hardware limitations [125], [126]. Hybrid architectures are particularly attractive in the current NISQ era, where practical quantum hardware remains resource constrained [99]. Consequently, hybrid quantum-classical systems provide a pragmatic pathway towards the gradual deployment of quantum communication technologies while maintaining compatibility with existing classical communication infrastructures, such

as fiber-optic and wavelength-division-multiplexed networks [124].

2.11 Quantum Noise Models in Quantum Communication Systems

In practical quantum communication systems, transmitted quantum states inevitably interact with the surrounding environment, resulting in quantum noise and the degradation of quantum information [127]. These noise effects are commonly modelled using the density matrix formalism together with Kraus operator representations. The general evolution of a noisy quantum state is expressed as in (2.18).

$$\rho' = \sum_k E_k \rho E_k^\dagger, \quad \sum_k E_k^\dagger E_k = I \tag{2.18}$$

where ρ represents the input density matrix, ρ' denotes the noisy output state, and E_k are the Kraus operators satisfying the completeness condition.

2.11.1 Bit-Flip Noise

Bit-flip noise models random state inversion errors in which the computational basis states are exchanged as $|0\rangle \leftrightarrow |1\rangle$. The corresponding density matrix evolution is given in (2.19).

$$\rho' = (1 - p_x)\rho + p_x X \rho X \tag{2.19}$$

where p_x denotes the bit-flip probability and X is the Pauli-X operator defined in (2.13). The associated Kraus operators are given in (2.20).

$$E_0 = \sqrt{1 - p_x}\, I, \quad E_1 = \sqrt{p_x}\, X \tag{2.20}$$

2.11.2 Phase-Flip Noise

Phase-flip noise alters the phase of a quantum state without modifying its amplitude. The corresponding noisy state evolution is expressed in (2.21).

$$\rho' = (1 - p_z)\rho + p_z Z\rho Z \tag{2.21}$$

where p_z represents the phase-flip probability and Z is the Pauli-Z operator defined in (2.17). The Kraus operators for phase-flip noise are given in (2.22).

$$E_0 = \sqrt{1 - p_z}\, I, \quad E_1 = \sqrt{p_z}\, Z \tag{2.22}$$

2.11.3 Depolarising Noise

Depolarising noise models random quantum errors that replace the transmitted quantum state with a maximally mixed state with probability p_D. The corresponding density matrix evolution is given in (2.23).

$$\rho' = (1 - p_D)\rho + p_D \frac{I}{2} \tag{2.23}$$

Its Kraus representation is expressed as in (2.24).

$$E_0 = \sqrt{1 - p_D}\, I, \quad E_1 = \sqrt{\frac{p_D}{3}} X, \quad E_2 = \sqrt{\frac{p_D}{3}} Y, \quad E_3 = \sqrt{\frac{p_D}{3}} Z \tag{2.24}$$

where the Pauli operators X, Y, and Z are defined in (2.13), (2.15), and (2.17), respectively.

2.11.4 Amplitude Damping Noise

Amplitude damping noise describes energy dissipation in quantum systems, such as spontaneous emission or photon loss. The noisy state evolution under amplitude damping is expressed as in (2.25).

$$\rho' = E_0 \rho E_0^\dagger + E_1 \rho E_1^\dagger \tag{2.25}$$

The corresponding Kraus operators are defined in (2.26), where λ denotes the amplitude damping probability.

$$E_0 = \begin{bmatrix} 1 & 0 \\ 0 & \sqrt{1-\lambda} \end{bmatrix}, \quad E_1 = \begin{bmatrix} 0 & \sqrt{\lambda} \\ 0 & 0 \end{bmatrix} \tag{2.26}$$

2.11.5 Phase Damping Noise

Phase damping (dephasing) noise describes the loss of quantum coherence without energy dissipation. Unlike amplitude damping, phase damping affects only the off-diagonal coherence terms of the density matrix while preserving the state populations. The evolution of the density matrix under phase damping is expressed as in (2.27).

$$\rho' = E_0 \rho E_0^\dagger + E_1 \rho E_1^\dagger \tag{2.27}$$

The corresponding Kraus operators are defined in (2.28), where γ denotes the dephasing probability.

$$E_0 = \begin{bmatrix} 1 & 0 \\ 0 & \sqrt{1-\gamma} \end{bmatrix}, \quad E_1 = \begin{bmatrix} 0 & 0 \\ 0 & \sqrt{\gamma} \end{bmatrix} \tag{2.28}$$

2.11.6 Summary

The quantum noise models presented in this section represent the principal error mechanisms encountered in quantum communication systems. Bit-flip and phase-flip noise describe discrete computational-basis and phase errors, respectively, while depolarising noise models random combined quantum disturbances. Amplitude damping and phase damping further represent physically realistic decoherence processes associated with energy dissipation and coherence loss. These noise processes significantly affect quantum-state fidelity and therefore play a critical role in the analysis and evaluation of robust quantum communication frameworks.

2.12 Quantum Error Correction (QEC)

QEC is a fundamental framework for protecting quantum information against noise, decoherence, and operational imperfections in quantum systems [127], [128]. Unlike classical error correction, where redundancy is introduced through direct copying of

bits, quantum systems are constrained by the no-cloning theorem, which prohibits the duplication of arbitrary unknown quantum states. Therefore, QEC encodes a single logical qubit into multiple entangled physical qubits, enabling error detection and correction without directly measuring the quantum information.

Quantum errors can be broadly categorised into bit-flip errors, which invert the state of a qubit, phase-flip errors, which alter the relative phase between quantum states, and combined errors that involve both types simultaneously. These errors are detected through syndrome measurements using stabiliser operators, which identify the type and location of the error without disturbing the encoded quantum information.

Several QEC schemes have been developed with varying levels of complexity and resource requirements. Multi-qubit QEC techniques are particularly important because quantum states are highly sensitive to environmental noise, decoherence, and operational imperfections during transmission and processing. By distributing the logical quantum information across multiple physical qubits, these techniques improve transmission reliability and enable the detection and correction of quantum errors without directly measuring the encoded quantum information. The three-qubit bit-flip code [129] is one of the simplest QEC schemes, capable of correcting a single bit-flip error by encoding one logical qubit into three physical qubits. The five-qubit code [130] is the smallest QEC code capable of correcting any arbitrary single-qubit error, encoding one logical qubit into five physical qubits. It achieves the theoretical minimum number of physical qubits required for full single-qubit error correction, making it an important benchmark in quantum coding theory. The Shor code [131] extends the error correction capability by encoding one logical qubit into nine physical qubits, enabling correction of arbitrary single-qubit errors including both bit-flip and phase-flip errors. The Steane code [132] offers a more efficient alternative by encoding one logical qubit into seven physical qubits based on the structure of classical Hamming codes.

Stabiliser codes [133] provide a general and widely used framework for constructing QEC codes. In the stabiliser formalism, a quantum code is defined by a set of commuting operators from the Pauli group, known as stabilisers, whose simultaneous eigenspace forms the protected code space. The syndrome measurements are performed by measuring these stabiliser operators, which reveal the presence and type of errors without

collapsing the encoded logical information. Many well-known QEC codes, including the five-qubit code, the Steane code, the Shor code, and surface codes, can be described within the stabiliser framework. For large-scale quantum systems, surface codes [134] are widely considered the most practical QEC approach due to their high fault-tolerance threshold and compatibility with scalable quantum architectures. In surface codes, qubits are arranged on a two-dimensional lattice, and error detection is performed using local stabiliser measurements over neighbouring qubits, enabling efficient error correction without requiring global operations. In quantum communication systems, QEC plays a crucial role in mitigating channel-induced noise such as depolarisation and amplitude damping, thereby improving the fidelity of transmitted quantum states and enhancing overall system performance.

2.13 Quantum Network Simulators

Several software platforms have been developed to facilitate the simulation and evaluation of quantum communication systems. Among the dedicated quantum network simulators, NetSquid [135] provides a discrete-event simulation environment for modelling large-scale quantum networks, including entanglement generation, quantum repeaters, and communication protocols. Similarly, SeQUeNCe [136] offers a modular framework for investigating quantum network architectures and protocol stacks across multiple network layers, while QuISP [137] is designed for large-scale quantum internet simulation, supporting the analysis of quantum repeater networks and distributed quantum communication. SimulaQron [138] focuses on the emulation of interconnected quantum processors for developing distributed quantum applications, whereas QuNetSim [139] provides a flexible framework for implementing and evaluating quantum networking protocols. Complementing these network simulators, quantum computing software development kits (SDKs) such as Qiskit [118] and Cirq [140] enable the design, implementation, and simulation of quantum circuits and algorithms for gate-based quantum computing.

Although these platforms provide valuable capabilities for modelling quantum circuits, distributed quantum computing, and quantum network protocols, their primary objective is the evaluation of network-layer functionalities such as routing, entanglement

distribution, quantum repeaters, resource management, and quantum internet protocols. Consequently, they are not designed for end-to-end multimedia communication system evaluation, where multimedia data are generated, compressed, represented as quantum states, transmitted over noisy quantum channels, decoded, reconstructed, and objectively assessed using communication quality metrics. In particular, these platforms do not provide integrated support for multimedia source coding, image and video compression, multidimensional quantum information representation, communication-theoretic channel modelling, or multimedia quality assessment. As a result, they cannot directly evaluate the performance of the proposed end-to-end quantum multimedia transmission framework.

Therefore, this work adopts an end-to-end communication-system modelling approach based on mathematical models rather than a full quantum network simulation. The proposed framework models the complete multimedia communication chain, including multimedia source compression, multidimensional quantum representation, quantum channel modelling, QEC, transmission over noisy quantum channels, and multimedia reconstruction at the receiver. The objective of this research is to evaluate the transmission performance of multimedia information over quantum communication channels at the physical and link layers instead of analysing network-layer operations such as routing, entanglement management, quantum repeaters, or quantum internet architectures. Consequently, end-to-end mathematical communication-system modelling provides a more appropriate and computationally efficient framework for investigating the proposed quantum multimedia transmission system.

2.14 Prior Works on Quantum Computing and Communication

Quantum mechanics underpins both quantum computing [141] and quantum communication [18]. Over the past several decades, quantum computing has experienced substantial technological advancement, leading to the development of practical quantum hardware and algorithms. A notable example is Google's Willow quantum processor [142], which demonstrates the rapid progress achieved in quantum hardware following decades of

theoretical and experimental research. Initially proposed as a theoretical concept more than 30 years ago, quantum computing has evolved significantly through continuous advancements in quantum devices, architectures, and algorithms.

In parallel, quantum communication research has primarily focused on secure communication protocols, QKD [23], quantum cryptography [27], and secure information exchange mechanisms. Furthermore, several quantum transform algorithms have been developed for computational and signal processing purposes, such as the quantum Fourier transform (QFT) [143], quantum discrete cosine transform (QDCT) [144], and quantum Haar wavelet transform (QHWT) [145]. These transforms have mainly been explored for quantum computation, image representation, compression, and secure protocol applications.

However, no prior research has investigated the integration of these quantum transform techniques into practical quantum communication frameworks for high-fidelity image and video transmission over noisy communication channels. Existing studies primarily focus either on secure communication protocols or isolated signal processing applications, without addressing end-to-end multimedia transmission challenges such as compression efficiency, channel robustness, reconstruction fidelity, and adaptive transmission strategies. This limitation reveals a clear research gap and motivates the proposed research work. Therefore, the following subsections critically analyse prior studies related to quantum communication and associated technologies:

1. Prior Works on Secure Quantum Communication
2. Prior Works Using Quantum Superposition for Communication Tasks
3. Prior Works on Transform-Domain Analysis in Quantum Systems
4. Prior Works on Quantum Error Correction
5. Prior Works on Quantum Image Representation and Compression
6. Prior Works on Quantum Communication Applications
7. Prior Works on Quantum Multimedia Transmission

2.14.1 Prior Works on Quantum Communication for Secure Transmission

Quantum communication was initially developed as a framework for secure information transfer. Early breakthroughs such as QKD [146], [147] and quantum teleportation [148], [149] laid the foundation for secure communication systems. These approaches rely on fundamental quantum mechanical principles, including superposition [21], entanglement [22], and the no-cloning theorem [100]. Superposition allows a quantum state to represent multiple values simultaneously, while entanglement enables strong correlations between quantum particles even when they are physically separated. In addition, the no-cloning theorem ensures that unknown quantum states cannot be copied, providing inherent protection against eavesdropping. Together, these properties enable levels of security that are not achievable using classical communication systems [27]. Building on these principles, several studies have explored secure image and video transmission using quantum communication techniques [150], [121], [122], [151]. These works primarily focus on encryption, privacy preservation, and secure multimedia delivery over quantum channels. However, their primary objective is to ensure secure transmission rather than to maintain high reconstruction quality under noisy channel conditions.

2.14.2 Prior Works Using Quantum Superposition for Communication Tasks

Quantum superposition has recently emerged as a promising resource for enhancing communication efficiency and reducing communication complexity in distributed communication systems. Unlike conventional quantum communication approaches that primarily rely on entanglement, these studies investigate the advantages obtained by placing communication directions or channel orders into quantum superposition states. Previous works demonstrated that quantum superposition of communication directions can improve the success probability of communication complexity tasks compared to classical or fixed-order communication protocols [152]. In these studies, multipartite communication tasks were introduced where separated parties cooperatively computed distributed functions while minimising communication resources. The results showed that superposing the direction of communication provides measurable advantages over

conventional fixed-order communication systems and enables semi-device-independent certification of indefinite communication order.

Further investigations analysed the impact of quantum superposition on communication complexity reduction [153]. These works established that communication protocols employing superpositions of communication directions can achieve substantial reductions in communication requirements compared to one-way classical and quantum communication schemes. In particular, exponential communication savings were demonstrated in specific tripartite communication tasks, even when bounded error probabilities were considered.

In addition, quantum superposition has been explored as a mechanism for detecting non-classical communication behaviour through coherence-based communication frameworks [154]. Prior studies introduced coherence equalities satisfied by classical communication systems operating with well-defined communication directions. These equalities were shown to be violated when communication carriers were prepared in coherent quantum superpositions of spatial directions, thereby demonstrating the non-classical advantages of quantum superposition in communication tasks. Moreover, these approaches enabled the operational detection of spatial quantum superposition states using only spatially separated local measurements without requiring conventional interferometric recombination techniques.

Another important research direction investigated indefinite causal order in quantum communication systems [155]. Previous studies showed that when the order of noisy quantum channels is placed in a quantum superposition, the ability to transmit quantum information can be significantly improved. Specifically, it was demonstrated that two completely dephasing channels, which individually cannot transmit quantum information, become partially capable of transmitting quantum bits when traversed in an indefinite causal order. Similar improvements were also observed for partially dephasing channels, where the achievable quantum information transmission exceeded that of individually applied channels.

Related studies further examined indefinite causal order using depolarising quantum channels [156]. Conventionally, fully depolarising channels are incapable of transmitting information due to complete noise corruption. However, prior works demonstrated

that combining depolarising channels within a superposition of channel orders enables non-zero information transmission. Experimental results confirmed that communication becomes feasible even when both channels are fully depolarising, highlighting the strong potential of indefinite causal order for future quantum communication strategies beyond traditional quantum Shannon theory.

Although these studies successfully demonstrate the theoretical advantages of quantum superposition and indefinite causal order for communication tasks and communication complexity reduction, they primarily focus on abstract communication protocols and low-dimensional information transmission scenarios. No prior research has investigated the application of these principles to practical high-fidelity multimedia communication systems, particularly for image and video transmission over noisy communication channels. Furthermore, challenges related to compression efficiency, adaptive transmission, reconstruction quality, and multimedia-oriented communication robustness remain largely unexplored. These limitations motivate the development of the proposed research framework.

2.14.3 Prior Works on Transform-Domain Analysis in Quantum Systems

Transform-domain processing has become an important component in quantum communication, quantum signal processing, and quantum image analysis systems. Various quantum transform techniques have been developed to improve information representation, spectral analysis, compression efficiency, and quantum state manipulation. Among the most widely used approaches, the Hadamard transform has been extensively applied in quantum communication systems because of its orthogonal basis representation and low computational complexity [108]. By uniformly distributing information across quantum states, the Hadamard transform can improve robustness against localised disturbances and simplify quantum encoding operations. However, its representation capability is limited by discrete phase structures, which restrict flexibility in representing complex signal characteristics.

The QFT is another fundamental transform widely investigated in quantum communication and quantum image processing applications [143], [157], [158]. QFT enables

frequency-domain representation of quantum states through phase-based transformations and has been employed for quantum signal analysis, image representation, and transform-domain processing. Due to its efficient spectral representation capability, QFT has become one of the core transform techniques in quantum information processing systems.

In addition to QFT, several other transform methods have been explored for quantum information representation and compression. The QDCT [144] has been investigated for energy compaction and redundancy reduction, while the QWT [145], [159] and QHWT [160], [161] provide multi-resolution analysis capabilities that enable efficient representation of localised image structures and spatial variations. These transform methods have demonstrated promising performance in quantum image representation and compression-oriented applications.

Despite these advancements, most existing transform-domain approaches are primarily designed for isolated processing tasks such as image representation, spectral analysis, or compression. Many current studies evaluate transform performance under idealised quantum environments without considering practical communication constraints, noisy transmission channels, adaptive transmission requirements, or reconstruction fidelity in multimedia communication systems. Furthermore, no existing transform-domain methods have been studied within end-to-end communication frameworks, limiting their applicability to practical high-fidelity image and video transmission scenarios. Consequently, several important challenges remain insufficiently explored, including robust transform-domain encoding under channel impairments, adaptive multimedia transmission, efficient integration of transform processing with communication systems, and reconstruction quality optimisation for practical multimedia communication applications.

2.14.4 Prior Works on Quantum Error Correction

Quantum communication systems are highly vulnerable to noise, decoherence, and quantum state disturbances introduced during transmission and processing. To improve transmission reliability and maintain quantum state fidelity, QEC techniques have been extensively investigated within quantum information processing research [127]. These

techniques aim to detect and correct errors affecting quantum states while preserving the encoded quantum information.

One of the major milestones in QEC research was the demonstration that multiple physical qubits can be used to protect a single logical qubit without violating the no-cloning theorem. Early foundational studies introduced several important QEC architectures for correcting different forms of quantum errors. Among them, the Shor code [131] employs nine physical qubits to protect a single logical qubit against both bit-flip and phase-flip errors, while the Steane code [132] provides similar protection using seven qubits. These pioneering approaches established the theoretical basis for fault-tolerant quantum information processing.

Following these developments, additional low-dimensional QEC methods were introduced, including five-qubit [130] and three-qubit quantum error correction codes [129]. The three-qubit code is considered one of the simplest and most fundamental QEC techniques, primarily designed to detect and correct single-qubit errors through logical qubit encoding across three physical qubits. Due to its relatively low implementation complexity, the three-qubit approach has been widely analysed in quantum computing studies [162], [163].

More advanced fault-tolerant QEC architectures have also been developed, including stabiliser codes [133] and surface codes [134]. Stabiliser codes provide a generalised framework for constructing quantum error correction schemes using stabiliser operators and form the basis for many modern QEC techniques. Surface codes, in particular, have attracted significant attention because of their high error thresholds, scalability, and suitability for large-scale fault-tolerant quantum computing systems. These methods offer improved robustness against quantum noise and decoherence but often require substantial physical qubit resources and increased implementation complexity.

Although significant progress has been achieved in the development of QEC methods, existing research has primarily focused on quantum computing applications, fault-tolerant quantum circuits, and quantum memory protection [164], [165]. Comparatively limited attention has been given to the integration of QEC techniques into practical quantum communication frameworks, particularly for multimedia communication tasks such as image and video transmission over noisy communication channels. In addi-

tion, many existing QEC studies evaluate error-correction performance independently rather than within complete end-to-end communication system architectures. Important practical considerations, including adaptive transmission behaviour, multimedia reconstruction fidelity, communication efficiency, and the trade-off between transmission robustness and computational complexity, remain insufficiently explored in current quantum communication research. These limitations reveal a significant research gap in the development of integrated quantum communication systems that combine quantum superposition, practical transmission strategies, and both low-complexity and advanced QEC mechanisms for reliable high-fidelity multimedia communication.

2.14.5 Prior Works on Quantum Image Representation and Compression

Quantum image processing research has introduced several representation frameworks for efficiently embedding classical image information into quantum states. Among the most widely studied approaches are the flexible representation of quantum images (FRQI), novel enhanced quantum representation (NEQR), and general quantum image representation (GQIR) frameworks [166], [28], [167]. These methods provide structured mechanisms for storing pixel intensity and positional information within quantum states, forming the foundation for quantum image representation and processing research.

In addition to image representation models, several quantum image compression techniques have been developed using transform-domain processing approaches. Methods based on the QFT [166], QDCT [144], and QWT [145] have demonstrated the potential to reduce redundancy and improve information compaction within quantum image representations. QDCT-based methods primarily focus on frequency-domain energy concentration, while wavelet-based approaches provide multi-scale decomposition capabilities that allow efficient representation of localised image structures.

Several additional studies have investigated compression-oriented quantum image processing and reconstruction frameworks under different computational settings [168], [169], [170], [171], [172], [173]. These works demonstrate the potential advantages of quantum-inspired image processing for storage efficiency and compact image representation. However, most existing methods are evaluated under theoretical or idealised

assumptions and often neglect practical communication constraints encountered during real-world transmission scenarios.

Furthermore, many current quantum image representation and compression techniques are studied independently from complete communication system architectures. Existing approaches generally focus on isolated representation or compression stages without integrating realistic noisy channel transmission, adaptive communication strategies, channel impairments, or perceptual reconstruction analysis into the overall framework. As a result, the practical applicability of these methods for high-fidelity multimedia communication, particularly for robust image and video transmission over error-prone communication channels, remains limited.

These limitations reveal a clear research gap in the development of integrated quantum-inspired multimedia communication systems that jointly address image representation, transform-domain compression, noisy channel transmission, adaptive processing, and reconstruction quality optimisation within a unified framework.

2.14.6 Prior Works on Quantum Communication Applications

Quantum communication research has expanded rapidly in recent years, with existing studies investigating a wide range of applications including quantum semantic communication, quantum secure communication, quantum teleportation, and entanglement-assisted wireless systems. However, most existing works focus on specific individual aspects of quantum communication rather than developing unified frameworks for high-fidelity multimedia transmission under practical noisy channel conditions.

In the area of quantum semantic communication, several quantum semantic communication systems have been proposed [174], [175], [176], [177]. These studies demonstrated efficient semantic information transmission with reduced communication resource consumption compared to conventional classical semantic communication systems [178]. Their primary objective is semantic-level information delivery with low complexity, rather than accurate reconstruction of high-quality multimedia content. Building on this direction, a scalable prototyping testbed integrating generative artificial intelligence (AI), quantum computing, and semantic communication is introduced in [179] to support goal-oriented 6G communication applications under noisy channel conditions. Similarly,

a sustainable big-AI-native quantum semantic communication framework was proposed in [180], combining lightweight generative AI models with quantum communication protocols to enable goal-oriented and quantum-safe communication. Although these studies demonstrated the potential of integrating AI and semantic intelligence with quantum communication, the proposed systems remained primarily limited to theoretical representations and did not investigate transmission over noisy channels or high-fidelity multimedia reconstruction.

In addition, research on MIMO techniques in quantum communication remains comparatively limited and has primarily focused on secure communication applications rather than multimedia transmission. Most existing quantum MIMO studies investigate entanglement-based communication approaches such as quantum teleportation [181], [182] and QKD systems [183]. These works mainly exploit quantum entanglement to improve secure information exchange and quantum state delivery. While these studies provide important insights into applying MIMO concepts within quantum communication systems, they do not investigate the effects of MIMO techniques on image and video transmission in quantum superposition-based communication frameworks.

In addition, several studies have explored the potential use of QFT in quantum communication applications, particularly in areas such as QKD [184] and quantum teleportation [185]. Some preliminary investigations have also considered hybrid quantum-classical OFDM architectures, entanglement-assisted transmission schemes, and early-stage QOFDM implementations for basic communication scenarios [186], [187], [188]. However, these studies mainly remain at a conceptual or limited implementation level and do not provide comprehensive analyses of fully integrated OFDM-based quantum communication systems. In particular, existing works generally lack rigorous mathematical modelling, scalable multi-qubit transmission frameworks, and practical end-to-end system evaluations under realistic quantum channel conditions. The effects of quantum noise, decoherence, and channel impairments throughout the complete transmission and reconstruction process have therefore not been thoroughly investigated. Furthermore, to the best of current knowledge, no prior work has presented a complete QOFDM framework specifically designed for robust high-fidelity image transmission over noisy quantum communication channels.

Overall, the majority of existing quantum communication studies focus on isolated communication aspects such as semantic transmission, secure communication, quantum teleportation, or entanglement-assisted information exchange. The integration of quantum encoding within a unified high-fidelity quantum multimedia communication framework remains largely unexplored. Therefore, a significant research gap exists in the development of practical and scalable quantum communication architectures specifically designed for robust image and video transmission over noisy wireless communication channels.

2.14.7 Prior Works on Quantum Multimedia Transmission

Quantum multimedia transmission is an emerging research area, and only a limited number of studies have investigated the application of quantum technologies for multimedia communication. Existing works have progressively extended quantum communication from one-dimensional secure information transfer towards image and video applications. Nevertheless, these studies remain focused on security, imaging, or encryption, rather than providing a complete end-to-end high-fidelity quantum multimedia communication framework.

One of the earliest multimedia-oriented approaches employed QKD to secure medical image transmission by integrating BB84 and differential phase shift protocols with quantum bit-plane representation and chaotic encryption techniques [189]. The framework demonstrated improved security for medical image transmission over free-space optical and optical fiber channels. However, the image information remained classically encoded and transmitted, while quantum communication was used only for secure key establishment.

Another study proposed a hybrid quantum-classical encryption framework for IoT-based medical image transmission. The framework combined QKD with one-time pad encryption, hyperchaotic systems, discrete cosine transform (DCT), and discrete wavelet transform (DWT) to enhance image security while reducing computational complexity through selective bit-plane encryption [190]. Similar to the previous approach, quantum techniques were employed exclusively for key generation, whereas multimedia encoding and transmission remained entirely classical.

A more direct quantum communication approach was introduced through a quantum-secured image transmission framework, in which image information was encoded using entangled photon pairs while communication security was verified through a BB84-inspired polarisation encoding scheme [122]. Unlike QKD-assisted encryption methods, this approach directly transmitted image information using quantum states. However, the framework primarily focused on physical-layer security and did not address multimedia compression, noisy quantum channel modelling, QEC, or multimedia reconstruction.

Another recent advancement demonstrated quantum image transmission through highly scattering media using entangled photon correlations and programmable optical transformations [191]. The proposed system successfully recovered images while remaining opaque to classical imaging techniques, highlighting the potential of quantum imaging. Nevertheless, the study focused on optical image formation rather than multimedia communication, and therefore did not consider source coding, communication channel impairments, transmission efficiency, or multimedia reconstruction.

In the video domain, a hybrid quantum-safe video transmission framework integrated quantum-inspired encryption with conventional Internet-based video communication [151]. The proposed method improved transmission security through quantum-assisted encryption and demonstrated superior encryption performance compared with existing video encryption techniques. However, the video content itself was transmitted through conventional communication channels, and quantum techniques were employed only as a security mechanism rather than as the communication medium.

Furthermore, quantum communication research can be traced along a clear trajectory of increasing information dimensionality, beginning with single-bit and single-qubit exchange and progressing towards structured, multidimensional multimedia content. A comparison of representative quantum transmission studies is presented in Table 2.2, illustrating the evolution from one-dimensional quantum-assisted secure communication to end-to-end multidimensional quantum multimedia communication.

The comparison presented in Table 2.2 illustrates that the role of quantum communication has gradually evolved from secure one-dimensional information exchange to increasingly sophisticated multimedia applications. However, existing research has not yet established a unified end-to-end multimedia communication framework capable of

Table 2.2: Evolution of Existing Quantum Multimedia Transmission Approaches.

Ref.	Multimedia	Quantum Role	Information Dimensionality	End-to-End Transmission
[146], [147], [185]	None	QKD / Quantum Teleportation	1-D quantum information	No
[189]	Medical Image	QKD-assisted encryption	2-D image (classical)	No
[190]	Medical Image	Hybrid quantum-classical encryption	2-D image (classical)	No
[122]	Image	Quantum-secured image transmission	High-dimensional image	Partial
[191]	Image	Quantum imaging	High-dimensional image	No
[151]	Video	Quantum-safe encryption	3-D video (classical)	No
Proposed	**Multimedia**	**High-fidelity communication**	**Multi-dimensional multimedia**	**Yes**

jointly addressing quantum information representation, transmission, error resilience, compression, and multimedia reconstruction. This observation motivates the development of the multimedia-oriented quantum communication paradigm proposed in this thesis, which integrates these complementary functionalities into a single communication framework.

2.14.8 Limitations of Existing Quantum Communication Research and Motivation

Although substantial progress has been achieved in quantum communication, no practical end-to-end quantum communication system has yet been fully developed for high-fidelity image and video transmission over noisy communication channels. Existing quantum communication research primarily focuses on isolated components of quantum systems, including secure communication protocols, quantum state representation, transform-domain processing, communication complexity reduction, and fault-tolerant quantum computation. As a result, integrated multimedia-oriented quantum communication frameworks remain largely underdeveloped.

A significant portion of prior quantum communication research has concentrated on secure communication applications such as QKD, teleportation, entanglement-based communication, and quantum cryptography. While these methods provide strong theoretical security guarantees, they are generally designed for low-dimensional information exchange and do not directly address practical multimedia communication requirements, including high-fidelity image reconstruction, adaptive transmission, bandwidth efficiency, perceptual quality preservation, and robustness against noisy communication environments.

Research involving quantum superposition and indefinite causal order has demon-

strated important theoretical advantages for communication complexity reduction and transmission efficiency improvement. However, these studies are mainly limited to abstract communication tasks and simplified communication models. Their applicability to practical multimedia transmission systems, particularly for robust image and video communication under realistic noisy channel conditions, remains insufficiently explored.

Similarly, existing transform-domain approaches in quantum systems, including the QFT, QDCT, and quantum wavelet-based methods, have mainly been investigated for signal representation, spectral analysis, and compression-related tasks. Although these techniques demonstrate promising theoretical capabilities, most current studies evaluate them under idealised assumptions and do not integrate them into complete communication frameworks capable of supporting adaptive high-fidelity multimedia transmission.

Quantum image representation and compression studies have also introduced several efficient image embedding and compression frameworks. However, most existing approaches primarily focus on representation efficiency and theoretical compression performance without considering practical communication constraints such as noisy transmission channels, adaptive communication behaviour, reconstruction fidelity, and end-to-end multimedia transmission performance. Consequently, their practical applicability for robust multimedia communication systems remains limited.

In the area of QEC, extensive research has focused on quantum computing, fault-tolerant quantum circuits, and quantum memory protection. Methods such as the Shor code, the Steane code, stabiliser codes, surface codes, and low-dimensional QEC schemes have demonstrated strong capabilities to protect quantum information against noise and decoherence. Nevertheless, the integration of these error correction methods into practical multimedia-oriented quantum communication systems remains largely unexplored, particularly for high-fidelity image and video transmission applications.

Another major limitation of existing research is the lack of comprehensive evaluation under practical communication environments. Many prior works assume ideal quantum conditions and do not sufficiently analyse the effects of realistic channel impairments, adaptive channel variations, computational complexity, or the trade-offs between communication robustness and multimedia reconstruction quality. Furthermore, limited research

has investigated unified frameworks that combine quantum-inspired transform-domain processing, quantum superposition, adaptive communication strategies, multimedia compression, and both quantum and classical error correction techniques within a single end-to-end system architecture.

These limitations collectively reveal a significant research gap in the development of robust, adaptive, and practical quantum multimedia communication systems. Motivated by these challenges, this research aims to develop quantum communication frameworks for high-fidelity image and video transmission over noisy communication channels. The proposed research investigates different encoding techniques, transform-domain quantum processing, adaptive transmission strategies, multimedia-oriented reconstruction techniques, and both quantum and classical error correction approaches within unified end-to-end communication architectures. Through this approach, the research seeks to improve communication robustness, transmission efficiency, reconstruction fidelity, and the practical applicability of future quantum multimedia communication systems.

2.15 Chapter Summary

This chapter has reviewed the theoretical and technological foundations relevant to the development of the quantum communication frameworks proposed in this thesis. The review proceeded in three parts. The first part examined classical multimedia communication systems, covering source coding, channel coding, modulation, OFDM, MIMO, MIMO-OFDM, multiple description coding, and semantic communication. While these technologies have driven decades of progress in image and video transmission, they remain constrained by the fundamental limitations of binary information representation and by their sensitivity to channel impairments in noisy and dynamically varying environments.

The second part introduced the principles of quantum mechanics, quantum computing, and quantum communication, together with the principal noise models and QEC frameworks that govern realistic quantum information processing. These foundations provide the theoretical basis for the encoding, transmission, and correction techniques developed in subsequent chapters.

The third part critically reviewed prior research on quantum communication ap-

plications, including secure transmission, superposition-based communication tasks, transform-domain processing, image representation and compression, QEC, and quantum multimedia transmission. Although these studies demonstrate the considerable potential of quantum communication technologies, they remain largely fragmented, with most focusing on individual communication components rather than complete multimedia transmission systems. Consequently, no unified end-to-end quantum communication framework has yet been established for reliable and high-fidelity image and video transmission over noisy quantum channels. This observation highlights the need for a multimedia-oriented quantum communication paradigm that integrates multimedia source coding, multidimensional quantum representation, quantum channel modelling, adaptive error resilience, compression, transmission, and multimedia reconstruction within a single end-to-end framework.

Motivated by this research gap, this thesis proposes such a paradigm by establishing a unified framework for reliable, scalable, and high-fidelity quantum multimedia communication. The remaining chapters progressively develop this paradigm through a series of interconnected contributions. Chapter 3 establishes the fundamental end-to-end quantum communication framework based on quantum superposition and QEC for reliable image and video transmission over noisy quantum channels, with subsequent chapters extending this foundation through scalable quantum representations, transform-domain processing, advanced quantum encoding strategies, and integration with emerging communication technologies.

Chapter 3

Design of a Single-Qubit Encoding Quantum Communication Framework for Image and Video Transmission

This chapter presents the design and development of a quantum communication framework for high-fidelity image and video transmission over error-prone communication channels. While conventional quantum communication research has primarily focused on secure data exchange through protocols such as QKD and quantum cryptography, practical image and video transmission demands a fundamentally different set of capabilities, including noise resilience, high reconstruction fidelity, efficient encoding, and adaptive error correction. This chapter addresses these requirements by developing a unified quantum communication framework that extends quantum superposition principles to image and video transmission scenarios. Throughout this chapter, JPEG, HEIF, and VVC are employed as transform-domain source encoders, each utilising conventional transform coding techniques to compress multimedia data prior to quantum processing. However, the proposed framework remains independent of the specific source transform because quantum encoding is performed only on the resulting compressed bitstream rather than on the underlying transform coefficients. Consequently, the proposed quantum

communication framework is compatible with a wide range of existing and future source coding standards without requiring modifications to the quantum encoding process.

The chapter is organised as a series of interconnected studies, each building upon the foundations established by its predecessor. Section 3.1 introduces the core quantum communication system for image transmission over noisy channels, establishing the fundamental encoding, channel modelling, and decoding framework that underpins all subsequent developments [192], [193]. Section 3.2 extends this framework by incorporating QEC mechanisms to improve transmission reliability under severe channel impairments [194]. Section 3.3 further advances the system by introducing an adaptive QEC strategy that dynamically adjusts error correction parameters based on channel conditions, thereby optimising the trade-off between transmission robustness and communication efficiency [195]. Finally, Section 3.4 extends the proposed framework to video transmission [196], demonstrating its applicability to more complex and data-intensive multimedia communication scenarios. Together, these contributions form a unified and scalable approach toward robust quantum multimedia communication systems.

3.1 Quantum Communications for Image Transmission over Error-Prone Channels

Publication Notice

The research presented in this section has been published in the following peer-reviewed journal publication:

U. Jayasinghe, P. Samarathunga, Y. Ganearachchi, T. Fernando, and A. Fernando, "Quantum communications for image transmission over error prone channels," *Electronics Letters*, vol. 60, no. 15, e13300, 2024, doi: 10.1049/ell2.13300.

This material is reproduced and adapted under the terms of the IET/Wiley Copyright policy for use in a doctoral thesis. The content has been revised and extended with additional explanations and expanded discussion.

Problem Statement: Image transmission over wireless channels is increasingly limited by the trade-off between bandwidth efficiency and robustness to channel impairments.

Classical communication systems rely on heavy redundancy through channel coding to maintain reliability under noisy conditions, but this redundancy is costly in bandwidth-constrained environments. Furthermore, in low-SNR regimes, the symbol-level mapping used by classical modulation schemes such as BPSK exposes every transmitted bit to direct corruption by additive noise, since each bit is represented by a single deterministic voltage level whose detection threshold is easily crossed by noise. This becomes particularly problematic for compressed image data, where even a small number of bit errors can cause severe perceptual degradation in the reconstructed image due to strong inter-bit dependencies in formats such as JPEG and HEIF.

Limitations of Existing Work: While entanglement-based quantum communication has been extensively studied (see Section 2.14.1) and successfully applied in tasks such as QKD and quantum teleportation, the direct utilisation of quantum superposition for practical communication system design remains relatively limited. Existing studies have primarily focused on theoretical models or isolated communication tasks (Section 2.14.2), such as quantum state representation, communication complexity reduction, transform-domain analysis, or secure communication protocols, without integrating source encoding, channel coding, quantum state mapping, transmission, and image reconstruction within a unified communication architecture. To the best of the author's knowledge, no practical end-to-end quantum communication framework has been fully developed for high-fidelity image transmission over error-prone channels.

Motivation and Proposed Contribution: To address this gap, this section proposes a superposition-based quantum communication framework specifically designed for end-to-end image transmission over noisy channels. The motivation is grounded in a fundamental property of quantum superposition: when classical bits are mapped into quantum superposition states via the Hadamard transform, information is distributed across probability amplitudes rather than concentrated in a single deterministic symbol level. This distribution makes the encoded information inherently more resilient to channel noise, since perturbations affect the amplitude distribution rather than directly corrupting a single binary decision. The proposed framework integrates classical source coding (JPEG and HEIF), classical channel coding (polar codes), quantum state mapping

via the Hadamard transform, transmission through a realistic composite quantum noise channel, and quantum measurement-based decoding into a single coherent pipeline. The system is evaluated using PSNR, SSIM, and BER metrics against a bandwidth-equivalent classical BPSK system, establishing one of the first integrated end-to-end quantum communication frameworks for high-fidelity image transmission and providing the foundation upon which the QEC-based, adaptive QEC-based, and video extensions presented in Sections 3.2–3.4 are built.

3.1.1 System Model

The proposed end-to-end quantum communication framework for image transmission is illustrated in Figure 3.1. The framework consists of five sequential processing stages: source encoding, channel encoding, quantum state mapping, quantum channel transmission, and quantum measurement-based decoding. Each stage is described in detail below.

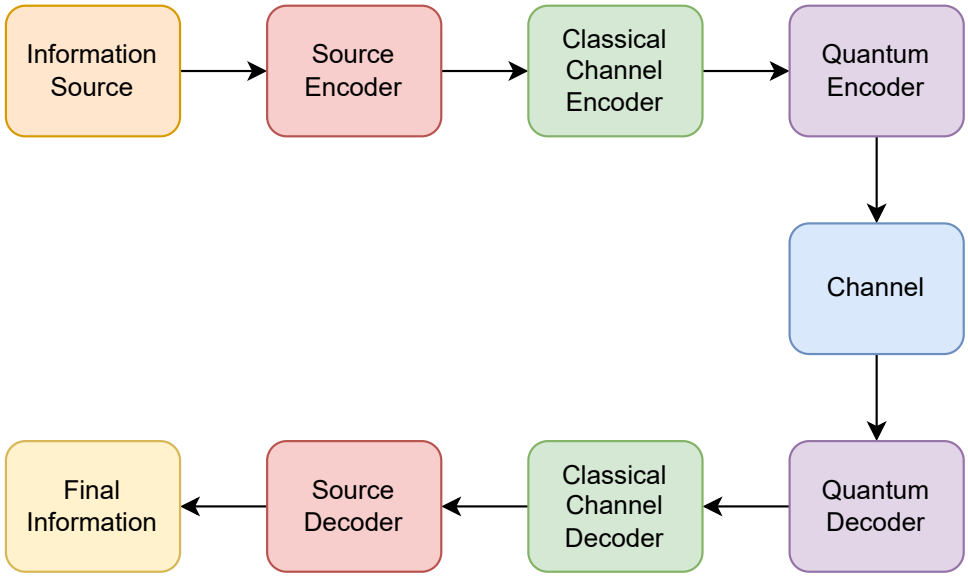


Figure 3.1: End-to-end information transmission system using quantum communications.

Dataset and Source Encoding: Fifty test images sourced from the Microsoft Common Objects in Context (COCO) dataset [197] are used as the information source.

The COCO dataset is chosen because it contains a diverse set of real-world images with varying resolutions, colour distributions, objects, scenes, and texture characteristics, providing a robust benchmark for evaluating the generalisation capability of the proposed framework. The use of diverse image characteristics further demonstrates the content-independent and input-agnostic nature of the proposed method, showing that the framework can operate effectively across different image resolutions, colour contents, and visual structures without requiring content-specific optimisation. This dataset is used consistently throughout all studies presented in this chapter.

The source encoder compresses the input images by reducing statistical redundancy using either the JPEG or HEIF codec. The quantisation parameter (QP) controls the compression level during encoding, where lower QP values correspond to higher quantisation and greater information loss upon decoding. A range of QP values (25, 50, 75, and 100) is explored to represent various levels of compression, enabling evaluation of the framework under both aggressive and conservative compression conditions. The output of the source encoder is a compressed bitstream $\mathbf{b} = [b_1, b_2, \ldots, b_L]$, where $b_i \in \{0, 1\}$ and L denotes the total number of bits.

Channel Encoding: Polar codes with a code rate of $R = 1/2$ are employed as the channel coding scheme. The code rate of 1/2 provides a balanced trade-off between transmission reliability and bandwidth efficiency by allocating an equal proportion of information bits and redundancy bits. Polar codes are selected due to their capacity-achieving properties under successive cancellation decoding and their well-established theoretical foundation for symmetric binary-input memoryless channels [39]. The channel polarisation property enables reliable transmission through highly reliable synthesised channels while reducing the impact of unreliable channels. The channel-encoded bitstream is denoted as $\mathbf{c} = [c_1, c_2, \ldots, c_N]$, where $N = 2L$ due to the rate-1/2 coding.

Quantum Encoder: The quantum encoder maps each channel-encoded classical bit c_i into a quantum superposition state suitable for transmission. Classical bits 0 and 1 are first mapped to the computational basis states $|0\rangle$ and $|1\rangle$, respectively, whose

matrix representations are given in (3.1) and (3.2).

$$|0\rangle = \begin{pmatrix} 1 \\ 0 \end{pmatrix} \tag{3.1}$$

$$|1\rangle = \begin{pmatrix} 0 \\ 1 \end{pmatrix} \tag{3.2}$$

The Hadamard gate H, defined in (3.3), is then applied to transform each basis state into a superposition state.

$$H = \frac{1}{\sqrt{2}} \begin{pmatrix} 1 & 1 \\ 1 & -1 \end{pmatrix} \tag{3.3}$$

The resulting superposition states are given in (3.4) and (3.5).

$$H|0\rangle = \frac{1}{\sqrt{2}} \begin{pmatrix} 1 \\ 1 \end{pmatrix} = \frac{1}{\sqrt{2}} (|0\rangle + |1\rangle) = |+\rangle \tag{3.4}$$

$$H|1\rangle = \frac{1}{\sqrt{2}} \begin{pmatrix} 1 \\ -1 \end{pmatrix} = \frac{1}{\sqrt{2}} (|0\rangle - |1\rangle) = |-\rangle \tag{3.5}$$

Thus, classical bit 0 is encoded as the $|+\rangle$ state and classical bit 1 is encoded as the $|-\rangle$ state. The key distinction from classical BPSK modulation is that the information is distributed across the probability amplitudes of the superposition state rather than being concentrated in a single deterministic voltage level. Table 3.1 compares the quantum (Hadamard-based) and classical (BPSK) encoding schemes.

Table 3.1: Comparison of classical and quantum encoding schemes.

Scheme	**Input Bit**	**Transmitted Symbol / State**
Classical (BPSK)	0	$+\frac{1}{2}$
Classical (BPSK)	1	$-\frac{1}{2}$
Quantum (Hadamard)	0	$\frac{1}{\sqrt{2}} (\|0\rangle + \|1\rangle)$
Quantum (Hadamard)	1	$\frac{1}{\sqrt{2}} (\|0\rangle - \|1\rangle)$

Quantum Channel: A composite quantum noise channel model is adopted to simulate realistic transmission conditions [198], incorporating five concurrent noise mechanisms: bit-flip, phase-flip, depolarising, amplitude damping, and phase damping [127]. This channel model is used consistently throughout all sections of this chapter.

The composite channel $\mathcal{N}(\sigma)$, where σ denotes the density matrix of the transmitted qubit, is expressed as in (3.6).

$$\mathcal{N}(\sigma) = (1 - q_{\text{tot}})\,\sigma + q_B\,\mathcal{B}_q(\sigma) + q_P\,\mathcal{P}_q(\sigma) + q_D\,\mathcal{D}_q(\sigma) + q_L\,\mathcal{L}_q(\sigma) + q_\Phi\,\mathcal{F}_q(\sigma) \quad (3.6)$$

where q_{tot} denotes the total noise probability, and q_B, q_P, q_D, q_L, and q_Φ represent the individual probabilities of bit-flip, phase-flip, depolarising, amplitude damping, and phase damping errors, respectively. The formulation constitutes a convex combination of completely positive trace-preserving (CPTP) maps, ensuring physical realisability under the normalisation condition given in (3.7).

$$(1 - q_{\text{tot}}) + q_B + q_P + q_D + q_L + q_\Phi = 1 \quad (3.7)$$

The total noise probability q_{tot} is related to the channel SNR (in dB) through (3.8), ensuring consistency with classical communication models where higher SNR corresponds to lower noise [199].

$$q_{\text{tot}} = \min\left(1,\ \frac{1}{1 + 10^{\text{SNR}/10}}\right) \quad (3.8)$$

To distribute q_{tot} among the five noise channels, independent random weights $v_i \sim \mathcal{U}(0, 1)$ are drawn and normalised as in (3.9).

$$[q_B,\, q_P,\, q_D,\, q_L,\, q_\Phi] = \frac{q_{\text{tot}}}{\sum_{i=1}^{5} v_i} \cdot [v_1,\, v_2,\, v_3,\, v_4,\, v_5] \quad (3.9)$$

The uniform distribution is chosen due to its maximum-entropy property under bounded support, ensuring that no noise type is preferentially weighted in the absence of prior knowledge. All stochastic components are controlled using a fixed random seed (seed = 42) to ensure reproducibility.

The individual noise channel operations are defined as follows.

Bit-flip noise $\mathcal{B}_q$ inverts the qubit state $|0\rangle \leftrightarrow |1\rangle$ with probability q_B, as expressed

in (3.10).

$$\mathcal{B}_q(\sigma) = (1 - q_B)\,\sigma + q_B\,X\sigma X^\dagger \tag{3.10}$$

Phase-flip noise $\mathcal{P}_q$ flips the relative phase of $|1\rangle$ with probability q_P, as shown in (3.11).

$$\mathcal{P}_q(\sigma) = (1 - q_P)\,\sigma + q_P\,Z\sigma Z^\dagger \tag{3.11}$$

Depolarising noise $\mathcal{D}_q$ randomly applies Pauli operators X, Y, or Z with equal probability $q_D/3$, as given in (3.12).

$$\mathcal{D}_q(\sigma) = (1 - q_D)\,\sigma + \frac{q_D}{3}\left(X\sigma X^\dagger + Y\sigma Y^\dagger + Z\sigma Z^\dagger\right) \tag{3.12}$$

Amplitude damping $\mathcal{L}_q$ models energy decay from $|1\rangle$ to $|0\rangle$ with probability q_L, via the Kraus operators defined in (3.13).

$$\mathcal{L}_q(\sigma) = K_0\,\sigma\,K_0^\dagger + K_1\,\sigma\,K_1^\dagger, \quad K_0 = \begin{bmatrix} 1 & 0 \\ 0 & \sqrt{1 - q_L} \end{bmatrix}, \quad K_1 = \begin{bmatrix} 0 & \sqrt{q_L} \\ 0 & 0 \end{bmatrix} \tag{3.13}$$

Phase damping $\mathcal{F}_q$ reduces off-diagonal coherence without altering populations with probability q_Φ, via the Kraus operators defined in (3.14).

$$\mathcal{F}_q(\sigma) = F_0\,\sigma\,F_0^\dagger + F_1\,\sigma\,F_1^\dagger, \quad F_0 = \begin{bmatrix} 1 & 0 \\ 0 & \sqrt{1 - q_\Phi} \end{bmatrix}, \quad F_1 = \begin{bmatrix} 0 & 0 \\ 0 & \sqrt{q_\Phi} \end{bmatrix} \tag{3.14}$$

where X, Y, and Z denote the Pauli operators. It is acknowledged that practical communication systems, including both classical and quantum systems, are affected by additional hardware-specific impairments and implementation non-idealities. However, such hardware-level effects are commonly excluded during the initial stages of communication system development in order to focus on the fundamental transmission behaviour and theoretical performance analysis. Therefore, the adopted abstraction is considered appropriate for evaluating the core communication characteristics of the proposed framework before incorporating more complex hardware-dependent effects in future investigations.

Furthermore, the proposed framework considers a single end-to-end quantum com-

munication channel between the transmitter and receiver. The primary objective is to investigate multimedia transmission over noisy quantum channels from a communication-system perspective, rather than addressing network-level communication involving multiple hops, quantum repeaters, or routing protocols. Although the proposed framework can be extended to support such network-level developments, including multi-hop quantum communication, this would require additional mechanisms such as entanglement swapping, quantum repeaters, routing strategies, and quantum resource management. These aspects are beyond the scope of this thesis and are left for future research.

Quantum Decoder: At the receiver, the quantum decoder employs projective measurement to extract classical information from the received qubit states. For a received quantum state $|\psi\rangle$, the post-measurement state $|\psi'\rangle$ corresponding to measurement outcome m is obtained using (3.15).

$$|\psi'\rangle = \frac{M_m|\psi\rangle}{\sqrt{\langle\psi|M_m^\dagger M_m|\psi\rangle}} \tag{3.15}$$

where M_m denotes the measurement operator corresponding to outcome m, and the denominator ensures normalisation. The measurement operators $M_0 = |0\rangle\langle 0|$ and $M_1 = |1\rangle\langle 1|$ project the received state onto the computational basis states $|0\rangle$ and $|1\rangle$, respectively. As an illustrative example, applying M_1 to an equal superposition state yields the result shown in (3.16) and (3.17).

$$|\psi'\rangle = \frac{|1\rangle\langle 1|\left(\frac{1}{\sqrt{2}}(|0\rangle + |1\rangle)\right)}{\sqrt{\left(\frac{1}{\sqrt{2}}\langle 0| + \frac{1}{\sqrt{2}}\langle 1|\right)(|1\rangle\langle 1|)\left(\frac{1}{\sqrt{2}}(|0\rangle + |1\rangle)\right)}} = +|1\rangle \tag{3.16}$$

$$|\psi'\rangle = \frac{|1\rangle\langle 1|\left(\frac{1}{\sqrt{2}}(|0\rangle - |1\rangle)\right)}{\sqrt{\left(\frac{1}{\sqrt{2}}\langle 0| - \frac{1}{\sqrt{2}}\langle 1|\right)(|1\rangle\langle 1|)\left(\frac{1}{\sqrt{2}}(|0\rangle - |1\rangle)\right)}} = -|1\rangle \tag{3.17}$$

The classical bit value is determined by examining the phase of the projected output state: a positive relative phase corresponds to bit 0 and a negative relative phase corresponds to bit 1. The recovered bitstream is subsequently channel decoded using

polar successive cancellation decoding and source decoded to reconstruct the transmitted image. This measurement framework is used consistently across all sections of this chapter.

Performance Metrics: The reconstructed image quality is evaluated using peak signal-to-noise ratio (PSNR) and structural similarity index measure (SSIM) [200]. PSNR quantifies pixel-level reconstruction accuracy, while SSIM measures the preservation of structural information, luminance, and contrast between the original and reconstructed images. Additionally, bit error rate (BER) is measured to evaluate the transmission-level accuracy of the recovered bitstream prior to source decoding.

3.1.2 Results

This subsection presents a comprehensive evaluation of the proposed quantum communication framework against the classical BPSK-based communication system. The analysis is organised into four parts: rate-distortion performance, visual quality assessment, BER analysis, and discussion of the underlying mechanisms.

Rate-Distortion Performance

The averaged PSNR and SSIM variations of the decoded images as a function of channel SNR for JPEG and HEIF source-encoded images across four QP settings (QP = 25, 50, 75, 100) are presented in Figure 3.2. Across all QP configurations, the proposed quantum communication system consistently achieves higher PSNR and SSIM values than the classical system. The performance advantage is most pronounced in the low-SNR regime (below 10 dB), where channel noise is severe. In this region, the classical system exhibits rapid degradation in both PSNR and SSIM due to increasing bit errors that propagate through the source decoding stage. In contrast, the quantum system maintains comparatively stable reconstruction quality, with significantly smaller reductions in both metrics.

The improvement is consistent across both JPEG and HEIF source-encoded formats, confirming that the performance gain originates from the transmission mechanism rather than the source coding format. Furthermore, the quantum system demonstrates

robust performance even under aggressive compression conditions (QP = 25), where the compressed bitstream is highly sensitive to transmission errors due to strong inter-bit dependencies. Under these conditions, the quantum approach still achieves noticeably better reconstruction fidelity, indicating that the superposition-based encoding effectively mitigates transmission-induced degradation regardless of the source compression level.

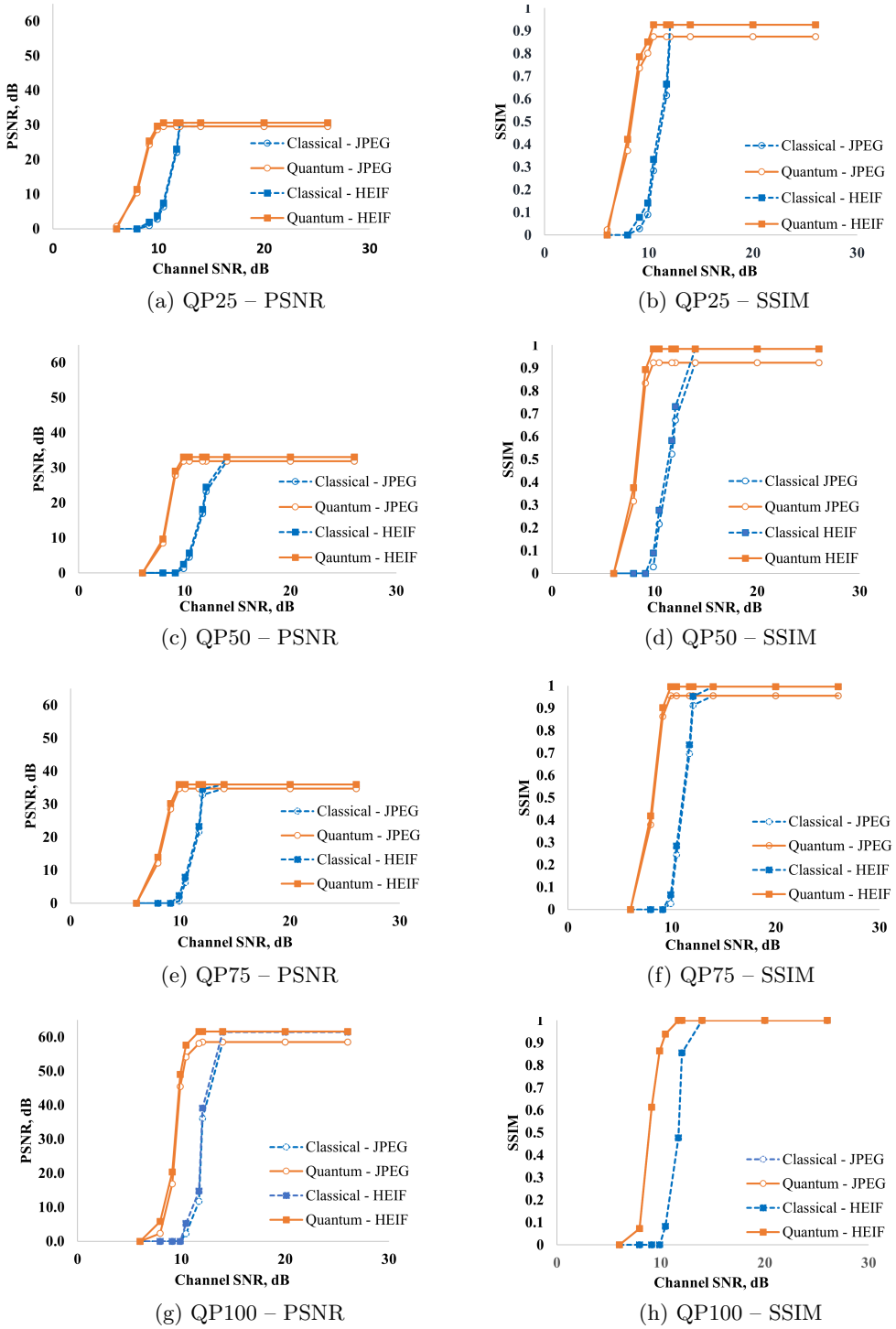
Visual Quality Assessment

Decoded image samples for JPEG-encoded images at QP100 and SNR = 10.45 dB are presented in Figure 3.3. The image reconstructed through the classical communication system exhibits severe visible distortions, including structural corruption, loss of fine details, and noticeable block artefacts caused by bitstream errors introduced during transmission. In contrast, the image reconstructed through the quantum communication system retains substantially better visual quality, with improved edge preservation, reduced artefacts, and clearer structural content. These visual observations are consistent with the quantitative PSNR and SSIM improvements presented in Figure 3.2 and confirm that the measured numerical improvements correspond to perceptually meaningful quality gains.

Bit Error Rate Analysis

The BER versus SNR performance for JPEG-encoded images across all QP settings is presented in Figure 3.4. The quantum communication system consistently achieves lower BER values than the classical system across the entire SNR range. This result directly explains the superior reconstruction quality observed in Figures 3.2 and 3.3: since image reconstruction quality is directly dependent on the accuracy of the recovered bitstream, the reduced BER achieved by the quantum system results in fewer corrupted bits entering the source decoder, thereby producing higher PSNR and SSIM values.

The BER advantage is particularly significant at low SNR levels (below 10 dB), where the classical system suffers from severe bit corruption. In compressed multimedia formats such as JPEG and HEIF, bit errors propagate through the entropy decoding and inverse quantisation stages, causing disproportionate degradation in the reconstructed image. The lower BER achieved by the quantum system substantially reduces this error



(a) QP25 – PSNR (b) QP25 – SSIM

(c) QP50 – PSNR (d) QP50 – SSIM

(e) QP75 – PSNR (f) QP75 – SSIM

(g) QP100 – PSNR (h) QP100 – SSIM

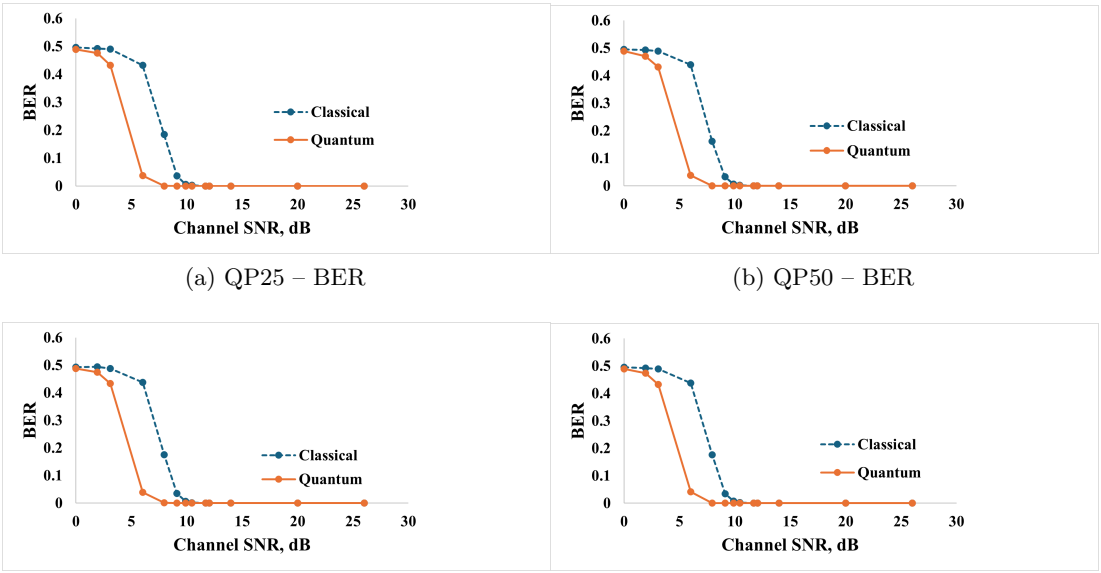
Figure 3.2: Rate-distortion performance measured by averaged PSNR and averaged SSIM of the test images for different QP values (QP = 25, 50, 75, 100).



(a) Classical (b) Quantum

Figure 3.3: Sample decoded images (JPEG) for QP100 and SNR = 10.45 dB.

propagation effect.



(a) QP25 – BER (b) QP50 – BER

(c) QP75 – BER (d) QP100 – BER

Figure 3.4: BER vs. SNR performance of JPEG-format images for quantum and classical communication systems.

Analysis of the Quantum Performance Advantage

The superior performance of the proposed quantum communication system can be attributed to two principal factors: the Hadamard-based superposition encoding mechanism and the resulting reduction in processing complexity.

Superposition-Based Noise Resilience: In classical BPSK transmission, each bit is mapped to a single deterministic voltage level ($+1/2$ or $-1/2$), and detection relies on a fixed binary decision boundary. Under low-SNR conditions, even small noise perturbations can push the received signal across this threshold, resulting in bit errors. In contrast, the proposed quantum framework encodes each bit into a superposition state ($|+\rangle$ or $|-\rangle$), distributing information across the probability amplitudes of the quantum state. When channel noise perturbs the transmitted state, it modifies the amplitude distribution rather than directly corrupting a single deterministic symbol. During reception, projective measurement estimates the transmitted bit by evaluating the probability distribution of the received quantum state, rather than comparing against a fixed threshold. This probabilistic detection mechanism improves the distinguishability between the encoded states $|+\rangle$ and $|-\rangle$ under noisy conditions, particularly when combined with polar channel coding, thereby reducing the probability of incorrect bit detection.

Reduced Latency and Computational Complexity: In addition to improved noise resilience, the proposed framework offers advantages in processing efficiency for image transmission when compared with conventional classical communication systems. Classical communication frameworks commonly require separate processing stages for modulation, channel encoding, demodulation, and iterative channel decoding in order to achieve reliable transmission under noisy channel conditions. These sequential operations introduce additional computational overhead and processing latency, particularly for large image bitstreams. In contrast, the proposed quantum communication framework utilises single-qubit superposition-based transmission, where information is represented directly using quantum state encoding through simple Hadamard operations. Since the framework relies on single-qubit processing rather than complex multi-qubit entanglement operations, the associated quantum circuit complexity remains comparatively low. Furthermore, the quantum state representation enables compact information processing within the transmission framework, reducing the dependence on highly complex signal processing operations commonly employed in classical systems. Although practical quantum communication systems still involve implementation challenges and hardware-related constraints, the proposed framework provides a computationally efficient and

low-complexity transmission model for investigating high-fidelity image communication over noisy channels.

Limitations

Despite the demonstrated performance improvements, the proposed quantum communication system has several limitations that motivate subsequent studies in this chapter. First, the quantum channel remains vulnerable to environmental noise and decoherence effects, and the current framework does not incorporate any QEC mechanism. Consequently, while the superposition-based encoding provides improved resilience compared to classical transmission, the system does not actively detect or correct quantum errors in the quantum domain. Instead, it employs classical error-correction codes after conversion to the classical domain. As a result, quantum errors accumulated during transmission may propagate through the quantum measurement process before correction is applied, potentially degrading the reconstructed image quality under severe channel conditions.

In addition, the proposed framework is based on end-to-end mathematical modelling and does not explicitly consider several practical implementation challenges associated with current quantum communication systems. These include imperfect quantum state preparation and measurement, gate implementation errors, limited qubit coherence times, photon loss, hardware scalability, synchronisation between quantum and classical processing, and the availability of high-fidelity quantum repeaters for long-distance communication. Furthermore, the present framework considers a point-to-point communication scenario and does not model multi-hop quantum networks involving multiple communication links, routing strategies, or entanglement distribution across intermediate nodes. These practical considerations may influence the achievable transmission performance in real-world deployments and require further investigation as quantum communication hardware continues to mature.

To address the absence of quantum-domain error mitigation, Section 3.2 introduces multi-qubit QEC mechanisms specifically designed for the proposed quantum modulation and transmission framework, with the aim of further improving transmission reliability and reconstruction fidelity. The broader practical implementation challenges identified above are considered beyond the scope of this work and represent promising directions

for future research.

3.1.3 Section Summary

This section proposed and evaluated an end-to-end quantum communication framework for image transmission over noisy channels, establishing the foundational system architecture upon which all subsequent sections in this chapter are built. The framework integrates classical source coding (JPEG and HEIF), polar channel coding, Hadamard-based quantum superposition encoding, composite quantum noise channel transmission, and projective measurement-based decoding within a unified pipeline. The experimental results demonstrated that the proposed quantum communication system consistently achieves higher PSNR and SSIM values and lower BER compared to the bandwidth-equivalent classical BPSK system across all tested QP settings and channel conditions. The performance advantage is most significant in the low-SNR regime, where the classical system suffers from rapid quality degradation due to direct bit corruption, whereas the quantum system maintains comparatively stable reconstruction quality. This improvement is attributed to the superposition-based encoding mechanism, which distributes information across probability amplitudes rather than concentrating it in deterministic symbol levels, thereby reducing the susceptibility of individual bits to channel noise. Despite the demonstrated improvements, the current framework does not incorporate any QEC mechanism, leaving the system vulnerable to uncorrected quantum channel errors. This limitation motivates the development of QEC schemes specifically designed for the proposed transmission framework, which is addressed in Section 3.2.

3.2 A Three-Qubit Quantum Error Correction Framework for Image Transmission

Publication Notice

The research presented in this section has been published in the following peer-reviewed journal publication:

U. Jayasinghe, P. Samarathunga, T. Fernando, Y. Ganearachchi, and A. Fernando, "Image transmission over quantum communication systems with three-qubit error correction," *Electronics Letters*, vol. 61, no. 1, e70205, 2025, doi: 10.1049/ell2.70205.

This material is reproduced and adapted under the terms of the IET/Wiley Copyright policy for use in a doctoral thesis. The content has been revised and extended with additional explanations and expanded discussion.

Problem Statement: The superposition-based quantum communication framework proposed in Section 3.1 demonstrated significant performance gains over classical communication for image transmission under noisy conditions. However, its protection against channel impairments relies solely on classical polar coding applied to the bitstream before quantum mapping. Under severe noise conditions or low SNR regimes, this strategy is insufficient: quantum states themselves remain unprotected once they enter the channel, and any corruption that occurs at the qubit level cannot be recovered by the classical channel decoder. This limitation is particularly problematic for compressed image formats such as JPEG and HEIF, where strong bit-level dependencies cause even minor transmission errors to propagate and severely degrade reconstructed image quality.

Limitations of Existing Work: Although QEC is a well-established area in quantum computing, the majority of existing studies focus on protecting stored quantum information for computational operations rather than safeguarding transmitted quantum information in practical communication systems, as discussed in Section 2.14.4 of the literature review. Existing research is therefore primarily directed toward fault-tolerant quantum computation, memory preservation, and logical qubit stability, with limited attention given to real-time multimedia transmission over noisy communication

channels. Furthermore, advanced QEC techniques such as surface codes and stabiliser codes, despite their strong theoretical error-correction capability, impose extremely high physical-qubit overhead, deep circuit requirements, complex syndrome-extraction procedures, and substantial decoding complexity, as identified in Chapter 2. These limitations make them unsuitable for latency-sensitive and bandwidth-constrained applications such as image transmission. In practical image communication scenarios, where large volumes of data must be transmitted efficiently and reconstructed with acceptable visual quality, the computational and qubit resource demands of such QEC schemes become a major limitation. To the best of the author's knowledge, no prior work has systematically investigated low-complexity QEC schemes as a practical quantum channel coding solution within a complete end-to-end image transmission framework, as evidenced by the research gaps identified in Section 2.14.8. In addition, existing studies have not benchmarked the performance of such quantum channel coding approaches against bandwidth-equivalent classical channel coding techniques under identical transmission conditions. This highlights a significant research gap in practical, communication-oriented QEC strategies for image transmission systems.

Motivation and Proposed Contribution: To address this gap, this section investigates the three-qubit QEC code as a practical quantum channel coding technique for image transmission. The three-qubit code is selected because it represents the simplest and most resource-efficient QEC scheme capable of correcting single bit-flip errors, requiring only one logical qubit to be encoded into three physical qubits. Unlike more complex QEC approaches that demand large qubit overhead, deep quantum circuits, and complicated syndrome extraction mechanisms, the three-qubit code provides a low-complexity and computationally feasible solution that is more suitable for bandwidth-constrained and high-throughput image communication systems. Its relatively small redundancy and reduced circuit complexity also make it more practical for near-term quantum communication implementations, where qubit availability and coherence time remain major limitations. The proposed approach integrates the three-qubit QEC directly into the quantum communication pipeline established in Section 3.1, protecting qubits during transmission rather than relying solely on classical bit-level coding. To ensure a fair evaluation, the proposed scheme is benchmarked against a classical rate-1/3 polar

code under identical bandwidth constraints, and its performance is assessed using PSNR, SSIM, and universal quality index (UQI) metrics. The aim is to demonstrate that even a minimal QEC strategy can provide meaningful improvements in transmission robustness and reconstructed image quality, thereby establishing a practical baseline for the more advanced multi-qubit QEC and adaptive QEC schemes presented in the subsequent sections.

3.2.1 System Model

The proposed quantum communication framework with three-qubit error correction is illustrated in Figure 3.5. The system extends the baseline quantum communication framework established in Section 3.1 by incorporating a three-qubit quantum channel coding scheme [162], [163] between the quantum encoder and the quantum channel. The quantum encoding, measurement, and channel model remain identical to those described in Section 3.1: classical bits are mapped to $|0\rangle$ and $|1\rangle$ (Equations (3.1)–(3.2)), transformed into superposition states via the Hadamard gate (Equations (3.3)–(3.5)), and transmitted over the composite noise channel (Equations (3.6)–(3.14)). The information source consists of 50 images from the Microsoft COCO dataset [197], compressed using JPEG or HEIF source encoders.

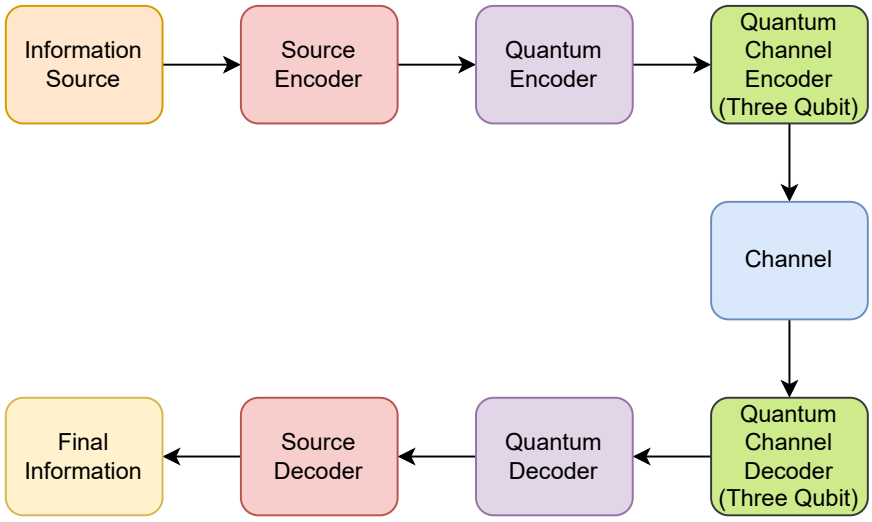


Figure 3.5: End-to-end quantum communication system with three-qubit QEC.

The three-qubit QEC code protects each transmitted logical qubit against single bit-flip errors by encoding it into three physical qubits. The encoding and decoding processes are illustrated in Figure 3.6 and described in the following paragraphs.

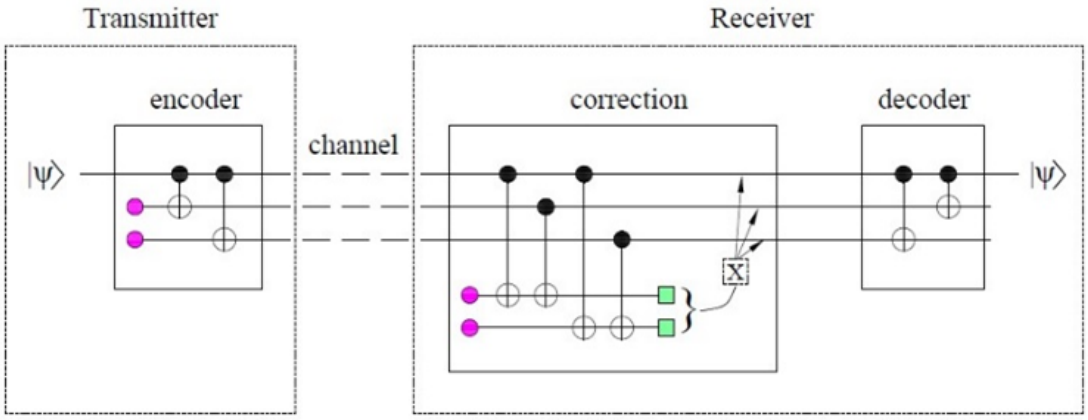


Figure 3.6: Encoding and decoding circuit of the three-qubit error correction method.

Encoding: Consider a logical qubit in the general superposition state $|\psi\rangle = \alpha|0\rangle + \beta|1\rangle$, where α and β are complex probability amplitudes satisfying $|\alpha|^2 + |\beta|^2 = 1$. To encode this qubit, two ancillary qubits initialised in the $|0\rangle$ state are appended, forming the initial three-qubit state given in (3.18).

$$|\psi\rangle \otimes |0\rangle \otimes |0\rangle = \alpha|000\rangle + \beta|100\rangle \tag{3.18}$$

Two sequential CNOT gates are then applied to entangle the three qubits. The first CNOT gate operates with the first qubit as control and the second qubit as target, and the second CNOT gate operates with the first qubit as control and the third qubit as target. The resulting encoding transformation is shown in (3.19).

$$\alpha|000\rangle + \beta|100\rangle \xrightarrow{\text{CNOT}_{1\to2}} \alpha|000\rangle + \beta|110\rangle \xrightarrow{\text{CNOT}_{1\to3}} \alpha|000\rangle + \beta|111\rangle \tag{3.19}$$

The final encoded state $|\psi_L\rangle = \alpha|000\rangle + \beta|111\rangle$ distributes the logical qubit information across three physical qubits. This redundant encoding ensures that if a single bit-flip error occurs on any one of the three qubits during transmission, the error can be detected and corrected without disturbing the encoded quantum information.

Transmission and Error Detection: The encoded three-qubit state is transmitted through the composite quantum noise channel defined in (3.6). During transmission, bit-flip errors may occur on one or more of the three physical qubits, resulting in one of eight possible received states. Table 3.2 lists all possible received states along with the corresponding error positions and ancilla measurement outcomes.

Table 3.2: Received states, error positions, and ancilla measurement outcomes for the three-qubit QEC code.

Received State	**Error Position**	**Ancilla State**
$\alpha\|000\rangle + \beta\|111\rangle$	No error	$\|00\rangle$
$\alpha\|100\rangle + \beta\|011\rangle$	First qubit	$\|11\rangle$
$\alpha\|010\rangle + \beta\|101\rangle$	Second qubit	$\|10\rangle$
$\alpha\|001\rangle + \beta\|110\rangle$	Third qubit	$\|01\rangle$
$\alpha\|110\rangle + \beta\|001\rangle$	First and second qubits	$\|01\rangle$
$\alpha\|101\rangle + \beta\|010\rangle$	First and third qubits	$\|10\rangle$
$\alpha\|011\rangle + \beta\|100\rangle$	Second and third qubits	$\|11\rangle$
$\alpha\|111\rangle + \beta\|000\rangle$	All three qubits	$\|00\rangle$

To identify the error location, two ancilla qubits initialised in the $|00\rangle$ state are coupled to the three data qubits through CNOT gates. The first ancilla qubit is coupled to the first and second data qubits, while the second ancilla qubit is coupled to the second and third data qubits. Measuring these ancilla qubits produces a two-bit syndrome that identifies the error position without collapsing the encoded logical state. Table 3.3 summarises the syndrome values and the corresponding corrective actions.

Table 3.3: Syndrome measurement outcomes and corresponding correction actions.

Syndrome	**Correction Action**
00	No correction required
01	Apply Pauli-X gate to third qubit
10	Apply Pauli-X gate to second qubit
11	Apply Pauli-X gate to first qubit

Decoding: After applying the appropriate corrective Pauli-X gate based on the measured syndrome, the decoder applies two reverse CNOT gates to disentangle the three physical qubits and recover the original logical qubit state $|\psi\rangle = \alpha|0\rangle + \beta|1\rangle$. The recovered logical qubit is then passed to the quantum measurement stage for classical bit extraction, as described in Section 3.1.

Matrix Representation: The entire encoding, error detection, and decoding process is implemented using matrix representations. Three-qubit states are constructed via the tensor product, as shown in (3.20).

$$|000\rangle = |0\rangle \otimes |0\rangle \otimes |0\rangle, \qquad |111\rangle = |1\rangle \otimes |1\rangle \otimes |1\rangle \tag{3.20}$$

The encoded state $\alpha|000\rangle + \beta|111\rangle$ is represented as the eight-dimensional state vector S given in (3.21).

$$S = \alpha \begin{pmatrix} 1 \\ 0 \\ 0 \\ 0 \\ 0 \\ 0 \\ 0 \\ 0 \end{pmatrix} + \beta \begin{pmatrix} 0 \\ 0 \\ 0 \\ 0 \\ 0 \\ 0 \\ 0 \\ 1 \end{pmatrix} \tag{3.21}$$

During decoding, the received state vector is compared against the set of eight possible state vectors listed in Table 3.4 to identify the error pattern and recover the logical qubit.

Baseline for Comparison: To ensure a fair comparison, the three-qubit QEC method is benchmarked against a classical communication system using BPSK modulation with rate-1/3 polar codes. The classical code rate of 1/3 is chosen to match the bandwidth utilisation of the three-qubit QEC scheme, which transmits three physical qubits for every one logical qubit. This bandwidth-equivalent comparison ensures that any observed performance difference is attributable to the encoding and error correction mechanism rather than differences in spectral efficiency. A range of images with varying spatial information content from the COCO dataset is used, and results are reported as averaged image quality metrics.

Table 3.4: Possible received states and corresponding eight-dimensional state vectors.

Received State	**State Vector**
$\frac{1}{\sqrt{2}}(\|000\rangle \pm \|111\rangle)$	$\begin{pmatrix} 1 \\ 0 \\ 0 \\ 0 \\ 0 \\ 0 \\ 0 \\ \pm 1 \end{pmatrix}$
$\frac{1}{\sqrt{2}}(\|001\rangle \pm \|110\rangle)$	$\begin{pmatrix} 0 \\ 1 \\ 0 \\ 0 \\ 0 \\ 0 \\ \pm 1 \\ 0 \end{pmatrix}$
$\frac{1}{\sqrt{2}}(\|010\rangle \pm \|101\rangle)$	$\begin{pmatrix} 0 \\ 0 \\ 1 \\ 0 \\ 0 \\ \pm 1 \\ 0 \\ 0 \end{pmatrix}$
$\frac{1}{\sqrt{2}}(\|100\rangle \pm \|011\rangle)$	$\begin{pmatrix} 0 \\ 0 \\ 0 \\ \pm 1 \\ 1 \\ 0 \\ 0 \\ 0 \end{pmatrix}$

3.2.2 Results

This subsection evaluates the performance of the proposed three-qubit QEC-based quantum communication system against both the quantum polar-coded system without QEC (presented in Section 3.1) and the bandwidth-equivalent classical system employing BPSK modulation with rate-1/3 polar codes. The analysis is organised into three parts: rate-distortion performance, visual quality assessment, and analysis of the error correction mechanism.

Rate-Distortion Performance

The averaged PSNR and SSIM of the decoded images as a function of channel SNR for JPEG and HEIF source-encoded images across four QP settings (QP = 25, 50, 75, 100) are presented in Figure 3.7. First, the proposed three-qubit QEC-based quantum system (green line) consistently achieves the highest PSNR and SSIM values among all three systems across every QP setting and channel condition. At low SNR values (below 5 dB), the three-qubit system achieves approximately 28–30 dB PSNR while both the quantum polar-coded system and the classical system remain near 0 dB, indicating complete reconstruction failure. This demonstrates that the three-qubit QEC scheme provides a substantial SNR gain of approximately 5–6 dB over the quantum polar-coded system and approximately 10–11 dB over the classical system in the low-SNR regime.

Second, the quantum polar-coded system (blue line) consistently outperforms the classical polar-coded system (orange line) across the entire SNR range, confirming the inherent advantage of superposition-based encoding over classical BPSK modulation as established in Section 3.1. However, the additional incorporation of three-qubit QEC further extends this advantage by shifting the performance curve to lower SNR values, demonstrating that quantum-level error correction provides complementary protection beyond what superposition encoding alone can achieve.

Third, the classical polar-coded system exhibits the poorest performance across all operating conditions, requiring significantly higher SNR values (approximately 10–15 dB) to achieve comparable PSNR and SSIM levels to those obtained by the three-qubit quantum system at 0–5 dB. This performance gap is particularly severe under aggressive compression (QP25), where the compressed bitstream is highly sensitive to residual bit

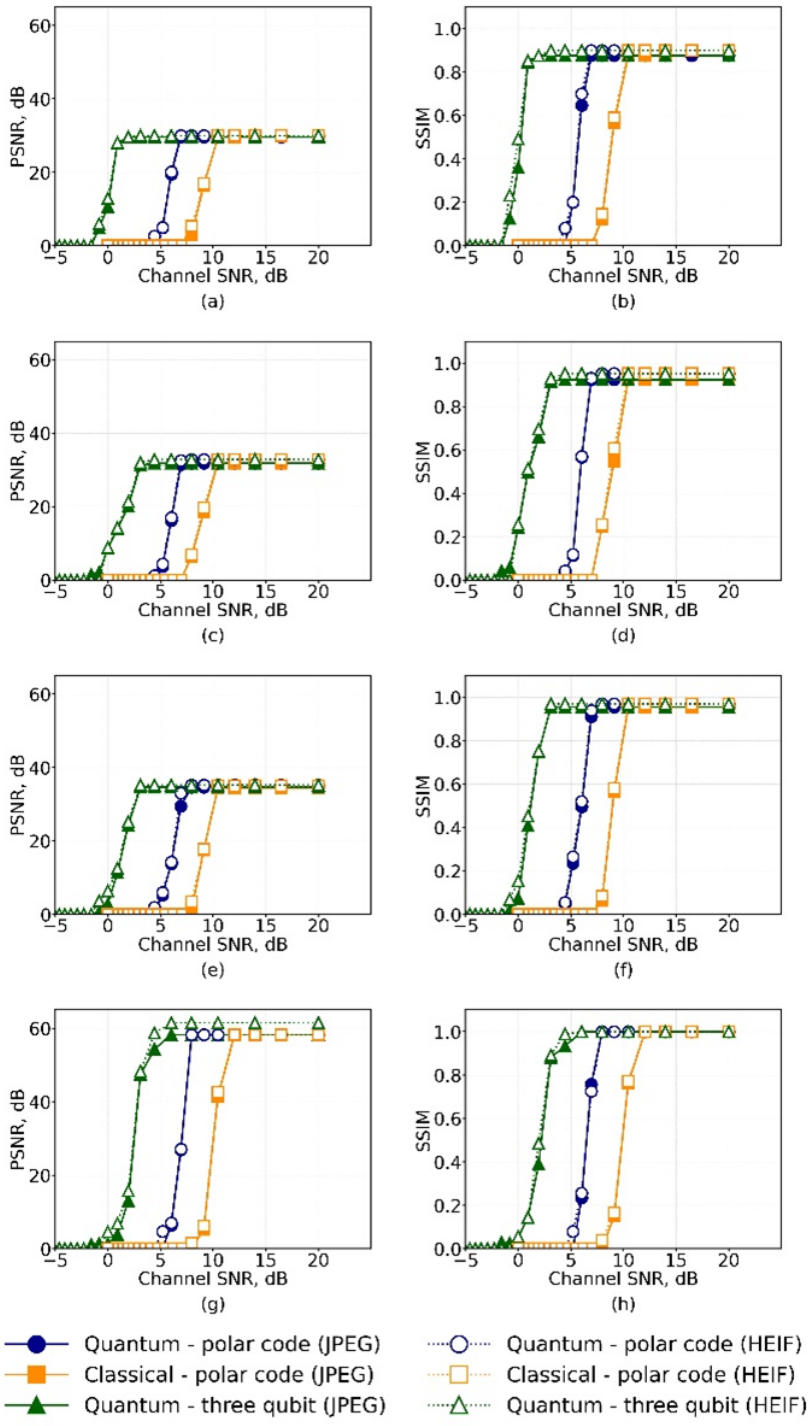


Figure 3.7: Rate-distortion performance measured by averaged PSNR and averaged SSIM of the test images for quantum three-qubit QEC, quantum polar-coded, and classical polar-coded systems across different QP values (QP = 25, 50, 75, 100) using JPEG and HEIF image formats: (a) QP25 - PSNR, (b) QP25 - SSIM, (c) QP50 - PSNR, (d) QP50 - SSIM, (e) QP75 - PSNR, (f) QP75 - SSIM, (g) QP100 - PSNR, (h) QP100 – SSIM.

errors. The classical system fails to produce meaningful reconstruction at SNR values below approximately 8 dB, whereas the proposed three-qubit QEC system maintains usable image quality even at SNR values as low as -2 dB.

The improvement is consistent across both JPEG and HEIF source coding formats for all three systems, confirming that the observed performance differences originate from the transmission and error correction mechanisms rather than the source coding method.

Visual Quality Assessment

Decoded image samples for JPEG-encoded images at QP25 and SNR = 6 dB, representing a challenging operating point with both aggressive source compression and severe channel noise, are presented in Figure 3.8. The image reconstructed through the classical polar-coded system exhibits severe visual corruption, including complete loss of structural content and widespread artefacts, indicating that the channel decoder was unable to recover a sufficient number of bits for meaningful source decoding. In contrast, the image reconstructed through the proposed three-qubit QEC-based quantum system retains substantially better visual quality, with preserved structural content, recognisable image features, and significantly reduced artefacts.

The visual comparison confirms that the quantitative PSNR and SSIM improvements reported in Figure 3.7 correspond to perceptually meaningful quality gains, particularly under low-SNR conditions where the classical system fails to produce a usable reconstruction.

Analysis of the Error Correction Mechanism

The superior performance of the proposed system is attributed to a fundamental difference in where error correction is applied within the transmission pipeline. In the proposed three-qubit QEC scheme, error detection and correction are performed directly at the quantum state level, prior to the measurement process. By encoding each logical qubit into three physical qubits, the system introduces controlled redundancy that enables the receiver to detect inconsistencies caused by channel noise through syndrome measurements and recover the original quantum state using majority-based correction.



(a) Quantum-three-qubit (b) Quantum-polar code

Figure 3.8: Sample decoded images (JPEG) for QP25 and SNR = 6 dB.

Critically, this correction occurs before the quantum state is projected onto classical bit values, meaning that transmission errors are resolved while the quantum information is still intact.

In contrast, classical channel coding operates on binary symbols that have already been obtained through detection or measurement. At this stage, any noise-induced corruption has already been committed to the detected bit sequence, and the channel decoder must attempt to reverse these errors using only the redundancy structure of the classical code. When the noise level is sufficiently high, the number of corrupted symbols exceeds the correction capability of the classical code, resulting in residual bit errors that propagate into the source decoder and cause significant image quality degradation.

The key advantage of the quantum approach is therefore that error correction is applied before the irreversible measurement step, whereas classical error correction is applied after detection. This distinction allows the three-qubit QEC scheme to prevent bit errors from entering the decoded bitstream in the first place, rather than attempting to correct them after they have already occurred. This mechanism directly accounts for the lower BER, higher PSNR, higher SSIM, and improved UQI performance observed in the experimental results, particularly under low-SNR conditions where channel noise is dominant.

Despite the demonstrated improvements, the proposed three-qubit QEC scheme has several limitations that must be acknowledged. From an error correction perspective,

the three-qubit code is designed exclusively to correct single bit-flip errors within each encoded block. It cannot detect or correct phase-flip errors, combined bit-and-phase errors, or simultaneous multi-qubit errors, all of which occur in practical quantum channels as modelled by the composite noise channel in (3.6). Consequently, when the channel noise level is sufficiently high that multiple errors occur within a single three-qubit block, the correction mechanism fails and the resulting bit errors propagate into the source decoder, degrading reconstruction quality.

From a bandwidth efficiency perspective, the three-qubit code operates at a fixed code rate of 1/3, requiring three physical qubits to protect every single logical qubit. This introduces a threefold increase in the number of transmitted qubits compared to an uncoded quantum transmission, resulting in significant bandwidth overhead. In bandwidth-constrained communication scenarios, this fixed overhead reduces spectral efficiency and limits the achievable data throughput, regardless of whether the channel conditions are favourable or severe.

Furthermore, the fixed code rate represents a fundamental inflexibility in the current design. Under high-SNR conditions, where channel noise is minimal and errors are infrequent, the full redundancy of the three-qubit code is unnecessary, leading to wasteful bandwidth consumption. Conversely, under very low-SNR conditions, the single-error correction capability may be insufficient to handle the increased error rate, resulting in residual uncorrected errors. An ideal system would dynamically adapt its error correction strategy based on the instantaneous channel conditions, applying stronger protection when noise is severe and reducing redundancy when the channel is favourable.

These limitations collectively motivate the development of an adaptive QEC framework that dynamically adjusts the error correction parameters based on real-time channel conditions. Such a framework would optimise the trade-off between transmission reliability, bandwidth efficiency, and reconstruction quality across varying channel environments. This adaptive approach is developed and evaluated in Section 3.3.

3.2.3 Section Summary

This section investigated the integration of three-qubit QEC into the proposed quantum communication framework for image transmission over noisy channels. The experimental

results demonstrated that the three-qubit QEC-based quantum system consistently outperforms both the quantum polar-coded system without QEC and the bandwidth-equivalent classical system employing rate-1/3 polar codes across all tested compression levels and channel conditions. At convergence, the proposed system achieved PSNR values of up to 64.5 dB for HEIF and 58.3 dB for JPEG-encoded images, SSIM values of up to 0.9997 for HEIF and 0.9994 for JPEG, and UQI values of up to 0.9999 for HEIF and 0.9998 for JPEG compared to the reference systems. Notably, the three-qubit QEC system maintained reliable image reconstruction at SNR values as low as 6 dB, where both the quantum polar-coded and classical systems exhibited significant quality degradation.

The performance improvement is attributed to the fundamental advantage of performing error correction at the quantum state level prior to measurement, which prevents bit errors from entering the decoded bitstream rather than attempting to correct them after detection. However, the three-qubit code is limited to correcting single bit-flip errors at a fixed code rate of 1/3, resulting in unnecessary bandwidth overhead under favourable channel conditions and insufficient protection under severe noise. These limitations motivate the development of an adaptive multi-qubit QEC framework capable of dynamically adjusting error correction parameters based on channel conditions, which is presented in Section 3.3.

3.3 An Adaptive Quantum Error Correction Framework for Reliable Quantum Image Transmission

Publication Notice

The research presented in this section has been published in the following peer-reviewed conference publication:

U. Jayasinghe, T. Fernando, and A. Fernando, "Optimizing quantum image transmission through an adaptive quantum error correction framework," in *Proc. IEEE Int. Conf. Consumer Electron. (ICCE)*, 2026, doi: 10.1109/ICCE67443.2026.11449609.

This material is reproduced and adapted under the terms of the IEEE Copyright policy for use in a doctoral thesis. The content has been revised and extended with additional explanations and expanded discussion.

Problem Statement: The three-qubit QEC scheme introduced in Section 3.2 significantly improves image transmission robustness compared to conventional classical channel coding approaches. However, the system operates using a fixed code rate, where every logical qubit is always encoded into the same number of physical qubits regardless of the current channel condition. As a result, the level of protection remains constant even when the channel quality changes. This fixed protection strategy creates important practical limitations. Under severe noisy channel conditions, the single-error-correction capability of the three-qubit code becomes insufficient to adequately protect the transmitted quantum information, leading to a rapid degradation in reconstructed image quality. Since the three-qubit scheme already represents the minimum redundancy required for single bit-flip error correction, the protection level cannot be further reduced to improve transmission efficiency or adjusted dynamically according to channel conditions. In practical wireless communication environments, the channel SNR continuously varies due to noise, interference, and environmental effects. Therefore, a fixed-rate QEC approach cannot efficiently adapt to changing channel conditions. A protection level that is sufficient under moderate noise conditions may become inadequate under more severe channel impairments. Consequently, fixed-rate QEC schemes remain limited in their ability to maintain consistently reliable multimedia transmission across dynamically

varying communication channels.

Limitations of Existing Work: The three-qubit QEC scheme significantly improves transmission robustness compared to conventional communication approaches; however, its error-correction capability remains limited under severe noisy channel conditions. Since the three-qubit code is designed primarily for single bit-flip error correction, its protection capability becomes insufficient as channel noise and decoherence effects increase. This limitation motivates the extension of the communication framework toward higher-order multi-qubit QEC schemes such as five, seven, and nine-qubit codes, which provide stronger error protection and improved transmission reliability. Although multi-qubit QEC schemes have been extensively studied in quantum computing literature, existing research primarily focuses on fault-tolerant computation and logical qubit preservation rather than practical image communication systems. In particular, limited attention has been given to evaluating the effectiveness of multi-qubit QEC techniques for quantum communication, especially in terms of transmission robustness, error resilience, and reconstructed image quality over noisy channels. Furthermore, existing studies have not systematically investigated how different multi-qubit QEC schemes influence communication performance under varying channel conditions within an end-to-end image transmission framework. To the best of the author's knowledge, no prior work has comprehensively analysed and compared the communication performance of multiple QEC schemes, including three, five, seven, and nine-qubit codes, specifically for image transmission applications. Therefore, investigating higher-order multi-qubit QEC schemes becomes important to address the limited error-protection capability of the three-qubit code and to improve transmission reliability under increasingly severe channel conditions.

Motivation and Proposed Contribution: To overcome the limited error-protection capability of the three-qubit QEC scheme, this section proposes an adaptive multi-qubit QEC framework that dynamically selects the QEC code configuration among three, five, seven, and nine-qubit schemes according to the prevailing channel SNR. These multi-qubit QEC schemes are specifically selected because they provide progressively stronger error-correction capability while maintaining a relatively structured and scalable

encoding framework suitable for practical quantum communication systems. Compared to more complex QEC approaches such as surface codes and stabiliser codes, multi-qubit repetition-based QEC schemes require lower circuit complexity, reduced syndrome-processing requirements, and more manageable physical-qubit overhead, making them more feasible for multimedia transmission applications under current quantum hardware limitations. The underlying principle of the proposed adaptive framework is that stronger QEC protection becomes necessary as channel conditions deteriorate. Under low-SNR conditions, higher-order QEC schemes such as seven and nine-qubit codes provide improved resilience against noise and decoherence by introducing greater redundancy and stronger quantum-state protection. Conversely, under favourable channel conditions, lower-order schemes such as the three-qubit code provide sufficient protection with lower complexity and reduced redundancy. By dynamically matching the QEC strength to the channel condition, the proposed framework avoids the limitations associated with relying on a single fixed QEC configuration across all operating scenarios. This adaptive strategy enables a more effective balance between transmission robustness, bandwidth utilisation, and computational complexity. The framework is evaluated against all fixed-rate QEC variants using both JPEG and HEIF source coding formats, with performance assessed using PSNR, SSIM, and UQI metrics. The experimental results demonstrate that adaptive multi-qubit QEC consistently achieves improved reconstructed image quality across a wide range of channel conditions, thereby establishing a practical foundation for the quantum video transmission framework presented in Section 3.4.

3.3.1 System Model

The proposed adaptive QEC-based quantum communication system for image transmission is illustrated in Figure 3.9. The system extends the three-qubit QEC framework presented in Section 3.2 by introducing two key enhancements: (i) support for multiple QEC code configurations (three, five, seven, and nine-qubit codes), and (ii) an adaptive code selection mechanism that dynamically switches among these configurations based on real-time channel conditions. The quantum encoding, measurement operators, and composite noise channel follow the framework established in Section 3.1 (Equations (3.1)–(3.14)).

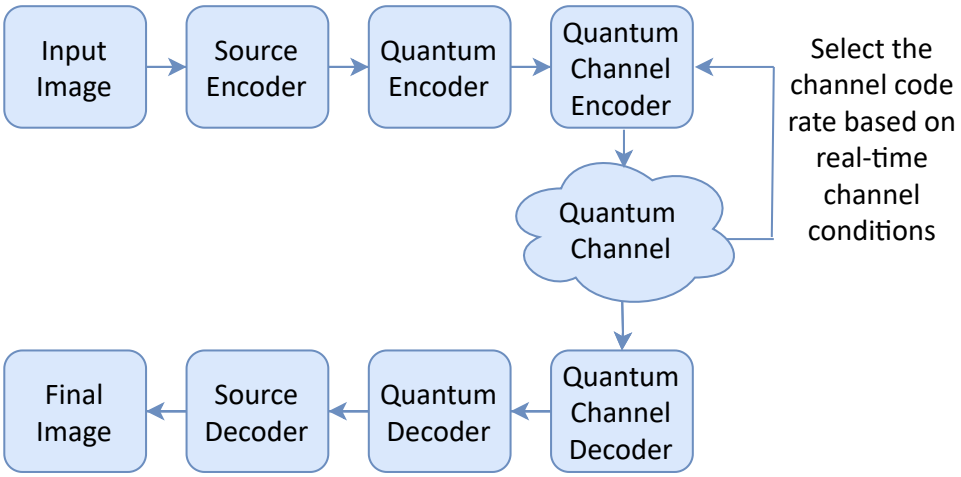


Figure 3.9: Proposed adaptive QEC-based quantum image communication system.

Dataset and Source Encoding: A total of 100 images from the Microsoft COCO dataset [197], each with a resolution of 256×192 pixels and varying spatial complexity, are used as input. Images are source encoded using both JPEG and HEIF formats. To ensure fair comparison across all QEC configurations, the source compression (QP values) are adjusted such that all configurations produce equal-length qubit streams after encoding. Specifically, higher-qubit QEC systems (which introduce greater redundancy) apply stronger source compression to maintain the same total transmission bandwidth as lower-qubit systems with lighter compression. This bandwidth normalisation ensures that observed performance differences are attributable to the error correction mechanism rather than differences in spectral efficiency.

Multi-Qubit QEC: Four QEC codes are employed in this study: three-qubit (Q3), five-qubit (Q5), seven-qubit (Q7), and nine-qubit (Q9). Each code encodes one logical qubit into n physical qubits ($n \in \{3, 5, 7, 9\}$), with the encoding and decoding procedures following the same CNOT-entanglement and syndrome-correction structure described in Section 3.2. These configurations are selected because these codes represent the canonical families of quantum error-correcting codes that established the foundations of QEC. The three-qubit repetition code is the simplest code capable of correcting a single bit-flip or phase-flip error, the five-qubit code is the smallest code that can correct an arbitrary single-qubit error, while the seven-qubit Steane code and nine-qubit Shor code

provide fault-tolerant error correction through increased redundancy. Owing to their well-defined theoretical properties, widespread adoption as benchmark QEC codes, and increasing levels of redundancy and error-correction capability, these codes provide a systematic basis for evaluating the trade-off between transmission reliability, coding overhead, and multimedia communication performance.

The three-qubit case, illustrated in Figure 3.10, serves as the basis; the five, seven, and nine-qubit codes extend the same principle by entangling additional physical qubits to provide progressively stronger error correction capability at the cost of increased redundancy.

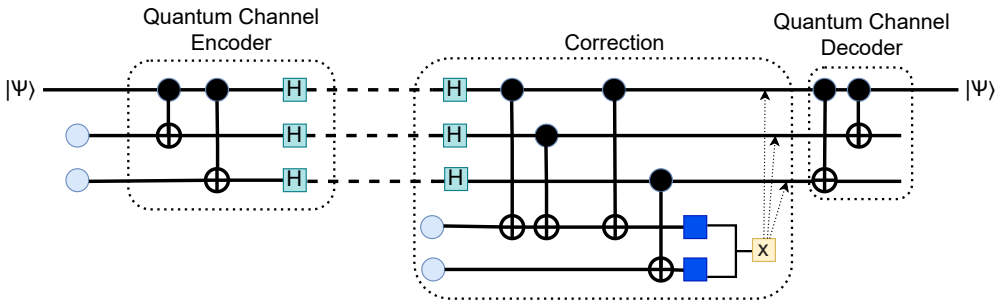


Figure 3.10: Quantum three-qubit encoder and decoder circuit.

A key distinction from the framework in Section 3.2 is that, in this study, the encoded states are additionally transformed using Hadamard operations prior to transmission. For the three-qubit case, the encoding proceeds as follows. The logical qubit $|\psi\rangle = \alpha|0\rangle + \beta|1\rangle$ is first encoded into the entangled state $\alpha|000\rangle + \beta|111\rangle$ using the CNOT-based procedure described in Section 3.2. Hadamard gates are then applied to each physical qubit, transforming the encoded state from the computational basis into the Hadamard basis, yielding the transmission state $\alpha|{+}{+}{+}\rangle + \beta|{-}{-}{-}\rangle$. This additional transformation distributes the encoded information across superposition states rather than deterministic basis states, improving robustness against channel noise by ensuring that perturbations affect the amplitude distribution rather than directly corrupting individual basis states.

At the receiver, the inverse Hadamard transformation is first applied to convert the received state back into the computational basis. Syndrome measurement is then performed using ancilla qubits to identify the error location, and the corresponding Pauli-X correction is applied based on the syndrome values listed in Section 3.2, Tables 3.2

and 3.3. The corrected logical qubit is subsequently passed to the quantum measurement stage for classical bit extraction.

Adaptive Code Selection Mechanism:

The adaptive QEC framework dynamically selects the optimal code configuration based on the estimated channel SNR. Under low-SNR conditions, where error rates are high, the system selects higher-qubit codes (Q7 or Q9) that provide stronger error correction capability at the reduced maximum achievable image quality due to stronger source compression. Under high-SNR conditions, where errors are infrequent, the system switches to lower-qubit codes (Q3 or Q5) that offer reduced redundancy, lower computational complexity, and higher maximum reconstruction quality. This adaptive switching optimises the trade-off between error resilience and reconstruction fidelity across the entire operating SNR range.

The proposed adaptive QEC framework emulates the operation of a practical adaptive communication system by dynamically selecting the QEC configuration according to the estimated channel quality. In a practical implementation, the receiver periodically estimates the channel condition using pilot symbols or reference signals transmitted through the communication channel. The estimated channel state information (CSI) is then returned to the transmitter through a reliable classical feedback channel, which reconfigures the QEC encoder for the subsequent transmission block. This adaptive procedure enables the communication system to continuously adjust the amount of error-correction redundancy according to the prevailing channel conditions.

In the proposed framework, this adaptive behaviour is represented through end-to-end mathematical modelling. At each transmission interval, the receiver estimates the channel SNR and feeds this information back to the transmitter, which selects the appropriate QEC configuration according to predefined SNR thresholds. Specifically, the operating SNR range is divided into four regions corresponding to the Q9, Q7, Q5, and Q3 configurations. Q9 is selected under the lowest SNR conditions, where transmission errors are most severe, followed by Q7 and Q5 for intermediate channel conditions, while Q3 is selected for high-SNR channels where the error probability is minimal.

The switching thresholds are determined empirically from the crossover regions of the individual QEC performance curves shown in Figure 3.11. These crossover regions represent the SNR values at which two adjacent QEC configurations achieve approximately equal reconstruction performance. Consequently, switching within these regions ensures that the selected QEC configuration consistently provides the highest reconstruction quality while avoiding unnecessary coding redundancy. This threshold-selection principle is consistent with adaptive communication techniques in conventional communication systems [201], where transmission parameters are selected according to channel quality to maximise overall system performance.

The proposed switching strategy is inherently robust because the threshold values are selected from relatively broad crossover regions rather than from isolated operating points. Around these regions, adjacent QEC configurations exhibit very similar reconstruction performance, resulting in smooth transitions between coding schemes. Consequently, small variations in the switching thresholds caused by practical channel estimation uncertainty or feedback delay are expected to have only a limited influence on the selected QEC configuration and the resulting reconstruction quality. Therefore, the performance improvements achieved by the proposed adaptive framework are not dependent on a single threshold selection but remain stable over a practical range of threshold values.

This threshold-based switching strategy enables the adaptive framework to operate along the upper envelope of the individual QEC performance curves across the entire SNR range, thereby achieving improved error resilience under low-SNR conditions while maintaining high reconstruction quality when channel conditions improve. Since the switching operation requires only a comparison between the estimated SNR and the stored threshold values, the additional computational overhead associated with adaptive code selection is negligible.

This study assumes perfect CSI at the receiver for SNR estimation, thereby establishing an upper performance bound for the proposed adaptive framework. In practical communication systems, the CSI estimate would be obtained from pilot or reference signals and returned to the transmitter through a classical feedback channel. Although estimation errors and feedback delays may occasionally result in suboptimal QEC selection, particularly near the switching boundaries, the adaptive framework is expected to

retain its overall performance advantages because adjacent QEC configurations exhibit similar reconstruction performance around their crossover regions. All reported performance metrics are averaged over 1,000 independent simulation runs to ensure statistical reliability.

Threshold Sensitivity Analysis:

To evaluate the robustness of the proposed adaptive switching strategy, a threshold sensitivity analysis is performed by varying all switching thresholds by ± 1 dB from their nominal values. Specifically, three switching configurations are considered: the nominal thresholds, thresholds reduced by 1 dB, and thresholds increased by 1 dB. All other simulation parameters are kept unchanged to ensure a fair comparison.

The average PSNR, SSIM, and UQI are evaluated for each threshold configuration over the entire SNR range. An average PSNR variation of less than 0.15 dB, an average SSIM variation of less than 0.002, and an average UQI variation of less than 0.00055 are observed across the three threshold configurations, while the adaptive framework consistently achieves higher reconstruction quality than the individual fixed-QEC schemes. These results indicate that the proposed adaptive framework is not highly sensitive to moderate variations in the switching thresholds.

This behaviour is attributed to the selection of switching thresholds within the crossover regions of adjacent QEC performance curves. Since neighbouring QEC configurations exhibit similar reconstruction performance around these regions, only a limited number of switching decisions are affected by small threshold variations. Consequently, the overall reconstruction quality is maintained, demonstrating that the performance improvement is achieved by the adaptive QEC selection mechanism rather than by a particular choice of threshold values.

3.3.2 Results

This subsection evaluates the proposed adaptive QEC framework in three stages: first, the individual performance of each fixed-qubit QEC configuration is analysed; second, the adaptive code selection mechanism is evaluated; and third, the proposed system is compared against classical error correction approaches. Performance is assessed

using PSNR, SSIM, and UQI, averaged over 100 test images under identical bandwidth conditions.

Performance of Individual QEC Configurations

The PSNR variation as a function of channel SNR for the four fixed-qubit QEC configurations (Q3, Q5, Q7, Q9) applied to HEIF-compressed images is presented in Figure 3.11 as an example case. Two competing effects are observed as the number of encoding qubits increases. First, higher-qubit codes achieve superior performance in the low-SNR regime. The Q9 configuration maintains usable image quality at SNR values as low as -10 dB, where the Q3, Q5, and Q7 configurations have already failed. This improvement arises because higher-qubit codes encode logical qubits into higher-dimensional Hilbert spaces (2^n-dimensional for n qubits), providing greater capacity to detect and correct multiple transmission errors.

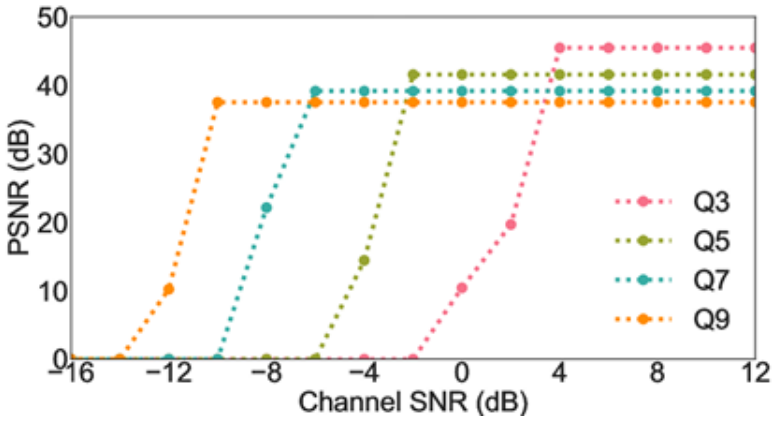
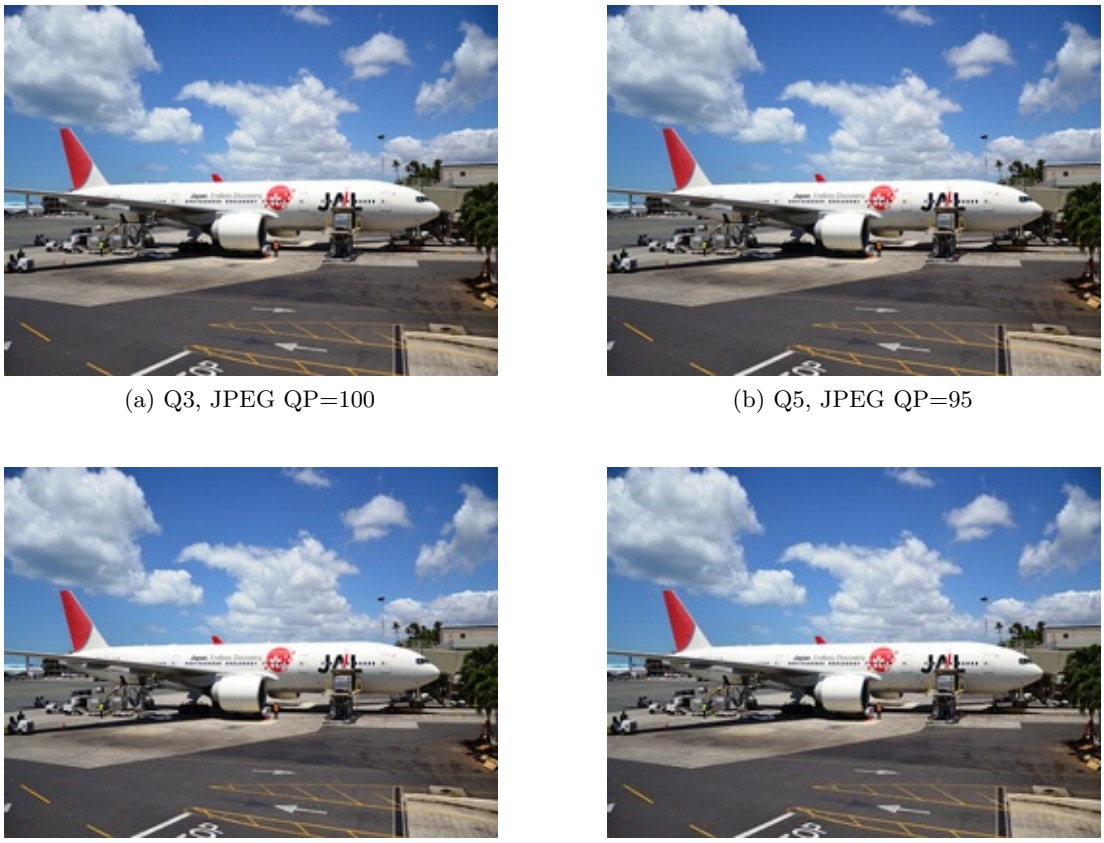


Figure 3.11: PSNR variation with channel SNR for different multi-qubit QEC configurations applied to HEIF-compressed images.

Second, higher-qubit codes achieve lower maximum PSNR values at high SNR. This is a direct consequence of the bandwidth normalisation constraint: since Q9 requires nine physical qubits per logical qubit, stronger source compression must be applied to maintain equal bandwidth, resulting in higher source distortion that limits the maximum achievable reconstruction quality. Conversely, Q3 requires only three physical qubits per logical qubit, allowing lighter compression and higher peak PSNR when channel errors are negligible. These competing effects confirm that no single fixed-qubit configuration is optimal across the entire SNR range, thereby motivating the adaptive code selection

approach. A similar performance trend can also be observed for the JPEG images.



(a) Q3, JPEG QP=100

(b) Q5, JPEG QP=95

(c) Q7, JPEG QP=93

(d) Q9, JPEG QP=88

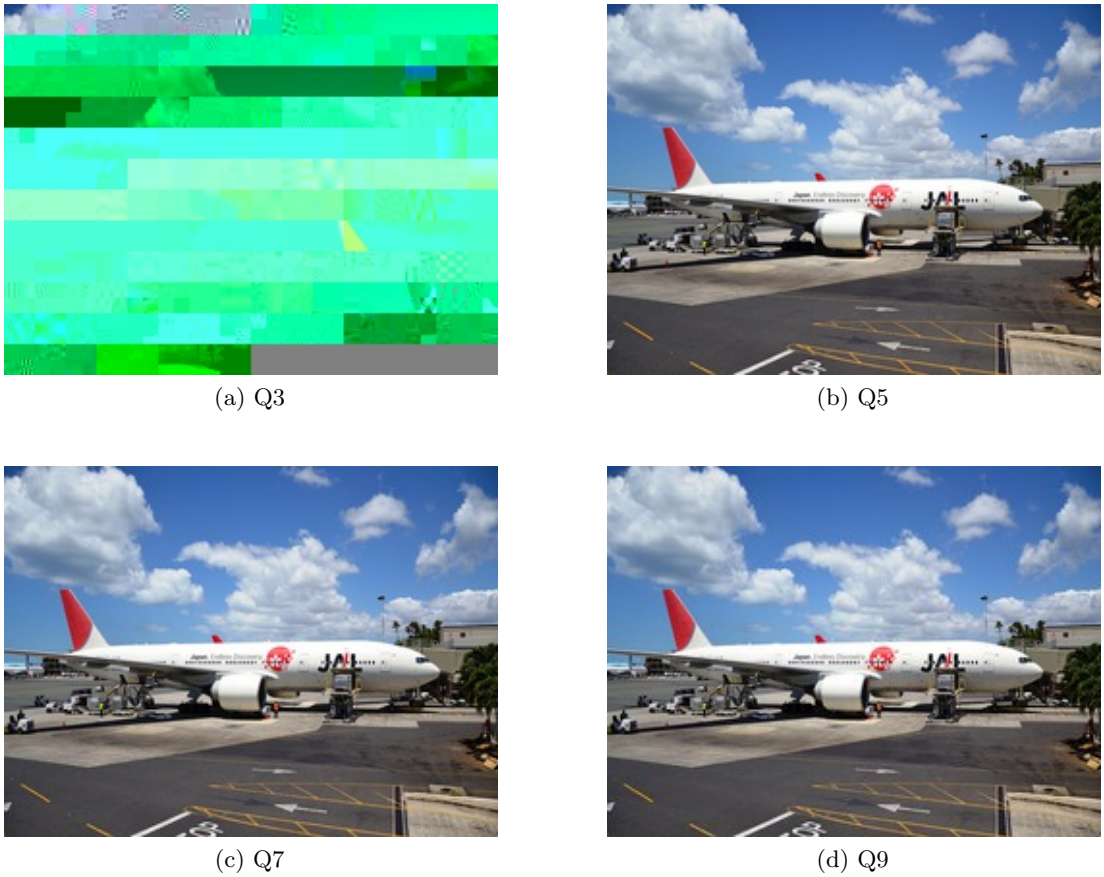
Figure 3.12: Input JPEG images for different QEC schemes: (a) Q3, (b) Q5, (c) Q7, and (d) Q9.

Table 3.5: Rate–distortion performance of JPEG compression at different QP settings.

Version	**QP**	**Size (B)**	**Bits**	**PSNR (dB)**	**SSIM**
Q3	100	48,540	388,320	37.33	0.9711
Q5	95	25,116	200,928	35.20	0.9478
Q7	93	20,979	167,832	34.39	0.9396
Q9	88	16,117	128,936	32.95	0.9276

To provide visual confirmation, Figure 3.12 presents representative input JPEG images for the Q3, Q5, Q7, and Q9 systems. These images exhibit different quality levels compared with the original image due to the compression mechanism applied to maintain equivalent transmission bandwidth across the different QEC schemes, as described in the source coding stage. The corresponding JPEG quality settings, file sizes, number

of bits, PSNR, and SSIM values are summarised in Table 3.5. It is important to note that the product of the QEC qubit size and the corresponding bitstream length remain approximately constant across all QEC configurations, ensuring that the total number of represented qubits remains unchanged irrespective of the selected QEC dimension.



(a) Q3 (b) Q5

(c) Q7 (d) Q9

Figure 3.13: Decoded JPEG images at an SNR of 0 dB for different QEC schemes: (a) Q3, (b) Q5, (c) Q7, and (d) Q9.

To further analyse the performance of the proposed QEC schemes over noisy channels, representative decoded JPEG images at different SNR levels are presented. At an SNR of 0 dB (Figure 3.13), the reconstructed image quality improves as the number of qubits in the QEC scheme increases. The Q3 scheme produces a visibly noisy image with noticeable blocking and compression artefacts, whereas the Q5, Q7, and Q9 schemes achieve their respective maximum reconstruction quality. This trend is consistent with the corresponding PSNR and SSIM results.

At an SNR of -5 dB (Figure 3.14), the Q3 scheme is unable to reconstruct a

decodable image because the high channel BER introduces excessive bit errors into the compressed JPEG bitstream. In contrast, the Q5 scheme exhibits noticeable artefacts, whereas the Q7 and Q9 schemes successfully recover the image. Among these, the higher-qubit QEC schemes achieve the highest visual quality, PSNR, and SSIM values under these severe channel conditions.

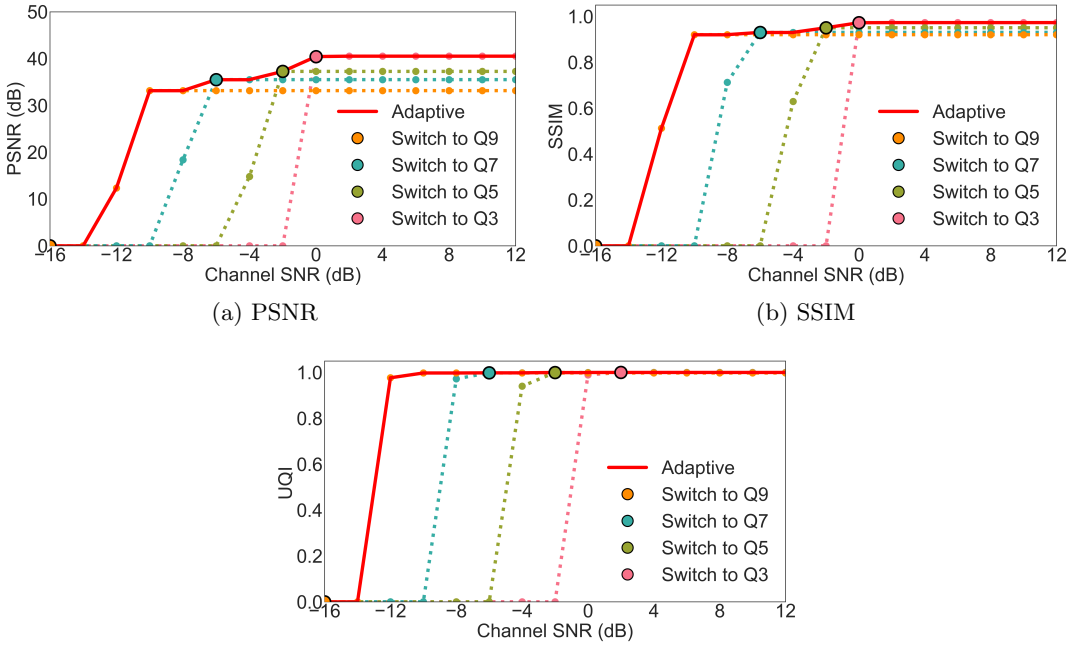


(a) Q3 (b) Q5

(c) Q7 (d) Q9

Figure 3.14: Decoded JPEG images at an SNR of −5 dB for different QEC schemes: (a) Q3, (b) Q5, (c) Q7, and (d) Q9.

As the SNR decreases further, the performance of the lower-qubit QEC schemes degrades more rapidly because of their limited error-correction capability, whereas the higher-qubit QEC schemes remain more robust and preserve acceptable image quality over a wider SNR range. These observations are consistent with the quantitative PSNR, SSIM, and UQI results and demonstrate the trade-off between QEC capability and robustness in noisy communication environments.



(a) PSNR (b) SSIM

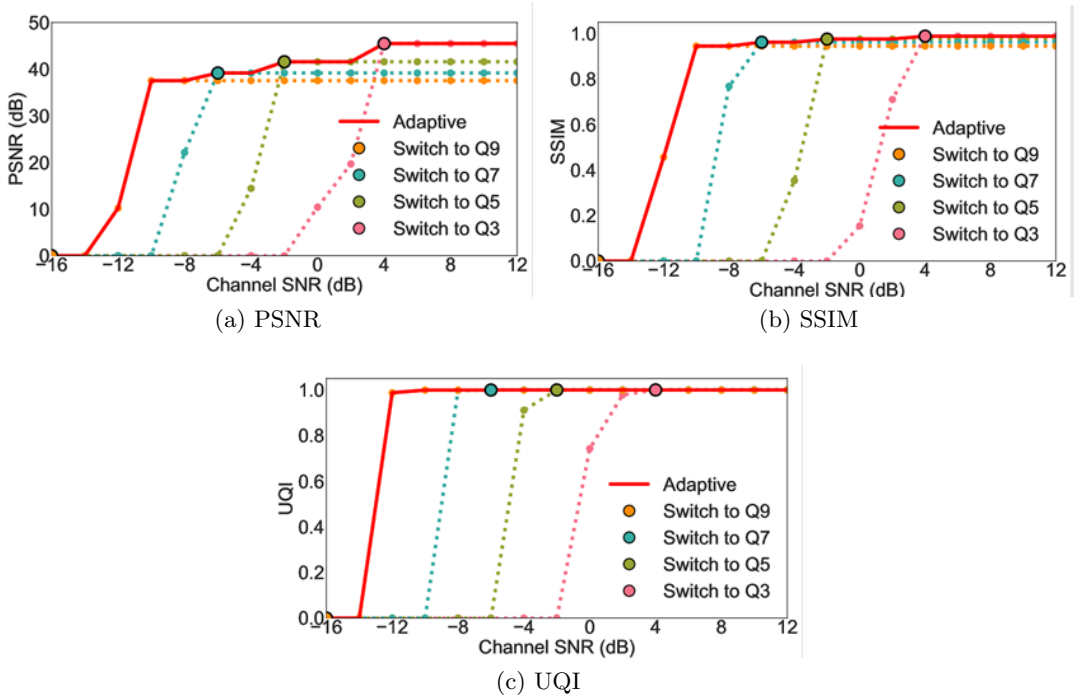
(c) UQI

Figure 3.15: Performance of adaptive QEC applied to JPEG-compressed images.

Performance of the Adaptive QEC Framework

The PSNR, SSIM, and UQI variations for the adaptive QEC system applied to JPEG-compressed images are presented in Figures 3.15a, 3.15b, and 3.15c, respectively. The adaptive system dynamically selects the optimal QEC configuration at each SNR operating point: higher-qubit codes (Q7, Q9) are employed at low SNR to maximise error resilience, while lower-qubit codes (Q3, Q5) are selected at high SNR to maximise reconstruction quality. This strategy produces an envelope curve that achieves the best performance of each individual configuration across the entire SNR range, effectively resolving the trade-off between error correction strength and source compression quality identified in the previous subsection. The SSIM and UQI results in Figures 3.15b and 3.15c exhibit trends consistent with the PSNR results, confirming that the adaptive approach preserves both perceptual and structural quality across all channel conditions.

The corresponding adaptive QEC results for HEIF-compressed images are presented in Figures 3.16a, 3.16b, and 3.16c. The HEIF results consistently outperform JPEG across all metrics and SNR conditions, which is attributed to HEIF's more efficient compression algorithm that better preserves structural and perceptual details under



(a) PSNR (b) SSIM

(c) UQI

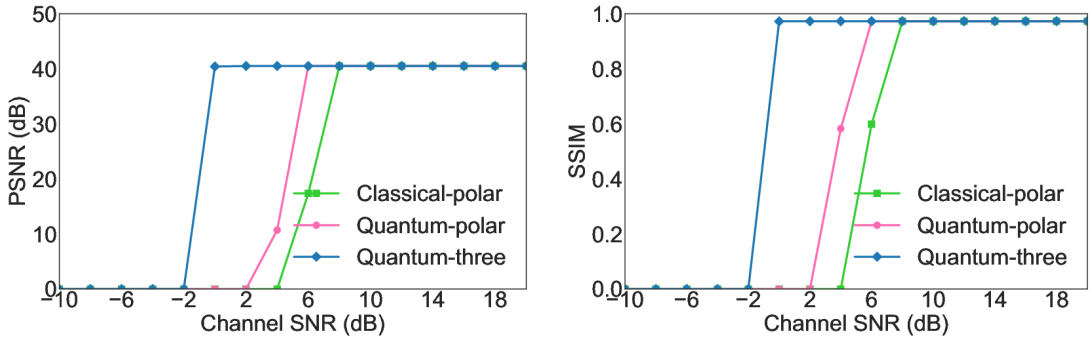
Figure 3.16: Performance of adaptive QEC applied to HEIF-compressed images.

the stronger compression required by higher-qubit QEC configurations. Importantly, the adaptive switching behaviour is equally effective for both source coding formats, confirming the generalisability of the proposed approach.

Comparison with Classical Error Correction

To contextualise the performance of the proposed QEC framework, Figure 3.17 presents a comparison of three systems under identical bandwidth conditions using the three-qubit configuration as a representative case: (i) the quantum three-qubit QEC system, (ii) a quantum system with rate-1/3 polar codes (without QEC), and (iii) a classical BPSK system with rate-1/3 polar codes. Both PSNR and SSIM results are presented.

The results demonstrate a clear performance hierarchy: the quantum three-qubit QEC system achieves the highest PSNR and SSIM across all SNR conditions, followed by the quantum polar-coded system, with the classical polar-coded system exhibiting the lowest performance. This ordering confirms two findings. First, quantum superposition-based encoding consistently outperforms classical BPSK encoding under identical channel coding conditions, as established in Section 3.1. Second, quantum-domain error



(a) PSNR (b) SSIM

Figure 3.17: PSNR and SSIM comparison of quantum three-qubit QEC, quantum polar-coded, and classical polar-coded systems under identical bandwidth conditions.

correction (three-qubit QEC) provides additional performance gains beyond classical channel coding (polar codes) when applied within the quantum transmission framework, as the QEC operates on quantum states prior to the irreversible measurement step, preventing errors from propagating into the decoded bitstream.

Practical Considerations

The multi-qubit QEC schemes employed in this framework exhibit linear complexity scaling with respect to the number of encoding qubits, making them substantially more practical than resource-intensive QEC schemes such as surface codes [202], or stabiliser codes. The adaptive switching mechanism introduces minimal additional overhead, as it requires only an SNR estimate to select the appropriate code configuration. Furthermore, the hardware feasibility of the proposed adaptive mechanism is expected to improve with advances in quantum technology, including the development of higher-fidelity multi-qubit gate operations and real-time adaptive control capabilities. By assuming perfect CSI, the current framework establishes a theoretical upper bound for system performance. In practical implementations, CSI estimation errors would introduce minor performance degradation, particularly near the adaptive switching boundaries where small SNR estimation inaccuracies could lead to suboptimal code selection. Nevertheless, the results presented under perfect CSI provide a meaningful benchmark against which future experimental implementations with realistic CSI estimation can be compared.

3.3.3 Section Summary

This section proposed and evaluated an adaptive QEC framework for image transmission over noisy quantum communication channels. The framework dynamically selects among four QEC configurations (Q3, Q5, Q7, Q9) based on the estimated channel SNR, employing higher-qubit codes under severe noise conditions to maximise error resilience and switching to lower-qubit codes under favourable conditions to maximise reconstruction quality and reduce computational overhead. The experimental results demonstrated that the adaptive approach consistently outperforms all individual fixed-qubit QEC configurations across the entire operating SNR range, achieving PSNR values of up to 40.51 dB, SSIM of up to 0.9730, and UQI of up to 0.9998 for JPEG-compressed images, and PSNR of up to 45.44 dB, SSIM of up to 0.9889, and UQI of up to 0.9999 for HEIF-compressed images. Furthermore, the comparative analysis confirmed that each quantum QEC configuration individually outperforms the bandwidth-equivalent classical polar-coded system, and that the quantum transmission frameworks consistently surpass classical BPSK-based communication across all tested conditions. The adaptive switching mechanism introduces negligible computational overhead while providing significant performance gains, particularly in the low-to-moderate SNR regime where fixed-qubit approaches suffer from either insufficient error correction or excessive bandwidth overhead. The linear complexity scaling of the employed QEC codes, combined with the threshold-based adaptive selection strategy, supports the practical scalability of the proposed framework for future quantum communication networks. Despite these improvements, the current framework is limited to image transmission. To address these limitations, Section 3.4 extends the proposed quantum communication framework to video transmission, which presents additional challenges including temporal correlation, higher data volumes, and stricter latency requirements.

3.4 Quantum Video Transmission over Noisy Communication Channels

Publication Notice

The research presented in this section has been published in the following peer-reviewed journal publication:

U. Jayasinghe, P. Samarathunga, N. Pollwaththage, Y. Ganearachchi, T. Fernando, and A. Fernando, "Quantum communication for video transmission over error-prone channels," *IEEE Transactions on Consumer Electronics*, vol. 71, no. 1, pp. 1148–1155, 2025, doi: 10.1109/TCE.2025.3552930.

This material is reproduced and adapted under the terms of the IEEE Copyright policy for use in a doctoral thesis. The content has been revised and extended with additional explanations and expanded discussion.

Problem Statement: Video has become the dominant component of global data traffic, driven by the proliferation of mobile devices, smart displays, and emerging platforms such as virtual and extended reality, making efficient and reliable video transmission a central challenge in contemporary communication systems. Sections 3.1–3.3 established a complete quantum communication framework for image transmission, including superposition-based encoding, multi-qubit QEC, and adaptive code selection. However, video transmission introduces fundamentally greater challenges. A compressed video bitstream is significantly larger than a single image and exhibits strong temporal dependencies between frames, where inter-coded P and B-frames depend on previously decoded reference frames within each group of pictures (GOP). Consequently, a single uncorrected bit error within a GOP can corrupt not only the affected frame but every subsequent inter-coded frame until the next intra-coded refresh point. This error propagation effect compounds the impact of channel noise compared to still-image transmission and makes video content substantially more vulnerable to quality degradation under noisy channel conditions.

Limitations of Existing Work: Existing research on quantum communication has focused almost exclusively on still-image transmission. Quantum communication

frameworks for video, which combine large data volumes, temporal correlation, and strict latency requirements, remain largely unexplored. Furthermore, no prior work has systematically compared, within a unified quantum communication framework, the use of quantum channel coding (multi-qubit QEC) versus classical channel coding (polar codes) for video transmission, nor evaluated how key video coding parameters such as GOP size, frame rate, and spatial resolution interact with the choice of channel coding strategy. Without such a comparison, it is unclear which configurations of quantum communication are best suited to which video transmission scenarios.

Motivation and Proposed Contribution: To address these gaps, this section extends the quantum communication framework of Sections 3.1–3.3 to video transmission and provides a comprehensive comparative analysis. Two distinct configurations are developed and evaluated: (i) a quantum communication system protected by multi-qubit QEC using three, five, and seven-qubit codes, and (ii) a hybrid quantum communication system protected by classical polar codes. Both configurations are benchmarked against a bandwidth-equivalent fully classical system to isolate the individual contributions of the quantum encoding layer and the QEC layer.

The nine-qubit code is excluded from this study due to the significantly higher computational complexity it introduces when applied to video data. Video bitstreams are substantially larger than image bitstreams, and encoding each logical qubit into nine physical qubits requires a proportionally greater number of CNOT gate operations, syndrome measurements, and correction steps across the entire bitstream. This increased processing demand makes the nine-qubit code computationally prohibitive for video transmission, where large data volumes must be processed efficiently. Similarly, the adaptive QEC switching mechanism proposed in Section 3.3 is not employed in this study, as the primary objective here is to isolate and characterise the individual performance of each fixed-qubit QEC configuration for video transmission. The adaptive framework established in Section 3.3 follows the same underlying system architecture and can be directly applied to video transmission once the individual code behaviours under video-specific conditions have been fully understood.

The proposed framework is evaluated using PSNR, SSIM, and VMAF across multiple GOP sizes, frame rates, and spatial resolutions, and is further validated through a

subjective user study. The objective is to demonstrate that quantum channel coding provides the most robust solution for video transmission under noisy conditions, while quantifying the trade-offs between reconstruction fidelity, bandwidth efficiency, and computational complexity across different multi-qubit configurations.

3.4.1 System Model

The proposed quantum communication frameworks for video transmission are illustrated in Figure 3.18. Two system configurations are developed to analyse the performance of the quantum communication process, both based on the quantum superposition encoding, composite noise channel model, and projective measurement decoding established in Section 3.1 (Equations (3.1)–(3.16)).



(a) Quantum error correction



(b) Classical error correction

Figure 3.18: Proposed quantum communication frameworks for video transmission with: (a) quantum error correction, and (b) classical error correction.

The first configuration (Figure 3.18a) utilises QEC with three-qubit (Q-T), five-qubit (Q-F), and seven-qubit (Q-S) codes. The compressed video bitstream is converted into qubit superposition states using the quantum encoder from Section 3.1, and these superposition states are then channel encoded using the multi-qubit QEC scheme described in Section 3.3. In the five-qubit and seven-qubit cases, the original video bitstream is further compressed to reduced quality to match the bitrate of the three-qubit channel-encoded qubit stream. The second configuration (Figure 3.18b) employs classical error correction with a rate-1/3 polar encoder to align the bitrate with the three-qubit error correction. The resulting channel-encoded bitstream is then converted into qubit superposition states using the quantum encoder.

In both configurations, the resulting qubit superposition states are transmitted

over the composite quantum noise channel defined in (3.6). In the first configuration, the received qubit states are quantum channel decoded to identify and correct errors, and then converted to a classical bitstream using the quantum decoder to recover the compressed video bitstream. In the second configuration, the quantum decoder is first applied to extract the classical information, which is then processed through the polar decoder to reconstruct the final bitstream.

The performance of the proposed quantum communication systems is evaluated against a bandwidth-equivalent classical communication system (C-P) employing BPSK modulation with rate-1/3 polar coding. All proposed quantum systems operate on compressed video bitstreams and can accommodate inputs from any standard video codec. For simulation purposes, the VVenC [203] implementation of VVC [204] is employed. Experiments are conducted using input videos in YUV420 format across three spatial resolutions (320×180, 1280×720, and 1920×1080), three frame rates (20, 30, and 50 fps), and three GOP sizes (8, 16, and 32) to comprehensively assess the robustness of the proposed framework. Simulations are performed using Python on a computing system with a 13^{th} Gen Intel® Core™ i5-1345U 1.60 GHz processor and 16.0 GB of RAM.

The following subsections provide detailed information on the main functional blocks of the quantum communication frameworks shown in Figure 3.18.

Quantum Encoding and Decoding

The quantum encoding and decoding processes follow the same architecture established in Section 3.1. Classical bits are mapped to the computational basis states $|0\rangle$ and $|1\rangle$ (Equations (3.1)–(3.2)), transformed into superposition states via the Hadamard gate (Equations (3.3)–(3.5)), and decoded using projective measurement operators (Equations (3.15)–(3.16)).

Quantum Channel Coding

After quantum encoding, the superposition states are processed by the quantum channel encoder using three-qubit, five-qubit, and seven-qubit channel coding techniques. All three codes follow the same CNOT-entanglement and syndrome-correction structure de-

scribed in Section 3.2, with the three-qubit code serving as the basis and the higher-qubit codes extending the same principle to provide progressively stronger error correction capability. The three-qubit encoder and decoder circuit is reproduced in Figure 3.19 for reference, and the corresponding syndrome measurement outcomes and correction actions are summarised in Section 3.2, Tables 3.2 and 3.3.

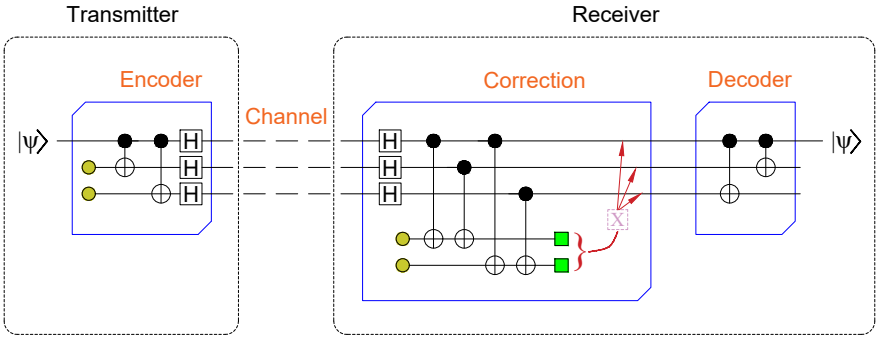


Figure 3.19: Three-qubit encoder and decoder circuit.

Quantum Channel

The composite quantum noise channel follows the model established in Section 3.1 (Equations (3.6)–(3.14)), incorporating bit-flip, phase-flip, depolarising, amplitude damping, and phase damping noise mechanisms. System performance is assessed across varying SNR levels by randomly adjusting the individual noise-type probabilities, enabling evaluation under diverse channel conditions.

3.4.2 Results

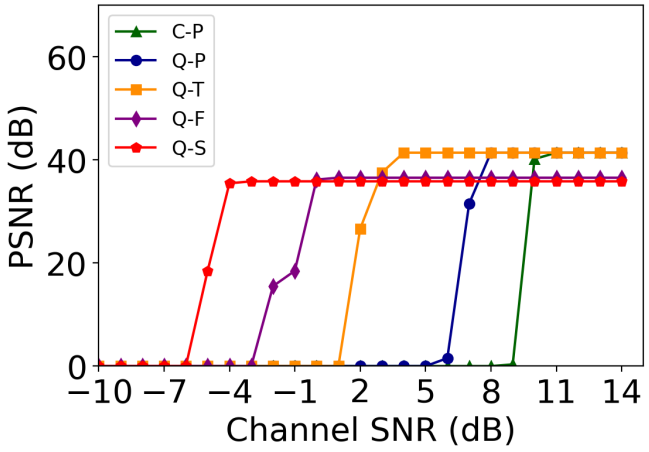
This subsection evaluates the proposed quantum video transmission framework across five system configurations: quantum communication with seven-qubit QEC (Q-S), five-qubit QEC (Q-F), three-qubit QEC (Q-T), classical polar codes (Q-P), and the fully classical baseline (C-P). The analysis is organised into five parts: objective quality assessment across GOP sizes, the effect of GOP size on error propagation, resolution and frame rate analysis, subjective quality evaluation, and computational complexity analysis.

Objective Quality Assessment

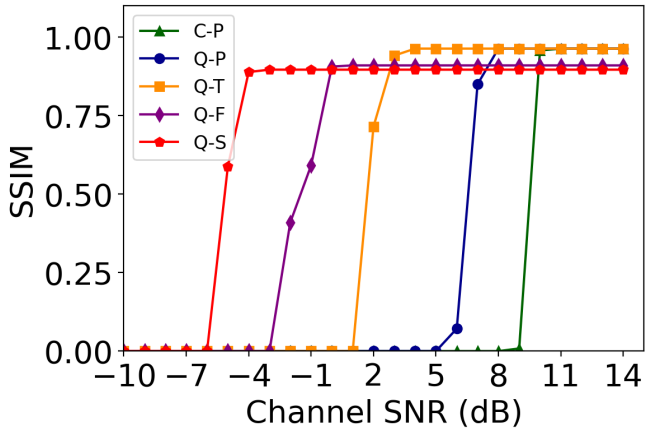
Three test videos with varying levels of spatial information (SI) and temporal information (TI) are used to evaluate performance: a high-motion video [205] with high SI and TI, a medium-motion video [206] with medium SI and TI, and a low-motion video [207] with medium SI and low TI. This selection ensures that the evaluation covers a representative range of video content characteristics, from fast-moving scenes with complex spatial detail that are challenging to compress and highly sensitive to transmission errors, to static scenes with minimal temporal variation that are easier to compress but still susceptible to channel noise. By evaluating across these diverse content types, the robustness and generalisability of the proposed framework can be assessed independently of specific video content characteristics. Performance is evaluated using PSNR, SSIM, and VMAF, with results presented across three GOP configurations (8, 16, 32) in Figures 3.20–3.22.

Three key observations emerge from the results. First, all quantum communication systems (Q-S, Q-F, Q-T, Q-P) consistently outperform the classical baseline (C-P) across all three metrics, all GOP sizes, and all SNR conditions. As shown in Figures 3.20a, 3.20b, and 3.20c, the quantum systems achieve higher PSNR, SSIM, and VMAF values than the classical system across the entire SNR range for GOP = 8, and this advantage is maintained for GOP = 16 (Figure 3.21) and GOP = 32 (Figure 3.22). The consistency across both spatial correlation metrics (PSNR and SSIM) and the spatial-temporal coherence metric (VMAF) confirms that the quantum superposition-based encoding advantage demonstrated for still-image transmission in Sections 3.1–3.3 extends directly to temporally correlated video content, preserving not only pixel-level accuracy but also perceptual quality across consecutive frames. The improvement is attributed to the Hadamard-based superposition encoding (Equations (3.4)–(3.5)), which distributes information across probability amplitudes of the quantum state rather than mapping it to deterministic binary symbol levels as in classical BPSK. Consequently, when channel noise perturbs the transmitted state through the composite noise channel (Equation (3.6)), it modifies the amplitude distribution rather than directly corrupting a single deterministic symbol, resulting in improved robustness against noise perturbations.

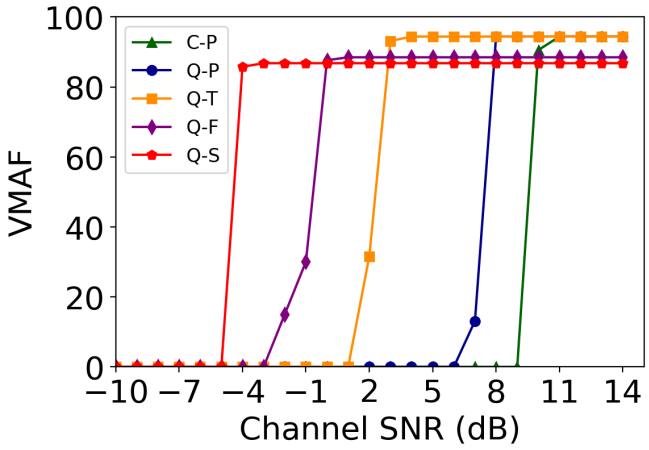
Second, a clear performance hierarchy is observed among the quantum configurations:



(a) PSNR

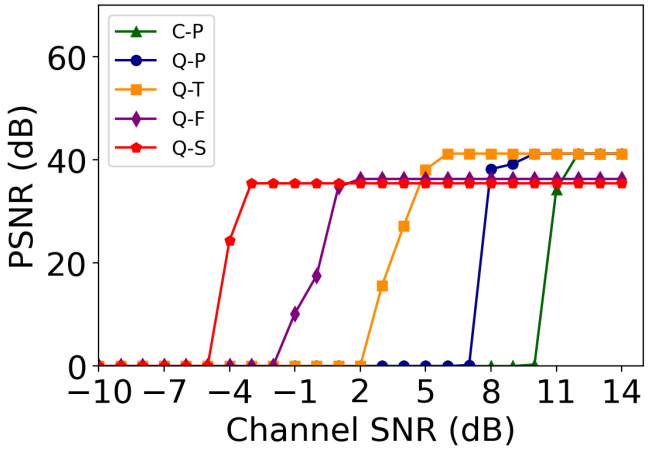


(b) SSIM

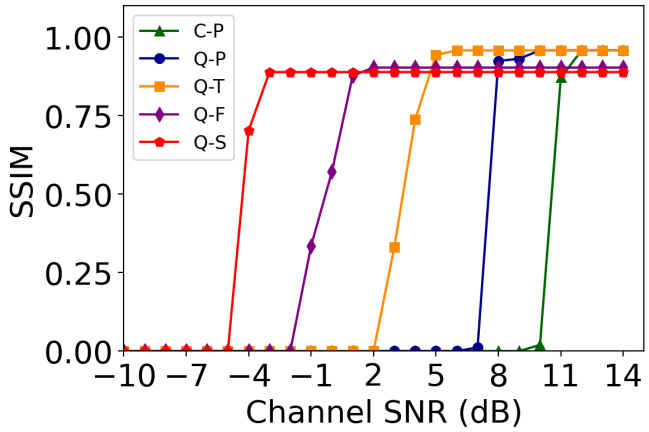


(c) VMAF

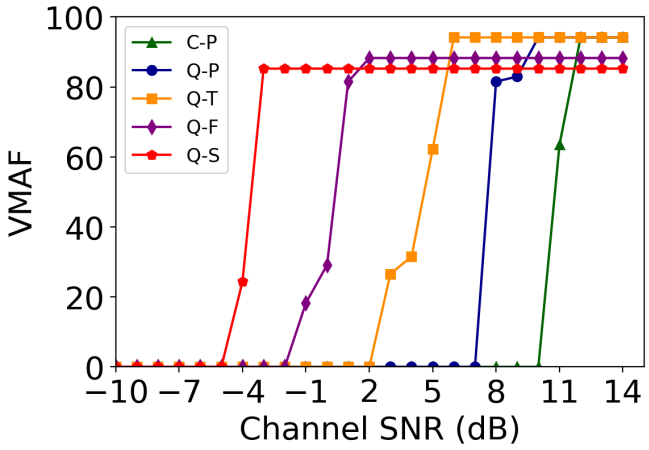
Figure 3.20: PSNR, SSIM, and VMAF variation for VVC videos with GOP = 8 for Q-S, Q-F, Q-T, Q-P, and C-P systems.



(a) PSNR

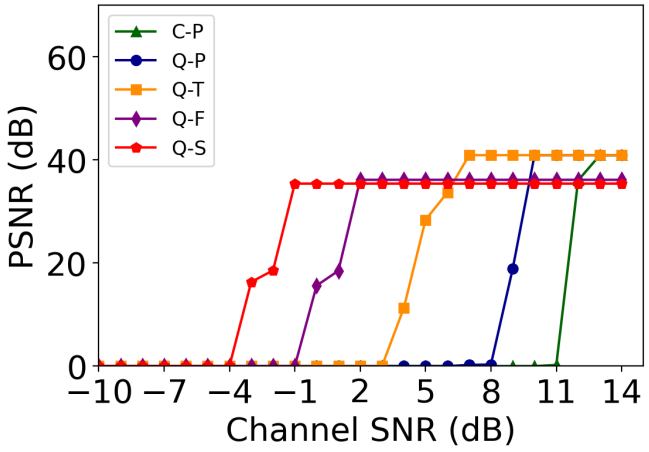


(b) SSIM

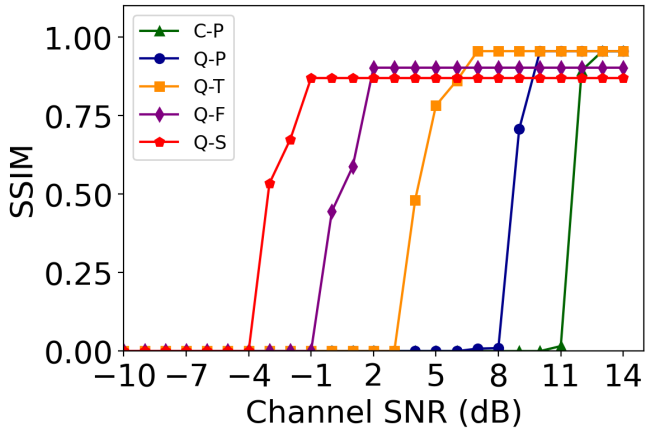


(c) VMAF

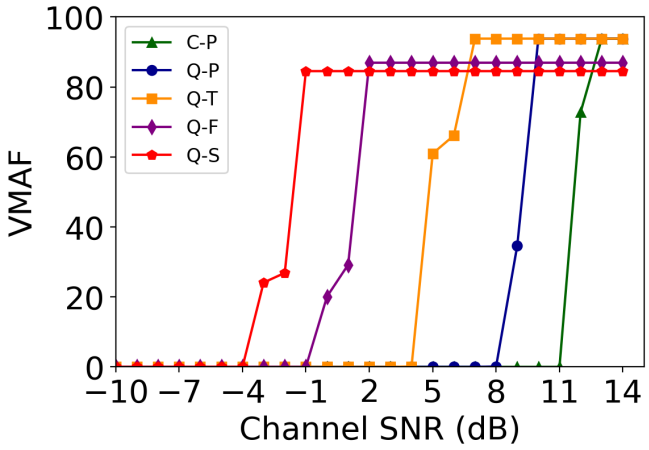
Figure 3.21: PSNR, SSIM, and VMAF variation for VVC videos with GOP = 16 for Q-S, Q-F, Q-T, Q-P, and C-P systems.



(a) PSNR



(b) SSIM



(c) VMAF

Figure 3.22: PSNR, SSIM, and VMAF variation for VVC videos with GOP = 32 for Q-S, Q-F, Q-T, Q-P, and C-P systems.

Q-S (seven-qubit) achieves the highest reconstruction fidelity, followed by Q-F (five-qubit), Q-T (three-qubit), and Q-P (polar-coded). This ordering is consistent across PSNR, SSIM, and VMAF and across all GOP sizes, as evident in Figures 3.20–3.22. The superior performance of higher-qubit codes arises because encoding a logical qubit into a larger number of physical qubits enables the system to detect and correct a greater number of transmission errors through the syndrome measurement process (Tables 3.2 and 3.3). The seven-qubit system is particularly effective under low-SNR conditions, where the increased error correction capability compensates for the stronger source compression required to maintain bandwidth equivalence. As shown in Figure 3.20c, the VMAF results further confirm that the spatial-temporal coherence of the reconstructed video improves with increasing QEC code strength, demonstrating that the error correction benefits extend beyond pixel-level accuracy to perceptual quality.

Third, the hybrid quantum system with classical polar codes (Q-P) achieves performance comparable to the classical system (C-P) at high SNR, but provides measurable gains at low SNR due to the inherent noise resilience of quantum superposition encoding. However, Q-P consistently lags behind all QEC-based quantum systems across all metrics and GOP sizes. This performance gap confirms that quantum-domain error correction, which operates on quantum states prior to the irreversible measurement step (Equation (3.15)), provides superior protection compared to classical channel coding that operates on binary symbols after detection. In the QEC-based systems, transmission errors are corrected while the quantum information is still intact, preventing corrupted bits from entering the source decoder. In contrast, the polar-coded system must attempt to correct errors after the quantum state has already been projected onto classical bit values, at which point noise-induced corruption has been irreversibly committed to the detected bit sequence.

Effect of GOP Size on Error Propagation

Comparing the results across Figures 3.20–3.22, all five systems exhibit reduced performance as the GOP size increases from 8 to 32. This degradation is attributed to the increased number of inter-coded frames within each GOP: errors occurring in the middle of a GOP propagate to all subsequent inter-coded frames until the next intra-coded

refresh point. With larger GOP sizes, this propagation chain is longer, resulting in greater cumulative quality degradation. Importantly, the quantum QEC-based systems (Q-S, Q-F, Q-T) exhibit smaller performance reductions with increasing GOP size compared to the classical system, indicating that quantum error correction partially mitigates the temporal error propagation effect. Nevertheless, the sensitivity to GOP size suggests that future work should investigate adaptive error correction strategies that account for the temporal structure of the GOP, applying stronger protection to reference frames and lighter protection to inter-coded frames.

Resolution and Frame Rate Analysis

The maximum SNR gains achieved by each quantum system relative to the classical baseline across different spatial resolutions and frame rates are summarised in Table 3.6 for the representative case of GOP = 8. The Q-S system achieves approximately 15 dB SNR gain, Q-F achieves approximately 13 dB, Q-T achieves approximately 8 dB, and Q-P achieves approximately 4 dB across all tested configurations. Crucially, the SNR gains remain nearly constant across all resolutions (320×180, 1280×720, 1920×1080) and frame rates (20, 30, 50 fps), confirming that the performance advantage of the proposed quantum framework is independent of both spatial resolution and temporal sampling rate. This resolution and frame rate-invariant behaviour demonstrates the scalability of the proposed approach to diverse video transmission scenarios.

Table 3.6: Maximum SNR gain (dB) for each quantum system compared to the classical system across different resolutions and frame rates (GOP = 8).

Frame Rate (fps)	**320×180**				**1280×720**				**1920×1080**			
	Q-S	Q-F	Q-T	Q-P	Q-S	Q-F	Q-T	Q-P	Q-S	Q-F	Q-T	Q-P
20	15.0	13.0	8.0	4.0	15.2	13.3	8.2	4.3	15.1	13.2	8.4	4.1
30	15.1	13.2	7.9	4.1	15.3	13.4	8.1	4.1	15.3	13.3	8.3	4.1
50	14.9	13.1	7.9	4.1	15.1	13.2	8.3	4.2	15.3	13.4	8.3	4.4

Subjective Quality Evaluation

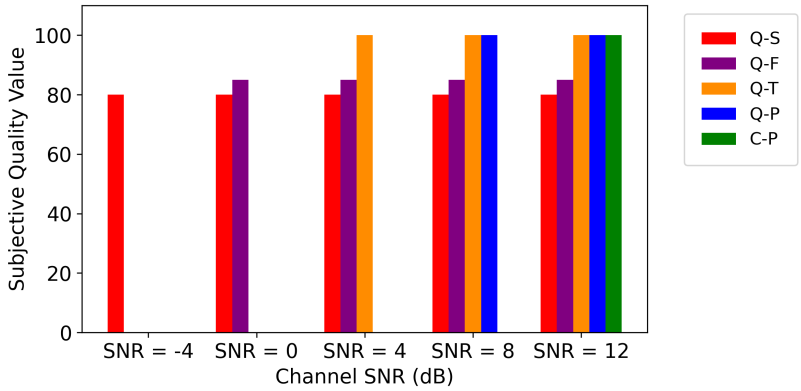
To complement the objective metrics, a subjective user experiment is conducted using the double stimulus impairment scale method recommended by ITU-R BT.500 [208]. A total of 50 participants aged 18 to 55 years evaluated the reconstructed video quality

across all five system configurations and three GOP sizes. The subjective results, presented in Figure 3.23, are consistent with the objective PSNR, SSIM, and VMAF findings: the QEC-based quantum systems receive the highest quality ratings, followed by the polar-coded quantum system, with the classical system receiving the lowest scores. This agreement between objective and subjective evaluations confirms that the measured performance improvements correspond to perceptually meaningful quality gains and strengthens the practical relevance of the proposed framework for consumer video applications.

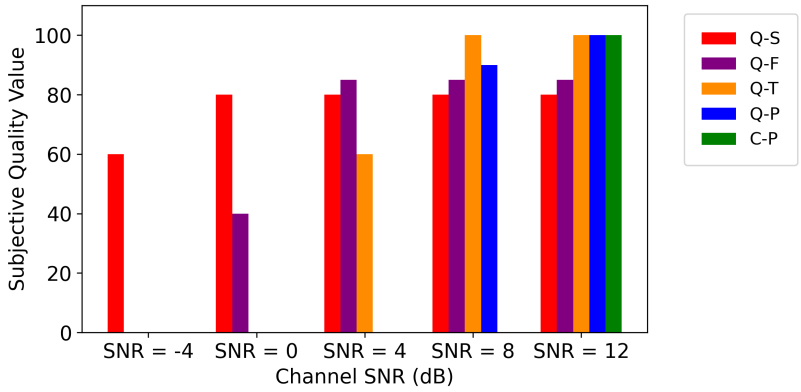
Computational Complexity Analysis

The multi-qubit QEC codes employed in this study exhibit linear complexity scaling with respect to the number of encoding qubits. The three-qubit system achieves approximately 30% reduction in encoding, transmission, and decoding time compared to the five-qubit system, and approximately 50% reduction compared to the seven-qubit system. This makes the three-qubit configuration particularly suitable for resource-constrained quantum devices where processing latency is a critical constraint. While the seven-qubit system achieves the strongest error correction performance, the three-qubit system offers a favourable trade-off between reconstruction fidelity and computational efficiency, particularly at moderate SNR levels where single-qubit error correction is sufficient.

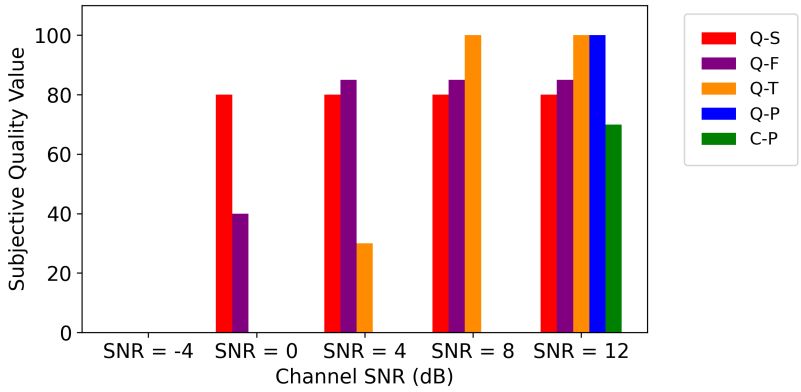
It is noted that the QEC codes employed in this study are designed to correct single-qubit bit-flip (X) and phase-flip (Z) errors. Noise types such as depolarisation and amplitude damping, which create mixed quantum states rather than discrete qubit-level errors, are captured by the composite noise channel model (Equation (3.6)) but are not fully correctable by the employed codes. Although the simulation framework accurately models the impact of these noise types on system performance, effectively addressing them would require more advanced QEC techniques, such as surface codes or stabiliser codes, which introduce substantially higher circuit complexity and qubit overhead. The development of communication-oriented QEC schemes capable of handling these noise types while maintaining practical complexity remains an important direction for future research.



(a) GOP = 8



(b) GOP = 16



(c) GOP = 32

Figure 3.23: Subjective experiment results for VVC videos with different GOP values over Q-S, Q-F, Q-T, Q-P, and C-P systems.

Limitations

Beyond the computational overhead associated with larger QEC codes, several practical implementation challenges must also be considered for real-world quantum communication systems. Current quantum hardware remains constrained by limited qubit coherence times, gate and measurement errors, photon loss, restricted qubit connectivity, and the availability of only a limited number of high-fidelity physical qubits. Furthermore, implementing large QEC codes requires additional ancilla qubits, more complex syndrome extraction circuits, and longer quantum circuit execution times, which increase susceptibility to decoherence and operational errors on present-day quantum devices. Long-distance multimedia transmission would additionally require scalable quantum repeaters, reliable entanglement distribution, and efficient synchronisation between quantum and classical processing, all of which remain active research challenges. Consequently, although the proposed framework demonstrates significant performance improvements through rigorous end-to-end mathematical modelling, its practical realisation will depend on continued advances in quantum hardware, fault-tolerant quantum technologies, and quantum networking infrastructures.

3.4.3 Section Summary

This section extended the quantum communication framework to video transmission, the most data-intensive and temporally complex multimedia scenario addressed in this chapter. Five system configurations were evaluated across multiple GOP sizes, frame rates, and spatial resolutions, and further validated through a subjective user study. The experimental results demonstrated a consistent performance hierarchy across all tested conditions: the seven-qubit QEC system (Q-S) achieved the highest reconstruction fidelity, followed by the five-qubit (Q-F), three-qubit (Q-T), and polar-coded (Q-P) quantum systems, with the classical baseline (C-P) exhibiting the lowest performance. The three-qubit system achieved PSNR values of up to 41.42 dB, SSIM of up to 0.9639, and VMAF of up to 94.40 under low-SNR conditions, while the seven-qubit system consistently achieved the best overall fidelity and noise resilience. The quantum system with classical polar codes (Q-P) surpassed the classical baseline but consistently lagged behind all QEC-based configurations, confirming that quantum-domain error correction

provides superior protection compared to classical channel coding within a quantum transmission framework. The SNR gains of the proposed quantum systems were shown to be invariant to spatial resolution and frame rate, demonstrating the scalability of the framework. Subjective evaluation results corroborated the objective metrics, confirming that the measured improvements correspond to perceptually meaningful quality gains.

3.5 Chapter Summary

This chapter presented the progressive development of a unified quantum communication framework for high-fidelity image and video transmission, comprising four interconnected studies (Sections 3.1–3.4). Section 3.1 established the foundational end-to-end quantum communication system, demonstrating that Hadamard-based superposition encoding inherently outperforms classical BPSK transmission by distributing information across probability amplitudes rather than deterministic symbol levels. Section 3.2 introduced three-qubit QEC into the framework, achieving significant performance gains over both quantum polar-coded and classical systems. Section 3.3 extended this to an adaptive QEC framework that dynamically selects among three, five, seven, and nine-qubit codes based on channel conditions, demonstrating that increasing the number of encoding qubits progressively improves error resilience, with the nine-qubit code achieving the strongest protection under severe noise conditions. Section 3.4 extended the framework to video transmission, where the seven-qubit code was the highest configuration evaluated, confirming that the performance hierarchy and quantum advantages hold for temporally correlated video content across diverse GOP sizes, frame rates, and spatial resolutions.

A critical insight emerging from the collective findings of this chapter is that achieving robust error resilience under severe noise conditions requires progressively larger QEC codes. The results consistently demonstrated that increasing the qubit code size from three to five, seven, and nine qubits yields progressively stronger error correction capability. However, this improvement comes at substantial practical costs: each increase in code size requires additional ancilla qubits for encoding and syndrome extraction, the quantum circuit depth grows with every additional encoding qubit, and the decoding complexity increases due to larger syndrome measurement spaces. Consequently, while higher-qubit QEC codes provide stronger error protection, the associated resource

demands make this approach increasingly impractical for data-intensive multimedia applications where large volumes of information must be transmitted efficiently.

This observation motivates a fundamental shift in approach: rather than relying solely on increasing QEC code size to improve error resilience at the cost of growing circuit complexity and ancilla requirements, the subsequent chapter investigates alternative encoding-level optimisation strategies that improve transmission robustness directly through the quantum state representation itself. Specifically, Chapter 4 introduces multi-qubit encoding techniques that map classical bitstreams into higher-dimensional Hilbert space representations, exploiting the increased dimensionality to achieve superior noise resilience without requiring ancilla qubits, additional quantum gates for syndrome extraction, or increased circuit depth. This encoding-driven approach offers a more resource-efficient and scalable pathway to improving quantum multimedia transmission performance.

Practical implementation of the proposed framework is influenced by several challenges that extend beyond the increased computational complexity associated with larger QEC codes. Current quantum communication hardware is still in the NISQ era, where limited coherence times, imperfect quantum operations, measurement inaccuracies, photon loss, restricted qubit connectivity, and the relatively small number of reliable physical qubits constrain the execution of large-scale quantum circuits. As the redundancy of the QEC scheme increases, additional physical qubits, more syndrome extraction operations, and deeper quantum circuits are required, making the system more vulnerable to accumulated hardware errors and decoherence.

Practical deployment over long communication distances introduces further challenges. Reliable operation would require supporting technologies such as scalable quantum repeaters, long-lived quantum memories, efficient entanglement distribution, and robust coordination between quantum and classical processing stages. Although considerable progress has been made in these areas, they have not yet reached the level of maturity necessary for large-scale multimedia communication applications.

Therefore, the proposed framework should be viewed as a communication-system model that investigates the feasibility and long-term potential of quantum multimedia communication under idealised communication assumptions rather than as an imple-

mentation intended for current quantum hardware. Continued advances in fault-tolerant quantum computing, quantum networking, hardware reliability, and scalable quantum devices are expected to progressively reduce these practical barriers, enabling future experimental validation and deployment of the proposed framework.

Chapter 4

Design and Analysis of Multi-Qubit Quantum Encoding Techniques for Image and Video Transmission

Chapter 3 established a progressive quantum communication framework for multimedia transmission, culminating in multi-qubit QEC schemes that achieved significant gains in image and video reconstruction quality under noisy channel conditions. However, QEC-based approaches introduce a fundamental scalability constraint: as the number of protection qubits grows, the required ancilla resources, syndrome measurement circuits, and decoding complexity increase substantially. For three-qubit QEC, two ancilla qubits are required per logical qubit; for five and seven-qubit codes, this overhead grows further. Extending QEC to protect blocks of classical bits simultaneously is therefore impractical for bandwidth-constrained multimedia applications, where ancilla overhead and circuit depth become prohibitive as channel conditions vary dynamically.

This chapter addresses that limitation by proposing a fundamentally different strategy. Rather than correcting errors after transmission, the proposed approach achieves noise resilience by *encoding more classical information per quantum transmission unit* through higher-dimensional multi-qubit superposition states. By grouping k classical

bits and mapping each group to one of 2^k orthogonal superposition states via the k-fold Hadamard transform $H^{\otimes k}$, the system exploits the exponential growth of the Hilbert space to reduce measurement ambiguity and improve reconstruction fidelity, without requiring any ancilla qubits or syndrome measurements. This represents a paradigmatic shift from *error correction after transmission* to *error-resilient representation during transmission*.

To realise this objective, the chapter introduces a structured framework that integrates multi-qubit quantum state construction, classical multimedia source coding, polar channel coding, quantum channel transmission, and reconstruction within a unified end-to-end architecture. An adaptive mechanism is further proposed that dynamically selects the optimal qubit group size k based on real-time channel SNR, minimising computational complexity under favourable conditions while maximising robustness under severe channel impairments. Throughout this chapter, transform-domain source coding is performed using the JPEG, HEIF, and VVC codecs. Since quantum encoding is applied to the compressed bitstream rather than to the transform coefficients, the proposed framework is not restricted to any particular source transform.

The remainder of this chapter is organised as follows. Section 4.1 presents the proposed multi-qubit encoding framework for image transmission [209] and evaluates its performance in comparison with the single-qubit transmission approaches introduced in Chapter 3. Section 4.2 extends the proposed framework to quantum video transmission, incorporating GOP-aware evaluation to analyse transmission performance under practical video coding conditions.

4.1 Error-Resistant Quantum Image Communication Based on Multi-Qubit Encoding

Publication Notice

The research presented in this section has been published in the following peer-reviewed journal publication:

U. Jayasinghe, N. Kushantha, T. Fernando, and A. Fernando, "A robust multi-qubit quantum communication system for image transmission over error-prone channels," *IEEE Transactions on Consumer Electronics*, vol. 71, no. 3, pp. 7551–7558, 2025, doi: 10.1109/TCE.2025.3594368.

This material is reproduced and adapted under the terms of the IEEE Copyright policy for use in a doctoral thesis. The content has been revised and extended with additional explanations and expanded discussion.

Problem Statement: Compressed image transmission over noisy quantum communication channels remains highly vulnerable to transmission errors, particularly under low-SNR conditions. In compressed image formats such as JPEG and HEIF, even a small number of bit errors can cause severe visual degradation due to the strong interdependency of entropy-coded bitstreams. Although the single-qubit superposition encoding framework presented in Section 3.1 demonstrates improved robustness compared to conventional classical BPSK transmission, its error resilience remains fundamentally constrained by the limited two-dimensional Hilbert space associated with single-qubit representation. The QEC-based approaches introduced in Section 3.2 improve transmission reliability through redundant qubit encoding; however, these schemes require additional ancilla qubits, increased circuit complexity, and higher computational overhead, which become increasingly impractical for large-scale multimedia transmission systems.

Limitations of Existing Work: No existing work has investigated higher-dimensional superposition encoding without ancilla-qubit overhead as an alternative mechanism for improving transmission robustness in end-to-end compressed image communication systems. Existing multi-qubit studies in the quantum computing literature primarily

focus on fault-tolerant computation and logical qubit preservation rather than practical multimedia communication performance. Furthermore, the relationship between qubit group size k, Hilbert space dimensionality, transmission robustness, and reconstructed image quality under realistic noisy channel conditions has not been systematically analysed. In addition, no prior work has proposed an adaptive multi-qubit encoding framework that dynamically adjusts the qubit configuration according to real-time channel SNR conditions for compressed image transmission.

Motivation and Proposed Contribution: The limitations of redundancy-based QEC approaches motivate the exploration of alternative mechanisms for improving transmission robustness in quantum image communication systems. Since compressed image bitstreams are highly sensitive to transmission errors, particularly under low-SNR conditions, there is a strong need for transmission frameworks that can enhance reliability without introducing excessive redundancy, ancilla qubits, or complex decoding operations. Motivated by the ability of multi-qubit systems to represent information within higher-dimensional Hilbert spaces, this work investigates whether higher-dimensional quantum state representations can improve robustness against channel impairments while maintaining practical transmission complexity. To address these challenges, this section proposes a robust multi-qubit quantum communication framework that enhances transmission resilience through higher-dimensional quantum state representation rather than redundancy-based QEC. The proposed approach groups k classical bits and maps them into one of 2^k orthogonal superposition states using the Hadamard transform $H^{\otimes k}$. By increasing the dimensionality of the encoded quantum state space, the proposed framework improves the robustness of state detection under noisy channel conditions, thereby enhancing reconstruction reliability without introducing ancilla qubits or additional redundancy. An adaptive multi-qubit transmission strategy is further proposed, where the qubit group size k is dynamically selected according to the instantaneous channel SNR. Under severe noisy conditions, larger qubit configurations improve robustness against channel impairments, whereas lower-dimensional configurations reduce computational complexity under favourable channel conditions. This adaptive strategy enables a practical balance between transmission reliability, computational complexity, and bandwidth efficiency across varying communication environments.

4.1.1 System Model

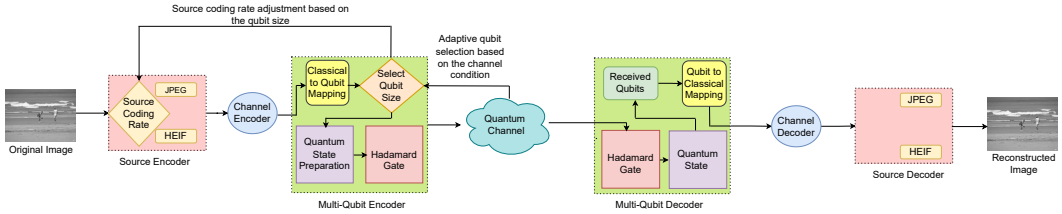


Figure 4.1: Proposed adaptive multi-qubit encoding based end-to-end quantum communication system for image transmission.

The proposed framework extends the single-qubit quantum communication architecture of Section 3.1 by introducing both fixed-size and adaptive multi-qubit encoding schemes, as illustrated in Figure 4.1. The fixed-size configuration evaluates performance across qubit group sizes $k \in \{1, 2, \ldots, 8\}$, while the adaptive configuration dynamically selects the optimal k based on real-time channel conditions. To maintain consistent bandwidth utilisation across all configurations, the source coding rate is adjusted according to the selected k, such that $k \times \text{bitrate}_k \approx \text{constant}$. Accordingly, the QP values for Q1–Q8 are set to $\{100, 94, 88, 79, 72, 60, 50, 40\}$ for JPEG and $\{100, 70, 60, 54, 50, 45, 43, 41\}$ for HEIF. These QP values are empirically selected such that the resulting bitrates are approximately equal across all qubit configurations. The resulting compressed bitstream then serves as the input to the subsequent quantum encoding stage. The system is evaluated using 100 images from the Microsoft COCO dataset [197], selected for their diverse SI characteristics. To ensure statistical reliability, 1,000 transmission trials are conducted per image and results are presented as averages. The system is evaluated in two configurations: without channel coding, to assess the intrinsic noise resilience of multi-qubit encoding alone; and with classical polar coding [210] at a rate of 1/2, to assess the combined benefit of multi-qubit encoding and classical error correction.

Multi-Qubit State Construction

The classical bitstream is first divided into groups of k bits. Each group is then mapped to one of 2^k orthogonal computational basis states by combining multiple single-qubit

basis representations, as expressed in (4.1).

$$|0\rangle = \begin{pmatrix} 1 \\ 0 \end{pmatrix}, \qquad |1\rangle = \begin{pmatrix} 0 \\ 1 \end{pmatrix} \tag{4.1}$$

For $k > 1$, higher-dimensional basis states are constructed using the tensor product operation between individual qubit basis states. For example, the four possible two-qubit basis states are represented in (4.2)–(4.3).

$$|00\rangle = \begin{pmatrix} 1 \\ 0 \end{pmatrix} \otimes \begin{pmatrix} 1 \\ 0 \end{pmatrix} = \begin{pmatrix} 1 \\ 0 \\ 0 \\ 0 \end{pmatrix}, \qquad |01\rangle = \begin{pmatrix} 1 \\ 0 \end{pmatrix} \otimes \begin{pmatrix} 0 \\ 1 \end{pmatrix} = \begin{pmatrix} 0 \\ 1 \\ 0 \\ 0 \end{pmatrix} \tag{4.2}$$

$$|10\rangle = \begin{pmatrix} 0 \\ 1 \end{pmatrix} \otimes \begin{pmatrix} 1 \\ 0 \end{pmatrix} = \begin{pmatrix} 0 \\ 0 \\ 1 \\ 0 \end{pmatrix}, \qquad |11\rangle = \begin{pmatrix} 0 \\ 1 \end{pmatrix} \otimes \begin{pmatrix} 0 \\ 1 \end{pmatrix} = \begin{pmatrix} 0 \\ 0 \\ 0 \\ 1 \end{pmatrix} \tag{4.3}$$

In general, for k qubits, the tensor product yields 2^k distinct orthogonal basis vectors, each of dimension 2^k.

Hadamard Superposition Encoding

The single-qubit Hadamard gate is defined in (4.4). For a multi-qubit system containing k qubits, the corresponding Hadamard operator is constructed using the k-fold tensor product, represented as $H_k = H^{\otimes k}$. This operation generates a $2^k \times 2^k$ transformation matrix that maps computational basis states into orthogonal superposition states.

$$H = \frac{1}{\sqrt{2}} \begin{pmatrix} 1 & 1 \\ 1 & -1 \end{pmatrix} \tag{4.4}$$

For the two-qubit case ($k = 2$), the Hadamard operator is obtained by taking the tensor product of two single-qubit Hadamard matrices, as shown in (4.5). The resulting two-qubit Hadamard transformation matrix is given in (4.6).

$$H_2 = H \otimes H = \left(\frac{1}{\sqrt{2}}\begin{pmatrix}1 & 1\\ 1 & -1\end{pmatrix}\right) \otimes \left(\frac{1}{\sqrt{2}}\begin{pmatrix}1 & 1\\ 1 & -1\end{pmatrix}\right) \tag{4.5}$$

$$H_2 = \frac{1}{2}\begin{pmatrix}1 & 1 & 1 & 1\\ 1 & -1 & 1 & -1\\ 1 & 1 & -1 & -1\\ 1 & -1 & -1 & 1\end{pmatrix} \tag{4.6}$$

Applying the two-qubit Hadamard operator H_2 to each computational basis state generates the corresponding orthogonal superposition transmission states. Specifically, the transformed states corresponding to the basis vectors $|00\rangle$, $|01\rangle$, $|10\rangle$, and $|11\rangle$ are presented in (4.7)–(4.10), respectively.

$$H_2\begin{pmatrix}1\\0\\0\\0\end{pmatrix} = \frac{1}{2}\begin{pmatrix}1\\1\\1\\1\end{pmatrix} \tag{4.7}$$

$$H_2\begin{pmatrix}0\\1\\0\\0\end{pmatrix} = \frac{1}{2}\begin{pmatrix}1\\-1\\1\\-1\end{pmatrix} \tag{4.8}$$

$$H_2\begin{pmatrix}0\\0\\1\\0\end{pmatrix} = \frac{1}{2}\begin{pmatrix}1\\1\\-1\\-1\end{pmatrix} \tag{4.9}$$

$$H_2\begin{pmatrix}0\\0\\0\\1\end{pmatrix} = \frac{1}{2}\begin{pmatrix}1\\-1\\-1\\1\end{pmatrix} \tag{4.10}$$

Similarly, higher-dimensional superposition states are constructed for multi-qubit configurations where $k \in \{3, \ldots, 8\}$. As the number of qubits increases, the dimensionality of the Hilbert space grows exponentially, enabling the representation of increasingly higher-dimensional quantum states. In particular, the $k = 8$ configuration produces a $2^8 = 256$-dimensional quantum state space, which directly corresponds to all possible 8-bit pixel intensity values. This property motivates restricting the evaluation to configurations with $k \leq 8$.

Quantum Channel

The superposition states are transmitted through the composite quantum noise channel defined in Section 3.1 (Equations (3.6)–(3.14)), incorporating bit-flip, phase-flip, depolarising, amplitude damping, and phase damping noise mechanisms. The same SNR-to-noise-probability mapping of (3.8) is applied consistently with Chapter 3.

Multi-Qubit Decoder

At the receiver, the Hadamard operator H_k is applied to the received noisy quantum state to recover an approximation of the original computational basis state. Since the Hadamard transform is self-inverse, applying the same operator during decoding reverses the encoding operation performed at the transmitter. In the absence of channel noise, this recovery process is exact. For example, the noiseless decoding operation for the two-qubit case is illustrated in (4.11), where the transmitted superposition state is perfectly transformed back into its original computational basis vector.

$$H_2 \left(\frac{1}{2} \begin{pmatrix} 1 \\ -1 \\ -1 \\ 1 \end{pmatrix} \right) = \begin{pmatrix} 0 \\ 0 \\ 0 \\ 1 \end{pmatrix} \tag{4.11}$$

In practical transmission scenarios, however, the received quantum state is affected by channel noise. The noisy received state is represented in (4.12), where $|\psi\rangle$ denotes the ideal transmitted superposition state and $\boldsymbol{\varepsilon}$ represents the noise perturbation introduced by the communication channel.

$$|\psi'\rangle = |\psi\rangle + \boldsymbol{\varepsilon} \tag{4.12}$$

After reception, the inverse Hadamard transformation is applied to the noisy state as shown in (4.13). This operation converts the received superposition state back into an estimated computational basis representation. Due to channel impairments, the resulting vector may not exactly match a valid basis state. Therefore, the receiver performs minimum Euclidean-distance detection to determine the most likely transmitted symbol.

$$|\phi'\rangle = H_k \, |\psi'\rangle \tag{4.13}$$

The decoding decision rule is defined in (4.14), where the estimated symbol $\hat{x}$ is selected as the valid computational basis vector that minimises the Euclidean distance from the received transformed state $|\phi'\rangle$.

$$\hat{x} = \arg\min_{x_i \in \mathcal{B}} \| \, |\phi'\rangle - x_i \| \tag{4.14}$$

Here, $\mathcal{B}$ denotes the complete set of 2^k valid computational basis vectors corresponding to the selected qubit configuration. Once symbol detection is completed, the recovered bit groups are reassembled to reconstruct the compressed image bitstream, which is subsequently decoded using the appropriate source decoder.

In the channel-coded configuration, the bitstream is first encoded with a rate-1/2 polar code before multi-qubit encoding. At the receiver, multi-qubit decoding is performed first, followed by polar decoding to recover the image bitstream.

Adaptive Qubit Selection

In both the uncoded and channel-coded configurations, an adaptive multi-qubit scheme is proposed based on the estimated channel quality, assuming perfect CSI. The adaptive selection methodology follows the same threshold-based framework described in Section 3.3.1, where the estimated channel SNR is used to determine the most appropriate transmission configuration. However, in this work, the adaptation is performed over the qubit size rather than the QEC configuration.

For each SNR level, the qubit size k that achieves the highest image reconstruction

quality in terms of PSNR, SSIM, and UQI is selected. Under low-SNR conditions, larger qubit sizes (e.g., $k = 6$–8) are selected to improve robustness against channel impairments through the higher-dimensional Hilbert space. As the channel quality improves, smaller qubit sizes (e.g., $k = 1$–4) are selected to reduce computational complexity, resource utilisation, and system latency while maintaining comparable reconstruction quality.

The switching thresholds are determined from the crossover regions of the performance curves for adjacent qubit sizes using the same procedure presented in Section 3.3.1. Consequently, the adaptive framework operates along the upper envelope of the individual qubit performance curves across the entire SNR range, enabling efficient utilisation of quantum resources while maintaining high image reconstruction quality under varying channel conditions.

4.1.2 Results

This section evaluates the proposed multi-qubit quantum encoding strategy for compressed image transmission under varying channel noise conditions, compared to the baseline single-qubit encoding method of Section 3.1.

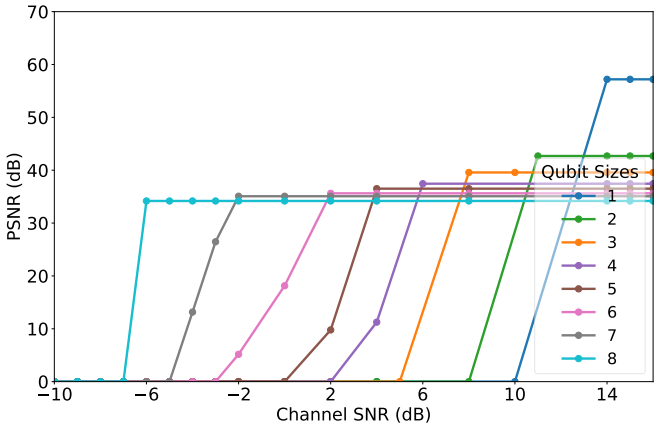
Effect of Qubit Size on Transmission Quality

To isolate the contribution of multi-qubit encoding, Figure 4.2 presents the performance of JPEG image transmission for all qubit sizes $k \in 1, \ldots, 8$ without channel coding. As the qubit size increases from 1 to 8, PSNR (Figure 4.2a), SSIM (Figure 4.2b), and UQI [211] (Figure 4.2c) consistently improve with increasing SNR, indicating enhanced transmission robustness and reconstructed image quality.

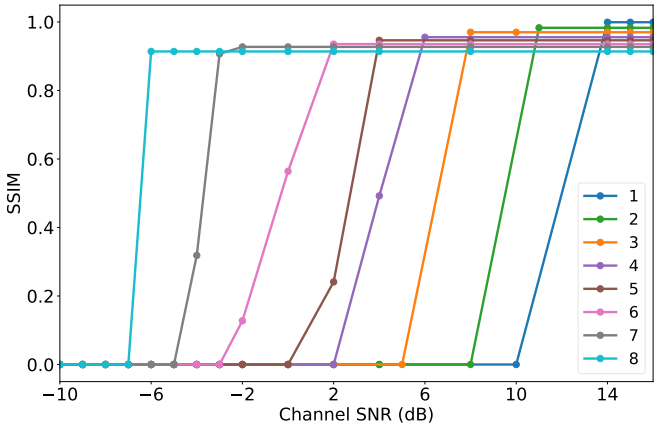
This improvement arises from the exponential increase in the dimensionality of the Hilbert space as the qubit group size k increases. For a k-qubit system, the dimensionality of the quantum state space increases to 2^k, enabling the transmitted information to be represented within a substantially larger Hilbert space. Consequently, the Euclidean distance and distinguishability between valid superposition states become more robust against channel perturbations. During transmission, channel noise affects the probability amplitudes of the quantum state; however, in higher-dimensional superposition

spaces, the transmitted states remain more distinguishable after the inverse Hadamard transformation and measurement process. As a result, the probability of incorrectly detecting the transmitted symbol decreases as the qubit dimension increases. This directly reduces the BER of the reconstructed bitstream, leading to fewer corrupted bits in the compressed JPEG data. Since compressed multimedia bitstreams are highly sensitive to transmission errors, even small BER reductions significantly improve reconstructed image quality. Therefore, the improved state distinguishability provided by higher-dimensional multi-qubit superposition encoding translates directly into higher PSNR, SSIM, and UQI values. At larger qubit configurations, particularly for $k = 8$, the system benefits from the full representation capability of $2^8 = 256$ orthogonal states, which directly corresponds to the range of 8-bit pixel intensity values commonly used in image representation. This enables highly efficient and robust symbol representation during transmission. Consequently, the eight-qubit configuration achieves the best overall performance, maintaining substantially lower distortion and significantly outperforming lower-dimensional qubit configurations under severe noisy channel conditions, even without explicit channel coding or quantum error correction.

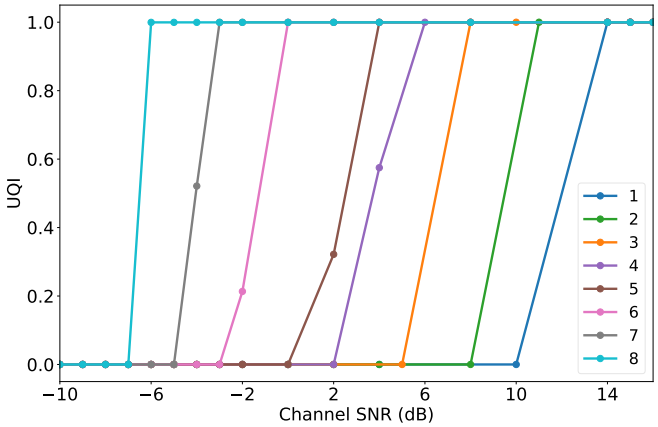
Notably, these gains are achieved without channel coding, demonstrating the intrinsic noise mitigation capability of multi-qubit encoding. This is in contrast to the QEC-based approach of Section 3.2, which requires ancilla qubits and syndrome circuits to achieve comparable robustness. While multi-qubit encoding significantly enhances performance, it introduces trade-offs in computational overhead, system complexity, and latency. Preparing a k-qubit superposition state requires $\mathcal{O}(k)$ single-qubit Hadamard operations, keeping encoding complexity linear. However, Euclidean distance decoding over 2^k basis states incurs $\mathcal{O}(2^k)$ operations, and the state vector representation requires $\mathcal{O}(2^k)$ memory. Consequently, both memory usage and decoding complexity grow exponentially with increasing k. Larger qubit configurations also increase latency and require longer coherence times, posing challenges for current quantum hardware implementations. Nevertheless, the maximum configuration considered in this study is limited to $k = 8$, corresponding to a 256-dimensional quantum state space, which remains computationally manageable and is considered compatible with the capabilities of near-future quantum communication hardware.



(a) PSNR



(b) SSIM



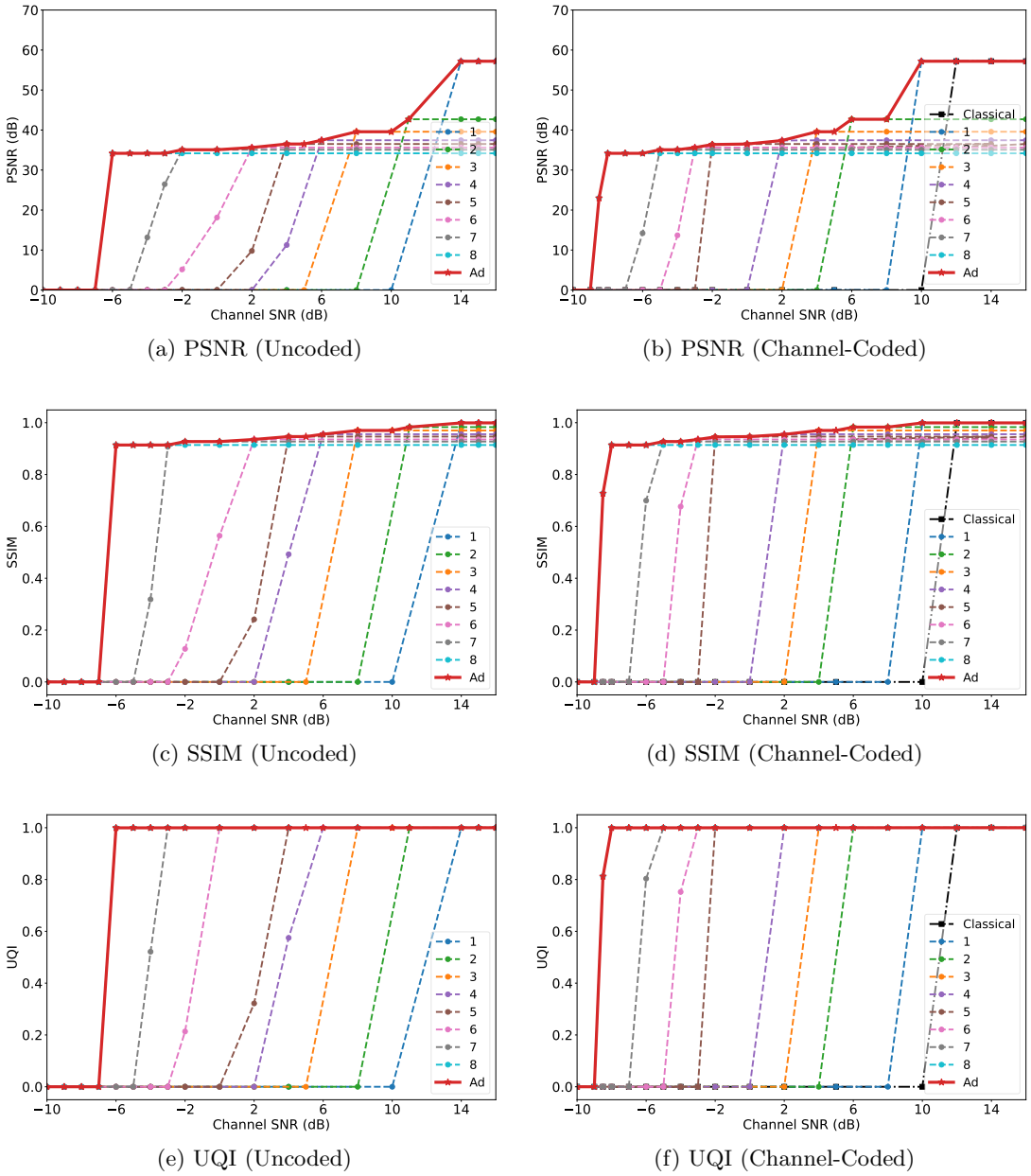
(c) UQI

Figure 4.2: Performance of all qubit configurations ($k = 1$–8) for JPEG image transmission without channel coding: (a) PSNR, (b) SSIM, (c) UQI.

Adaptive Multi-Qubit Encoding for JPEG Images

To address the trade-off between transmission robustness and computational complexity, Figure 4.3 presents the performance of the proposed adaptive multi-qubit transmission framework for JPEG-compressed images under both uncoded and channel-coded transmission scenarios. The results demonstrate that the integration of classical polar coding further enhances the robustness of the proposed quantum communication system across all qubit configurations. In the uncoded transmission case, shown in Figures 4.3a, 4.3c, and 4.3e, the adaptive multi-qubit framework already achieves substantial improvements in reconstructed image quality compared to lower-dimensional fixed-qubit configurations. When polar channel coding is incorporated, as illustrated in Figures 4.3b, 4.3d, and 4.3f, additional gains are observed in PSNR, SSIM, and UQI performance across the entire SNR range. The channel-coded system therefore combines the advantages of higher-dimensional quantum state representation with the error-correction capability of classical polar coding, resulting in significantly improved transmission reliability under noisy channel conditions.

Furthermore, the proposed adaptive framework (Ad) consistently outperforms conventional classical communication systems that rely solely on polar coding. The performance improvement is particularly noticeable in the low-SNR region, where the adaptive quantum system maintains substantially higher PSNR and structural similarity values despite severe channel impairments. This demonstrates the effectiveness of combining adaptive multi-qubit superposition encoding with classical channel coding for robust multimedia transmission. The adaptive transmission scheme, represented by the solid red curve in Figure 4.3, dynamically selects the most suitable qubit configuration according to the instantaneous channel SNR. Under severe noisy conditions, the framework automatically selects higher-dimensional qubit configurations ($k = 6$–8) to maximise transmission robustness and improve quantum-state distinguishability during decoding. As the channel quality improves and the SNR increases, the system progressively switches to lower-dimensional configurations ($k = 1$–4), thereby reducing computational complexity and transmission overhead while still maintaining high reconstructed image quality. This adaptive behaviour enables the proposed framework to efficiently balance error resilience, complexity, and bandwidth utilisation across varying channel conditions.



(a) PSNR (Uncoded)

(b) PSNR (Channel-Coded)

(c) SSIM (Uncoded)

(d) SSIM (Channel-Coded)

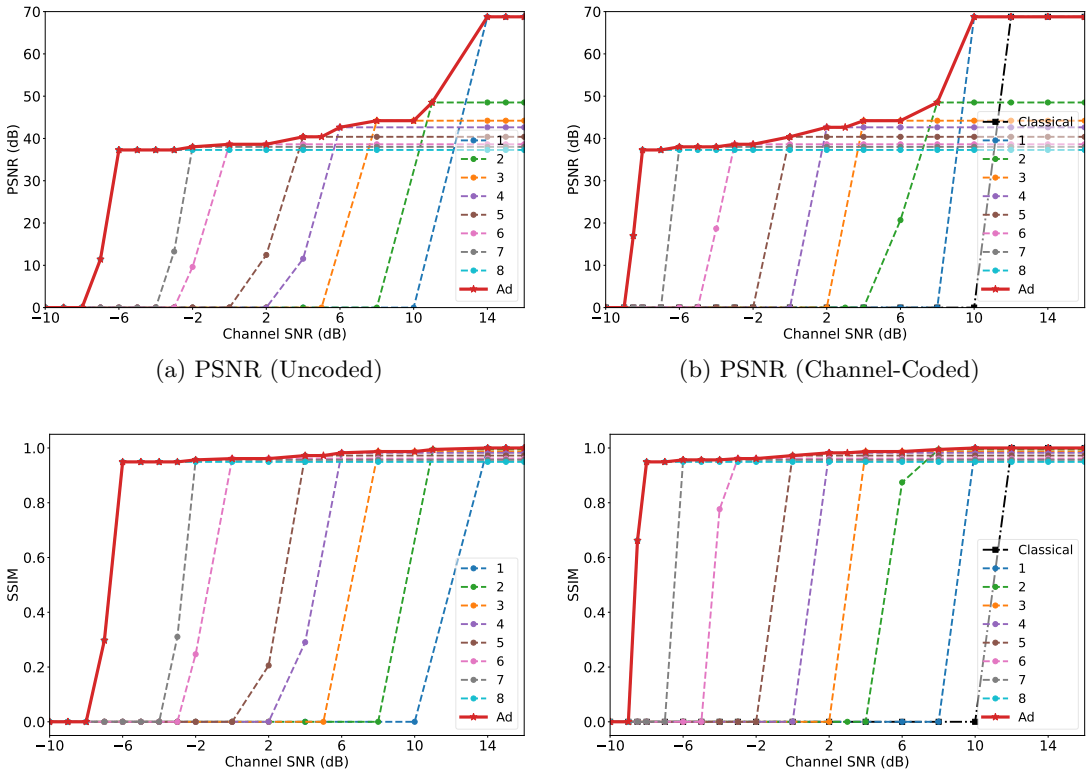
(e) UQI (Uncoded)

(f) UQI (Channel-Coded)

Figure 4.3: Performance of JPEG image transmission using adaptive (Ad) qubit encoding.

Adaptive Multi-Qubit Encoding for HEIF Images

The proposed adaptive multi-qubit transmission framework is equally effective for HEIF-compressed images. The performance results presented in Figure 4.4 demonstrate consistent improvements for both uncoded and channel-coded transmission scenarios across the full SNR range. In the uncoded case, the adaptive framework achieves clear gains in PSNR and SSIM performance, as illustrated in Figure 4.4a and Figure 4.4c, respectively. Similar improvements are also observed in the channel-coded transmission results shown in Figure 4.4b and Figure 4.4d, where the combination of adaptive multi-qubit encoding and polar channel coding provides enhanced robustness against channel noise.



(a) PSNR (Uncoded)

(b) PSNR (Channel-Coded)

(c) SSIM (Uncoded)

(d) SSIM (Channel-Coded)

Figure 4.4: Performance of HEIF image transmission using adaptive (Ad) qubit encoding.

Compared to the corresponding JPEG transmission results, the HEIF-based system consistently achieves higher reconstruction quality under identical channel conditions. This improvement is mainly due to the superior compression efficiency of the HEIF

format, which preserves structural information and perceptual image quality more effectively at comparable bitrates. Consequently, the reconstructed HEIF images maintain higher PSNR and SSIM values after transmission through noisy quantum communication channels. The results further confirm that the performance advantages of the proposed adaptive framework are not limited to a specific source coding format. Instead, the consistent improvements observed for both JPEG and HEIF images demonstrate that the proposed adaptive multi-qubit transmission strategy provides a robust and versatile solution for compressed image transmission over error-prone quantum communication channels.

To provide a visual comparison, Figure 4.5 presents the JPEG input images for different qubit encoding sizes ranging from 1 to 8. To achieve bandwidth equalisation, different JPEG quality settings are applied for each qubit encoding size. Consequently, each configuration has a different file size, number of bits, PSNR, and SSIM, as summarised in Table 4.1. Lower QP values are used for the higher-qubit encoding schemes to achieve higher compression, whereas higher QP values are used for the lower-qubit encoding schemes, resulting in lighter compression. Accordingly, the product of the qubit encoding size and the corresponding bitstream length remains approximately constant across all encoding configurations, ensuring that an equal amount of source information is represented. As a result, the higher compression applied to the higher-qubit encoding schemes leads to lower maximum achievable reconstruction quality. In contrast, the lower-qubit encoding schemes utilise lighter compression and therefore achieve higher maximum PSNR and SSIM values.

To further evaluate the performance of the proposed system under noisy channel conditions, Figures 4.6 and 4.7 present representative decoded images (JPEG, uncoded) at SNRs of 11 dB and 9 dB, respectively. The visual results closely follow the corresponding PSNR and SSIM trends. As the qubit encoding size increases, the reconstructed images exhibit improved robustness against channel noise. At an SNR of 11 dB (Figure 4.6), the qubit size 1 configuration shows noticeable compression and transmission artefacts, whereas the higher-qubit configurations produce significantly better visual quality. When the channel condition deteriorates to an SNR of 9 dB (Figure 4.7), the qubit size 1 configuration is unable to reconstruct a decodable image because of the high

BER, while the qubit size 2 configuration exhibits noticeable artefacts. The higher-qubit configurations (3-8) continue to preserve acceptable image quality under these conditions. As the SNR decreases further, the noise resilience of each qubit configuration gradually degrades; however, higher-qubit encoding schemes (7-8) maintain reliable image reconstruction over a wider SNR range than lower-qubit encoding schemes.



(a) 1 (b) 2 (c) 3 (d) 4



(e) 5 (f) 6 (g) 7 (h) 8

Figure 4.5: Input JPEG images for different multi-qubit configurations: (a) 1, (b) 2, (c) 3, (d) 4, (e) 5, (f) 6, (g) 7, and (h) 8.

Table 4.1: Rate–distortion performance of JPEG compression for different multi-qubit configurations.

Qubit Size	**QP**	**Size (B)**	**Bits**	**PSNR (dB)**	**SSIM**
1	100	73,710	589,680	50.88	0.9978
2	95	31,265	250,120	40.90	0.9877
3	92	24,006	192,048	38.52	0.9813
4	86	18,273	146,184	35.88	0.9710
5	79	14,505	116,040	34.01	0.9594
6	71	12,252	98,016	32.74	0.9487
7	62	10,507	84,056	31.64	0.9379
8	52	9,266	74,128	30.76	0.9273



(a) 1 (b) 2 (c) 3 (d) 4

(e) 5 (f) 6 (g) 7 (h) 8

Figure 4.6: Decoded JPEG images (uncoded) for different multi-qubit configurations at an SNR of 11 dB: (a) 1, (b) 2, (c) 3, (d) 4, (e) 5, (f) 6, (g) 7, and (h) 8.



(a) 1 (b) 2 (c) 3 (d) 4

(e) 5 (f) 6 (g) 7 (h) 8

Figure 4.7: Decoded JPEG images (uncoded) for different multi-qubit configurations at an SNR of 9 dB: (a) 1, (b) 2, (c) 3, (d) 4, (e) 5, (f) 6, (g) 7, and (h) 8.

Practical Considerations and Deployment Potential

The experimental results indicate that the proposed adaptive multi-qubit encoding framework provides several advantages for reliable high-quality image transmission in bandwidth-constrained and error-prone communication environments. These characteristics make the framework well suited for emerging multimedia applications including augmented reality devices, ultra-high-definition display systems, and intelligent IoT platforms. By dynamically selecting appropriate qubit dimensions according to transmission conditions, the framework is able to maintain image quality while reducing unnecessary transmission overhead and energy consumption, both of which are important considerations for resource-limited devices.

The proposed system further benefits from the use of separable multi-qubit superposition states, which improves compatibility with near-term quantum hardware while avoiding the substantial complexity associated with entanglement-based implementations. Although increasing the qubit dimension introduces additional computational and hardware requirements, the adaptive nature of the framework enables a practical balance between transmission quality, system complexity, and resource utilisation. Consequently, the proposed approach represents a feasible direction for future practical quantum communication systems.

Another important contribution of this work is the development of a scalable and adaptable quantum communication architecture capable of operating under varying channel conditions and hardware constraints. Such adaptability is essential for enabling future quantum-enabled multimedia communication applications requiring reliable and high-fidelity data delivery. The proposed framework therefore establishes a foundation for the continued development of efficient and practical quantum image transmission technologies as quantum communication hardware continues to mature.

Despite these advantages, several limitations remain within the proposed adaptive multi-qubit transmission framework. One of the primary challenges is the absence of low-complexity and scalable quantum error correction techniques suitable for higher-dimensional multi-qubit states. Although classical polar coding provides useful error mitigation capability, its effectiveness decreases under severely noisy channel conditions. In comparison, low-complexity three-qubit QEC schemes can improve transmission

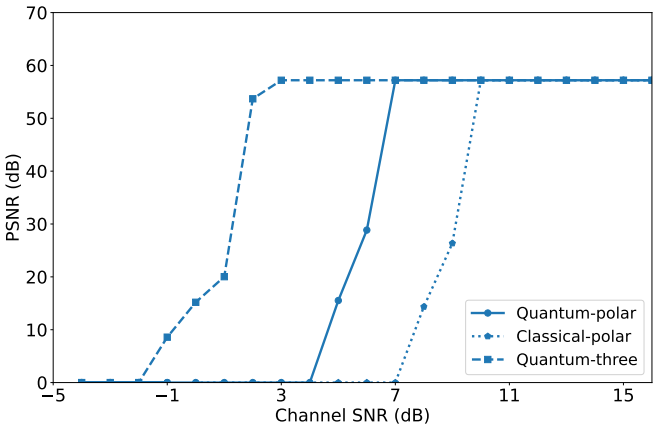


Figure 4.8: PSNR comparison of three-qubit QEC, multi-qubit superposition encoding, and classical polar-coded systems for JPEG image transmission.

reliability for single-qubit encoding scenarios, as illustrated in Figure 4.8. However, these approaches require substantial additional qubit and ancilla resources, which significantly limits scalability. Extending similar quantum error correction strategies to larger multi-qubit systems would result in rapidly increasing implementation complexity and resource consumption, thereby reducing practical feasibility for robust large-scale quantum communication applications.

4.1.3 Section Summary

This section proposed a multi-qubit quantum encoding strategy for compressed image transmission, demonstrating that higher-dimensional Hilbert space representations provide substantial noise resilience. Increasing the qubit group size from $k = 1$ to $k = 8$ yielded consistent gains in PSNR, SSIM, and UQI under all tested noise conditions, with eight-qubit encoding achieving SNR gains of up to 15 dB for JPEG and 17 dB for HEIF relative to single-qubit encoding when combined with polar channel coding. These improvements arose from the combined benefits of higher-dimensional superposition encoding, improved transmission robustness, and enhanced compression efficiency. Statistical analysis over 30,000 transmissions confirmed consistent and reliable results, with 95% confidence intervals of ± 0.0068 dB (JPEG) and ± 0.0045 dB (HEIF) for PSNR. The adaptive scheme further reduced unnecessary complexity at high SNR while preserving fidelity under severe impairments, offering a scalable and practical

complement to the QEC-based approaches of Chapter 3. Section 4.2 extends this multi-qubit framework to video transmission, incorporating temporal quality assessment and GOP-aware evaluation.

4.2 An Adaptive Multi-Qubit Encoding Framework for Robust Video Transmission over Noisy Quantum Channels

Publication Notice

The research presented in this section has been submitted as the following manuscript and is currently under review:

U. Jayasinghe, P. Samarathunga, T. Fernando, Y. Ganearachchi, and A. Fernando, "An Adaptive Variable-Qubit Encoding Framework for Robust Video Transmission over Noisy Quantum Channels," submitted to *IEEE Communications Letters*.

Portions of this chapter are based on the above submitted manuscript. The material has been revised and expanded with additional explanations, analysis, and discussion for inclusion in this doctoral thesis.

Problem Statement: Section 4.1 demonstrated that multi-qubit encoding significantly improves transmission robustness for compressed image communication without requiring ancilla-qubit overhead. However, compressed video transmission presents a substantially more challenging communication scenario. Compared to still images, compressed video bitstreams are considerably larger and contain strong temporal dependencies introduced by inter-frame prediction structures such as P-frames and B-frames. Consequently, transmission errors can propagate across multiple consecutive frames within a GOP, causing severe degradation in reconstructed video quality. Even a small number of bit errors may corrupt not only the current frame but also subsequent dependent frames until the next intra-coded refresh frame is reached. As a result, video transmission is significantly more sensitive to channel impairments than still-image transmission. Under severe noisy channel conditions, conventional single-qubit quantum encoding approaches, which operate within a limited two-dimensional Hilbert space, are

insufficient to maintain acceptable visual quality and temporal consistency throughout the transmitted video sequence.

Limitations of Existing Work: Existing research on quantum multimedia communication has primarily focused on image transmission and QEC techniques, while adaptive multi-qubit encoding strategies for compressed video transmission over noisy quantum channels remain largely unexplored. In particular, no prior work has systematically investigated how the qubit group size influences reconstructed video quality under varying channel conditions, especially in terms of spatial fidelity, temporal consistency, and inter-frame error propagation. Furthermore, adaptive qubit allocation driven by real-time CSI has not been explored for quantum video communication systems. In addition, the multi-qubit encoding framework presented in Section 4.1 has not previously been extended to compressed video transmission, where factors such as GOP structure, frame rate, temporal prediction dependencies, and spatial resolution introduce substantially greater transmission and reconstruction challenges compared to static image communication systems.

Motivation and Proposed Contribution: Compressed video transmission over noisy quantum channels presents significantly greater challenges than static image communication due to temporal prediction dependencies, inter-frame error propagation, and continuously varying channel conditions. In practical communication environments, a fixed qubit configuration cannot simultaneously provide high transmission robustness under severe noisy conditions and low computational complexity under favourable channel conditions. These limitations motivate the development of adaptive quantum transmission strategies capable of dynamically balancing robustness and system complexity according to instantaneous channel quality. To address these challenges, this section proposes an adaptive variable-qubit quantum communication framework for robust compressed video transmission over noisy quantum channels. Building upon the multi-qubit image transmission framework introduced in Section 4.1, the proposed system dynamically adjusts the qubit group size k according to the instantaneous channel condition obtained through CSI. Under favourable channel conditions, lower-dimensional qubit configurations are selected to reduce computational complexity and transmission

overhead. Conversely, under severe noisy channel conditions, higher-dimensional qubit configurations are employed to improve transmission robustness and enhance decoding reliability. The proposed framework is evaluated under different GOP sizes, frame rates, and spatial resolutions to analyse its effectiveness across diverse video transmission scenarios. System performance is assessed using both spatial and perceptual quality metrics, including PSNR, SSIM, and VMAF, and compared against fixed-qubit quantum transmission schemes as well as a conventional classical BPSK-based communication framework.

4.2.1 System Model

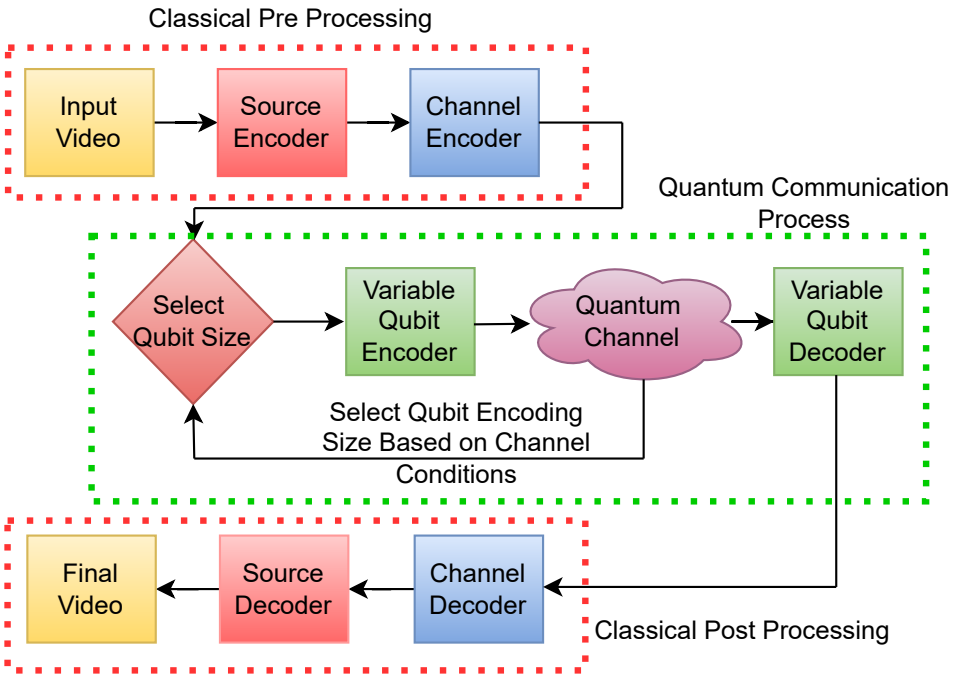


Figure 4.9: Proposed variable-qubit encoding system for video transmission.

The end-to-end variable-qubit video communication framework is illustrated in Figure 4.9. The system employs VVC [204] (H.266) compression via the VVenC encoder to produce a binary bitstream, which is protected using a rate-1/2 polar code [210] before quantum encoding. Experiments are conducted using three YUV420 video sequences representing high-motion [205], medium-motion [206], and low-motion [207]

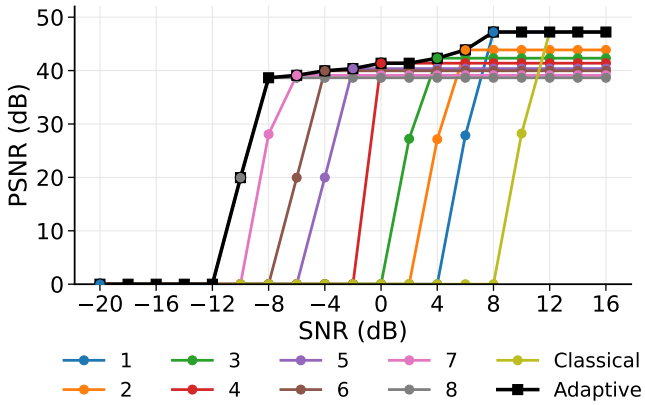
content. Each sequence is evaluated at resolutions of 320×180, 1280×720, and 1920×1080, frame rates of 20, 30, and 50 fps, and GOP sizes of 8, 16, and 32, thereby providing a representative range of practical multimedia transmission scenarios. All qubit configurations are evaluated under equal bandwidth conditions, with the QP values adjusted to ensure a fair comparison. The classical reference system uses BPSK modulation with a rate-1/2 polar code under the same bandwidth. Simulations assume perfect CSI as the standard upper-bound baseline.

Multi-Qubit Encoding and Decoding for Video

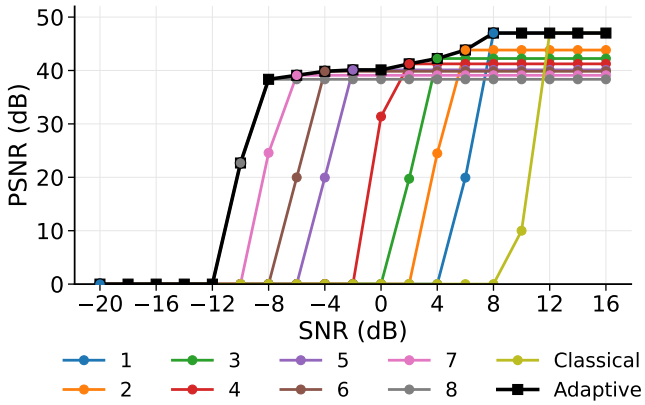
The quantum state construction, Hadamard superposition encoding, composite noise channel model, and minimum Euclidean distance decoding follow the framework established in Section 4.1.1 (Equations (4.1)–(4.14)). For a qubit group size $k \in \{1, \ldots, 8\}$, the polar-coded video bitstream is segmented into groups of k bits, each mapped to one of 2^k orthogonal superposition states via $H_k = H^{\otimes k}$ and transmitted through the composite quantum noise channel of Section 3.1. At the receiver, the inverse Hadamard transform is applied and the decoded symbol is selected by minimum Euclidean distance as in (4.14). The recovered bitstream is then passed through the polar decoder and VVC source decoder to reconstruct the video. The adaptive variable-qubit scheme selects k per SNR level using the same strategy as Section 4.1: larger k at low SNR for maximum noise resilience, smaller k at high SNR to minimise complexity.

4.2.2 Results

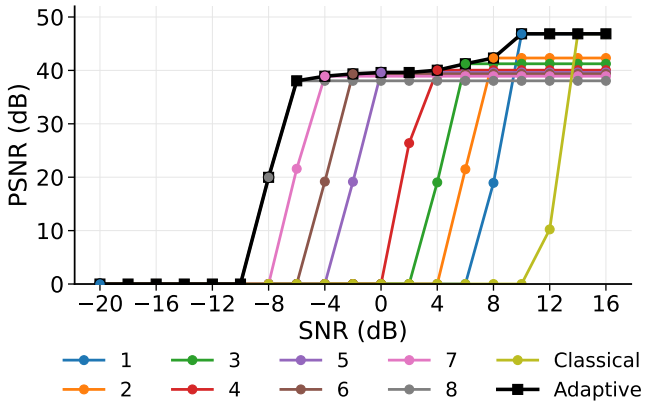
Three video sequences with contrasting motion and spatial characteristics are used for evaluation. The first [205] features rapid motion and frequent scene changes, making compression and transmission challenging. The second [206] has moderate motion with balanced spatial and temporal complexity. The third [207] shows minimal movement, resulting in low temporal variation and easier compression. Performance is evaluated using average PSNR, SSIM, and VMAF across all three sequences.



(a) PSNR, GOP = 8

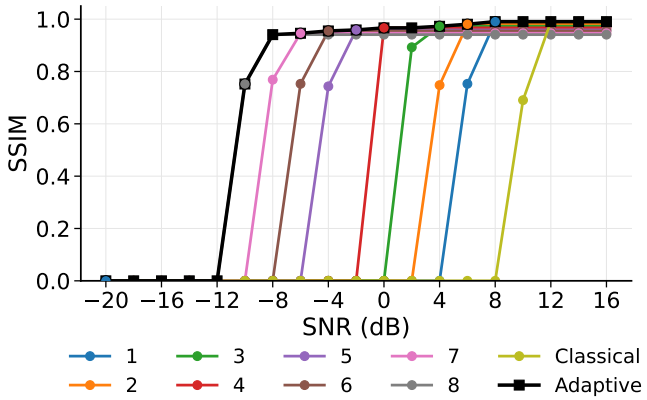


(b) PSNR, GOP = 16

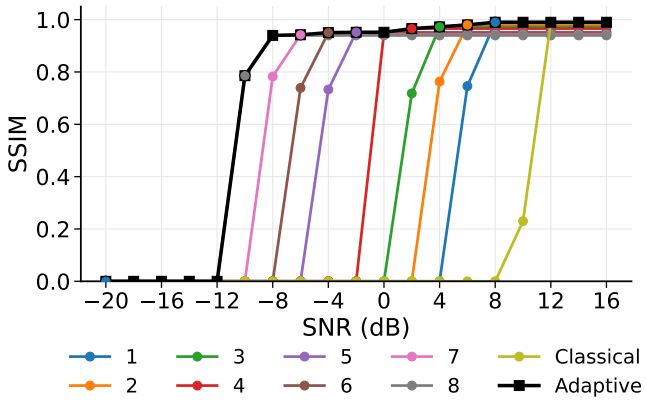


(c) PSNR, GOP = 32

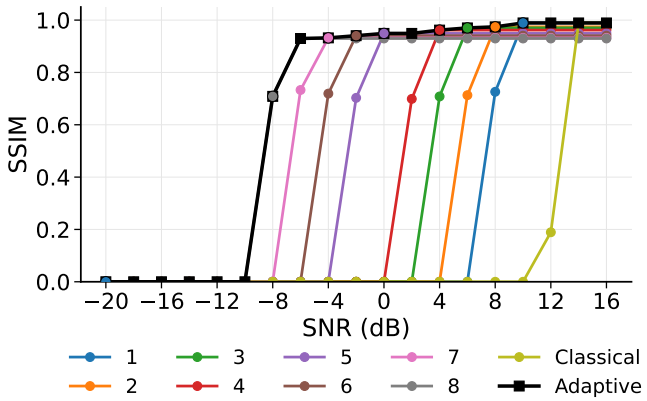
Figure 4.10: PSNR performance variation with qubit size and GOP size in quantum and classical video communication systems at 320×180 resolution.



(a) SSIM, GOP = 8

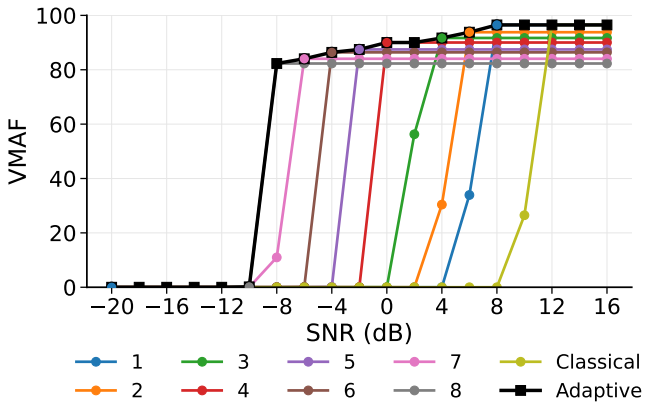


(b) SSIM, GOP = 16

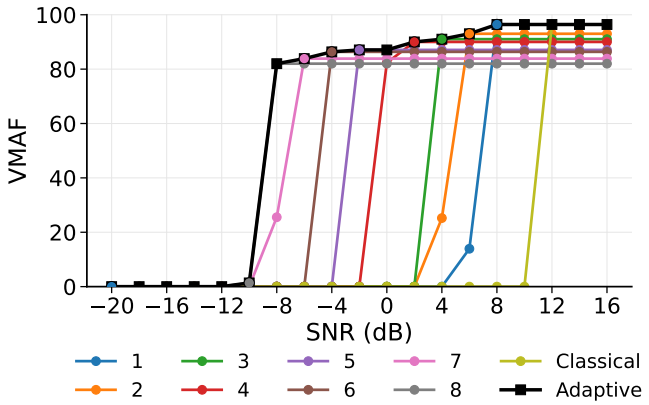


(c) SSIM, GOP = 32

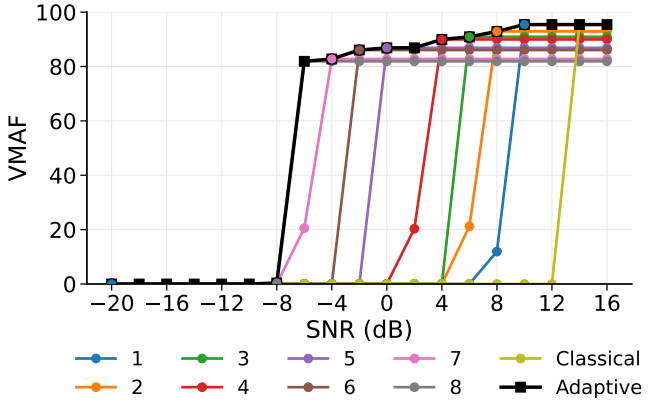
Figure 4.11: SSIM performance variation with qubit size and GOP size in quantum and classical video communication systems at 320×180 resolution.



(a) VMAF, GOP = 8



(b) VMAF, GOP = 16



(c) VMAF, GOP = 32

Figure 4.12: VMAF performance variation with qubit size and GOP size in quantum and classical video communication systems at 320×180 resolution.

Effect of Qubit Size and GOP on Video Quality

Performance variations with qubit size and GOP size at the 320×180 resolution are presented in Figures 4.10–4.12. The results show that quantum communication systems using qubit configurations from $k = 1$ to $k = 8$ consistently outperform the classical baseline system (light green curve) across all evaluated channel conditions. In general, reconstructed video quality improves as the qubit group size increases, demonstrating the effectiveness of higher-dimensional Hilbert space representations for improving transmission robustness in compressed video communication. However, fixed-qubit transmission schemes exhibit two important limitations. Lower-dimensional qubit configurations provide reduced robustness against channel noise, leading to faster degradation in PSNR, SSIM, and VMAF under low-SNR conditions. Conversely, higher-dimensional configurations provide stronger noise resilience but introduce increased computational complexity and reduced maximum reconstruction quality due to bandwidth equalisation constraints and the stronger compression required to maintain constant transmission bandwidth across different qubit settings.

The proposed adaptive variable-qubit framework effectively resolves this trade-off by dynamically selecting the most suitable qubit configuration according to the instantaneous channel condition. As shown by the black curve in Figures 4.10–4.12, the adaptive scheme maintains strong robustness against channel noise while simultaneously preventing unnecessary quality degradation and excessive computational overhead. Consequently, the adaptive framework consistently achieves the best overall transmission performance, outperforming all fixed-qubit transmission configurations and achieving an approximate channel SNR gain of 20 dB relative to the classical communication system. The adaptive framework also provides consistent improvements across all GOP configurations in terms of both spatial reconstruction quality (PSNR and SSIM) and perceptual spatio-temporal quality (VMAF). As the GOP size increases, a larger proportion of frames become inter-coded, increasing the dependency between consecutive frames. Under these conditions, transmission errors occurring in earlier frames propagate through subsequent predicted frames, causing cumulative degradation in reconstructed video quality. This error-propagation behaviour is clearly observed in Figures 4.10–4.12, where all transmission systems experience gradual reductions in PSNR, SSIM, and

VMAF performance as the GOP size increases from 8 to 32. Nevertheless, the proposed adaptive framework consistently maintains superior performance compared to both fixed-qubit quantum systems and the classical baseline across all GOP configurations.

Effect of Frame Rate and Resolution

Table 4.2 summarises the maximum SNR gain of the adaptive variable-qubit scheme over the classical baseline across all evaluated resolutions and frame rates for GOP = 8. The gain remains essentially unchanged across these parameters, confirming that frame rate and resolution do not materially affect the SNR advantage of the proposed framework.

Table 4.2: Relative SNR advantage of adaptive variable-qubit quantum communication compared with the classical reference, across spatial resolutions and frame rates (GOP = 8).

Frame Rate (fps)	Resolution		
	320×180	1280×720	1920×1080
20	20.0 dB	19.9 dB	20.1 dB
30	20.1 dB	20.0 dB	20.2 dB
50	20.0 dB	20.1 dB	20.1 dB

These results confirm that the approximately 20 dB gain over the classical system is a robust and consistent property of the adaptive variable-qubit framework, independent of the specific video encoding parameters tested.

4.2.3 Section Summary

This section introduced an adaptive variable-qubit encoding framework for quantum video transmission, extending the multi-qubit image encoding strategy of Section 4.1 to the more demanding temporal domain. The proposed system consistently outperforms both fixed-qubit quantum baselines and the classical BPSK reference, achieving a robust ∼20 dB SNR gain across all tested resolutions (320×180 to 1920×1080), frame rates (20–50 fps), and GOP sizes (8, 16, 32). Larger GOP sizes reduce performance for all systems due to inter-frame error propagation, highlighting the importance of adaptive QP and GOP-aware error resilience strategies as a direction for future work. Together, the two contributions of this chapter establish a comprehensive, scalable, and ancilla-

free multi-qubit quantum multimedia communication framework, providing a practical and resource-efficient pathway toward high-fidelity quantum-enabled image and video transmission for next-generation consumer and network applications.

4.3 Chapter Summary

This chapter presented the development of a novel multi-qubit encoding paradigm for robust quantum multimedia transmission, covering both compressed image (Section 4.1) and compressed video (Section 4.2) communication scenarios. The proposed framework demonstrated that increasing the qubit group size enables multimedia information to be represented within progressively higher-dimensional Hilbert spaces, thereby improving transmission robustness under noisy channel conditions without relying on ancilla qubits or redundancy-based QEC mechanisms.

For compressed image transmission, the proposed multi-qubit framework achieved substantial improvements in reconstructed image quality compared to single-qubit and classical transmission approaches, while the adaptive qubit-selection strategy provided an effective balance between transmission robustness and computational complexity across varying channel conditions. The framework was subsequently extended to compressed video transmission, where adaptive variable-qubit encoding demonstrated consistent improvements in both spatial and perceptual video quality across different resolutions, frame rates, and GOP configurations. The results confirmed that the robustness advantages of higher-dimensional multi-qubit encoding remain effective even in temporally correlated video transmission environments.

However, this encoding-driven robustness is achieved entirely in the *time domain*, where classical bits are mapped directly into computational-basis quantum states. Consequently, channel noise acts within the same domain in which the information is encoded, and the resulting quantum states do not exploit the spectral structure that classical multimedia processing techniques, such as DCT and FFT, have long demonstrated to provide superior energy compaction and noise robustness. This observation motivates a fundamental shift in approach. Rather than continuing to scale the dimensionality of time-domain encoding, the subsequent chapter investigates how quantum transmission can be moved into the *frequency domain* through native quantum transforms.

Specifically, Chapter 5 introduces frequency-domain multi-qubit encoding based on the QFT, projecting multi-qubit states into the quantum frequency domain to enable spectral processing, transform-domain compression, and improved noise immunity. This transform-domain extension complements the time-domain multi-qubit framework established in this chapter, providing a broader design space for high-fidelity quantum-enabled image and video transmission across diverse channel conditions.

Chapter 5

Design and Analysis of Quantum Frequency-Domain Techniques for Quantum Communication

The frameworks developed in Chapters 3 and 4 established that quantum superposition encoding, combined with multi-qubit information representation, can deliver substantial gains over classical communication systems for image and video transmission over noisy channels. However, all of these frameworks operate entirely in the *time domain*, where classical bits are mapped directly into computational-basis quantum states, or their corresponding multi-qubit superposition states, and transmitted through the communication channel. While these approaches demonstrated improved transmission robustness, they did not exploit the transform-domain properties that have long been fundamental to classical multimedia processing for energy compaction, sample decorrelation, compression, and improved transmission resilience. The QFT provides a native and exponentially efficient mechanism for projecting multi-qubit quantum states into the quantum frequency domain, thereby enabling transform-domain quantum multimedia processing. This raises three important research questions that were not addressed in Chapters 3 and 4: (i) can quantum frequency-domain encoding using the QFT provide improved transmission robustness compared to time-domain multi-qubit encoding? (ii) can QFT-based quantum-state representation be exploited not only for transmission

but also for symbol-level quantum compression that reduces channel utilisation without relying solely on classical source coding techniques? and (iii) when residual channel distortions and reconstruction artefacts remain after transmission, can semantic-aware post-processing, targeting both quantum channel noise and compression artefacts, further enhance the reconstructed image or video quality? This chapter addresses each of these research questions in sequence.

The QFT is selected in this chapter because it provides a native unitary transform that is naturally compatible with multi-qubit quantum-state representations while offering exponentially efficient and low-complexity implementation using elementary quantum gates, such as Hadamard and controlled-phase gates. In addition to its well-established role in quantum algorithms, the QFT enables direct manipulation of frequency-domain quantum amplitudes, making it particularly suitable for investigating transform-domain quantum communication, frequency-domain encoding, and quantum compression within a unified framework. By contrast, other quantum transforms, such as quantum wavelet transforms, provide attractive multiresolution properties and improved spatial localisation. However, their circuit implementations are generally more complex, depend on the specific wavelet basis adopted, and are still under active development. Consequently, the QFT is selected as the primary transform in this dissertation to establish the fundamental principles of quantum frequency-domain multimedia communication. Although JPEG, HEIF, and VVC employ conventional transform coding (e.g., DCT or related transforms) prior to entropy coding, these operations only influence the statistical characteristics and length of the compressed bitstream. Since the proposed quantum encoder operates directly on the compressed bitstream rather than on transform coefficients, the quantum encoding process remains independent of the particular source transform adopted.

The chapter is organised in six sections. Section 5.1 develops a frequency-domain multi-qubit encoding framework for image transmission [212], [213], comparing it directly against the time-domain multi-qubit framework of Chapter 4. Section 5.2 extends the frequency-domain framework to video transmission, where temporal correlation amplifies the cost of channel errors. Section 5.3 introduces a QFT-based *compression* scheme for image transmission, in which the QFT itself performs symbol-level data reduction instead

of relying on classical source coding [214]. Section 5.4 extends QFT-based compression to quantum video transmission [215]. To address the reconstruction artefacts and perceptual degradation introduced by aggressive QFT compression and channel noise, Section 5.5 introduces a semantic-aware diffusion-based restoration framework for image transmission, which is further extended to video transmission in Section 5.6.

5.1 A Quantum Multi-Qubit Frequency-Domain Approach for Reliable Image Transmission

Publication Notice

The research presented in this section has been published in the following peer-reviewed journal publication:

U. Jayasinghe, T. Fernando, and A. Fernando, "High-Fidelity Image Transmission in Quantum Communication with Frequency-Domain Multi-Qubit Techniques," *Algorithms*, vol. 18, no. 8, p. 501, 2025, doi: 10.3390/a18080501.

This material is reproduced and adapted under the terms of the MDPI copyright policy for inclusion in this doctoral thesis. The content has been revised and extended with additional explanations and expanded discussion.

Problem Statement: Chapter 4 demonstrated that multi-qubit time-domain encoding significantly improves image transmission performance compared to single-qubit baselines. However, in that framework each transmitted quantum state directly represents a block of classical bits in the time domain, which means channel noise acts on the same domain in which the information is encoded. Under low-SNR conditions, perturbations of the state vector therefore translate directly into measurement errors and, ultimately, image-bit corruption. Classical multimedia processing has long shown that frequency-domain representations (DCT, FFT) provide superior noise robustness and energy compaction, yet the time-domain quantum framework of Chapter 4 does not exploit any analogous structure in the quantum domain.

Limitations of Existing Work: Existing quantum communication research, including the multi-qubit framework presented in Chapter 4, has primarily relied on direct computational-basis encoding for transmission. Although the QFT offers several theoretical advantages, including frequency-domain representation, improved information distribution across quantum states, and potential robustness against channel noise, its use as a direct encoding and transmission mechanism for compressed image bitstreams has not been sufficiently explored. In addition, previous studies have not systematically compared QFT-based frequency-domain encoding with conventional time-domain multi-qubit encoding under identical bandwidth and channel conditions. Consequently, the influence of QFT-based transmission on multi-qubit communication performance and noise resilience remains largely uncharacterised.

Motivation and Proposed Contribution: To address these identified gaps, this section proposes a frequency-domain multi-qubit quantum communication framework for image transmission over error-prone channels. Similar to the framework presented in Chapter 4, compressed image bitstreams are first grouped and mapped into multi-qubit computational-basis vectors. However, instead of transmitting these encoded vectors directly, the proposed method applies the QFT to project the encoded quantum states into the quantum frequency domain prior to transmission. At the receiver, the IQFT is applied to reconstruct the computational-basis representation for measurement and decoding. The motivation for adopting frequency-domain quantum encoding lies in the change in information representation introduced by the QFT. In direct computational-basis transmission, the encoded information is represented primarily through the identity of the mapped computational-basis vector. In contrast, the QFT transforms the encoded state into a structured superposition spanning the 2^k-dimensional Hilbert space, where the information is distributed through amplitude and relative phase relationships across multiple basis components. Consequently, the transmitted information is represented in a distributed spectral form rather than solely through the original computational-basis mapping. Because channel disturbances act on the transformed superposition prior to reconstruction, the resulting degradation is expected to be distributed across the spectral representation rather than directly affecting only the original mapped basis structure. After transmission, the IQFT coherently recombines

the distributed components to recover the computational-basis information. Therefore, the central hypothesis investigated in this section is that QFT-based frequency-domain representation can improve robustness against channel-induced degradation compared to direct computational-basis transmission. To further isolate the contribution of frequency-domain processing, system performance is evaluated using both JPEG and HEIF source coding schemes, with and without rate-1/2 polar channel coding. This enables the contribution of QFT-based spectral representation to be distinguished from the gains provided by classical channel coding alone. The main contributions of this section are summarised as follows.

- A frequency-domain quantum communication framework is proposed for compressed image transmission, in which QFT-based multi-qubit encoding is integrated with classical source and channel coding to improve robustness against channel noise.
- The proposed framework is benchmarked against the time-domain multi-qubit scheme introduced in Chapter 4 under matched bandwidth conditions, allowing the performance gain attributable to frequency-domain processing to be isolated.
- A comprehensive evaluation is conducted across qubit group sizes $k \in [1, 8]$, for both JPEG and HEIF compressed inputs, and under configurations with and without rate-1/2 polar channel coding, identifying the operating regimes in which frequency-domain encoding provides the greatest benefit.

5.1.1 System Model

The end-to-end frequency-domain multi-qubit quantum image transmission framework is illustrated in Figure 5.1. The model is engineered to be highly flexible, modular, and scalable, supporting multi-qubit configuration bounds where each distinct logical state can encapsulate between 1 and 8 qubits (Q1–Q8). The 8-qubit maximum threshold was intentionally selected to align precisely with the traditional 8-bit allocation utilised for pixel brightness scales (0–255), facilitating a direct and highly seamless pixel-to-state mapping. Nevertheless, the underlying structural logic is not restricted to this cap; it can be dynamically scaled to accommodate larger qubit blocks based on hardware

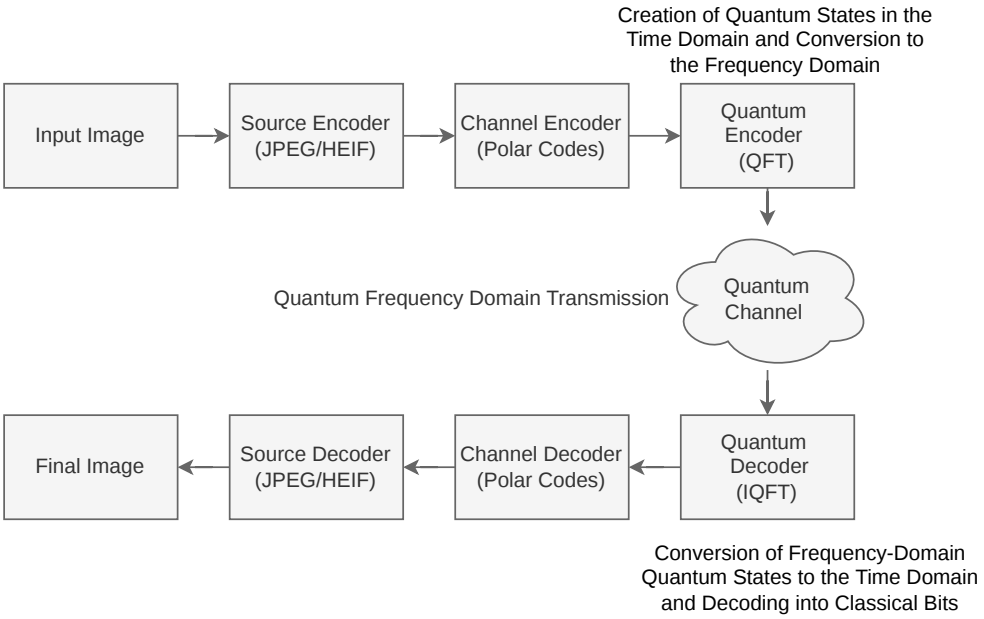


Figure 5.1: Complete block architecture of the proposed frequency-domain multi-qubit quantum communication pipeline.

viability and application-specific parameters.

The processing architecture operates completely independent of the source type, comfortably handling diverse inputs regardless of resolution variations, content profiles, or spatial complexities. For experimental validation, this research utilises 50 carefully selected images extracted from the Microsoft COCO dataset [197], an industry-standard benchmark in computer vision research. These target images showcase a wide spectrum of SI and integrate diverse real-world landscapes, object categories, and structural variations, offering a representative cross-section of typical visual data. While the core sample size comprises 50 images, their deep structural diversity ensures sufficient statistical confidence to reflect real-world performance hurdles. This selection balances data management efficiency with empirical rigour. Furthermore, every single test image undergoes thousands of independent transmission iterations across an expansive multidimensional configuration space, encompassing shifting channel constraints, variable encoding size parameters ($k = 1$ to 8 qubits), and different operating domains (time vs. frequency). This extensive simulation framework generates a large volume of performance data, enabling reliable statistical analysis of both average-case and worst-

case communication behaviour. Consequently, the consolidated data accurately maps the system's resilience and functional agility under realistic deployment scenarios.

Detailed operational breakdowns of each distinct block within the introduced framework are provided in the subsequent subsections.

Source Coding

The initial stage of the processing pipeline involves source encoding, which structurally compacts raw visual data matrices into highly dense binary sequences. In this analysis, JPEG [11] and HEIF [12] compression methodologies are adopted due to their favourable efficiency in reducing data size while preserving high visual fidelity. To guarantee a fair and objective evaluation across different multi-qubit systems, the source compression metrics are dynamically adjusted so that all configuration alternatives consume roughly matching channel bandwidth. Because high-capacity systems (such as Q8) carry significantly more qubits per transmitted symbol than lower-capacity setups (such as Q1), more intensive compression parameters are applied at the higher qubit levels to prevent bandwidth expansion. This is managed by calibrating specific QP values to ensure that the mathematical product of the active qubit count (k) and the per-symbol bitrate remains substantially static, satisfying the relation: $k \times \text{bitrate}_k \approx \text{constant}$.

Channel Encoding/ Decoding

After source compression, a classical channel encoder injects systematic redundancy into the binary data to ensure reliable reconstruction over imperfect channels. The system utilises polar codes configured with a standard code rate of 1/2, dictating that for every k bits of incoming data, the encoder outputs a $2k$-bit block.

Quantum Encoding

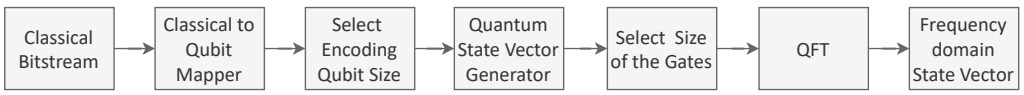


Figure 5.2: Schematic design of the introduced frequency-domain multi-qubit quantum encoding unit.

The quantum encoder is responsible for translating classical binary sequences from a time-domain format into specialised quantum states mapped inside the frequency domain. This transformation creates highly optimised quantum representations tailored for communication channels. As shown in Figure 5.2, the encoder relies on a sequence of progressive layers detailed below, where each tier executes a specific mathematical transformation.

Classical-to-Quantum Mapping and Multi-Qubit State Construction: The foundational operations regarding classical-to-quantum state transitions, the generation of multi-qubit basis layouts using tensor products, and the definitive relationship linking qubit count to overall Hilbert space dimensions match precisely the mathematical formulations outlined in Chapter 3 (Equations 3.1–3.2) and subsequently expanded to any arbitrary size k in Chapter 4 (Section 4.1). In brief, the incoming classical binary stream is partitioned into distinct blocks of length $k \in [1, 8]$. Each segment maps smoothly onto a computational-basis state within the matching 2^k-dimensional Hilbert space $\mathcal{H}_{2^k}$. The defining novelty introduced in this section resides in the subsequent phase: leveraging the QFT to project these multi-qubit time-domain states into the quantum frequency domain.

Quantum Gate Dimension Selection and Quantum Fourier Transform: To accurately shift a quantum state vector out of time coordinates and into the frequency spectrum, it is mandatory to deploy a QFT gate dimensioned precisely to match the state vector's size. The exact length of this quantum vector is governed by the number of active qubits (k) engaged in the encoding step, yielding a dimension of $2^k \times 1$. Consequently, the corresponding QFT gate operator must be configured as a square matrix of dimension $2^k \times 2^k$ to execute accurately on the state. For instance, a quantum state vector with an operational length of 4×1 (corresponding to a $k = 2$ qubit system) demands a 4×4 QFT matrix. For a 3-qubit array ($k = 3$), the state length expands to 8, necessitating an 8×8 matrix. This structural scaling logic applies uniformly across all qubit depths.

Furthermore, the QFT algorithm for a framework utilising k qubits, where the total dimension is given by $N = 2^k$, can be modelled as a unitary matrix F_N. When

executed upon a standard computational basis state $|x\rangle$, the QFT reorganises it into a frequency-domain superposition state defined via (5.1).

$$F_N |x\rangle = \frac{1}{\sqrt{N}} \sum_{y=0}^{N-1} e^{2\pi i\, xy/N} |y\rangle \tag{5.1}$$

This formula redefines the initial input $|x\rangle$ as a proportional linear combination spanning all available basis states $|y\rangle$, where every component incorporates a complex phase factor $e^{2\pi i\, xy/N}$ that explicitly holds frequency data. The normalisation coefficient $\frac{1}{\sqrt{N}}$ ensures that the overall process remains unitary, thereby protecting the total quantum state norm.

Additionally, the exact structural compilation of the QFT matrix F_N, where $N = 2^k$, is executed according to the layout in (5.2).

$$F_N = \frac{1}{\sqrt{N}} \begin{pmatrix} 1 & 1 & 1 & \cdots & 1 \\ 1 & \omega & \omega^2 & \cdots & \omega^{N-1} \\ 1 & \omega^2 & \omega^4 & \cdots & \omega^{2(N-1)} \\ \vdots & \vdots & \vdots & \ddots & \vdots \\ 1 & \omega^{N-1} & \omega^{2(N-1)} & \cdots & \omega^{(N-1)^2} \end{pmatrix} \tag{5.2}$$

In this framework, ω represents the primitive N^{th} root of unity, defined explicitly in (5.3).

$$\omega = e^{\frac{2\pi i}{N}} \tag{5.3}$$

To illustrate, inside a configuration with an encoding depth of $k = 2$, the resulting QFT matrix F_4 takes the form of the 4×4 matrix detailed in (5.4).

$$F_4 = \frac{1}{2} \begin{pmatrix} 1 & 1 & 1 & 1 \\ 1 & i & -1 & -i \\ 1 & -1 & 1 & -1 \\ 1 & -i & -1 & i \end{pmatrix} \tag{5.4}$$

This mathematical definition transitions seamlessly to any higher qubit volume k, where every independent coordinate of F_N is calculated utilising the matrix structure

established in (5.2). The QFT matrix directly acts on the incoming quantum state vector, shifting it out of its native time-based representation and into the frequency domain by multiplying the state vector by F_N. As a concrete example, let us observe the four basic vectors that map out a two-qubit environment: $|00\rangle$, $|01\rangle$, $|10\rangle$, and $|11\rangle$. Subjecting each discrete input to the F_4 transformation matrix outputs distinct, complex vectors within the frequency spectrum, as derived in (5.5) through (5.8).

$$F_4 |00\rangle = \frac{1}{2} \begin{pmatrix} 1 & 1 & 1 & 1 \end{pmatrix}^T = \frac{1}{2} (|00\rangle + |01\rangle + |10\rangle + |11\rangle) \tag{5.5}$$

$$F_4 |01\rangle = \frac{1}{2} \begin{pmatrix} 1 & i & -1 & -i \end{pmatrix}^T = \frac{1}{2} (|00\rangle + i\,|01\rangle - |10\rangle - i\,|11\rangle) \tag{5.6}$$

$$F_4 |10\rangle = \frac{1}{2} \begin{pmatrix} 1 & -1 & 1 & -1 \end{pmatrix}^T = \frac{1}{2} (|00\rangle - |01\rangle + |10\rangle - |11\rangle) \tag{5.7}$$

$$F_4 |11\rangle = \frac{1}{2} \begin{pmatrix} 1 & -i & -1 & i \end{pmatrix}^T = \frac{1}{2} (|00\rangle - i\,|01\rangle - |10\rangle + i\,|11\rangle) \tag{5.8}$$

These derivations highlight how the QFT systematically modifies every individual two-qubit basis state in the time domain into a highly distinct complex-valued vector situated in the frequency domain. This unitary QFT matrix serves as an essential channel, enabling the representation of quantum information within a spectral domain, a trait highly beneficial for advanced quantum communication networks. Furthermore, these derived vectors demonstrate how each original qubit basis combination maps to an explicit column within the QFT matrix structure, a characteristic that is foundational for communication frameworks built around phase-space analysis.

Quantum Channel

The composite quantum noise channel utilised across this chapter perfectly mirrors the structural model defined in Chapter 3 Section 3.1 (specifically Equations 3.6–3.14). In short, propagating quantum states are subjected to a randomised blend of five primary error mechanisms: bit-flip, phase-flip, depolarising, amplitude damping, and phase damping. Their independent error likelihoods $(q_B, q_P, q_D, q_L, q_\Phi)$ aggregate to define

the total channel noise threshold q_{tot}, calculated relative to the active channel SNR as: $q_{\text{tot}} = \min(1, 1/(1+10^{\text{SNR}/10}))$. To faithfully replicate the unpredictable environment of physical quantum communication links, the total parameter q_{tot} is distributed across the five channels using uniformly randomised weightings. A static random seed guarantees that identical noise combinations are administered across all comparative configurations, validating the fairness of the evaluation. These QFT-encoded frequency-domain states pass through the composite channel under identical noise conditions.

Quantum Decoding

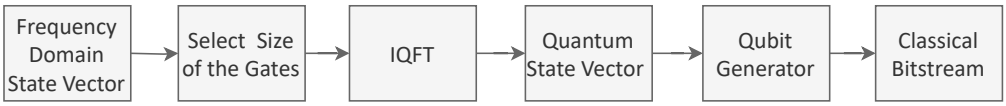


Figure 5.3: Operational architecture of the proposed frequency-domain quantum decoding system.

The quantum decoder serves to invert the entire encoding chain, converting the incoming frequency-domain quantum vector back into its initial time-domain coordinates. As illustrated in Figure 5.3, the decoder natively processes the complete frequency-domain vector as a single entity. Initially, the decoder assesses the dimensionality of the incoming state to accurately determine the required size for the IQFT gate. Following this dimensional measurement, the appropriate IQFT operation is executed, shifting the state from frequency coordinates back to the standard time domain. Ultimately, the qubit processing unit executes quantum measurements, verifying the recovered states, associating them with the correct qubits, and generating the final classical binary sequence that mirrors the original transmission.

Mathematical Process of Quantum Decoding in Noiseless Situation: In mathematical terms, the IQFT functions as the conjugate transpose of the primary QFT matrix, detailed in (5.9).

$$\mathbf{F}_{\text{IQFT}} = \mathbf{F}_{\text{QFT}}^{\dagger} \tag{5.9}$$

Let the captured frequency-domain state be represented as $|\Psi_f\rangle \in \mathbb{C}^{2^k}$, where k

is the number of qubits involved in the quantum representation, and $\mathbb{C}^{2^k}$ denotes the complex Hilbert space of dimension 2^k that describes all possible superpositions of the k-qubit system. The decoder applies the IQFT transformation as in (5.10), to convert the quantum state from the frequency domain to the time domain.

$$|\Psi_t\rangle = \mathbf{F}_{\text{IQFT}} |\Psi_f\rangle \tag{5.10}$$

Within this equation, $|\Psi_t\rangle$ represents the successfully restored time-domain quantum state. The conclusive measurement procedure projects $|\Psi_t\rangle$ accurately onto the computational basis to retrieve the initial bitstring.

Mathematical Process of Quantum Decoding in Noisy Situation: Channel interference inevitably causes the received vector to drift from the theoretical QFT basis states. We define $|\Phi_f\rangle$ as the corrupted incoming vector in (5.11).

$$|\Phi_f\rangle = |\Psi_f\rangle + |\nu\rangle \tag{5.11}$$

where $|\nu\rangle$ is a complex-valued noise vector with $\| |\nu\rangle \| \ll 1$. To identify the original transmitted frequency state, we perform a nearest-vector match in the frequency domain. Suppose the set of ideal QFT basis states is $\mathcal{B} = \{|\phi_j\rangle\}_{j=0}^{2^k-1}$. The decoder estimates the symbol index j' according to (5.12).

$$j' = \arg\min_j \| |\Phi_f\rangle - |\phi_j\rangle \| \tag{5.12}$$

Once the best match $|\phi_{j'}\rangle$ is determined, it is assumed that it is the transmitted basis state. The IQFT transform is then applied as in (5.13).

$$|\tilde{\Psi}_t\rangle = \mathbf{F}_{\text{IQFT}} |\phi_{j'}\rangle \tag{5.13}$$

Measurement of $|\tilde{\Psi}_t\rangle$ yields the estimated classical bitstream $\hat{\mathbf{b}} \in \{0, 1\}$.

In summary, the full quantum state is preserved throughout transmission, and recovery is based on comprehensive vector matching. Unlike schemes that rely on inspecting individual elements (such as a particular amplitude or phase), this approach enhances robustness by utilising the global structure of the quantum state in the

frequency domain.

Hardware Implementation of Quantum Fourier Transform

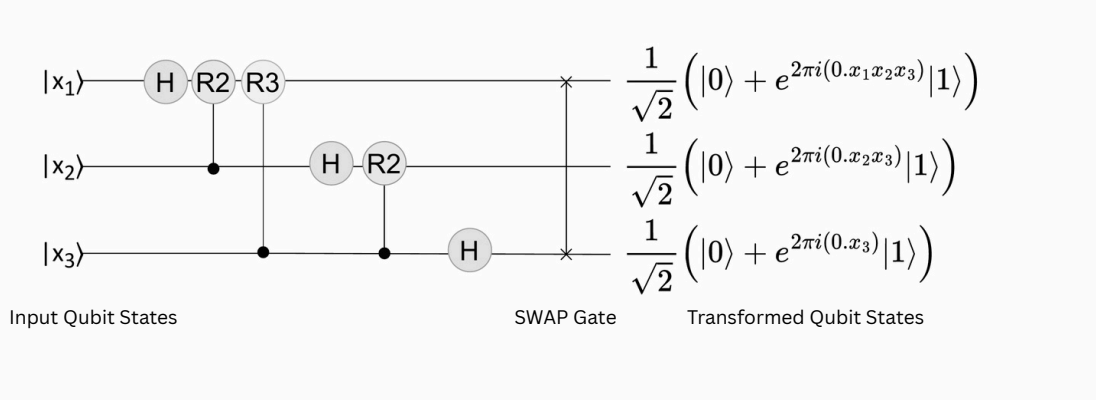


Figure 5.4: Hardware circuit layout for a three-qubit QFT processing system.

The physical realisation of a QFT network is executed via a coordinated sequence of physical quantum gates that manipulate individual qubits to run the discrete Fourier transform within a quantum framework. The essential building blocks enabling this hardware layout are Hadamard gates combined with controlled phase-rotation gates. The Hadamard gate acts on a single qubit, instantly generating a balanced superposition linking the computational basis states. Its matrix formula is presented in (5.14).

$$H = \frac{1}{\sqrt{2}} \begin{bmatrix} 1 & 1 \\ 1 & -1 \end{bmatrix} \tag{5.14}$$

This gate transforms a qubit state $|0\rangle$ into $\frac{1}{\sqrt{2}}(|0\rangle + |1\rangle)$ and $|1\rangle$ into $\frac{1}{\sqrt{2}}(|0\rangle - |1\rangle)$, thereby enabling the superposition necessary for parallel phase encoding.

To encode phase relationships between qubits, the QFT circuit employs controlled phase-rotation gates. The general phase gate applied conditionally is given by (5.15).

$$P(\theta) = \begin{bmatrix} 1 & 0 \\ 0 & e^{i\theta} \end{bmatrix} \tag{5.15}$$

where the rotation angle θ depends on the relative position between the control and target qubits. Specifically, for the controlled-R_k gate, the phase angle is $\theta = \frac{2\pi}{2^k}$, with k indicating the distance between qubits.

For the three-qubit QFT circuit example as shown in Figure 5.4, the rotation matrices for R_2 and R_3 are shown in (5.16) and (5.17).

$$R_2 = \begin{bmatrix} 1 & 0 \\ 0 & e^{2\pi i/4} \end{bmatrix} \tag{5.16}$$

$$R_3 = \begin{bmatrix} 1 & 0 \\ 0 & e^{2\pi i/8} \end{bmatrix} \tag{5.17}$$

In the three-qubit QFT circuit as shown in Figure 5.4, the procedure begins by applying a Hadamard gate to the most significant qubit x_1. This operation generates a superposition, setting the stage for subsequent phase rotations. Following this, controlled phase rotations R_2 and R_3 are applied, controlled by x_1 and targeting x_2 and x_3 respectively, introducing precise phase shifts conditioned on the qubit states. Next, the second qubit x_2 undergoes a Hadamard transformation to form its own superposition, followed by a controlled-R_2 gate between x_2 and x_3. The least significant qubit x_3 only experiences a Hadamard gate, as no qubits lie beyond it for further conditional phase encoding. Due to the construction of the QFT circuit, the final qubit order is reversed relative to the input. To correct this ordering in hardware, the SWAP gates [216] are applied, exchanging the qubit positions to restore the original logical sequence. The output state of the QFT circuit can be expressed as a tensor product of superposition and phase-encoded qubits as shown in (5.18).

$$\mathrm{QFT}(|x_1x_2x_3\rangle) = \frac{1}{\sqrt{8}} \left(|0\rangle + e^{2\pi i \cdot 0.x_3} |1\rangle\right) \otimes \left(|0\rangle + e^{2\pi i \cdot 0.x_2x_3} |1\rangle\right) \otimes \left(|0\rangle + e^{2\pi i \cdot 0.x_1x_2x_3} |1\rangle\right) \tag{5.18}$$

Here, each qubit accumulates phase information corresponding to the binary fractional values formed by itself and the less significant qubits, confirming both the accuracy of the QFT operation and its underlying theoretical principles. Similarly, by reversing these quantum gates, we can construct the IQFT hardware implementation [217].

Time-Domain Multi-Qubit System

To evaluate the performance of the proposed frequency-domain multi-qubit communication framework, a corresponding time-domain quantum communication system is implemented under identical bandwidth, source coding, and channel coding conditions. A fair and consistent comparison between the two transmission approaches is therefore ensured. The benchmark time-domain system follows the multi-qubit quantum communication framework introduced in Chapter 4.

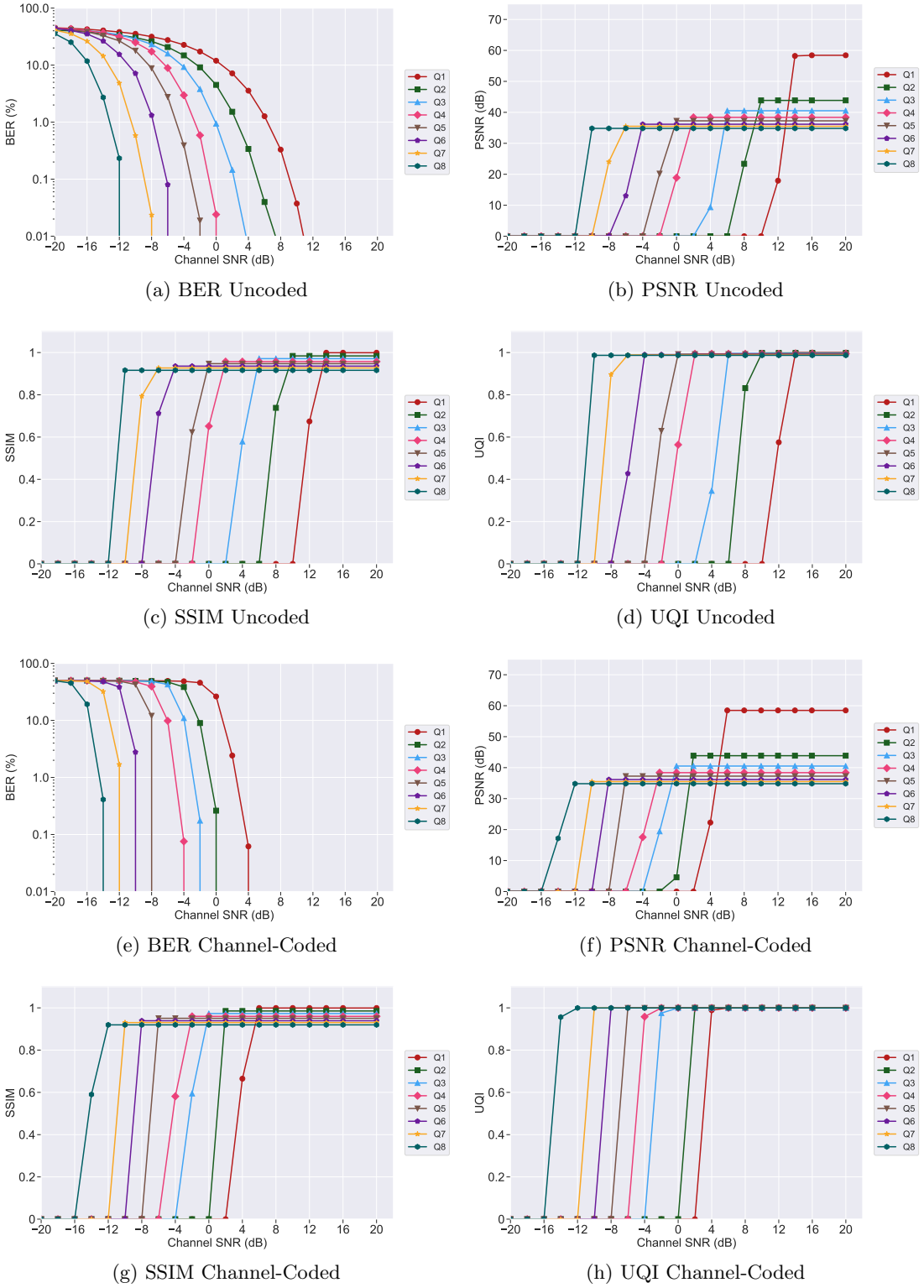
5.1.2 Results

This section presents the performance evaluation of the proposed framework using BER, PSNR, SSIM, and UQI as key performance metrics. Results are reported for both frequency-domain and time-domain multi-qubit systems. A comparative analysis between these two domains is conducted to highlight their respective strengths and weaknesses. To ensure statistical reliability, the evaluation is conducted on a dataset of 50 images, with 1000 trials per image. The reported results represent the average performance across all test cases. The framework is tested using JPEG and HEIF image formats in channel-coded and uncoded transmission scenarios, allowing a thorough examination of its performance under varied source coding and channel conditions. The results validate the robustness and efficiency of the proposed system across different communication environments.

The following subsections provide a detailed presentation and analysis of the results for each communication system.

Frequency-Domain Multi-Qubit Framework for JPEG Image Transmission

The performance of the frequency-domain multi-qubit framework for JPEG image transmission is presented in Figure 5.5. Under uncoded conditions (Figures 5.5a–5.5d), increasing the qubit size from Q1 to Q8 consistently improves all evaluated metrics. Q8 achieves the lowest BER and the highest PSNR, SSIM, and UQI across the entire SNR range, indicating stronger transmission reliability and better preservation of structural and perceptual image quality. These improvements arise from the larger representational capacity of higher-dimensional Hilbert spaces combined with the enhanced state



(a) BER Uncoded

(b) PSNR Uncoded

(c) SSIM Uncoded

(d) UQI Uncoded

(e) BER Channel-Coded

(f) PSNR Channel-Coded

(g) SSIM Channel-Coded

(h) UQI Channel-Coded

Figure 5.5: Performance evaluation of BER, PSNR, SSIM, and UQI for JPEG images transmitted using frequency-domain encoding across varying SNR levels, under both uncoded and channel-coded conditions.

distinguishability provided by QFT-based amplitude and phase encoding.

The introduction of channel coding (Figures 5.5e–5.5h) yields substantial further gains across all qubit configurations. Q8 achieves near-zero BER at considerably lower SNR values than lower-dimensional systems, with corresponding improvements in reconstructed image quality. Overall, the combination of higher-dimensional multi-qubit encoding with classical channel coding provides significant performance gains, establishing the effectiveness of the proposed framework for robust image transmission over noisy quantum channels.

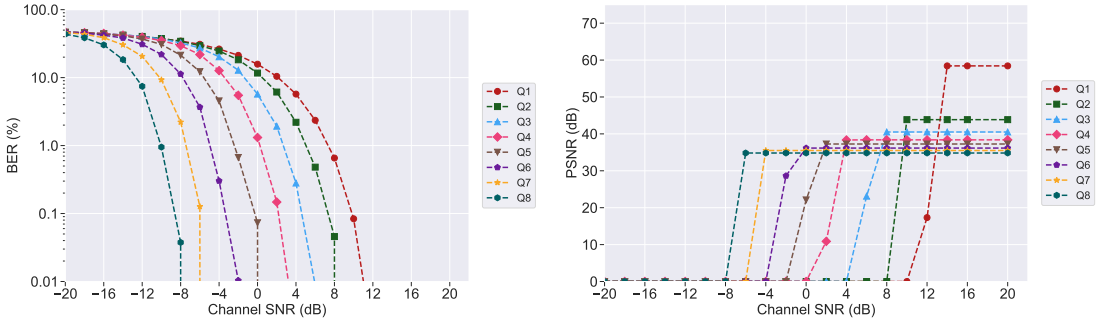
Time-Domain Multi-Qubit Framework for JPEG Image Transmission

The performance of the time-domain multi-qubit framework for JPEG image transmission is shown in Figure 5.6. As in the frequency-domain case, increasing the qubit size from Q1 to Q8 consistently improves BER, PSNR, SSIM, and UQI under both uncoded (Figures 5.6a–5.6d) and channel-coded (Figures 5.6e–5.6h) conditions. However, the absolute performance remains lower than that of the frequency-domain framework, as the time-domain encoding relies solely on amplitude-based superposition without the additional phase representation provided by the QFT.

Comparing Transmission Efficiency Between Time-Domain and Frequency-Domain Systems for JPEG Image Transmission

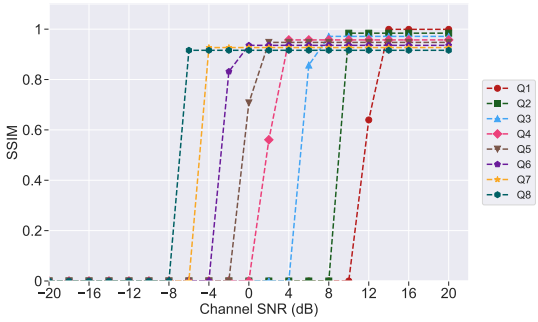
A direct comparison between time-domain (TQ1–TQ8) and frequency-domain (FQ1–FQ8) multi-qubit systems is presented in Figure 5.7. Across all evaluated metrics, the frequency-domain framework consistently outperforms the time-domain framework under both uncoded and channel-coded conditions. This advantage stems from the QFT-based phase encoding combined with high-dimensional superposition, which improves quantum-state distinguishability and resistance to channel perturbations, whereas the time-domain framework is restricted to amplitude-based encoding.

The performance gap is relatively small at single-qubit dimensionality, where the benefits of QFT-based processing are limited because only a two-dimensional state space is available, restricting the degree of spectral distribution introduced by the QFT. As the qubit size increases, however, the frequency-domain framework can exploit

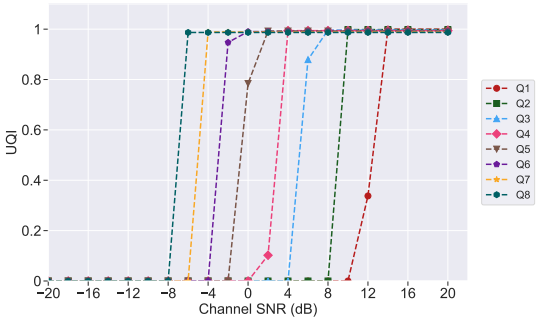


(a) BER Uncoded

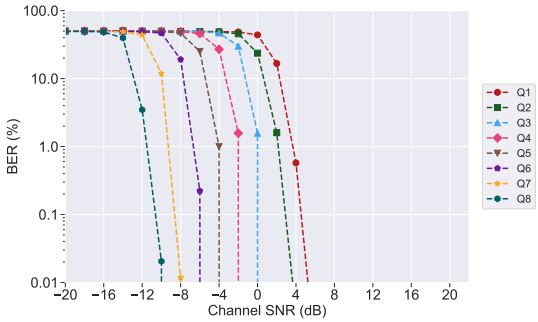
(b) PSNR Uncoded



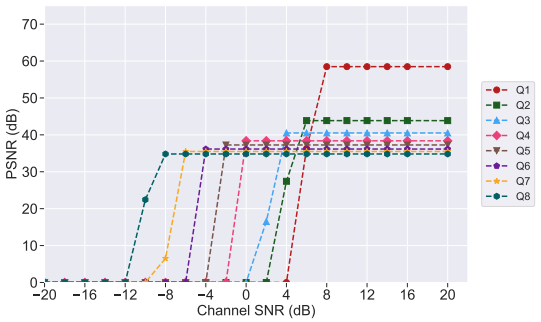
(c) SSIM Uncoded



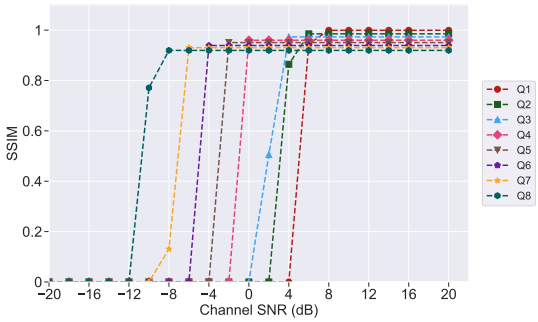
(d) UQI Uncoded



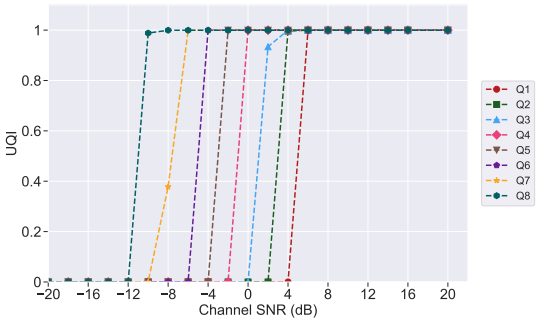
(e) BER Channel-Coded



(f) PSNR Channel-Coded

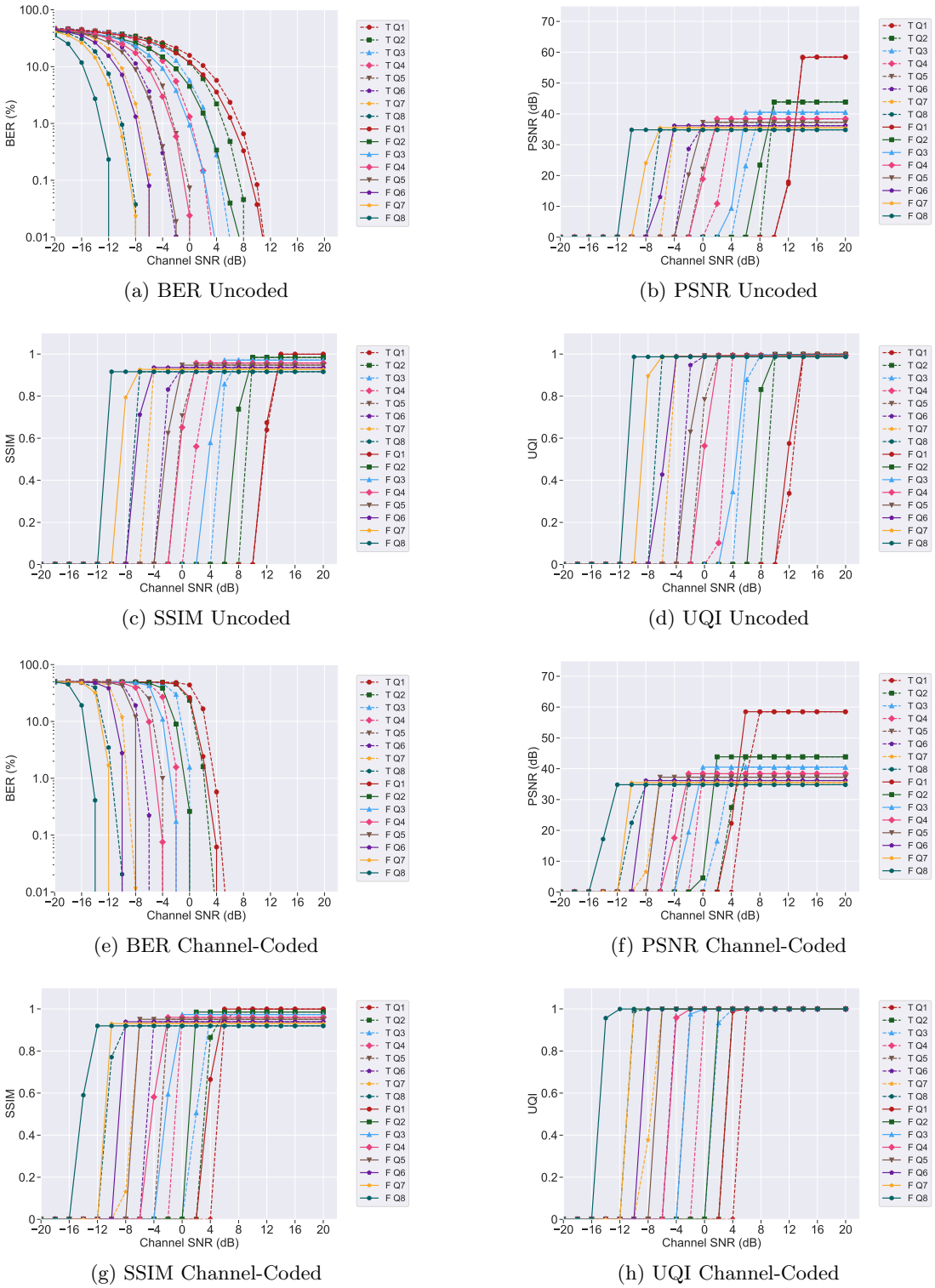


(g) SSIM Channel-Coded



(h) UQI Channel-Coded

Figure 5.6: Performance evaluation of BER, PSNR, SSIM, and UQI for JPEG images transmitted using time-domain encoding across varying SNR levels, under both uncoded and channel-coded conditions.



(a) BER Uncoded

(b) PSNR Uncoded

(c) SSIM Uncoded

(d) UQI Uncoded

(e) BER Channel-Coded

(f) PSNR Channel-Coded

(g) SSIM Channel-Coded

(h) UQI Channel-Coded

Figure 5.7: Comparative analysis of BER, PSNR, SSIM, and UQI for JPEG image transmission using time-domain and frequency-domain encoding schemes over varying SNR levels, under both uncoded and channel-coded conditions.

richer multi-qubit phase relationships and higher-dimensional interference effects across the 2^k-dimensional Hilbert space. Consequently, the encoded information becomes distributed across a larger set of correlated spectral components, enabling channel-induced distortions to be spread over the transformed representation rather than directly affecting the original computational-basis structure. After applying the IQFT at the receiver, this distributed representation improves the recovery of the transmitted information, yielding substantially enhanced transmission robustness and reconstructed image quality.

Frequency-Domain Multi-Qubit Framework for HEIF Image Transmission

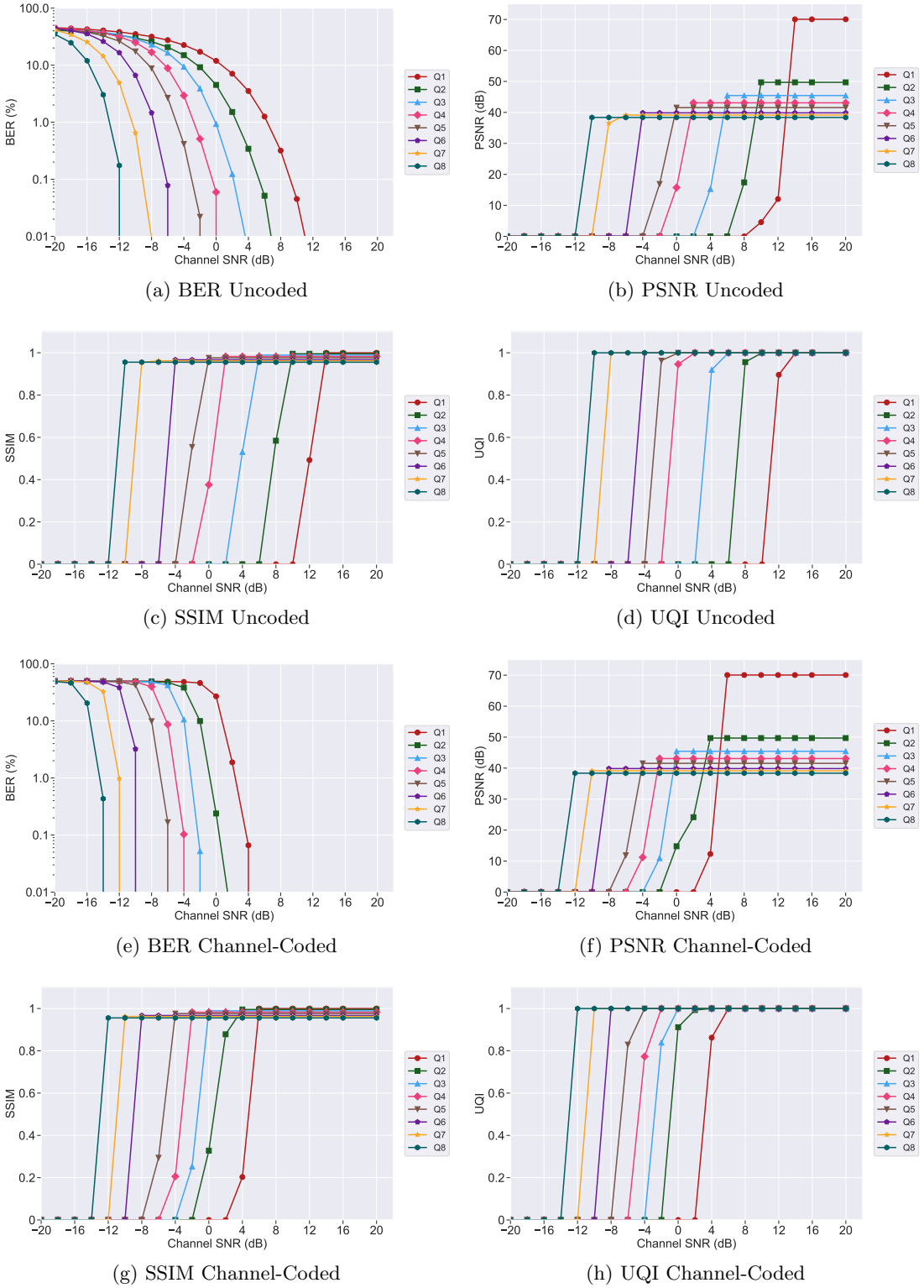
The performance of the frequency-domain framework for HEIF image transmission is presented in Figure 5.8. The observed trends closely follow those reported for JPEG transmission: increasing the qubit size consistently improves BER, PSNR, SSIM, and UQI under both uncoded and channel-coded conditions, with the largest gains observed for Q6–Q8. The consistency of these trends across two distinct compression formats confirms that the proposed QFT-based framework provides scalable and compression-independent robustness.

Time-Domain Multi-Qubit Framework for HEIF Image Transmission

The performance of the time-domain framework for HEIF image transmission is shown in Figure 5.9. As with JPEG transmission, increasing the qubit size improves all evaluated metrics, and the application of channel coding yields substantial further gains. However, the time-domain framework remains consistently less robust than the corresponding frequency-domain system, particularly under low and moderate SNR conditions, reflecting the absence of phase-domain representation.

Comparing Transmission Efficiency Between Time-Domain and Frequency-Domain Systems for HEIF Image Transmission

A direct comparison between time-domain and frequency-domain frameworks for HEIF transmission is shown in Figure 5.10. The same trends observed for JPEG hold here: the frequency-domain framework achieves lower BER and higher PSNR, SSIM, and



(a) BER Uncoded

(b) PSNR Uncoded

(c) SSIM Uncoded

(d) UQI Uncoded

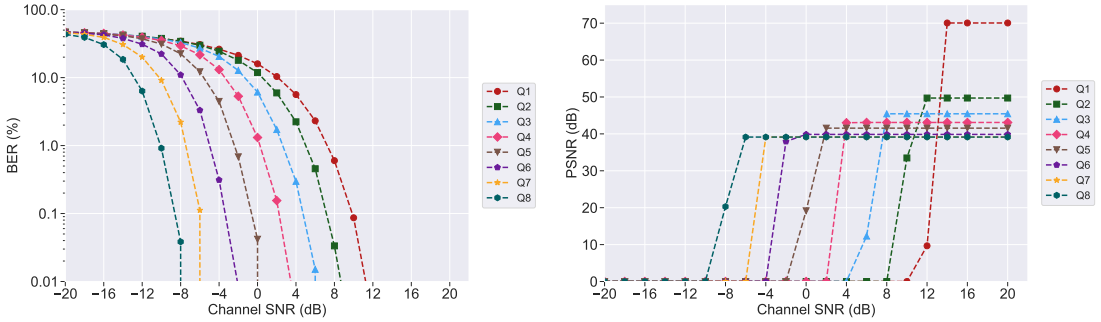
(e) BER Channel-Coded

(f) PSNR Channel-Coded

(g) SSIM Channel-Coded

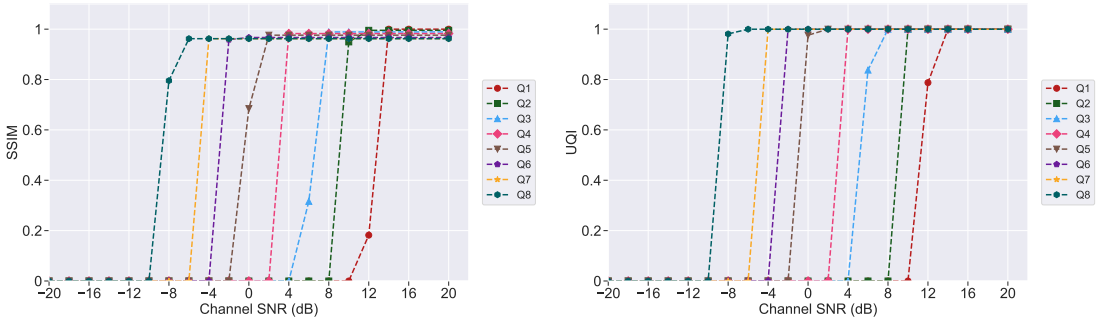
(h) UQI Channel-Coded

Figure 5.8: Performance evaluation of BER, PSNR, SSIM, and UQI for HEIF images transmitted using frequency-domain encoding across varying SNR levels, under both uncoded and channel-coded conditions.



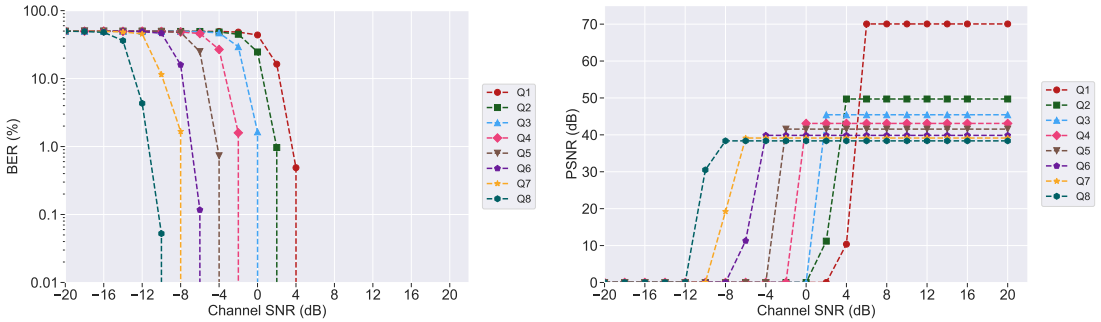
(a) BER Uncoded

(b) PSNR Uncoded



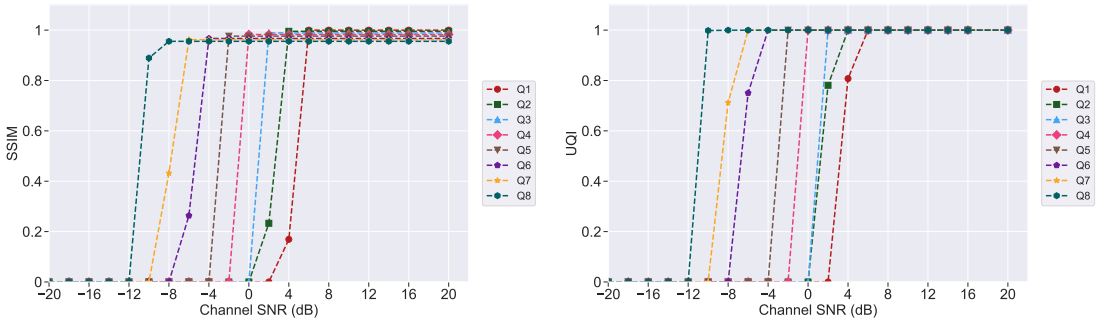
(c) SSIM Uncoded

(d) UQI Uncoded



(e) BER Channel-Coded

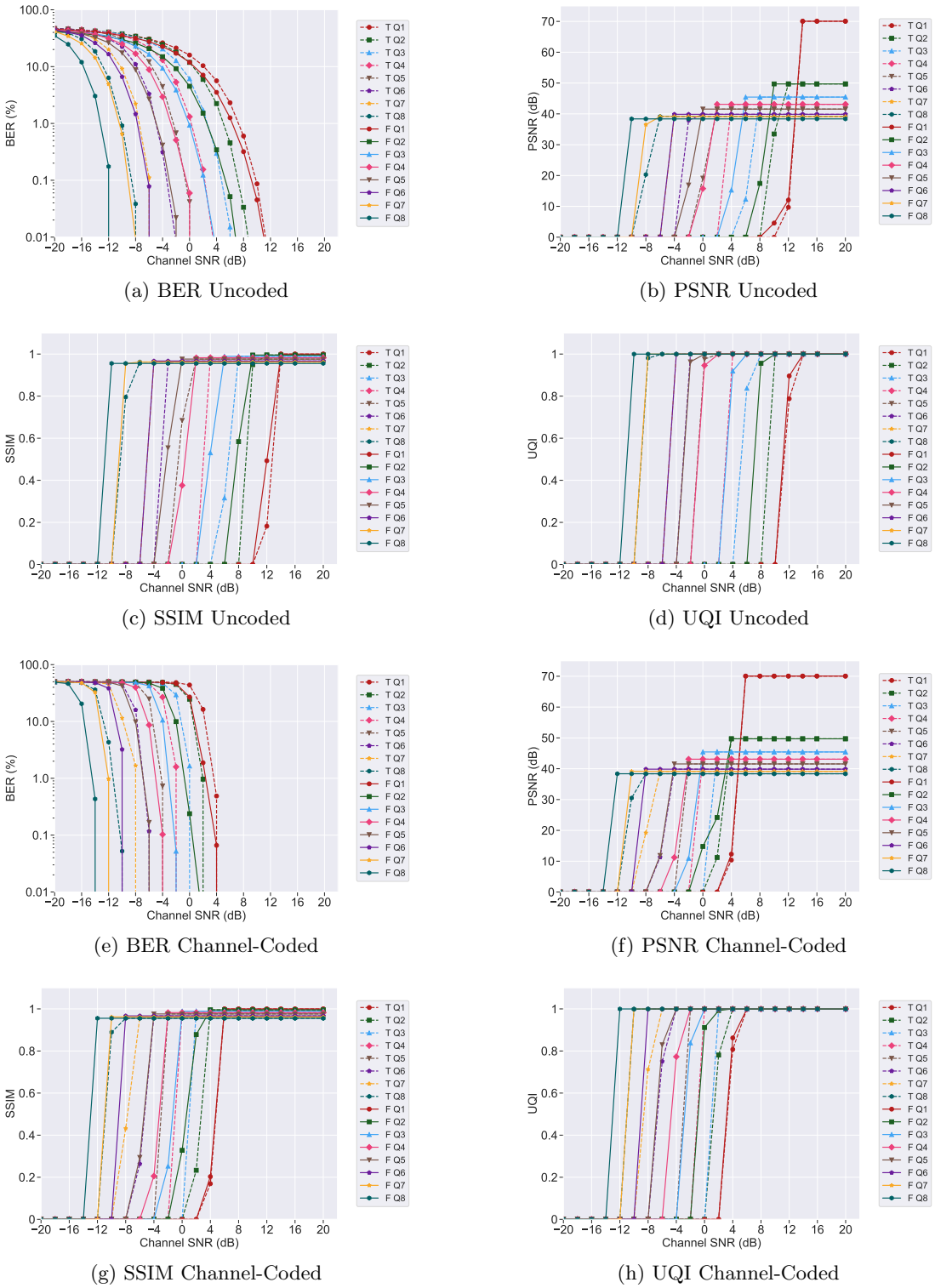
(f) PSNR Channel-Coded



(g) SSIM Channel-Coded

(h) UQI Channel-Coded

Figure 5.9: Performance evaluation of BER, PSNR, SSIM, and UQI for HEIF images transmitted using time-domain encoding across varying SNR levels, under both uncoded and channel-coded conditions.



(a) BER Uncoded

(b) PSNR Uncoded

(c) SSIM Uncoded

(d) UQI Uncoded

(e) BER Channel-Coded

(f) PSNR Channel-Coded

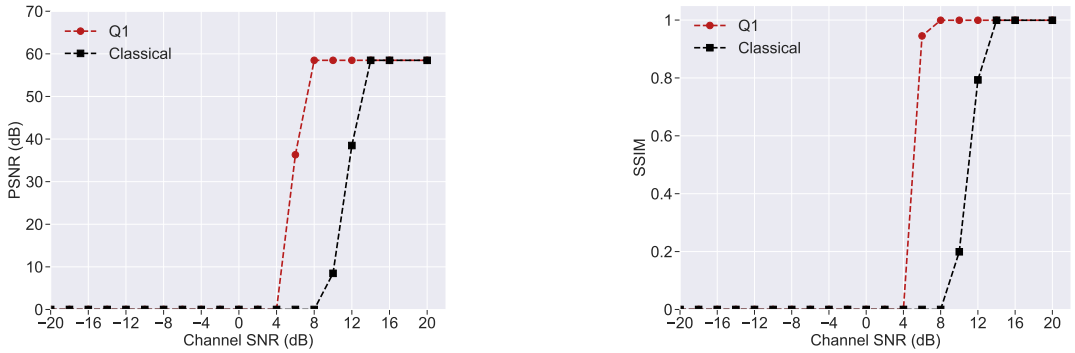
(g) SSIM Channel-Coded

(h) UQI Channel-Coded

Figure 5.10: Comparative analysis of BER, PSNR, SSIM, and UQI for HEIF image transmission using time-domain and frequency-domain encoding schemes over varying SNR levels, under both uncoded and channel-coded conditions.

UQI values across both uncoded and channel-coded conditions, with the performance gap widening as the qubit dimensionality increases. This consistency across JPEG and HEIF confirms that the advantages of QFT-based encoding are independent of the underlying compression format.

Furthermore, as shown in Figure 5.11, single-qubit time-domain quantum communication systems already outperform conventional classical communication systems operating under identical bandwidth and power constraints using rate-1/2 polar coding and BPSK modulation. Consequently, the proposed frequency-domain multi-qubit framework is expected to achieve even greater performance improvements over the corresponding classical approaches.

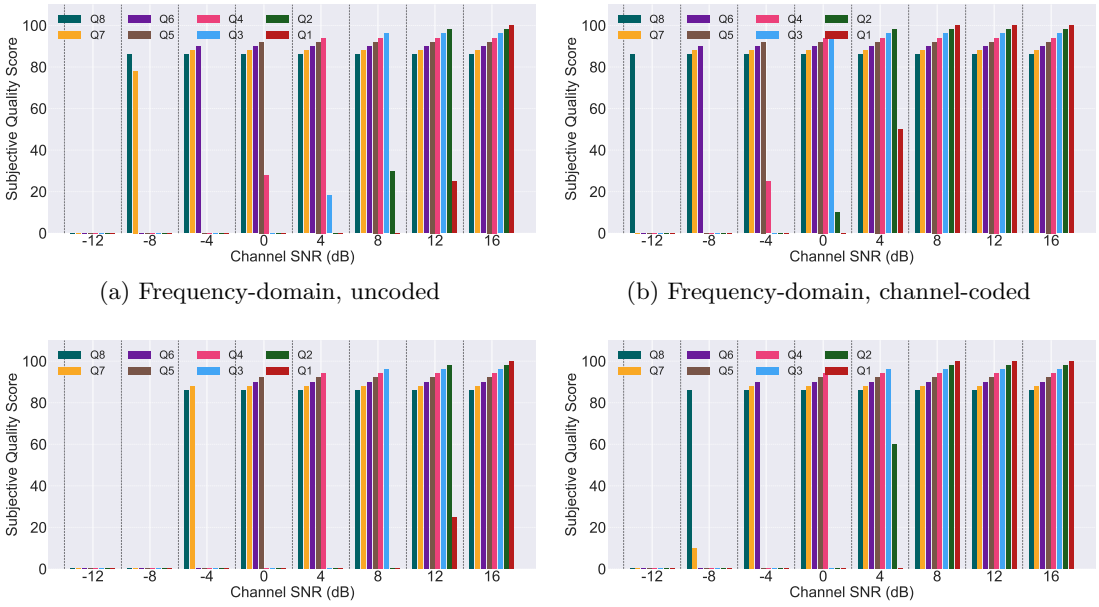


(a) PSNR (b) SSIM

Figure 5.11: Performance comparison between time-domain single-qubit quantum system and classical system at the same bandwidth.

Furthermore, the perceived visual quality of the transmitted images is assessed using a subjective evaluation based on the double stimulus method [208]. A total of 100 participants, aged 18 to 55 years, are involved in the study. JPEG image transmission is used for evaluation across both time-domain and frequency-domain multi-qubit systems, under both uncoded and channel-coded conditions. For each SNR level, images generated by the quantum systems are presented to the participants, who are asked to rate the visual quality of each image. Ratings are assigned according to the standard mean opinion score (MOS) scale, which ranges from 0 to 100, where 0–20 indicates bad, 21–40 poor, 41–60 fair, 61–80 good, and 81–100 excellent quality. The final MOS values are computed as the average of all participant scores, representing the overall perceived

image quality.



(a) Frequency-domain, uncoded

(b) Frequency-domain, channel-coded

(c) Time-domain, uncoded

(d) Time-domain, channel-coded

Figure 5.12: Subjective quality assessment results for JPEG image transmission using frequency-domain and time-domain multi-qubit systems under uncoded and channel-coded conditions.

Figures 5.12a through 5.12d present the results of this subjective evaluation under four distinct configurations. Figure 5.12a shows the MOS results for the frequency-domain system without channel coding, while Figure 5.12b displays the frequency-domain system with channel coding. Figure 5.12c illustrates the performance of the time-domain system without channel coding, and Figure 5.12d presents the results of the time-domain system with channel coding. These visual comparisons provide information on the impact of both the encoding domain and channel coding on perceived image quality under varying SNR conditions. All subjective results are found to be consistent with the corresponding objective quality metrics, confirming the reliability of the evaluation. Among all configurations, the frequency-domain system with channel coding consistently achieves the highest MOS scores, indicating superior visual quality. This suggests that the combination of frequency domain processing and channel coding provides the most effective strategy to preserve image fidelity under noisy channel conditions.

The analysis of both time-domain and frequency-domain multi-qubit systems shows

that increasing the qubit encoding size from Q1 to Q8 improves transmission robustness and reconstructed image quality, but also increases system complexity due to the larger number of quantum operations required for encoding and decoding. Higher-dimensional qubit configurations provide stronger resistance against channel noise and achieve lower BER together with improved PSNR, SSIM, and UQI performance.

However, these gains come at the cost of increased computational overhead and quantum resource requirements. Consequently, a clear trade-off exists between performance and implementation complexity: lower-dimensional systems such as Q1 offer reduced complexity but limited noise resilience, whereas higher-dimensional configurations such as Q8 achieve significantly improved transmission fidelity at the expense of greater processing complexity.

When comparing the complexity of time-domain and frequency-domain multi-qubit systems, a key difference emerges in the types and number of quantum gate operations required. The time-domain system uses only Hadamard gates to encode classical information into quantum superposition states. These gates are applied independently to each qubit, allowing for full parallelism and resulting in a shallow circuit with low gate complexity. Specifically, the total number of gates scales linearly with the number of qubits, with a gate count of k and a constant circuit depth of 1, since the encoding is performed using a single-layer transformation. This leads to an overall encoding complexity of $\mathcal{O}(k)$, making the time domain system highly efficient and well-suited for near-term quantum devices. In contrast, the frequency-domain system employs the QFT, which consists of both Hadamard and controlled-phase gates. Due to inter-qubit dependencies, these gates must be applied sequentially, increasing both the gate count and the circuit depth. For a k-qubit system, the total number of gates required is $\frac{k(k+1)}{2}$, and the circuit depth grows linearly as k, resulting in an overall complexity of $\mathcal{O}(k^2)$.

Although the frequency-domain system introduces greater computational overhead, this added complexity enables more advanced encoding that incorporates both amplitude and phase information. As a result, it offers enhanced noise resistance and superior image fidelity preservation, particularly in challenging transmission environments. Therefore, despite its higher quantum resource demands, the frequency-domain approach presents a compelling solution for high-fidelity quantum image communication. A detailed

breakdown of gate count, circuit depth, and error resilience for qubit sizes from $k = 1$ to 8 in both time-domain and frequency-domain systems is summarised in Table 5.1.

Table 5.1: Comparison of encoding complexity and error resilience (based on BER at an SNR of −8 dB) for JPEG uncoded images across time-domain and frequency-domain systems (Q1–Q8).

Qubit Size (k)	**Domain**	**Gate Count**	**Circuit Depth**	**BER (%)**
Q1	Time	1	1	34.51
Q2	Time	2	1	34.26
Q3	Time	3	1	32.37
Q4	Time	4	1	29.52
Q5	Time	5	1	31.36
Q6	Time	6	1	11.31
Q7	Time	7	1	2.21
Q8	Time	8	1	0.03
Q1	Frequency	1	1	31.56
Q2	Frequency	3	2	26.17
Q3	Frequency	6	3	23.17
Q4	Frequency	10	4	17.36
Q5	Frequency	15	5	8.83
Q6	Frequency	21	6	1.31
Q7	Frequency	28	7	0.02
Q8	Frequency	36	8	0

Both the time-domain and frequency-domain frameworks remain suitable for near-term quantum implementations because they rely on relatively simple quantum gate operations. The time-domain framework offers lower circuit complexity and reduced gate requirements, making it particularly suitable for noisy intermediate-scale quantum (NISQ) devices and resource-constrained quantum communication scenarios. In contrast, the frequency-domain framework introduces higher computational complexity due to the QFT, but achieves substantially improved transmission robustness and reconstructed image quality. QEC codes are not incorporated in this study because existing QEC methods introduce significant implementation complexity and are not directly compatible with frequency-domain processing. Instead, classical channel coding is applied after quantum decoding to improve transmission reliability while maintaining practical implementation feasibility. Overall, the proposed simulation framework establishes a scalable and theoretically validated foundation for future quantum image communication systems. By focusing on architectural feasibility under generalised quantum noise condi-

tions, the study demonstrates the potential of multi-qubit quantum encoding for robust, bandwidth-efficient, and noise-resilient multimedia transmission, providing a practical basis for future hardware implementations and real-world quantum communication applications.

5.1.3 Section Summary

This study proposed a novel frequency-domain multi-qubit quantum image transmission framework that integrates QFT-based encoding with JPEG/HEIF source coding and classical channel coding to improve transmission robustness over noisy quantum channels. By exploiting both quantum superposition and QFT-based phase encoding, the proposed framework achieved enhanced error resilience and more efficient quantum state representation compared with time-domain encoding. Experimental results demonstrated consistent improvements in BER, PSNR, SSIM, and UQI as the number of qubits increased, with frequency-domain encoding providing up to a 4 dB channel SNR gain, particularly for eight-qubit configurations. In contrast, the single-qubit system exhibited only a modest performance gap between time and frequency-domain encoding, reflecting its limited capacity to exploit the advantages offered by frequency-domain processing. Overall, the proposed framework offers an effective balance between transmission performance, bandwidth efficiency, and system complexity, demonstrating its potential for high-fidelity quantum image communication.

5.2 A Quantum Multi-Qubit Frequency-Domain Approach for Reliable Video Transmission

Publication Notice

The research presented in this section has been published in the following peer-reviewed conference publication:

U. Jayasinghe, T. N. Atulugama, and A. Fernando, "A quantum frequency-domain multi-qubit encoding framework for robust video transmission," in *Proc. IEEE Int. Conf. Consumer Electron. (ICCE)*, 2025 (in press).

This material is reproduced and adapted under the terms of the IEEE Copyright policy for use in a doctoral thesis. The content has been revised and extended with additional explanations and expanded discussion.

Problem Statement: Section 5.1 demonstrated that frequency-domain multi-qubit encoding offers measurable robustness gains over time-domain multi-qubit encoding for image transmission. Video transmission, however, presents a substantially more demanding scenario than still-image transmission. Compressed video bitstreams are much larger, exhibit strong temporal dependencies between inter-coded frames, and are highly susceptible to error propagation across a GOP. A single corrupted bit early in a GOP can degrade every subsequent inter-coded frame until the next intra refresh, magnifying the impact of even rare transmission errors. The frequency-domain multi-qubit framework of Section 5.1 is image-specific and has not been evaluated under the temporal-correlation conditions that dominate practical video communication.

Limitations of Existing Work: Existing quantum communication studies on video transmission, including the time-domain framework of Chapter 4, operate in the computational basis and therefore inherit the same noise-sensitivity limitations identified in Section 5.1. No prior work has applied QFT-based frequency-domain encoding to compressed video bitstreams, nor evaluated how key video coding parameters (GOP size, frame rate, spatial resolution) interact with the choice of quantum encoding domain. Without such analysis, it is unclear whether the per-symbol robustness gains of frequency-domain encoding observed for images carry over to the temporally correlated

video case.

Motivation and Proposed Contribution: To address these limitations, this section extends the frequency-domain multi-qubit framework of Section 5.1 to compressed video transmission over noisy quantum channels. Unlike still images, compressed video streams contain strong temporal dependencies between consecutive frames due to inter-frame prediction and GOP-based coding structures. As a result, transmission errors affecting one frame can propagate to subsequent frames, significantly degrading overall video quality. Therefore, improving transmission robustness is more critical in video communication systems. The proposed framework investigates whether QFT-based frequency-domain encoding can reduce the impact of channel noise on compressed video bitstreams compared with conventional time-domain quantum transmission. In the proposed system, VVC-compressed video bitstreams generated under multiple GOP configurations are first protected using rate-1/2 polar coding. The encoded bitstreams are then grouped and mapped into multi-qubit superposition states before being transformed into the quantum frequency domain using the QFT for transmission over the composite quantum noise channel established in Chapter 3 Section 3.1. At the receiver, the IQFT, multi-qubit decoding, polar decoding, and VVC reconstruction are sequentially applied to recover the transmitted video. The framework is evaluated under multiple GOP sizes, frame rates, and spatial resolutions using PSNR, SSIM, and VMAF quality metrics. The objective is to analyse how frequency-domain quantum encoding influences error propagation, reconstructed video quality, and transmission robustness under different video coding conditions.

5.2.1 System Model

The proposed framework for quantum video transmission is designed to deliver high-fidelity video over noisy quantum channels while supporting multiple multi-qubit configurations, as shown in Figure 5.13. To evaluate system performance, videos with varying SI and TI are selected, covering low, medium, and high-motion content. High-motion videos [205] feature rapid movements, medium-motion videos [206] show moderate activity, and low-motion videos [207] have minimal movement. These datasets provide a comprehensive test of the framework's robustness and adaptability across diverse video

characteristics. This flexibility ensures that the framework can handle a wide variety of content types, making it robust for any input video.

All videos are encoded using the VVenC [203] implementation of VVC in YUV420 format, covering multiple spatial resolutions (320×180, 1280×720, 1920×1080), frame rates (20, 30, 50 fps), and GOP sizes of 8, 16, and 32. For each multi-qubit configuration, videos are compressed according to their GOP size, and source coding rates are adjusted to ensure consistent bandwidth across different qubit levels. Higher-qubit systems, which transmit more information per quantum symbol, are compressed more aggressively, while lower-qubit systems use lighter compression. This ensures that the overall qubit stream lengths are approximately equal, allowing fair and meaningful comparisons across all multi-qubit configurations. The compressed video bitstreams are then channel-encoded using polar codes with a rate of 1/2.

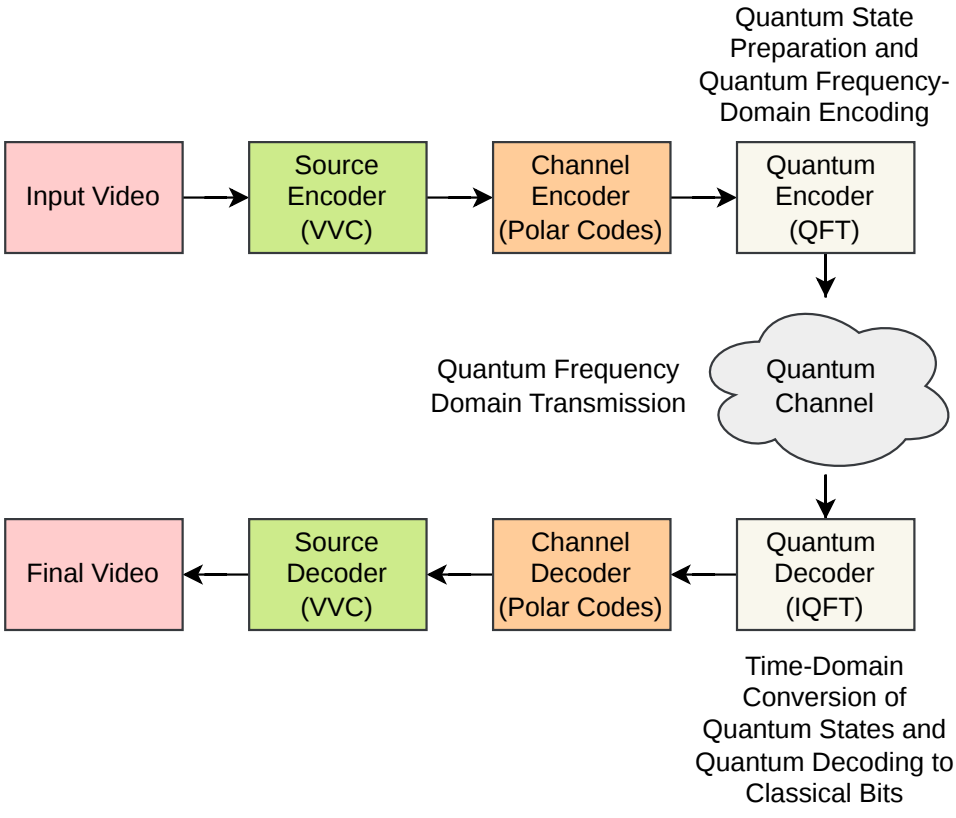


Figure 5.13: Proposed end-to-end video transmission system.

Quantum Encoder

The multi-qubit mapping and QFT-based frequency-domain encoding follow the framework introduced in Section 5.1. Classical video bitstreams are grouped into blocks of $k \in [1, 8]$ bits and mapped into computational-basis quantum states. The QFT is then applied to generate frequency-domain superposition states for transmission, enabling high-dimensional quantum-state representation and improved robustness against channel noise.

Quantum Channel

The transmitted frequency-domain quantum states pass through the same generalised composite quantum noise model described in Section 5.1, incorporating bit-flip, phase-flip, depolarising, amplitude-damping, and phase-damping effects under varying SNR conditions.

Quantum Decoder

At the receiver, IQFT-based decoding follows the framework introduced in Section 5.1. The received noisy frequency-domain states are first mapped to the nearest valid basis vector using minimum Euclidean-distance detection. The IQFT is then applied to reconstruct the corresponding time-domain quantum states, whose measurements produce the estimated classical video bitstream.

Time-Domain Quantum and Classical Systems

For benchmarking, a corresponding time-domain multi-qubit communication system, similar to the framework presented in Section 4.2, is implemented under identical bandwidth, source coding, and channel coding conditions. In addition, a classical BPSK-based communication system operating under the same bandwidth constraints is also considered for performance comparison.

5.2.2 Results

This section presents the performance evaluation of the proposed quantum video communication systems using frequency-domain multi-qubit encoding. The results are reported

as average values across test video sequences at a resolution of 320×180 and frame rates of 20, 30, and 50 fps, providing a comprehensive assessment of system performance under varying SNR conditions, qubit sizes, and GOP configurations. Performance metrics considered include PSNR, SSIM, and VMAF, which together capture objective reconstruction fidelity, perceptual video quality, and temporal coherence.

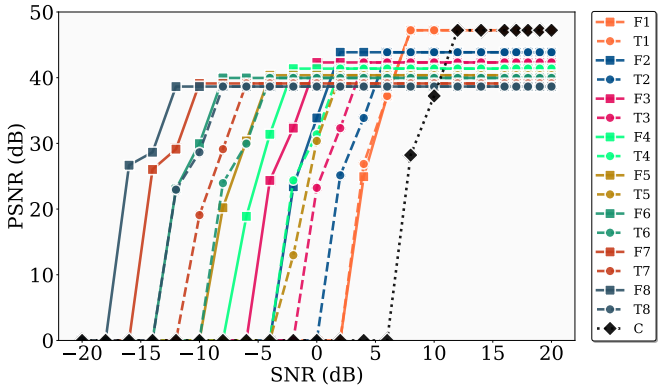
Figures 5.14–5.16 present the performance comparison of time-domain quantum systems (T1–T8), frequency-domain quantum systems (F1–F8), and the classical benchmark system (C) for GOP sizes of 8, 16, and 32, respectively. In all cases, both time-domain and frequency-domain quantum systems exhibit clear performance improvements with increasing qubit size across PSNR, SSIM, and VMAF metrics. This demonstrates that larger qubit allocations provide higher-dimensional quantum state representations, enabling more accurate preservation of video information during transmission.

At the lowest allocation of one qubit, the performance of the time-domain (T1) and frequency-domain (F1) systems becomes nearly identical across all SNR values. This occurs because the limited state-space dimensionality and reduced circuit depth restrict the ability of the systems to exploit temporal and frequency-domain correlations effectively. Consequently, the theoretical advantages of QFT-based encoding cannot be fully utilised in the single-qubit configuration.

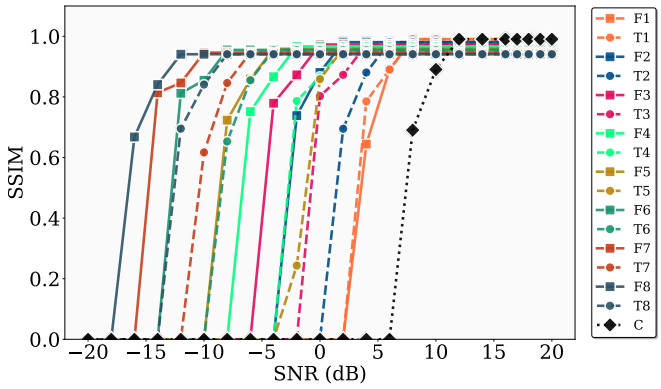
As the qubit size increases, the performance gap between the time-domain and frequency-domain systems becomes more pronounced. The frequency-domain systems scale more efficiently due to the improved frequency representation provided by the QFT, which better aligns with the structure of VVC-compressed video bitstreams. At the highest qubit allocation of eight qubits, the frequency-domain system (F8) significantly outperforms the time-domain system (T8) across all quality metrics, particularly at low and moderate SNR levels, achieving an approximate channel SNR gain of 4 dB.

The classical communication system consistently exhibits the lowest performance among all evaluated systems and is outperformed even by the single-qubit time-domain configuration (T1) by approximately 4 dB in channel SNR. Overall, the frequency-domain eight-qubit system (F8) achieves the highest reconstruction quality and noise robustness, demonstrating the effectiveness of QFT-based frequency-domain quantum encoding when sufficient quantum resources are available. These results indicate that

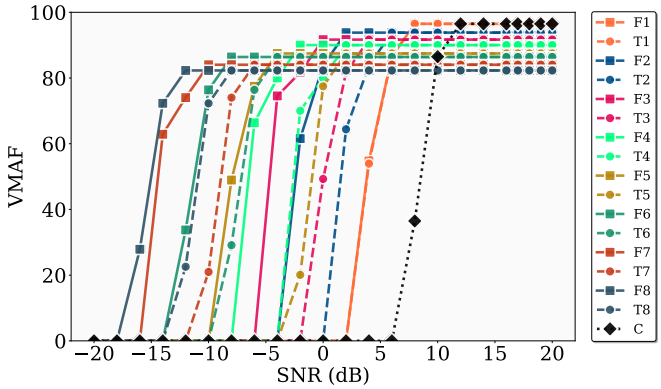
exploiting both amplitude and phase information through the QFT improves resistance to channel noise and enhances reconstructed video quality under realistic transmission conditions.



(a) GOP8 – PSNR



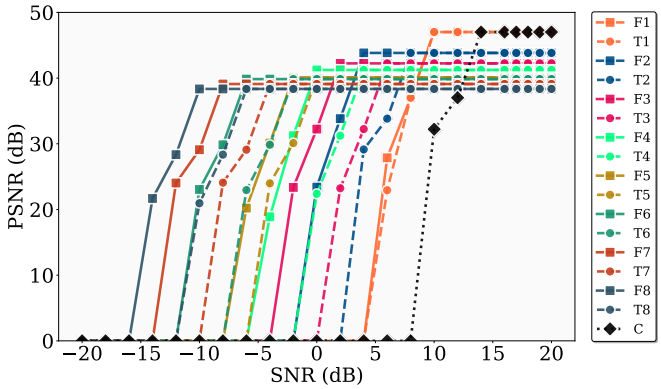
(b) GOP8 – SSIM



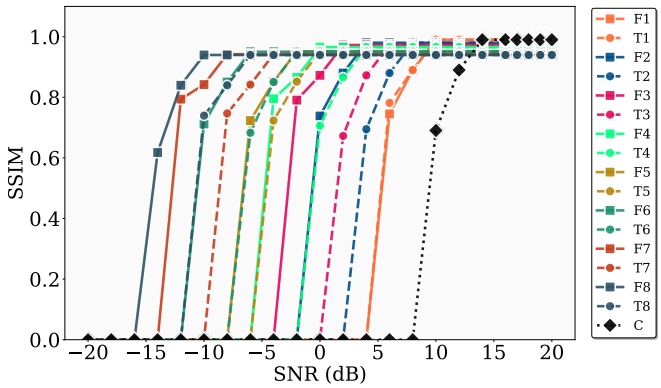
(c) GOP8 – VMAF

Figure 5.14: Performance comparison of quantum video communication systems for GOP8 using PSNR, SSIM, and VMAF metrics.

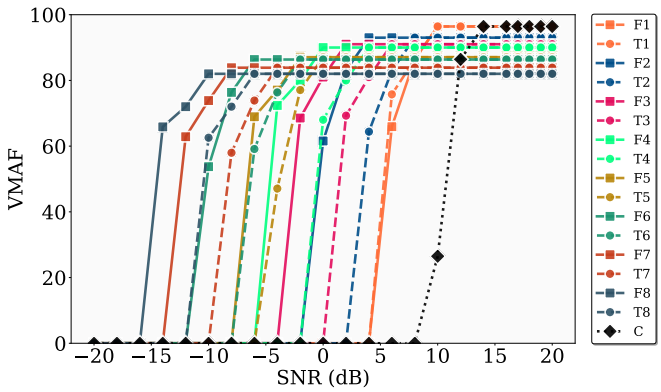
All systems exhibit reduced PSNR, SSIM, and VMAF performance as the GOP



(a) GOP16 – PSNR



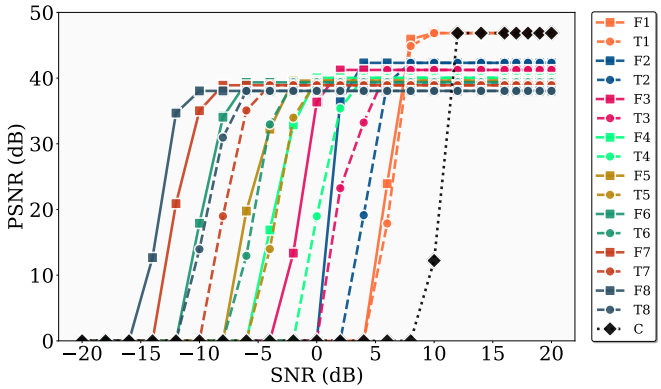
(b) GOP16 – SSIM



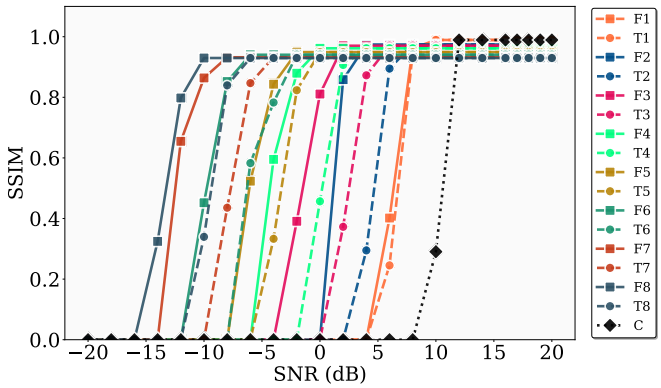
(c) GOP16 – VMAF

Figure 5.15: Performance comparison of quantum video communication systems for GOP16 using PSNR, SSIM, and VMAF metrics.

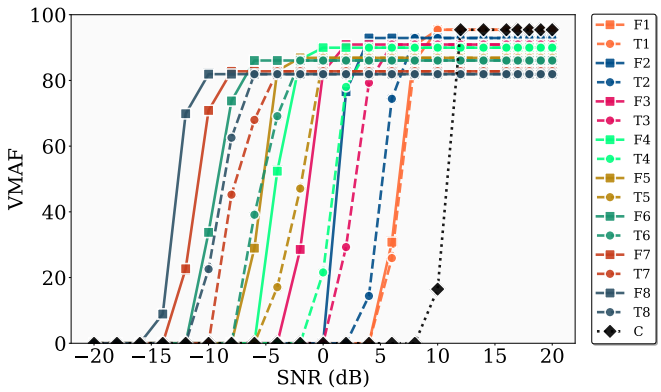
size increases, as illustrated in Figures 5.15 and 5.16. This occurs because larger GOP sizes introduce a higher number of inter-coded frames that rely on previously reconstructed frames for prediction. Consequently, transmission errors affecting earlier frames can propagate to subsequent frames, resulting in cumulative quality degradation.



(a) GOP32 – PSNR



(b) GOP32 – SSIM



(c) GOP32 – VMAF

Figure 5.16: Performance comparison of quantum video communication systems for GOP32 using PSNR, SSIM, and VMAF metrics.

To mitigate such degradation, adaptive error correction and GOP-aware error-resilient encoding strategies can be employed.

The proposed systems are also evaluated across different frame rates and spatial resolutions (1280×720 and 1920×1080) for GOP8, and the results are summarised in

Table 5.2. The analysis indicates that the relative SNR gains achieved by the quantum systems remain approximately unchanged across different frame rates and resolutions. This occurs because both the classical and quantum communication systems are similarly affected by these parameters.

Overall, the frequency-domain quantum encoding framework demonstrates superior robustness against channel noise while effectively preserving both structural and perceptual video quality. This improvement arises from the combined use of amplitude superposition and phase-domain representation through the QFT, which enhances quantum state separability and reduces susceptibility to transmission noise. In contrast, the time-domain framework relies primarily on amplitude superposition, making it more vulnerable to degradation under noisy channel conditions. Furthermore, to limit error accumulation and excessive quantum circuit complexity, the proposed framework restricts the qubit size to a maximum of eight qubits, ensuring manageable QFT circuit depth and reduced decoherence effects.

Table 5.2: Maximum SNR gain compared to classical communication systems across different resolutions and frame rates for frequency (F1–F8) and time (T1–T8) domain quantum systems.

Frame Rate (fps)	1280×720								1920×1080							
	F1	F2	F3	F4	F5	F6	F7	F8	T1	T2	T3	T4	T5	T6	T7	T8
20	4.5	8.2	12.3	14.0	16.5	20.0	21.7	24.0	4.2	6.3	7.8	10.3	13.7	16.2	17.8	20.3
30	4.1	8.2	12.4	14.1	16.3	20.1	21.9	24.3	4.3	6.4	7.9	10.4	13.8	16.3	17.9	20.4
50	4.1	8.1	12.3	14.0	16.0	20.2	22.1	24.1	4.1	6.2	8.0	10.0	14.0	16.3	18.0	20.4

To visually illustrate the difference between frequency-domain and time-domain systems, a representative decoded video frame is shown in Figures 5.17 at a channel SNR of –12 dB, using GOP8 and qubit encoding size 8. The figure clearly demonstrates the superior reconstruction quality of frequency-domain encoding, highlighting the effectiveness of phase-based superposition in preserving structural and perceptual video details compared to time-domain encoding.

Although the proposed framework is conceptually strong, it is fully simulation-based, and practical implementations require consideration of circuit complexity, gate depth, and processing latency. For an 8-qubit QFT-based frequency-domain encoding, the circuit involves 36 sequential gates (8 Hadamard gates and 28 controlled-phase rotations), whereas time-domain Hadamard-only encoding requires only 8 gates. This increase



(a) Frequency-domain decoded frame (F8) (b) Time-domain decoded frame (T8)

Figure 5.17: Decoded video frames at –12 dB channel SNR for GOP 8 and qubit size 8: (a) frequency-domain, (b) time-domain.

in circuit depth can impact the susceptibility to decoherence in near-term quantum hardware, which is critical for real-time video applications. Furthermore, polar coding (rate 1/2) introduces classical processing with complexity $\mathcal{O}(E \log E)$, where E is the block length of the polar code. Larger block lengths improve error correction but may add latency, affecting real-time performance. By constraining the system to moderate qubit counts (≤ 8) and avoiding QEC, the framework remains compatible with future hardware, while still demonstrating the advantages of frequency-domain encoding.

5.2.3 Section Summary

This section extended the frequency-domain multi-qubit framework of Section 5.1 to video transmission, demonstrating that the per-symbol robustness gains observed for images also carry over to the temporally correlated video case. Across all GOP sizes, frame rates, and resolutions evaluated, frequency-domain encoding (F1–F8) consistently outperforms its time-domain counterpart (T1–T8) and the classical BPSK baseline at equal bandwidth. The performance advantage grows with qubit dimensionality: at $k = 1$ the time and frequency domains converge, but at $k = 8$ frequency-domain encoding achieves an additional 4 dB channel-SNR gain over the time-domain system. Resolution and frame rate have negligible influence on the relative gain, while larger GOP sizes amplify error propagation and reduce absolute quality across all systems. These results confirm that the dual amplitude–phase encoding provided by the QFT delivers a robust, bandwidth-efficient, and content-agnostic framework for video transmission over noisy quantum channels, at a moderate increase in gate count and circuit depth compared with time-domain Hadamard-only encoding.

5.3 Quantum Fourier Transform for Image Compression and Transmission over Error-Prone Channels

Publication Notice

The research presented in this section has been submitted as the following manuscript and is currently under review:

U. Jayasinghe and A. Fernando, "Quantum Fourier Transform for Image Transmission over Error-Prone Channels," submitted to *IEEE Transactions on Consumer Electronics*.

Portions of this chapter are based on the above submitted manuscript. The material has been revised and expanded with additional explanations, analysis, and discussion for inclusion in this doctoral thesis.

Problem Statement: Sections 5.1 and 5.2 established that frequency-domain multi-qubit encoding improves transmission robustness for both image and video communication. In those frameworks, however, the QFT is used only as a transmission representation; data reduction is still performed entirely by classical source coding (JPEG, HEIF, VVC) applied *before* quantum mapping. This leaves an opportunity unexplored: the QFT itself concentrates a real-valued input signal into a small number of dominant frequency components, which is exactly the property that classical transform coding exploits for compression. If the QFT representation could be truncated or quantised in the quantum domain, the resulting framework would perform symbol-level data reduction natively, without requiring a separate classical compression stage.

Limitations of Existing Work: Although the QFT provides several theoretical advantages, including compact frequency-domain representation, improved information distribution across quantum states, and enhanced robustness against channel noise, its potential for jointly performing image compression and transmission has not been fully explored. Existing QFT-related studies mainly focus on quantum algorithms or standalone quantum image compression techniques rather than integrated communication systems. Furthermore, prior work has not investigated symbol-level compression and transmission directly in the quantum frequency domain within a unified framework. Consequently, the interaction between frequency-domain quantum representation, com-

pression efficiency, transmission robustness, and reconstructed image quality remains largely uncharacterised.

Motivation and Proposed Contribution. To overcome the limitations, this section investigates the use of the QFT as a unified frequency-domain mechanism for both image compression and transmission. The motivation for this approach is that frequency-domain representations can distribute image information more efficiently across quantum states while enabling selective retention of dominant frequency components, thereby reducing transmission redundancy and improving robustness against channel noise. Unlike conventional approaches that separately perform compression and transmission, the proposed framework integrates both operations within a single quantum processing pipeline. In the proposed system, image pixel groups are first mapped into multi-qubit computational-basis states and transformed into the quantum frequency domain using the QFT. The transformed coefficients are then selectively quantised to retain dominant frequency components before transmission through the noisy quantum channel. At the receiver, the IQFT and Euclidean-distance decoding are applied to reconstruct the transmitted pixel groups, which are subsequently reassembled into the output image. The framework is evaluated both with and without classical polar channel coding and compared against bandwidth-equivalent classical and time-domain quantum communication systems. The results demonstrate that the QFT can effectively operate as a unified compression-and-transmission mechanism for quantum multimedia communication.

5.3.1 System Model

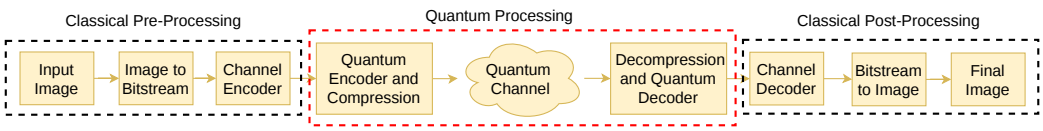


Figure 5.18: Proposed framework of quantum Fourier transform-based image compression and transmission.

As illustrated in Figure 5.18, the proposed method adopts a quantum frequency-domain image compression and transmission strategy, implemented within a hybrid

quantum-classical communication framework. The proposed method is designed to be adaptable to any image, making it suitable for diverse real-world applications. To evaluate its performance, 20 images are selected from the Microsoft COCO dataset at a resolution of 256×192 [197], 20 images are chosen from the ImageNet dataset [218] at 450×450 resolution, and 20 high-resolution (4K) images are taken from the Kaggle 4K dataset [219]. All are initially evaluated in their uncompressed form. To demonstrate the framework's compatibility with different source coding formats, the JPEG standard is also employed as a representative example. Additionally, the proposed framework is input-agnostic because it operates directly on the bitstream using a deterministic quantum encoding and transmission process, without any training, parameter tuning, or dataset-dependent adaptation. Processing begins with converting images into classical bitstreams. These bitstreams are then channel encoded using polar codes with a code rate of 1/2. Additionally, the non-channel coded (without channel coding) scenario is also analysed to evaluate the intrinsic performance of the QFT rather than its error correction capabilities.

The subsequent subsections elaborate on the detailed process of each main functional block illustrated in Figure 5.18.

Quantum Encoder and Decoder

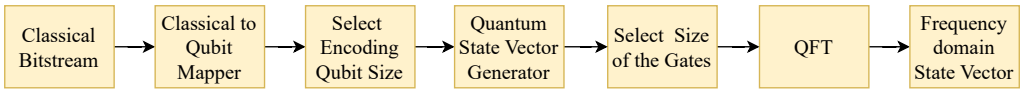


Figure 5.19: Proposed quantum encoder.

The quantum encoder, illustrated in Figure 5.19, converts classical time-domain data into frequency-domain quantum data. The first stages of the encoder, namely classical-to-qubit mapping, encoding qubit size selection, and multi-qubit state vector construction via the tensor product, follow the formulation established in Chapter 4 (Section 4.1). Briefly, each block of $k \in [1, 8]$ classical bits is mapped to a computational-basis state in the 2^k-dimensional Hilbert space $\mathcal{H}_{2^k}$. The contribution of this section lies in the subsequent layers, which perform the time-to-frequency-domain transformation via the QFT and exploit the structure of QFT-transformed basis states for symbol-level

compression, as detailed below.

The next layer projects each computational-basis state into the frequency domain using the QFT operator F_N ($N = 2^k$) defined in Section 5.1 (Equations 5.1–5.3), with explicit basis-state transformations $F_4 |00\rangle, \ldots, F_4 |11\rangle$ given in (5.5)–(5.8). According to the results, each qubit state in the time domain corresponds to a unique column vector in the QFT matrix when converted to the frequency domain. Upon careful examination of these QFT column vectors, it is evident that the second element of each vector uniquely identifies the entire column. Therefore, instead of transmitting the full quantum state vector in the frequency domain, it is sufficient to transmit only the second element. For example, with $k = 2$, the full state vector has 4 elements, and transmitting just one achieves a $4:1$ compression ratio. As k increases, the compression becomes more significant: at $k = 8$, only 1 out of 256 elements is transmitted, yielding a $256:1$ compression.

In physical implementation, the quantum state can be prepared directly using deterministically computed coefficients via unitary operations, without performing any projective measurement or extracting amplitudes from an existing superposition. The second QFT coefficient of each symbol can then be computed from the bit pattern and encoded as a discrete phase on the complex unit circle, and 2^k such coefficients are combined to synthesise a valid multi-qubit state in the 2^k-dimensional Hilbert space, fully preserving the quantum coherence. The so-prepared state allows the nearest-vector reconstruction at the receiver to exactly recover the quantum frequency-domain state vector, and the IQFT subsequently reconstructs the original classical bitstream in noiseless or very low-noise channels, making the claim of near-lossless reconstruction fully consistent with quantum mechanics. By transmitting only these phase coefficients, the method significantly reduces the quantum symbol payload while enabling near-lossless reconstruction in low-noise environments. Under higher channel noise, however, perturbations in the transmitted coefficients can cause the nearest-vector reconstruction to select an incorrect state, introducing errors in the recovered bitstream. Consequently, while the framework remains theoretically lossless, practical transmission over noisy channels results in progressively lossy reconstruction, with the degree of fidelity loss depending on noise intensity and system dimensionality.

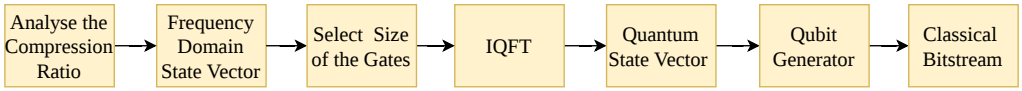


Figure 5.20: Proposed quantum decoder.

In the quantum decoder, as shown in Figure 5.20, the process mirrors the encoder with multiple layers. It begins by analysing the compression ratio and reconstructing the full frequency domain state vector. Next, the appropriate IQFT is applied to convert the frequency-domain representation back to the time domain. The IQFT is simply the Hermitian adjoint (conjugate transpose) of the QFT, and is analogous to the inverse DFT in classical systems. Finally, the resulting time-domain quantum state is mapped into classical bits using the corresponding quantum measurements.

Mathematically, IQFT is expressed as (5.19).

$$\text{IQFT} = \text{QFT}^{\dagger} \tag{5.19}$$

Therefore, the IQFT matrix is the conjugate transpose of the QFT matrix, differing only in the sign of the exponent in its phase factors. The QFT and IQFT equations are defined in (5.20) and (5.21), respectively.

$$F_N \left|x\right\rangle = \frac{1}{\sqrt{N}} \sum_{y=0}^{N-1} e^{+2\pi i\, xy/N} \left|y\right\rangle \tag{5.20}$$

$$F_N^{-1} \left|y\right\rangle = \frac{1}{\sqrt{N}} \sum_{x=0}^{N-1} e^{-2\pi i\, xy/N} \left|x\right\rangle \tag{5.21}$$

where F_N and F_N^{-1} denote the forward and inverse quantum Fourier transform operators acting on an N-dimensional quantum system, respectively, with $N = 2^k$ representing the Hilbert-space dimension for a k-qubit system. In the forward transform (5.20), $|x\rangle$ is the input computational-basis state (time-domain) with $x \in \{0, 1, \ldots, N-1\}$, and $|y\rangle$ denotes the basis states output frequency-domain with $y \in \{0, 1, \ldots, N-1\}$. In the inverse transform (5.21), $|y\rangle$ is the input frequency-domain basis state and $|x\rangle$ denotes the output computational-basis states. The factor $i = \sqrt{-1}$ is the imaginary unit, and the exponential terms $e^{\pm 2\pi i\, xy/N}$ represent the complex phase factors that distinguish the forward $(+)$ and inverse $(-)$ transformations.

In addition, the compression and decoding process can be mathematically simulated as follows. The QFT matrix $F \in \mathbb{C}^{N\times N}$ is defined as in (5.22).

$$F_{k,l} = \frac{1}{\sqrt{N}} e^{2\pi i \frac{kl}{N}}, \quad k,l \in \{0,1,\ldots,N-1\} \tag{5.22}$$

Let $\mathbf{q}_j \in \mathbb{C}^N$ denote the j^{th} column of the QFT matrix as in (5.23).

$$\mathbf{q}_j = \frac{1}{\sqrt{N}} \begin{bmatrix} 1 \\ e^{2\pi ij/N} \\ e^{2\pi i 2j/N} \\ \vdots \\ e^{2\pi i(N-1)j/N} \end{bmatrix} \tag{5.23}$$

The second element of each column can be represented as (5.24).

$$q_j^{(2)} = \frac{1}{\sqrt{N}} e^{2\pi ij/N} \tag{5.24}$$

The values represent N equally spaced points on the complex unit circle, scaled by $\frac{1}{\sqrt{N}}$. Each second element $q_j^{(2)}$ is distinct, enabling a unique one-to-one mapping to the original column index j.

Following the transmission process, $\tilde{q}^{(2)}$ denotes the received (possibly noisy) complex value, where $\eta \in \mathbb{C}$ represents the noise introduced during transmission. The received value is thus expressed as shown in (5.25).

$$\tilde{q}^{(2)} = q_j^{(2)} + \eta \tag{5.25}$$

Therefore, the reconstruction process is as follows.

1. Define the set of ideal second elements as in (5.26).

$$\mathcal{Q} = \left\{ \frac{1}{\sqrt{N}} e^{2\pi ij/N} \mid j = 0, ..., N-1 \right\} \tag{5.26}$$

2. Find the nearest element as in (5.27).

$$j^* = \arg\min_j \left| \tilde{q}^{(2)} - \frac{1}{\sqrt{N}} e^{2\pi ij/N} \right| \tag{5.27}$$

3. Retrieve the corresponding QFT columns as in (5.28).

$$\hat{\mathbf{q}} = \mathbf{q}_{j^*} \tag{5.28}$$

4. Apply IQFT to reconstruct as in (5.29).

$$\hat{\mathbf{x}} = F^{\dagger}\hat{\mathbf{q}} \tag{5.29}$$

After applying the IQFT, projective measurements are performed on all k qubits in the computational (Z) basis, using projection operators $\{|x\rangle\langle x|\}$ for $x \in \{0,1\}^k$. A single result $|x\rangle$ is sampled based on the probability $|\langle x|\psi\rangle|^2$, producing a k-bit classical string that represents the decoded symbol for bitstream reconstruction. It is important to note that the simulation process strictly follows the theoretical model, maintaining mathematical consistency throughout.

Quantum Channel

The quantum channel uses the same composite noise model established in Chapter 3 Section 3.1 and reused in Section 5.1 of this chapter, combining bit-flip, phase-flip, depolarising, amplitude-damping, and phase-damping mechanisms in a probabilistic mixture whose total noise probability scales with the channel SNR.

5.3.2 Results

This study evaluates quantum frequency-domain unified image compression and transmission system across varying qubit encoding sizes and channel conditions using key performance metrics: PSNR, SSIM, and BER. To ensure statistical reliability, input images are tested with 1000 trials each, and average results are reported, offering a robust and realistic performance assessment.

Performance Evaluation Under Non-Channel Coding

The variation in BER for different qubit encoding sizes, ranging from 1 to 8, is shown in Figure 5.21a for uncompressed image inputs. For a k-qubit encoding, the QFT maps

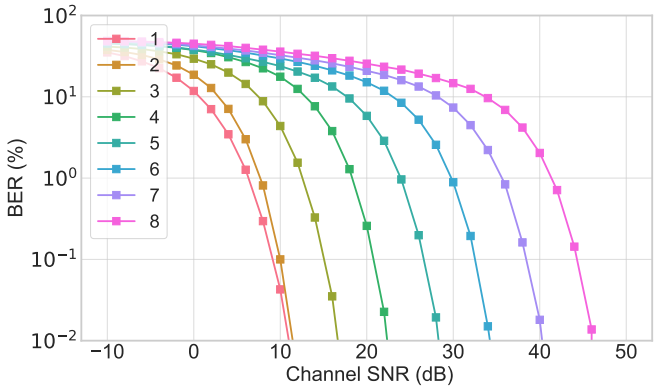
each block into a 2^k-dimensional frequency-domain vector with 2^k frequency components. Since the QFT matrix is unitary, each basis state corresponds to one orthogonal column, and in the ideal noise-free case a single coefficient is sufficient to uniquely identify the state. This enables symbol-level compression with an effective ratio of $2^k : 1$, which grows exponentially with k.

However, larger k also reduces the angular separation between neighbouring frequency components, given by (5.30).

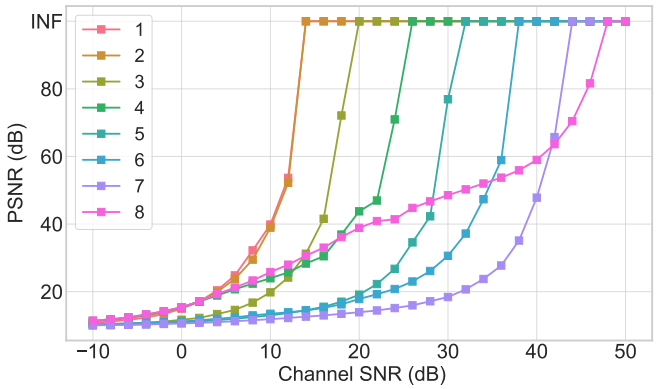
$$\Delta\theta = \frac{2\pi}{N_{\text{freq}}} = \frac{2\pi}{2^k} \tag{5.30}$$

Where N_{freq} is the number of frequency components, which is equal to 2^k. As k increases, $\Delta\theta$ decreases, causing denser clustering in the angular domain and higher phase noise sensitivity, which directly increases the BER. For instance, with $k = 2$, $\Delta\theta = \pi/2$ provides robust separation and a $4 : 1$ compression ratio, whereas with $k = 8$, $\Delta\theta \approx 0.0245$ radians yields a $256 : 1$ compression ratio (99.6% reduction) but with significantly reduced robustness. This establishes the fundamental trade-off: small k offers strong noise resilience with modest compression, while large k provides exponential compression at the cost of higher error rates, making intermediate block sizes (e.g., $k = 2$) the most practical choices under noisy channel conditions.

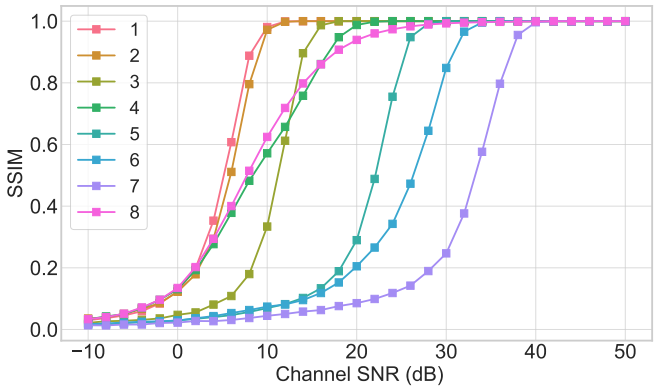
The variation of PSNR for the decoded images with respect to SNR for different qubit encoding sizes (1 to 8) is shown in Figure 5.21b for uncompressed image inputs. The general trend indicates that PSNR improves as SNR increases for all systems, leading to better image reconstruction. As expected, the PSNR performance of the proposed system decreases with increasing encoding sizes of the qubit. An anomalous behaviour is observed with the eight-qubit encoding, where PSNR fluctuates differently compared to lower-qubit encodings. This occurs because each pixel is mapped into 2^8 QFT frequency components, resulting in dense angular spacing $\Delta\theta = 2\pi/2^8$ between adjacent states, which increases sensitivity to channel noise. Noise primarily perturbs the least significant bits (LSBs) that correspond to smaller angular differences, while the most significant bits (MSBs), which determine the dominant pixel intensity, remain largely intact. The IQFT spreads frequency-domain perturbations across all basis states, and the strong spatial correlations in natural images allow neighbouring pixels to absorb



(a) BER

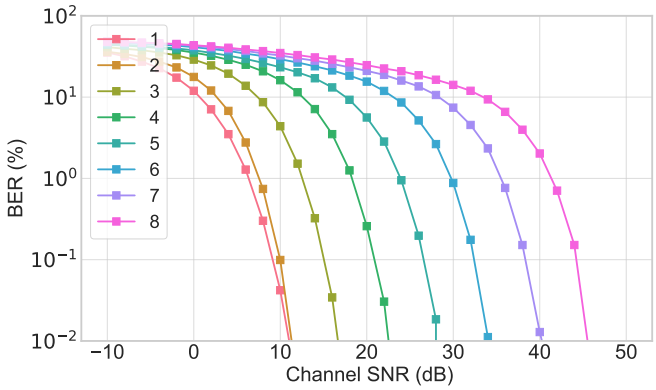


(b) PSNR

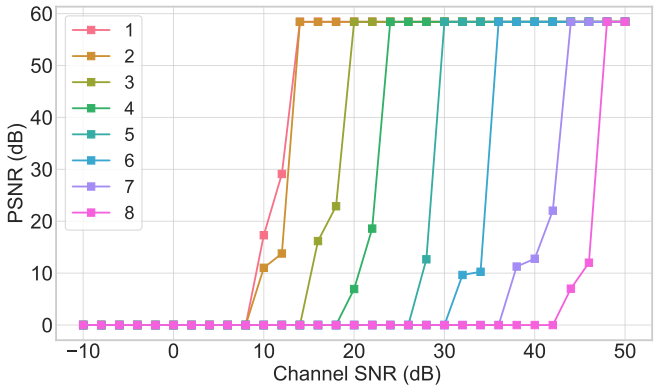


(c) SSIM

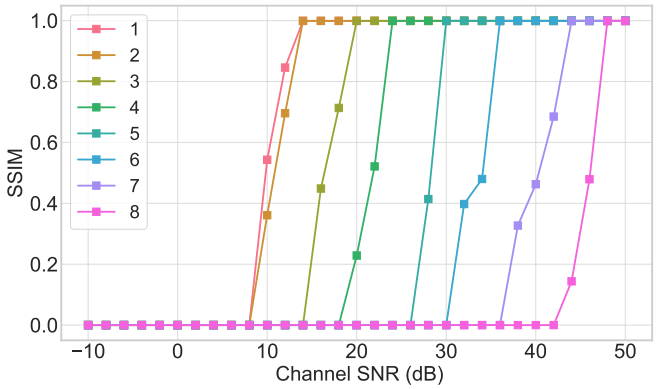
Figure 5.21: Performance of the proposed system for different qubit sizes in a non-channel coding scenario for uncompressed image inputs.



(a) BER



(b) PSNR



(c) SSIM

Figure 5.22: Performance of the proposed system for different qubit sizes in a non-channel coding scenario for JPEG images.

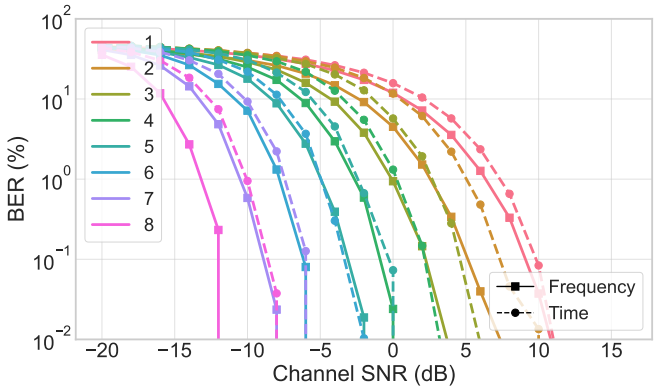
minor deviations. Consequently, despite an increased BER, the reconstructed pixel values preserve the main image structure, yielding high PSNR and SSIM. Additionally, qubit sizes 1 and 2 provide better error resilience with lower compression, while the two-qubit system is optimal with a compression ratio of 4:1. Furthermore, the variation in SSIM, as shown in Figure 5.21c, further validates the performance of the system for different qubit encoding sizes in decoded images, similar to the PSNR variation.

The performance of the proposed framework on classically source-coded image formats is evaluated using JPEG-compressed images, as depicted in Figure 5.22. A performance trend similar to that of uncompressed inputs is observed with increasing qubit sizes from 1 to 8, where higher qubit counts generally lead to improved compression but reduced noise resilience. However, for JPEG-compressed images, the image quality deviates at eight-qubit encoding due to the altered data structure. Unlike uncompressed images, where spatial redundancy and frequency leakage help mitigate noise effects, JPEG compression involves quantisation and block-based decorrelation, which reduce tolerance to distortions. As a result, eight-qubit mappings become more sensitive to noise, leading to greater perceptual degradation despite similar BER levels.

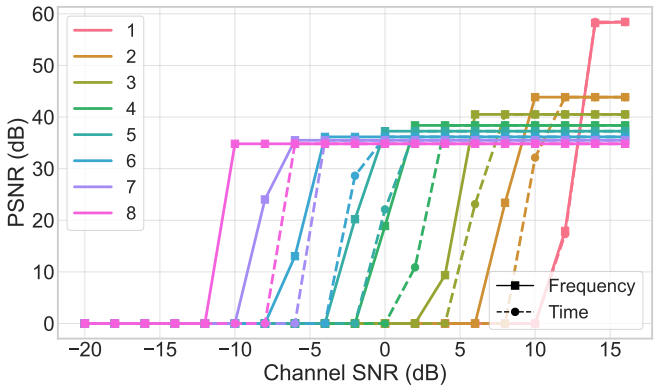
The proposed system is also compared with compression-free frequency-domain and time-domain quantum communication systems for JPEG images under identical bandwidth conditions, as shown in Figure 5.23. In the reference systems, the full quantum state is transmitted, resulting in improved performance with higher qubit encodings but at the cost of increased bandwidth. The compression-free frequency-domain system is more resistant to noise than the time-domain approach because of its structured phase encoding. In contrast, the proposed method achieves comparable performance while transmitting fewer quantum symbols through selective QFT coefficient transmission, providing a more favourable trade-off between fidelity and bandwidth efficiency.

Performance Evaluation Under Channel Coding

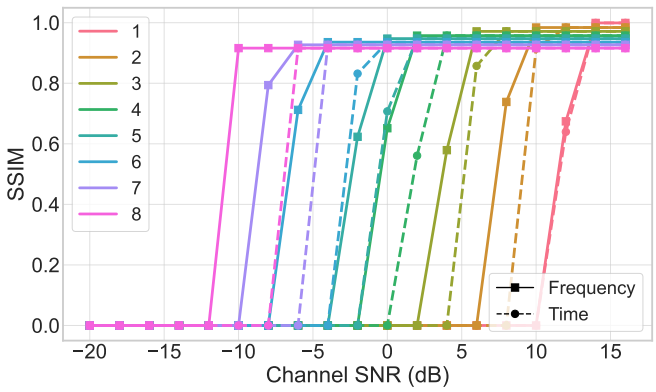
The variation in BER as a function of channel SNR for different encoding sizes of the qubits is presented in Figure 5.24a for uncompressed image inputs, which shows improved error performance with channel coding. At low SNR (0–10 dB), BER remains high but lower than in the uncoded system. As SNR increases beyond 20 dB, BER



(a) Comparison - BER

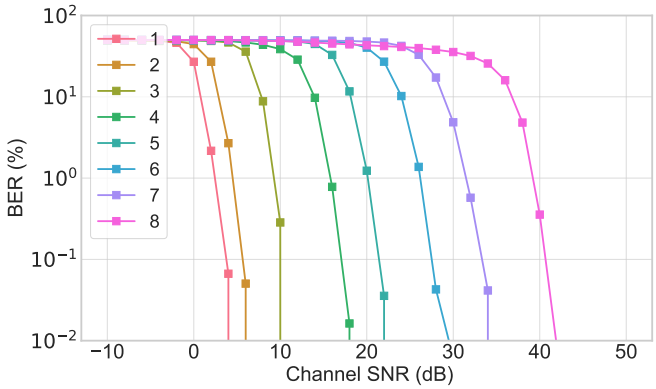


(b) Comparison - PSNR

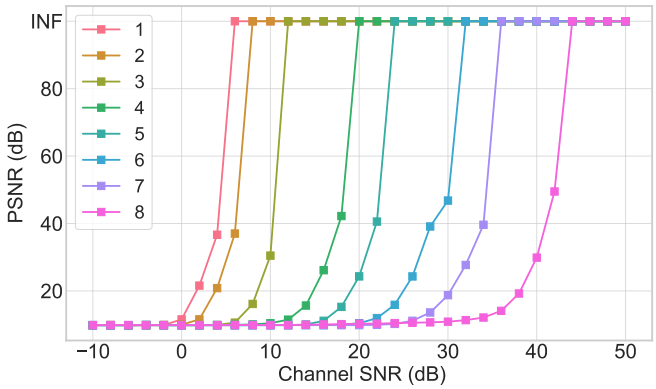


(c) Comparison - SSIM

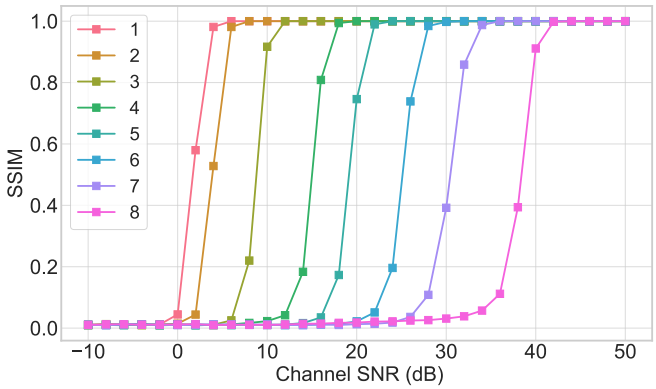
Figure 5.23: Performance of JPEG image transmission for different qubit sizes in a non-channel coding scenario across two different communication systems: time-domain without compression (dash lines), frequency-domain without compression (solid lines).



(a) BER



(b) PSNR



(c) SSIM

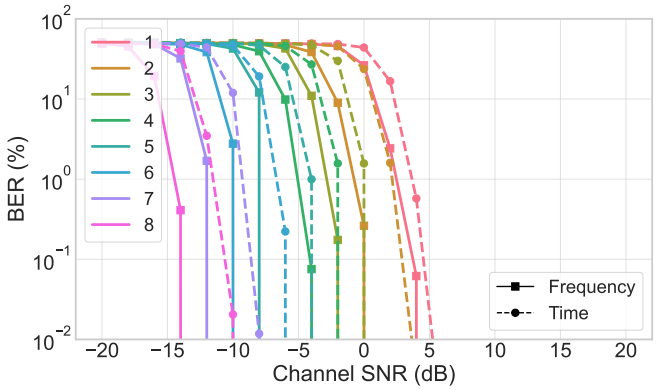
Figure 5.24: Performance of the proposed system for different qubit sizes with channel coding for uncompressed image inputs.

decreases exponentially, confirming effective error mitigation. As shown in Figure 5.24b, channel coding significantly enhances PSNR for uncompressed image inputs, especially at low SNR levels, and achieves perfect reconstruction (infinite PSNR) at high SNR. Similar to the non-channel-coded case, PSNR decreases with larger qubit sizes, indicating increased noise sensitivity. However, unlike the non-channel-coded system where eight-qubit encoding directly maps pixel values and shows some resilience, channel coding introduces redundancy that disrupts this mapping. As a result, qubit size eight exhibits the worst performance among all encoding sizes, highlighting that increasing qubit encoding size leads to performance degradation due to the impact of closely spaced frequency components. In contrast, single-qubit encoding offers the best resilience with a 2:1 compression ratio. SSIM results in Figure 5.24c further confirm this trend, showing lower SSIM for higher qubit sizes, consistent with PSNR trends.

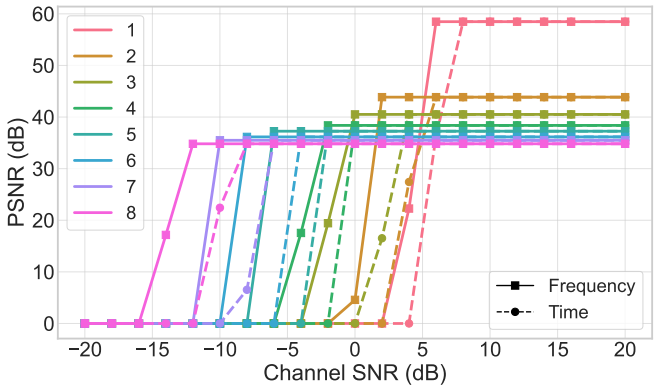
Furthermore, as shown in Table 5.3, the summarised maximum channel SNR gains illustrate the performance of each qubit system compared to the eight-qubit system, which offers maximum compression but low noise resilience. According to the results, both channel-coded and non-channel-coded scenarios enable variable compression rates through different qubit encoding sizes, and the maximum channel SNR gains are similar regardless of the image format. In addition, highly compressed systems are more susceptible to noise, whereas less compressed systems exhibit greater robustness due to increased phase separation and reduced encoding complexity. However, this compression applies only to transmission, not storage, as reconstructing the classical bitstream requires the full quantum state with quantum measurements.

Table 5.3: Maximum SNR gains (in dB) achieved by each qubit system compared to the 8-qubit configuration.

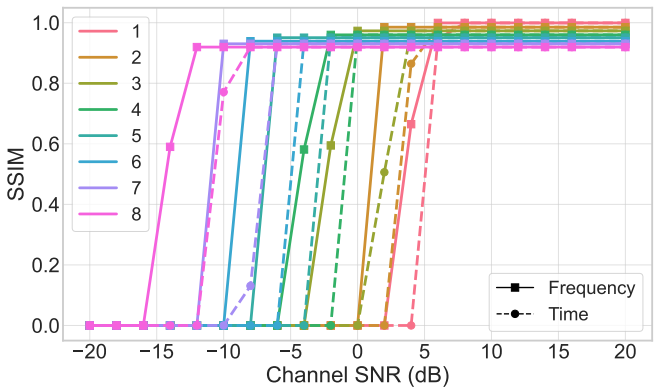
Configuration	**Qubit Encoding Size**							
	1	**2**	**3**	**4**	**5**	**6**	**7**	**8**
Compression Ratio	2:1	4:1	8:1	16:1	32:1	64:1	128:1	256:1
Non-channel coded, 256×192	34 dB	34 dB	28 dB	22 dB	16 dB	10 dB	4 dB	–
Non-channel coded, 450×450	34 dB	34 dB	28 dB	22 dB	16 dB	10 dB	4 dB	–
Non-channel coded, 4K (UHD)	34 dB	34 dB	28 dB	22 dB	16 dB	10 dB	4 dB	–
Channel coded, 256×192	38 dB	36 dB	32 dB	24 dB	20 dB	12 dB	8 dB	–
Channel coded, 450×450	38 dB	36 dB	32 dB	24 dB	20 dB	12 dB	8 dB	–
Channel coded, 4K (UHD)	38 dB	36 dB	32 dB	24 dB	20 dB	12 dB	8 dB	–



(a) Comparison - BER



(b) Comparison - PSNR



(c) Comparison - SSIM

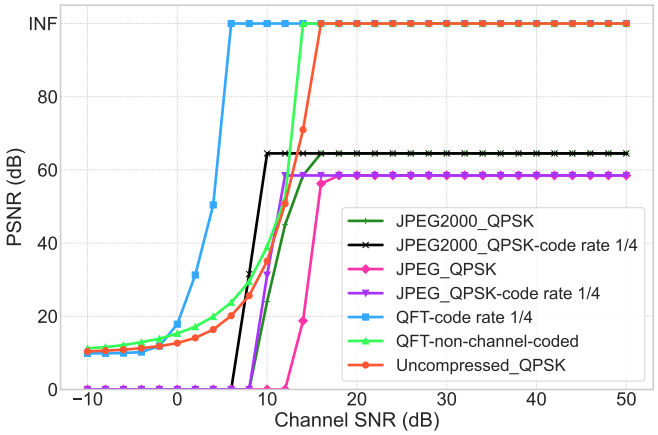
Figure 5.25: Performance of JPEG image transmission for different qubit sizes with channel coding across two different communication systems: time-domain without compression (dash lines), frequency-domain without compression (solid lines).

As shown in Figure 5.25, the time and frequency-domain systems without compression exhibit improved robustness due to the application of error correction, while operating under the same bandwidth constraints across all qubit sizes for JPEG images. Similarly to the uncoded scenario, the performance of these two multi-qubit systems improves with increasing qubit size; however, this comes at the cost of higher bandwidth consumption compared to the proposed unified compression and transmission method. This shows that the proposed framework provides a balance between transmission fidelity and bandwidth efficiency.

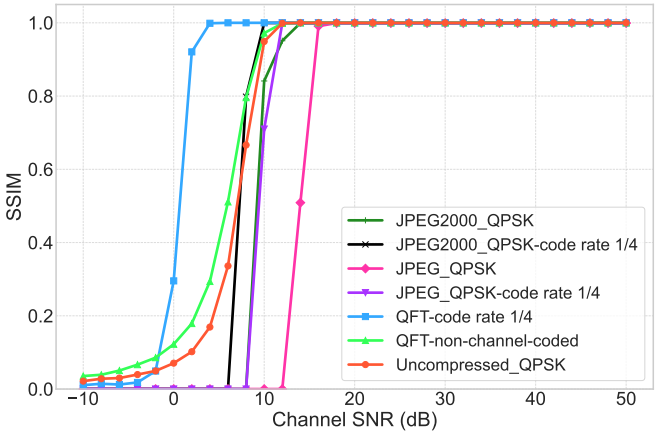
Performance Evaluation for Two Qubit System

To contextualise our results, we compare the proposed method with representative classical baselines, as shown in Figure 5.26. QPSK provides a modulation-level reference with comparable bandwidth to the two-qubit system, while JPEG and JPEG2000 are chosen as standard image compression benchmarks based on DCT and wavelets, respectively. It is important to note that all systems are analysed under similar bitrates, ensuring equal bandwidth utilisation. Due to the lack of comparable state-of-the-art quantum systems with integrated compression–transmission designs, direct comparison with existing quantum approaches is not technically consistent. This is because these systems are based on fundamentally different operational principles.

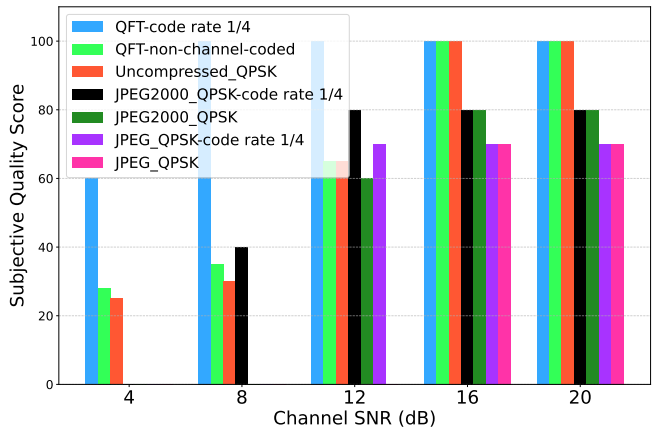
The QFT-based system, even without channel coding, enables frequency-domain image transmission that performs comparably to the uncompressed classical QPSK system while achieving a 4:1 compression advantage. When polar coding is applied at a rate of 1/4, maintaining the same channel bitrate without compression gain, the QFT system demonstrates up to a 10 dB PSNR gain, surpassing the uncompressed classical QPSK system in both error resilience and image quality under noisy conditions. Although JPEG and JPEG2000 are lossy compression methods, their performance with and without channel coding lags behind the proposed QFT-based approach as shown in Figure 5.26a. SSIM results (Figure 5.26b) follow the same trend, confirming the efficiency and reliability of quantum frequency domain image compression and transmission. However, the proposed framework differs by exploiting exponential Hilbert-space scaling, achieving symbol-level compression ratios up to $256:1$, transmitting only one coefficient



(a) PSNR



(b) SSIM



(c) Subjective Quality Score

Figure 5.26: Comparison of the proposed system with classical communication systems: (a) Peak Signal-to-Noise Ratio (PSNR), (b) Structural Similarity Index Measure (SSIM), and (c) Subjective Quality Score.

per block, and showing stronger resilience under noisy conditions. Although JPEG and JPEG2000 remain superior in terms of hardware maturity, the proposed QFT-based method highlights the potential of quantum encoding strategies for bandwidth-limited and noise-prone scenarios.

In addition, a subjective user experiment is conducted, using a double stimulus quality assessment [208], with 50 participants (aged 18 to 55) to assess image quality at different SNR levels. The results, shown in Figure 5.26c, align with the objective metrics, reinforcing the study's relevance for consumer applications. Furthermore, a histogram-based analysis is performed at selected SNR levels to further validate the proposed system, as shown in Figure 5.27. This analysis is conducted for the eight-qubit encoding configuration without channel coding, since it represents the highest compression and the most noise-sensitive case. The histogram comparison between the original and reconstructed images shows that the overall intensity distribution is largely preserved, supporting the visual observations and objective quality metrics.

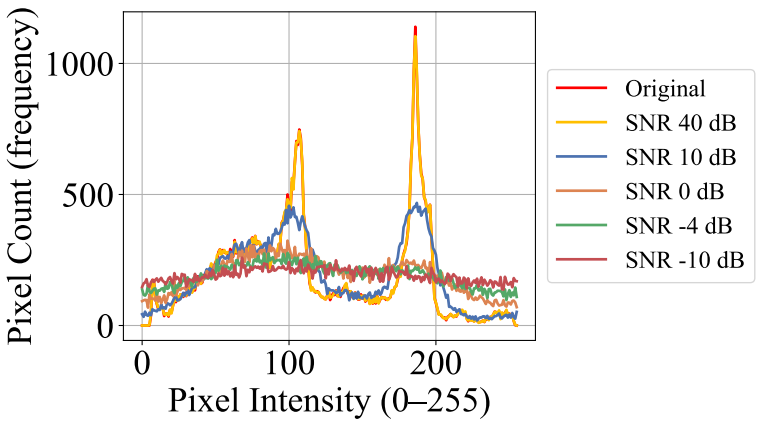


Figure 5.27: Histogram comparison between the original image and the reconstructed images at different SNR levels using eight-qubit encoding.

In this study, the QFT is selected for the framework due to its efficient and low-depth circuit implementation, distinctive frequency-domain characteristics that enable vector identification from a single coefficient, and its natural compatibility with multi-qubit states. Additionally, QFT exhibits inherent unitarity, supports coherent phase manipulation, and offers better integration with quantum algorithms such as phase estimation. These features make it particularly well-suited for scalable, selective quantum compression and transmission frameworks, offering significant benefits over alternative

transforms such as the QDCT, which often involve more complex gate structures and lack frequency-domain sparsity in quantum representations.

Furthermore, the proposed QFT-based framework enables theoretically lossless symbol-domain compression during transmission under noiseless conditions due to the unitary nature of the QFT and IQFT operations. The transmitted compressed representation is reconstructed at the receiver using the received symbols and the corresponding inverse transformation. Consequently, the compression process affects only the transmission stage and does not introduce the permanent information loss associated with conventional lossy down-sampling methods. In practice, however, higher qubit encodings experience PSNR and SSIM degradation due to channel noise and smaller angular separation between frequency coefficients, making transmission effectively lossy despite ideal reconstruction. In addition, the proposed QFT-based transmission scheme achieves accurate image reconstruction while maintaining low computational demands. The quantum processing stage is implemented using Hadamard and controlled phase operations, and the overall circuit complexity increases polynomially as $\mathcal{O}(k^2)$ with the number of qubits. This is significantly more efficient than the equivalent classical discrete Fourier transform, which requires $\mathcal{O}(2^{2k})$ operations in the corresponding state space. As a result, higher-dimensional configurations such as eight-qubit encoding can be supported without a significant increase in computational cost, making the framework scalable and practical. Moreover, with parallel gate scheduling, the circuit depth grows approximately linearly with the number of qubits. In this research, the qubit encoding size is limited to $k \leq 8$ to balance computational complexity and noise robustness. Increasing k raises the QFT/IQFT cost and reduces angular separation between quantum states, making the system more sensitive to noise. Thus, $k \leq 8$ provides an effective trade-off between compression efficiency, computational feasibility, and reconstruction quality.

While the proposed QFT-based framework shows strong theoretical potential, its practical implementation is currently limited by quantum hardware constraints. Experiments are conducted on a conventional CPU (Intel Core i5-1345U, 16 GB RAM) using MATLAB and Python, with execution times from less than one minute for low-qubit configurations to roughly ten minutes for eight-qubit encodings. The framework is

therefore presented as a theoretical feasibility study, with potential applications in real-time multimedia scenarios such as augmented and virtual reality, medical image transmission, remote sensing, and future quantum internet services.

5.3.3 Section Summary

This work presented a QFT-based quantum communication framework that jointly performed image compression and transmission in the frequency domain. Instead of separating source coding and channel transmission, image information was directly embedded into quantum frequency components. The system was evaluated across different qubit encoding sizes and channel conditions, both with and without channel coding, using BER, PSNR, and SSIM metrics. The results highlighted a clear trade-off between compression efficiency and noise robustness. As the qubit encoding size increased, compression efficiency improved significantly. Eight-qubit encoding achieved up to a 256:1 symbol-level compression ratio, providing substantial bandwidth savings. However, higher-dimensional frequency states reduced the phase separation between components, making the system more sensitive to noise. Although the eight-qubit configuration performed well under high-SNR conditions, its performance degraded more rapidly in noisy channels, while moderate SNR levels still enabled acceptable reconstruction due to preserved local pixel correlations. In contrast, lower qubit configurations offered stronger noise resilience. The two-qubit system, in particular, maintained stable performance across a wide SNR range while achieving a practical 4:1 compression ratio. This made it a balanced and practical choice for channels with varying or uncertain conditions. Compared with classical schemes, the two-qubit QFT system achieved performance comparable to an uncompressed QPSK system while using significantly less bandwidth. With polar coding at a rate of 1/4, it provided up to a 10 dB PSNR improvement at the same bitrate. Classical JPEG and JPEG2000 approaches demonstrated lower efficiency and reduced robustness under comparable transmission conditions. Overall, the proposed framework provided a unified quantum frequency-domain architecture that integrated compression and transmission. By enabling adjustable multi-qubit encoding, the system offered a flexible trade-off between compression efficiency and noise tolerance, demonstrating strong potential for bandwidth-efficient and high-quality

image communication.

5.4 Quantum Fourier Transform for Video Compression and Transmission over Error-Prone Channels

Publication Notice

The research presented in this section has been published in the following peer-reviewed journal publication:

U. Jayasinghe and A. Fernando, "Rethinking video transmission: A quantum Fourier transform-based approach for error-prone channels," *Electronics*, vol. 15, no. 6, art. no. 1323, 2026, doi: 10.3390/electronics15061323.

This material is reproduced and adapted under the terms of the MDPI Copyright policy for use in a doctoral thesis. The content has been revised and extended with additional explanations and expanded discussion.

Problem Statement: Section 5.3 showed that the QFT can serve as a symbol-level compression primitive for image transmission, removing the dependence on a separate classical source coder. Extending this idea to video, however, exposes a tension: video transmission demands aggressive data reduction, because raw video bitrates are orders of magnitude higher than those of still images, while video is simultaneously far more sensitive to compression-induced errors due to the strong temporal correlation between frames. Whether QFT-based compression remains effective when applied to video bitstreams under both uncompressed and VVC-precompressed inputs, and how quantum compression interacts with the GOP structure, are open questions left unanswered by Section 5.3.

Limitations of Existing Work: Existing quantum video communication frameworks exhibit three key limitations that motivate the work in this section. First, current approaches rely entirely on classical source coders (e.g., HEVC, VVC) for data reduction prior to quantum encoding, meaning the quantum layer contributes only to transmission and not to compression itself. Second, the QFT-based compression framework introduced in Section 5.3 has been validated only on still images, and its applicability to temporally

correlated video data remains unverified, particularly under varying GOP configurations where inter-frame dependencies amplify the impact of residual transmission errors. Third, no prior study has systematically analysed the joint interaction between QFT-based symbol-level compression and transmission within a unified framework, leaving the practical operating regimes of quantum video compression largely unexplored.

Motivation and Proposed Contribution: To address these limitations, this section investigates the use of the QFT as a unified mechanism for both video compression and transmission in the quantum frequency domain. Unlike conventional quantum video communication systems that depend entirely on classical source coding for data reduction, the proposed framework performs symbol-level compression directly during the quantum transmission process. The motivation behind this approach is that QFT-based frequency-domain representation can distribute video information more efficiently across quantum states, enabling reduced transmission redundancy while improving robustness against channel noise.

The proposed system extends the QFT-based compression-and-transmission framework of Section 5.3 to video communication. The framework supports both uncompressed (raw) and VVC-pre-encoded video inputs and applies QFT-based symbol-level compression using multi-qubit configurations ($k \in [1, 8]$). The resulting quantum states are transmitted through the composite noise channel established in Chapter 3. At the receiver, the IQFT and multi-qubit decoding reconstruct the transmitted video data for final video recovery. The proposed framework is evaluated under both uncoded and rate-1/2 polar-coded transmission scenarios across multiple spatial resolutions, frame rates, and GOP sizes using PSNR, SSIM, and VMAF quality metrics. The objective is to investigate the trade-off between compression efficiency, transmission robustness, and reconstructed video quality under different qubit configurations, while comparing the proposed framework against classical and time-domain quantum communication systems operating under equivalent bandwidth conditions.

5.4.1 System Model

The processing pipeline developed in this work is illustrated in Figure 5.28. Its purpose is twofold: video data is compressed efficiently and delivered reliably through noisy



Figure 5.28: Proposed quantum communication pipeline for joint video compression and transmission.

quantum channels. Because the quantum encoder, decoder, and channel model are reused from the structures introduced in Section 5.3 for image transmission, those derivations are not repeated here. The discussion below is therefore concentrated only on the modifications that are required when the source signal is a video stream rather than a still image.

Video-Specific Considerations

Video is distinguished from a single image in one obvious but important respect: it has a time axis. Frames are arranged sequentially, the frame rate is set by the temporal sampling, and redundancies between frames are exploited by modern codecs through GOP structures. To capture these dynamics in the evaluation, test material with a range of motion characteristics is required. Three sequences are therefore selected: a high-motion clip [205], a sequence with moderate movement [206], and a low-activity sample [207].

Each sequence is processed at three spatial resolutions, 320×180, 1280×720, and 1920×1080, and at frame rates of 20, 30, and 50 fps. The test matrix is composed of raw frames as well as VVC bitstreams produced with two GOP lengths (8 and 32), so that the interaction between the depth of temporal prediction and the proposed quantum transmission scheme can be observed. Qubit grouping sizes are swept over $k \in [1, 8]$, and rate-1/2 polar codes are applied where channel coding is used; these choices are matched to the protocol from Section 5.3. As is anticipated from the image experiments, the same tension between compression depth and noise tolerance is observed in the video case.

Performance Evaluation Methodology

The evaluation is conducted along two parallel tracks, each of which is designed to isolate a different aspect of the system's behaviour under channel noise:

- **Raw video tests:** Uncompressed frames are fed directly into the multi-qubit encoder, with k ranging from 1 to 8. By this arrangement, the contribution of quantum-domain compression and the role of channel coding are isolated, without any classical codec in the loop. Both uncoded and polar-coded variants are measured.

- **Pre-compressed video tests:** VVC bitstreams (GOP8 and GOP32) are used as the input, so that the interaction between the quantum layer and an already-compressed source can be observed. Again, both uncoded and channel-coded runs are performed.

Simulation Configuration

A custom numerical simulator is developed in MATLAB and Python to reproduce the complete encode–transmit–decode pipeline. The simulator implements the proposed source encoding, qubit mapping, quantum state preparation, composite quantum noise model, quantum decoding, and image reconstruction using numerical linear algebra based on the mathematical models presented in this chapter. To obtain statistically meaningful results under stochastic channel conditions, Monte Carlo averaging is employed. For every combination of source sequence and channel SNR, the complete transmission pipeline is executed 1000 times. In each simulation run, a new set of channel noise weights is independently generated from a uniform distribution ($U(0,1)$) and normalised to ensure that the total error probability satisfies the composite channel model.

The correctness of the simulator is verified by confirming that the implemented unitary operations preserve quantum-state normalisation, the simulated quantum channels satisfy the corresponding Kraus operator completeness conditions, and the obtained transmission behaviour is consistent with the theoretical properties of the proposed framework. Since this work focuses on system-level evaluation of the proposed communication framework rather than hardware-specific quantum circuit execution, a custom numerical simulator is adopted instead of quantum hardware simulators such as Qiskit Aer. This approach provides greater flexibility for evaluating large-scale multimedia transmission scenarios involving long bitstreams, multiple qubit configurations, and extensive Monte Carlo simulations.

After propagation through this composite noise channel, the reconstructed frames are scored using BER, PSNR, SSIM, and VMAF. The curves shown in the subsequent figures are obtained as averages over these 1000 trials, which accounts for their smoothness despite the underlying randomness. All simulation parameters are listed in Table 5.4.

Table 5.4: Experimental environment parameters.

Parameter	**Value / Description**
Video resolutions	320×180, 1280×720, 1920×1080
Frame rates	20 fps, 30 fps, 50 fps
Video motion types	Low-motion, Medium-motion, High-motion sequences
Input formats	Uncompressed video and VVC-encoded bitstreams
Source encoder	VVC (Versatile Video Coding)
Qubit grouping size (k)	1–8 qubits
Compression ratio	$2^k : 1$ (2:1 to 256:1)
Quantum transform	Quantum Fourier Transform (QFT)
Receiver transform	Inverse Quantum Fourier Transform (IQFT)
Channel model	Composite quantum noise channel
Noise weighting	Random weighting in noise process ($w_i \sim U(0,1)$)
SNR range	50 dB to −10 dB
SNR step size	2 dB
Monte Carlo runs	1000 runs per SNR value
Channel coding	Polar coding (rate 1/2) and no coding scenarios
Evaluation metrics	BER, PSNR, SSIM, VMAF
Simulation platform	MATLAB and Python 3

5.4.2 Results

This section presents and discusses the results from the simulation experiments. Four metrics are used to evaluate the system: BER for transmission reliability, PSNR for pixel-level reconstruction quality, SSIM for structural similarity, and VMAF for perceived visual quality. Together, these metrics give a full picture of both signal quality and visual quality. The analysis follows the method described in Section 5.4.1.

Uncompressed Video Inputs without Channel Coding

Figure 5.29 shows how the QFT-based system performs when raw video frames are sent without forward error correction. The four panels show BER, PSNR, SSIM, and VMAF against channel SNR for register sizes $F1$ to $F8$ (i.e., $k = 1, \ldots, 8$).

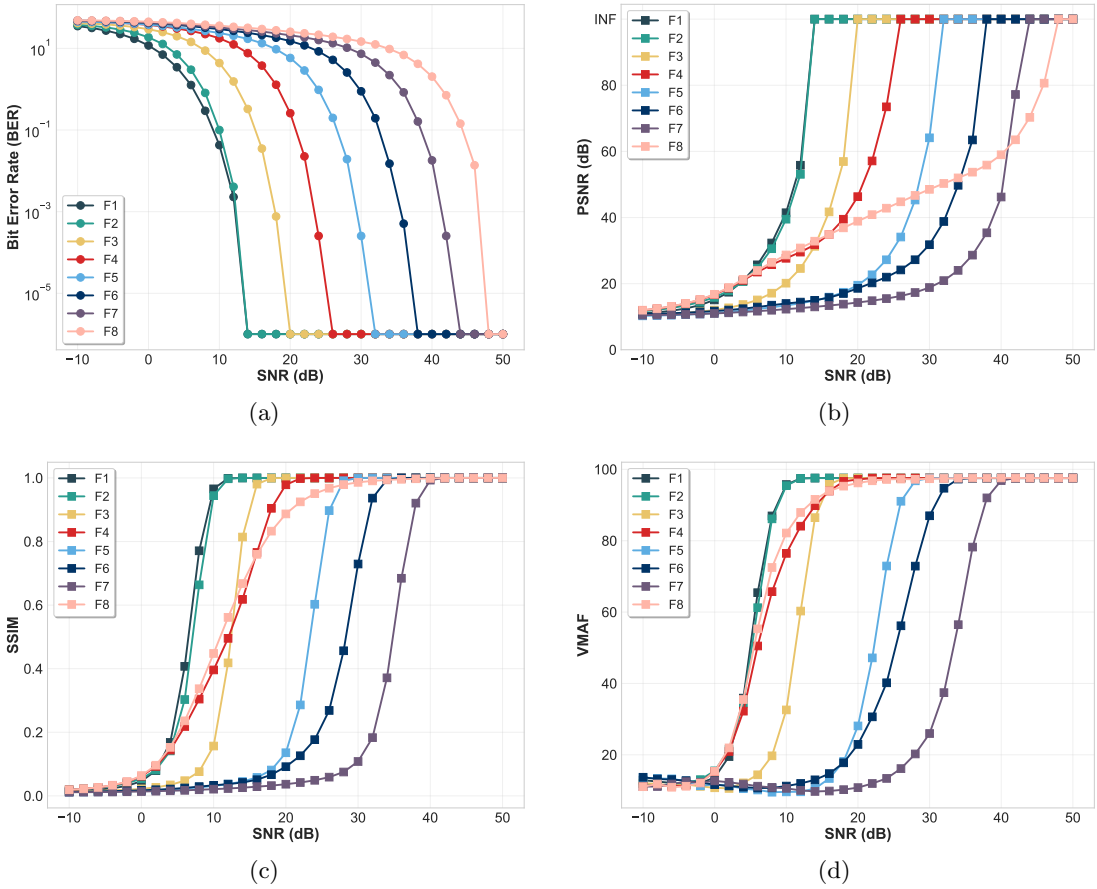


Figure 5.29: Objective quality results for raw video processed through the proposed QFT pipeline without channel coding.

The BER plot in Figure 5.29a shows a clear trade-off that depends on k. The QFT maps each k-bit block into a 2^k-dimensional frequency-domain vector. Because the transform is unitary, the receiver can rebuild the input by sending only the largest coefficient. This is how the system reaches the $2^k : 1$ compression limit.

Higher compression comes at the cost of lower noise tolerance. From Section 5.3 (Equation 5.30), the angular gap between neighbouring frequency states is $\Delta\theta = 2\pi/2^k$. A larger k packs more states into the same phase space, so even small phase shifts can

push a symbol into the wrong decision region. The $F8$ case ($k = 8$) therefore has the worst BER curve, even though it gives the highest compression of $256 : 1$. On the other hand, $F2$ has a wide $\pi/2$ gap between adjacent states, which explains why it handles phase noise well even though its compression is only $4 : 1$. The $F1$ baseline is even more robust, but it only halves the payload. Overall, these results show that the best balance is in the $F2$ to $F4$ range, where the system gives useful compression without losing too much margin against the channel.

The visual quality metrics in Figures 5.29b, 5.29c, and 5.29d follow the same order across PSNR, SSIM, and VMAF. All three metrics rise as SNR increases, which is expected because cleaner channels allow better quantum-state recovery. Low-k settings give the best results at every SNR point, which matches the wider symbol spacing discussed above. The strong result for $F2$ confirms that it is a good balanced choice.

One curve behaves in an unexpected way. The $F8$ PSNR trace does not match what its BER would suggest. The reason is structural. With $k = 8$, each pixel value is mapped directly onto one of the eight-qubit basis states, so each pixel is encoded as one of 2^8 closely spaced QFT coefficients. Phase noise corrupts these coefficients easily, but the errors mostly affect the least significant bits that carry fine phase detail. The most significant bits, which hold the main brightness information, stay mostly correct. In addition, the IQFT spreads any frequency-domain error across the reconstructed pixel basis instead of placing it at one point. Because natural video has strong spatial and temporal correlation, neighbouring pixels and frames smooth out these spread-out errors. The result is a visible image that scores fairly well on PSNR, SSIM, and VMAF even though the BER is high. In other words, reconstruction quality is partly separated from the raw error rate. The main message from Figure 5.29 is familiar: higher compression means lower robustness. When the channel quality cannot be guaranteed, register sizes in the $F2$ to $F4$ range give the best balance, keeping usable video quality while still saving a lot of bandwidth.

Uncompressed Video Inputs with Channel Coding

Adding forward error correction changes the results in important ways, as Figure 5.30 shows. Compared with the uncoded results in Figure 5.29, every curve shifts to the left.

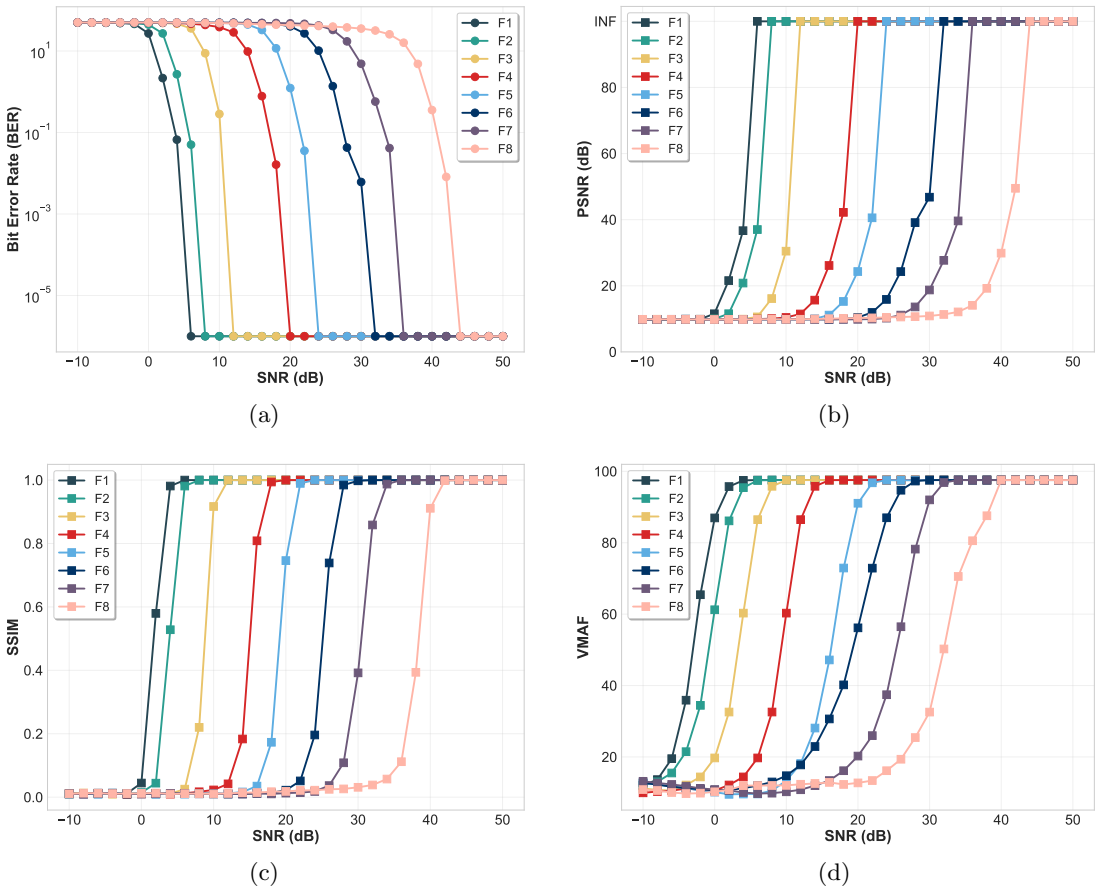


Figure 5.30: Objective quality results for raw video processed through the proposed QFT pipeline with polar channel coding.

This means the same quality is now reached at a lower SNR. This is the expected coding gain, which makes reliable decoding possible in SNR ranges where the uncoded system fails. The BER traces in Figure 5.30a make this clear. The basic trade-off between k and noise sensitivity is still there, but its effect is much smaller: BER values for all register sizes drop a lot compared to the uncoded case. Settings that did not work in moderate noise before now become usable. The biggest improvement is in the 10 to 25 dB range, where the polar decoder works near its best point. In this range, the BER curves drop sharply, marking the change from heavy errors to almost error-free recovery as SNR increases.

The PSNR results in Figure 5.30b show something more subtle. With channel coding, the $F8$ resilience effect described earlier disappears. The order of the configurations becomes regular and predictable, with $F8$ now at the bottom of the ranking instead of

doing better than expected. The reason is that forward error correction changes how quantisation errors spread during reconstruction. The added redundancy protects the bitstream, but it also breaks the spatial correlation that gave $F8$ its earlier masking effect. Without this masking, the weakness of dense constellations is exposed, and $F8$ ends up where its phase margins would predict.

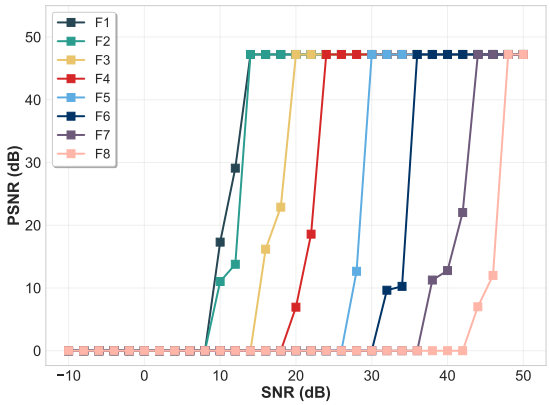
The SSIM results in Figure 5.30c tell the same story, but for structural rather than pixel-level accuracy. Coding improves structural reconstruction across all settings, with the biggest gain in the mid-SNR range where structural information is most at risk. The usual drop with higher k is still there, which confirms that forward error correction raises the overall performance but does not remove the basic compression-versus-robustness limit in the QFT framework.

VMAF, shown in Figure 5.30d, gives the closest match to human visual judgement. The result is encouraging: channel coding gives a much better viewer experience for all settings. The same order is kept. Settings $F1$ to $F3$ reach excellent scores (VMAF > 80) at moderate SNR, while higher-k settings need cleaner channels to reach the same level. VMAF clearly shows the strength of $F2$, which gives useful $4:1$ compression with consistently high perceptual scores.

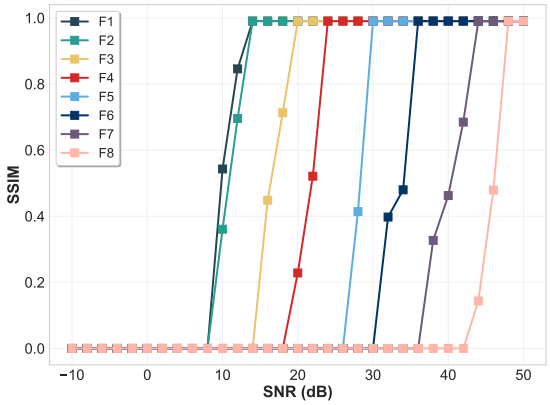
Together, the four metrics suggest clear operating recommendations. $F1$ is the best choice when channel quality is poor and reliability matters more than payload reduction, since it handles the heaviest noise while still halving the payload. $F2$ gives the best overall balance, with $4:1$ reduction and strong PSNR, SSIM, VMAF, and BER over a wide SNR range. High-k settings $F6$ to $F8$ are only useful when the channel is reliably clean; they give the highest compression but cannot deliver consistent quality under stress.

VVC Encoded Video Inputs without Channel Coding (GOP8)

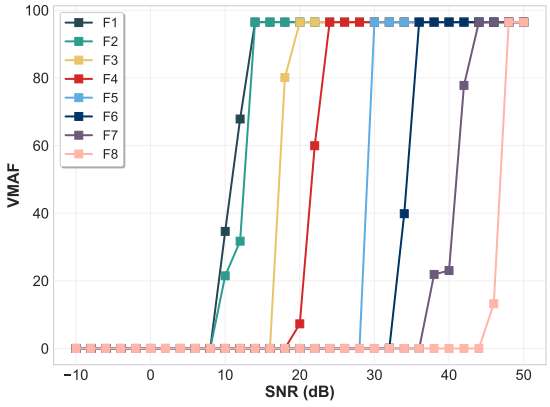
When VVC-encoded bitstreams are used instead of raw frames, the system behaves quite differently. Figure 5.31 shows the curves for GOP8 inputs without channel coding. PSNR, SSIM, and VMAF all follow the same trend: low-k settings ($F1$ to $F3$) keep good quality across the SNR axis, while high-k settings ($F6$ to $F8$) fail, especially at low and mid SNR. The PSNR plot in Figure 5.31a shows clearly that pre-compressed



(a)



(b)



(c)

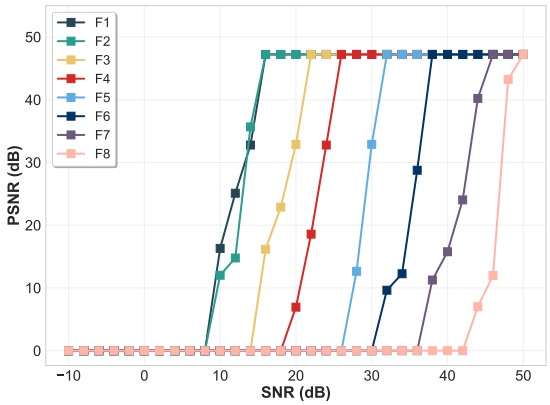
Figure 5.31: Quality metrics for VVC-encoded input video (GOP8) transmitted through the proposed QFT pipeline without channel coding.

bitstreams are less tolerant of channel errors than raw frames.

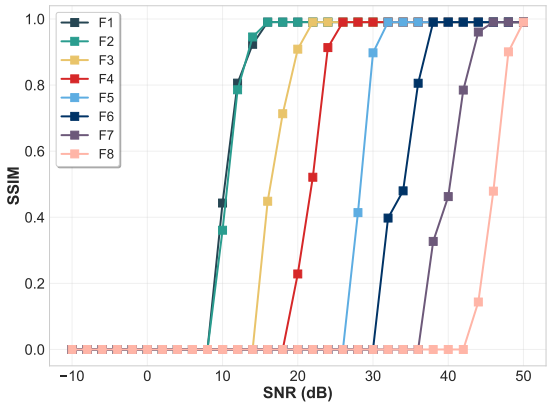
The SSIM and VMAF panels (Figures 5.31b and 5.31c) support this finding, each in its own way. Low-k SSIM values stay safely above 0.8 for SNR $>$ 10 dB, which shows that structural information is kept during transmission. The high-k settings, however, lose even basic structural agreement; $F8$ in particular stays at low quality across most of the SNR range. VMAF separates the settings most clearly: $F1$ reaches strong perceptual scores (VMAF $>$ 80) across almost the full SNR axis, while $F8$ cannot get past a VMAF of about 40 until SNR reaches around 40 dB, which is rarely available in practice.

The reason is simple. A VVC bitstream is already a highly compressed form in which most redundancy has been removed. Adding a second compression stage on top leaves very little room for error correction at either layer. When the quantum layer also uses a dense constellation (high k), VVC stream errors combine with phase-noise errors in the quantum domain. The result is compound distortion that quickly damages every quality metric. For pre-compressed sources, the quantum layer must stay conservative ($F1$ or $F2$) to keep structural integrity. Although high-k configurations provide substantial theoretical bandwidth savings, these gains are effectively offset in practice by the associated degradation in visual quality.

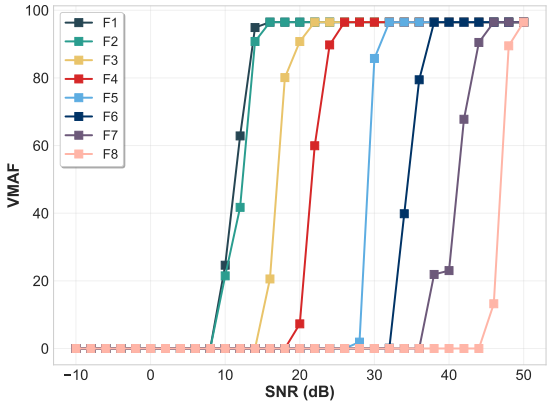
When the GOP length is increased to 32 (Figure 5.32), the effect of temporal dependency on transmitted video becomes very clear. For all eight register sizes, the PSNR, SSIM, and VMAF results drop compared to GOP8. The cause is structural, not statistical. A longer GOP uses fewer intra-coded keyframes and more inter-coded predicted frames, so the decoder relies more heavily on temporal references. When transmission damages a keyframe, the error does not stay in one place: it spreads through every frame that depends on it, building up until the next keyframe arrives. This effect shows even in the usually robust $F1$ and $F2$ settings, which now show measurable quality drops compared to GOP8. The design implication is clear. Long-GOP transmission needs either keyframe-aware unequal protection (for example, stronger coding on anchor frames) or quantum-side mappings designed to limit error spread. Without such measures, GOP32 trades robustness for compression efficiency in a way that may not be acceptable in noisy channels.



(a)



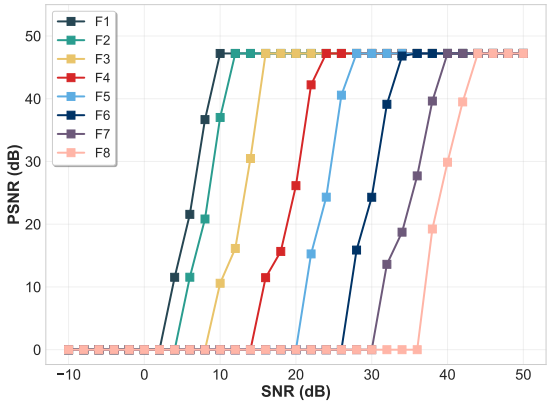
(b)



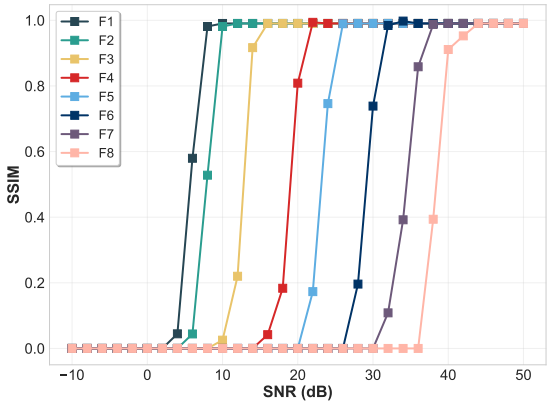
(c)

Figure 5.32: Quality metrics for VVC-encoded input video (GOP32) transmitted through the proposed QFT pipeline without channel coding.

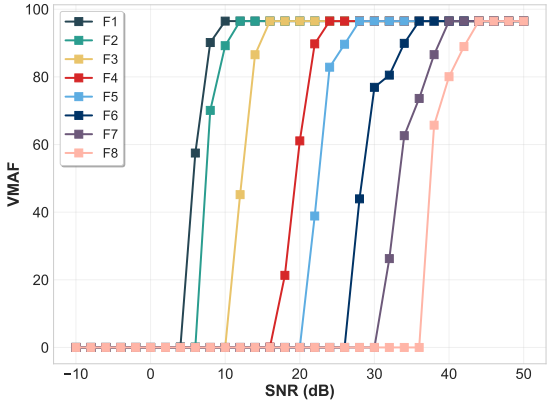
VVC Encoded Video Inputs with Channel Coding



(a)



(b)



(c)

Figure 5.33: Quality metrics for VVC-encoded input video (GOP8) processed by the QFT pipeline with polar channel coding.

Adding polar coding to the GOP8 VVC case (Figure 5.33) recovers much of what was lost in the uncoded case. PSNR, SSIM, and VMAF all improve a lot compared to

Figure 5.31, and the system now gives acceptable output in mid-SNR regions where the uncoded pipeline already failed. Forward error correction breaks the error-spread chain that temporal prediction in VVC creates. The relative order of settings does not change, but the overall floor rises for all of them. Low-k settings ($F1$ to $F3$) reach excellent reconstruction quality, with $F1$ and $F2$ keeping PSNR above 25 dB, SSIM above 0.8, and VMAF above 80 across almost the full SNR axis. Mid-k settings ($F4$ to $F6$), which were marginal in the uncoded case, now become usable when SNR is reasonable. The high-end $F7$ and $F8$ settings remain limited; their phase margins are simply too narrow for coding alone to save. Overall, the combination of VVC, QFT-based quantum compression, and polar coding gives a workable transmission scheme for real networks. The two-qubit setting ($F2$) again stands out as the best overall, giving 4 : 1 reduction with consistently high quality on every metric. This balance between bandwidth efficiency and reliability makes it well suited for capacity-limited deployments.

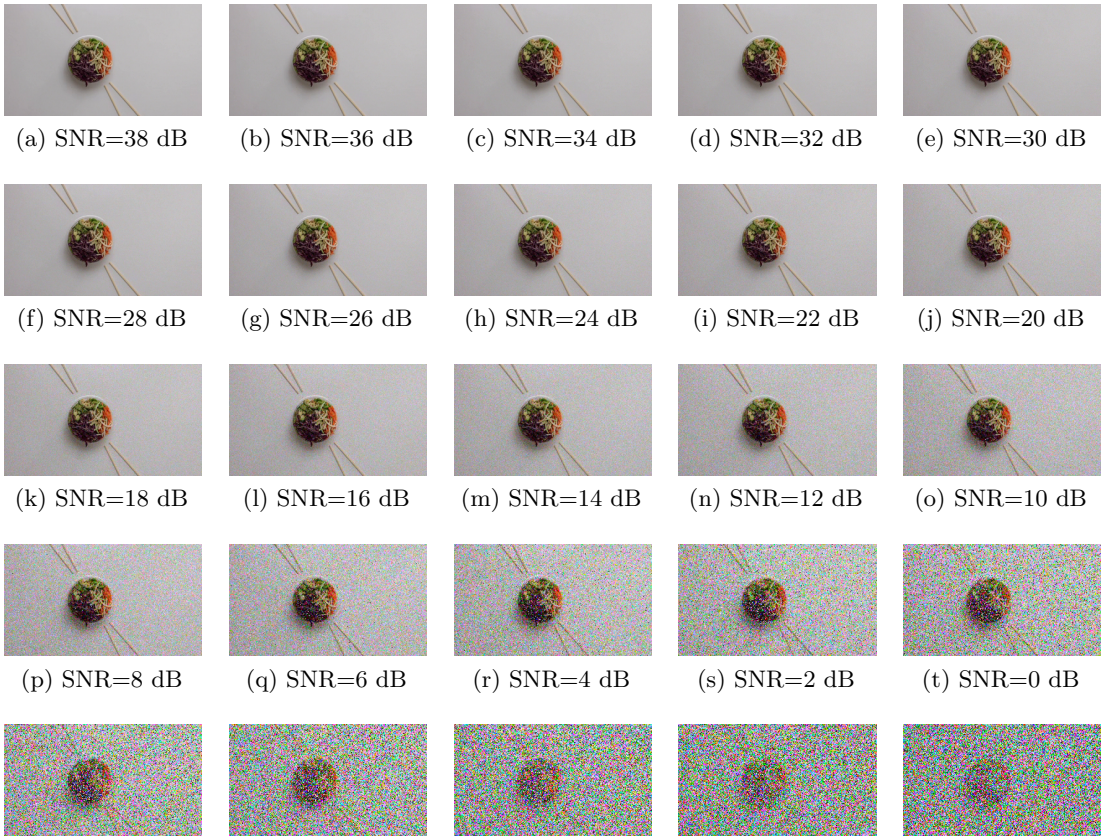
Effect of Resolution and Frame Rate

Table 5.5: Maximum SNR gain (dB) achieved by each qubit configuration relative to the 8-qubit baseline, across resolutions and frame rates.

Resolution	**Frame Rate**	**Maximum Channel SNR Gains**						
		1 (2:1)	2 (4:1)	3 (8:1)	4 (16:1)	5 (32:1)	6 (64:1)	7 (128:1)
320×180	20 fps	38	36	32	24	20	12	8
320×180	30 fps	38	36	32	24	20	12	8
320×180	50 fps	38	36	32	24	20	12	8
1280×720	20 fps	38	36	32	24	20	12	8
1280×720	30 fps	38	36	32	24	20	12	8
1280×720	50 fps	38	36	32	24	20	12	8
1920×1080	20 fps	38	36	32	24	20	12	8
1920×1080	30 fps	38	36	32	24	20	12	8
1920×1080	50 fps	38	36	32	24	20	12	8

Table 5.5 shows the maximum SNR improvement that each setting gives over the $F8$ baseline, across every resolution and frame rate in the test set. Two points stand out. First, the values are the same across rows: neither resolution nor frame rate has any measurable effect on the gain values. Second, only k controls those gains. This shows that the performance of the proposed pipeline depends on the quantum encoding

itself, not on the visual properties of the source. From a deployment point of view, this is helpful, because the system can be characterised once and the same SNR–quality relationship applies to a wide range of content.



(a) SNR=38 dB (b) SNR=36 dB (c) SNR=34 dB (d) SNR=32 dB (e) SNR=30 dB

(f) SNR=28 dB (g) SNR=26 dB (h) SNR=24 dB (i) SNR=22 dB (j) SNR=20 dB

(k) SNR=18 dB (l) SNR=16 dB (m) SNR=14 dB (n) SNR=12 dB (o) SNR=10 dB

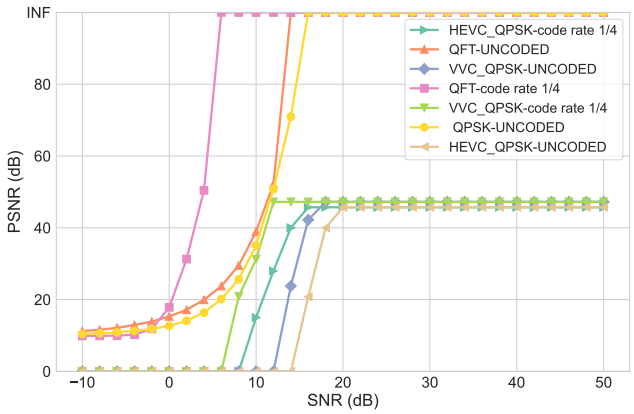
(p) SNR=8 dB (q) SNR=6 dB (r) SNR=4 dB (s) SNR=2 dB (t) SNR=0 dB

(u) SNR=-2 dB (v) SNR=-4 dB (w) SNR=-6 dB (x) SNR=-8 dB (y) SNR=-10 dB

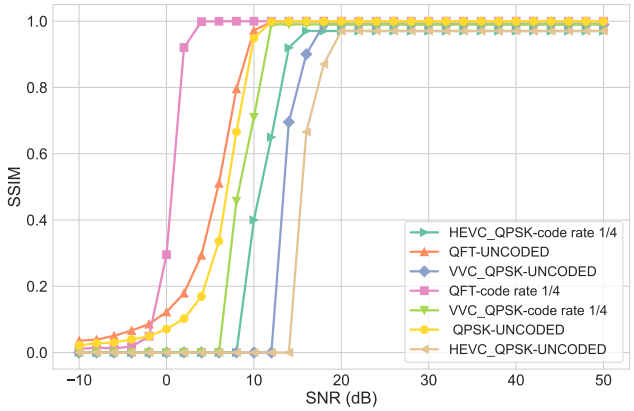
Figure 5.34: Reconstructed video frames at SNR values from 38 dB down to -10 dB using the 8-qubit configuration ($F8$) at $256:1$ compression on raw input.

Figure 5.34 gives a visual view of how reconstruction quality drops as the channel gets worse. The sample frames go from 38 dB down to -10 dB and are labelled alphabetically for easy reference. To make the test as hard as possible, the $F8$ setting is used, which compresses raw input at $256:1$. At high SNR, the reconstructed frames keep fine visual detail, which confirms that the essential information is recovered correctly. As SNR drops, the usual signs of channel damage appear: artefacts, blocking effects, and colour distortion all become stronger, showing the growing disturbance of the transmitted quantum states.

Comparison with Classical Communication Systems



(a) PSNR



(b) SSIM

Figure 5.35: Performance comparison between the proposed two-qubit configuration and classical communication baselines.

To put the results in a wider context, Figure 5.35 compares the two-qubit setting with several well-known classical references. QPSK is used as the modulation baseline at matched bandwidth, while VVC and HEVC are taken as the current state of the art in classical compression. All schemes use the same bitrate budget, so the comparison reflects bandwidth efficiency on equal terms.

The QFT-based scheme sends video by mapping frame-level data into quantum states, which gives a compact spatial representation. Even without forward error correction, its performance is similar to uncompressed QPSK, but it provides an additional $4:1$ compression benefit due to the structure of the underlying quantum states. Adding

polar coding at rate 1/4 moves the quantum scheme well ahead in noise robustness, with PSNR gains of about 10 dB over uncompressed QPSK at matched bit rates, as Figure 5.35a shows.

An important difference is the shape of the degradation curve. HEVC and VVC use strong inter-frame prediction, which makes them sensitive to channel errors: a single bit-error can affect every following frame in a GOP until the next keyframe. The collapse at low SNR is therefore sudden and severe. The QFT-based scheme, in contrast, works on independent frequency-domain representations, so disturbances stay local. Its degradation is gradual instead of catastrophic, which explains the behaviour shown in the PSNR plot of Figure 5.35a and in the SSIM plot of Figure 5.35b: the proposed scheme keeps structural information far longer than classical alternatives.

Classical codecs are of course unbeatable in clean, error-free channels, where decades of work have given them excellent rate-distortion behaviour. But for channels that are bandwidth-limited and prone to errors, the proposed quantum scheme offers a useful complementary set of properties: gradual degradation under stress and mathematically lossless reconstruction in the noise-free limit. The lossless property comes from the fact that the QFT and IQFT operations are unitary.

Advantages and Practical Implications

The proposed framework can be summarised as *symbol-level compression carried out inside the quantum domain.* The reduction happens at the encoding stage, where only a chosen subset of QFT coefficients is sent. It is important to note that this compression applies only to the transmission path; the source file itself is not reduced, because decoding still needs the full uncompressed state vector. This approach is therefore best understood as a bandwidth-saving method for the active channel rather than a storage compression method, which separates it clearly from classical codecs. Because the forward and inverse transforms are unitary, ideal reconstruction is possible in noise-free conditions. In real channels, the system instead shows a controllable trade-off between compression depth and quality, set by the choice of k. For deployment, three ranges are useful: $k = 1, 2$ for safety-critical low-SNR transmission, $k = 3$ to 5 for normal multimedia delivery, and $k = 6$ to 8 for cases where saving bandwidth matters more

than quality.

Effective Channel Capacity and QFT Compression Trade-offs

In the proposed scheme, each k-bit input block is encoded into one of 2^k computational basis states, transformed using the QFT, and sent across the channel as a single representative phase coefficient. A single channel use therefore corresponds to one such transmission per encoded block. The effect on throughput is direct: increasing k reduces the number of channel uses needed to send a given video bitstream by the same factor.

The starting point for the analysis is the standard Shannon–Hartley expression in (5.31).

$$C_{\text{raw}} = B \log_2(1 + \text{SNR}) \tag{5.31}$$

Here B is the channel bandwidth (Hz) and SNR is the linear SNR. Using the dB form $\text{SNR} = 10^{\text{SNR}_{\text{dB}}/10}$ gives (5.32).

$$C_{\text{raw}} = B \log_2\Big(1 + 10^{\text{SNR}_{\text{dB}}/10}\Big) \tag{5.32}$$

Under the proposed compression scheme, only one frequency coefficient per k-qubit block is actually sent, so the achievable capacity is reduced by a factor of 2^k, giving (5.33).

$$C_{\text{eff}}(k) = \frac{C_{\text{raw}}}{2^k} = \frac{B \log_2(1 + \text{SNR})}{2^k} \tag{5.33}$$

This expression captures the main trade-off: while k gives exponential gains in compression, it reduces the effective bit throughput per second of channel time by the same factor.

A numerical example helps make this clear. Let $B = 1$ Hz and SNR = 10 dB. From Equation (5.32), $C_{\text{raw}} = \log_2(1 + 10) \approx 3.46$ bits/s. Sweeping k from 1 to 8 raises the compression ratio from 2:1 to 256:1, while $C_{\text{eff}}(k)$ drops from 1.73 bits/s to just 0.013 bits/s, as shown in Table 5.6. In the context of the proposed framework, this reduction is not a problem; the small remaining capacity is used to carry highly concentrated, error-protected quantum states, which reduces hardware load and limits exposure to noise while keeping high reconstruction quality per active qubit.

Table 5.6: Effective channel capacity for QFT-based compression at SNR = 10 dB and $B = 1$ Hz.

Qubit Size (k)	**Compression Ratio (2^k:1)**	$C_{\text{eff}}(k)$ **(bits/s/Hz)**
1	2:1	1.73
2	4:1	0.87
3	8:1	0.43
4	16:1	0.22
5	32:1	0.11
6	64:1	0.054
7	128:1	0.027
8	256:1	0.013

Computational Complexity and System Scalability

A useful practical feature of the proposed QFT-based scheme is its low computational cost. For a k-qubit block, the gate count scales as $\mathcal{O}(k^2)$, using only Hadamard and controlled-phase rotations. Both are standard operations on current quantum processors. Circuit depth, which controls latency, can be as low as $\mathcal{O}(k)$ when gates are run in parallel on separate qubits. In practice, hardware limits (such as nearest-neighbour connectivity) usually require extra SWAP operations, which push the actual depth back towards $\mathcal{O}(k^2)$. Using widely supported phase and Hadamard implementations, and optionally combining them with approximate QFT variants that drop very small rotation angles, keeps both gate count and circuit depth within practical limits without any measurable loss of fidelity.

Scalability with increasing k is good in principle. Larger registers pack more information into each transmitted quantum state, which increases payload efficiency. The cost is a denser arrangement of phase states, which narrows noise margins and makes each qubit more sensitive to channel imperfections. The choice of k is therefore an engineering decision that balances compression efficiency against the channel conditions in which the system will operate.

Furthermore, the proposed framework follows a hybrid quantum-classical architecture in which computationally intensive multimedia processing tasks, including source coding and optional channel coding, are performed in the classical domain, while the QFT-based encoding, quantum transmission, and inverse QFT decoding are performed in the quantum domain. This partitioning exploits the respective strengths of classical

and quantum processing, enabling efficient multimedia compression while leveraging quantum-state representations for communication. Such hybrid architectures are considered a practical approach for near-term quantum communication systems, where classical processing complements the current limitations of quantum hardware.

Hardware Feasibility and Resource Requirements

The proposed architecture is designed to match what near-term quantum hardware can support. On the encoding side, the operations needed are standard basis-state preparation (initialisation to $|0\rangle$ and application of Pauli-X where needed), QFT execution using Hadamard and controlled-phase operations with a total of $G(k) = k + k(k-1)/2$ gates, channel transmission, IQFT at the receiver, and computational-basis measurement. For the range $k = 1$ to $k = 8$ used in this study, the qubit counts and gate budgets listed in Table 5.7 are well within the capabilities of current NISQ devices and of experimental quantum communication setups reported in the literature.

Table 5.7: Estimated hardware resource requirements for different QFT register sizes.

Qubits (k)	**Register Size (Qubits)**	**Hadamard Gates** $H = k$	**Phase Gates** $\frac{k(k-1)}{2}$	**Total Gates** $k + \frac{k(k-1)}{2}$
1	1	1	0	1
2	2	2	1	3
3	3	3	3	6
4	4	4	6	10
5	5	5	10	15
6	6	6	15	21
7	7	7	21	28
8	8	8	28	36

5.4.3 Section Summary

This section examined the proposed QFT-based scheme for joint compression and transmission of video over noisy quantum channels. The results showed that the qubit grouping parameter k controls a clear trade-off between payload reduction and tolerance to channel noise. Larger registers gave higher symbol-level compression (up to 256:1 at $k = 8$) but at the cost of narrower phase separations between adjacent states. This made the encoded symbols more easily disturbed by noise and led to faster quality loss under

poor channel conditions. Smaller registers gave better quality protection in exchange for more modest compression. Under an ideal noise-free channel, the scheme was lossless for any value of k, because the QFT and IQFT are unitary. In real deployments, however, keeping both high compression and acceptable visual quality at large k was difficult. These limits gave direct motivation for the semantic restoration framework developed in Section 5.5, which keeps perceptual fidelity and structural detail while still benefiting from the high compression that larger QFT registers give.

5.5 Semantic-Aware Quantum Frequency-Domain Image Transmission with Channel-Aware Denoising

Publication Notice

The research presented in this section has been submitted as the following manuscript and is currently under review:

U. Jayasinghe, V. Gowrisetty, and A. Fernando, "Semantic-aware quantum frequency-domain image transmission with channel-aware denoising," submitted to *IEEE Transactions on Communications*.

Portions of this chapter are based on the above submitted manuscript. The material has been revised and expanded with additional explanations, analysis, and discussion for inclusion in this doctoral thesis.

Problem Statement: Sections 5.3 and 5.4 demonstrated that QFT-based quantum frequency-domain communication can achieve substantial compression efficiency for image and video transmission by reducing transmission redundancy at the symbol level. However, increasing the compression ratio through larger multi-qubit configurations also increases sensitivity to channel noise due to the reduced angular separation between frequency-domain components. Consequently, under low-SNR conditions and high compression ratios, the reconstructed outputs suffer from both compression artefacts and quantum channel distortions, leading to degradation in structural quality and semantic consistency. Conventional reconstruction and filtering methods are unable to effectively recover semantically important content once it has been corrupted or lost

during transmission.

Limitations of Existing Work: Existing quantum communication systems, including the QFT-based frameworks proposed earlier in this chapter, mainly focus on reliable transmission and reconstruction quality without incorporating semantic-aware restoration mechanisms. Furthermore, current quantum communication methods are predominantly based on time-domain operations, which do not inherently support compression and remain highly sensitive to noise. Although QFT-based frequency-domain transmission enables structured redundancy reduction and symbol-level compression, existing QFT approaches focus primarily on signal representation and transmission rather than semantic preservation and perceptual reconstruction. To the best of the author's knowledge, no prior work has integrated quantum compression, channel-noise compensation, and image restoration with semantic fidelity within a unified quantum communication framework, nor investigated the interaction between quantum frequency-domain compression, quantum channel noise, and learned semantic reconstruction.

Motivation and Proposed Contribution: To address these limitations, this section proposes a semantic-aware QFT-based quantum image communication framework that jointly integrates compression, transmission, and semantic reconstruction within the quantum frequency domain. Building upon the QFT-based compression-and-transmission framework developed in Section 5.3, the proposed system introduces a denoising diffusion probabilistic model (DDPM)-based reconstruction network designed to recover structural, contextual, and perceptual information degraded by both QFT compression and quantum channel noise. In the proposed framework, input images are converted into binary bitstreams, optionally protected using polar coding, and mapped into multi-qubit quantum states with qubit encoding sizes ranging from 1 to 8. The QFT is then applied to transform the encoded states into the quantum frequency domain, where only selected frequency-domain coefficients are retained to achieve symbol-level compression while preserving semantically important information. After transmission through the noisy quantum channel, IQFT and quantum measurement reconstruct the classical bitstreams, followed by DDPM-based semantic restoration to enhance fine details and contextual consistency. The proposed framework establishes a unified

quantum semantic communication pipeline that simultaneously addresses compression efficiency, transmission robustness, and semantic fidelity. Experimental results demonstrate that the DDPM-assisted framework achieves higher reconstruction performance under low-SNR conditions while operating with significantly reduced effective channel capacity. Furthermore, the results reveal a robustness–compression trade-off in QFT-based transmission, motivating the proposed hybrid semantic-aware reconstruction strategy for maintaining image quality at high compression ratios. It is important to distinguish the respective contributions of the QFT-based communication framework and the DDPM-based semantic restoration network. The QFT is responsible for the transmission-related improvements by providing frequency-domain quantum encoding, symbol-level compression, and robustness against channel impairments, as demonstrated in Section 5.3. Operating in the frequency domain enables the multimedia information to be represented in terms of spectral components rather than individual pixel values, allowing the proposed framework to exploit the energy compaction properties of transform-domain representations. This facilitates more efficient compression, reduces transmission redundancy, and enables transmission errors to be distributed across the reconstructed signal rather than remaining localised, thereby improving overall reconstruction quality under noisy channel conditions. In contrast, the DDPM operates solely as a receiver-side post-processing module that restores residual channel distortions and compression artefacts after QFT-based reconstruction without modifying the transmission process or compression strategy. Consequently, the improvements reported in this section represent the additional reconstruction gains achieved by the semantic restoration network beyond the underlying QFT-based communication framework.

5.5.1 System Model

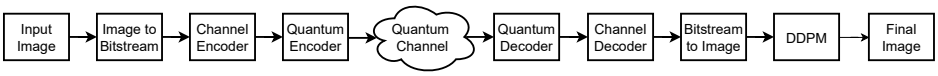


Figure 5.36: Proposed framework for quantum Fourier transform-based image compression, transmission, and semantic-aware image reconstruction.

The proposed system, illustrated in Figure 5.36, adopts a semantic-aware hybrid framework that integrates quantum and classical processing to enable efficient and

resilient image transmission. Rather than emphasising pixel-level accuracy, the approach prioritises the preservation of semantic content, ensuring that the reconstructed images retain their essential meaning and contextual information even when subjected to noise and distortions during transmission. The processing pipeline up to image reconstruction remains identical and consistent with the framework presented in Section 5.3. Input images are converted into binary bitstreams, optionally protected using rate-1/2 polar codes, and segmented according to the selected multi-qubit encoding size k (up to 8 qubits). These segments are mapped into quantum states of dimension 2^k and processed using the QFT, which acts as a semantic transformer by projecting the data into the frequency domain. A reduced set of QFT coefficients is then encoded into a valid artificial quantum state of dimension 2^k for transmission, thereby achieving compression while preserving essential structural and contextual information. At the receiver, the qubit encoding size is conveyed as minimal side information to enable decoder synchronisation and reconstruction of the frequency-domain quantum state. After applying the IQFT and quantum measurement, a semantically meaningful image bitstream is obtained, followed by optional channel decoding and standard image reconstruction. To further enhance perceptual quality, a quantum-noise-customised DDPM is developed. The DDPM acts as a semantic restorer, refining textures and recovering structural details that may have been degraded during transmission. Additionally, an adaptive denoising network is proposed under the assumption of perfect CSI. In practical communication systems, however, CSI is typically estimated using pilot-based feedback mechanisms, which may introduce estimation errors, additional overhead, and latency. The assumption of perfect CSI is therefore adopted to isolate and evaluate the effectiveness of the proposed semantic-aware reconstruction framework under ideal channel estimation conditions. This assumption is sufficient for analysing the network's performance and establishing an upper-bound benchmark.

The evaluation is conducted on MNIST [220] (70,000 images at 28×28), CIFAR-10 [221] (60,000 images at 32×32), COCO [197] (80,000 images resized to 256×192), and ImageNet [218] (approximately 80,000 images resized to 450×450). An 80%/20% training–testing split is applied, enabling comprehensive evaluation across varying image complexity and semantic richness.

It is important to note that within the quantum communication process, any image can be accommodated as input regardless of its resolution, since the QFT-based encoding operates directly on the bitstream representation rather than fixed pixel dimensions. In contrast, the training stage of the proposed denoising network requires standardised input sizes to ensure stable learning and computational efficiency, depending on the training environment.

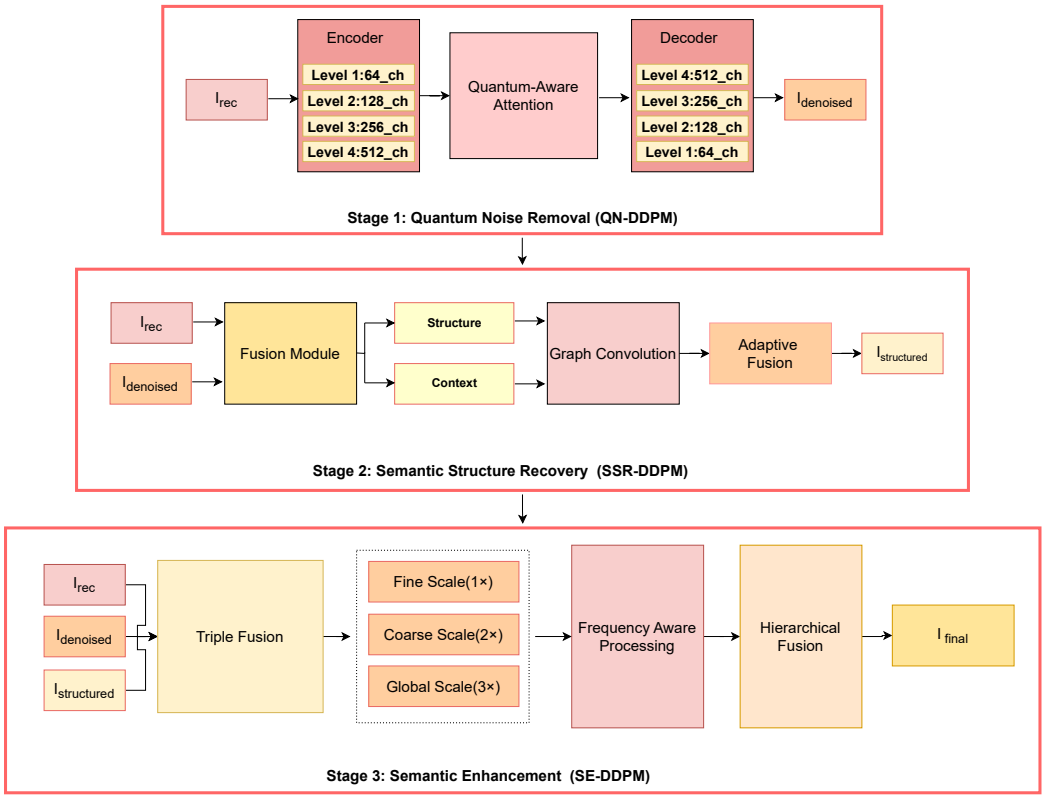


Figure 5.37: Multi-stage denoising diffusion probabilistic model (DDPM) architecture for quantum image reconstruction.

The following subsections provide a detailed description of each functional component of the proposed DDPM module depicted in Figure 5.37. To enhance the semantic fidelity and visual quality of the QFT-reconstructed images (I_{rec}) under high-noise conditions, this learning-based reconstruction method is employed using a three-stage progressive diffusion framework, as illustrated in Figure 5.37. Each stage iteratively refines the noisy reconstructed outputs to mitigate quantum-induced degradations and recover semantically meaningful image details.

Stage 1: Quantum Noise Removal DDPM (QN-DDPM)

The first stage focuses on mitigating quantum noise using a modified U-Net diffusion architecture with quantum-aware attention mechanisms. The reconstructed image obtained after the quantum communication process, denoted as I_{rec}, is first passed through the attention module and then processed by a four-level encoder-decoder hierarchy with channel dimensions $64 \to 128 \to 256 \to 512$. The key technical innovation is the quantum-aware attention mechanism, which explicitly captures correlation patterns induced by quantum noise, as formulated in (5.34).

$$\text{QAttention}(X) = \text{Softmax}\left(\frac{QK^T}{\sqrt{d_k}} + M_{\text{quantum}}\right)V \tag{5.34}$$

Here, $Q \in \mathbb{R}^{n\times d_k}$, $K \in \mathbb{R}^{n\times d_k}$, and $V \in \mathbb{R}^{n\times d_v}$ represent the query, key, and value matrices, respectively, with d_k denoting the dimensionality of the key vectors. The additional bias term $M_{\text{quantum}} \in \mathbb{R}^{n\times n}$ embeds structured noise correlations arising from quantum processes.

The structure of M_{quantum} is defined as in (5.35).

$$M_{\text{quantum}}[i,j] = \alpha \exp\big(-\beta \|f_i - f_j\|_2^2\big)\, \xi(i,j) \tag{5.35}$$

Here, $M_{\text{quantum}}[i,j]$ denotes the (i,j)-th entry of the quantum similarity matrix, α is a normalisation constant controlling the overall scale, β is a sharpness parameter that regulates sensitivity to feature distance, f_i and f_j are the feature vectors corresponding to the i-th and j-th quantum-encoded components, $\|f_i - f_j\|_2^2$ represents the squared Euclidean distance between the two feature vectors, and $\xi(i,j)$ is a weighting function that incorporates prior structural or correlation constraints. The matrix M_{quantum} encodes correlations induced by quantum decoherence, since pixels originating from the same QFT block and frequency coefficient undergo correlated phase and amplitude perturbations; this allows the diffusion model to denoise coherently across spatial locations that share a common quantum-frequency origin rather than treating them as independent pixels.

Unlike standard U-Net architectures, our quantum noise removal network integrates a dual-pooling attention mechanism that combines global average pooling (GAP) and

global max pooling (GMP). This design enables the model to effectively capture both gradual amplitude decay and abrupt noise-induced intensity variations, which are characteristic of quantum decoherence. The resulting denoised image output from this stage is represented as I_{denoised}.

Stage 2: Semantic Structure Recovery DDPM (SSR-DDPM)

The second stage employs a dual-pathway diffusion model that reconstructs semantic relationships distorted by frequency-domain compression and transmission. This stage jointly leverages the denoised output from stage 1 (I_{denoised}) and the I_{rec} to enhance semantic consistency. The recovered structural image is defined in (5.36).

$$I_{\text{structured}} = \mathcal{F}_{\text{fusion}}(\mathcal{P}_{\text{struct}}(I_{\text{denoised}}),\ \mathcal{P}_{\text{context}}(I_{\text{rec}})) \tag{5.36}$$

Here, $\mathcal{F}_{\text{fusion}}(\cdot)$ denotes the fusion operator that jointly leverages structural and contextual representations. The structural pathway, $\mathcal{P}_{\text{struct}}(\cdot)$, is designed to recover fine details by employing a U-Net backbone enriched with graph convolutional layers, enabling explicit modelling of local semantic relationships, as formulated in (5.37), where $\text{UNet}_{\text{struct}}(\cdot)$ provides multi-scale feature extraction and GraphConv$(\cdot)$ models spatial dependencies using graph-based message passing.

$$\mathcal{P}_{\text{struct}}(x) = \text{GraphConv}(\text{UNet}_{\text{struct}}(x)) \tag{5.37}$$

The second pathway, $\mathcal{P}_{\text{context}}(\cdot)$, focuses on contextual coherence by integrating self-attention with U-Net features, as expressed in (5.38), where $\text{UNet}_{\text{context}}(\cdot)$ extracts hierarchical representations and SelfAttention$(\cdot)$ captures global dependencies across spatial positions.

$$\mathcal{P}_{\text{context}}(x) = \text{SelfAttention}(\text{UNet}_{\text{context}}(x)) \tag{5.38}$$

The semantic structure recovery mechanism jointly reinforces fine-grained details and global contextual coherence through the combined operations defined in (5.36)–(5.38). Spatial semantic dependencies are explicitly modelled using a graph convolutional layer with an adaptive adjacency matrix A_{ij}, as specified in (5.39), where $\phi(\cdot)$ is a feature

embedding function, $\mathrm{sim}(\cdot,\cdot)$ denotes a similarity measure (e.g., cosine similarity), and τ is a temperature scaling parameter.

$$A_{ij} = \mathrm{Softmax}\left(\frac{\mathrm{sim}(\phi(x_i), \phi(x_j))}{\tau}\right) \tag{5.39}$$

By jointly exploiting complementary structural and contextual cues, the dual-pathway architecture compensates for spatial semantic distortions introduced by quantum frequency-domain compression and transmission that cannot be resolved by single-stream models. The output of this stage is denoted as $I_{\text{structured}}$.

Stage 3: Semantic Enhancement DDPM (SE-DDPM)

The final stage refines semantic content by hierarchically integrating complementary representations produced by earlier stages within a multi-scale diffusion framework. The resulting fused reconstruction is defined in (5.40), where $\mathcal{C}(\cdot)$ denotes channel-wise concatenation, $\mathcal{T}_s(\cdot)$ represents the transformation at scale s, and w_s is the scale-specific weight learned during training.

$$I_{\text{final}} = \sum_{s=1}^{S} w_s \cdot \mathcal{T}_s\left(\mathcal{C}(I_{\text{structure}}, I_{\text{denoised}}, I_{\text{rec}})\right) \tag{5.40}$$

Feature refinement is achieved through a frequency-aware enhancement module that jointly exploits spatial and spectral representations. The spatial-domain processing is described in (5.41), while the corresponding frequency-domain operation is defined in (5.42).

$$F_{\text{spatial}} = \mathrm{SpatialAttention}(x) \tag{5.41}$$

$$F_{\text{freq}} = \mathrm{IFFT}(\mathrm{FreqMask} \odot \mathrm{FFT}(x)) \tag{5.42}$$

Here, x denotes the input feature map, F_{spatial} represents the spatially enhanced features, F_{freq} represents the frequency-enhanced features, $\mathrm{SpatialAttention}(\cdot)$ denotes the spatial attention operator, $\mathrm{FFT}(\cdot)$ and $\mathrm{IFFT}(\cdot)$ denote the fast Fourier and inverse fast Fourier transforms, respectively, $\odot$ indicates element-wise multiplication, and

FreqMask is a learnable frequency-domain mask.

At each scale s, the outputs of the spatial and frequency pathways are fused using a convex combination, as formulated in (5.43).

$$\text{FreqEnhance}(x) = \lambda F_{\text{spatial}} + (1 - \lambda) F_{\text{freq}} \tag{5.43}$$

The coefficient $\lambda \in [0, 1]$ controls the balance between the two domains, producing the enhanced representation FreqEnhance(x). By operating on multiple scales, the framework effectively addresses both local distortions and global semantic degradation, with learnt scale-dependent weights (w_s) dynamically prioritising the features that carry the most semantic relevance.

Overall, the framework employs a hierarchical U-Net operating at three resolution levels, fine (1×), coarse (2×), and global (4×). Frequency-aware modules incorporate learnable spectral masks in the FFT domain to emphasise perceptually significant components. The multi-scale outputs are then fused using learned importance weights to generate the final semantically enhanced image. The resulting denoised output image from this stage is represented as I_{final}.

Progressive Training Strategy

Due to the high sensitivity of quantum-distorted images and the complex dependencies introduced by QFT-based processing, a progressive training strategy is employed in which each stage is trained independently prior to joint integration. This staged optimisation approach improves training stability by reducing gradient instabilities that commonly occur in end-to-end learning on quantum-reconstructed data.

Phase 1 (30 epochs): The QN-DDPM module is optimised for noise reduction using a loss function dominated by L_1 and L_2 terms to enforce pixel-level accuracy, as defined in (5.44). Training is conducted for 30 epochs, which offers a practical balance between convergence stability and computational efficiency without introducing overfitting.

Phase 2 (25 epochs): The SSR-DDPM module is then trained to recover structural information, with the optimisation objective placing greater emphasis on SSIM to main-

tain perceptual and contextual consistency. Training for 25 epochs provides adequate capacity to learn structural relationships while limiting overfitting and supporting robust generalisation.

Phase 3 (20 epochs): In the final stage, the SE-DDPM module is trained to enhance semantic content, with perceptual loss playing the primary role in optimising high-level semantic consistency. The training is restricted to 20 epochs to achieve effective refinement while avoiding over-adaptation, thereby maintaining generalisation across diverse image scenarios.

Quantum-Adapted Loss Function: The overall optimisation objective integrates multiple complementary loss functions to balance pixel-level accuracy, structural fidelity, and perceptual quality. The total loss (L_{total}) is formulated as in (5.44). The loss function is designed to account for quantum-specific distortions introduced by QFT-based compression and transmission, while the weighting coefficients are fixed throughout the training process.

$$L_{\text{total}} = 0.4 \cdot L_{L1} + 0.2 \cdot L_{L2} + 0.3 \cdot L_{\text{SSIM}} + 0.1 \cdot L_{\text{perceptual}} \tag{5.44}$$

Here, L_{L1} and L_{L2} correspond to pixel-wise reconstruction losses computed using the mean absolute error and mean squared error norms, which stabilise optimisation and ensure pixel-level fidelity. L_{SSIM} denotes the structural similarity loss, which is essential for preserving edges, textures, and semantic consistency across quantum-distorted images. $L_{\text{perceptual}}$ represents a high-level feature loss derived from the intermediate activations of a pretrained deep network (e.g., VGG-19), allowing the model to capture semantic details that extend beyond low-level pixel alignment.

The weighting configuration in (5.44) is empirically chosen to prioritise L_{L1} (0.4) for strong pixel-level convergence and L_{SSIM} (0.3) for structure and semantics-preserving reconstruction. A smaller weight is assigned to L_{L2} (0.2) to stabilise gradient behaviour and penalise larger deviations, while $L_{\text{perceptual}}$ (0.1) provides complementary high-level feature alignment without overwhelming the optimisation. The parameter weights are selected to achieve an optimal balance between pixel-level fidelity and structural

preservation under the characteristic distortions introduced by QFT-based quantum transmission, such as phase-induced blurring and structural artefacts. Pixel-accuracy terms optimally suppress residual numerical noise, while structure-aware terms optimally preserve edges and contextual features that are critical for semantic integrity. The loss weights are empirically selected based on extensive experimental evaluation across multiple datasets, SNR conditions, and encoding configurations, rather than derived from a theoretical optimisation.

5.5.2 Results

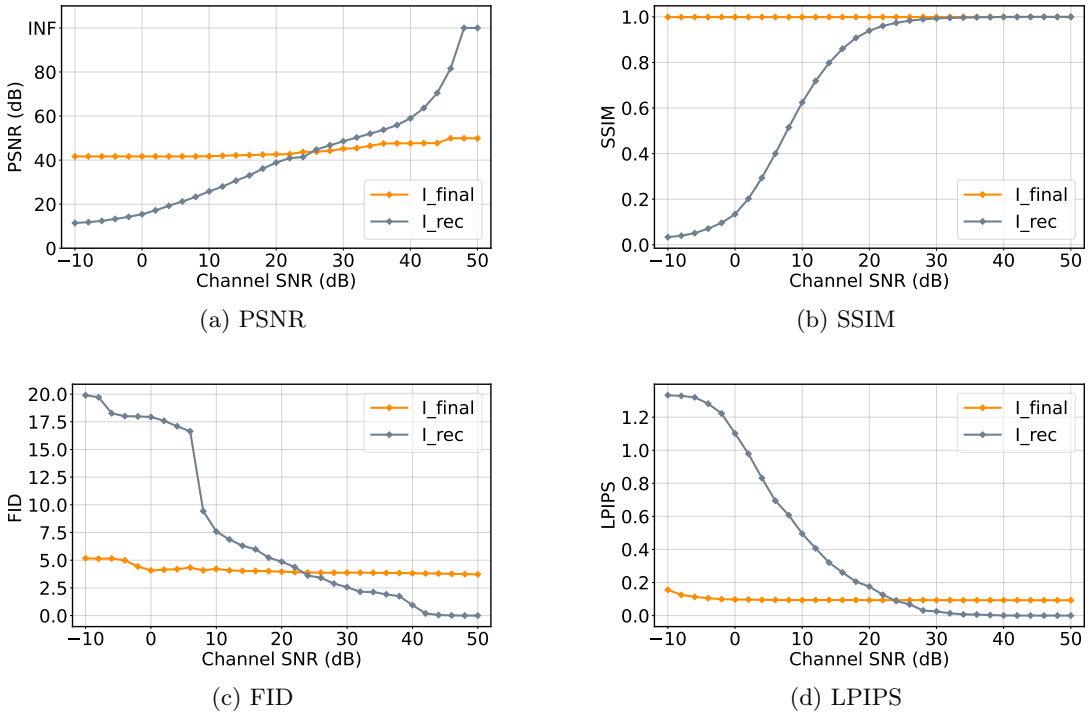
In this section, a comprehensive evaluation of the proposed semantic-aware QFT-based communication framework is presented. The evaluation is performed under both uncoded and channel-coded transmission scenarios with the proposed DDPM-based semantic restoration framework. The reported results represent the average values across all the datasets. The corresponding QFT-only transmission performance, objective quality evaluation, and compression–robustness trade-offs have already been analysed in detail in Section 5.3, including the results shown in Figures 5.21, and 5.24, and are therefore not repeated here.

To evaluate the perceptual quality as well as the structural and semantic fidelity of the reconstructed images, a two-pronged evaluation strategy is employed. Standard distortion-based metrics, including PSNR, SSIM, and UQI [211], are used to assess pixel-level and structural fidelity. In addition, advanced perceptual metrics such as Frechet Inception Distance (FID) and Learned Perceptual Image Patch Similarity (LPIPS) [222] are employed to evaluate semantic realism and perceptual consistency. All reported results are presented as average values over the corresponding test datasets.

Perceptual and Semantic Restoration using DDPM

To fully leverage the high compression efficiency achieved by large qubit encodings, the reconstructed images must also preserve perceptual quality and semantic consistency under noisy channel conditions. Although higher qubit configurations provide substantial compression gains, they become increasingly sensitive to channel noise, leading to degradation in reconstructed image quality. To address this limitation, the proposed

DDPM-based semantic restoration framework is incorporated to recover structural details and perceptual information from noisy QFT-reconstructed outputs. The following results focus on the eight-qubit configuration, representing the highest compression scenario, and demonstrate the effectiveness of the proposed semantic restoration mechanism across different datasets.



(a) PSNR (b) SSIM

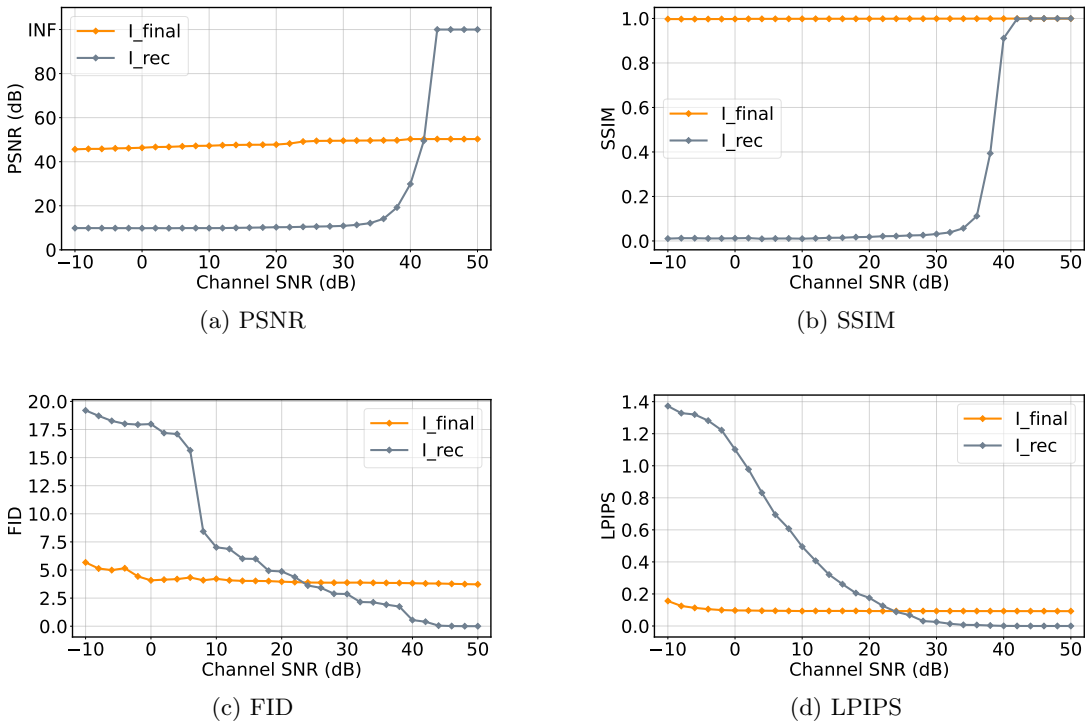
(c) FID (d) LPIPS

Figure 5.38: DDPM reconstruction performance on uncompressed images without channel coding.

Based on the uncoded results shown in Figure 5.38, the effectiveness of the DDPM framework strongly depends on the channel noise conditions. While the quality of the QFT-reconstructed images improves with increasing SNR, the DDPM-refined outputs exhibit significant improvements not only in distortion-based metrics such as PSNR and SSIM, but also in semantic fidelity metrics including FID and LPIPS. These improvements are particularly evident under medium and low-SNR conditions, where the proposed DDPM effectively mitigates channel-induced degradations and restores perceptual consistency.

At high SNR values, however, the DDPM provides limited benefit and may slightly underperform compared to direct QFT reconstruction due to the introduction of restora-

tion artefacts. This behaviour indicates that the primary benefit of the DDPM lies in noisy transmission environments. Furthermore, the denoising process normalises reconstructed outputs into a perceptually stable distribution, resulting in relatively stable PSNR, SSIM, FID, and LPIPS values across varying SNR conditions. Among these metrics, SSIM remains the most stable indicator of structural and semantic consistency.



(a) PSNR (b) SSIM

(c) FID (d) LPIPS

Figure 5.39: DDPM reconstruction performance on uncompressed images with channel coding.

As shown in Figure 5.39, the DDPM-assisted reconstruction framework maintains stable perceptual and semantic reconstruction quality under channel-coded transmission conditions. Similar to the uncoded scenario, the DDPM significantly improves PSNR, SSIM, FID, and LPIPS performance under low and medium-SNR conditions by mitigating channel-induced degradations and restoring semantically meaningful image structures. The inclusion of polar channel coding further improves robustness by reducing transmission errors before semantic restoration.

At high SNR levels, however, the improvement introduced by the DDPM becomes less significant because the QFT-reconstructed images already contain minimal distortion. In some cases, the DDPM may introduce slight reconstruction artefacts due to unnecessary

denoising operations. Nevertheless, the combined use of channel coding and DDPM-based semantic restoration provides consistently robust performance across varying channel conditions while preserving the high compression efficiency of the proposed QFT-based transmission framework.

In addition, a task-oriented evaluation is conducted using a convolutional neural network (CNN)-based image classification model [223], where classification accuracy on reconstructed images is used as a measure of semantic preservation. This evaluation is performed using channel-coded transmitted images from the MNIST dataset, as summarised in Table 5.8. All comparisons are conducted under identical compression ratios and SNR conditions to ensure fairness.

The results demonstrate that the proposed DDPM framework achieves significantly higher classification accuracy under low and medium-SNR conditions compared to QFT-only reconstruction, indicating improved semantic preservation. The improvement is particularly evident in noisy environments, where DDPM effectively compensates for channel-induced degradations. At high SNR levels, however, the performance gain decreases and may slightly degrade due to restoration artefacts. Overall, the proposed framework provides stable and robust semantic reconstruction performance across varying channel conditions. Furthermore, as an example, the proposed DDPM method reduces the effective channel capacity of the eight-qubit system to 0.0044 bits/s at an SNR of –10 dB, as calculated in Section 5.4.2.

Table 5.8: Classification accuracy (%) vs. SNR under identical compression settings.

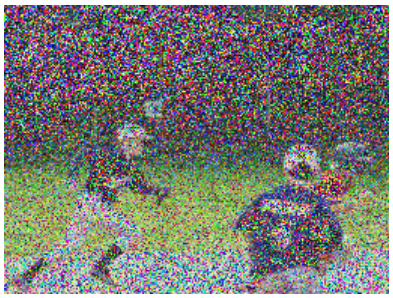
SNR (dB)	**DDPM+QFT**	**QFT Only**
-10	92.3	31.5
0	92.7	55.2
10	93.6	78.4
20	94.2	88.9
30	94.5	96.5
40	94.8	97.1
50	95.1	97.3

To further assess perceptual quality, Figure 5.40 illustrates qualitative visual comparisons using the uncompressed and uncoded COCO dataset. The figure presents the original image, the QFT-only reconstructed image, and the DDPM-refined reconstruction at an example SNR of -4 dB. The DDPM reconstruction clearly preserves improved

visual consistency and semantic structure under severe channel noise conditions.



(a) Original



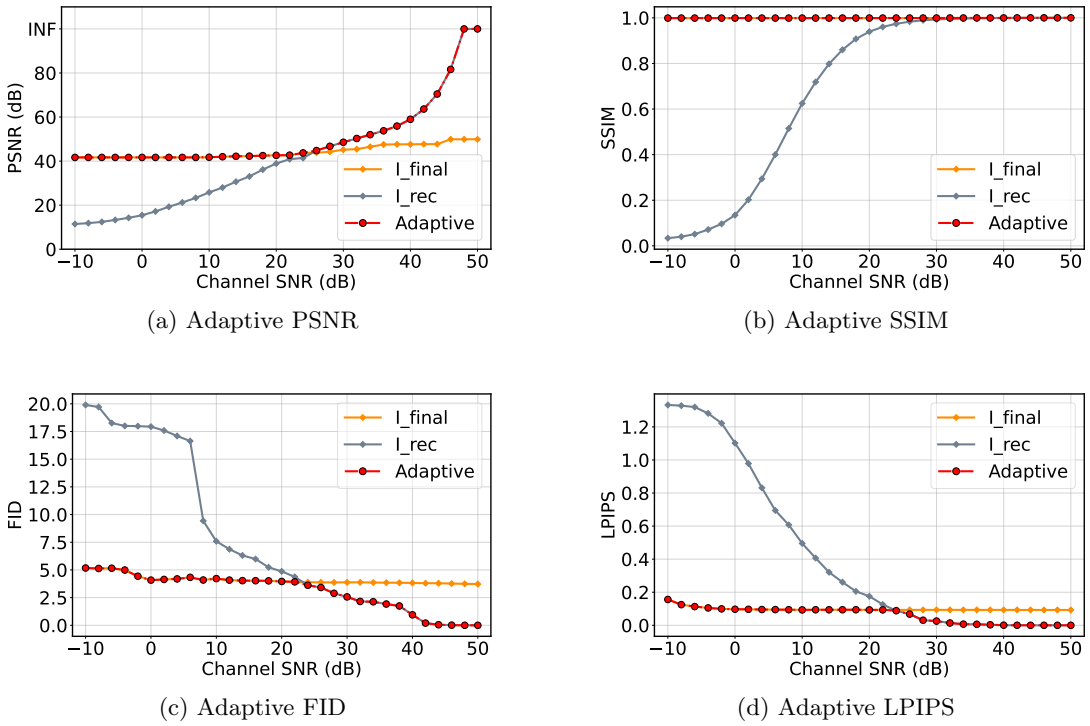
(b) QFT



(c) DDPM

Figure 5.40: Sample reconstructed images from the uncompressed and uncoded COCO dataset at SNR = −4 dB, comparing QFT-based and DDPM-based reconstructions.

The results shown in Figure 5.41 demonstrate that the proposed framework adopts a two-stage adaptive reconstruction strategy for efficient and robust semantic image communication. QFT-based compression provides a 256:1 transmission compression ratio by retaining only dominant frequency-domain coefficients, thereby significantly reducing transmission redundancy, qubit requirements, and effective channel capacity. At the receiver, the DDPM-based semantic restoration framework recovers structural and contextual details lost during noisy transmission. While DDPM provides significant improvements under low-SNR conditions, its benefit becomes limited at high SNR and may introduce unnecessary restoration artefacts. To address this issue, the proposed adaptive reconstruction mechanism dynamically selects the optimal reconstruction strategy based on the estimated channel conditions. This channel-aware reconstruction approach balances QFT-based compression efficiency with DDPM-assisted robustness, ensuring stable perceptual and semantic image quality while avoiding unnecessary computational overhead. In a practical implementation, the receiver periodically estimates



(a) Adaptive PSNR

(b) Adaptive SSIM

(c) Adaptive FID

(d) Adaptive LPIPS

Figure 5.41: Performance of the proposed channel-aware adaptive reconstruction mechanism on the uncoded dataset.

the channel quality using pilot or reference symbols embedded within the transmitted signal to obtain the CSI and the corresponding operating SNR. This information is then conveyed to the transmitter or the receiver-side controller through a reliable control or feedback channel, where it is compared with predefined switching thresholds determined from the crossover regions of the reconstruction performance curves. Based on this comparison, a simple threshold-based decision mechanism is employed to determine whether DDPM-based semantic restoration should be activated. When the estimated SNR falls below the selected threshold, semantic restoration is enabled to compensate for channel-induced degradation. Conversely, when the estimated SNR exceeds the threshold, the image reconstructed directly after IQFT is used, thereby avoiding unnecessary computational complexity, processing latency, and the possibility of introducing restoration artefacts under favourable channel conditions. This adaptive decision process is analogous to adaptive modulation and coding strategies employed in conventional communication systems, where transmission parameters are dynamically selected according to the estimated channel conditions.

The joint integration of QFT-based transmission and semantic reconstruction involves important technical trade-offs between structured, interpretable encoding and robustness to physical noise sources such as phase errors and decoherence. While QFT-based encoding is hardware-feasible and analytically well defined, it remains susceptible to hardware-induced impairments, leading to an inherent trade-off between structured representation and physical robustness. Rather than attempting to eliminate these impairments at the physical layer through complex error correction, the proposed framework combines QFT-based encoding with semantic-oriented reconstruction at the receiver, shifting part of the robustness requirement to classical post-processing. The framework targets application scenarios where semantic fidelity is prioritised over exact symbol recovery, such as low-rate image transmission and exploratory hybrid quantum–classical communication systems.

The proposed framework consists of two complementary components with distinct roles. The QFT-based communication framework forms the core transmission pipeline, where it performs frequency-domain quantum encoding, enables symbol-level compression, and improves resilience to channel impairments during data transmission, as presented in Section 5.3. Following transmission and QFT-based reconstruction, the DDPM is applied exclusively at the receiver as a post-processing stage. Rather than influencing the communication process itself, it enhances the reconstructed images by reducing residual noise and compression-induced distortions, resulting in improved perceptual fidelity and semantic consistency while leaving the transmission framework unchanged. Although the learned generative prior demonstrates substantial improvements in reconstruction quality under noisy channel conditions, its performance is inherently influenced by the characteristics of the training data. A key strength of learned generative priors is their ability to exploit statistical image priors to recover missing or corrupted visual information, enabling robust reconstruction even when the transmitted data are significantly degraded. However, their performance may deteriorate when the characteristics of the test images differ substantially from those represented in the training data. In particular, the CIFAR-10 dataset contains relatively simple visual structures, low-resolution images, and limited scene complexity, which may simplify the restoration task compared with more challenging natural image datasets.

To evaluate the generalisation capability of the proposed framework, the restoration network is also assessed using the more diverse COCO and ImageNet datasets, which exhibit greater variations in object categories, scene complexity, textures, and image resolution. The reported performance metrics are presented as average values across all evaluated datasets, providing a representative assessment of the framework's robustness and reducing the potential bias associated with any individual dataset.

Complexity Analysis

The computational complexity of the proposed multi-stage framework can be analysed by considering its main components: QFT-based encoding, minimum-distance detection, IQFT reconstruction, and DDPM-based refinement. The QFT-based encoding and IQFT reconstruction exhibit low computational complexity, scaling as $\mathcal{O}(k^2)$, or $\mathcal{O}(k \log k)$ when approximate implementations are used. Since the system is constrained to $k \leq 8$, these operations introduce only a modest computational cost while enabling an exponential compression ratio of 2^k:1. At the receiver, minimum-distance detection requires comparison with all possible symbols, resulting in a complexity of $\mathcal{O}(2^k)$ per symbol. Although this grows exponentially with k, the small qubit size ensures that the overall cost remains tractable. The dominant computational cost arises from the DDPM-based reconstruction stage, which performs iterative denoising over T timesteps. Its complexity can be expressed as $\mathcal{O}(T \cdot C_{\text{net}})$. Here, C_{net} denotes the cost of a single network evaluation. This stage significantly increases computational load but provides substantial gains in reconstruction quality under low-SNR conditions.

The overall system complexity (C_{total}) is given in (5.45), with the terms corresponding to encoding, detection, reconstruction, and DDPM refinement, respectively.

$$C_{\text{total}} = \mathcal{O}(k^2) + \mathcal{O}(2^k) + \mathcal{O}(k^2) + \mathcal{O}(T \cdot C_{\text{net}}) \tag{5.45}$$

To improve efficiency, the proposed adaptive mechanism bypasses the DDPM stage under high-SNR conditions. In this case, the reduced complexity is given in (5.46), with the terms corresponding to encoding, detection, and reconstruction.

$$C_{\text{reduced}} = \mathcal{O}(k^2) + \mathcal{O}(2^k) + \mathcal{O}(k^2) \tag{5.46}$$

This design ensures a practical trade-off between computational complexity and reconstruction performance.

5.5.3 Section Summary

In this study, we introduced a quantum frequency-domain framework for image communication that integrated QFT-based compression and transmission with DDPM-based channel-aware reconstruction. The proposed system effectively balanced resource efficiency and robustness. Our analysis across different datasets revealed a fundamental trade-off: higher qubit encodings offered significant compression gains but were more sensitive to noise, whereas lower qubit encodings provided greater robustness at the expense of reduced compression efficiency. The DDPM-based reconstruction framework addressed this limitation by achieving consistently high-quality reconstruction under low-SNR conditions, reaching a maximum average SSIM of approximately 0.9996. At the same time, it reduced the effective channel capacity requirement for the eight-qubit system to 0.0044 bits/s, although its performance at high SNR was slightly lower compared to the standalone QFT-based reconstruction. This trade-off was effectively balanced through an adaptive mechanism that dynamically selected between raw quantum reconstructions and DDPM-enhanced outputs, resulting in consistent quality improvements across varying channel conditions.

5.6 Semantic-Aware Quantum Frequency-Domain Video Transmission with Post-Channel Noise Reduction

Publication Notice

The research presented in this section has been submitted as the following manuscript and is currently under review:

U. Jayasinghe, V. Gowrisetty, and A. Fernando, "Semantic-aware quantum frequency-domain video transmission with post-channel noise reduction," submitted to *IEEE Transactions on Vehicular Technology*.

Portions of this chapter are based on the above submitted manuscript. The material has been revised and expanded with additional explanations, analysis, and discussion for inclusion in this doctoral thesis.

Problem Statement: Section 5.5 demonstrated that diffusion-based semantic-aware restoration can recover compression artefacts and channel-induced distortions in QFT-compressed image transmission. Video transmission, however, introduces an additional restoration challenge that does not arise in still images: temporal coherence. Per-frame restoration without temporal awareness causes flickering artefacts, inconsistent denoising across frames, and visible discontinuities at GOP boundaries, all of which severely degrade perceived video quality even when per-frame PSNR appears acceptable.

Limitations of Existing Work: Existing quantum video communication frameworks, including those of Section 5.4 and earlier sections, do not include any post-channel semantic restoration stage. Classical learned video-restoration methods exist but assume classical degradation models (Gaussian noise, compression blockiness) and are not designed for the dual quantum compression-and-channel degradation studied here. The combination of QFT-based video compression, composite quantum channel noise, and temporally coherent semantic restoration has not been explored.

Motivation and Proposed Contribution: These limitations motivate the development of a restoration framework capable of jointly addressing quantum compression artefacts, quantum channel noise, and temporal semantic consistency within QFT-

compressed video transmission systems. To address this gap, this section extends the semantic-aware diffusion-based restoration framework of Section 5.5 to video transmission. A three-stage U-Net architecture, trained progressively using a quantum-adapted loss function, performs quantum-noise removal, semantic structure recovery, and semantic enhancement on each video frame while preserving temporal coherence across the sequence. The framework is evaluated using QFT-compressed video transmissions across multiple GOP sizes and resolutions, demonstrating that semantic-aware restoration substantially improves both per-frame objective quality and end-to-end VMAF perceptual scores compared to the unrestored baseline.

5.6.1 System Model

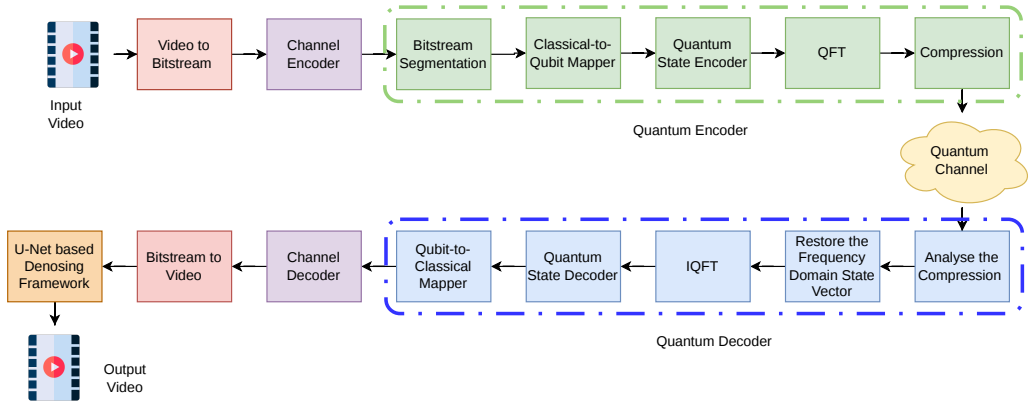


Figure 5.42: Proposed end-to-end framework for video compression, transmission, reconstruction, and denoising.

The proposed semantic-aware quantum video transmission system, shown in Figure 5.42, consists of video preprocessing, bitstream generation, multi-qubit quantum encoding, QFT-based frequency-domain compression, transmission over a noisy quantum channel, IQFT-based reconstruction, bitstream-to-video recovery as described in Section 5.4, and a U-Net-based semantic-aware restoration framework consistent with Section 5.5, where the diffusion model is specifically trained for video data restoration to recover spatial, temporal, and contextual details.

To improve both semantic fidelity and perceptual quality in video frames degraded by high quantum noise, we employ a customised three-stage U-Net pipeline, as illustrated

in Figure 5.43.

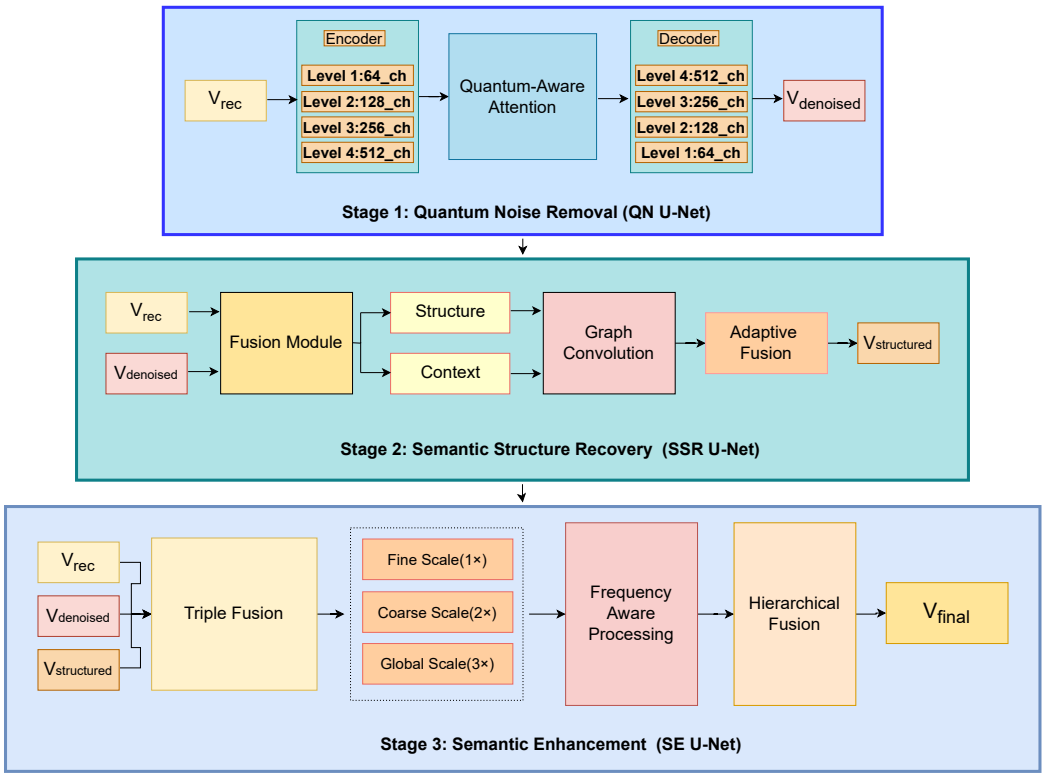


Figure 5.43: Three-stage U-Net architecture for video denoising.

Let the reconstructed video, $\mathbf{V}_{rec}$, after the QFT reconstruction process, be denoted as in (5.47).

$$\mathbf{V}_{rec} = \{I_{rec}^{t}\}_{t=1}^{T}, \quad I_{rec}^{t} \in \mathbb{R}^{H \times W \times 3} \tag{5.47}$$

where T is the total number of frames, H and W are the frame height and width, respectively, and each frame I_{rec}^{t} is an RGB image. Each stage of the pipeline is designed to reduce quantum-induced distortions while preserving temporal coherence across consecutive frames.

Stage 1: Quantum Noise Removal (QN U-Net)

The first stage focuses on suppressing quantum noise at the frame level while maintaining short-range temporal consistency. Each reconstructed frame I_{rec}^{t} is processed using a modified diffusion U-Net with quantum-aware spatiotemporal attention. The encoder–

decoder hierarchy consists of four levels with channel dimensions, as shown in (5.48).

$$64 \rightarrow 128 \rightarrow 256 \rightarrow 512 \tag{5.48}$$

The quantum-aware attention for frame t, which models correlation patterns induced by quantum noise, is defined as in (5.49).

$$QAttention(\mathbf{X}^t) = \text{Softmax}\Big(\frac{QK^\top}{\sqrt{d_k}} + M^t_{quantum}\Big)V \tag{5.49}$$

where $\mathbf{X}^t$ denotes the spatiotemporal feature representation of the reconstructed frame at time t, constructed from a local temporal window $\{I^{t-\Delta}_{rec}, \ldots, I^{t+\Delta}_{rec}\}$, with t being the current video frame index and Δ the temporal half-window size. Q, K, and V are the spatiotemporal query, key, and value matrices derived from $\mathbf{X}^t$, and d_k represents the dimensionality of the key vectors.

The quantum correlation bias term ($M^t_{quantum}$), which incorporates quantum-induced correlations and temporal priors, is defined as in (5.50).

$$M^t_{quantum}[i,j] = \alpha \exp\Big(-\beta \|f^t_i - f^t_j\|^2_2\Big) \cdot \xi(i,j) \tag{5.50}$$

where f^t_i and f^t_j are feature vectors associated with quantum-encoded components at spatial positions i and j in frame t, α and β are scaling hyperparameters, and $\xi(i,j)$ encodes temporal adjacency or short-term correlation priors between positions i and j.

A dual-pooling attention mechanism, combining global average and max pooling, is included to handle both gradual amplitude decay and abrupt decoherence artefacts. The output of this stage is the denoised video ($\mathbf{V}_{denoised}$), as shown in (5.51)

$$\mathbf{V}_{denoised} = \{I^t_{denoised}\}^T_{t=1} \tag{5.51}$$

where $I^t_{denoised}$ denotes the denoised frame at time index t.

Stage 2: Semantic Structure Recovery (SSR U-Net)

The second stage reconstructs semantic structure distorted by quantum-frequency compression and transmission. SSR U-Net employs a dual-pathway spatiotemporal

diffusion model that uses both $\mathbf{V}_{denoised}$ and $\mathbf{V}_{rec}$ to recover structured frames, as defined in (5.52).

$$I^t_{structured} = F_{fusion}\Big(P_{struct}(I^t_{denoised}),\, P_{context}(I^t_{rec})\Big) \tag{5.52}$$

where $P_{struct}(\cdot)$ extracts fine spatial details, $P_{context}(\cdot)$ captures global semantic context, and $F_{fusion}(\cdot,\cdot)$ fuses the two pathways. Fine-grained spatial features are restored via a graph-augmented U-Net as in (5.53) with an adaptive spatiotemporal adjacency matrix defined in (5.54).

$$P_{struct}(x^t) = \text{GraphConv}\big(\text{UNet}_{struct}(x^t)\big) \tag{5.53}$$

$$A^t_{ij} = \text{Softmax}\left(\frac{\text{sim}(\phi(x^t_i), \phi(x^t_j))}{\tau}\right) \tag{5.54}$$

where x^t denotes the feature map of frame t, x^t_i represents the feature vector at spatial location i within that frame, $\phi(x^t_i)$ is the corresponding learned embedding, τ is a temperature scaling parameter, and $\text{sim}(\cdot,\cdot)$ computes pairwise similarity. Temporal edges may connect the same spatial position across consecutive frames ($i^t \leftrightarrow i^{t\pm1}$). Global semantic context is preserved using temporal self-attention as represented in (5.55).

$$P_{context}(x^t) = \text{SelfAttention}\big(\text{UNet}_{context}(x^t)\big) \tag{5.55}$$

The structured video sequence ($\mathbf{V}_{structured}$) after stage 2 is represented as in (5.56).

$$\mathbf{V}_{structured} = \{I^t_{structured}\}_{t=1}^{T} \tag{5.56}$$

where $I^t_{structured}$ denotes the denoised frame at time index t.

Stage 3: Semantic Enhancement (SE U-Net)

The third stage performs hierarchical enhancement across spatial and temporal dimensions. The final reconstructed frame (I^t_{final}) at time t is represented as in (5.57).

$$I^t_{final} = \sum_{s=1}^{S} w_s\, T_s\Big(C(I^t_{structured}, I^t_{denoised}, I^t_{rec})\Big) \tag{5.57}$$

where $C(\cdot)$ denotes channel-wise concatenation, T_s represents the s-th multi-scale U-Net, and w_s is the corresponding scale weight. Frequency-aware enhancement is applied in both the spatial and frequency domains as represented in (5.58) and (5.59), and fused as in (5.60).

$$F^t_{spatial} = \text{SpatialAttention}(x^t) \tag{5.58}$$

$$F^t_{freq} = \text{IFFT}\big(\text{FreqMask} \odot \text{FFT}(x^t)\big) \tag{5.59}$$

$$\text{FreqEnhance}(x^t) = \lambda F^t_{spatial} + (1-\lambda) F^t_{freq} \tag{5.60}$$

Here, $x^t \in \mathbb{R}^{H\times W\times C}$ denotes the intermediate feature representation of frame t, $F^t_{spatial}$ is the spatially enhanced feature map obtained through spatial attention, F^t_{freq} is the frequency-enhanced feature map derived by applying a frequency mask (FreqMask) in the Fourier domain, $\odot$ represents element-wise multiplication, FFT and IFFT denote the fast Fourier transform and its inverse, and $\lambda \in [0,1]$ controls the contribution of spatial versus frequency components in the fused representation $\text{FreqEnhance}(x^t)$.

The final restored video sequence ($\mathbf{V}_{final}$) is represented as in (5.61).

$$\mathbf{V}_{final} = \{I^t_{final}\}^T_{t=1} \tag{5.61}$$

where I^t_{final} is the enhanced output frame.

Progressive Training Strategy for Video

The model is trained on a large-scale video dataset collected from the Pexels platform with an 80:20 train/validation split, using the same progressive strategy as Section 5.5 (each stage optimised independently before joint integration). The only video-specific changes are (a) longer per-stage training schedules (Stage 1: 100 epochs; Stage 2: 90 epochs; Stage 3: 80 epochs) and (b) the addition of three temporal-consistency loss terms used at the corresponding stages, defined in (5.62)–(5.64).

$$L_{temp} = \frac{1}{T-1}\sum_{t=1}^{T-1} \|I^t_{denoised} - I^{t+1}_{denoised}\|_1 \tag{5.62}$$

$$L_{ssim\_temp} = \frac{1}{T-1} \sum_{t=1}^{T-1} \Big(1 - \mathrm{SSIM}(I^{t}_{structured}, I^{t+1}_{structured})\Big) \tag{5.63}$$

$$L_{warp} = \frac{1}{T-1} \sum_{t=1}^{T-1} \|\mathrm{Warp}(I^{t}_{final}, F^{t\to t+1}) - I^{t+1}_{final}\|_1 \tag{5.64}$$

Here, L_{temp} enforces smooth intensity transitions across consecutive frames in Stage 1; L_{ssim_temp} penalises structural differences between consecutive structured frames in Stage 2; and L_{warp} aligns motion in Stage 3 using the optical-flow field $F^{t\to t+1} \in \mathbb{R}^{H\times W\times 2}$ from frame t to frame $t+1$, where $\mathrm{Warp}(\cdot, F^{t\to t+1})$ warps a frame according to the estimated flow.

The overall quantum-adaptive loss for video, which augments the image-domain loss with the temporal terms above, is given in (5.65).

$$\begin{aligned} L_{\text{total}} = {} & 0.35\, L_{L1} + 0.15\, L_{L2} + 0.25\, L_{SSIM} \\ & + 0.10\, L_{\text{perceptual}} + 0.10\, L_{temp} + 0.05\, L_{warp} \end{aligned} \tag{5.65}$$

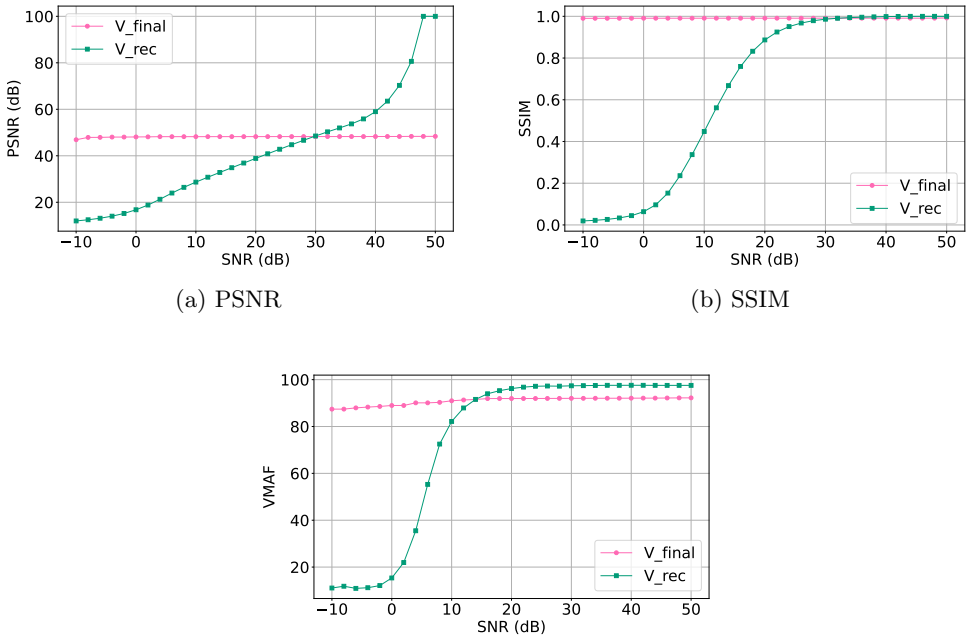
The weights balance pixel, structural, semantic, and temporal consistency for accurate reconstruction of quantum-noise-corrupted video frames.

5.6.2 Results

In this section, a detailed performance evaluation of the proposed video transmission framework is presented. The analysis investigates the behaviour of the system under both uncoded and channel-coded transmission scenarios and further evaluates the perceptual and semantic restoration capability of the integrated U-Net-based denoising framework. The detailed quantitative analysis of the QFT-based compression and transmission framework is presented in Section 5.4. Therefore, this section primarily focuses on evaluating the perceptual contribution of the U-Net-based denoising framework under different transmission conditions. The evaluation employs objective video quality metrics, including PSNR, SSIM, and VMAF, with all reported values averaged over the complete test set of video sequences. PSNR is used to evaluate pixel-level reconstruction quality, while SSIM measures structural preservation and semantic consistency within the reconstructed video frames. In addition, VMAF is employed to assess perceptual

video quality by incorporating both spatial and temporal characteristics associated with human visual perception. These metrics are used to analyse how effectively the proposed denoising framework restores meaningful visual content under noisy transmission conditions. The reported results represent the average values across all the video sequences.

To evaluate the restoration capability, PSNR, SSIM, and VMAF metrics are analysed for both uncoded and channel-coded transmission scenarios using eight-qubit encoding, corresponding to the highest compression ratio of 256:1. The U-Net operates on the reconstructed frames generated by the QFT-based transmission system and aims to recover perceptual quality, structural consistency, and semantic information lost during transmission.



(a) PSNR

(b) SSIM

(c) VMAF

Figure 5.44: Performance evaluation of the U-Net-based video reconstruction framework for uncompressed and uncoded video inputs using eight-qubit encoding.

The restoration performance of the proposed U-Net framework for uncoded transmission of uncompressed video inputs is illustrated in Figure 5.44. Under low-SNR conditions, the reconstructed frames generated by the QFT-based transmission system suffer from significant perceptual and structural degradation due to the increased sen-

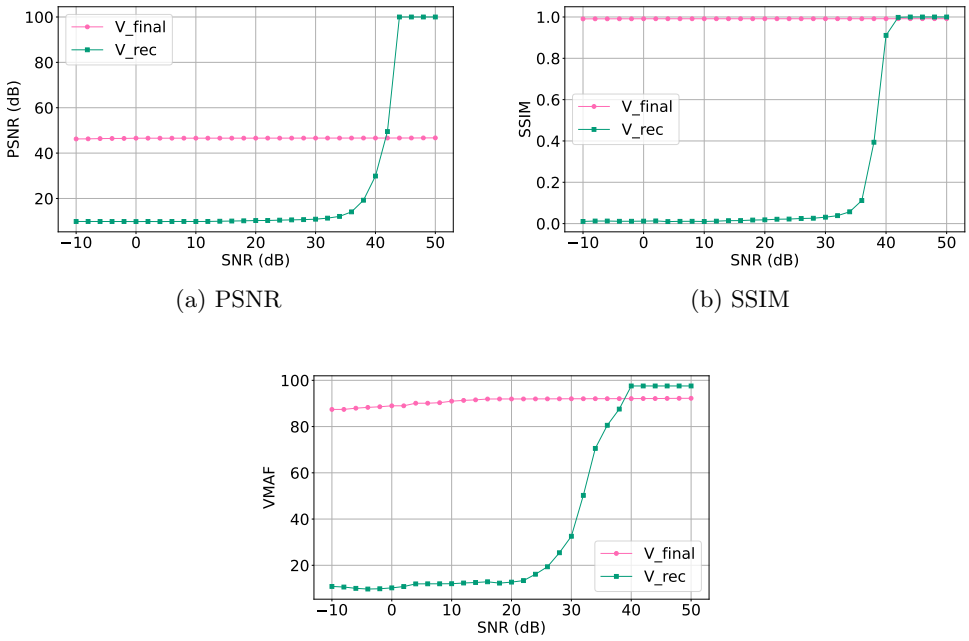
sitivity of higher-qubit encodings to channel noise. The proposed U-Net framework effectively suppresses these distortions and restores meaningful visual content.

The PSNR results demonstrate moderate numerical improvement after U-Net refinement, indicating partial recovery of pixel-level distortions introduced during transmission. However, the most significant improvements are observed in SSIM and VMAF. The increase in SSIM confirms that the U-Net preserves structural information and spatial consistency more effectively than the original QFT reconstruction alone. Since semantic preservation prioritises the retention of meaningful visual content rather than exact pixel-wise reconstruction, SSIM becomes particularly important for evaluating semantic fidelity.

Similarly, the VMAF results show substantial improvement across low and medium SNR regions. Unlike conventional distortion metrics, VMAF incorporates perceptual characteristics associated with the human visual system together with spatial and temporal quality assessment. The improved VMAF scores therefore indicate that the U-Net reconstruction produces video sequences that are perceptually more natural and semantically more interpretable to human observers. At high SNR values, only marginal improvements are observed because the reconstructed frames already possess high visual quality before denoising. This behaviour confirms that the U-Net framework is particularly beneficial in noisy transmission environments where semantic and perceptual information is severely degraded.

The corresponding restoration performance for channel-coded transmission is illustrated in Figure 5.45. Compared with the uncoded scenario, channel coding already improves the baseline reconstructed video quality by reducing transmission errors prior to U-Net refinement. Nevertheless, residual distortions remain visible at lower SNR levels, particularly for eight-qubit encoding, where the dense frequency-domain representation remains highly sensitive to noise perturbations.

The integration of the U-Net further enhances perceptual reconstruction quality by refining edges, restoring structural consistency, and reducing visually disturbing artefacts. The PSNR improvements remain relatively moderate because pixel-wise restoration alone does not fully capture perceptual enhancement. In contrast, the improvements in SSIM and VMAF are more pronounced, confirming that the denoising



(a) PSNR

(b) SSIM

(c) VMAF

Figure 5.45: Performance evaluation of the U-Net-based video reconstruction framework for uncompressed and channel-coded video inputs using eight-qubit encoding.

framework effectively restores semantic structures and perceptual continuity within the reconstructed video frames. These observations are particularly important for semantic reconstruction, where the objective is not necessarily perfect pixel reconstruction, but rather preservation of meaningful and interpretable visual information. The improved VMAF scores further demonstrate that the reconstructed videos exhibit enhanced perceptual realism and temporal consistency from a human visual perspective.

A visual comparison of the restoration capability under highly noisy transmission conditions at SNR $= -4$ dB is presented in Figure 5.46. The figure compares the original frame, the QFT-reconstructed frame (V_{rec}), and the U-Net-enhanced frame (V_{final}). The QFT-reconstructed frame contains noticeable noise distortions, loss of fine structural details, and reduced perceptual clarity due to the severe channel impairments associated with high compression and low-SNR transmission.

After U-Net refinement, the reconstructed frame exhibits substantially improved visual quality. Structural edges become clearer, noise artefacts are significantly suppressed, and semantically meaningful content becomes more recognisable. The restored frame



(a) Original

(b) V_{rec}



(c) V_{final}

Figure 5.46: Sample reconstructed video frames at SNR $= -4$ dB for uncompressed and uncoded inputs using eight-qubit encoding, comparing the original frame, QFT-reconstructed frame (V_{rec}), and the U-Net-enhanced frame (V_{final}).

more closely resembles the original scene while preserving important perceptual and contextual information. These observations confirm that the proposed denoising framework successfully enhances semantic interpretability even under challenging transmission conditions.

Overall, the results demonstrate that the proposed U-Net-based denoising framework substantially improves perceptual and semantic reconstruction quality within the QFT-based video transmission system. The framework is particularly effective in low-SNR environments and high-compression scenarios where transmission noise severely affects perceptual fidelity. By restoring structural consistency, perceptual realism, and semantic information, the proposed approach enables more reliable and meaningful video delivery over noisy quantum communication channels. The computational complexity and performance trade-offs associated with the proposed restoration framework remain consistent with those discussed in Section 5.5. Similar to the adaptive restoration strategy proposed in Section 5.5, an adaptive quality-balancing mechanism can also be applied within the proposed video restoration framework to dynamically balance

between direct QFT-based reconstruction and U-Net-enhanced outputs under varying channel conditions. Although such adaptive switching is not explicitly implemented in this section, the presented framework remains compatible with the same adaptive reconstruction principle for future quality-aware video transmission optimisation.

5.6.3 Section Summary

In this work, a quantum frequency-domain video transmission framework was presented, integrating QFT-based compression and transmission with U-Net-based reconstruction to enable efficient and reliable video delivery. The QFT-based system exhibited a trade-off between compression efficiency and noise robustness: lower-qubit encodings provided higher resilience with limited compression, while higher-qubit encodings achieved greater compression ratios (up to 2^k:1) at the cost of reduced noise tolerance. To address this limitation, the U-Net refinement significantly enhanced perceptual quality under low-SNR conditions, achieving PSNR values up to 48.36 dB, SSIM values up to 0.9921, and VMAF scores up to 92.22, making it particularly effective in low to mid-SNR regimes. In contrast, the standalone QFT-based system achieved PSNR approaching infinity, SSIM values near 1, and VMAF scores up to 98 under high-SNR conditions. Overall, the results highlighted a practical pathway for high-fidelity and semantically meaningful video transmission over noisy quantum channels, with the U-Net-based reconstruction proving especially advantageous in noisy transmission environments.

5.7 Chapter Summary

This chapter presented the progressive development of a quantum frequency-domain framework for high-fidelity multimedia transmission, comprising six interconnected studies (Sections 5.1–5.6). Section 5.1 established the foundational frequency-domain multi-qubit encoding scheme for image transmission, demonstrating that QFT-based projection into the quantum frequency domain distributes information across both amplitude and phase components of the encoded state, yielding up to a 4 dB channel-SNR gain over the time-domain multi-qubit framework of Chapter 4 for eight-qubit configurations on both JPEG and HEIF inputs. Section 5.2 extended this framework to VVC-compressed video transmission across multiple GOP sizes, frame rates, and

spatial resolutions, confirming that the per-symbol robustness gains of frequency-domain encoding carry over to temporally correlated content and that the eight-qubit frequency-domain system (F8) consistently outperforms its time-domain counterpart (T8) and a bandwidth-matched classical baseline. Section 5.3 reformulated QFT as a unified compression and transmission primitive, in which symbol-level reduction up to 256:1 is achieved by transmitting a single representative coefficient per k-qubit block, eliminating the dependence on a separate classical source coder and providing up to a 10 dB PSNR gain over bandwidth-equivalent QPSK with polar coding for the two-qubit configuration. Section 5.4 extended QFT-based compression to video, showing that the same compression–robustness trade-off governs temporally correlated inputs and remains invariant to resolution and frame rate, with maximum SNR gains determined by qubit encoding size rather than video content characteristics. Section 5.5 addressed the residual perceptual and semantic degradation introduced by aggressive QFT compression and channel noise through a three-stage diffusion-based restoration framework (QN-DDPM, SSR-DDPM, SE-DDPM), achieving SSIM values approaching 0.9996 under low-SNR conditions and substantially improving the classification accuracy in QFT-compressed transmissions. Section 5.6 extended this restoration framework to video transmission through a three-stage U-Net pipeline trained with temporal-consistency loss terms, achieving PSNR values up to 48.36 dB, SSIM up to 0.9921, and VMAF up to 92.22 for the eight-qubit configuration under severe channel impairments.

A critical insight emerging from the collective findings of this chapter is that frequency-domain quantum encoding consistently outperforms time-domain encoding because the QFT spreads each computational-basis state uniformly across the full 2^k-dimensional Hilbert space, exploiting both amplitude and phase components rather than amplitude alone. However, this robustness gain comes at a substantial circuit cost: the QFT requires $\mathcal{O}(k^2)$ gates with the circuit depth scaling linearly with k, compared to the constant-depth $\mathcal{O}(k)$ gate count of the Hadamard time-domain encoding of Chapter 4. Furthermore, the QFT achieves its Hilbert-space spreading using a fixed and structured set of phases, namely the roots of unity, leaving the broader design space of amplitude–phase combinations unexplored.

A second, equally important insight is that the effect of qubit size on error resilience

depends fundamentally on whether the QFT is used purely for transmission or for joint compression and transmission. In Sections 5.1–5.2, where the QFT serves only as a transmission representation and the full 2^k-dimensional state vector is transmitted, increasing the qubit encoding size *improves* error resilience. This is because larger Hilbert spaces distribute the encoded information across more basis components, allowing channel-induced perturbations to be diluted across a higher-dimensional spectral representation. Consequently, higher-qubit configurations (e.g., $k = 8$) consistently achieve lower BER and better reconstruction quality than lower-qubit configurations under identical bandwidth conditions.

In contrast, in Sections 5.3–5.4, where the QFT is additionally exploited for symbol-level compression by transmitting only a single representative coefficient per k-qubit block, increasing the qubit encoding size *degrades* error resilience. This reversal arises because the angular separation between adjacent frequency components scales as $\Delta\theta = 2\pi/2^k$, shrinking exponentially with k. As the constellation of transmitted coefficients becomes denser on the complex unit circle, the receiver-side nearest-vector detector becomes progressively more susceptible to channel phase noise, and the compression ratio of 2^k:1 is purchased at the cost of reduced noise tolerance. This trade-off becomes particularly acute at $k = 7$–8, motivating the receiver-side restoration mechanisms of Sections 5.5–5.6 to preserve perceptual and semantic fidelity when high compression ratios are required.

This observation motivates a fundamental shift in approach: rather than relying on the structured phase pattern of the QFT to obtain Hilbert-space spreading at the cost of growing circuit depth, the subsequent chapter returns to the time domain and investigates encoding-level strategies that exploit the joint amplitude–phase representation of qubits directly, without invoking any frequency-domain transformation. Specifically, Chapter 6 introduces complex-valued orthogonal unitary superposition (COUS) encoding, a new time-domain encoding mechanism that combines orthogonal amplitude components with deliberately chosen phase components to occupy directions in the complex Hilbert space that are simultaneously orthogonal in both magnitude and phase. This encoding achieves Hilbert-space-spreading benefits comparable to the QFT while requiring only constant-depth $\mathcal{O}(1)$ circuits per qubit, using only single-qubit Hadamard and phase gates with

no transform-domain reconstruction overhead at the decoder, offering a complementary and computationally efficient alternative to the frequency-domain framework developed in this chapter.

Chapter 6

Introduction of Novel Quantum Encoding Techniques for Noise Resilience and Computational Efficiency

Chapters 3–5 progressively developed a quantum image and video communication framework through two distinct encoding domains. Chapters 3 and 4 operated in the *time domain* using Hadamard-based superposition encoding: Chapter 3 established the foundational framework with quantum error correction, and Chapter 4 extended it through multi-qubit encoding into higher-dimensional Hilbert spaces. Both achieved their robustness through real-valued amplitude superposition with constant-depth circuits, but distributed information primarily through amplitude-domain encoding while leaving the phase degrees of freedom largely unexploited. Chapter 5 then moved into the *frequency domain* through the QFT, demonstrating that representing information jointly through amplitude and structured phase relationships across the 2^k-dimensional Hilbert space provides measurable robustness gains over the earlier time-domain frameworks. However, as established in Chapter 5, these robustness gains came at a substantial circuit cost, requiring $\mathcal{O}(k^2)$ gates and circuit depth that scales linearly with the number of qubits.

These observations reveal an important unaddressed design question. The perfor-

mance gains observed in the QFT-based framework of Chapter 5 suggest that jointly exploiting amplitude and phase degrees of freedom improves noise resilience compared with purely amplitude-based encoding. However, in the QFT framework this joint amplitude–phase representation is achieved only through a frequency-domain transformation with relatively high computational complexity. This naturally raises the following question: can similar Hilbert-space spreading and robustness advantages be achieved directly within the time domain through a low-complexity encoding strategy that jointly exploits amplitude and phase by design, without requiring any frequency-domain transform?

This chapter answers that question by introducing complex-valued orthogonal unitary superposition (COUS) encoding. COUS constructs each multi-qubit state from orthogonal amplitude components combined with deliberately selected phase components, producing encoded states that are simultaneously separated in both magnitude and phase. Unlike the QFT-based framework presented in Chapter 5, Section 5.1 and Section 5.2, which requires transform-domain processing and inverse reconstruction, COUS operates entirely in the time domain while still exploiting joint amplitude–phase diversity. Consequently, the proposed framework investigates whether the robustness advantages previously observed in the frequency domain can instead be achieved through low-complexity time-domain encoding.

COUS provides three architectural advantages: constant circuit depth $\mathcal{O}(1)$ per qubit, implementation using only single-qubit Hadamard and phase gates, and elimination of any transform-domain reconstruction stage at the decoder. In contrast to the QFT-based compression scheme of Sections 5.3–5.4, where shrinking angular separation between frequency coefficients caused error resilience to degrade with increasing qubit encoding size, COUS selects its phase components to maximise minimum-distance separation in the complex Hilbert space. Consequently, increasing the qubit encoding size improves robustness rather than reducing it.

The proposed framework is therefore evaluated against both categories of previously developed systems: the time-domain Hadamard-based multi-qubit framework of Chapter 4 and the frequency-domain QFT-based framework of Chapter 5, Section 5.1 and Section 5.2, together with equivalent classical communication baselines under matched

bandwidth conditions. This comparison enables the contribution of joint amplitude–phase encoding to be isolated from the influence of transform-domain processing and computational complexity. Throughout this chapter, the proposed framework is evaluated using JPEG, HEIF, and VVC-compressed multimedia. Although these standards employ transform-domain source coding, the subsequent quantum encoding remains independent of the underlying transform because it is performed on the compressed bitstream.

The chapter is organised in two sections. Section 6.1 formulates COUS encoding for quantum image transmission, derives the orthogonality conditions on the amplitude and phase components, analyses noise resilience through minimum-distance and amplitude–phase diversity arguments, and benchmarks against the Hadamard-based multi-qubit framework of Chapter 4, the QFT-based framework of Chapter 5, and classical baselines under matched bandwidth. Section 6.2 extends the framework to quantum video transmission [224], where temporal inter-frame correlation amplifies the impact of residual transmission errors and the encoding-stage robustness of COUS becomes particularly valuable. Together, these contributions complete the encoding-side design space explored in this thesis: time-domain real-valued amplitude encoding (Chapters 3–4), frequency-domain QFT-based encoding (Chapter 5), and time-domain complex-valued orthogonal unitary superposition encoding (this chapter).

6.1 A Complex-Valued Orthogonal Unitary Superposition Encoding-Based Multi-Qubit System for Quantum Image Transmission

Publication Notice

The research presented in this section has been submitted as the following manuscript and is currently under review:

U. Jayasinghe, T. Fernando, and A. Fernando, "A novel complex-valued orthogonal unitary superposition encoding-based multi-qubit system for quantum image transmission," submitted to *IEEE Transactions on Communications*.

Portions of this chapter are based on the above submitted manuscript. The material has been revised and expanded with additional explanations, analysis, and discussion for inclusion in this doctoral thesis.

Problem Statement: Chapters 4 and 5 demonstrated that both time domain multi-qubit superposition encoding and QFT-based frequency-domain encoding can improve the robustness of image transmission over noisy quantum communication channels. In particular, the QFT-based framework achieves enhanced robustness by exploiting transform-domain amplitude and phase characteristics that improve the separability of encoded quantum states. However, these gains come at the cost of substantial computational and implementation complexity due to the transform-domain processing stages, including QFT and IQFT operations, increased circuit depth, and higher gate-count requirements. Such complexity limits the practicality of QFT-based approaches for near-term quantum hardware and real-time multimedia transmission systems.

Limitations of Existing Work: Existing Hadamard-based multi-qubit encoding frameworks provide low-complexity implementations but primarily exploit amplitude-domain superposition diversity using fixed ± 1 amplitude patterns. As a result, their robustness remains lower than that achievable with transform-domain approaches such as QFT-based encoding. Conversely, QFT-based systems improve transmission performance through additional phase diversity in the frequency domain, but require

complex transform-domain operations and increased computational overhead. To the best of the author's knowledge, no prior work has developed a low-complexity multi-qubit encoding framework that can exploit flexible complex-valued amplitude–phase relationships to achieve robustness comparable to frequency-domain quantum transmission approaches while avoiding the complexity associated with transform-domain processing.

Motivation and Proposed Contribution: To address these limitations, this section proposes a COUS encoding strategy for multi-qubit quantum image transmission. The proposed framework directly constructs complex-valued orthogonal quantum states in the encoding stage without requiring QFT-based transform-domain operations. By jointly engineering amplitude and phase characteristics through orthogonal unitary superposition design, the proposed method increases the separability between encoded states while maintaining low implementation complexity. COUS provides three architectural advantages: low circuit complexity with constant-depth $\mathcal{O}(1)$ operations per qubit, encoding based primarily on Hadamard and phase-controlled state construction, and elimination of any transform-domain reconstruction stage at the decoder.

The framework is evaluated for qubit group sizes from 1 to 8, corresponding to standard 8-bit pixel representations, using both JPEG and HEIF source coding formats, with and without rate-1/2 polar channel coding. The proposed system is compared against the Hadamard-based multi-qubit framework presented in Section 4.1, a QFT-based frequency-domain framework presented in Section 5.1, and a classical BPSK reference system. The objective is to demonstrate that the proposed complex-valued encoding mechanism can achieve robustness comparable to transform-domain quantum communication approaches while substantially reducing encoding and decoding complexity.

The main contributions of this section are as follows.

- Proposes a novel quantum encoding technique utilising the COUS encoding scheme.
- Analyses the COUS encoding scheme to evaluate its performance and robustness in a multi-qubit system.
- Develops a low-complexity and scalable multi-qubit framework.

- Evaluates the system performance for high-fidelity image transmission.
- Compares the performance of the proposed system with state-of-the-art quantum multi-qubit encoding schemes, demonstrating superior image quality and noise resilience.

6.1.1 System Model

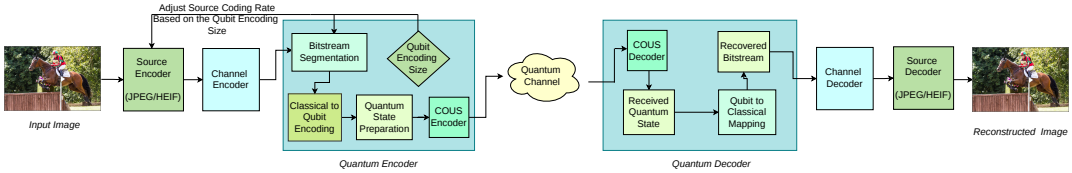


Figure 6.1: Architecture of the proposed COUS-based multi-qubit quantum communication system for high-fidelity image transmission.

The proposed system, as illustrated in Figure 6.1, begins with input images, which are first compressed using standard source coding techniques such as JPEG or HEIF to remove statistical and perceptual redundancies. This compression produces compact binary bitstreams suitable for transmission, with the compression level controlled via the quantisation parameter (QP); lower QP values result in more compact streams, while higher QP values preserve more image detail. To ensure fair comparison across different qubit configurations (k), QP values are adaptively adjusted such that the effective bandwidth remains approximately constant, i.e., $k \times$ bitstream length $\approx$ constant. Specifically, for JPEG, QP values of 100, 94, 88, 79, 72, 60, 50, and 40 are used for qubit sizes 1 to 8, respectively, while for HEIF, the corresponding QP values are 100, 70, 60, 54, 50, 45, 43, and 41. Consequently, the single-qubit configuration requires the least source compression and therefore achieves the highest maximum reconstruction quality under high-SNR conditions, where performance is primarily limited by source coding distortion. In contrast, higher-qubit configurations require progressively stronger source compression to compensate for the increased number of transmitted qubits and maintain bandwidth equivalence. This additional compression introduces greater source coding distortion, resulting in lower quality values.

For performance evaluation, 100 images from the Microsoft COCO dataset [197] with a resolution of 256 $\times$ 192 and 20 high-spatial-complexity 4K images from the

Kaggle dataset [219] are selected to ensure diversity in scene content and spatial characteristics. All reported results are averaged over the dataset, with 1000 Monte Carlo trials performed for each SNR value. Importantly, the proposed framework is input-agnostic and operates solely on the compressed bitstream, making it independent of image content, resolution, or dataset-specific features.

The source-encoded bitstreams are optionally protected using polar codes [210] with a code rate of 1/2, which are particularly well-suited for this system due to their capacity-achieving nature and low computational complexity [209]. An uncoded system is also evaluated to clearly analyse the intrinsic performance gains. The absence of quantum QEC is intentional, as existing QEC schemes introduce significant computational and implementation overhead due to additional qubits, syndrome measurements, and complex decoding operations. A detailed analysis of COUS encoding combined with three-qubit QEC under single-qubit encoding is presented in Appendix A. Since three-qubit QEC codes are not directly compatible with multi-qubit encoding schemes, this study is conducted under single-qubit encoding as a separate investigation. Appendix A describes the methodology and reports the effect of COUS encoding on three-qubit QEC encoded state transmission, error detection, and error correction performance.

To provide a clearer understanding, the following subsections describe the main functional blocks of the proposed system in greater detail.

The Proposed Quantum Encoder

The channel-encoded bitstream is first segmented according to the qubit encoding size, ranging from 1 to 8. The upper limit of 8 qubits is chosen because the images have an 8-bit depth, allowing each pixel to be fully represented using a single multi-qubit state. However, the system is flexible and can, in principle, use any qubit size; 8 qubits are used in this study to balance pixel representation and system complexity.

Classical-to-Qubit Encoding: In the proposed framework, each classical bit $b \in \{0, 1\}$ is transformed into a quantum state using the qubit computational basis. Specifically, a bit value of 0 is represented by the state $|0\rangle$, and a bit value of 1 is represented by $|1\rangle$. These two states form the basis of the qubit Hilbert space $\mathcal{H}_2$ and can be expressed

in vector form as in (6.1).

$$|0\rangle = \begin{pmatrix} 1 \\ 0 \end{pmatrix}, \quad |1\rangle = \begin{pmatrix} 0 \\ 1 \end{pmatrix} \tag{6.1}$$

This mapping converts classical data into a quantum-compatible format, preparing it for subsequent multi-qubit encoding and quantum processing steps. Physically, this can be implemented as follows. The quantum register is first initialised such that all qubits are in the ground state $|0\rangle$. A classical control key determines the applied operation: a key value of 0 results in no action, leaving the qubit unchanged, whereas a key value of 1 activates a Pauli-X gate, flipping the qubit from $|0\rangle$ to $|1\rangle$.

Quantum State Preparation: In the multi-qubit encoding scheme, the classical bitstream is first segmented according to the qubit encoding size k. Each segment forms a binary string, as shown in (6.2).

$$b_1 b_2 \dots b_k, \quad b_i \in \{0, 1\} \tag{6.2}$$

Then, it is mapped to individual qubits as described in (6.1). The complete quantum state for the block is constructed by taking the tensor product of the corresponding single-qubit states, as shown in (6.3).

$$|b_1 b_2 \dots b_n\rangle = |b_1\rangle \otimes |b_2\rangle \otimes \cdots \otimes |b_n\rangle \tag{6.3}$$

As an example, for single-qubit encoding ($k = 1$), each bit is directly mapped to the standard computational basis states $|0\rangle$ and $|1\rangle$. For two-qubit encoding ($k = 2$), the four possible combinations of bits are mapped to the following 4-dimensional quantum states, as shown from (6.4) to (6.7).

$$|00\rangle = |0\rangle \otimes |0\rangle = \begin{pmatrix} 1 & 0 & 0 & 0 \end{pmatrix}^T \tag{6.4}$$

$$|01\rangle = |0\rangle \otimes |1\rangle = \begin{pmatrix} 0 & 1 & 0 & 0 \end{pmatrix}^T \tag{6.5}$$

$$|10\rangle = |1\rangle \otimes |0\rangle = \begin{pmatrix} 0 & 0 & 1 & 0 \end{pmatrix}^T \tag{6.6}$$

$$|11\rangle = |1\rangle \otimes |1\rangle = \begin{pmatrix} 0 & 0 & 0 & 1 \end{pmatrix}^T \tag{6.7}$$

The same quantum state preparation procedure applies for qubit blocks with sizes ranging from $k = 3$ to $k = 8$. In general, a block of k classical bits can be mapped to a quantum state within a Hilbert space of dimension 2^k. Using the tensor-product operation, multiple classical bits can be efficiently encoded into a single high-dimensional quantum state, enabling the system to scale smoothly for different qubit encoding sizes while maintaining compact representation of the data.

COUS Quantum Encoder: After preparing the multi-qubit states, the next step is to encode them into complex-valued quantum superposition states with phase information using the proposed COUS method. This is achieved by applying the COUS unitary gate to each qubit, as shown in (6.8).

$$G_{\text{COUS}} = \frac{1}{\sqrt{2}} \begin{bmatrix} 1 & i \\ i & 1 \end{bmatrix} \tag{6.8}$$

For a single qubit ($k = 1$), the action of the COUS gate on the computational basis states produces the following superpositions, as shown in (6.9) and (6.10).

$$\psi_0 = G_{\text{COUS}}|0\rangle = \frac{1}{\sqrt{2}}(|0\rangle + i|1\rangle) \tag{6.9}$$

$$\psi_1 = G_{\text{COUS}}|1\rangle = \frac{1}{\sqrt{2}}(i|0\rangle + |1\rangle) \tag{6.10}$$

In photonic systems, the computational basis $\{|0\rangle, |1\rangle\}$ is equivalent to the linear polarisation basis $\{|H\rangle, |V\rangle\}$, while circular polarisation states are defined as in (6.11).

$$|R\rangle = \frac{1}{\sqrt{2}}(|H\rangle + i|V\rangle), \quad |L\rangle = \frac{1}{\sqrt{2}}(|H\rangle - i|V\rangle) \tag{6.11}$$

By identifying $|0\rangle \equiv |H\rangle$ and $|1\rangle \equiv |V\rangle$, it follows as shown in (6.12), where the factor i represents a global phase and does not affect physical observables.

$$G_{\text{COUS}}|0\rangle = |R\rangle, \quad G_{\text{COUS}}|1\rangle = i|L\rangle, \tag{6.12}$$

Therefore, the COUS transformation maps the computational basis to the circular

polarisation basis up to a global phase, consistent with standard linear-to-circular polarisation transformations in quantum optics [225]. Furthermore, the resulting states are properly normalised, satisfying the following condition, as shown in (6.13).

$$\left|\frac{1}{\sqrt{2}}\right|^2 + \left|\frac{i}{\sqrt{2}}\right|^2 = 1 \tag{6.13}$$

For multi-qubit blocks of size k, the overall COUS operation is obtained by taking the tensor product of k individual COUS gates, as given in (6.14).

$$G_{\text{COUS}}^{(k)} = \bigotimes_{l=1}^{k} G_{\text{COUS}} \tag{6.14}$$

The COUS gate is unitary, satisfying the condition $G_{\text{COUS}}^{\dagger} G_{\text{COUS}} = I$, which ensures that the transformation preserves total probability and produces physically valid quantum states.

As an example, for a two-qubit system ($k = 2$), the overall COUS gate is obtained by taking the tensor product of two single-qubit COUS gates, as shown in (6.15).

$$G_{\text{COUS}}^{(2)} = G_{\text{COUS}} \otimes G_{\text{COUS}} = \frac{1}{2}\begin{bmatrix} 1 & i & i & -1 \\ i & 1 & -1 & i \\ i & -1 & 1 & i \\ -1 & i & i & 1 \end{bmatrix} \tag{6.15}$$

The matrix in (6.15) acts on the two-qubit computational basis states $\{|00\rangle, |01\rangle, |10\rangle, |11\rangle\}$ to produce complex-valued superposition states. The transformation of each basis vector is expressed in (6.16) to (6.19).

$$G_{\text{COUS}}^{(2)}|00\rangle = \frac{1}{2}\left(|00\rangle + i|01\rangle + i|10\rangle - |11\rangle\right) \tag{6.16}$$

$$G_{\text{COUS}}^{(2)}|01\rangle = \frac{1}{2}\left(i|00\rangle + |01\rangle - |10\rangle + i|11\rangle\right) \tag{6.17}$$

$$G_{\text{COUS}}^{(2)}|10\rangle = \frac{1}{2}\left(i|00\rangle - |01\rangle + |10\rangle + i|11\rangle\right) \tag{6.18}$$

$$G_{\text{COUS}}^{(2)}|11\rangle = \frac{1}{2}\left(-|00\rangle + i|01\rangle + i|10\rangle + |11\rangle\right) \tag{6.19}$$

Each of the resulting states is properly normalised and exhibits distinct complex phase

relationships among the basis states. This phase diversity increases the distinguishability of quantum states within the complex Hilbert space, enabling more reliable quantum information transmission under noisy channel conditions.

Quantum Channel

The quantum channel used in this section is the composite noise model defined in Chapter 3 Section 3.1 (Equations (3.6)–(3.14)). The channel combines bit-flip, phase-flip, depolarising, amplitude damping, and phase damping mechanisms in a probabilistic mixture whose total noise probability scales with channel SNR as $q_{\text{tot}} = \min(1, 1/(1 + 10^{\text{SNR}/10}))$. Individual channel probabilities are obtained by normalising independent uniform weights, ensuring a heterogeneous and physically realistic abstraction of quantum decoherence. The COUS-encoded states constructed in the preceding subsection are transmitted through this composite channel without modification to the noise model, and identical channel realisations are applied across all configurations evaluated below for fair comparison.

Quantum Decoder

At the receiver, the inverse COUS operation $G_{\text{COUS}}^{(k)\dagger}$ is applied to decode the received multi-qubit quantum states and recover the original computational basis states. The single-qubit inverse COUS gate, which corresponds to the Hermitian adjoint (conjugate transpose) of the forward COUS gate, is shown in (6.20).

$$G_{\text{COUS}}^{\dagger} = \frac{1}{\sqrt{2}} \begin{bmatrix} 1 & -i \\ -i & 1 \end{bmatrix} \tag{6.20}$$

For a k-qubit block, the overall inverse COUS operation is constructed through the tensor product of k single-qubit inverse gates, as expressed in (6.21), or equivalently by taking the Hermitian adjoint of the corresponding qubit size forward COUS gate.

$$G_{\text{COUS}}^{(k)\dagger} = \bigotimes_{l=1}^{k} G_{\text{COUS}}^{\dagger} \tag{6.21}$$

During transmission, noise and decoherence may distort the encoded quantum states. Therefore, prior to inverse decoding, a nearest-state mapping (minimum-distance)

procedure is performed to identify the most likely transmitted encoded state.

Let $\psi_r^{(k)}$ denote the received (noisy) 2^k-dimensional state vector and let $\{ G_{\text{COUS}}^{(k)}|x\rangle : x \in \{0,1\}^k \}$ denote the set of all possible COUS-encoded basis states. The estimated encoded state $\hat{\psi}^{(k)}$ is obtained as defined in (6.22).

$$\hat{\psi}^{(k)} \;=\; \arg \min_{x \in \{0,1\}^k} \left\| \psi_r^{(k)} - G_{\text{COUS}}^{(k)}|x\rangle \right\| \tag{6.22}$$

where $\| \cdot \|$ is the Euclidean norm in $\mathbb{C}^{2^k}$, the 2^k-dimensional complex Hilbert space corresponding to a k-qubit system.

The nearest-state decoding in (6.22) can be interpreted as a nearest-neighbour search in a high-dimensional Hilbert space, where each k-qubit input maps to one of 2^k valid constellation states. Due to channel noise, the received state is a perturbed version of the transmitted state, and decoding is performed by selecting the closest reference state in Euclidean distance, which is equivalent to maximum likelihood (ML) detection under Gaussian noise. Although this formulation uses the full state vector for analytical convenience, it corresponds to a physically realisable quantum state discrimination process, where the receiver performs measurements and selects the state with maximum overlap (fidelity) using projective measurements. The COUS encoding improves robustness by increasing constellation separation via joint amplitude-phase representation. However, since decoding requires comparison over 2^k candidate states, the complexity grows exponentially with the number of qubits; while this is tractable for small k considered in this work, reduced-complexity or approximate decoding strategies may be required for large-scale systems.

After selecting $\hat{\psi}^{(k)}$, the multi-qubit inverse COUS decoder, as represented in (6.21), is applied to reconstruct the recovered quantum state $|\phi_{\text{rec}}^{(k)}\rangle$, as shown in (6.23).

$$|\phi_{\text{rec}}^{(k)}\rangle \;=\; G_{\text{COUS}}^{(k)\dagger}\, \hat{\psi}^{(k)} \tag{6.23}$$

Finally, projective measurements [192] are performed on each qubit of the recovered multi-qubit state $|\phi_{\text{rec}}^{(k)}\rangle$ to obtain the corresponding classical bitstream. Mathematically, this can be expressed as in (6.24).

$$b_i \;=\; \text{Measure}\big(|\phi_{\text{rec}}^{(k)}\rangle_i\big), \qquad b_i \in \{0,1\},\; i = 1,\ldots,k, \tag{6.24}$$

Here, b_i denotes the i-th classical bit in the recovered bitstream, $|\phi_{\text{rec}}^{(k)}\rangle_i$ represents the i-th qubit of the recovered multi-qubit state, and Measure$(\cdot)$ denotes a projective measurement in the computational basis $\{|0\rangle, |1\rangle\}$. After quantum decoding, the recovered bitstreams are processed by the channel and source decoders to reconstruct the final image.

Benchmark System Implementations

To assess the performance of the proposed quantum transmission framework, three bandwidth-equivalent benchmark systems are considered: a state-of-the-art Hadamard-based quantum communication system proposed in Section 4.1, a QFT-based frequency-domain quantum communication system presented in Section 5.1, and a classical communication system employing BPSK modulation. Since a single qubit represents one bit of information, its bandwidth characteristics align directly with those of BPSK modulation, which also transmits one bit per symbol. This ensures that both the classical and quantum communication systems operate under identical effective bandwidth and data-rate constraints, enabling a fair performance comparison. Furthermore, BPSK modulation is selected due to its strong robustness under noisy channel conditions, whereas higher-order modulation schemes generally exhibit increased sensitivity to channel impairments and noise-induced transmission errors.

6.1.2 Results

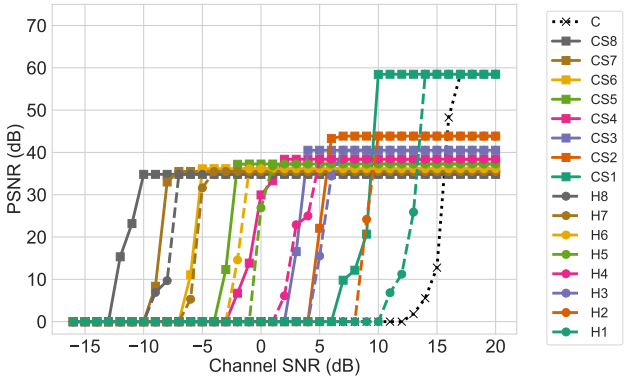
In this section, the performance of the proposed quantum communication system is evaluated and compared with the benchmark systems. The evaluation is carried out using key performance metrics including PSNR, SSIM, and UQI. The results demonstrate the impact of the proposed encoding strategy on transmission robustness and reconstructed image quality under different channel conditions. Throughout this section, the proposed COUS encoding schemes with qubit sizes 1–8 are denoted as CS1–CS8, the Hadamard-based benchmark systems with qubit sizes 1–8 are denoted as H1–H8, and the classical BPSK benchmark system is denoted as C.

The performance of the proposed system is first evaluated using JPEG-encoded images without additional channel coding. As illustrated in Figure 6.2, the proposed COUS-based encoding framework consistently outperforms both the Hadamard-based benchmark and the classical communication system across all considered performance metrics. Similar to the trend observed in Hadamard-based encoding, the performance of the proposed framework improves progressively as the number of qubits increases. Even the single-qubit configuration demonstrates a clear advantage, achieving approximately 4 dB channel SNR improvement relative to the Hadamard-based system. Higher-qubit configurations further enhance robustness against channel noise due to the improved separability of the encoded complex-valued quantum states.

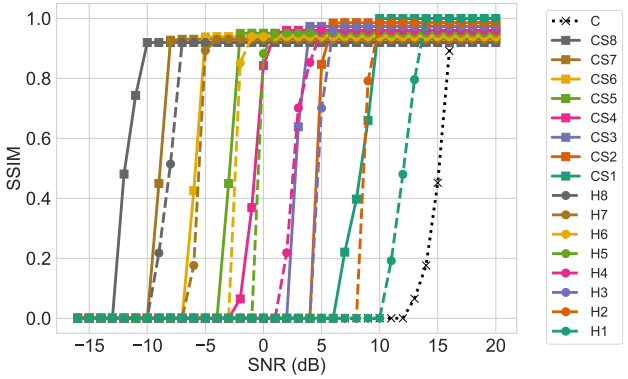
In contrast, the classical BPSK system exhibits the lowest performance, trailing the single-qubit Hadamard system by approximately 3 dB in terms of maximum tolerable channel SNR. Owing to the bandwidth normalisation process, higher-qubit configurations require stronger source compression, resulting in slightly lower peak PSNR, SSIM, and UQI values at high SNR conditions. Nevertheless, their significantly improved robustness under noisy conditions enables superior overall performance compared with lower-qubit and benchmark systems. These results demonstrate that the proposed complex-valued encoding strategy substantially improves both image fidelity and transmission robustness relative to existing quantum and classical benchmark approaches.

The proposed system is also evaluated using HEIF-encoded uncoded images, with the corresponding results presented in Figure 6.3. Similar trends to the JPEG scenario are observed. Increasing the number of qubits improves the transmission robustness and reconstructed image quality for both the proposed and Hadamard-based systems. The proposed single-qubit COUS configuration again provides an approximate 4 dB channel SNR improvement over the Hadamard-based benchmark, while the classical BPSK system remains significantly inferior under noisy conditions.

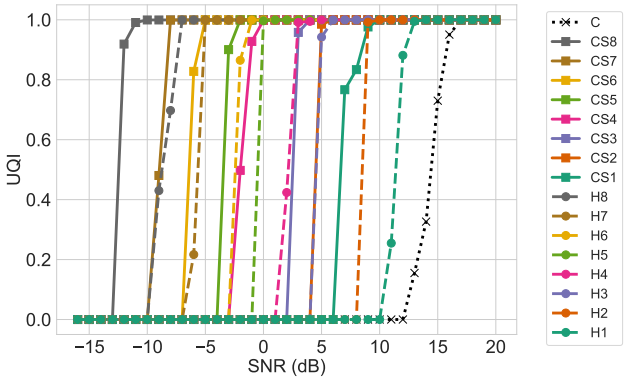
Furthermore, the HEIF-based systems achieve higher maximum PSNR, SSIM, and UQI values compared with JPEG-based systems due to the superior compression efficiency of the HEIF source coding framework. Despite the stronger compression introduced by bandwidth normalisation at higher qubit sizes, the proposed encoding method maintains strong resilience against channel noise and consistently outperforms



(a) JPEG Uncoded-PSNR



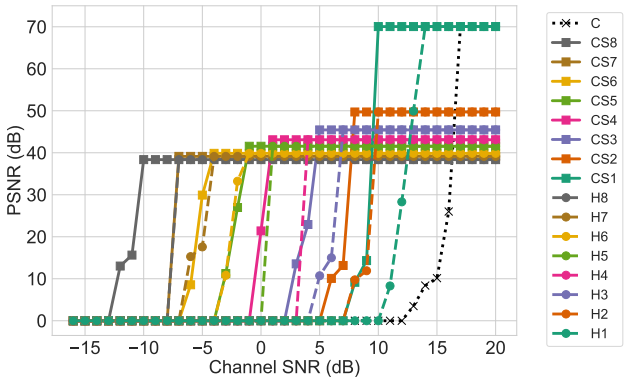
(b) JPEG Uncoded-SSIM



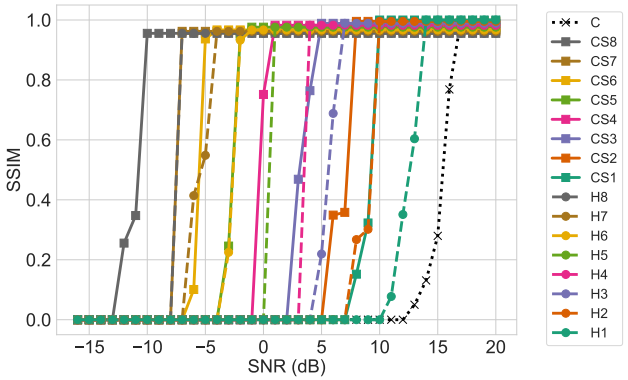
(c) JPEG Uncoded-UQI

Figure 6.2: Performance comparison of the proposed COUS-based quantum transmission system (CS1–CS8), the Hadamard-based encoding framework (H1–H8), and the classical BPSK system (C) for JPEG uncoded images.

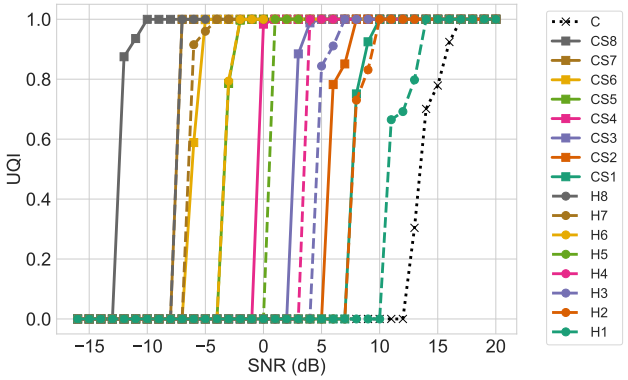
the benchmark systems.



(a) HEIF Uncoded-PSNR



(b) HEIF Uncoded-SSIM



(c) HEIF Uncoded-UQI

Figure 6.3: Performance comparison of the proposed COUS-based quantum transmission system (CS1–CS8), the Hadamard-based encoding framework (H1–H8), and the classical BPSK system (C) for HEIF uncoded images.

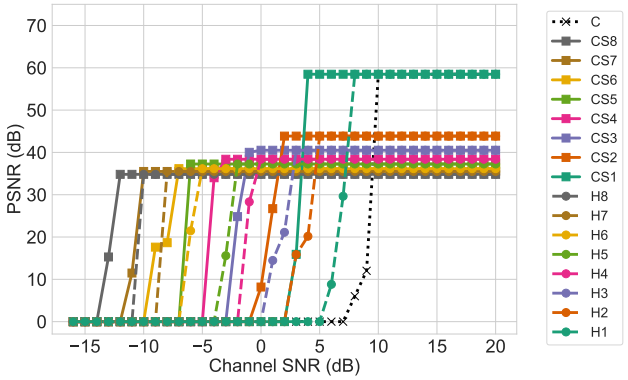
The proposed framework is further evaluated using rate-1/2 polar channel coding together with JPEG source coding. As illustrated in Figure 6.4, the incorporation of polar coding shifts the performance curves approximately 3–4 dB towards lower channel SNR regions for all systems, indicating substantial robustness improvements due to channel coding. The proposed COUS-based framework continues to outperform both the Hadamard-based and classical benchmark systems across all evaluated metrics.

The combined use of quantum encoding and classical channel coding significantly improves reconstructed image quality under severe channel conditions. Nevertheless, the relative performance differences between the proposed and benchmark systems remain similar to those observed in the uncoded scenario. This indicates that the primary performance advantage arises from the inherent properties of the proposed encoding strategy rather than solely from the additional error correction capability provided by polar coding.

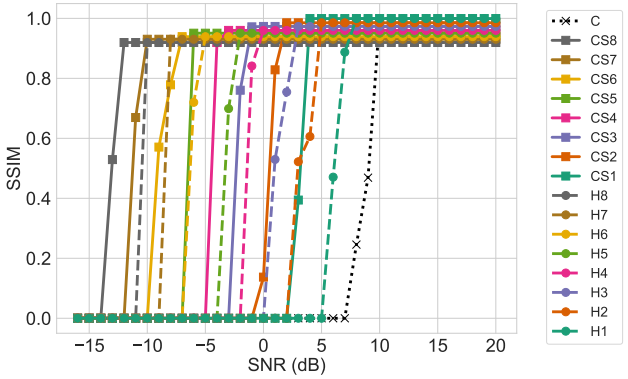
Finally, the proposed system is evaluated using HEIF source coding together with rate-1/2 polar channel coding. The corresponding results shown in Figure 6.5 demonstrate similar trends to the JPEG channel-coded scenario. Polar coding substantially improves transmission robustness for all systems, while the proposed COUS-based framework consistently achieves the highest PSNR, SSIM, and UQI values across the evaluated channel SNR range.

The HEIF-based channel-coded framework achieves the best overall performance due to the combined advantages of efficient source compression, robust channel coding, and the proposed complex-valued quantum encoding strategy. These results confirm that the proposed framework can provide strong robustness improvements while maintaining lower implementation complexity compared with transform-domain QFT-based systems.

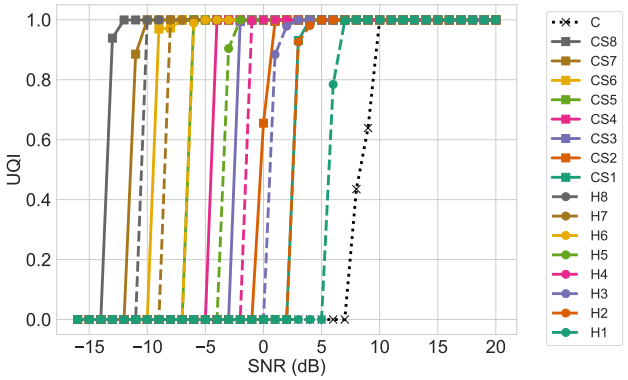
To ensure statistical reliability, a representative statistical summary of the results, averaged over all images and 1000 Monte Carlo runs, is provided in Table 6.1, where the standard deviation of PSNR, SSIM, and UQI is reported for uncoded JPEG images using the CS1 scheme. The observed variations are extremely small across all metrics, indicating strong stability of the proposed system. These results confirm that the reported averages are statistically robust and that the stochastic nature of the quantum noise model does not significantly affect the overall performance trends.



(a) JPEG Channel Coded-PSNR

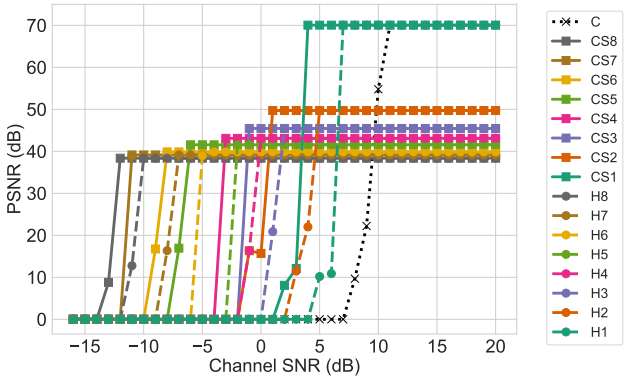


(b) JPEG Channel Coded-SSIM

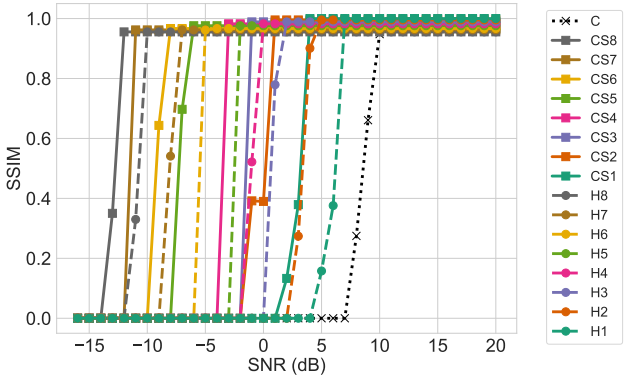


(c) JPEG Channel Coded-UQI

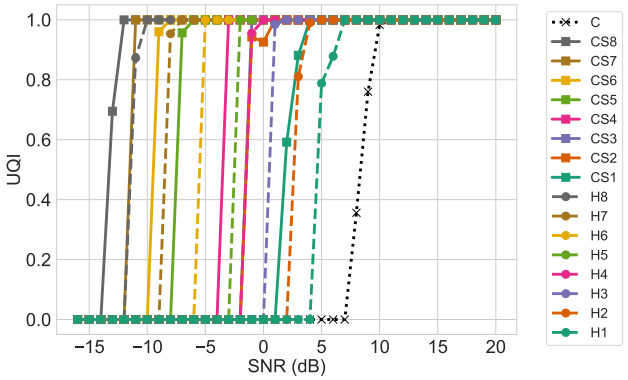
Figure 6.4: Performance comparison of the proposed COUS-based quantum transmission system (CS1–CS8), the Hadamard-based encoding framework (H1–H8), and the classical BPSK system (C) for JPEG images with rate-1/2 polar channel coding.



(a) HEIF Channel Coded-PSNR



(b) HEIF Channel Coded-SSIM



(c) HEIF Channel Coded-UQI

Figure 6.5: Performance comparison of the proposed COUS-based quantum transmission system (CS1–CS8), the Hadamard-based encoding framework (H1–H8), and the classical BPSK system (C) for HEIF images with rate-1/2 polar channel coding.

Table 6.1: Statistical summary of performance metrics for JPEG-based uncoded transmission for CS1.

SNR (dB)	**PSNR (dB)**	**SSIM**	**UQI**
11	58.48 ± 0.03	$0.99932 \pm 1 \times 10^{-5}$	$0.999998 \pm 1 \times 10^{-6}$
10	58.45 ± 0.03	$0.99931 \pm 1 \times 10^{-5}$	$0.999998 \pm 1 \times 10^{-6}$
9	20.69 ± 0.05	0.65988 ± 0.002	0.97613 ± 0.001
8	12.16 ± 0.06	0.39737 ± 0.003	0.83371 ± 0.002
7	9.79 ± 0.07	0.22056 ± 0.004	0.76675 ± 0.003

Robustness Advantages: The COUS encoding, defined as G_{COUS}, is a unitary operation and therefore preserves orthogonality of the encoded states. The encoded basis states satisfy the orthogonality and distance properties given in (6.25).

$$\langle \psi_0^{(k)} \mid \psi_1^{(k)} \rangle = 0, \quad \|\psi_0^{(k)} - \psi_1^{(k)}\|^2 = 2 \tag{6.25}$$

Here, $\psi_0^{(k)}, \psi_1^{(k)} \in \mathbb{C}^{2^k}$ denote encoded k-qubit quantum states, and $\| \cdot \|$ denotes the Euclidean norm. These properties are identical to those of Hadamard encoding, indicating that nominal distinguishability remains unchanged in the absence of noise.

Under noisy conditions, the received state $\psi_r^{(k)}$ in (6.22) can be modelled as in (6.26).

$$\psi_r^{(k)} = \psi^{(k)} + \eta^{(k)} \tag{6.26}$$

Here, $\psi^{(k)} \in \mathbb{C}^{2^k}$ is the transmitted state and $\eta^{(k)} \in \mathbb{C}^{2^k}$ represents complex noise. The decoding rule in (6.22) depends on the projection of noise onto the decision vector defined in (6.27).

$$\mathbf{d}^{(k)} = \psi_1^{(k)} - \psi_0^{(k)} \tag{6.27}$$

For the single-qubit case, the corresponding decision vectors for Hadamard and COUS encoding are given in (6.28) and (6.29), respectively.

$$\mathbf{d}_H = \frac{1}{\sqrt{2}} \begin{bmatrix} 0 \\ -2 \end{bmatrix} \tag{6.28}$$

$$\mathbf{d}_C = \frac{1}{\sqrt{2}} \begin{bmatrix} i-1 \\ 1-i \end{bmatrix} \tag{6.29}$$

The Hadamard decision vector lies entirely in the real subspace, whereas the COUS decision vector spans both real and imaginary components. The decoding process depends on the projection of noise onto the decision vector, given by (6.30).

$$\Re\{\eta^{\dagger}\mathbf{d}\} \tag{6.30}$$

Here, $(\cdot)^{\dagger}$ denotes the Hermitian transpose, and $\Re\{\cdot\}$ denotes the real part. In COUS encoding, the decision vector spans both real and imaginary dimensions in $\mathbb{C}^{2^k}$, whereas Hadamard encoding is confined to a real subspace. As a result, noise is distributed across multiple dimensions in COUS, reducing the likelihood of strong alignment with the decision boundary. This improves the robustness of the decoding regions defined by (6.22). Therefore, the observed performance gains arise from enhanced noise resilience due to amplitude-phase representation, rather than increased intrinsic separability.

Based on the results, the COUS encoding achieves outstanding performance by exploiting both phase encoding and the energy-preserving characteristics of unitary transformations. By simultaneously encoding information in amplitude and phase, COUS encoding distributes image data across multiple orthogonal components in the complex Hilbert space, making it inherently robust against noise and channel distortions. The COUS encoded states physically correspond to circular polarisation states, right-handed ($|R\rangle$) and left-handed ($|L\rangle$), which serve as the encoding basis. This allows each qubit to carry more information than linear polarisation alone, as the phase component introduces additional degrees of freedom. The approach preserves orthogonality and energy, ensuring that the overall probability amplitude remains normalised and that high fidelity is maintained even under severe channel impairments.

Moreover, the dual encoding in amplitude and phase introduces intrinsic redundancy without requiring extra qubits, improving both efficiency and error resilience. This redundancy allows partial recovery of information even when some qubit components are degraded by noise, enhancing the robustness of the transmission. COUS encoding also achieves high distinguishability between quantum states, which is critical for accurate decoding and reducing the probability of misidentification. In contrast, Hadamard encoding operates solely in the linear polarisation basis, horizontal ($|H\rangle$) and vertical ($|V\rangle$), using only real-valued amplitudes without phase information. This limits both the

information per qubit and the separation between states, reducing robustness against channel noise and decoding accuracy.

To further validate the proposed method, Table 6.2 presents the channel SNR gains compared with the classical system for both COUS and Hadamard-based encoding in the JPEG uncoded and channel-coded system. The results are reported for both standard 256×192 resolution images and high-resolution 4K images, covering multiple multi-qubit configurations. Across all tested scenarios, COUS consistently outperforms Hadamard-based encoding, demonstrating higher SNR gains and indicating superior robustness against channel noise and distortions. The observed improvements are attributed to COUS's ability to encode information in both amplitude and phase, which increases the effective separability of quantum states and enhances error resilience.

Additionally, the performance trends are consistent across different qubit configurations, indicating that the COUS scheme scales effectively with the number of qubits and maintains similar SNR gains regardless of image resolution, as the proposed encoding operates at the bitstream level. This demonstrates that COUS not only improves fidelity for conventional image resolutions but also retains robustness and high distinguishability for ultra-high-definition (4K) content, which is more susceptible to noise due to the larger information content. These results empirically confirm the advantages of COUS over Hadamard-based encoding, supporting its effectiveness as a reliable and scalable solution for high-fidelity quantum image transmission.

Table 6.2: Maximum SNR gains of COUS (CS1–CS8) and Hadamard (H1–H8) encoding schemes over the classical communication (C) system for JPEG images.

Type	**Resolution**	**COUS (CS1–CS8)**								**Hadamard (H1–H8)**							
		CS1	CS2	CS3	CS4	CS5	CS6	CS7	CS8	H1	H2	H3	H4	H5	H6	H7	H8
Uncoded	256×192	7.0	10.0	12.0	14.0	16.0	19.0	21.0	23.0	3.0	6.0	8.0	10.0	12.0	15.0	17.0	19.0
	4K	7.0	10.0	12.0	14.0	16.0	19.0	21.0	23.0	3.0	6.0	8.0	10.0	12.0	15.0	17.0	19.0
Channel-Coded	256×192	7.0	10.0	12.0	14.0	16.0	19.0	21.0	23.0	3.0	6.0	8.0	10.0	12.0	15.0	17.0	19.0
	4K	7.0	10.0	12.0	14.0	16.0	19.0	21.0	23.0	3.0	6.0	8.0	10.0	12.0	15.0	17.0	19.0

Furthermore, the results are compared with an advanced QFT-based frequency-domain encoding scheme for further validation, as shown in Table 6.3. Importantly, the proposed COUS framework achieves comparable and, in several configurations, superior SNR gains compared with the QFT-based framework despite operating entirely within the time domain. For low and intermediate-qubit configurations, COUS consistently outperforms the QFT-based approach, while at higher qubit dimensions its performance

remains nearly identical, differing by only approximately 1 dB at the largest qubit sizes. These results indicate that the robustness gains previously attributed to frequency-domain QFT processing can instead be achieved through carefully designed amplitude–phase encoding directly within the time domain. Unlike the QFT-based framework, which requires $\mathcal{O}(k^2)$ controlled phase-gate operations and increased circuit depth, the proposed COUS framework achieves these robustness gains with substantially lower computational complexity using only $\mathcal{O}(k)$ encoding operations. Consequently, COUS provides a more computationally efficient and practically scalable solution while maintaining robustness performance comparable to or better than the frequency-domain QFT-based framework.

Table 6.3: Comparison of SNR gains (dB) under identical system conditions compared with classical baseline.

Scheme	**Qubit Size**							
	1	2	3	4	5	6	7	8
Frequency Domain (QFT)	4.0	8.0	12.0	14.0	16.0	20.0	21.0	24.0
Hadamard	3.0	6.0	8.0	10.0	12.0	15.0	17.0	19.0
COUS (Proposed)	7.0	10.0	12.0	14.0	16.0	19.0	21.0	23.0

Hardware Feasibility and Complexity Analysis: The COUS gate, $G_{\text{COUS}} = S \cdot H \cdot S$, can be implemented using standard single-qubit gates, where H is the Hadamard gate and S is the phase gate. The full derivation is provided in Appendix B. In multi-qubit systems, COUS is applied independently to each qubit, allowing parallel execution across all qubits. All gates in this decomposition are native to most quantum platforms, including superconducting qubits, trapped ions, and photonic systems, making the COUS gate feasible for future hardware. It is important to note that the COUS operation is a composition of standard quantum gates and does not represent a new fundamental quantum gate. Instead, its contribution lies in its use as a structured encoding strategy that enables enhanced amplitude-phase representation for improved robustness in quantum communication systems.

From a computational perspective, the proposed COUS encoding requires three single-qubit gates per qubit, resulting in a total gate count of $3k$ for a k-qubit system. Therefore, the gate complexity scales linearly as $O(k)$, while the circuit depth remains

Table 6.4: Complexity and runtime comparison between COUS and Hadamard encoding.

Qubits (k)	**State (2^k**	**COUS Encoding**				**Hadamard Encoding**			
		Runtime (s)	**Memory (KB)**	**Gates ($3k$)**	**Depth**	**Runtime (s)**	**Memory (KB)**	**Gates (k)**	**Depth**
1	2	0.13	1.2	3	const	0.12	1.2	1	const
2	4	0.17	1.5	6	const	0.15	1.5	2	const
3	8	0.22	2.0	9	const	0.19	2.0	3	const
4	16	0.29	3.2	12	const	0.25	3.2	4	const
5	32	0.39	5.0	15	const	0.34	5.0	5	const
6	64	0.55	8.5	18	const	0.48	8.5	6	const
7	128	0.81	15.8	21	const	0.72	15.8	7	const
8	256	1.18	30.4	24	const	1.05	30.4	8	const

constant $O(1)$ due to the parallel application of single-qubit operations. In comparison, the Hadamard-based encoding requires only a single gate per qubit, leading to a total of k gates with the same $O(k)$ complexity and $O(1)$ depth. Although COUS employs a higher number of gates, it provides enhanced noise resilience and improved fidelity due to its ability to encode both amplitude and phase information.

The practical computational cost of the simulation is summarised in Table 6.4, which reports runtime, memory usage, number of quantum gates, and circuit depth for qubit sizes ranging from 1 to 8. Both encoding schemes exhibit identical memory requirements, as they rely on a representation of a 2^k-dimensional quantum state, resulting in an exponential memory complexity of $\mathcal{O}(2^k)$. The minimum-distance decoding employed in (6.22) involves evaluating distances to all 2^k candidate states, each defined in a 2^k-dimensional Hilbert space. As a result, the decoding complexity scales as $\mathcal{O}(2^k \cdot 2^k) = \mathcal{O}(4^k)$ under exhaustive search. However, for the considered system with $k \leq 8$, this corresponds to at most 256 candidate states, and the resulting computational cost remains tractable, as confirmed by the runtime analysis in Table 6.4. Furthermore, the decoding process is inherently parallelisable, enabling efficient implementation within the targeted system scale. While the COUS scheme introduces a slight runtime overhead compared with the Hadamard approach, this increase remains marginal across all qubit sizes. Overall, the results demonstrate that the proposed COUS encoding maintains manageable computational complexity with linear gate scaling and constant circuit depth, while the dominant cost arises from the inherent exponential nature of classical quantum simulation. This confirms the practical feasibility and scalability of the proposed framework, making it suitable for early-stage evaluation of multi-qubit quantum communication systems.

Scalability, Comparative Analysis, and Potential Applications: The system achieves efficient scalability through linear gate count, constant circuit depth, and parallel operations, enabling extension to higher qubit counts for high-resolution quantum communication, while maintaining low execution time; although decoding complexity grows exponentially, it is mitigated using structured constellations and efficient approximate strategies. However, COUS utilises both amplitude and phase components, resulting in a more expressive state representation compared with the purely amplitude-based Hadamard scheme. This enhanced representation improves robustness under stochastic noise conditions and leads to better performance in terms of PSNR, SSIM, and UQI, with only a marginal increase in computational overhead. A concise comparison of the two approaches is provided in Table 6.5.

Table 6.5: Comparison between COUS and Hadamard encoding schemes.

Aspect	**COUS Encoding**	**Hadamard Encoding**
Information Representation	Uses both amplitude and phase components	Uses amplitude superposition only
State Structure	Complex-valued unitary superposition states	Real-valued superposition states
Constellation Representation	Complex-valued constellation in $\mathbb{C}^{2^k}$	Real-valued constellation in $\mathbb{R}^{2^k}$
Noise Behaviour	Improved tolerance under certain noise conditions due to amplitude-phase representation	More sensitive to phase-related perturbations due to real-valued structure
Decoding Behaviour	Nearest-state decoding in complex Hilbert space	Nearest-state decoding in real subspace
Multi-Qubit Representation	Information distributed across amplitude and phase dimensions	Information represented primarily through amplitude superposition
Gate Count	$3k$ (linear complexity)	k (linear complexity)
Circuit Depth	$O(1)$ (parallel implementation)	$O(1)$ (parallel implementation)
Computational Complexity	$O(k)$ (encoding), dominated by $O(2^k)$ simulation	Same $O(k)$, dominated by $O(2^k)$ simulation
Decoding Complexity	$\mathcal{O}(4^k)$ (exhaustive search in 2^k-dimensional space)	$\mathcal{O}(4^k)$ (exhaustive search in 2^k-dimensional space)
Runtime Impact	Slightly higher due to additional gates	Lower
Performance (Observed)	Higher PSNR, SSIM, and UQI under evaluated stochastic noise conditions	Lower performance under the same experimental conditions

Potential Real-Time Applications: If supported by future large-scale quantum communication infrastructure, the proposed COUS framework could enable a range of real-time multimedia applications requiring reliable and low-latency image and video transmission. Potential applications include live video streaming, telemedicine, remote robotic operation, autonomous vehicles, immersive virtual and augmented

reality, industrial monitoring, and emergency response systems, where both transmission efficiency and resilience to channel impairments are essential. The low-complexity quantum encoding employed by the proposed framework makes it well suited for latency-sensitive multimedia communication, while future advances in quantum processors, quantum networking, and fault-tolerant technologies are expected to facilitate practical deployment in these application domains.

Simulation-Based Nature: Quantum communication is still in its early stages, with practical implementations limited by hardware availability, qubit coherence times, and gate fidelity. Consequently, the performance evaluation in this study is conducted using classical simulations that model standard quantum gate operations and noise effects. Classical simulation is both valid and widely accepted because it faithfully implements the mathematical framework of quantum mechanics, including unitary operations, superposition, and density-matrix-based noise channels [209]. This approach enables systematic testing across various channel conditions, qubit configurations, and noise levels, allowing for quantitative evaluation of performance metrics such as fidelity, robustness, and scalability. Moreover, simulation provides a controlled and reproducible environment to explore novel multi-qubit encoding strategies, such as COUS, without the constraints of current hardware limitations. While hardware-based experiments are ultimately necessary for full validation, simulation-based studies represent a standard and crucial first step for developing and validating novel quantum communication frameworks, offering critical insights that guide future experimental implementations.

Implications for Practical Quantum Hardware: The performance reported in this section is obtained under a simulation framework that assumes ideal quantum gate operations, accurate state preparation, and the composite quantum channel model described in Chapter 3. To achieve comparable performance on practical quantum hardware, several physical requirements are important. First, high single-qubit gate fidelity is required to ensure that the implemented COUS encoding closely matches the intended unitary transformation, thereby limiting the accumulation of operational errors during state preparation and decoding. Second, the coherence time of the physical qubits should exceed the total execution time of the encoding, transmission, and decoding

operations so that quantum coherence is preserved throughout the communication process. Third, hardware-level error sources, including gate imperfections, measurement errors, qubit relaxation, and dephasing, should remain sufficiently low to prevent significant degradation of the encoded quantum states. Since the proposed COUS framework employs only native single-qubit gate operations with constant circuit depth, the overall execution time is shorter than that of transform-domain approaches requiring deeper quantum circuits. Consequently, the proposed framework is expected to be less susceptible to cumulative gate errors and decoherence, making it well suited for implementation on NISQ devices. Nevertheless, experimental validation on emerging quantum hardware remains an important direction for future work to quantify the impact of practical hardware imperfections on the proposed communication framework.

6.1.3 Section Summary

This work presented a COUS-based quantum encoding framework for high-fidelity image transmission over noisy communication channels. The experimental results demonstrated that the proposed framework consistently outperformed conventional Hadamard-based quantum systems and classical BPSK communication systems across all evaluated SNR conditions and qubit configurations. In particular, the single-qubit COUS configuration surpassed the advanced QFT-based frequency-domain framework by approximately 4 dB in channel SNR, while higher-qubit COUS configurations achieved comparable transmission performance. The observed performance improvements resulted from the joint exploitation of amplitude and phase diversity, which enhanced the separability and robustness of the encoded quantum states under noisy channel conditions. Consequently, the proposed framework achieved improved decoding reliability and superior reconstructed image quality in terms of PSNR, SSIM, and UQI performance metrics. Importantly, these robustness gains were achieved without increasing circuit depth, while maintaining linear gate complexity with respect to the number of qubits. Furthermore, the proposed framework avoided the transform-domain processing overhead associated with QFT-based systems, resulting in significantly reduced implementation complexity. The proposed system remained computationally tractable within the evaluated range ($k \leq 8$), where the decoding process involved at most $2^8 = 256$ candidate states. Run-

time analysis further confirmed the practical feasibility of the framework, with execution time increasing from approximately 0.13 s to 1.18 s as the qubit size increased.

6.2 A Complex-Valued Orthogonal Unitary Superposition Encoding-Based Multi-Qubit System for Quantum Video Transmission

Publication Notice

The research presented in this section has been published in the following peer-reviewed journal publication:

U. Jayasinghe and A. Fernando, "Complex-valued unitary superposition-driven multi-qubit encoding for quantum video transmission," *Electronics*, vol. 15, no. 9, art. no. 1906, 2025, doi: 10.3390/electronics15091906.

This material is reproduced and adapted under the terms of the MDPI Copyright policy for use in a doctoral thesis. The content has been revised and extended with additional explanations and expanded discussion.

Problem Statement: Section 6.1 established that COUS encoding delivers superior image-transmission robustness compared with Hadamard-based multi-qubit encoding and QFT-based systems at low and intermediate-qubit configurations, while achieving performance comparable to advanced QFT-based frequency-domain systems at higher qubit sizes. These performance gains are achieved through the joint exploitation of amplitude–phase diversity within the encoded quantum states. Video transmission, however, represents a significantly more challenging scenario than still-image transmission. Compressed video bitstreams are substantially larger, exhibit strong temporal dependencies between inter-coded frames within a GOP, and are highly susceptible to error propagation when even a small number of corrupted bits occur early in the GOP structure. Consequently, transmission errors can propagate across multiple subsequent frames, severely degrading overall video quality. Although the COUS framework presented in Section 6.1 demonstrated strong robustness for image transmission, its performance has not yet been investigated under the temporal-correlation characteristics

and error-propagation behaviour associated with practical video compression systems. Furthermore, the interaction between COUS-based encoding robustness and the GOP-dependent transmission characteristics of modern video codecs remains unexplored.

Limitations of Existing Work: Quantum video communication studies, including the time-domain framework presented in Chapter 4, Section 4.2, and the frequency-domain framework presented in Chapter 5, Section 5.2, have primarily evaluated encoding strategies in terms of per-symbol transmission robustness. However, to the best of the author's knowledge, no prior work has applied complex-valued orthogonal unitary superposition encoding to quantum video transmission, nor systematically investigated how amplitude–phase diversity at the encoding stage can mitigate the compounded effects of inter-frame error propagation. Consequently, the trade-off between encoding-side robustness improvements and temporally accumulated error sensitivity remains largely unexplored in the existing quantum video communication literature.

Motivation and Proposed Contribution: Although the COUS framework presented in Section 6.1 demonstrated strong robustness improvements for quantum image transmission, it remains unclear whether these advantages can be maintained in practical video transmission scenarios, where temporal dependencies and GOP-based error propagation significantly amplify the impact of channel errors. To address this limitation, this section extends the COUS encoding framework of Section 6.1 to end-to-end quantum video transmission. Compressed video bitstreams generated using the VVC standard under multiple GOP configurations, frame rates, and spatial resolutions are protected using rate-1/2 polar channel coding and subsequently mapped into COUS-based multi-qubit superposition states for transmission over the composite quantum noise channel. At the receiver, inverse COUS decoding, polar decoding, and VVC reconstruction are performed to recover the transmitted video sequence. Performance is benchmarked against the Hadamard-based multi-qubit quantum video framework presented in Chapter 4, Section 4.2, the frequency-domain framework presented in Chapter 5, Section 5.2, and a classical BPSK communication system. The primary objective is to investigate whether the amplitude–phase diversity introduced by COUS encoding can effectively mitigate temporally propagated transmission errors in compressed

video systems while maintaining lower implementation complexity than QFT-based frequency-domain approaches.

6.2.1 System Model

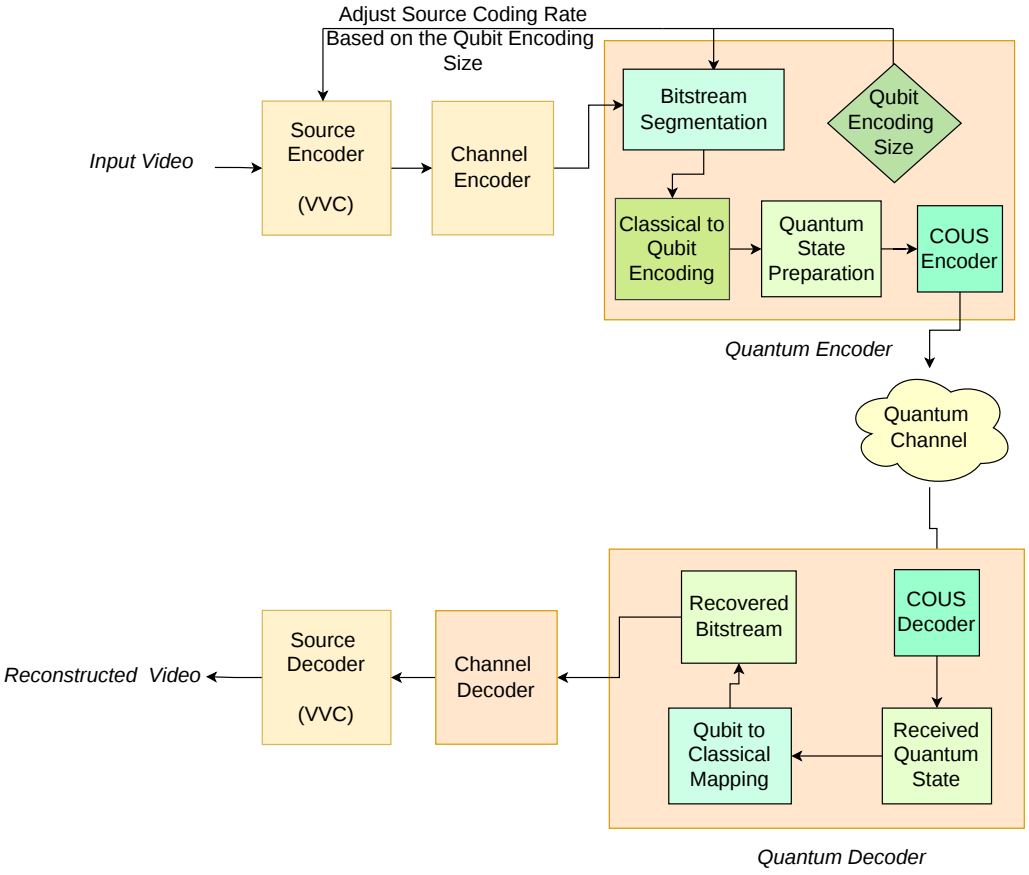


Figure 6.6: Block diagram illustrating the proposed COUS-driven multi-qubit framework optimised for quantum video delivery.

The communication architecture illustrated in Figure 6.6 is derived directly from the image-transmission framework introduced in Section 6.1, with the only major modification being the replacement of the compressed image source by a compressed video bitstream. All remaining functional blocks are retained from the earlier framework, including the quantum encoder, the composite quantum-noise environment presented in Section 6.1, the quantum decoding process incorporating inverse COUS operations, minimum-distance detection, and projective measurement, as well as the

benchmark transmission schemes based on classical BPSK with rate-1/2 polar coding, Hadamard-based multi-qubit encoding, and QFT-assisted transmission. The same bandwidth-normalisation methodology across varying qubit dimensions is also preserved; consequently, the mathematical derivations and architectural details previously introduced in Section 6.1 are not repeated here.

To ensure a comprehensive performance evaluation under diverse multimedia conditions, three YUV420 VVC video sequences representing different levels of spatial and temporal complexity are selected. These comprise a high-motion sequence [205], characterised by rapid movement and frequent scene transitions; a medium-motion sequence [206], exhibiting moderate temporal activity and intermediate scene complexity; and a low-motion sequence [207], characterised by relatively limited motion while preserving meaningful structural content. Each sequence is evaluated at resolutions of 320×180, 1280×720, and 1920×1080, frame rates of 20, 30, and 50 fps, and GOP sizes of 8, 16, and 32. Through the combination of different motion characteristics, spatial resolutions, frame rates, and GOP structures, a representative range of practical video transmission scenarios is covered, enabling a comprehensive assessment of the proposed framework under diverse multimedia conditions.

The full simulation configuration adopted throughout the video-transmission evaluation is summarised in Table 6.6.

Table 6.6: Simulation parameters adopted for evaluating the proposed COUS-based multi-qubit video-transmission framework.

Parameter	**Value**
Video Resolutions	320×180, 1280×720, 1920×1080
Frame Rates	30, 50, 60 fps
GOP Sizes	8, 16, 32
SNR Range	20 dB to -16 dB, step size 1 dB
Number of Trials	1,000 independent trials per video
Video Characteristics	High motion, medium motion, low motion
Hardware	Intel Core i5-1345U CPU (1.60 GHz), 16 GB RAM
Simulation Environment	Python 3.10

6.2.2 Results

This section presents a comprehensive evaluation of the proposed COUS-based multi-qubit video-transmission framework under a wide range of communication settings and channel conditions. The analysis focuses on the influence of COUS-based encoding on reconstruction quality, transmission robustness, and resilience against channel impairments. To ensure statistical reliability, 1000 independent transmission trials are performed for each video sequence. The reported performance metrics correspond to the average values obtained across all trials, frame rates, and spatial resolutions considered for each video category. Statistical analysis of the obtained results revealed only minor variation between repeated simulations, with standard deviations generally remaining below 0.5 for VMAF, 0.003 for SSIM, and 0.15 dB for PSNR. Since these variations are negligible compared with the overall performance improvements achieved by the proposed framework, error bars and confidence intervals are omitted in the presented figures to maintain visual clarity. Performance improvements are quantified using the channel SNR gain metric, defined as the difference between the SNR required by the benchmark transmission system and the SNR required by the corresponding quantum framework to achieve the same reconstruction quality level.

The performance of the proposed COUS-based multi-qubit framework under the GOP8 configuration is evaluated using PSNR, SSIM, and VMAF metrics, with the corresponding results presented in Figure 6.7. The obtained results demonstrate a clear and consistent performance advantage over both the classical communication baseline (C) and the Hadamard-based multi-qubit framework (H) across the entire investigated SNR range. Even under the single-qubit configuration, the proposed COUS-based system (CS1) achieves noticeable improvements, providing an approximate 4 dB channel SNR gain relative to the corresponding Hadamard-based configuration (H1) while simultaneously delivering higher PSNR, improved SSIM, and better perceptual quality according to the VMAF metric. Increasing the qubit dimension further strengthens performance, indicating that higher-dimensional COUS encoding improves robustness against channel impairments and maintains more reliable frame reconstruction in the presence of transmission errors.

Although the bandwidth-equalisation process requires stronger source compression

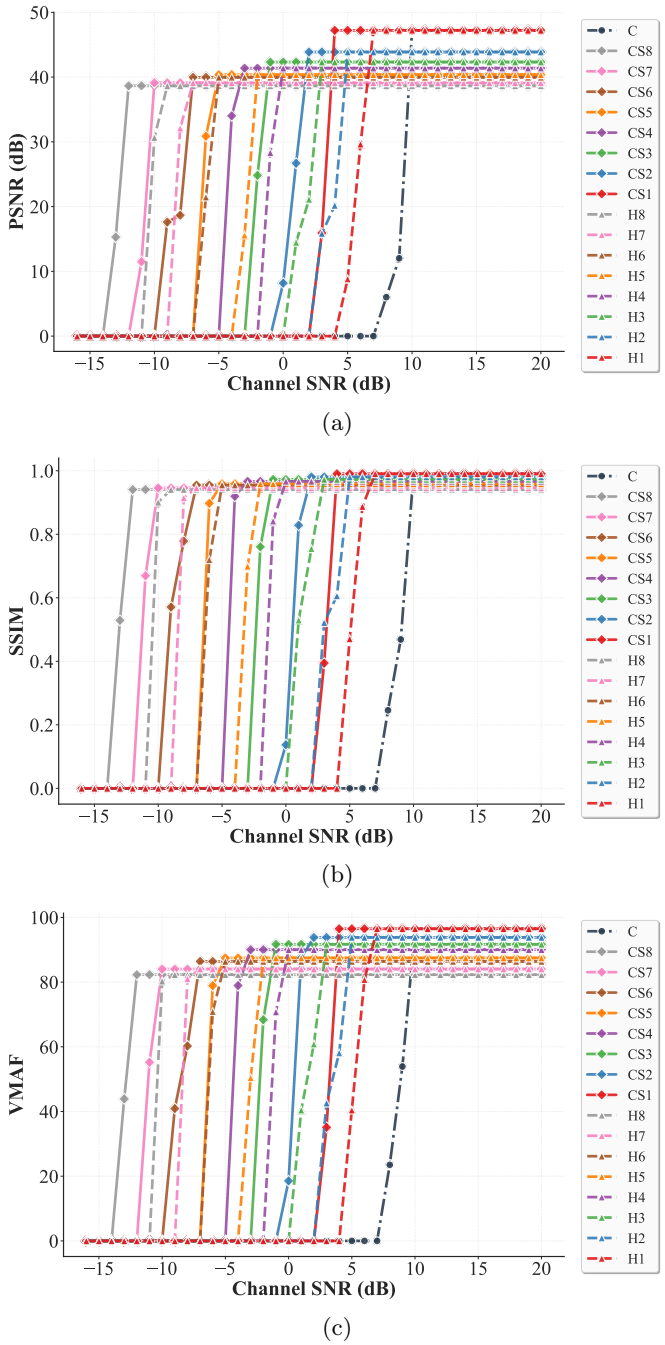
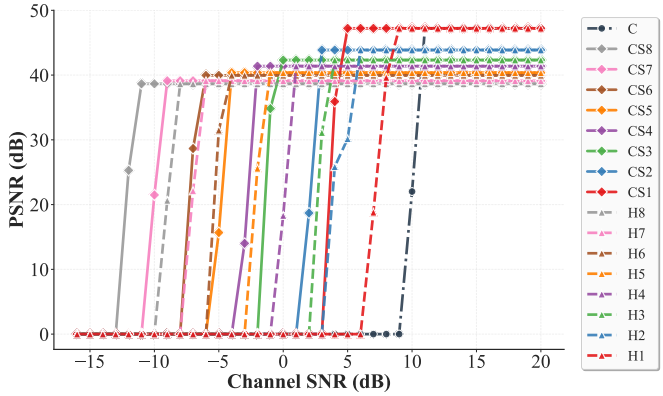


Figure 6.7: Analytical evaluation of video reconstruction fidelity across the classical (C), Hadamard (H1–H8), and COUS (CS1–CS8) setups utilising a GOP8 framework.

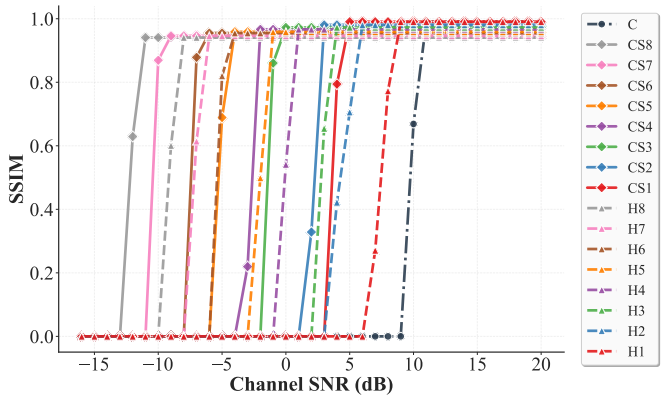
for larger qubit dimensions, which introduces a slight reduction in peak quality under high-SNR conditions, the higher-dimensional COUS configurations continue to outperform both the lower-dimensional and benchmark systems throughout low and moderate-SNR operating regions. In contrast, the classical communication framework (C) consistently records the lowest reconstruction quality across all evaluated metrics. The classical baseline also performs approximately 3 dB below the single-qubit Hadamard configuration (H1) in terms of channel SNR performance and exhibits noticeably weaker perceptual quality under noisy channel conditions. Overall, the GOP8 results confirm that the proposed COUS-based multi-qubit framework provides substantial improvements in reconstruction fidelity, structural preservation, and perceptual video quality, particularly under noise-dominated transmission conditions. These findings demonstrate the suitability of the proposed framework for robust quantum video-transmission applications.

Increasing the GOP size to 16 introduces stronger temporal dependencies between successive frames, thereby increasing the sensitivity of the transmission process to channel-induced errors, as illustrated in Figure 6.8. Despite this increase in temporal dependency, the overall performance behaviour remains consistent with the observations obtained for the GOP8 configuration. Across all evaluated SNR values, the proposed COUS-based multi-qubit framework (CS1–CS8) consistently outperforms both the classical communication baseline (C) and the corresponding Hadamard-based multi-qubit configurations (H1–H8). Even under the single-qubit setting, the COUS-based configuration (CS1) maintains an approximate 3–4 dB channel SNR advantage over the equivalent Hadamard-based framework (H1) while simultaneously achieving improved PSNR, SSIM, and VMAF performance. Increasing the qubit dimension further strengthens transmission robustness, allowing higher-dimensional COUS configurations to maintain stable reconstruction quality under increasingly noisy channel conditions. These improvements become particularly evident within low-SNR operating regions, where temporal error propagation significantly degrades the reconstruction quality of weaker transmission frameworks.

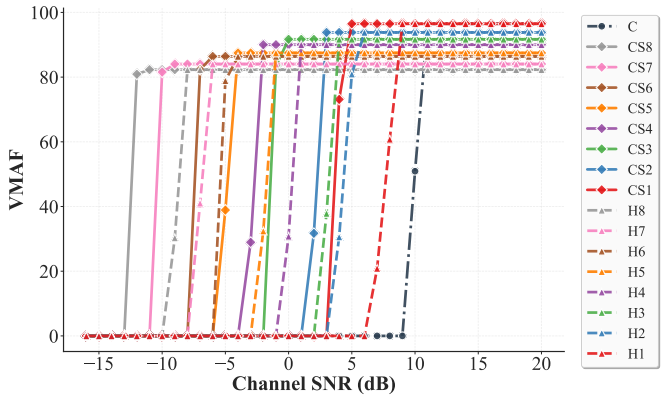
By comparison, the Hadamard-based multi-qubit configurations exhibit a more noticeable degradation in quality as the GOP size increases, indicating reduced resistance



(a)



(b)



(c)

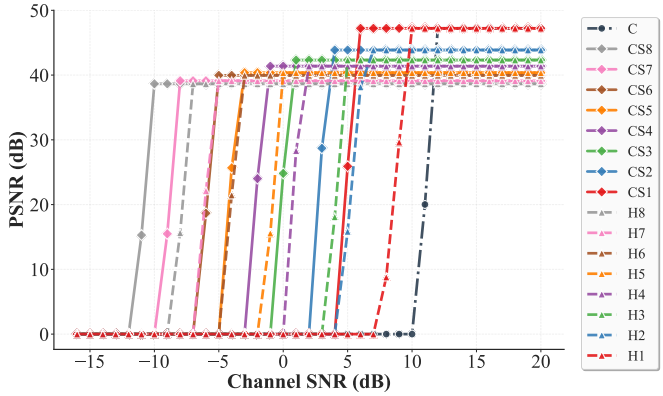
Figure 6.8: Analytical evaluation of video reconstruction fidelity across the classical (C), Hadamard (H1–H8), and COUS (CS1–CS8) setups utilising a GOP16 framework.

to accumulated temporal transmission errors. The classical baseline continues to produce the lowest performance across all investigated quality metrics and remains several decibels below even the lowest-dimensional quantum configurations, particularly under severe channel-noise conditions. Overall, the GOP16 evaluation confirms that the proposed COUS-based multi-qubit transmission framework effectively mitigates the impact of temporal error propagation associated with compressed video transmission. The consistently improved PSNR, SSIM, and VMAF performance demonstrates the scalability, robustness, and reliability of the proposed framework for quantum video communication under realistic noisy-channel environments.

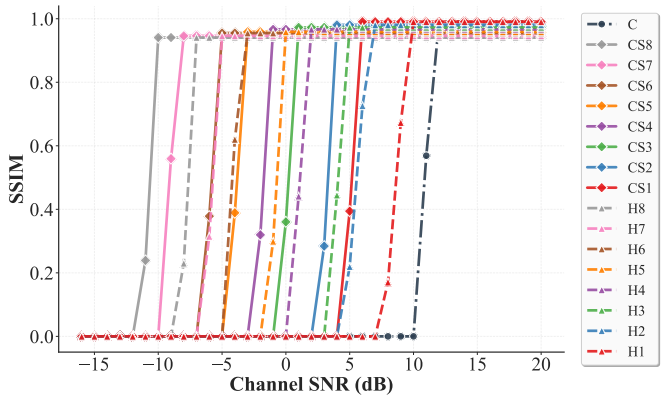
Operating with the largest evaluated GOP structure of 32 creates a significantly more challenging transmission environment because of the stronger temporal dependencies introduced by extended prediction chains, as shown in Figure 6.9. Under these conditions, the performance differences between the investigated transmission frameworks become increasingly pronounced. Across the entire SNR range, the proposed COUS-based multi-qubit configurations (CS1–CS8) maintain substantially greater stability than both the classical communication baseline and the corresponding Hadamard-based multi-qubit systems (H1–H8), preserving higher PSNR, SSIM, and VMAF performance even under severe channel degradation.

Higher-dimensional COUS configurations demonstrate particularly strong resistance to noise-induced distortion and significantly reduce the quality degradation commonly associated with long-GOP compressed video transmission. Although the stronger compression required for bandwidth equalisation introduces a slight reduction in peak reconstruction quality at high SNR values, the proposed COUS-based framework continues to provide superior perceptual and structural quality throughout moderate and low-SNR operating regions. By contrast, the classical transmission baseline experiences severe quality degradation under the same conditions because transmission errors propagate through the extended prediction chain of dependent frames.

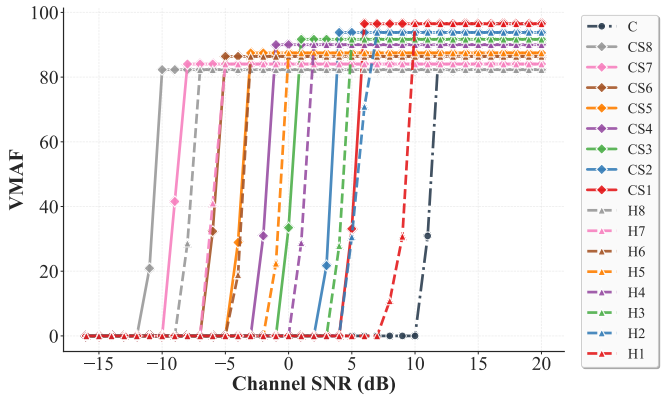
Across all evaluated GOP structures, the proposed COUS-based multi-qubit framework consistently outperforms both the classical benchmark and the Hadamard-based quantum configurations. The ability of the COUS encoding mechanism to represent information simultaneously through amplitude and phase components improves state



(a)



(b)



(c)

Figure 6.9: Analytical evaluation of video reconstruction fidelity across the classical (C), Hadamard (H1–H8), and COUS (CS1–CS8) setups utilising a GOP32 framework.

separability and strengthens robustness against channel impairments. Even lower-dimensional COUS configurations achieve noticeable performance gains, while larger qubit dimensions provide progressively stronger resilience under hostile transmission environments. These results confirm that the proposed framework achieves an effective balance between perceptual quality, transmission robustness, and compression efficiency, supporting its suitability for high-quality quantum video transmission over realistic noisy communication channels.

As the GOP size increases to 16 and 32, as illustrated in Figures 6.8 and 6.9, the influence of temporal dependency becomes increasingly significant. Larger GOP structures create longer prediction chains in which P-frames depend not only on the original I-frame but also on previously reconstructed inter-coded frames. Consequently, the transmitted video stream becomes more vulnerable to transmission-induced errors, since corruption affecting earlier frames propagates through subsequent predicted frames and generates cumulative visual artefacts such as blocking distortion, temporal flickering, and motion smearing. This progressive error propagation causes an overall reduction in reconstruction quality and requires increasingly higher SNR conditions to maintain acceptable visual fidelity.

Despite these more demanding transmission conditions, the proposed COUS-based multi-qubit framework continues to outperform both the classical and Hadamard-based transmission systems. Higher-dimensional COUS configurations further improve robustness by distributing encoded information across multiple qubits, thereby preserving more reliable reference-frame reconstruction and reducing the accumulation of errors throughout inter-coded video frames.

The obtained results demonstrate that the proposed COUS-based encoding framework significantly improves video reconstruction quality by jointly exploiting both the phase and amplitude properties of the quantum states. In contrast to the Hadamard-based approach, which primarily operates using linear polarisation states such as vertical $|V\rangle$ and horizontal $|H\rangle$ states associated with real-valued amplitudes, the COUS framework employs circular polarisation states, namely left-handed $|L\rangle$ and right-handed $|R\rangle$ states. This additional phase representation increases the information-carrying capability of each qubit and provides greater flexibility for quantum-state encoding. By

distributing the encoded video information across orthogonal quantum states within a complex Hilbert space, the proposed framework inherently improves robustness against channel impairments and transmission noise.

One of the principal advantages of the COUS-based encoding strategy is its unitary and energy-preserving structure, which ensures that the total probability amplitude remains normalised throughout transmission. This property plays an important role in maintaining stable reconstruction quality even under severe low-SNR conditions and hostile transmission environments. The simultaneous use of phase and amplitude information also introduces an inherent form of redundancy, allowing partially corrupted quantum states to retain recoverable information and thereby reducing the influence of localised transmission errors.

The proposed multi-qubit COUS framework further strengthens these advantages by distributing the encoded information across larger quantum-state dimensions. Increasing the qubit dimension improves the separability between encoded quantum states, reduces decoding ambiguity, and enhances the reliability of reconstructed reference frames. These improvements are reflected consistently through higher PSNR, SSIM, and VMAF performance, particularly within moderate and low-SNR operating regions where the classical communication framework and the Hadamard-based quantum configurations experience substantial quality degradation.

In addition, deriving a simple closed-form analytical relationship between perceptual quality metrics, channel SNR, and qubit dimension is difficult because of the highly nonlinear and multi-layered structure of the proposed communication framework. Nevertheless, several clear quantitative trends can still be observed from the simulation results. In particular, PSNR increases approximately logarithmically with increasing SNR, indicating diminishing performance improvements at very high SNR values. Increasing the qubit dimension also improves reconstruction quality through enhanced quantum-state representation; however, this improvement gradually approaches a saturation region as the representational capacity of the framework is reached. Similar saturation behaviour is observed for both SSIM and VMAF at larger qubit dimensions and high-SNR operating points. These trends remain consistent with established communication-theory behaviour and provide a clear quantitative interpretation of the

performance characteristics of the proposed framework without relying on oversimplified analytical approximations.

To provide additional validation of the proposed framework, Table 6.7 summarises the maximum channel SNR gains achieved by the Hadamard-based and COUS-based encoding approaches relative to the classical communication baseline for multiple video resolutions under the GOP8 configuration. For clarity and ease of interpretation, the reported SNR-gain values in Table 6.7 are rounded to the nearest integer value. This rounding does not affect the observed performance trends because the underlying statistical variations remain very small, typically within ≤ 0.3 dB, as further indicated in Table 6.8.

The evaluation includes full-HD (1920×1080), HD (1280×720), and low-resolution (320×180) video sequences. Across all investigated resolutions, the proposed COUS-based multi-qubit configurations (CS1–CS8) consistently outperform the corresponding Hadamard-based configurations (H1–H8), achieving larger channel SNR gains and demonstrating stronger robustness against transmission errors and channel impairments. The obtained results further indicate that the performance advantages provided by the proposed framework remain largely independent of the input video resolution, with similar gains observed across both high-resolution and low-resolution video content. This behaviour suggests that the proposed communication framework operates effectively irrespective of spatial video resolution.

Table 6.7: Maximum channel SNR gains achieved by the Hadamard-based (H1–H8) and COUS-based (CS1–CS8) multi-qubit frameworks relative to the classical communication baseline across different video resolutions.

Resolution	**COUS (CS1–CS8)**								**Hadamard (H1–H8)**							
	CS1	CS2	CS3	CS4	CS5	CS6	CS7	CS8	H1	H2	H3	H4	H5	H6	H7	H8
320×180	7.0	10.0	12.0	14.0	16.0	19.0	21.0	23.0	3.0	6.0	8.0	10.0	12.0	15.0	17.0	19.0
1280×720	7.0	10.0	12.0	14.0	16.0	19.0	21.0	23.0	3.0	6.0	8.0	10.0	12.0	15.0	17.0	19.0
1920×1080	7.0	10.0	12.0	14.0	16.0	19.0	21.0	23.0	3.0	6.0	8.0	10.0	12.0	15.0	17.0	19.0

To further examine the consistency of the observed performance improvements, Table 6.8 presents the channel SNR gains obtained under individual operating conditions together with the corresponding standard deviations across different spatial resolutions. The reported values demonstrate that the statistical variation remains extremely small, typically within ≤ 0.3 dB, for both the Hadamard-based and COUS-based multi-qubit

frameworks. These results confirm the strong statistical reliability and stability of the obtained performance improvements.

Table 6.8: Channel SNR gains (dB) together with the corresponding standard deviations across different video resolutions for representative transmission configurations.

Resolution	**COUS**			**Hadamard**		
	CS1	CS4	CS8	H1	H4	H8
320×180	7.02 ± 0.05	14.03 ± 0.06	23.05 ± 0.07	2.94 ± 0.12	9.92 ± 0.15	18.85 ± 0.18
1280×720	7.01 ± 0.04	14.01 ± 0.05	23.02 ± 0.06	2.97 ± 0.10	9.98 ± 0.13	18.92 ± 0.16
1920×1080	7.00 ± 0.05	14.02 ± 0.05	23.03 ± 0.06	2.95 ± 0.11	9.95 ± 0.14	18.88 ± 0.17

These minor variations arise primarily from the inherent randomness associated with Monte Carlo simulation processes, including stochastic channel generation and finite-sample averaging effects, and are generally considered statistically insignificant within communication-system evaluations. It is further observed that the channel SNR gains achieved by both the Hadamard-based and COUS-based transmission frameworks remain largely unchanged across different motion categories and spatial resolutions. This behaviour is attributed to the fact that the proposed encoding frameworks operate directly on the compressed and channel-coded bitstreams rather than on the raw pixel-domain video data itself. Owing to the inter-frame prediction and entropy-coding mechanisms employed within the VVC compression process, the resulting bitstreams exhibit relatively stable statistical characteristics, causing the transmission efficiency to remain largely independent of the original video content and spatial resolution.

To further analyse the influence of video motion characteristics, the proposed COUS-based framework is evaluated using high-motion, medium-motion, and low-motion video sequences across multiple spatial resolutions. The corresponding results are summarised in Table 6.9, which reports the maximum channel SNR gains achieved for different multi-qubit configurations.

The results presented in Table 6.9 show that the achieved channel SNR gains remain largely consistent across different spatial resolutions and motion categories. This indicates that the performance of the proposed framework is only minimally affected by the motion characteristics of the transmitted video content. This behaviour can be explained by the structure of the transmission pipeline itself. Initially, the source video undergoes VVC compression, where temporal prediction and spatiotemporal redundancy are exploited to generate a compact compressed bitstream. High-motion video sequences

Table 6.9: Maximum channel SNR gains (dB) achieved by the proposed COUS-based framework relative to the classical communication baseline for different motion categories and spatial resolutions at 30 fps.

Resolution	**Motion Type**	CS1	CS2	CS3	CS4	CS5	CS6	CS7	CS8
320 × 180	Low	7.0	10.0	12.0	14.0	16.0	19.0	21.0	23.0
	Medium	7.0	10.0	12.0	14.0	16.0	19.0	21.0	23.0
	High	7.0	10.0	12.0	14.0	16.0	19.0	21.0	23.0
1280 × 720	Low	7.0	10.0	12.0	14.0	16.0	19.0	21.0	23.0
	Medium	7.0	10.0	12.0	14.0	16.0	19.0	21.0	23.0
	High	7.0	10.0	12.0	14.0	16.0	19.0	21.0	23.0
1920 × 1080	Low	7.0	10.0	12.0	14.0	16.0	19.0	21.0	23.0
	Medium	7.0	10.0	12.0	14.0	16.0	19.0	21.0	23.0
	High	7.0	10.0	12.0	14.0	16.0	19.0	21.0	23.0

generally produce bitstreams with higher entropy, while low-motion sequences compress more efficiently. However, once compression has been completed, the transmission framework operates exclusively on the resulting binary bitstream rather than on the original video frames. As a result, the overall transmission performance becomes primarily dependent on factors such as qubit dimension, channel-coding efficiency, and channel quality rather than on the motion intensity of the source video itself.

To complement the objective simulation metrics, a subjective visual-quality assessment was conducted for the proposed COUS-based framework and the corresponding classical transmission baselines under the GOP8 configuration using the double-stimulus evaluation methodology defined in ITU-R BT.500 [208], with the resulting scores illustrated in Figure 6.10. Within this evaluation procedure, participants were first shown the original reference video sequence followed immediately by the reconstructed version, enabling direct perceptual comparison between the source and transmitted outputs.

The assessment involved 20 participants aged between 18 and 65 years, recruited through university distribution channels. The participant group included individuals from both technical and non-technical backgrounds, all reporting normal or corrected-to-normal vision. To minimise subjective bias, the participants were not informed about the technical details or transmission configurations associated with the evaluated video sequences.

Each participant evaluated a selected collection of video samples representing the

classical baseline, Hadamard-based configurations (H1–H8), and COUS-based configurations (CS1–CS8) across different channel SNR conditions. The number of test samples was selected to ensure statistical consistency while limiting session duration in accordance with ITU-R BT.500 recommendations [208]. All videos were displayed using a colour-calibrated monitor under controlled ambient-lighting conditions, with the viewing distance maintained at approximately three times the display height. Furthermore, all sequences were presented using their original resolutions and frame rates to preserve perceptual accuracy.

To reduce the effects of viewer fatigue and sequential bias, mandatory rest intervals were introduced throughout the testing sessions, and the presentation order of the video sequences was randomised independently for each participant. Participants provided continuous quality ratings based on overall perceptual quality, visual sharpness, and the visibility of reconstruction artefacts. The final subjective quality scores were obtained by averaging the responses across all participants. Prior to participation, informed consent was obtained from all volunteers. The subjective evaluation procedure complied fully with institutional ethical guidelines and received approval from the Ethics Committee of the University of Strathclyde (protocol code 3048, approved on 9 December 2025). Overall, the controlled and randomised evaluation methodology ensured reliable and reproducible perceptual-quality measurements, thereby providing an effective complement to the objective PSNR, SSIM, and VMAF simulation results.

The subjective visual-quality assessment conducted across channel SNR values ranging from 16 dB to -12 dB reveals clear performance differences between the classical communication baseline (C) and the proposed COUS-based multi-qubit configurations (CS1–CS8). Under favourable high-SNR conditions between 12 dB and 16 dB, nearly all investigated quantum configurations achieve excellent perceptual quality comparable to the classical framework, indicating that both classical and quantum transmission systems perform effectively when channel impairments are limited. As the channel SNR decreases to 8 dB, the visual quality of the classical transmission framework begins to degrade noticeably, whereas the COUS-based configurations continue to preserve high perceptual quality across all investigated qubit dimensions. At 4 dB SNR, the COUS-based configurations maintain stable and visually clear reconstruction quality

while the classical baseline experiences severe degradation. Under increasingly noisy conditions at 0 dB SNR, the lower-dimensional quantum configurations begin to show visible quality reduction, although higher-dimensional configurations continue to preserve acceptable reconstruction fidelity. Within severe low-SNR environments such as −4 dB and −8 dB, only the larger multi-qubit COUS configurations retain stable visual quality, with the highest-dimensional configurations (CS7 and CS8) demonstrating the strongest perceptual robustness. Under the most challenging operating condition of −12 dB SNR, only the eight-qubit configuration (CS8) continues to maintain visually interpretable video reconstruction quality. The subjective observations obtained from the participant study closely match the objective simulation results measured using PSNR, SSIM, and VMAF metrics. This strong agreement confirms the consistency between the theoretical performance analysis and the perceived visual quality experienced by human observers.

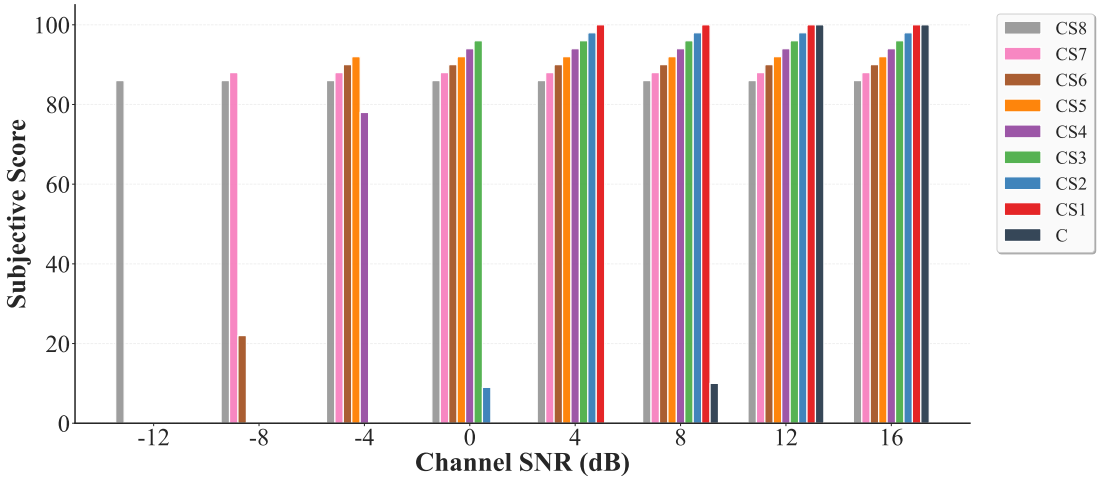


Figure 6.10: Subjective perceptual-quality scores comparing the classical communication baseline (C) with the proposed COUS-based multi-qubit configurations (CS1–CS8) under the GOP 8 transmission setting.

To further illustrate the perceptual differences between the Hadamard-based multi-qubit framework and the proposed COUS-based system, Figure 6.11 presents a representative reconstructed video frame obtained at an SNR value of 6 dB for the H1 and CS1 configurations. The reconstructed frame generated by the proposed COUS-based framework exhibits noticeably improved visual quality, including sharper edge preservation and reduced reconstruction artefacts, compared with the corresponding Hadamard-based configuration operating under the same channel conditions.



(a) CS1 (b) H1

Figure 6.11: Representative reconstructed video frames produced by the Hadamard-based (H1) and COUS-based (CS1) transmission frameworks at an SNR of 6 dB.

To further validate the effectiveness of the proposed framework, an additional comparison was conducted against two established quantum transmission approaches, under identical operating conditions. The corresponding results are summarised in Table 6.10. The obtained data show that the proposed COUS-based framework consistently outperforms the Hadamard-based approach across all investigated qubit dimensions (Q1–Q8), achieving an approximate channel SNR improvement of 3–4 dB. This performance advantage arises from the ability of the COUS framework to encode information simultaneously within both the phase and amplitude components of the quantum states, thereby increasing the representational flexibility of the encoded information.

When compared with the QFT-based transmission framework, the proposed COUS-based system achieves nearly identical performance across most qubit dimensions, with only minor deviations observed at larger qubit scales. Importantly, this comparable performance is achieved without the additional computational complexity associated with QFT-based frequency-domain processing, highlighting the computational efficiency of the proposed COUS framework.

For the single-qubit configuration (Q1), the proposed COUS framework slightly outperforms the QFT-based system, achieving an approximate 3 dB channel SNR

improvement. This behaviour occurs because the QFT-based framework cannot fully exploit frequency-domain characteristics when operating with only a single qubit, since meaningful frequency-domain decomposition requires multiple qubits. In contrast, the COUS framework continues to exploit both phase and amplitude encoding even within the single-qubit case, enabling improved information representation and transmission robustness.

Although the QFT-based framework achieves marginally higher peak performance at very large qubit dimensions, this improvement comes at the cost of significantly increased computational complexity due to the larger circuit depth and the controlled-rotation operations required by QFT processing. Specifically, QFT-based encoding exhibits computational complexity on the order of $\mathcal{O}(k^2)$ together with circuit depth scaling approximately as $\mathcal{O}(k)$. By comparison, the proposed COUS-based framework operates with computational complexity approximately proportional to $\mathcal{O}(k)$, while maintaining gate counts close to $3k$ and near-constant effective circuit depth because the encoding operations are applied independently across individual qubits. Consequently, the proposed COUS-based framework represents a more practical candidate for future real-world implementation, particularly for near-term quantum communication hardware where limiting circuit depth and reducing cumulative quantum-gate errors remain critical design considerations.

Table 6.10: Contrast of SNR improvements (dB) achieved at a 1280×720 resolution (30 fps) against the classical system under standardised testing variables.

Encoding Scheme	Q1	Q2	Q3	Q4	Q5	Q6	Q7	Q8
Frequency Domain	4.0	8.0	12.0	14.0	16.0	20.0	21.0	24.0
Hadamard (Time Domain)	3.0	6.0	8.0	10.0	12.0	15.0	17.0	19.0
COUS (Proposed)	7.0	10.0	12.0	14.0	16.0	19.0	21.0	23.0

Positioning of the Proposed COUS Encoding

The proposed COUS-based encoding framework differs substantially from both conventional basis-rotation approaches and frequency-domain quantum transmission frameworks in several important aspects. Although the practical implementation of the COUS operation can be decomposed into a sequence of standard quantum operations,

S–H–S gates, the contribution of the proposed framework does not lie in introducing a fundamentally new physical quantum gate. Instead, the primary innovation is the development of a structured complex-valued orthogonal encoding framework specifically designed for robust video transmission over noisy quantum communication channels.

Unlike conventional Hadamard-based encoding schemes, which generate only real-valued quantum superposition states, the proposed COUS framework introduces an additional $\pi/2$ phase component that produces complex-valued quantum-state representations. This enables information to be distributed simultaneously across both the phase and amplitude dimensions of the quantum state, thereby increasing the diversity and separability of the encoded states within the underlying Hilbert space. As a consequence, the resulting quantum states become more distinguishable under noisy channel conditions, improving robustness against transmission impairments and decoding ambiguity.

Compared with frequency-domain frameworks based on the QFT, the proposed COUS framework achieves comparable amplitude–phase diversity while relying only on a small number of independent single-qubit operations, resulting in a significantly shallower circuit structure. This provides an advantageous balance between encoding capability and computational efficiency, which becomes particularly important for high-dimensional multimedia-transmission applications such as compressed video communication.

Furthermore, the proposed COUS encoding strategy is integrated directly within a complete multimedia-transmission architecture incorporating multi-qubit transmission, polar channel coding, and modern video-compression techniques. This end-to-end integration demonstrates how carefully structured complex-valued quantum-state mapping can improve the robustness of compressed multimedia transmission under realistic noisy quantum-channel conditions.

Theoretical Justification of COUS Performance Improvements

The performance improvements achieved by the proposed COUS-based encoding framework are supported by several fundamental principles related to quantum-state representation, Hilbert-space geometry, and quantum-state distinguishability under noisy-channel conditions.

Complex Hilbert-Space Representation: For a k-qubit system, the encoded quantum states exist within a complex Hilbert space $\mathbb{C}^{2^k}$. The robustness of a quantum encoding framework depends strongly on how effectively the available Hilbert-space dimensions are utilised.

The conventional Hadamard-based encoding framework produces real-valued superposition states, expressed in (6.31).

$$|+\rangle = \frac{1}{\sqrt{2}}(|0\rangle + |1\rangle), \quad |-\rangle = \frac{1}{\sqrt{2}}(|0\rangle - |1\rangle) \tag{6.31}$$

These states are confined primarily to the real-valued region of the Hilbert space. By contrast, the proposed COUS-based framework generates complex-valued quantum states, as described in (6.32).

$$|\psi_0\rangle = \frac{1}{\sqrt{2}}(|0\rangle + i|1\rangle), \quad |\psi_1\rangle = \frac{1}{\sqrt{2}}(i|0\rangle + |1\rangle) \tag{6.32}$$

The incorporation of complex phase components allows information to be represented simultaneously through both phase and amplitude dimensions, increasing the diversity and spatial distribution of the encoded quantum states within the complex Hilbert space. This richer representation contributes directly to improved robustness against channel disturbances and decoding ambiguity.

State Distinguishability and Noise Robustness: For two normalised quantum states $|\psi_0\rangle$ and $|\psi_1\rangle$, the Euclidean separation between the corresponding state vectors is given by (6.33).

$$d^2 = 2 - 2\,\mathrm{Re}\{\langle\psi_0|\psi_1\rangle\} \tag{6.33}$$

Under ideal noise-free conditions, both the Hadamard-based and COUS-based frameworks generate orthogonal states, yielding identical initial Euclidean separation. However, once the encoded states propagate through a noisy communication channel, the resulting quantum states become distorted according to (6.34).

$$\rho_i' = \mathcal{E}(|\psi_i\rangle\langle\psi_i|), \quad i \in \{0, 1\} \tag{6.34}$$

The distinguishability between the degraded states is then quantified using the trace distance defined in (6.35).

$$D(\rho_0', \rho_1') = \frac{1}{2}\|\rho_0' - \rho_1'\|_1 \tag{6.35}$$

For a composite noisy quantum channel represented by (6.36).

$$\mathcal{E}(\rho) = \sum_k p_k \mathcal{E}_k(\rho) \tag{6.36}$$

where $\mathcal{E}_k$ denotes individual CPTP quantum operations and p_k represents the corresponding probability coefficients satisfying $\sum_k p_k = 1$. Under the composite quantum channel defined in (6.36), the trace-distance contractivity property from quantum information theory [127] guarantees that the distinguishability between the output states cannot increase after the action of the noisy channel, as expressed in (6.37).

$$D(\rho_0', \rho_1') \leq D(\rho_0, \rho_1) \tag{6.37}$$

Although trace distance decreases under noise for all encoding strategies, the proposed COUS framework preserves greater effective distinguishability after channel degradation because the encoded information is distributed jointly across both phase and amplitude dimensions. Consequently, the degraded COUS states maintain larger post-channel separation than the corresponding Hadamard-based states, as represented in (6.38).

$$D\big(\rho_0'^{\text{COUS}}, \rho_1'^{\text{COUS}}\big) > D\big(\rho_0'^{\text{Hadamard}}, \rho_1'^{\text{Hadamard}}\big) \tag{6.38}$$

This improved post-channel distinguishability directly contributes to the improved decoding reliability and transmission robustness observed throughout the simulation results.

Bloch-Sphere Interpretation: A general single-qubit quantum state can be expressed on the Bloch sphere according to (6.39).

$$|\psi\rangle = \cos\left(\frac{\theta}{2}\right)|0\rangle + e^{i\phi}\sin\left(\frac{\theta}{2}\right)|1\rangle \tag{6.39}$$

Within the Hadamard-based framework, the phase parameter is restricted to $\phi \in$

$\{0, \pi\}$, constraining the resulting quantum states primarily along the X-axis of the Bloch sphere. In contrast, the proposed COUS framework introduces phase values of $\phi = \pm\frac{\pi}{2}$, shifting the quantum-state representation towards orthogonal directions on the Bloch sphere.

Under noisy-channel conditions, quantum states experience contraction and rotation on the Bloch sphere. States distributed across multiple orthogonal directions maintain greater angular separation after channel degradation, improving distinguishability and reducing decoding ambiguity.

Hardware Feasibility and Complexity Analysis: The computational complexity, scalability behaviour, and practical hardware feasibility of the proposed COUS-based encoding framework were analysed previously in Section 6.1. Since the video-transmission framework presented in this section directly adopts the same encoding and decoding architecture, the associated circuit requirements, implementation considerations, and scalability characteristics remain unchanged and are therefore not repeated here.

6.2.3 Section Summary

This section presented a comprehensive evaluation of the proposed COUS-based multi-qubit framework for robust video transmission over noisy quantum communication channels. The proposed COUS encoding strategy jointly exploited both phase and amplitude information within multi-qubit quantum states, producing a richer and more resilient representation of compressed video data compared with conventional Hadamard-based encoding approaches that rely primarily on real-valued superposition states. By utilising the additional representational flexibility introduced through phase encoding, the proposed framework improved robustness against channel noise, temporal error propagation, and transmission distortions while maintaining relatively low computational complexity and shallow circuit depth. Extensive simulation studies were conducted across multiple GOP structures and qubit dimensions in order to evaluate the performance of the proposed framework under diverse transmission conditions. The obtained results consistently demonstrated that the COUS-based configurations achieved superior reconstruction quality across all investigated PSNR, SSIM, and VMAF metrics when compared with both the bandwidth-matched classical communication baseline

and the corresponding Hadamard-based quantum configurations. For example, the eight-qubit COUS configuration (CS8) achieved channel SNR gains of up to 23 dB, exceeding the corresponding Hadamard-based configuration (H8), which achieved a maximum improvement of approximately 19 dB. Even under the single-qubit setting, the proposed COUS framework (CS1) maintained an approximate 3–4 dB channel SNR advantage over the equivalent Hadamard-based configuration (H1).

In addition, the proposed COUS-based framework achieved robustness levels comparable to those of significantly more computationally demanding QFT-based transmission frameworks while avoiding the substantial complexity associated with QFT and inverse-QFT operations. In particular, the single-qubit COUS configuration achieved an approximate 4 dB channel SNR improvement relative to the corresponding QFT-based framework, while larger multi-qubit COUS configurations maintained similar transmission robustness with considerably lower computational overhead. Importantly, these performance improvements remained consistent across all investigated GOP configurations, confirming the effectiveness of the proposed framework in mitigating temporal error propagation during compressed video transmission.

6.3 Chapter Summary

This chapter introduced COUS encoding as a time-domain multi-qubit encoding strategy that jointly exploits amplitude and phase diversity, and presented two interconnected studies (Sections 6.1–6.2) that establish its effectiveness across both still-image and video transmission scenarios. Section 6.1 formulated COUS encoding for quantum image transmission, deriving the orthogonality conditions on the amplitude and phase components and constructing encoded states that are simultaneously separated in both magnitude and phase within the complex Hilbert space. Across qubit group sizes $k \in [1, 8]$, for both JPEG and HEIF source coding and under configurations with and without rate-1/2 polar channel coding, COUS consistently outperformed the Hadamard-based multi-qubit framework of Chapter 4 and the classical BPSK baseline. In particular, the single-qubit COUS configuration (CS1) surpassed the QFT-based frequency-domain framework of Section 5.1 by approximately 4 dB in channel SNR, while higher-qubit COUS configurations achieved robustness comparable to QFT-

based transmission without invoking any frequency-domain transformation. Runtime analysis further confirmed the practical feasibility of the framework, with execution time increasing from approximately 0.13 s at $k = 1$ to 1.18 s at $k = 8$. Section 6.2 extended the COUS framework to VVC-compressed video transmission across multiple GOP sizes, frame rates, and spatial resolutions, confirming that the encoding-stage amplitude–phase diversity provided by COUS effectively mitigates the temporally compounded effects of inter-frame error propagation. The eight-qubit COUS configuration (CS8) delivered channel SNR gains of up to 23 dB over the classical baseline, exceeding the 19 dB maximum achieved by the Hadamard-based framework (H8). At the single-qubit level, CS1 provided a 3–4 dB improvement over H1, with this advantage remaining consistent across all evaluated GOP structures. CS1 further outperformed QFT-based frequency-domain single-qubit encoding by 4 dB in channel SNR. Moreover, it achieved robustness comparable to that of higher-qubit QFT-based transmissions, despite operating entirely in the time domain without any frequency-domain transformation.

A central insight emerging from the collective findings of this chapter is that the joint amplitude–phase diversity that drives the robustness advantages of the QFT-based framework of Chapter 5 is not intrinsic to frequency-domain representation itself, but rather to the underlying use of complex-valued, phase-structured encoded states. By directly engineering orthogonal amplitude components together with deliberately chosen phase components in the time domain, COUS recovers the Hilbert-space-spreading benefits previously attributed to the QFT while requiring only constant-depth $\mathcal{O}(1)$ circuits per qubit, using single-qubit Hadamard and phase gates with no two-qubit operations and no transform-domain reconstruction stage at the decoder. This represents a substantial reduction relative to the $\mathcal{O}(k^2)$ gate count and linearly scaling circuit depth of the QFT framework of Chapter 5.

Taken together with the time-domain real-valued amplitude encoding of Chapters 3–4 and the frequency-domain QFT-based encoding of Chapter 5, the time-domain complex-valued orthogonal unitary superposition encoding developed in this chapter completes the encoding-side design space explored in this thesis. Having established this design space, the natural next question is no longer how to further refine the encoding stage in isolation, but how the quantum encoding mechanisms developed in Chapters 3–6 interact

with the practical communication architectures that govern multimedia transmission in modern wireless networks. Chapter 7 takes up this question.

Chapter 7

Design of an Integrated Quantum Communication Framework with Existing Image and Video Transmission Systems

Chapters 3–6 progressively developed the encoding-side design space of quantum multimedia communication. Chapter 3 established the foundational superposition-based encoding framework together with QEC. Chapter 4 extended this framework into higher-dimensional Hilbert spaces through time-domain multi-qubit Hadamard encoding. Chapter 5 moved into the frequency domain through QFT-based encoding, exploiting joint amplitude and structured phase representation, repurposing the QFT as a unified compression-and-transmission primitive, and introducing diffusion-based semantic-aware restoration at the receiver. Chapter 6 then returned to the time domain and introduced COUS encoding, which recovered the joint amplitude–phase robustness advantages of the QFT framework using only constant-depth $\mathcal{O}(1)$ circuits per qubit. Collectively, these chapters demonstrated that quantum signal representations can significantly improve transmission robustness, compression efficiency, and reconstruction fidelity under noisy channel conditions.

However, all of the frameworks developed in Chapters 3–6 have been investigated as

standalone quantum-domain transmission systems, in which classical bits or compressed bitstreams are mapped directly into quantum superposition states and transmitted without incorporating the communication architectures that underpin modern wireless and multimedia systems. In practice, image and video transmission must operate under limited bandwidth, dynamic channel conditions, multipath fading, packet losses, and high data-rate requirements. To address these challenges, contemporary communication systems employ complementary mechanisms operating at different layers of the communication stack.

At the physical layer, robustness is achieved through spatial diversity and frequency diversity. Spatial diversity is provided by MIMO systems, which mitigate fading through multiple transmit and receive antennas. Frequency diversity is achieved through OFDM, which improves resilience against frequency-selective fading by distributing data across multiple orthogonal subcarriers. These two mechanisms can be combined within MIMO-OFDM, simultaneously exploiting both spatial and frequency diversity to provide enhanced transmission reliability under dynamic wireless channel conditions. Collectively, these techniques represent the principal physical-layer robustness mechanisms used in modern wireless communication systems.

Beyond the physical layer, additional robustness can be introduced at higher communication layers. At the source layer, MDC improves transmission robustness by generating multiple independently decodable descriptions of the source content, enabling graceful degradation in reconstruction quality when one or more descriptions are lost or corrupted during transmission. At the content layer, semantic communication enhances robustness by prioritising semantically important information, thereby preserving perceptual quality even under severe channel impairments. Despite their widespread adoption in classical communication systems, the interaction between these architectures and the quantum encoding frameworks developed in Chapters 3–6 remains largely unexplored.

This observation raises several research questions that were not addressed in the preceding chapters: (i) can the robustness advantages of quantum encoding be combined with the spatial-diversity gains of MIMO systems to mitigate fading and channel impairments more effectively than either mechanism in isolation? (ii) can quantum-domain processing be integrated with frequency-selective multicarrier transmission

(frequency diversity) through OFDM to improve spectral efficiency and robustness under noisy conditions? (iii) can spatial and multicarrier mechanisms be jointly exploited within a unified quantum MIMO-OFDM architecture? (iv) beyond physical-layer improvements, can quantum representations be combined with MDC to provide source-layer robustness against transmission impairments through multiple independently decodable descriptions? (v) can quantum representations be integrated with semantic communication to provide content-layer robustness by preserving semantically important information under severe channel impairments? This chapter addresses each of these research questions in sequence.

Throughout this chapter, although transform-domain compression is employed by the JPEG, HEIF, and VVC source encoders, the proposed frameworks remain independent of the specific source transform because quantum encoding is performed on the resulting compressed bitstream rather than on the transform coefficients.

As illustrated in Figure 7.1, this chapter is organised into three complementary integration stages. The first stage focuses on physical-layer robustness, where the proposed quantum communication framework is integrated with MIMO, OFDM, and MIMO-OFDM systems to exploit spatial diversity, frequency diversity, and their combined benefits. The second stage extends the framework to source-layer robustness through quantum MDC (Q-MDC), enhancing robustness under unreliable transmission conditions. Finally, the third stage investigates content-layer robustness by integrating the framework with semantic communication, enabling content-aware transmission that prioritises semantically important information. Together, these three stages demonstrate the compatibility and adaptability of the proposed quantum communication framework across the physical, source, and content layers, encompassing the three principal aspects of modern image and video communication systems.

Therefore, the chapter is organised in seven sections. Sections 7.1 and 7.2 develop quantum communication frameworks for image and video transmission integrated with MIMO systems employing transmit and receive diversity [226], [227], combining quantum encoding with spatial diversity mechanisms to improve robustness against fading and channel impairments while maintaining high-fidelity reconstruction. Sections 7.3 and 7.4 investigate quantum OFDM (QOFDM)-based image and video transmission frame-

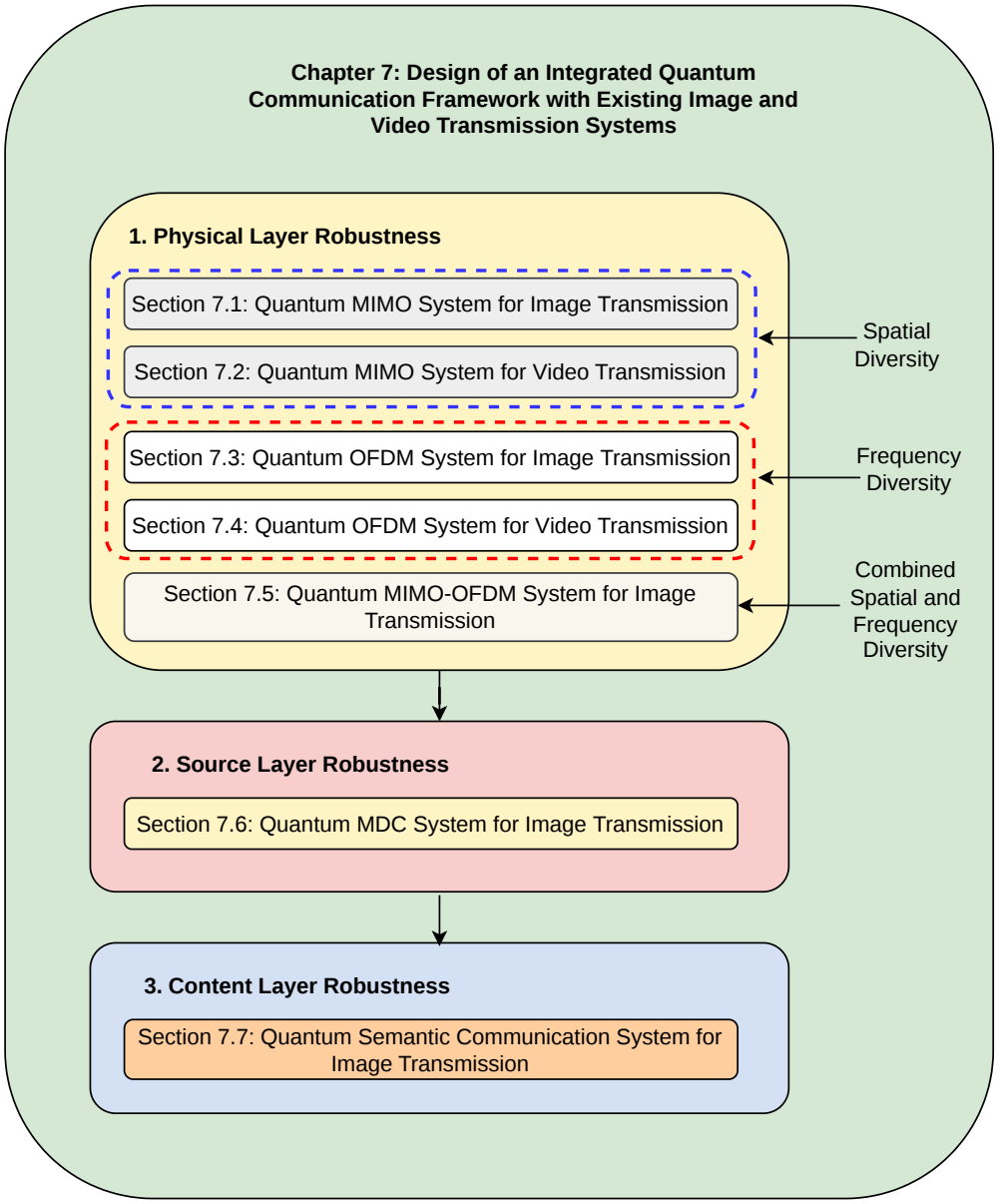


Figure 7.1: Organisation of Chapter 7.

works [228], [229], in which quantum-domain processing is integrated with frequency-selective multicarrier transmission to improve spectral efficiency and robustness under noisy conditions. Section 7.5 introduces a hybrid quantum MIMO-OFDM architecture with transmit and receive diversity [230] that jointly exploits spatial diversity and multicarrier communication advantages within the quantum communication domain. Section 7.6 introduces a Q-MDC framework that exploits quantum-domain correlations for robust image transmission, providing improved resilience against packet loss and channel impairments through distributed quantum representations. Finally, Section 7.7 presents a quantum semantic communication framework [223] that investigates how quantum representations can preserve semantically important image information under noisy transmission conditions while reducing transmission overhead.

7.1 Quantum Communication Techniques for Image Transmission in Diversity-Assisted MIMO Systems

Publication Notice

The research presented in this section has been published in the following peer-reviewed journal publication:

U. Jayasinghe, T. Fernando, Y. Ganearachchi, P. Samarathunga, and A. Fernando, "Quantum communication based image transmission with transmit and receive diversity in MIMO communication systems," *IEEE Transactions on Consumer Electronics*, vol. 71, no. 2, pp. 2500–2507, 2025, doi: 10.1109/TCE.2025.3559634.

This material is reproduced and adapted under the terms of the IEEE Copyright policy for use in a doctoral thesis. The content has been revised and extended with additional explanations and expanded discussion.

Problem Statement: Previous chapters demonstrated that quantum superposition encoding frameworks can improve image transmission robustness under noisy communication environments. However, most existing quantum communication studies have primarily focused on single-antenna transmission models and have not investigated the integration of spatial diversity techniques into the quantum communication process.

In practical wireless multimedia transmission, spatial diversity plays a critical role in improving link reliability, spectral efficiency, and reconstructed image quality, particularly for compressed image formats such as JPEG and HEIF. Consequently, analysing the performance of quantum image transmission systems under transmit and receive diversity configurations remains an important and largely unexplored research direction for practical communication applications.

Limitations of Existing Work: Conventional classical communication systems widely employ diversity techniques within MIMO architectures to improve transmission reliability. Transmit diversity, receive diversity, and combined spatial diversity mechanisms have been extensively studied and deployed to enhance robustness and spectral efficiency. However, existing quantum-inspired image transmission frameworks have largely concentrated on encoding-domain improvements without integrating spatial diversity mechanisms into the quantum communication pipeline. Furthermore, prior studies have not comprehensively analysed how quantum superposition-based image transmission behaves under different MIMO diversity configurations, nor have they provided a fair comparison against equivalent classical communication frameworks operating under identical bandwidth and channel conditions.

Motivation and Proposed Contribution: To address these limitations, this section proposes a quantum communication-based image transmission framework integrated with transmit and receive diversity techniques in MIMO communication systems. The proposed framework combines superposition-based quantum encoding with spatial diversity mechanisms to analyse how diversity gains translate into improved image reconstruction performance in quantum communication systems. The system is investigated under multiple diversity configurations, including (1×1) single-input single-output (SISO), (2×1) transmit diversity multiple-input single-output (MISO), and (1×2) receive diversity single-input multiple-output (SIMO) architectures over Rayleigh communication channels. The proposed quantum communication framework is compared against an equivalent classical communication system operating under identical bandwidth, diversity, and channel conditions. The objective is to analyse the impact of transmit and receive diversity on quantum image transmission and to demonstrate that integrating

quantum superposition encoding with MIMO diversity techniques yields measurable improvements in image reconstruction fidelity and transmission robustness. The main contributions of this section are as follows.

- Analyse the performance of superposition-based quantum communication systems employing transmit and receive diversity techniques in MIMO configurations for image transmission.
- Compare the performance of the proposed quantum communication framework with that of an equivalent classical communication system utilising the same diversity techniques under identical bandwidth and channel conditions.
- Propose a more robust end-to-end image transmission system that leverages spatial diversity gains to improve reconstruction quality in practical wireless communication environments.

7.1.1 System Model



Figure 7.2: Block diagram of the proposed quantum-enabled MIMO image transmission framework.

The realisation of the proposed framework, depicted in Figure 7.2, begins by drawing a 100 representative subset of images from the Microsoft COCO database [197]. This collection is chosen because it spans a broad spectrum of scene types and visual complexities, which makes it well suited for stress-testing communication pipelines under heterogeneous content.

The chosen images are next passed through a source coding stage, where either JPEG or HEIF is employed to reduce the payload size prior to transmission. The compressed bit sequence is subsequently passed to the channel encoder, where a rate-1/2 polar code [210] is applied, consistent with the approach adopted in the previous chapters.

Following channel encoding, the coded bitstream is forwarded to the quantum encoder, which maps each classical bit onto a single qubit. A classical 0 is associated

with the computational basis state $|0\rangle$ and a classical 1 with $|1\rangle$. This direct mapping prepares the data for quantum-domain transmission while keeping the encoding strategy simple and hardware friendly.

The two computational basis states have the column-vector representations given in (7.1) and (7.2).

$$|0\rangle = \begin{pmatrix} 1 \\ 0 \end{pmatrix} \tag{7.1}$$

$$|1\rangle = \begin{pmatrix} 0 \\ 1 \end{pmatrix} \tag{7.2}$$

Once the bits have been mapped to basis states, a Hadamard gate, written in matrix form in (7.3), is applied at the quantum encoder to drive each qubit into an equal superposition.

$$H = \frac{1}{\sqrt{2}} \begin{pmatrix} 1 & 1 \\ 1 & -1 \end{pmatrix} \tag{7.3}$$

Acting with H on $|0\rangle$ yields the superposition shown in (7.4), whose explicit column-vector form is given in (7.5).

$$H\,|0\rangle = \frac{1}{\sqrt{2}}\left(|0\rangle + |1\rangle\right) \tag{7.4}$$

$$H \begin{pmatrix} 1 \\ 0 \end{pmatrix} = \frac{1}{\sqrt{2}} \begin{pmatrix} 1 & 1 \\ 1 & -1 \end{pmatrix} \begin{pmatrix} 1 \\ 0 \end{pmatrix} = \frac{1}{\sqrt{2}} \begin{pmatrix} 1 \\ 1 \end{pmatrix} \tag{7.5}$$

The same gate acting on $|1\rangle$ produces the orthogonal superposition expressed in (7.6), with its matrix-form counterpart given in (7.7).

$$H\,|1\rangle = \frac{1}{\sqrt{2}}\left(|0\rangle - |1\rangle\right) \tag{7.6}$$

$$H\begin{pmatrix}0\\1\end{pmatrix} = \frac{1}{\sqrt{2}}\begin{pmatrix}1 & 1\\1 & -1\end{pmatrix}\begin{pmatrix}0\\1\end{pmatrix} = \frac{1}{\sqrt{2}}\begin{pmatrix}1\\-1\end{pmatrix} \tag{7.7}$$

Because the MIMO link in this work operates on complex baseband symbols, a real-valued superposition alone is not sufficient. To embed a phase component in the transmitted state, the Hadamard output is further processed by the phase gate S defined in (7.8).

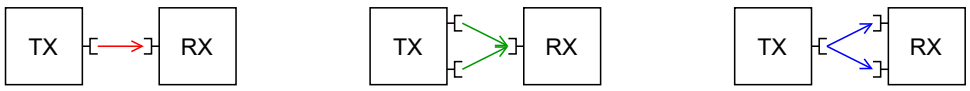
$$S = \begin{bmatrix}1 & 0\\0 & i\end{bmatrix} \tag{7.8}$$

Cascading the S gate after the Hadamard for the two input bits produces the transmitted states given in (7.9) and (7.10).

$$SH\,|0\rangle = \frac{1}{\sqrt{2}}(|0\rangle + i\,|1\rangle) \tag{7.9}$$

$$SH\,|1\rangle = \frac{1}{\sqrt{2}}(|0\rangle - i\,|1\rangle) \tag{7.10}$$

The resulting phase-bearing superposition states are then handed to the transmit front-end and launched into the channel under three antenna configurations, namely 1×1 SISO, 2×1 MISO, and 1×2 SIMO, as illustrated in Figure 7.3.



(a) 1×1 SISO (b) 2×1 MISO (c) 1×2 SIMO

Figure 7.3: Antenna configurations adopted in the simulation study: (a) a single-antenna baseline without diversity, (b) a transmit-diversity arrangement, and (c) a receive-diversity arrangement.

The propagation environment is captured by a flat-fading Rayleigh channel, which reflects the kind of multipath conditions typically encountered in mobile wireless links without a dominant line-of-sight component. Under this model, the envelope of the received signal follows a Rayleigh distribution [231], making it a standard choice for

non-line-of-sight scenarios.

In the multi-antenna variants, each transmit–receive antenna pair is taken to experience statistically independent fading. This independence assumption is what underpins the diversity gain offered by MIMO schemes, since it allows the receiver to combine effectively decorrelated copies of the signal and thereby improve reliability. CSI is further assumed to be known perfectly at the receiver, which provides a clean reference point for assessing the coding and modulation stages without conflating their performance with channel-estimation errors.

To make this classical channel model compatible with the transmission of qubits, it is augmented with mechanisms that capture the quantum-domain impairments encountered along the link. The noise processes affecting quantum signals are qualitatively different from their classical counterparts and are usually modelled by quantum operations acting on the transmitted state. Typical mechanisms [127] include bit-flip and phase-flip errors, depolarisation, phase damping, and amplitude damping, all of which can degrade or destroy the information carried by a qubit through its interaction with the environment. The Rayleigh model used here is therefore extended to incorporate such decoherence effects, so as to reflect the difficulty of preserving qubit integrity over a noisy, time-varying wireless link.

On the receive side, the incoming qubit states are routed to the quantum decoder, whose task is to map the received superpositions back into classical bits. The decoder first strips out the phase component that was introduced at the transmitter. This is achieved by applying the Hermitian conjugate of the phase gate, denoted $S^\dagger$ and defined in (7.11).

$$S^\dagger = \begin{bmatrix} 1 & 0 \\ 0 & -i \end{bmatrix} \tag{7.11}$$

After the phase has been reversed, the decoder performs quantum measurement, which converts the quantum information into classical observations, as described in Section 3.1 and Equation (3.15). After demapping, the recovered bitstream is delivered to the polar decoder, which exploits the redundancy injected at the encoder to detect and correct residual errors and to estimate the most likely transmitted sequence. The

decoded bits are then handed back to the source decoder corresponding to the format originally used at the transmitter, that is, JPEG or HEIF. This last stage inverts the compression step and produces the reconstructed image, which is what we ultimately evaluate.

For benchmarking, the proposed quantum link is compared against a classical baseline that employs complex baseband BPSK together with the same rate 1/2 polar code, so that both systems occupy comparable bandwidth. In the classical case, bit 0 is mapped to $(1 + 0i)$ and bit 1 to $(-1 + 0i)$. In the quantum case, the cascade of Hadamard and phase gates produces the constellation-like states $\frac{1}{\sqrt{2}}(|0\rangle + i\,|1\rangle)$ for bit 0 and $\frac{1}{\sqrt{2}}(|0\rangle - i\,|1\rangle)$ for bit 1.

Simulations evaluate system performance over a range of channel SNR values from -3 dB to 19 dB and emulate a low-mobility urban deployment, accounting for multipath fading, dynamic interference, and a specific set of channel parameters. The sampling rate is set to 1000 Hz, the path delays are taken as $(0, 3 \times 10^{-6}, 8 \times 10^{-6}, 20 \times 10^{-6})$ seconds, and the corresponding average path gains are $(0, -3, -6, -9)$ dB. A maximum Doppler shift of 10 Hz is also applied. The pipeline is content-agnostic and can be exercised with arbitrary images, including high-resolution ones, and still yield accurate reconstruction. To obtain statistically meaningful results, twenty images of varying spatial-information content are transmitted and the metrics averaged. Reconstruction quality is quantified using PSNR and SSIM, complemented by the variation of BER, which together constitute a well-established set of objective quality indicators.

7.1.2 Results

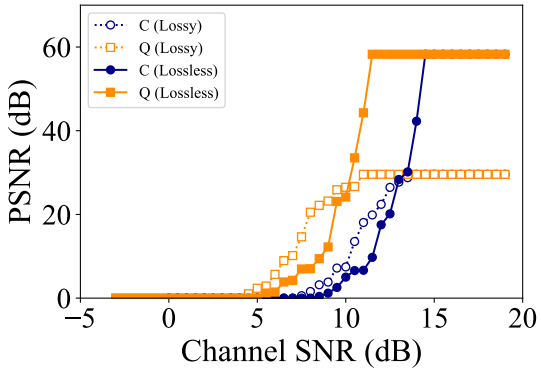
This subsection examines the behaviour of the proposed superposition-based quantum image transmission system across the 1×1 SISO, 2×1 MISO, and 1×2 SIMO configurations, alongside a matched classical baseline. The evolution of the average PSNR and SSIM of the reconstructed images with channel SNR for JPEG-compressed inputs at both a lossy operating point (QP25) and a near-lossless one (QP100), across the three antenna configurations, is illustrated in Figure 7.4. Across all cases, the quantum-based link (denoted Q) yields markedly higher PSNR and SSIM values than the classical counterpart (denoted C), and the advantage is most pronounced in the

low-SNR regime. A further point worth flagging is the 3 dB offset between 2×1 MISO and 1×2 SIMO that appears in both the quantum and classical curves; this is a direct consequence of constraining the total transmit power to be the same across all configurations.

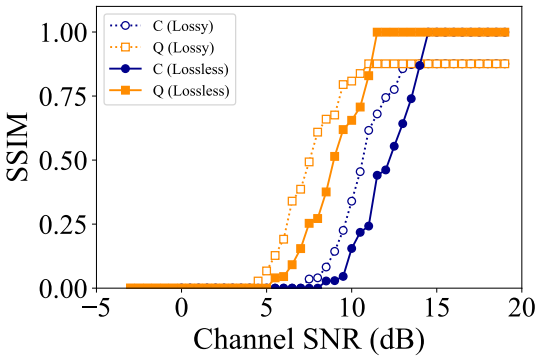
The reconstructed JPEG samples presented in Figure 7.5 further validate the performance trends observed in the PSNR and SSIM results. The displayed images correspond to a channel SNR of 10 dB for the SISO configuration and 7 dB for the diversity-assisted schemes. Visually, the proposed quantum transmission framework achieves noticeably superior reconstruction quality compared with the classical counterpart. Moreover, the ability of the diversity-enabled quantum configurations to attain image quality at 7 dB comparable to that achieved by the SISO quantum system at 10 dB highlights the enhanced resilience provided by spatial diversity. This demonstrates the effectiveness of the proposed approach in maintaining reliable and visually acceptable image transmission even under challenging channel conditions.

Switching from JPEG to HEIF source coding, Figure 7.6 compares the quantum and classical pipelines at QP25 and QP100 under the same set of antenna configurations. The behaviour mirrors that observed for JPEG, with the quantum-based MIMO system retaining a consistent PSNR and SSIM advantage over the classical baseline at every SNR point considered. This is attributable to the noise tolerance and error-handling characteristics of the quantum link, which together translate into cleaner reconstructions even under adverse channel conditions. A second observation, common to both quantum and classical pipelines, is that HEIF outperforms JPEG in absolute terms because its more sophisticated compression strategy preserves perceptual quality more effectively and produces fewer compression artefacts. In other words, the gain provided by quantum transmission is largely independent of the choice of source coder, while HEIF supplies an additional, orthogonal improvement on top.

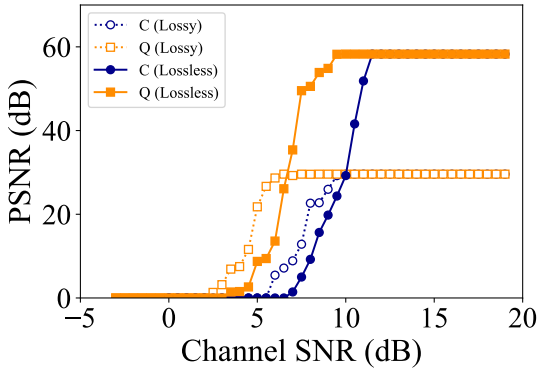
The BER curves for the JPEG and HEIF lossy operating points, presented in Figure 7.7, supply a third, independent view of the same trend. Taken together with the PSNR and SSIM data, these results confirm that the quantum image transmission pipeline outperforms its classical counterpart, particularly when transmit or receive diversity is in use (i.e. 2×1 MISO and 1×2 SIMO). The quantum link delivers



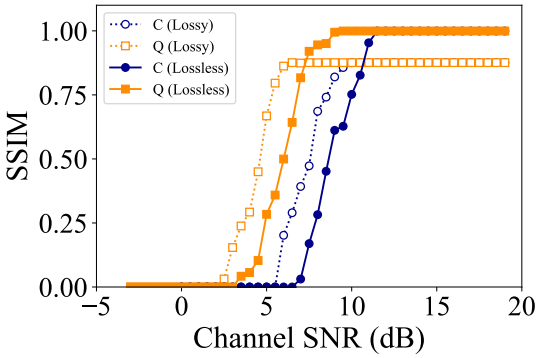
(a) No diversity (1×1/SISO)



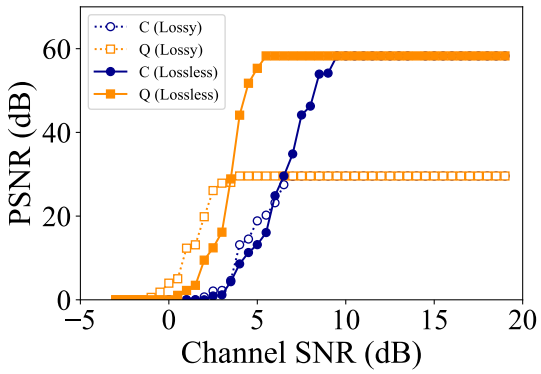
(b) No diversity (1×1/SISO)



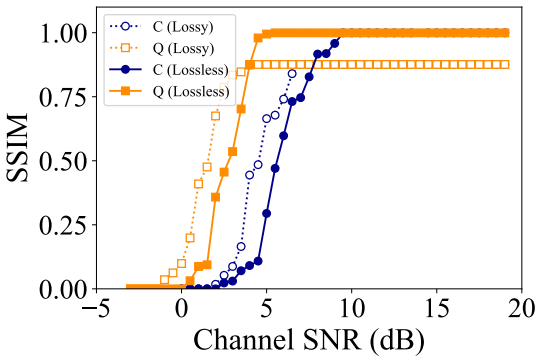
(c) Transmit diversity (2×1 MISO)



(d) Transmit diversity (2×1 MISO)



(e) Receive diversity (1×2 SIMO)



(f) Receive diversity (1×2 SIMO)

Figure 7.4: Average PSNR (left column) and SSIM (right column) achieved by the classical (C) and quantum (Q) pipelines for JPEG-coded images at QP = 25 (lossy) and QP = 100 (near-lossless), across (a), (b) the SISO baseline, (c), (d) the 2×1 MISO configuration, and (e), (f) the 1×2 SIMO configuration.



(a) Classical (1×1 SISO)



(b) Quantum (1×1 SISO)



(c) Classical (2×1 MISO)



(d) Quantum (2×1 MISO)

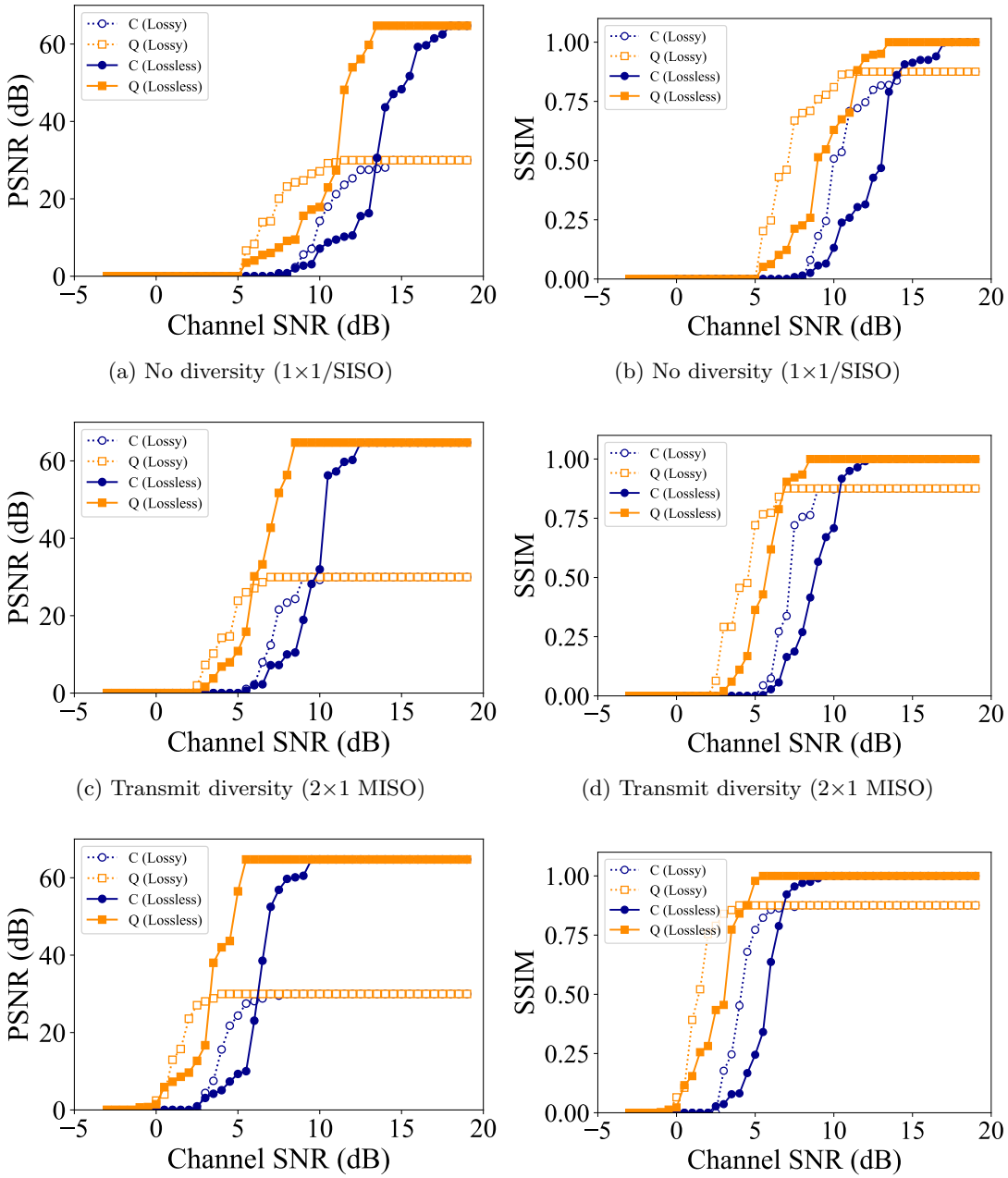


(e) Classical (1×2 SIMO)



(f) Quantum (1×2 SIMO)

Figure 7.5: Reconstructed lossy JPEG images for the classical and quantum pipelines under each configuration: (a), (b) SISO at 10 dB channel SNR; (c), (d) 2×1 MISO at 7 dB channel SNR; (e), (f) 1×2 SIMO at 7 dB channel SNR.



(a) No diversity (1×1/SISO)

(b) No diversity (1×1/SISO)

(c) Transmit diversity (2×1 MISO)

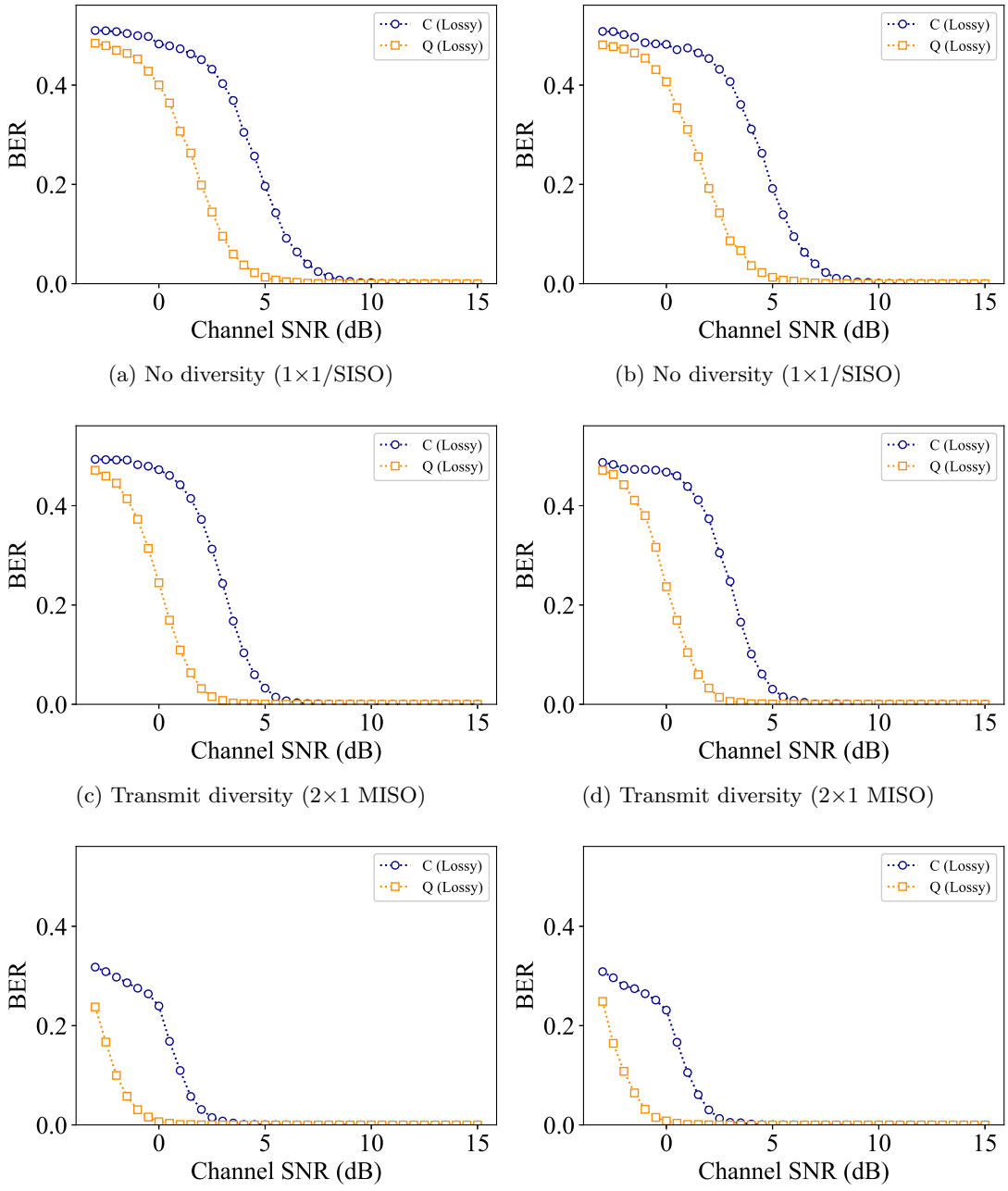
(d) Transmit diversity (2×1 MISO)

(e) Receive diversity (1×2 SIMO)

(f) Receive diversity (1×2 SIMO)

Figure 7.6: Average PSNR (left column) and SSIM (right column) for classical (C) and quantum (Q) pipelines applied to HEIF-coded images at QP = 25 (lossy) and QP = 100 (near-lossless), under (a), (b) SISO, (c), (d) 2×1 MISO, and (e), (f) 1×2 SIMO.

higher reconstruction quality through its noise tolerance and error-handling properties while keeping computational cost and latency low. The robustness of the proposed framework is supported by several key design considerations. First, the use of single-



(a) No diversity (1×1/SISO)

(b) No diversity (1×1/SISO)

(c) Transmit diversity (2×1 MISO)

(d) Transmit diversity (2×1 MISO)

(e) Receive diversity (1×2 SIMO)

(f) Receive diversity (1×2 SIMO)

Figure 7.7: BER as a function of channel SNR for JPEG-coded (left column) and HEIF-coded (right column) images at QP = 25 under the classical (C) and quantum (Q) pipelines, with (a), (b) SISO, (c), (d) 2×1 MISO, and (e), (f) 1×2 SIMO.

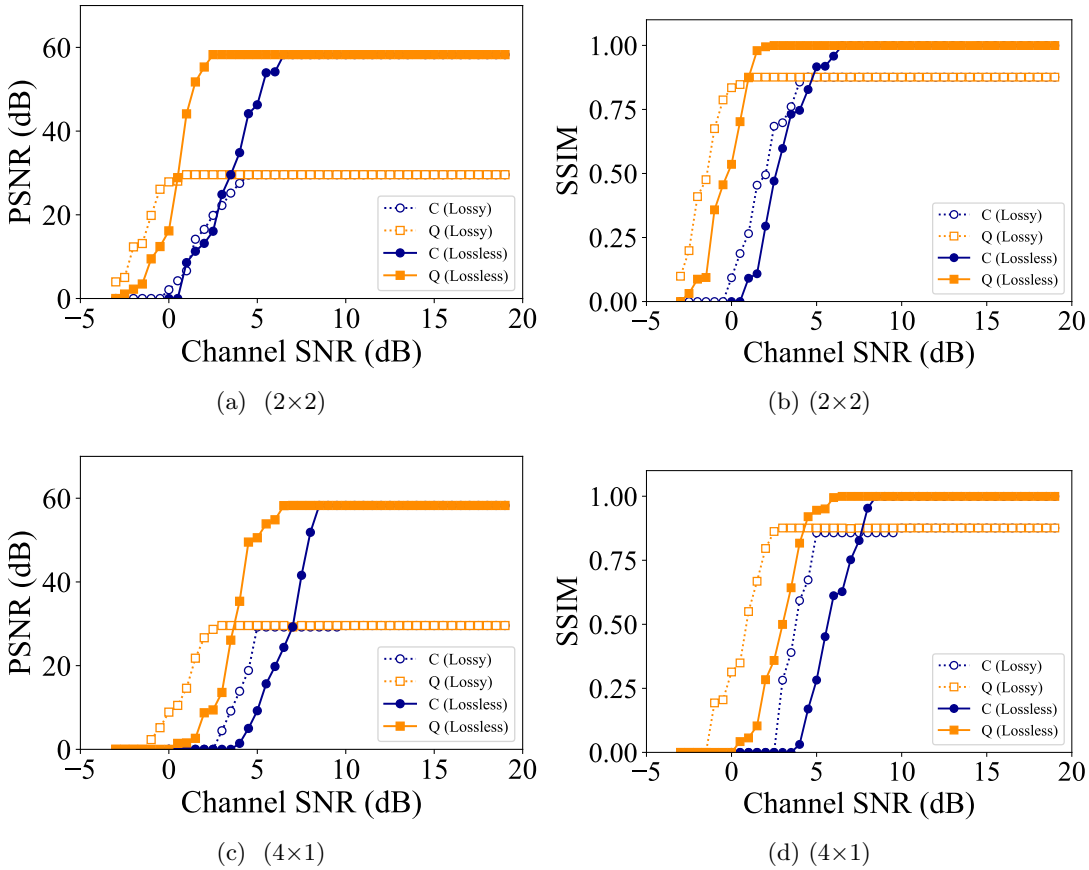
qubit encoding avoids the susceptibility commonly associated with multi-qubit entangled states. In addition, residual transmission errors are mitigated through classical polar coding, while MIMO-inspired spatial diversity further enhances communication reliability. Furthermore, the adoption of a low-dimensional qubit representation helps limit noise accumulation throughout the transmission process, thereby improving overall system stability under imperfect channel conditions.

The decision to focus on 2×2 MIMO at most reflects the experimental nature of this study, in which low complexity is prioritised over more elaborate configurations. Larger antenna arrays could be expected to yield additional improvements, but at the cost of greater implementation overhead. The application implications are nevertheless attractive: the framework points towards consumer-facing use cases such as high-fidelity multimedia streaming, remote collaboration tools, and emerging AR/VR experiences. It also lends itself to domains where confidentiality and reliability are paramount, including telemedicine and financial data exchange. Finally, the robustness to channel impairments suggests it could support stable, high-definition live video distribution even when the underlying link is far from ideal.

To investigate the scalability of the approach, we also evaluated higher-order configurations, specifically 4×1 and 2×2, with the results shown in Figure 7.8. As anticipated, raising the diversity order improves end-to-end performance, but it does so at the price of increased system complexity. Although these results suggest favourable scaling behaviour and good resistance to fading and noise, deploying such systems in larger real-world networks will require addressing a number of practical issues, including the limitations of current quantum hardware, the impact of imperfect channel estimation, and the more pronounced effect of decoherence at higher dimensions.

Taken as a whole, these results indicate that quantum superposition, when paired with lightweight single-qubit encoding, decoding, and classical polar coding for error correction, provides a tangible benefit for image transmission in MIMO settings. Avoiding QEC at this stage keeps the architecture tractable, but it also motivates future work on tailored QEC codes that could be folded into the same framework without prohibitive overhead. Multi-qubit encoding represents another promising direction, with the potential for further performance gains traded against a larger gate count and more

demanding hardware.



(a) (2×2) (b) (2×2)

(c) (4×1) (d) (4×1)

Figure 7.8: Average PSNR (left column) and SSIM (right column) for the classical (C) and quantum (Q) pipelines applied to JPEG-coded images at QP = 25 and QP = 100, under (a), (b) the 2×2 configuration and (c), (d) the 4×1 configuration.

In summary, the proposed quantum MIMO system offers a route to lowering the computational and energy footprint relative to classical alternatives while taking advantage of the strengths intrinsic to quantum hardware. Despite the fact that quantum MIMO hardware is still in an early stage of maturity, the simulation evidence presented here demonstrates the promise of the approach and provides a theoretical foundation that supports future experimental and real-world deployment.

7.1.3 Section Summary

This section established that quantum MIMO-based image transmission outperforms the matched classical MIMO system across the three antenna configurations considered:

the no-diversity 1×1 SISO baseline, the transmit-diversity 2×1 MISO arrangement, and the receive-diversity 1×2 SIMO arrangement. The diversity-assisted configurations demonstrated strong robustness against channel impairments, maintaining more reliable and stable performance in the presence of severe noise and fading conditions. Overall, the findings demonstrate that combining MIMO diversity with quantum superposition is a promising approach for mitigating fading and improving reconstruction fidelity in image transmission systems.

7.2 Quantum Communication Techniques for Video Transmission in Diversity-Assisted MIMO Systems

Publication Notice

The research presented in this section has been published in the following peer-reviewed journal publication:

U. Jayasinghe, P. Samarathunga, T. Fernando, and A. Fernando, "Transmit and receive diversity in MIMO quantum communication for high-fidelity video transmission," *Algorithms*, vol. 18, no. 7, p. 436, 2025, doi: 10.3390/a18070436.

This material is reproduced and adapted under the terms of the MDPI Copyright policy for use in a doctoral thesis. The content has been revised and extended with additional explanations and expanded discussion.

Problem Statement: The Section 7.1 established that integrating quantum communication with MIMO transmit and receive diversity can substantially improve the robustness and reconstruction quality of static image transmission over noisy quantum channels. Extending this approach from images to video transmission, however, is non-trivial. Video introduces temporal dependencies and inter-frame motion information that must be preserved alongside spatial fidelity, and its bandwidth requirements are an order of magnitude higher than those of single-image transmission. Under fading wireless channels, these characteristics make video especially vulnerable: channel impairments translate not only into per-frame distortion but also into motion artefacts, temporal inconsistency, and visible quality fluctuations during playback. The central problem

addressed in this section is therefore whether quantum communication, combined with classical MIMO spatial diversity, can deliver high-fidelity video transmission, preserving both spatial quality and temporal continuity, over fading channels.

Limitations of Existing Work: Two bodies of prior work bear on this problem, and each leaves a clear gap. First, existing quantum MIMO-based communication studies have focused predominantly on static image transmission; video transmission under spatial diversity configurations has not been comprehensively investigated, despite its significantly higher sensitivity to channel impairments and stricter bandwidth and latency requirements. Second, conventional classical video communication systems do employ diversity, channel coding, and advanced signal processing to combat fading and packet loss, but they remain bounded by classical limitations and degrade sharply under severe channel conditions. Critically, no prior work has examined how quantum superposition-based encoding can be combined with classical MIMO spatial diversity to jointly preserve spatial reconstruction quality and temporal continuity for video transmitted over fading channels.

Motivation and Proposed Contribution: To address these limitations, this section proposes a quantum MIMO communication framework for high-fidelity video transmission employing transmit and receive diversity techniques over fading communication channels. The proposed framework combines quantum superposition-based encoding with spatial diversity mechanisms to improve robustness against multipath fading and channel impairments during video transmission. By exploiting the advantages of quantum encoding together with MIMO diversity schemes, the proposed system aims to preserve both spatial video quality and temporal consistency under challenging wireless communication environments. The framework is evaluated under multiple diversity configurations, including 1×1 SISO, 2×1 MISO, and 1×2 SIMO communication architectures over fading quantum channels. The proposed quantum communication framework is compared against equivalent classical communication systems operating under identical bandwidth and channel conditions. The objective is to investigate whether integrating quantum communication with spatial diversity techniques can improve video reconstruction fidelity, robustness, and transmission reliability for next-generation video

communication systems.

7.2.1 System Model

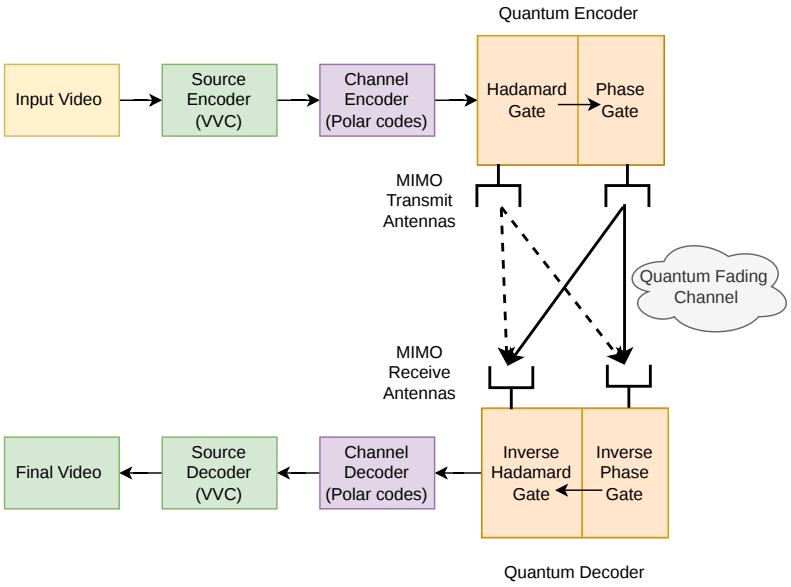


Figure 7.9: Block diagram of the proposed quantum-enabled MIMO link for video transmission.

This section describes the proposed pipeline for transmitting video over a quantum MIMO link, the high-level structure of which appears in Figure 7.9. The pipeline is built upon the quantum MIMO image transmission framework established in Section 7.1. Accordingly, only the modifications required to support video transmission are described below, while the complete description of the quantum encoding, channel coding, and diversity combining procedures is provided in Section 7.1.

On the transmit side, source coding is performed first, where the input video is compressed into a bitstream using the VVenC [203] implementation of the VVC standard. To ensure a comprehensive evaluation under diverse multimedia conditions, three YUV420 video sequences representing high-motion [205], medium-motion [206], and low-motion [207] content are employed. Each sequence is evaluated at three spatial resolutions (320×180, 1280×720, and 1920×1080), three frame rates (20, 30, and 50 fps), and three GOP sizes (8, 16, and 32). These combinations encompass diverse

levels of spatial information (SI), temporal information (TI), and coding configurations, thereby providing a representative range of practical video transmission scenarios rather than a single operating condition. The compressed bitstream is subsequently protected by a rate-1/2 polar code before being mapped into quantum superposition states by the proposed quantum encoder.

Propagation takes place over a quantum MIMO channel with Rayleigh fading, which is adopted here as a representative model for noisy quantum wireless environments. Three antenna configurations are examined, SISO, MISO, and SIMO, as shown earlier in Figure 7.3. At the receiver, the quantum decoder maps the incoming superposition states back into a classical bit sequence, which is then processed by the polar decoder and the source decoder to recover the video. For benchmarking purposes, an equivalent set of experiments is conducted using a classical MIMO communication system operating under the same bandwidth constraints and antenna configurations, with BPSK employed as the modulation scheme.

Simulation Environment

All simulations are performed in Python 3 on a workstation with the following specifications:

- CPU: 13th Gen Intel® Core™ i5-1345U, 1.60 GHz (Intel Corporation, Santa Clara, CA, USA).
- RAM: 16 GB DDR4 memory (SK hynix Inc., Icheon, Gyeonggi-do, South Korea).
- Operating System: Windows 11 (Microsoft Corporation, Redmond, WA, USA).
- Programming Language: Python 3.14.6 (Python Software Foundation, Wilmington, DE, USA).
- Main Libraries: NumPy for numerical computation, OpenCV for image and video processing, and Matplotlib for result visualisation.

The receiver is assumed to have perfect CSI, providing the decoder with an ideal channel estimate and eliminating channel-estimation errors as a confounding factor. Each video sequence is transmitted over the communication link for 1000 independent

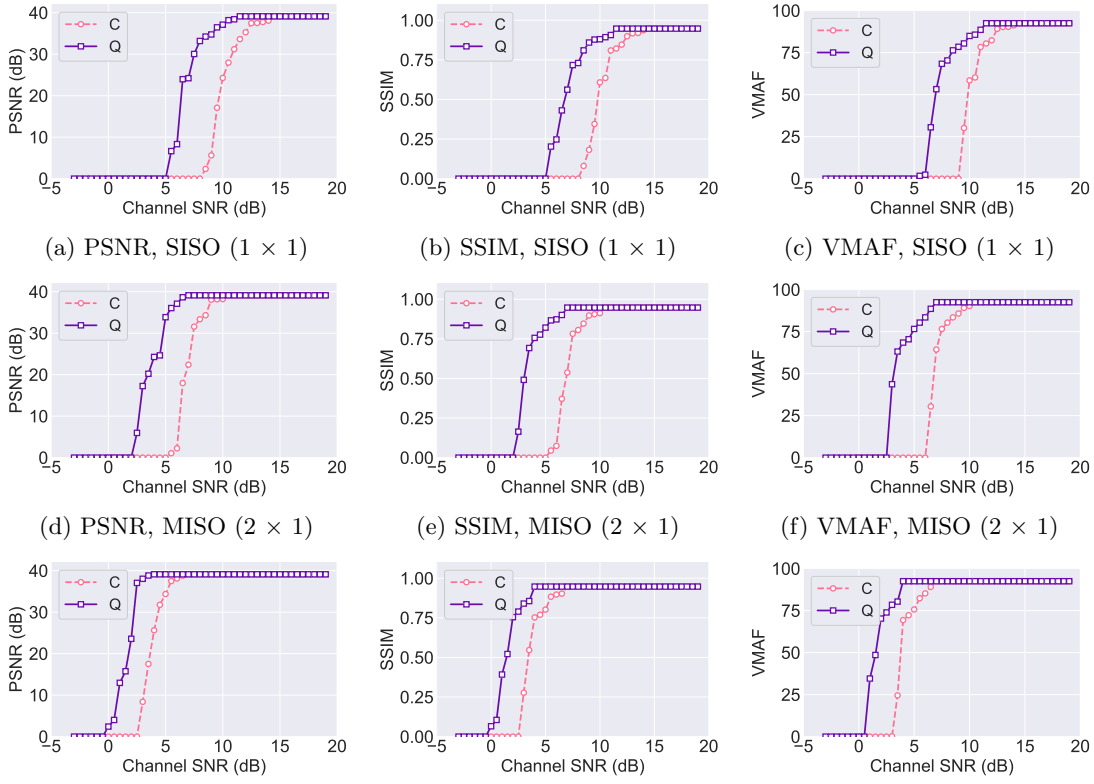
Monte Carlo trials, and the reported performance metrics are obtained by averaging the results across all trials to ensure statistical reliability. The reconstructed video quality is evaluated using PSNR, SSIM, and VMAF.

7.2.2 Results

This study characterises the proposed superposition-based quantum system for video transmission under three antenna configurations: 1×1 SISO, 2×1 MISO, and 1×2 SIMO. Rather than treating GOP size alone as the independent variable, the evaluation draws on three reference video sequences whose spatial and temporal information levels span high, medium, and low-motion content. The high-motion clip [205] contains fast object motion and frequent shot changes, producing elevated SI and TI scores and posing a stiff test for both compression and transmission. The medium-motion clip [206] sits in the middle, with moderate movement and scene change, and thus represents an intermediate-complexity case. The low-motion clip [207] is largely static, with limited movement; its SI is moderate but the TI is low, making it the easiest of the three to compress and convey. Because three different sequences are used, the metrics reported throughout this section are averages over all three, which gives a more representative picture of how the system behaves across heterogeneous content.

Figure 7.10 plots PSNR, SSIM, and VMAF as a function of channel SNR for a GOP size of 8, a spatial resolution of 320×180, and a frame rate of 50 fps. The data make it clear that the quantum-based pipeline (Q) consistently delivers better video quality than the classical baseline (C) on all three metrics, with the gap widening at low channel SNRs and present across all three antenna configurations (MISO, SIMO, and SISO). As the channel noise grows, more qubits are received in error during transmission, those errors propagate into the recovered classical bitstream, and the resulting distortions show up as visible artefacts and a drop in perceptual quality of the reconstructed frames. Diversity helps in both pipelines: the transmit-diversity (MISO) and receive-diversity (SIMO) arrangements outperform the no-diversity SISO baseline in classical and quantum settings alike. The benefit is particularly visible in the quantum versions of 2×1 MISO and 1×2 SIMO, where, for example, the PSNR remains respectable down to a channel SNR of around 7 dB.

In comparison, the SISO configuration requires a channel SNR of approximately 10 dB to achieve a similar level of reconstruction quality. This performance difference highlights the effectiveness of spatial diversity in enhancing the robustness of the proposed quantum transmission framework against noise and fading. By combining diversity techniques with quantum encoding, the system is able to maintain higher reconstruction fidelity even under challenging channel conditions. Similar trends can also be observed in the SSIM and VMAF results, where the quantum-based transmission approach consistently outperforms the classical counterpart across all antenna configurations, further demonstrating the benefits of integrating spatial diversity with quantum communication.



(a) PSNR, SISO (1 × 1) (b) SSIM, SISO (1 × 1) (c) VMAF, SISO (1 × 1)

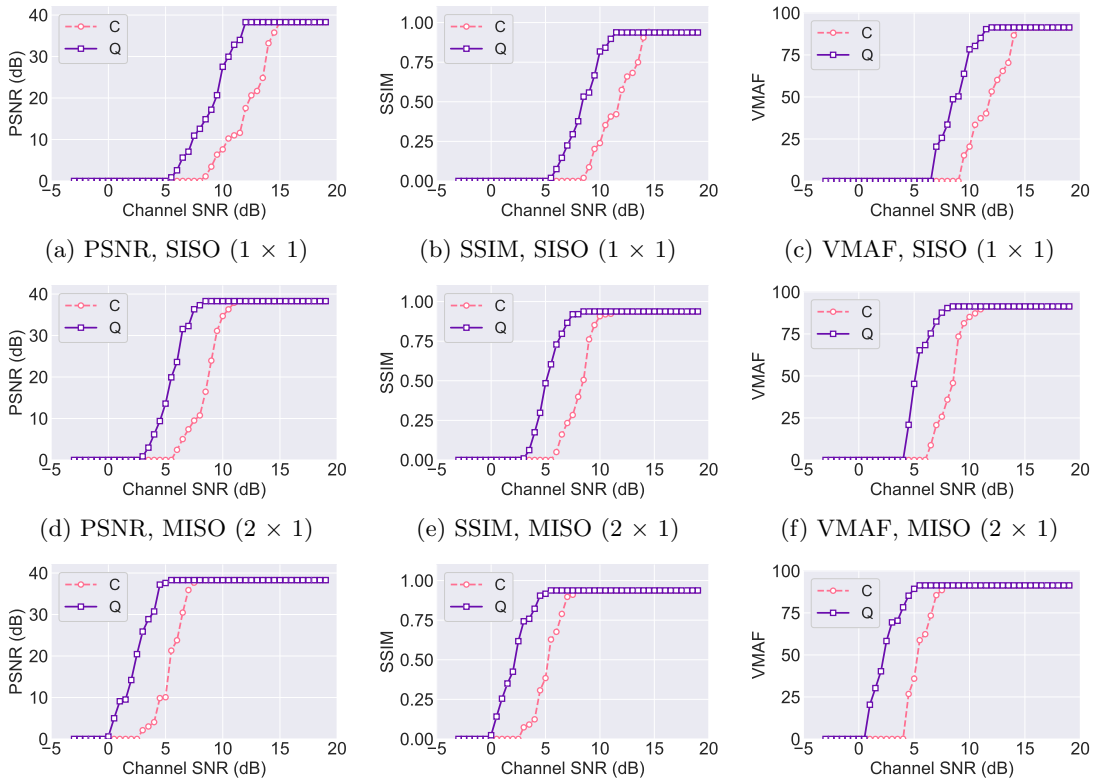
(d) PSNR, MISO (2 × 1) (e) SSIM, MISO (2 × 1) (f) VMAF, MISO (2 × 1)

(g) PSNR, SIMO (1 × 2) (h) SSIM, SIMO (1 × 2) (i) VMAF, SIMO (1 × 2)

Figure 7.10: Average PSNR (left column), SSIM (centre column), and VMAF (right column) obtained with the classical (C) and quantum (Q) pipelines for GOP size 8 under three antenna configurations: (a–c) 1 × 1 SISO, (d–f) 2 × 1 MISO, and (g–i) 1 × 2 SIMO.

An additional observation from the performance curves is the approximate 3 dB

advantage achieved by the 1×2 SIMO configuration over the 2×1 MISO configuration in both classical and quantum transmission scenarios. This behaviour arises from the assumption of equal total transmit power across all antenna setups, which naturally provides a performance benefit to receive diversity schemes.



(a) PSNR, SISO (1×1) (b) SSIM, SISO (1×1) (c) VMAF, SISO (1×1)

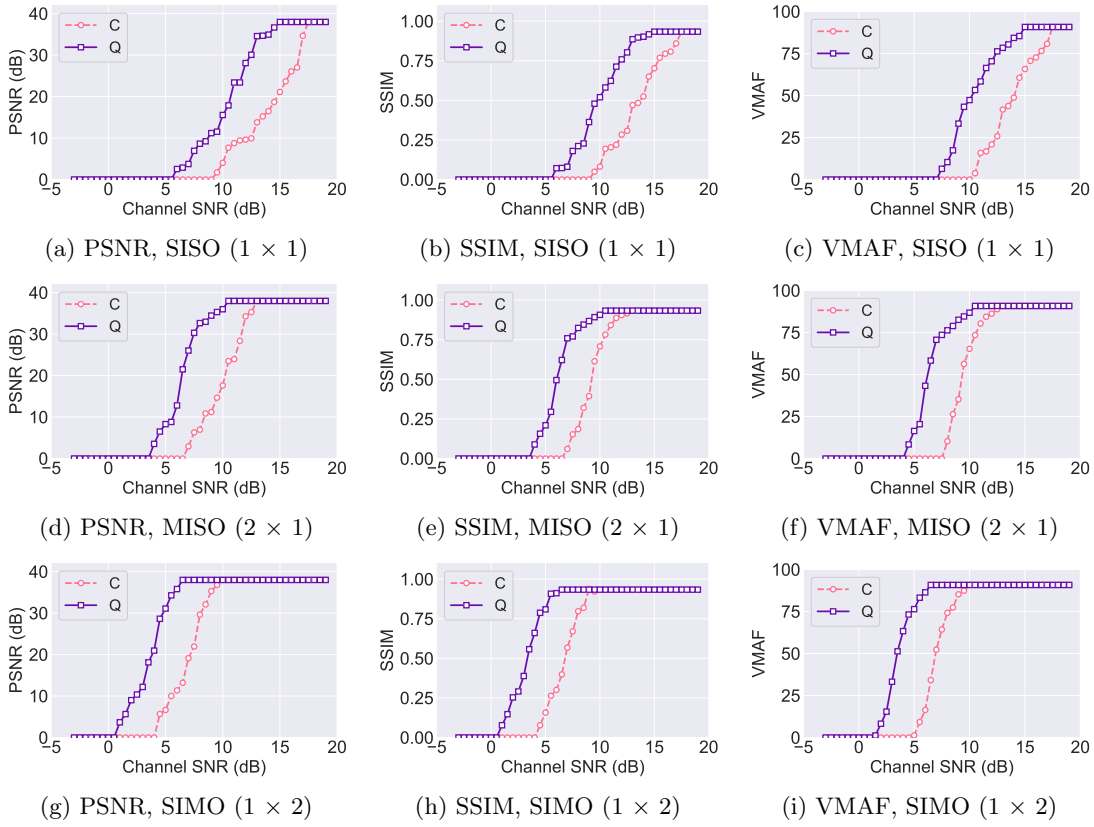
(d) PSNR, MISO (2×1) (e) SSIM, MISO (2×1) (f) VMAF, MISO (2×1)

(g) PSNR, SIMO (1×2) (h) SSIM, SIMO (1×2) (i) VMAF, SIMO (1×2)

Figure 7.11: Average PSNR (left column), SSIM (centre column), and VMAF (right column) obtained with the classical (C) and quantum (Q) pipelines for GOP size 16 under three antenna configurations: (a–c) 1×1 SISO, (d–f) 2×1 MISO, and (g–i) 1×2 SIMO.

Figure 7.11 presents the performance results obtained with a GOP size of 16. Similar trends to those observed for GOP8 can be identified, where the proposed quantum transmission framework consistently achieves superior performance compared with the classical baseline across all antenna configurations. In addition, the diversity-assisted MISO and SIMO configurations continue to outperform the conventional SISO arrangement, further demonstrating the benefits of incorporating spatial diversity into the transmission system. The notable change is that absolute quality is slightly lower

at GOP16 than at GOP8, signalling that the longer prediction structures interact unfavourably with channel impairments.



(a) PSNR, SISO (1 × 1) (b) SSIM, SISO (1 × 1) (c) VMAF, SISO (1 × 1)

(d) PSNR, MISO (2 × 1) (e) SSIM, MISO (2 × 1) (f) VMAF, MISO (2 × 1)

(g) PSNR, SIMO (1 × 2) (h) SSIM, SIMO (1 × 2) (i) VMAF, SIMO (1 × 2)

Figure 7.12: Average PSNR (left column), SSIM (centre column), and VMAF (right column) obtained with the classical (C) and quantum (Q) pipelines for GOP size 32 under three antenna configurations: (a–c) 1 × 1 SISO, (d–f) 2 × 1 MISO, and (g–i) 1 × 2 SIMO.

Figure 7.12 continues this analysis at a GOP size of 32. The relative ranking of the systems is preserved, quantum system still surpasses classical system, and the diversity-aided variants still surpass SISO, but absolute quality falls below the levels reached at GOP16. This behaviour can be explained by the increased reliance on inter-frame prediction associated with larger GOP sizes. As the GOP length increases, a greater number of frames are encoded using information from previously reconstructed frames within the same GOP. Consequently, transmission errors affecting one frame can propagate to subsequent predicted frames, resulting in cumulative distortion and a corresponding reduction in overall reconstruction quality.

This monotonic degradation with GOP is visible across Figures 7.10–7.12: each step from 8 to 16 to 32 brings down the metrics. Sustaining quality in this regime therefore calls for adaptive error-protection techniques that allocate stronger protection to frames higher up in the GOP dependency tree. Pairing such unequal protection with error-resilient encoding strategies, for instance flexible macroblock ordering or intra-refresh, can confine the spread of errors and prevent localised failures from contaminating the rest of the GOP. The combination is a sensible direction for hardening video transmission over both quantum and classical channels.

Beyond the influence of GOP size, the MISO and SIMO diversity configurations provide additional robustness benefits in both classical and quantum communication systems. In conventional classical systems, spatial diversity is primarily used to mitigate the effects of multipath fading and interference, thereby improving the effective received SNR through diversity combining techniques. In quantum communication systems, however, the transmission process is additionally affected by quantum-specific impairments such as decoherence, quantum noise, and quantum fading, which can disturb the integrity of the superposition states used for information encoding. Unlike classical fading, which mainly alters signal amplitude and phase, these quantum effects directly impact the stability of the encoded quantum states themselves. Despite these additional challenges, spatial diversity remains highly beneficial in the quantum framework. The use of MISO and SIMO configurations introduces multiple transmission or reception paths, increasing redundancy and improving the probability of successful signal recovery. As a result, the diversity-assisted quantum systems achieve greater robustness against channel impairments and maintain more reliable video reconstruction performance under adverse transmission conditions.

Quantum superposition itself contributes a further layer of resistance. By holding multiple bit values simultaneously, the quantum encoding spreads information across parallel components of the state, giving the system an intrinsic tolerance to noise and fading. The improved performance of the proposed quantum framework at low channel SNRs can be attributed to the combined effect of spatial diversity at the antenna level and superposition-based encoding at the quantum level. This integration enhances transmission robustness and enables more accurate reconstruction of the

received video data under challenging channel conditions. The resulting performance gains are consistently reflected in the PSNR, SSIM, and VMAF evaluations across all antenna configurations and GOP sizes.

Next, we examine how varying the frame rate and resolution affects the quantum MIMO pipeline, using GOP8 as a representative working point. The findings are summarised in Table 7.1. Across the configurations tested, changes in resolution and frame rate have only a marginal impact on the maximum channel SNR gain achieved by the quantum system relative to the classical baseline. This gain is computed using (7.12).

$$\Delta\mathrm{SNR}(Q) = \mathrm{SNR}_{\mathrm{classical}}(Q) - \mathrm{SNR}_{\mathrm{quantum}}(Q) \tag{7.12}$$

where $\mathrm{SNR}_{\mathrm{classical}}(Q)$ and $\mathrm{SNR}_{\mathrm{quantum}}(Q)$ are the channel SNRs that the classical baseline and the proposed system, respectively, need in order to reach the same quality level Q. The fact that the gain is essentially flat across resolutions and frame rates indicates that the two systems scale similarly with these video parameters, and that the advantage of the quantum approach is largely insensitive to format choices. From a practical standpoint, this means the quantum gain should carry over to a wide variety of streaming scenarios, and it also speaks to the scalability and flexibility of the proposed framework when faced with content of differing complexity and quality.

Table 7.1: Comparison of the highest channel SNR reduction achieved by the proposed quantum transmission framework relative to the equivalent classical system for different antenna diversity configurations under varying spatial resolutions and frame rates.

Frame Rate (fps)	**1280 × 720**			**1920 × 1080**		
	1 × 1	**2 × 1**	**1 × 2**	**1 × 1**	**2 × 1**	**1 × 2**
20	3.0 dB	3.0 dB	3.1 dB	3.0 dB	2.8 dB	3.0 dB
30	3.0 dB	2.9 dB	3.0 dB	3.0 dB	3.0 dB	3.0 dB
50	3.0 dB	3.1 dB	3.0 dB	2.8 dB	2.8 dB	3.0 dB

To make these findings tangible, Figure 7.13 provides a representative decoded frame from each configuration for both pipelines. The MISO and SIMO frames are decoded at a channel SNR of 7.5 dB. For SISO, however, 7.5 dB lies below what the pipeline can sustain because the BER is too high, so the corresponding frame is shown at 10 dB instead. The obtained results validate the robustness of the proposed transmission

system.



(a) Classical (1×1 SISO) (b) Classical (2×1 MISO) (c) Classical (1×2 SIMO)



(d) Quantum (1×1 SISO) (e) Quantum (2×1 MISO) (f) Quantum (1×2 SIMO)

Figure 7.13: Representative reconstructed video frames for classical (top row) and quantum (bottom row) transmission under different antenna configurations: 1×1 SISO at 10.0 dB SNR, and 2×1 MISO and 1×2 SIMO at 7.5 dB SNR.

Motivated by the demand for low-complexity transmission schemes capable of maintaining high perceptual quality with near-real-time performance, the proposed framework integrates classical and quantum communication techniques within a hybrid architecture. The system is specifically designed to support efficient operation while minimising computational complexity, making it well suited for deployment in resource-limited communication environments.

Within the quantum transmission stage, the bitstream is encoded by applying Hadamard operations to the qubits representing the input data segments. The computational complexity of this process scales as $\mathcal{O}(k)$, where k denotes the number of encoded qubits. Since the proposed framework employs single-qubit encoding ($k = 1$), the encoding complexity reduces to $\mathcal{O}(1)$, resulting in a highly lightweight quantum encoding process. Similarly, the decoding stage relies solely on single-qubit measurements, each requiring constant computational complexity. Furthermore, the framework avoids the use of entanglement, deep quantum gate structures, and QEC mechanisms, thereby significantly reducing both implementation complexity and hardware requirements.

Conventional communication systems benefit from decades of technological development, standardisation, and highly optimised reliability mechanisms. Quantum

communication systems, however, offer a different advantage in the form of reduced algorithmic and computational complexity arising from the characteristics of quantum-state processing. In the proposed framework, this benefit is further strengthened through the use of single-qubit operations and Hadamard-based modulation, both of which maintain a low computational overhead throughout the transmission process. It should also be noted that the reported performance results are obtained entirely through classical simulation of quantum operations. Since practical quantum hardware exhibits fundamentally different behaviour in terms of state evolution and parallel processing, runtime comparisons based solely on classical simulations are not representative of actual hardware performance and are therefore not considered in this work. Furthermore, to preserve the low-complexity nature of the framework and maintain practical implementability, QEC techniques are intentionally excluded.

Despite the simulation-based nature of the present study, the obtained results establish a foundation for future experimental validation, including hardware prototyping, laboratory implementation, and real-world performance measurements. In addition to the primary antenna configurations, a 2×2 MIMO arrangement is also investigated to evaluate the combined effects of transmit and receive diversity and to demonstrate the adaptability of the framework to more advanced spatial diversity structures without significant architectural modifications.

Furthermore, the proposed framework remains scalable to higher-order MIMO configurations such as 4×4 and 8×8, provided that adequate quantum processing and hardware resources are available. Although increasing the number of antennas inevitably introduces additional complexity, the modular structure and inherently low baseline complexity of the proposed design make such extensions feasible. These characteristics position the hybrid quantum–classical communication framework as a promising candidate for future applications including telemedicine, remote diagnostics, and real-time multimedia transmission over bandwidth-constrained or error-prone communication channels.

7.2.3 Section Summary

Extending the Section 7.1 framework from images to video, this section showed that the same superposition-plus-diversity approach carries over to compressed video, consistently exceeding the classical baseline in PSNR, SSIM, and VMAF across all evaluated GOP sizes, resolutions, and frame rates. The architecture retains the low-complexity, scalable design of the image case, supporting the same near-future hardware realisation path.

7.3 Quantum OFDM-Based Image Transmission for Noise-Impaired Communication Channels

Publication Notice

The research presented in this section has been published in the following peer-reviewed journal publication:

U. Jayasinghe and A. Fernando, "A quantum OFDM framework for high-fidelity image transmission," *IEEE Transactions on Consumer Electronics*, vol. 71, no. 4, pp. 9628–9636, 2025, doi: 10.1109/TCE.2025.3619569.

This material is reproduced and adapted under the terms of the IEEE Copyright policy for use in a doctoral thesis. The content has been revised and extended with additional explanations and expanded discussion.

Problem Statement: Sections 7.1 and 7.2 showed that combining quantum superposition based encoding with MIMO transmit and receive diversity substantially improves robustness and reconstruction fidelity for both image and video transmission under fading conditions. Those frameworks, however, exploited only the spatial dimension of the wireless channel; the frequency-selective impairments that dominate wideband multimedia transmission were left unaddressed. Modern multimedia communication systems are required to deliver reliable high-data-rate image transmission under challenging wireless environments involving multipath fading, interference, bandwidth limitations, and dynamic channel variations. Although conventional OFDM systems have been widely adopted to mitigate frequency-selective fading and improve spectral efficiency, maintaining high-fidelity image reconstruction under severe noisy channel conditions

remains a significant challenge for classical communication systems. Quantum communication has recently emerged as a promising direction for next-generation wireless systems, offering potential advantages in robustness, spectral efficiency, and resilience to channel impairments that classical systems alone cannot fully overcome. Integrating quantum communication with OFDM is therefore important, as it could combine the frequency-selective fading mitigation and spectral efficiency of OFDM with the noise-resilience advantages of quantum-domain transmission, providing a path toward reliable high-data-rate image transmission under severe channel conditions. To date, however, no QOFDM system has been developed for image transmission, leaving the feasibility and performance benefits of such an integration an open problem.

Limitations of Existing Work: Classical OFDM communication systems improve robustness by dividing high-rate data streams into orthogonal low-rate subcarriers. However, these systems remain vulnerable to noise, synchronisation errors, interference, and high peak-to-average power ratio (PAPR) effects, which degrade transmission reliability and reconstructed image quality under adverse communication conditions. At the same time, existing quantum communication studies have primarily focused on standalone quantum transmission frameworks and have not comprehensively investigated OFDM-based multicarrier transmission within the quantum communication domain. To the best of the author's knowledge, no prior work has developed a complete end-to-end QOFDM framework specifically designed for high-fidelity image transmission over noisy fading communication channels.

Motivation and Proposed Contribution: To address these limitations, this section proposes a QOFDM-based image transmission framework for robust image communication over noisy quantum communication channels. The proposed framework integrates multi-qubit quantum encoding with QFT-based orthogonal subcarrier generation to construct a complete end-to-end quantum multicarrier transmission system. By exploiting the orthogonality and parallel transmission characteristics of OFDM together with quantum signal representations, the proposed framework aims to improve transmission robustness, spectral efficiency, and reconstructed image quality under noisy and fading communication conditions. The proposed system converts source-coded image data

into quantum superposition states using multi-qubit encoding and applies the QFT to generate orthogonal quantum subcarriers analogous to classical OFDM systems. The framework further incorporates cyclic prefix insertion, noisy fading channel modelling, inverse quantum Fourier processing, and quantum decoding for complete end-to-end transmission and reconstruction. The proposed QOFDM framework is compared against equivalent classical OFDM systems employing different modulation schemes under identical channel conditions. The objective is to demonstrate that integrating quantum communication with OFDM-based multicarrier communication can significantly improve image transmission fidelity and robustness under challenging communication environments.

The main contributions of this section are as follows.

- Proposes a complete end-to-end QOFDM framework for high-fidelity image transmission over noisy communication channels.
- Integrates multi-qubit quantum encoding with QFT-based orthogonal multicarrier transmission for robust image communication.
- Investigates the performance of the proposed QOFDM framework under different qubit encoding sizes and noisy channel conditions.
- Evaluates the system performance using objective quality assessment metrics, including BER, PSNR, and SSIM.
- Compares the proposed QOFDM framework against equivalent classical OFDM communication systems employing different modulation schemes, demonstrating improved robustness and reconstructed image quality.

7.3.1 System Model

This section introduces the QOFDM architecture proposed for image transmission. To benchmark its behaviour, we compare it against a classical OFDM system constrained to operate within the same bandwidth budget. The approach exploits core quantum mechanics ideas, including superposition, unitary evolution, and Hilbert-space encoding, to obtain a degree of parallelism, spectral efficiency, and noise tolerance that classical

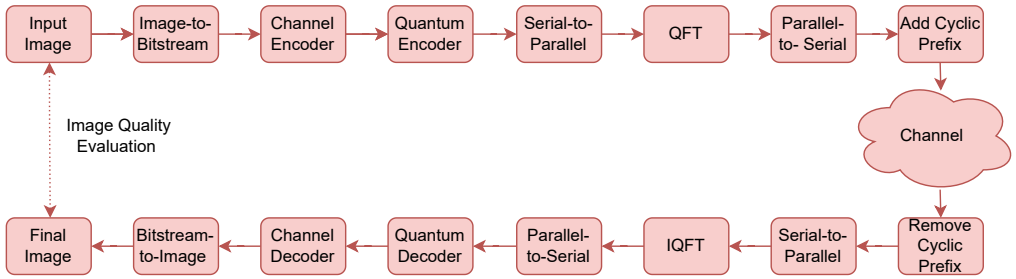


Figure 7.14: Block diagram of the proposed QOFDM pipeline for image transmission.

OFDM cannot match. As shown in Figure 7.14, the QOFDM pipeline retains the overall block structure of conventional OFDM but reinterprets each stage in quantum terms. The chain starts from an input image; for the simulation campaign we use twenty uncompressed PNG images of resolution 256×192 pixels from the Microsoft COCO dataset [197], chosen so as to span a wide range of spatial content. That said, the pipeline is agnostic to image format and can accept arbitrary inputs. The selected images are serialised into bitstreams, which are then fed to a channel encoder. We use polar codes [210] with a code rate of $1/2$ to add redundancy prior to quantum mapping.

Each coded classical bit is converted into a qubit by the quantum encoder. The resulting qubit sequence is reshaped from serial to parallel and forwarded to the QFT stage, which produces a set of orthogonal subcarriers suitable for OFDM-style transmission. The parallel subcarriers are then linearised back into a serial stream, a cyclic prefix (CP) is prepended to each symbol, and the resulting quantum states are launched into the quantum channel.

At the receiver, the operations of the transmitter are reversed in order. The CP is stripped first, followed by a serial-to-parallel rearrangement. The IQFT then maps the orthogonal frequency-domain components back into the corresponding time-domain quantum representation. From there, the quantum decoder recovers the underlying classical bits, the polar decoder undoes the redundancy added at the encoder, and the image is finally reassembled from the recovered bitstream.

To make the operation of each quantum block in Figure 7.14 clear, the next subsections expand on the main blocks individually.

Quantum Encoder/Decoder and QFT/IQFT

Once the bitstream emerges from the polar encoder, it is mapped onto qubits using the same computational-basis convention introduced in Section 7.1 ($|0\rangle$ and $|1\rangle$, as defined in (7.1)–(7.2)); this correspondence is not re-derived here. The qubit stream is then partitioned into groups whose size matches a chosen "qubit width" between 1 and 8. The framework itself supports arbitrarily large qubit sizes, but we cap the study at eight qubits because that matches the natural 8-bit grouping used in standard image representations.

For the single-qubit case, the basis states defined in Section 7.1 are sufficient to represent the encoded state directly. For multi-qubit encoding, however, composite states are constructed by taking the tensor products of single-qubit basis vectors. This is the standard approach for constructing multi-qubit basis states, as described in Section 4.1.1, Equations (4.2)–(4.3).

After this encoding step, the QFT is applied to turn the prepared quantum states into a set of orthogonal subcarriers, which forms the heart of the QOFDM scheme. In classical OFDM systems, the IFFT is employed to generate orthogonal subcarriers by converting modulated complex-valued symbols into time-domain signals. Since the IFFT operates on frequency-domain coefficients, its quantum counterpart would naturally be the IQFT. However, in the proposed QOFDM system, the quantum encoder produces quantum states directly rather than frequency-domain quantum coefficients requiring inverse transformation. As a result, the IQFT cannot be directly applied in the same manner as the classical IFFT. Instead, the QFT itself is utilised to transform the encoded quantum states into orthogonal quantum subcarriers within the quantum domain. For the transformation to be well-defined, the dimension of the QFT matrix must match that of the input state vector. Specifically, an input vector of size $2^k \times 1$ calls for a QFT matrix of size $2^k \times 2^k$. The general form of the QFT matrix is given in (7.13).

$$F_N = \frac{1}{\sqrt{N}} \begin{pmatrix} 1 & 1 & 1 & \cdots & 1 \\ 1 & \omega & \omega^2 & \cdots & \omega^{N-1} \\ 1 & \omega^2 & \omega^4 & \cdots & \omega^{2(N-1)} \\ \vdots & \vdots & \vdots & \ddots & \vdots \\ 1 & \omega^{N-1} & \omega^{2(N-1)} & \cdots & \omega^{(N-1)(N-1)} \end{pmatrix} \tag{7.13}$$

Here, ω is the complex N-th root of unity, defined in (7.14), and $N = 2^k$ with k the number of qubits.

$$\omega = e^{2\pi i/N} \tag{7.14}$$

The matrix in (7.13) follows directly from the standard QFT definition [127] expressed in (7.15).

$$F_N |x\rangle = \frac{1}{\sqrt{N}} \sum_{y=0}^{N-1} e^{\frac{2\pi i x y}{N}} |y\rangle \tag{7.15}$$

This expression maps a computational basis state $|x\rangle$ onto a superposition spanning all basis states $|y\rangle$, with each component weighted by a complex exponential phase whose argument depends on both x and y.

As a concrete example, for a two-qubit register ($N = 4$) the QFT matrix takes the form shown in (7.16).

$$F_4 = \frac{1}{2} \begin{pmatrix} 1 & 1 & 1 & 1 \\ 1 & i & -1 & -i \\ 1 & -1 & 1 & -1 \\ 1 & -i & -1 & i \end{pmatrix} \tag{7.16}$$

When this 4×4 matrix F_4 acts on each of the two-qubit basis states defined in (4.2)–(4.3), the resulting transformed vectors are those listed in (7.17)–(7.20).

$$T_1 = F_4 |00\rangle = \frac{1}{2} \begin{pmatrix} 1 & 1 & 1 & 1 \end{pmatrix}^T \tag{7.17}$$

$$T_2 = F_4 |01\rangle = \frac{1}{2} \begin{pmatrix} 1 & i & -1 & -i \end{pmatrix}^T \tag{7.18}$$

$$T_3 = F_4 \left|10\right\rangle = \frac{1}{2}\begin{pmatrix}1 & -1 & 1 & -1\end{pmatrix}^T \tag{7.19}$$

$$T_4 = F_4 \left|11\right\rangle = \frac{1}{2}\begin{pmatrix}1 & -i & -1 & i\end{pmatrix}^T \tag{7.20}$$

Because the columns of the QFT matrix constitute an orthonormal basis, the transformed subcarriers in (7.17)–(7.20) are mutually orthogonal. This orthogonality is easy to verify by computing pairwise Hermitian inner products: any two distinct vectors that yield a zero inner product are, by definition, orthogonal in the complex Hilbert space, as demonstrated in (7.21).

$$\begin{aligned}\langle T_1|T_2\rangle &= \left(\frac{1}{2}\begin{pmatrix}1 & 1 & 1 & 1\end{pmatrix}\right)\left(\frac{1}{2}\begin{pmatrix}1\\ i\\ -1\\ -i\end{pmatrix}\right)\\ &= \frac{1}{4}(1+i-1-i)\\ &= 0\end{aligned} \tag{7.21}$$

Carrying out the same computation for every remaining pair confirms that all four transformed states are mutually orthogonal. This feature is central to QOFDM, since orthogonality among subcarriers is exactly what allows ICI to be kept to a minimum.

Beyond establishing orthogonality, the QFT effectively spreads the original information across the resulting subcarriers, so that each output state carries a portion of the input. This information-spreading property can be read off from the relations given in (7.22)–(7.25).

$$T_1 = S_1 + S_2 + S_3 + S_4 \tag{7.22}$$

$$T_2 = S_1 + S_2 i - S_3 - S_4 i \tag{7.23}$$

$$T_3 = S_1 - S_2 + S_3 - S_4 \tag{7.24}$$

$$T_4 = S_1 - S_2 i - S_3 + S_4 i \tag{7.25}$$

This pattern mirrors what the IFFT does in classical OFDM: every subcarrier carries a linear combination of the original symbols while the set as a whole remains mutually orthogonal.

At the receive side, the IQFT is applied to undo the QFT operation. Conceptually, this brings the frequency-domain quantum subcarriers back to the time-domain representation in which the encoded states originally lived, which is then handed to the quantum decoder. The role played here by the IQFT is the quantum counterpart of the FFT in classical OFDM, and it is a prerequisite for any subsequent demapping back to classical bits.

By construction, the IQFT is the Hermitian adjoint (†) of the QFT operator, as expressed in (7.26).

$$\text{IQFT} = \text{QFT}^{\dagger} \tag{7.26}$$

For an N-dimensional system, acting with the IQFT on a computational basis state $|y\rangle$ produces the result given in (7.27).

$$F_N^{-1} |y\rangle = \frac{1}{\sqrt{N}} \sum_{x=0}^{N-1} e^{-2\pi i x y/N} |x\rangle \tag{7.27}$$

where F_N^{-1} denotes the N-point inverse quantum Fourier transform operator, N represents the dimension of the quantum system, $|y\rangle$ is the input computational basis state, and $|x\rangle$ denotes the output basis states in the superposition. The variables x and y are integer indices ranging from 0 to $N-1$, while $i = \sqrt{-1}$ represents the imaginary unit. The exponential term $e^{-2\pi i x y/N}$ defines the complex phase rotation associated with the IQFT operation. Overall, this process reverses the spreading effect introduced by the QFT, reconstructing the information distributed across the orthogonal subcarriers back into its original computational-basis form.

Before the IQFT is applied, however, the decoder performs a Euclidean-distance-based detection step in the frequency domain. The received vector is compared against the candidate set of frequency-domain basis states, and the nearest candidate is selected as the most likely transmitted state. The chosen state is then propagated through the IQFT to recover its time-domain basis representation, after which an inverse tensor mapping is used to extract the underlying classical bit sequence. In the proposed QOFDM pipeline, channel effects are equalised after the IQFT under an assumption of perfect CSI. In a deployed system, the CSI would have to be obtained via quantum pilot-assisted estimation, where specially prepared probe qubits are transmitted and measured at the receiver to characterise the channel.

In this QOFDM scheme, the number of subcarriers N sets how the total bandwidth B is partitioned, with the subcarrier spacing Δf following from (7.28).

$$\Delta f = \frac{B}{N} \tag{7.28}$$

Choosing N as a power of two is standard practice, as it strikes a useful balance between spectral resolution and computational cost while keeping subcarriers strictly orthogonal and ICI under control. Throughout this work, $N = 2^k$, where k is the number of qubits per encoded group.

Cyclic Prefix in QOFDM

To suppress ISI arising from multipath propagation, a CP is inserted by copying the samples of the QFT output (L_{CP}) and prepending them to the symbol. This lengthens the transmitted symbol as captured by (7.29).

$$T_{\mathrm{symbol}} = N + L_{\mathrm{CP}} \tag{7.29}$$

The presence of the CP preserves quantum-subcarrier orthogonality by absorbing the channel-induced spread of successive symbols and preventing them from leaking into one another. In the reported experiments, the CP length is selected as one quarter of the total number of subcarriers associated with the corresponding qubit dimension, as defined in (7.30).

$$L_{\mathrm{CP}} = \mathrm{round}(N \times 0.25) \tag{7.30}$$

Quantum Channel

To make the quantum transmission stage realistic, this work adopts a generalised Rayleigh fading model that has been extended to handle quantum signals. Whereas classical channels typically introduce noise primarily through amplitude and phase distortions, quantum channels additionally suffer from decoherence processes such as bit-flips, phase-flips, amplitude damping, phase damping, and depolarisation. To accommodate these quantum-specific impairments, the standard Rayleigh fading model is augmented with operators that mimic the corresponding decoherence effects, giving a more faithful description of how a quantum state degrades over a time-varying, noisy link. Less common noise mechanisms and hardware-specific artefacts are left out of the present analysis to keep the discussion focused. To evaluate the proposed QOFDM framework under different propagation conditions, two commonly adopted Rayleigh fading channel models representing urban and indoor environments are considered. Each channel model consists of four multipath components, representing relatively severe and moderate multipath fading conditions, respectively. These channel profiles provide sufficient variability to assess the robustness and reliability of the proposed system without exhaustively modelling every possible wireless propagation scenario. The urban profile uses path delays of $(0,\ 0.2,\ 0.5,\ 1.0)$ μs, gains of $(0,\ -3,\ -10,\ -15)$ dB, and a Doppler shift of 100 Hz. The indoor profile uses delays of $(0,\ 0.05,\ 0.15,\ 0.3)$ μs, gains of $(0,\ -2,\ -8,\ -12)$ dB, and a 5 Hz Doppler shift. Quantum noise probabilities are swept to emulate different effective SNR conditions, and the impact of the channel on quantum-state fidelity is recorded.

A classical OFDM benchmark is set up to operate within the same bandwidth and under the same conditions as the QOFDM system. The benchmark uses common digital modulation schemes, including BPSK, QPSK, and 16-QAM. The number of OFDM subcarriers is fixed at $N = 256$, matching the largest configuration used by the quantum system and giving the classical baseline a fair, optimised operating point for the comparison. The QOFDM framework is evaluated in a normalised baseband-equivalent

setting, which puts the carrier frequency aside and keeps the focus on how modulation behaves in the presence of multipath fading and quantum noise.

7.3.2 Results

In this section, the performance of the proposed QOFDM transmission framework is investigated through BER, PSNR, and SSIM analysis. To provide a clearer understanding of the contribution of the quantum transmission process itself, the system is evaluated under two operating conditions: with channel coding and without channel coding. This allows the impact of the quantum modulation framework and the additional protection offered by classical coding techniques to be examined independently. For comparative assessment, all results are benchmarked against an equivalent classical OFDM transmission system. The evaluation is carried out under both urban and indoor Rayleigh fading environments in order to analyse system behaviour across different wireless propagation conditions. Performance metrics are computed as average values over the complete set of twenty test images considered in the study. The subsequent subsections present and discuss the obtained results for each transmission scenario separately.

Performance Evaluation of QOFDM under Urban Rayleigh Fading Environments

The uncoded transmission results obtained under the urban Rayleigh fading channel demonstrate that the proposed QOFDM framework achieves progressively lower BER as the qubit dimension increases, as illustrated in Figure 7.15a. Under severe low-SNR conditions, all transmission schemes experience performance degradation due to the strong effects of fading and channel noise. However, the QOFDM configurations consistently outperform the corresponding classical OFDM schemes throughout the evaluated SNR range. Among all tested configurations, the eight-qubit QOFDM system achieves the lowest BER performance. Even the best-performing classical OFDM configuration based on BPSK modulation remains inferior to the proposed quantum transmission approach.

Several characteristics of the QOFDM framework contribute to this performance

advantage. By representing information within a higher-dimensional Hilbert space, the system achieves improved robustness against channel impairments while maintaining compact signal representation. The use of the QFT generates orthogonal quantum subcarriers that reduce interference effects during transmission. In addition, the distributed nature of quantum-state encoding allows transmission errors to have a less significant impact on the reconstructed information. The normalisation property of quantum states also contributes to improved transmission stability by avoiding the high PAPR commonly observed in conventional OFDM systems.

The image reconstruction quality follows trends consistent with the BER behaviour. As shown in Figure 7.15b, increasing the qubit width produces higher PSNR values, indicating reduced distortion and improved image recovery performance. For larger qubit dimensions, the proposed framework is capable of achieving near-lossless reconstruction even at comparatively low channel SNR levels. Similar behaviour is observed in the SSIM analysis presented in Figure 7.15c, where the proposed QOFDM system maintains strong structural similarity despite the absence of channel coding. As the number of qubits increases, the SSIM curves progressively shift towards lower SNR values, indicating improved robustness against channel impairments. In particular, the 8-qubit configuration achieves near-perfect reconstruction at a substantially lower SNR than the lower-dimensional quantum schemes and classical modulation techniques. This behaviour demonstrates that higher-dimensional quantum encoding improves transmission reliability while maintaining excellent reconstruction quality. These observations collectively demonstrate that the proposed framework scales effectively with increasing qubit dimensions, leading to progressively improved image transmission performance.

When polar channel coding is incorporated into the transmission framework, additional performance improvements are observed for both QOFDM and classical OFDM systems. The coded transmission results shown in Figure 7.16a indicate a substantial reduction in BER across all considered modulation schemes compared with the uncoded transmission case. Within the proposed framework, the eight-qubit configuration again achieves the strongest overall BER performance, while even the single-qubit configuration continues to outperform the classical OFDM baseline.

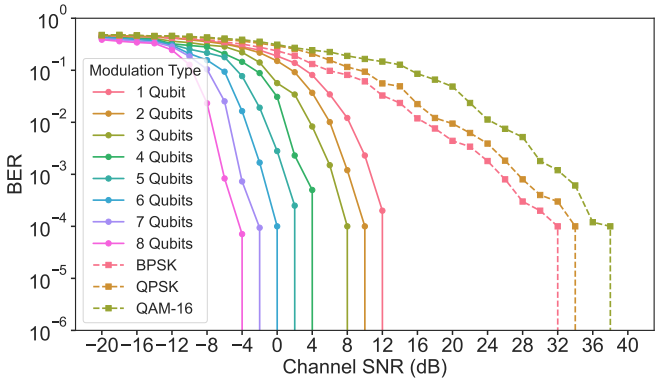
The inclusion of channel coding also improves reconstruction quality in terms of

PSNR and SSIM. As illustrated in Figure 7.16b, the proposed QOFDM framework consistently achieves superior image quality compared with classical OFDM, with the performance improvement becoming increasingly significant for larger qubit dimensions. In particular, the eight-qubit configuration achieves extremely high PSNR values even at relatively low channel SNR levels. Overall, the application of channel coding provides an approximate channel SNR improvement of 2–4 dB relative to the uncoded transmission scenarios. The SSIM results shown in Figure 7.16c further confirm that the proposed QOFDM system preserves perceptual image quality more effectively than the corresponding classical OFDM framework under urban Rayleigh fading conditions.

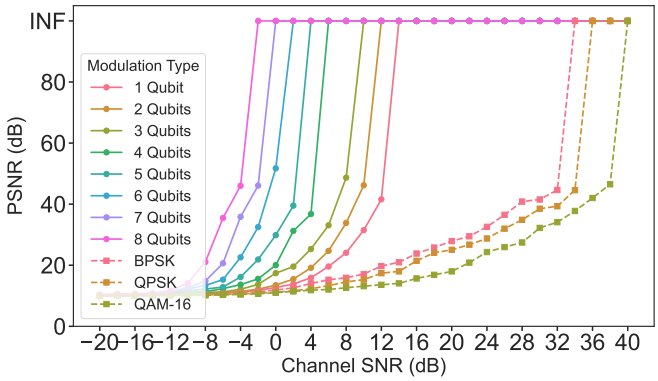
Performance Analysis of QOFDM under Indoor Rayleigh Fading Conditions

The performance results obtained for the uncoded indoor Rayleigh fading scenario indicate that the proposed QOFDM framework maintains strong transmission reliability across the evaluated SNR range, as shown in Figure 7.17a. Similar to the observations made under urban fading conditions, increasing the qubit dimension leads to improved BER performance. All investigated QOFDM configurations consistently achieve lower BER values than the corresponding classical OFDM schemes, with the performance gap becoming more pronounced as the qubit width increases. Since indoor propagation environments generally experience less severe multipath fading compared with urban channels, both classical and quantum transmission systems achieve lower overall BER levels for a given SNR. Nevertheless, the proposed QOFDM framework continues to demonstrate a clear robustness advantage over conventional OFDM transmission.

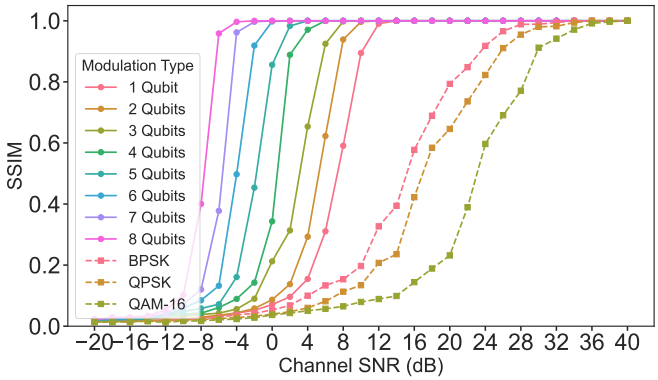
The reconstruction-quality results obtained for the uncoded indoor scenario further support the BER analysis. As illustrated in Figure 7.17b, larger qubit dimensions produce progressively higher PSNR values, demonstrating improved image recovery capability and reduced reconstruction distortion. Compared with the classical OFDM configurations, the proposed QOFDM framework consistently delivers higher image quality and visually improved reconstructed outputs, even under relatively moderate indoor fading conditions. Similar conclusions can be drawn from the SSIM results presented in Figure 7.17c, where the proposed quantum framework preserves structural image information more effectively than the classical baseline system.



(a) BER

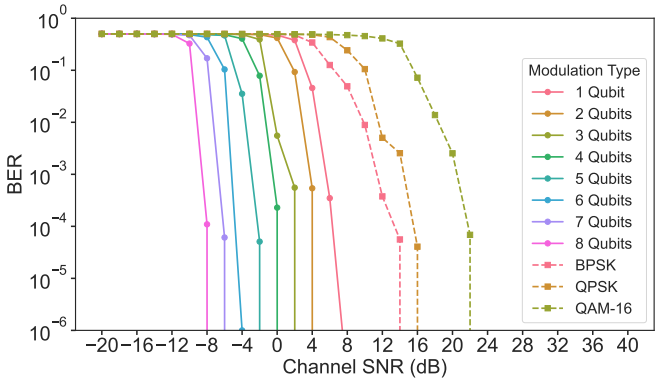


(b) PSNR

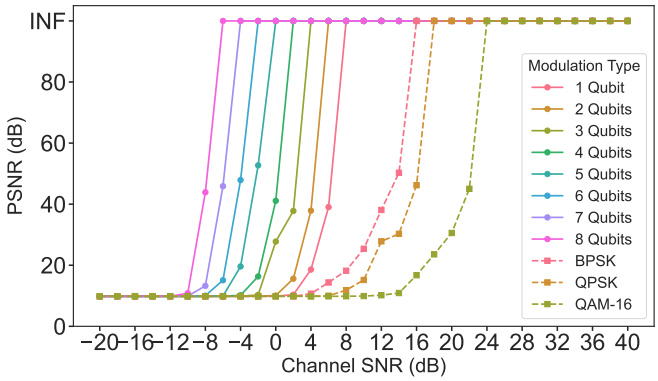


(c) SSIM

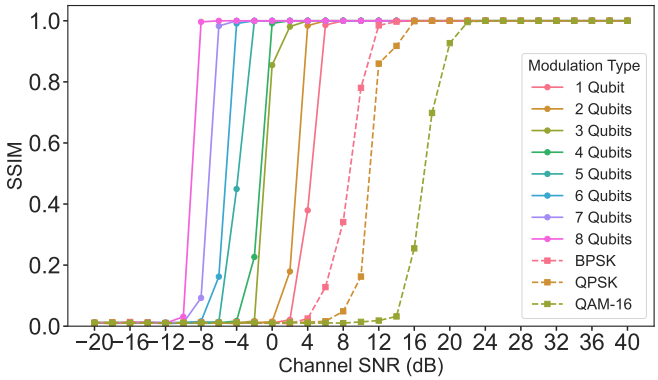
Figure 7.15: Behaviour of the proposed QOFDM pipeline without channel coding under urban Rayleigh fading for the different qubit widths considered: (a) BER, (b) PSNR, and (c) SSIM.



(a) BER

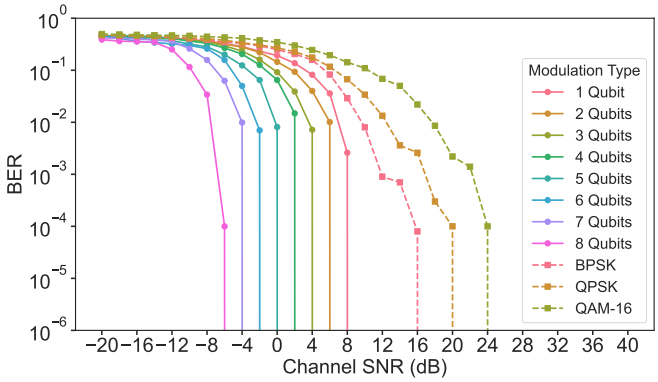


(b) PSNR

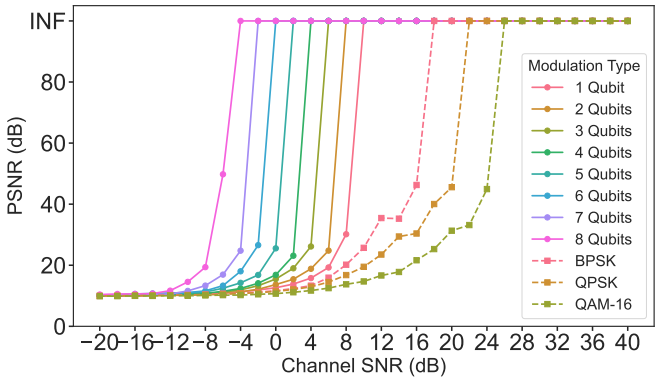


(c) SSIM

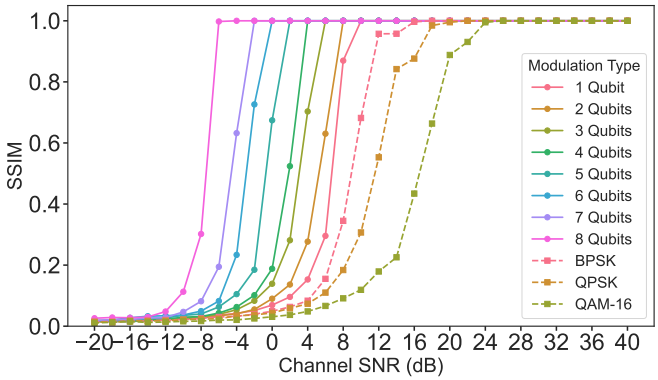
Figure 7.16: Behaviour of the proposed QOFDM pipeline with channel coding under urban Rayleigh fading for the different qubit widths considered: (a) BER, (b) PSNR, and (c) SSIM.



(a) BER

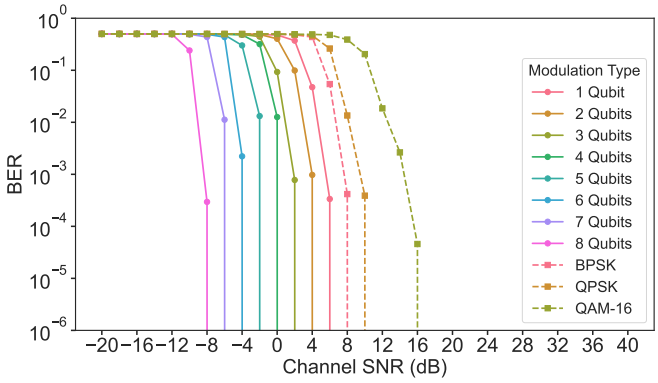


(b) PSNR

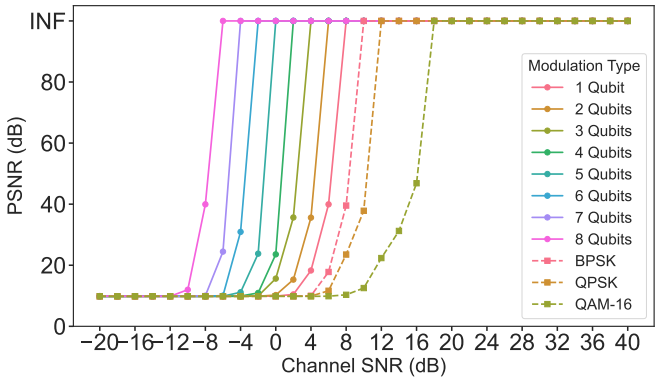


(c) SSIM

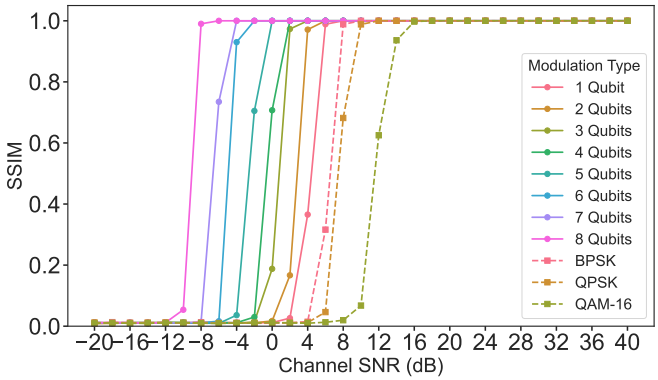
Figure 7.17: Behaviour of the proposed QOFDM pipeline without channel coding under indoor Rayleigh fading for the different qubit widths considered: (a) BER, (b) PSNR, and (c) SSIM.



(a) BER



(b) PSNR



(c) SSIM

Figure 7.18: Behaviour of the proposed QOFDM pipeline with channel coding under indoor Rayleigh fading for the different qubit widths considered: (a) BER, (b) PSNR, and (c) SSIM.

Additional performance improvements are observed when polar channel coding is incorporated into the indoor transmission framework. The BER results shown in Figure 7.18a demonstrate that channel coding significantly improves transmission reliability for both quantum and classical OFDM systems. Although classical modulation schemes such as BPSK benefit from the added redundancy introduced by channel coding, the proposed QOFDM configurations continue to achieve superior BER performance across the entire SNR range.

The PSNR performance shown in Figure 7.18b follows trends consistent with the BER behaviour, where image reconstruction quality improves as the qubit width increases. The proposed QOFDM framework again achieves higher reconstruction quality than the classical OFDM baseline across all evaluated SNR values. Likewise, the SSIM analysis presented in Figure 7.18c confirms the ability of the proposed framework to preserve perceptual image fidelity effectively under indoor fading conditions. These results collectively demonstrate the effectiveness of the proposed QOFDM system in maintaining reliable and high-quality image transmission performance even in the presence of channel impairments.

Table 7.2: Observed channel SNR advantages of the proposed QOFDM framework compared with conventional BPSK modulation-based OFDM under different fading environments and coding conditions for varying qubit dimensions.

Transmission Scenario	**1-Qubit**	**2-Qubit**	**3-Qubit**	**4-Qubit**	**5-Qubit**	**6-Qubit**	**7-Qubit**	**8-Qubit**
Urban Fading (Uncoded)	20 dB	22 dB	24 dB	28 dB	30 dB	32 dB	34 dB	36 dB
Urban Fading (Coded)	6 dB	10 dB	12 dB	14 dB	16 dB	18 dB	20 dB	22 dB
Indoor Fading (Uncoded)	8 dB	10 dB	12 dB	14 dB	16 dB	18 dB	20 dB	22 dB
Indoor Fading (Coded)	2.5 dB	4 dB	6 dB	8 dB	10 dB	12 dB	14 dB	16 dB

The performance advantages achieved by the proposed QOFDM framework over conventional BPSK-based OFDM transmission are summarised in Table 7.2 for all evaluated qubit dimensions under both coded and uncoded transmission conditions. The largest channel SNR improvements are observed in the uncoded urban fading scenario, where severe multipath effects significantly degrade the performance of the classical OFDM system. In contrast, the proposed QOFDM framework maintains substantially stronger transmission reliability under the same channel conditions. In several cases, the reconstructed images obtained through QOFDM achieve effectively distortion-free recovery at relatively low channel SNR levels, while the corresponding classical OFDM

system experiences considerable degradation.

These improvements originate from the quantum-mechanical principles integrated into the transmission framework. The use of superposition and QFT-based processing enables efficient representation and transmission of information across orthogonal quantum subcarriers. By employing multi-qubit state representations within higher-dimensional Hilbert spaces, the system gains additional robustness against transmission errors and fading-induced distortions. The inclusion of polar channel coding further enhances transmission reliability by providing additional protection against channel impairments. Consequently, the combined framework maintains lower BER levels and enables more accurate image reconstruction under challenging propagation environments, thereby reducing the minimum SNR required to achieve acceptable image quality.

Although the indoor fading environment produces less severe multipath distortion compared with the urban channel, the proposed QOFDM framework still consistently outperforms the classical OFDM baseline. Another important factor contributing to this robustness is the distributed nature of information representation within the quantum transmission process. In classical OFDM systems, information is directly associated with specific amplitude and phase values, making the transmitted signal highly sensitive to channel fluctuations. In contrast, QOFDM distributes information across quantum states and orthogonal subcarriers, reducing the direct impact of amplitude and phase distortions introduced by the channel. The preservation of quantum-state coherence during transmission, together with the advantages of superposition-based encoding, enables more efficient utilisation of spectral resources while improving resistance against fading and interference effects. As a result, the proposed framework achieves improved reconstruction fidelity and enhanced quality of service under noisy communication conditions.

An additional advantage of the proposed QOFDM framework relates to its PAPR characteristics. Conventional OFDM modulation schemes such as BPSK, QPSK, and 16-QAM typically exhibit relatively high PAPR values, often in the range of 10–12 dB, which can reduce amplifier efficiency and introduce nonlinear distortion effects. In contrast, the proposed QOFDM framework maintains a constant PAPR of approximately 0 dB regardless of the selected qubit dimension. This behaviour results from the normalisation

property of quantum-state vectors and the unitary characteristics of the QFT and IQFT operations, leading to improved power efficiency compared with classical OFDM systems.

Increasing the qubit dimension also improves robustness against channel noise and fading by enabling higher-dimensional quantum representations. Among the evaluated configurations, the eight-qubit system achieves the strongest overall performance in terms of both reconstruction quality and transmission reliability. However, larger qubit dimensions also increase computational complexity and implementation requirements. In practical near-term applications, lower-dimensional configurations involving up to four qubits may represent a more balanced trade-off between performance improvement and implementation feasibility. These lower-qubit QOFDM configurations continue to outperform the classical OFDM baseline while maintaining reduced computational and hardware demands.

From a computational perspective, the QFT operation provides significant complexity advantages relative to classical Fourier-based processing. For a quantum system with dimension 2^k, the QFT can be implemented using approximately $O(k^2)$ quantum gate operations. Although increasing the qubit dimension leads to greater circuit depth and more demanding gate control requirements, the resulting complexity remains substantially lower than that of the classical FFT and IFFT operations, which require approximately $O(k2^k)$ operations for k-bit classical inputs. In the proposed framework, the total QFT gate count grows quadratically with the number of qubits, while the circuit depth scales approximately linearly with $2k$. These characteristics make the proposed QOFDM framework computationally efficient for small and medium-scale quantum configurations. The estimated QFT gate counts and corresponding circuit depths for the considered qubit dimensions are summarised in Table 7.3. It should be noted that these values represent approximate estimates, since certain SWAP operations may be omitted depending on implementation strategy, compiler optimisations, and hardware-specific constraints.

From a latency perspective, the proposed QOFDM framework offers structural advantages over conventional OFDM systems due to the parallel processing capabilities of quantum-state evolution and the computational efficiency of the QFT operation. The QFT requires approximately $O(k^2)$ computational complexity, which is significantly lower

Table 7.3: Estimated quantum computational resources required for QFT processing under different qubit dimensions in the proposed image transmission framework.

Qubit Dimension (k)	Hadamard Operations	Controlled Phase Operations	Estimated Total Gate Count	Estimated Circuit Depth
1	1	0	1–2	1–2
2	2	1	3–4	2–3
3	3	3	6–7	4–6
4	4	6	10–12	8–10
5	5	10	15–17	10–12
6	6	15	21–23	12–14
7	7	21	28–30	14–18
8	8	28	36–38	16–20

than the $O(k2^k)$ complexity associated with the classical FFT implementation. For lower qubit dimensions, particularly configurations involving up to four qubits, the resulting symbol duration is noticeably shorter than that of an equivalent classical OFDM symbol. This improvement arises because a single k-qubit quantum state can simultaneously represent information distributed across 2^k orthogonal subcarriers through quantum superposition, eliminating the need for sequential subcarrier processing.

As summarised in Table 7.3, the circuit depth of the QFT operation increases approximately linearly with the number of qubits, following an estimated scaling trend of roughly $2k$. Consequently, the associated processing delay remains relatively moderate even as the qubit dimension increases. For example, a four-qubit QOFDM configuration requires an estimated circuit depth of approximately 8–10 gate layers, whereas the equivalent 16-point classical IFFT implementation requires a substantially larger number of arithmetic operations involving complex multiplications. The reduced computational overhead, together with the inherent parallelism provided by quantum-state processing, contributes to lower end-to-end transmission latency. These characteristics make the proposed QOFDM framework particularly attractive for delay-sensitive applications such as augmented reality, virtual reality, real-time multimedia streaming, and intelligent surveillance systems.

Although the obtained simulation results demonstrate promising performance characteristics, practical realisation of QOFDM on physical quantum hardware remains associated with several challenges. Current quantum computing platforms are still constrained by limited qubit availability, relatively short coherence durations, and imperfect gate fidelities, all of which directly affect the reliability and scalability of operations such as the QFT and IQFT. Furthermore, integrating quantum communication modules

with conventional classical processing hardware introduces additional implementation challenges related to synchronisation, real-time control, and decoding operations.

Despite these limitations, rapid advancements in quantum hardware technologies continue to improve the feasibility of practical quantum communication systems. Therefore, the simulation-based investigation presented in this work should be regarded as an initial feasibility study establishing a theoretical and architectural foundation for future implementations. As quantum technologies continue to mature, the framework and design principles developed in this study may support future hardware prototyping, experimental validation, and large-scale deployment of practical QOFDM-based communication systems.

7.3.3 Section Summary

This section demonstrated the effectiveness of the proposed QOFDM framework for reliable high-quality image transmission over noisy quantum communication channels. The obtained results showed that the proposed system consistently achieves superior performance compared with conventional OFDM in terms of image reconstruction quality and transmission robustness under equivalent bandwidth conditions. Improvements in PSNR and SSIM indicate that the integration of quantum superposition with QFT-generated orthogonal subcarriers enables more reliable information transmission in the presence of channel impairments. Overall, the proposed QOFDM architecture demonstrates strong potential for future quantum-enabled communication applications requiring reliable, high-fidelity, and low-latency multimedia transmission. This QOFDM architecture is naturally extended to video next, before the spatial and frequency-domain gains are unified in Section 7.5.

7.4 Quantum OFDM-Based Video Transmission for Noise-Impaired Communication Channels

Publication Notice

The research presented in this section has been published in the following peer-reviewed journal publication:

U. Jayasinghe and A. Fernando, "A quantum OFDM framework for next-generation video transmission over noisy channels," *Electronics*, vol. 15, no. 2, art. no. 284, 2026, doi: 10.3390/electronics15020284.

This material is reproduced and adapted under the terms of the MDPI Copyright policy for use in a doctoral thesis. The content has been revised and extended with additional explanations and expanded discussion.

Problem Statement: The previous section demonstrated that integrating quantum-domain processing with OFDM architectures can significantly improve the robustness and reconstruction quality of image transmission under noisy communication conditions. However, extending these advantages from static image transmission to compressed video transmission introduces substantially greater challenges due to temporal dependencies, motion continuity, inter-frame prediction structures, and significantly higher bandwidth requirements. In practical communication environments, compressed video bitstreams are highly sensitive to noise, fading, and error propagation, where even small transmission errors can severely degrade both spatial video quality and temporal playback consistency. Consequently, developing robust quantum-domain multicarrier communication frameworks capable of maintaining high-fidelity video transmission under noisy channel conditions remains a major challenge for next-generation video communication systems.

Limitations of Existing Work: Conventional classical OFDM-based video transmission systems improve spectral efficiency and robustness against frequency-selective fading through orthogonal multicarrier communication. However, these systems remain vulnerable to noise, interference, synchronisation errors, and error propagation effects caused by compressed video prediction structures. Furthermore, existing quantum

communication studies have primarily focused on static image transmission and have not comprehensively investigated quantum-domain OFDM frameworks for compressed video communication. To the best of the author's knowledge, no prior work has developed a complete end-to-end QOFDM framework integrating modern video compression, multi-qubit encoding, and quantum multicarrier transmission specifically for robust high-fidelity video transmission over noisy communication channels.

Motivation and Proposed Contribution: To address these limitations, this section proposes a QOFDM-based framework for next-generation high-fidelity video transmission over noisy communication channels. The proposed framework integrates VVC-based source compression, polar channel coding, multi-qubit quantum encoding, and QFT-based orthogonal multicarrier transmission to improve robustness against noisy channel impairments while preserving perceptual video quality. Within the proposed framework, compressed video bitstreams are converted into multi-qubit quantum superposition states and processed using QFT-based orthogonal subcarrier generation analogous to classical OFDM systems. At the receiver, IQFT-based reconstruction and quantum decoding operations are employed to recover the transmitted video information. By combining quantum-domain signal representations with multicarrier communication principles, the proposed framework aims to improve transmission reliability, robustness against noise, and reconstructed video quality under adverse communication environments. The proposed QOFDM framework is evaluated under different noisy channel conditions and qubit configurations using objective video quality assessment metrics, including BER, PSNR, SSIM, and VMAF. Comparative analysis is further conducted against equivalent classical OFDM communication systems operating under identical channel conditions. The objective is to investigate whether quantum-domain multicarrier communication can provide improved robustness and high-fidelity video reconstruction for next-generation multimedia communication systems.

7.4.1 System Model

This section presents the proposed QOFDM framework for video transmission as an extension of the QOFDM-based image transmission framework presented in Section 7.3. The end-to-end communication architecture remains unchanged, as shown in Figure 7.19,

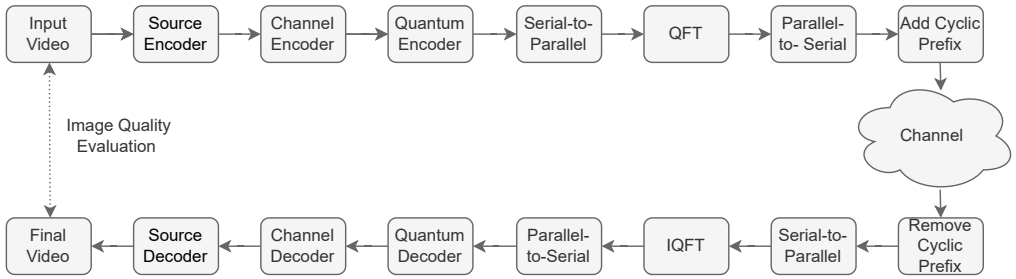


Figure 7.19: Block diagram of the proposed QOFDM pipeline for video transmission.

with the primary difference being that video sequences, rather than still images, are used as the input. To ensure a comprehensive performance evaluation under different multimedia conditions, three VVC encoded video sequences representing different levels of spatial and temporal complexity are selected. These include a high-motion sequence [205] containing rapid movement and frequent scene transitions, a medium-motion sequence [206] with moderate temporal activity and intermediate scene complexity, and a low-motion sequence [207] characterised by relatively limited motion while preserving meaningful structural content. The selected video sequences are evaluated at spatial resolutions of 320×180, 1280×720, and 1920×1080, together with frame rates of 20, 30, and 50 fps. These settings enable the communication framework to be assessed under varying spatial and temporal transmission requirements. Both the classical OFDM benchmark and the proposed QOFDM system are inherently content-independent, allowing arbitrary video formats, resolutions, frame rates, and scene characteristics to be processed without architectural modification.

To evaluate the proposed framework under realistic transmission conditions, the quantum communication channel is modelled using three separate channel scenarios, each incorporating both classical propagation impairments and quantum decoherence effects.

- **Indoor Rayleigh fading with quantum decoherence:** This scenario represents indoor wireless propagation conditions using a four-path Rayleigh fading model with delay values of $(0, 0.05, 0.15, 0.3)$ μs, corresponding path gains of $(0, -2, -8, -12)$ dB, and a Doppler frequency of $f_D = 5$ Hz. In addition to the fading effects, the transmitted quantum states are subjected to the quantum-

noise processe, including bit-flip, phase-flip, depolarising, amplitude-damping, and phase-damping mechanisms.

- **Urban Rayleigh fading with quantum decoherence:** This channel configuration models a more severe urban multipath environment using four propagation components with delays of $(0, 0.2, 0.5, 1.0)$ μs, path gains of $(0, -3, -10, -15)$ dB, and a Doppler frequency of $f_D = 100$ Hz. The same set of quantum decoherence mechanisms described previously is incorporated simultaneously within the transmission process.

Within the proposed QOFDM receiver, channel impairments are compensated after the IQFT stage under the assumption of perfect CSI. In practical quantum communication systems, however, CSI estimation would require dedicated quantum pilot signals, where predefined quantum states are transmitted through the channel and measured at the receiver to estimate the corresponding channel characteristics.

Simulation Setup

The complete simulation configuration adopted for evaluating the classical OFDM benchmark and the proposed QOFDM framework is summarised in Table 7.4.

7.4.2 Results

The proposed QOFDM framework and the conventional OFDM benchmark are evaluated under identical bandwidth constraints to ensure a fair performance comparison. By integrating multi-qubit quantum encoding with QFT-based multicarrier processing, the proposed QOFDM system is able to maintain high video reconstruction quality across all investigated transmission scenarios, including environments affected by severe channel impairments and quantum-noise effects. The obtained results are analysed according to the considered channel conditions, video resolutions, and GOP configurations. Reconstruction quality is assessed using PSNR, SSIM, and VMAF metrics, which collectively provide insight into the robustness and transmission advantages of the proposed quantum communication framework relative to the classical OFDM system.

The following subsection presents a detailed discussion of the obtained results under the different channel environments and GOP configurations considered in this study.

Table 7.4: Simulation setup used for the classical OFDM baseline and the proposed QOFDM scheme.

Category	**Parameters / Description**
	Simulation Environment
Software	MATLAB R2025a, Quantum Computing Toolbox v2.1, Communications Toolbox
Hardware	Intel Core i5-1345U CPU, 16 GB RAM
Random seeds	12345, 23456, 34567 (each Monte Carlo run uses a fixed seed for reproducibility)
	Video Sequences
High-motion	Rapid movement, frequent scene changes, high SI/TI
Medium-motion	Moderate movement, medium SI/TI
Low-motion	Minimal movement, medium SI, low TI
Resolutions	320×180, 1280×720, 1920×1080
Frame rates	20, 30, 50 fps
GOP sizes	8, 16, 32
	Classical OFDM Parameters
Number of subcarriers	256
Cyclic prefix	25% of N
Modulation schemes	BPSK, QPSK, 16-QAM
Polar code rate	1/2
	Channel Models
SNR Range	-20 to 30 dB
AWGN	Additive White Gaussian Noise
Indoor Rayleigh	Delays: $(0, 0.05, 0.15, 0.3)$ μs; Gains: $(0, -2, -8, -12)$ dB; Doppler: 5 Hz
Urban Rayleigh	Delays: $(0, 0.2, 0.5, 1.0)$ μs; Gains: $(0, -3, -10, -15)$ dB; Doppler: 100 Hz
	QOFDM Parameters
Qubit sizes (k)	1–8
Number of subcarriers	2^k
Cyclic prefix	25% of 2^k
Polar code rate	1/2
Quantum noise channels	bit-flip, phase-flip, depolarising, amplitude damping, phase damping
Noise allocation	Proportional to $p_{\text{total}} = 1/(1 + 10^{\text{SNR}/10})$
	Monte Carlo Simulation
Runs per SNR	100
Statistical analysis	Mean values; standard deviation at representative SNR points: PSNR < 0.1 dB, SSIM < 0.01, VMAF < 0.09
	Power Normalisation and SNR
Symbol power	Unit average power per OFDM symbol/subcarrier
SNR calculation	SNR (dB) $= 10 \log_{10} \frac{P_{\text{signal}}}{P_{\text{noise}}}$
	Notes
Reproducibility	Fixed seeds, multiple runs, and variability reporting ensure results can be independently replicated
Comparison	Bandwidth-equivalent comparison between classical and QOFDM systems

Analysis of the Proposed QOFDM System under Indoor Fading Conditions

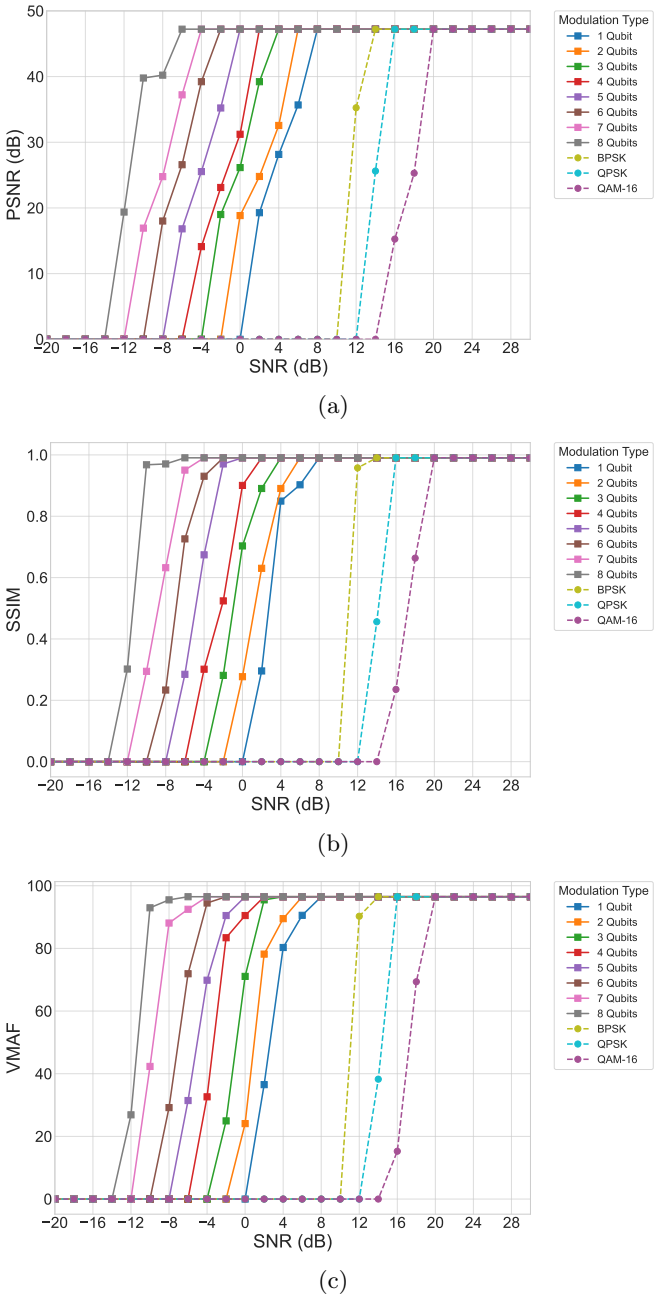


Figure 7.20: Behaviour of the proposed QOFDM pipeline at GOP8 under an indoor Rayleigh fading channel: (a) PSNR, (b) SSIM, and (c) VMAF.

The results obtained for GOP8 transmission over the indoor Rayleigh fading channel demonstrate that the proposed QOFDM framework maintains strong video reconstruction quality under multipath propagation conditions, as illustrated in Figure 7.20. The

PSNR performance shown in Figure 7.20a improves consistently as the qubit dimension increases, indicating the scalability advantages provided by the proposed quantum encoding framework. Higher qubit configurations correspond to larger quantum-state dimensions and increased numbers of orthogonal subcarriers, enabling each transmitted quantum symbol to represent and preserve greater amounts of information during transmission. Consequently, the transmitted video content becomes more resistant to the amplitude and phase fluctuations introduced by the indoor Rayleigh fading channel. This allows the proposed QOFDM system to maintain significantly higher PSNR values than classical OFDM schemes employing BPSK, QPSK, and 16-QAM modulation, particularly at low and moderate channel SNR levels. The performance improvement is especially noticeable within these SNR regions, where the proposed quantum encoding mechanism more effectively preserves GOP frame integrity and temporal consistency throughout the reconstructed video sequence.

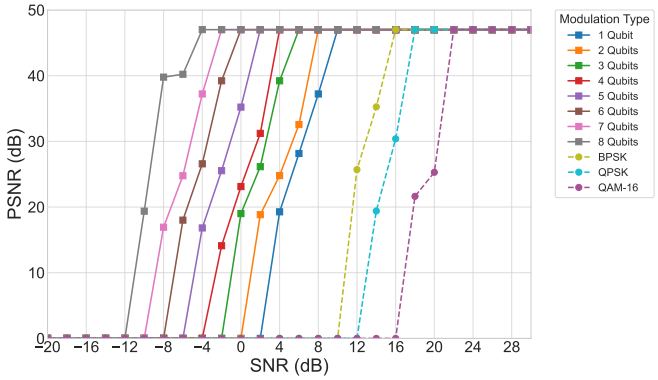
The SSIM analysis presented in Figure 7.20b further confirms the structural preservation capability of the proposed framework. Unlike PSNR, which primarily measures pixel-level reconstruction accuracy, SSIM evaluates structural similarity, luminance consistency, and spatial correlation between frames. The higher SSIM values achieved by QOFDM indicate that the proposed transmission system more effectively preserves edges, textures, and object relationships throughout the video sequence. This characteristic is particularly important for GOP8 transmission, since transmission errors affecting earlier frames may propagate into dependent predictive frames within the same GOP structure. Across all evaluated SNR levels and qubit configurations, the proposed QOFDM framework consistently maintains higher SSIM values than the classical OFDM baseline, indicating improved control over temporal error propagation and more reliable reconstruction of motion-dependent content.

Additional perceptual evaluation is provided through the VMAF results shown in Figure 7.20c. Since VMAF incorporates perceptual characteristics such as detail preservation, blur, blocking artefacts, and temporal smoothness, it provides a more comprehensive assessment of perceived video quality. The proposed QOFDM framework consistently achieves higher VMAF values than classical OFDM across the full SNR range considered in the study. The performance gap becomes particularly evident at

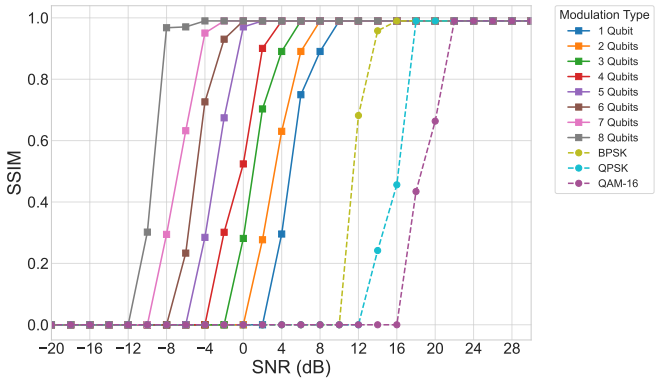
moderate SNR levels, where the classical OFDM configurations begin to exhibit visible impairments including flickering, motion degradation, and frame inconsistency. In contrast, the proposed QOFDM system maintains more stable perceptual quality due to the robustness provided by quantum frequency-domain encoding and the balanced energy distribution generated through QFT-based processing. As a result, the reconstructed reference frames supplied to the decoder remain more reliable, thereby improving the quality of subsequent predicted frames within the GOP structure.

When the PSNR, SSIM, and VMAF results are considered collectively, the proposed QOFDM framework demonstrates clear performance advantages for GOP8 video transmission under indoor Rayleigh fading conditions. The performance difference between QOFDM and classical OFDM becomes increasingly significant as the qubit dimension increases, indicating that the proposed quantum encoding strategy improves both individual frame reconstruction and overall temporal consistency. Although BPSK achieves the strongest performance among the classical OFDM configurations, even the single-qubit QOFDM system maintains a clear performance advantage. This observation suggests that the obtained improvements are not solely related to higher-dimensional representations, but also arise from the inherent benefits of quantum-based information encoding and transmission. Overall, the results demonstrate that the proposed QOFDM framework effectively preserves both objective and perceptual video quality, highlighting its suitability for future indoor multimedia communication applications operating under mild fading conditions.

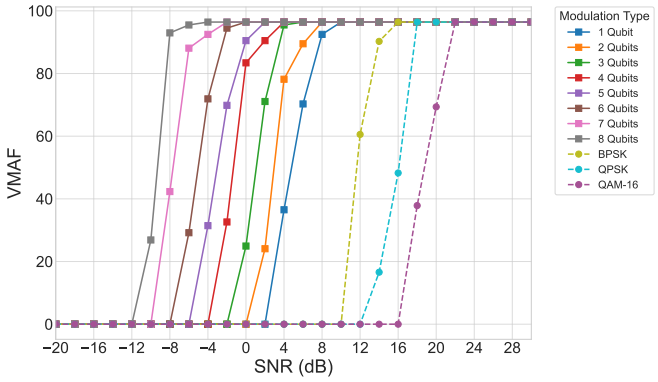
The performance results obtained for GOP16 (Figure 7.21) and GOP32 (Figure 7.22) exhibit trends generally consistent with those observed for GOP8, although the influence of temporal dependency becomes increasingly pronounced as the GOP size increases. Across all evaluated SNR values, the proposed QOFDM framework continues to achieve superior PSNR, SSIM, and VMAF performance compared with the classical OFDM transmission schemes. The preservation of this performance advantage at larger GOP sizes demonstrates that the benefits provided by the proposed quantum encoding framework are not restricted to a specific temporal prediction structure. Even under extended prediction intervals, the higher-dimensional quantum-state representation employed by QOFDM continues to improve resilience against channel impairments,



(a)

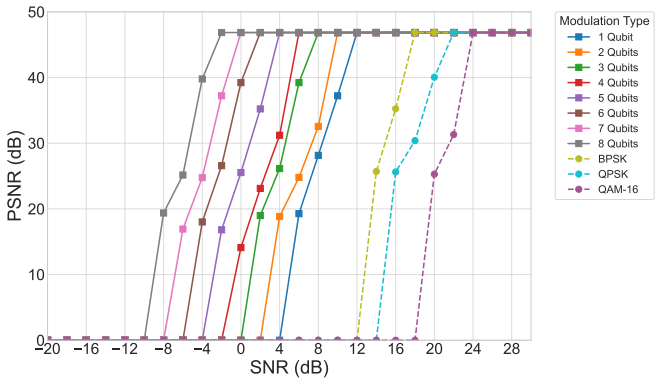


(b)

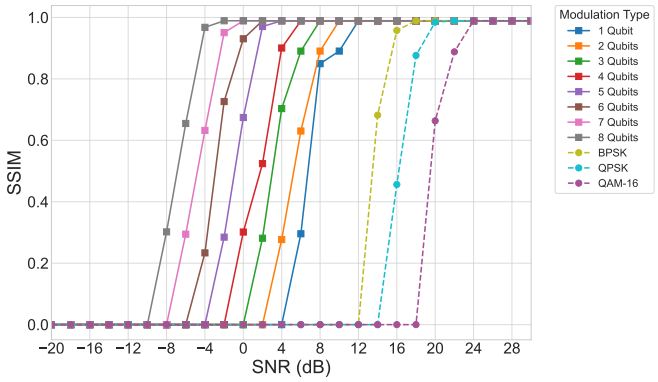


(c)

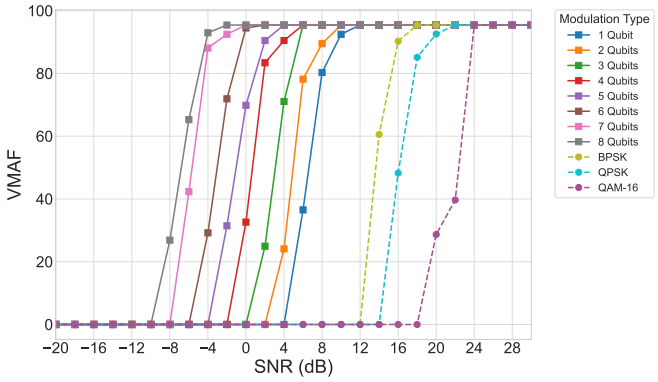
Figure 7.21: Behaviour of the proposed QOFDM pipeline at GOP16 under an indoor Rayleigh fading channel: (a) PSNR, (b) SSIM, and (c) VMAF.



(a)



(b)



(c)

Figure 7.22: Behaviour of the proposed QOFDM pipeline at GOP32 under an indoor Rayleigh fading channel: (a) PSNR, (b) SSIM, and (c) VMAF.

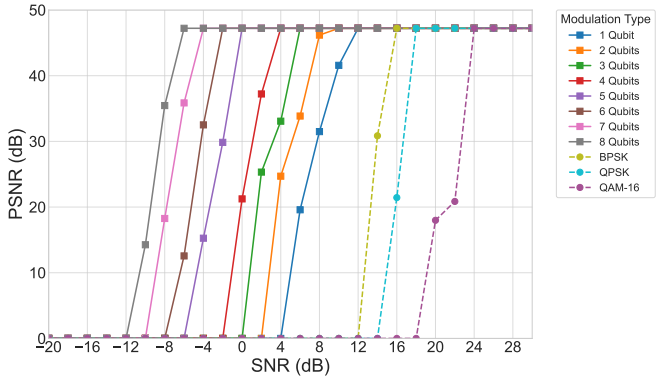
enabling the decoder to reconstruct more reliable reference frames and subsequently improve the quality of predictive frames within the GOP.

As the GOP size increases, a larger proportion of frames are encoded using inter-frame prediction mechanisms. Consequently, reconstructed frames become increasingly dependent on previously decoded intra and predictive frames. This extended prediction dependency increases the susceptibility of the video stream to transmission errors, since impairments affecting earlier frames can propagate throughout subsequent predictive frames within the same GOP. Such propagation effects commonly appear as temporal flickering, blurring artefacts, and block-based distortions in the reconstructed video sequence. This behaviour explains the gradual reduction in absolute reconstruction quality observed across all transmission schemes as the GOP size increases from 8 to 16 and subsequently to 32. The corresponding quality-performance curves shift towards higher SNR regions, indicating that increasingly favourable channel conditions are required to maintain equivalent reconstruction quality as temporal dependency grows. In practical terms, longer GOP structures amplify the accumulation of transmission errors, thereby increasing the channel quality requirements necessary to preserve perceptual video fidelity.

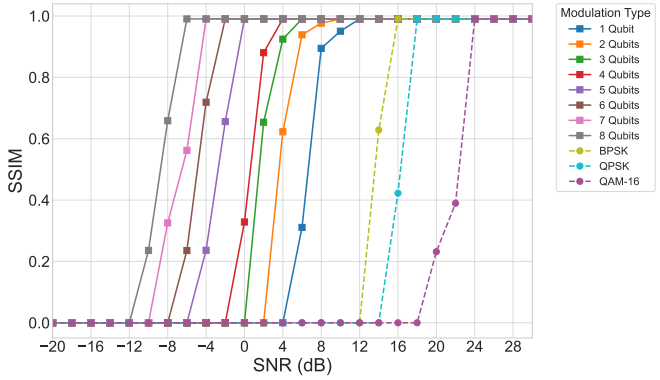
Despite the expected degradation associated with larger GOP configurations, the proposed QOFDM framework consistently maintains a significant performance advantage over classical OFDM transmission. Even under GOP16 and GOP32 configurations, the proposed system achieves higher reconstruction accuracy and more stable perceptual quality, as reflected by the PSNR, SSIM, and VMAF evaluations. These results demonstrate the robustness and scalability of the proposed quantum encoding strategy, which effectively limits error propagation while preserving both spatial detail and temporal continuity over extended prediction intervals in fading wireless communication environments.

Analysis of the Proposed QOFDM System in Urban Fading Conditions

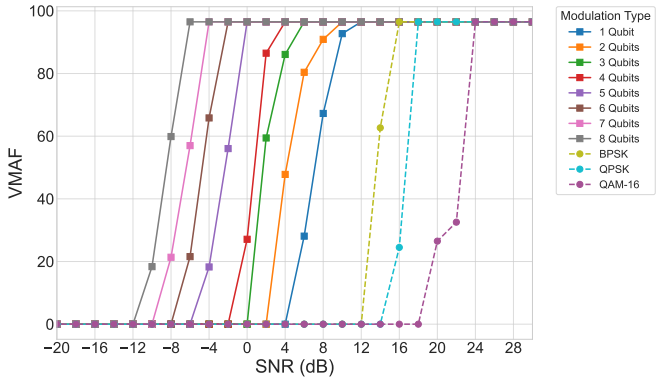
To evaluate the proposed QOFDM framework under more demanding propagation conditions, GOP8 video sequences are transmitted through an urban Rayleigh fading environment, with the corresponding results presented in Figure 7.23. The PSNR



(a)



(b)



(c)

Figure 7.23: Behaviour of the proposed QOFDM pipeline at GOP8 under an urban Rayleigh fading channel: (a) PSNR, (b) SSIM, and (c) VMAF.

performance shown in Figure 7.23a increases consistently as the qubit dimension grows, demonstrating the scalability and transmission efficiency of the proposed quantum encoding strategy. Compared with the indoor fading scenario, the urban channel introduces more severe multipath distortions and stronger time-varying fading effects, which reduce overall transmission robustness for both classical and quantum systems. Nevertheless, larger qubit configurations within the QOFDM framework generate higher-dimensional quantum states capable of representing and preserving greater amounts of information during transmission. This additional encoding capability improves resistance against amplitude and phase distortions introduced by the urban fading channel, thereby enabling higher PSNR values even at relatively low and moderate SNR levels. Across all evaluated SNR conditions, the proposed QOFDM system consistently outperforms classical OFDM schemes employing BPSK, QPSK, and 16-QAM modulation, with the most significant improvements observed in the low-to-medium SNR region. These results indicate that the proposed framework preserves the integrity of both intra-coded and predictive frames sufficiently well to maintain temporal continuity throughout the GOP structure despite the challenging urban propagation environment.

The SSIM analysis presented in Figure 7.23b further confirms the structural reconstruction advantages of the proposed QOFDM framework. Higher SSIM values are consistently achieved across all evaluated qubit dimensions and channel SNR conditions, indicating more effective preservation of edges, textures, and inter-frame structural relationships. The obtained results also demonstrate that the proposed framework significantly reduces the propagation of transmission errors while maintaining both spatial and temporal consistency under rapidly varying urban fading conditions. Similar observations can be made from the perceptual-quality analysis shown in Figure 7.23c, where the proposed QOFDM framework consistently achieves higher VMAF values than the classical OFDM baseline across the entire SNR range. Furthermore, the performance gap becomes increasingly pronounced as the qubit dimension increases.

When considered collectively, the PSNR, SSIM, and VMAF results demonstrate that the proposed QOFDM framework provides substantial performance improvements for GOP8 video transmission under urban Rayleigh fading conditions. The progressive performance enhancement observed with increasing qubit dimension confirms that the

proposed quantum encoding strategy improves robustness at both the individual frame level and the temporal prediction level. These findings highlight the suitability of the proposed QOFDM framework for future high-quality video transmission applications operating in challenging urban wireless communication environments.



(a) Qubit 1 (b) Classical BPSK

Figure 7.24: Representative reconstructed video frames for GOP8 sequences under an urban Rayleigh fading channel at an SNR of 13 dB.

The reconstructed video samples shown in Figure 7.24 provide visual evidence of the performance advantage achieved by the proposed QOFDM framework for GOP8 transmission under urban Rayleigh fading conditions at an SNR of 13 dB. The left-hand reconstruction corresponds to the single-qubit QOFDM configuration, whereas the right-hand reconstruction is obtained from the classical OFDM benchmark employing BPSK modulation. A clear visual difference can be observed between the two outputs, with the proposed quantum framework preserving noticeably higher image clarity, structural detail, and frame consistency despite the severe multipath fading environment.

These visual observations closely align with the previously presented PSNR, SSIM, and VMAF results, further confirming the robustness of the proposed transmission framework under challenging wireless conditions. An important outcome highlighted by these reconstructed frames is that even the lowest-dimensional quantum configuration, corresponding to $k = 1$, achieves superior reconstruction quality compared with the strongest classical OFDM configuration evaluated in this study. This result demonstrates that the performance improvements offered by QOFDM arise not only from increased dimensionality at larger qubit widths, but also from the inherent advantages associated with quantum-based information representation and transmission.

The proposed QOFDM framework is further evaluated using all three motion

Table 7.5: Highest channel SNR improvements achieved by the proposed QOFDM framework relative to classical BPSK modulation-OFDM under urban Rayleigh fading conditions for different qubit dimensions, video resolutions, and motion categories (dB).

Motion Type	Resolution	1 Qubit	2 Qubit	3 Qubit	4 Qubit	5 Qubit	6 Qubit	7 Qubit	8 Qubit
Low Motion	320×180	6.1	10.0	12.1	14.1	16.0	17.9	20.1	22.0
	1280×720	5.9	9.8	12.1	14.1	15.9	18.0	19.9	22.0
	1920×1080	6.0	9.9	12.0	14.1	15.8	17.9	20.0	22.1
Medium Motion	320×180	5.9	9.9	12.0	13.9	16.0	18.0	20.0	21.9
	1280×720	6.1	10.1	12.0	13.9	16.0	18.1	20.1	22.0
	1920×1080	6.0	10.1	11.9	14.1	15.9	18.0	20.0	22.0
High Motion	320×180	5.9	9.9	11.9	14.0	16.1	18.0	20.0	22.0
	1280×720	5.9	10.0	12.0	14.1	16.0	18.0	20.1	22.0
	1920×1080	5.9	10.0	12.1	14.1	15.9	18.1	20.0	21.9

categories and across the three considered spatial resolutions (320×180, 1280×720, and 1920×1080), with performance compared directly against the classical BPSK-OFDM benchmark. The resulting channel SNR gains are summarised in Table 7.5. The obtained gains remain relatively consistent across both the different motion characteristics and spatial resolutions, indicating that the performance advantage provided by the proposed quantum transmission framework is not strongly dependent on the underlying video content. This behaviour can be attributed to the fact that channel noise affects both the classical and quantum transmission schemes under the same operating conditions, causing the relative improvement introduced by QOFDM to remain comparatively stable across varying resolutions and motion levels. In addition, the results demonstrate that increasing the qubit dimension consistently produces larger channel SNR gains throughout all evaluated scenarios. These observations further confirm the scalability, robustness, and transmission efficiency of the proposed QOFDM framework across a broad range of video content characteristics and spatial resolutions.

Discussion

The obtained results demonstrate that the proposed QOFDM framework significantly outperforms conventional OFDM for video transmission over Rayleigh fading channels. This improvement is primarily attributed to quantum superposition and higher-dimensional Hilbert-space representations, which enable each quantum symbol to encode more information than classical modulation while improving robustness against channel impairments. The framework also exhibits enhanced resilience to transmission errors. Multi-qubit encoding and QFT-based orthogonal subcarrier generation distribute infor-

mation across quantum states and subcarriers, reducing the impact of channel noise and limiting error propagation within GOP-based video transmission. Consequently, both spatial reconstruction quality and temporal consistency are better preserved under challenging channel conditions. In addition, the proposed QOFDM framework provides improved power efficiency. Unlike conventional OFDM, which typically exhibits a high PAPR, the use of normalised quantum states together with unitary QFT and IQFT operations results in a nearly constant transmission power, corresponding to an approximate PAPR of 0 dB. This characteristic improves energy efficiency and makes the framework well suited for high-quality multimedia communication. Finally, the framework offers flexibility through scalable multi-qubit encoding, allowing a trade-off between reconstruction quality and computational complexity. These characteristics make the proposed QOFDM framework a promising solution for robust, energy-efficient, and high-fidelity quantum video transmission.

Computational Complexity and Scalability: The computational complexity and scalability analysis of the proposed QOFDM framework are identical to those presented for the QOFDM-based image transmission system in Section 7.3. Since the same quantum encoding, QFT/IQFT processing, multi-qubit architecture, and decoding framework are employed in the proposed video transmission system, the computational complexity, quantum gate requirements, circuit depth, and scalability characteristics remain unchanged and are therefore not repeated here. The detailed complexity analysis and scalability discussion can be found in Section 7.3.

For QOFDM-based video transmission, the scalability of the framework enables support for a wide range of video resolutions, frame rates, and quality-of-service requirements by selecting appropriate multi-qubit configurations. This flexibility makes the proposed framework suitable for future high-fidelity video communication applications, including live video streaming, immersive multimedia services, augmented and virtual reality, intelligent surveillance, and other bandwidth-intensive multimedia systems. As quantum hardware continues to mature, the proposed QOFDM framework provides a promising foundation for practical quantum-enhanced video communication over future wireless and quantum communication networks.

7.4.3 Section Summary

Extending the Section 7.3 QOFDM architecture to VVC-compressed video, this section confirmed the same pattern: consistent gains over classical OFDM across all GOP configurations, with the eight-qubit setting again giving the largest channel SNR improvement. With both the spatial (Sections 7.1–7.2) and frequency (this section and Section 7.3) dimensions now characterised individually, the next section combines them into a single hybrid architecture.

7.5 Enhanced Quantum Image Transmission Using MIMO-OFDM with Transmit and Receive Diversity

Publication Notice

The research presented in this section has been published in the following peer-reviewed journal publication:

U. Jayasinghe, T. Fernando, and A. Fernando, "A quantum MIMO-OFDM framework with transmit and receive diversity for high-fidelity image transmission," *Telecom*, vol. 6, no. 4, art. no. 96, 2025, doi: 10.3390/telecom6040096.

This material is reproduced and adapted under the terms of the MDPI Copyright policy for use in a doctoral thesis. The content has been revised and extended with additional explanations and expanded discussion.

Problem Statement: The previous sections demonstrated that integrating quantum communication with MIMO diversity and QOFDM frameworks can significantly improve the robustness and reconstruction quality of image and video transmission under noisy and fading channel conditions. However, achieving reliable high-fidelity image transmission over practical wireless communication channels remains a major challenge due to severe fading, channel noise, synchronisation errors, bandwidth limitations, and interference effects. In practical communication environments, compressed image bitstreams are highly sensitive to transmission impairments, where even small channel errors can cause significant degradation in reconstructed image quality. Furthermore, rapidly varying fading conditions and multipath propagation introduce additional

transmission distortions that reduce communication reliability and visual reconstruction performance. Consequently, developing robust communication frameworks capable of jointly mitigating fading effects, channel noise, and frequency-selective impairments while maintaining high-fidelity image reconstruction remains a critical challenge for next-generation multimedia communication systems.

Limitations of Existing Work: Conventional MIMO-OFDM communication systems improve transmission reliability using spatial diversity and orthogonal multicarrier transmission techniques. MIMO systems enhance robustness against fading through transmit and receive diversity, while OFDM mitigates frequency-selective fading using orthogonal subcarriers. However, despite these advantages, classical MIMO-OFDM systems remain vulnerable to high PAPR, ICI, imperfect CSI, synchronisation errors, and performance degradation under highly dynamic channel conditions. Furthermore, existing quantum communication studies have primarily investigated quantum MIMO systems and QOFDM frameworks independently rather than within a unified communication architecture. Most existing quantum communication frameworks also rely on simple single-qubit or basic encoding structures and do not comprehensively exploit the combined advantages of multi-qubit quantum encoding, spatial diversity, and frequency-domain quantum processing for high-fidelity image transmission, as a combined approach. To the best of the author's knowledge, no prior work has developed a complete end-to-end quantum MIMO-OFDM framework integrating transmit diversity, receive diversity, multi-qubit quantum encoding, and QFT-based orthogonal subcarrier transmission specifically for robust high-fidelity image transmission over noisy and fading communication channels.

Motivation and Proposed Contribution: To address these limitations, this section proposes a quantum MIMO-OFDM framework with transmit and receive diversity for next-generation high-fidelity image transmission over noisy and fading communication channels. The proposed framework integrates multi-qubit quantum encoding, quantum MIMO spatial diversity, and QFT-based orthogonal multicarrier transmission into a unified communication architecture to improve robustness against fading, channel noise, and frequency-selective impairments while preserving reconstructed image qual-

ity. Within the proposed framework, compressed image bitstreams are converted into multi-qubit quantum superposition states and transmitted using QFT-based orthogonal quantum subcarriers analogous to classical OFDM systems. The proposed MIMO architecture further exploits transmit and receive diversity mechanisms to improve resilience against multipath fading and dynamic channel variations. At the receiver, quantum-domain signal recovery, IQFT-based reconstruction, and quantum decoding operations are employed to recover the transmitted image information. By jointly combining quantum-domain spatial diversity and frequency-domain multicarrier processing, the proposed framework aims to improve transmission reliability, spectral efficiency, robustness against channel impairments, and reconstructed image quality under adverse communication environments.

7.5.1 System Model

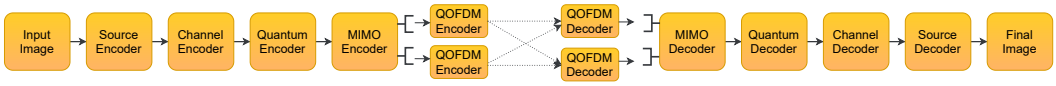


Figure 7.25: Block diagram of the proposed quantum MIMO-OFDM framework for high-fidelity image transmission.

The overall operation of the proposed quantum MIMO-OFDM framework is illustrated in Figure 7.25. The complete transmission and reception process consists of the following stages.

- **Input image stage:** The experimental dataset consists of 100 images with a spatial resolution of 256×192 pixels obtained from the Microsoft COCO dataset [197], together with 50 high-resolution 4K images collected from the Kaggle dataset [219]. These datasets provide diverse image characteristics and spatial complexities for performance evaluation. The proposed framework is independent of image format and supports both greyscale and colour image transmission across different resolutions and compression conditions.

- **Source encoding stage:** At this stage, the input image may either be compressed using conventional image-compression techniques such as JPEG or HEIF. The output of this stage is a classical binary bitstream that serves as the input to the

subsequent communication stages.

- **Channel encoding stage:** The generated bitstream is protected using polar channel coding with a coding rate of $1/2$ to improve robustness against transmission errors.

- **Quantum encoding stage:** The channel-coded bitstream is partitioned into groups according to the selected qubit dimension k, where $1 \leq k \leq 8$. Each group of classical bits is then mapped into a quantum superposition state using multi-qubit encoding. Although the framework can theoretically support larger quantum dimensions, the maximum qubit width is restricted to eight qubits in this work, since $2^8 = 256$ is sufficient to represent the standard 8-bit pixel intensity range used in digital image processing.

- **MIMO processing stage:** Spatial diversity is incorporated by applying one of three antenna configurations to the quantum-encoded symbols, namely SISO (1×1), MISO (2×1), or SIMO (1×2). The transmitted quantum symbols are distributed across the available antennas according to the selected diversity configuration.

- **QOFDM modulation stage:** Each transmit branch independently performs quantum-domain OFDM modulation. In place of the classical IFFT operation, the proposed framework employs the QFT directly on the quantum-encoded states to generate orthogonal quantum subcarriers. Prior to QFT processing, the serial quantum-state sequence is rearranged into parallel form. The resulting orthogonal quantum subcarriers improve robustness under frequency-selective fading conditions by distributing the encoded information across multiple subcarrier components.

- **Transmission stage:** Following QOFDM modulation, the parallel quantum subcarriers are converted back into serial form, after which a cyclic prefix is inserted to reduce inter-symbol interference arising from multipath propagation. The resulting signals are transmitted through the noisy quantum communication channel. Depending on the considered scenario, the channel model includes both

quantum-noise effects and wireless fading characteristics. Flat-fading channels are employed for simplified narrowband transmission cases, whereas frequency-selective fading channels are considered for more realistic wideband communication conditions.

- **QOFDM demodulation stage:** At the receiver, the cyclic prefix is first removed before the received signals are transformed from serial to parallel form. The IQFT operation is then applied to recover the corresponding time-domain quantum representation from the received quantum subcarriers.

- **MIMO decoding stage:** The receiver performs spatial decoding to separate the transmitted data streams originating from the different antennas according to the selected MIMO configuration.

- **Quantum decoding stage:** The reconstructed quantum states are subsequently converted back into the corresponding classical binary representation through the quantum decoding process.

- **Channel decoding stage:** The recovered classical bitstream is processed by the polar decoder with coding rate 1/2 to correct any remaining transmission errors introduced by the communication channel.

- **Source reconstruction stage:** Finally, the transmitted image is reconstructed using the appropriate source-decoding operation associated with the original image format, such as JPEG or HEIF decoding. In uncompressed transmission scenarios, this stage directly reconstructs the transmitted image without additional source decoding.

The following subsections provide a more detailed discussion of the individual quantum-processing blocks incorporated within the proposed communication framework.

Quantum MIMO-OFDM Transmitter Design

The transmitter structure of the proposed quantum MIMO-OFDM framework is illustrated in Figure 7.26. The transmitter consists of three principal processing stages,

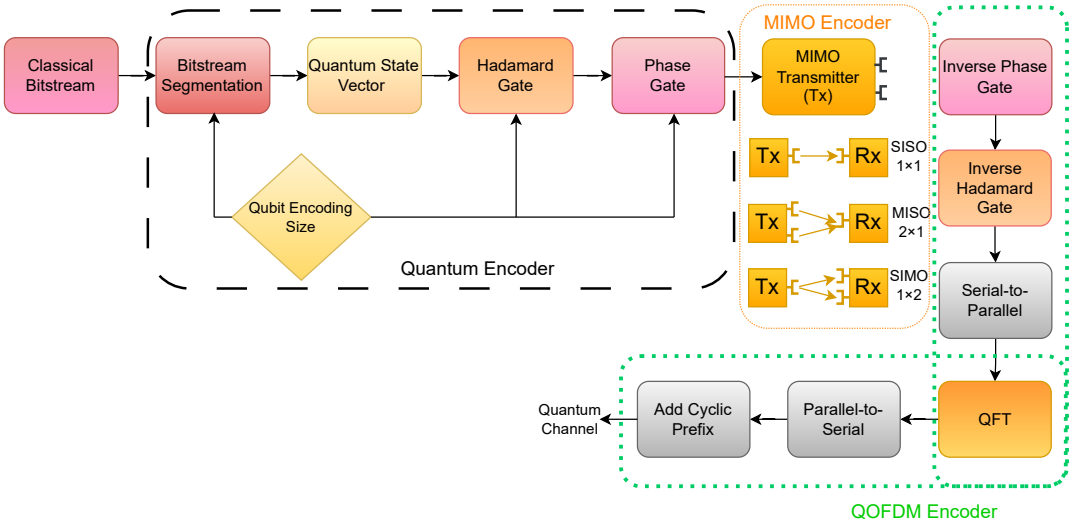


Figure 7.26: Architecture of the proposed quantum MIMO-OFDM transmitter.

namely quantum encoding, MIMO processing, and QOFDM modulation. Each stage performs a distinct role in preparing the image bitstream for reliable transmission through noisy quantum communication channels. The individual encoding and modulation processes are described in detail in the following subsections.

Quantum Encoder

The quantum encoder is responsible for transforming the channel-coded classical bitstream into quantum states appropriate for quantum-domain transmission. Initially, the encoded binary sequence is divided into fixed-length groups according to the selected qubit dimension k. For the single-qubit case ($k = 1$), each classical bit is mapped onto the computational basis state and then carried through the Hadamard and phase-gate cascade exactly as defined for the MIMO image framework in Section 7.1 (basis mapping, H, and S as in (7.1)–(7.2) and the surrounding equations), so this construction is not repeated here.

For multi-qubit configurations ($k > 1$), the corresponding basis states and gates are formed through tensor-product combinations of the single-qubit vectors and operators, following the same construction used for the QOFDM image framework in Section 7.3. In general, a k-qubit state lives in a Hilbert space of dimension 2^k, so the corresponding state vector is $2^k \times 1$ and the associated gates are $2^k \times 2^k$ matrices built via tensor

products of the single-qubit operators. A composite superposition state is produced by applying the Hadamard and phase gates in sequence, $|\psi'\rangle = H^{\otimes k}|\psi\rangle$ followed by $|\psi''\rangle = S^{\otimes k}|\psi'\rangle$, giving an efficient and compact mechanism for encoding and modulating classical information prior to transmission through the quantum communication channel.

MIMO Encoder

Within the proposed framework, the generated quantum symbols are transmitted using different spatial-diversity configurations in order to improve communication reliability and robustness against channel impairments. For the present study, a 2×2 MIMO framework is considered, representing the quantum-domain counterpart of conventional classical MIMO communication systems in terms of spatial-diversity utilisation. The adopted spatial-processing strategies are derived from established classical MIMO techniques but are extended here to support quantum-symbol transmission while preserving the underlying principle of exploiting multiple antennas to improve transmission performance. The investigated antenna configurations include SISO, MISO, and SIMO arrangements. Distributing the quantum symbols across antennas using the SISO, MISO, and SIMO configurations improves the overall reliability of the quantum communication system and enhances the fidelity of the transmitted information.

QOFDM Encoder

The QOFDM modulation stage employs the same QFT-based orthogonal-subcarrier framework previously introduced for image transmission in Section 7.3 and later extended for video transmission in Section 7.4. In the proposed architecture, the quantum-symbol sequence generated from each MIMO branch is initially processed using the inverse phase operation $(S^\dagger)^{\otimes k}$ followed by the inverse Hadamard transformation $(H^\dagger)^{\otimes k}$. These inverse operations remove the complex-valued superposition introduced during the MIMO encoding stage and return the quantum states to their corresponding computational-basis representation prior to QFT processing.

The QFT subsequently transforms each k-qubit computational-basis state into a 2^k-dimensional quantum superposition, thereby generating a set of mutually orthogonal quantum subcarriers with subcarrier spacing defined as $\Delta f = B/2^k$. The complete

mathematical representation of the QFT operation, including the matrix formulation, the transformation applied to computational-basis states $|x\rangle$, the illustrative F_4 example, and the orthogonality verification using the Hermitian inner product, follows the formulation previously presented in Section 7.3 (equations (7.13)–(7.21)) and is therefore not repeated in this section.

After generating the orthogonal quantum subcarriers, the parallel quantum-state streams are converted back into serial form. A cyclic prefix with length $L_{\text{CP}} = \text{round}(N \times 0.25)$ is then inserted to reduce ISI arising from multipath propagation. The resulting symbol duration is expressed as $T_{\text{symbol}} = N + L_{\text{CP}}$, consistent with the cyclic-prefix configuration adopted previously in Section 7.3.

Quantum Channel Modelling

The transmission of quantum symbols through realistic wireless communication environments is modelled in this work using a layered channel framework that combines environmental Rayleigh fading with intrinsic quantum decoherence effects. This channel representation extends the models introduced earlier in this chapter by jointly incorporating classical wireless propagation impairments and the quantum-noise mechanisms described previously in Section 7.3. For the simulation analysis, the urban Rayleigh fading environment is characterised using four propagation paths with delays of $(0, 0.2, 0.5, 1.0)$ μs and corresponding path gains of $(0, -3, -10, -15)$ dB. A Doppler frequency of 100 Hz is incorporated to model the relative movement between the transmitter and receiver, thereby capturing the time-varying behaviour typical of urban wireless communication scenarios.

Proposed Quantum MIMO-OFDM Receiver

As shown in Figure 7.27, the receiver mirrors the transmitter and consists of a sequence of decoding stages. These are summarised in the subsections that follow.

QOFDM Decoder

At the receiver, the QOFDM demodulation process follows the same procedure as that described in Section 7.3. The received signal first undergoes cyclic prefix removal

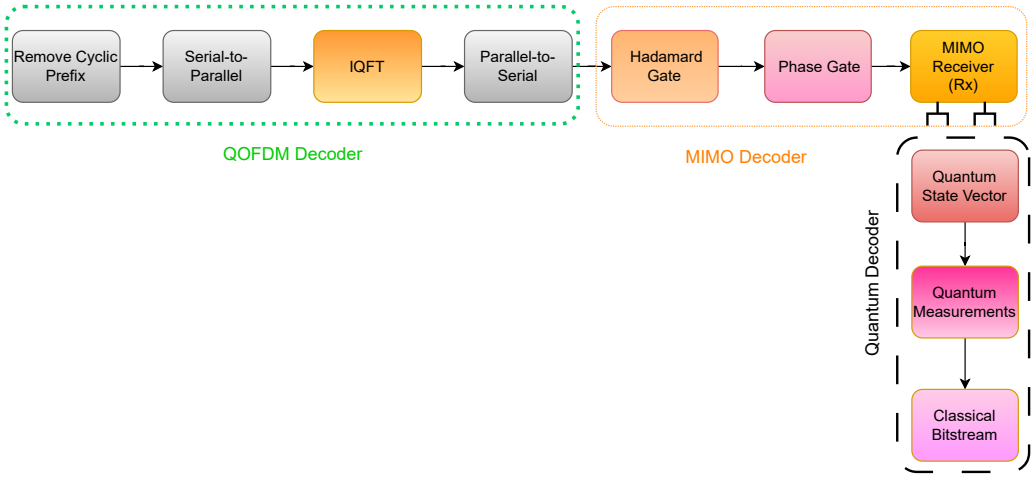


Figure 7.27: Block diagram of the proposed quantum MIMO-OFDM receiver.

and serial-to-parallel conversion, after which the IQFT is applied to reverse the QFT operation performed during transmission. Since the IQFT implementation and the subsequent parallel-to-serial conversion are identical to those presented in Section 7.3, these operations are not repeated here.

MIMO Decoder

Each recovered quantum state is subsequently processed using Hadamard and phase-gate operations in order to reconstruct the complex-valued superposition representation required by the MIMO receiver. These operations effectively mirror the transformations applied during the MIMO transmission stage. Following this reconstruction process, the decoding strategy corresponding to the selected spatial-diversity configuration is applied, consistent with the procedure described in Section 7.1, to recover the quantum state at the output of the complete MIMO decoding framework.

Quantum Decoder

At the input of the quantum decoder, each received k-qubit state has already been affected by channel impairments and therefore appears as a noisy quantum superposition. To recover the transmitted information, the decoder first applies the transformation $H^{\otimes k}$, which reverses the Hadamard operation introduced during the quantum encoding stage and maps the state back into the computational basis. A projective measurement

is subsequently performed, causing the quantum state to collapse onto one of the possible 2^k computational basis states and producing the corresponding classical bit sequence.

Because the transmitted quantum states may have been altered by noise and fading during propagation, the measured bit sequence may not exactly match the originally transmitted data. To improve decoding reliability, the observed measurement outcome is compared against the set of valid bit patterns, and the closest candidate is selected according to the Euclidean-distance criterion. This procedure enables reliable recovery of the transmitted classical information from the distorted quantum states.

It should also be noted that the proposed framework assumes perfect CSI at the receiver. Under this assumption, the equalisation process is treated as ideal, allowing the performance characteristics of the proposed communication framework to be analysed without the additional influence of channel-estimation errors.

Classical MIMO-OFDM Benchmark Framework

To provide a fair performance benchmark, a classical MIMO-OFDM communication system is configured under the same bandwidth and operating conditions as the proposed quantum framework. The classical reference system employs widely used digital modulation schemes, including BPSK, QPSK, and 16-QAM. In order to maintain consistency between the classical and quantum transmission frameworks, the number of OFDM subcarriers is fixed at $N = 256$, corresponding to the maximum subcarrier configuration considered within the proposed QOFDM system.

7.5.2 Results

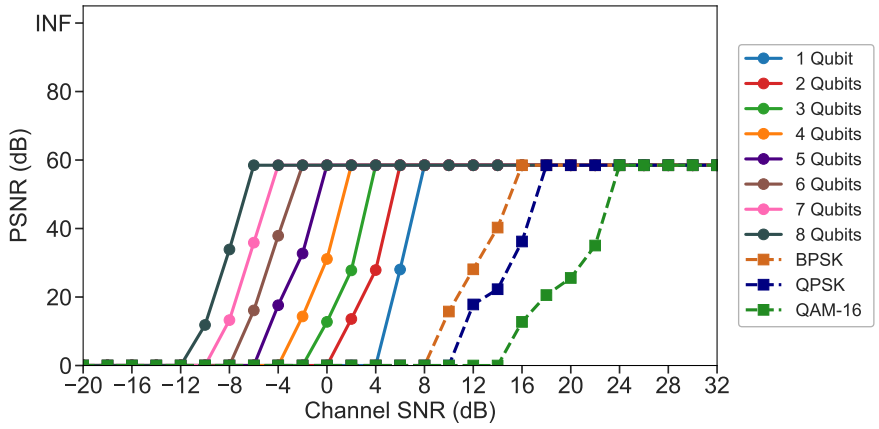
This section presents a comparative evaluation of the proposed quantum MIMO-OFDM framework and the corresponding classical MIMO-OFDM benchmark under multiple source-coding conditions. Three transmission scenarios are considered, namely JPEG-compressed images, HEIF-compressed images, and uncompressed image transmission, with the compressed cases evaluated using a quantisation parameter (QP) value of 100. To ensure a fair and balanced comparison, both communication frameworks are tested under identical transmission and channel conditions. Performance results are averaged over a dataset consisting of 100 test images, while reconstruction quality is

assessed using PSNR, SSIM [200], and UQI [211]. Together, these metrics provide a comprehensive evaluation of both objective reconstruction fidelity and structural image quality. All simulations are implemented in Python 3 and executed on a workstation equipped with a 13$^{\text{th}}$ Gen Intel® Core™ i5-1345U processor operating at 1.60 GHz together with 16 GB of RAM. The following subsections discuss the obtained results for each transmission scenario individually.

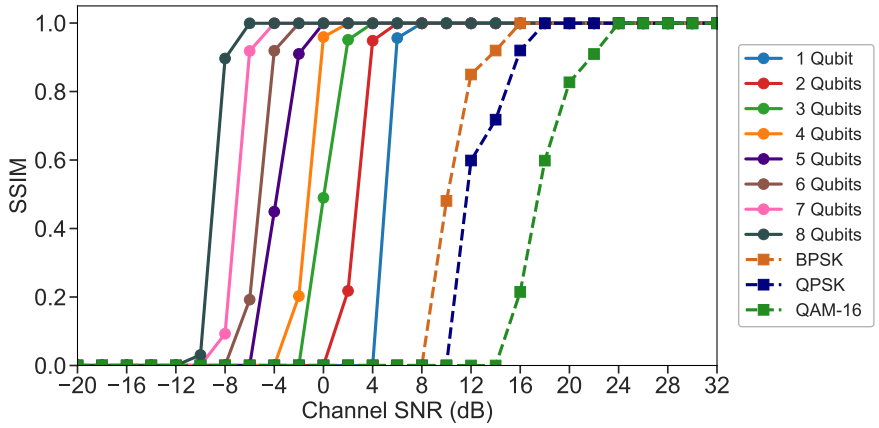
Performance Comparison of JPEG Image Transmission using Quantum MIMO-OFDM and Classical MIMO-OFDM Systems

JPEG image transmission is evaluated under the three antenna configurations: SISO (1×1) in Figure 7.28, MISO (2×1) in Figure 7.29, and SIMO (1×2) in Figure 7.30, for both the proposed quantum framework and the classical MIMO-OFDM benchmark. The quantum framework employs Hadamard-based superposition encoding together with phase-gate operations to generate the quantum MIMO symbols, followed by QFT-based QOFDM processing using qubit dimensions ranging from 1 to 8. The classical benchmark uses BPSK, QPSK, and 16-QAM modulation schemes. Performance is evaluated using PSNR, SSIM, and UQI across channel SNR values from -20 dB to 32 dB.

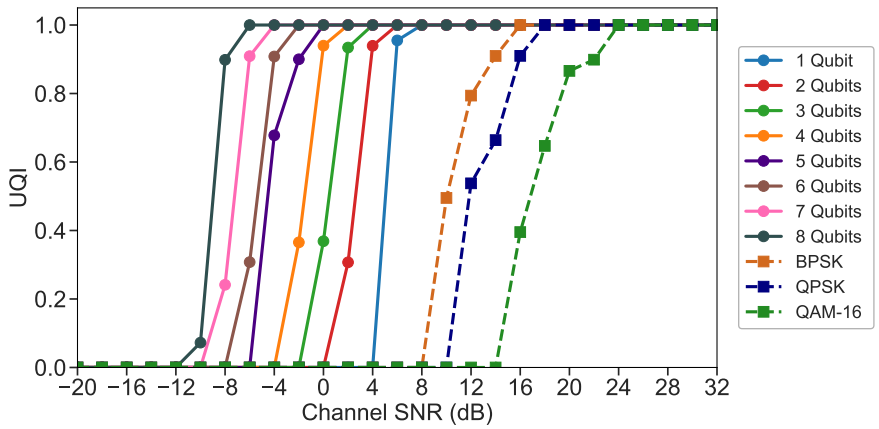
Across all antenna configurations, the qubit dimension has the strongest influence on robustness against noise. In the SISO configuration, quantum systems using $k = 1$ to 3 qubits exhibit a noticeable reduction in reconstruction quality below 0 dB SNR. In contrast, larger configurations using 6, 7, or 8 qubits maintain significantly higher robustness. The eight-qubit SISO configuration, for example, preserves peak PSNR, SSIM, and UQI values down to approximately -6 dB SNR without visible quality degradation. Smaller qubit configurations deteriorate earlier, while the classical transmission schemes begin to degrade below approximately 12 dB SNR. A consistent trend observed in the SISO results is a crossover region near 8 dB SNR, where the classical modulation schemes approach near-zero PSNR, SSIM, and UQI values, whereas even the single-qubit quantum configuration continues to outperform all classical schemes across the evaluated quality metrics. This performance gap increases further as the qubit dimension grows, with the eight-qubit configuration producing the strongest overall



(a) PSNR

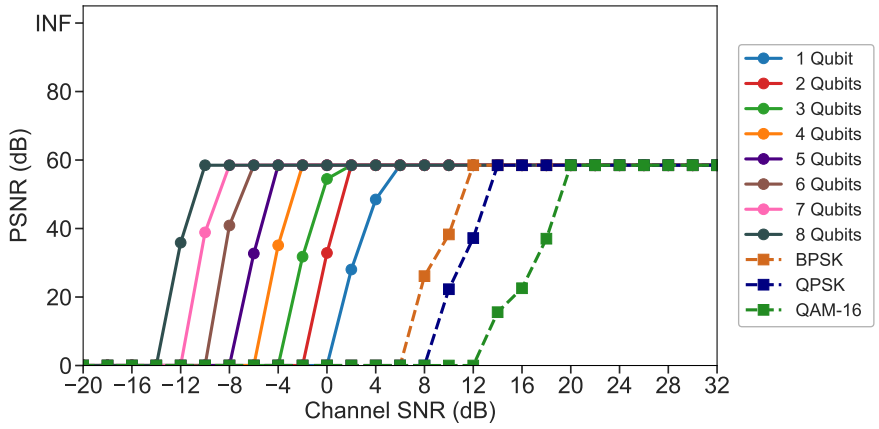


(b) SSIM

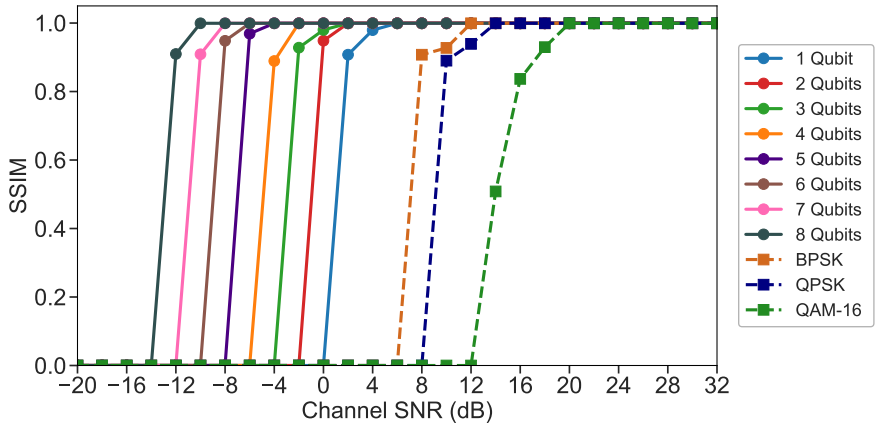


(c) UQI

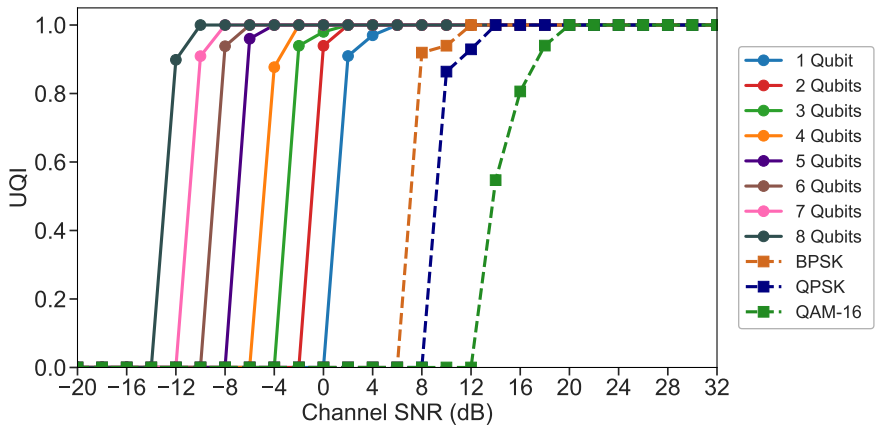
Figure 7.28: PSNR, SSIM, and UQI curves for JPEG image transmission using the proposed quantum MIMO-OFDM and the classical MIMO-OFDM benchmark, 1×1 (SISO).



(a) PSNR

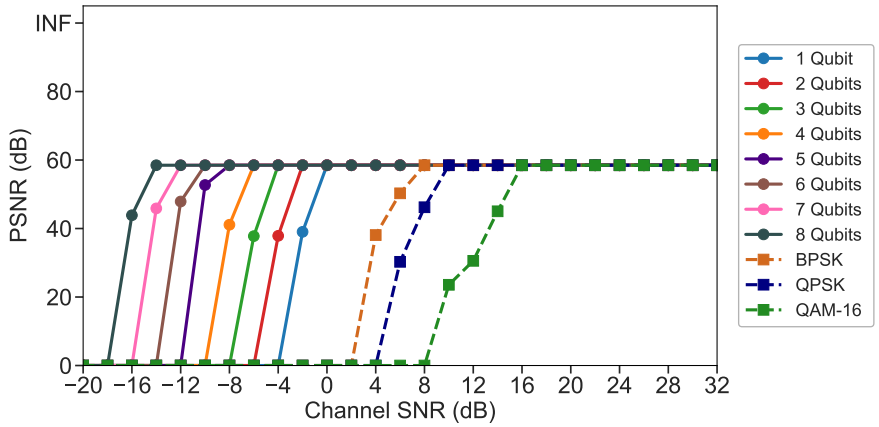


(b) SSIM

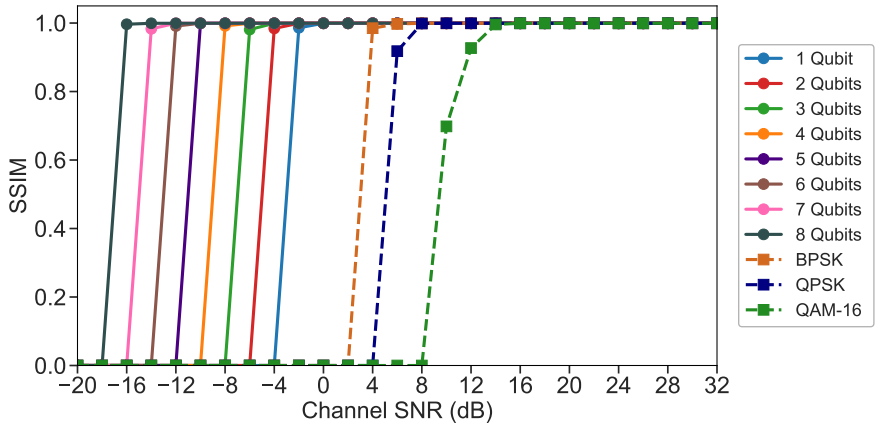


(c) UQI

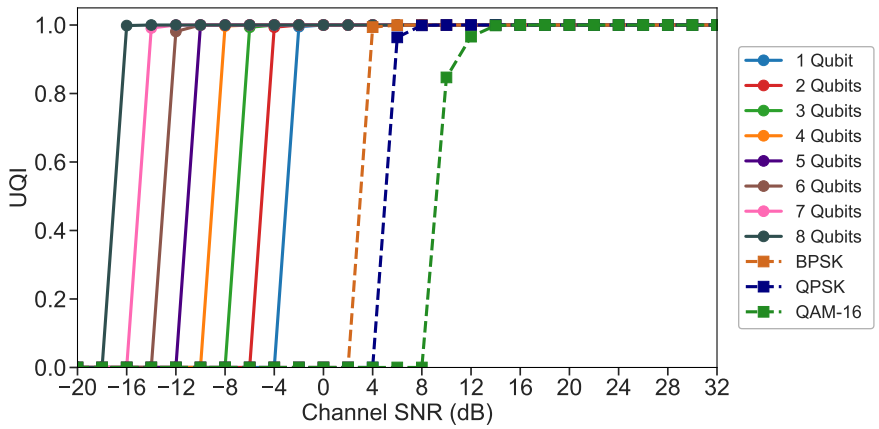
Figure 7.29: PSNR, SSIM, and UQI curves for JPEG image transmission using the proposed quantum MIMO-OFDM and the classical MIMO-OFDM benchmark, 2×1 (MISO).



(a) PSNR



(b) SSIM



(c) UQI

Figure 7.30: PSNR, SSIM, and UQI curves for JPEG image transmission using the proposed quantum MIMO-OFDM and the classical MIMO-OFDM benchmark, 1×2 (SIMO).

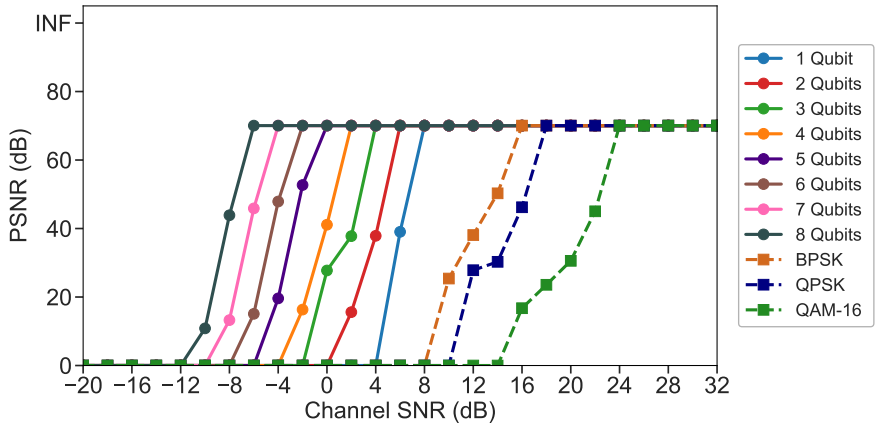
performance. Among the classical modulation schemes, BPSK remains the most robust under noisy conditions, outperforming both QPSK and 16-QAM. Similar behaviour is observed for the SIMO and MISO configurations, where spatial diversity improves performance for both the classical and quantum frameworks relative to SISO operation, while the proposed quantum framework still maintains a clear advantage in both noise tolerance and reconstruction quality due to the multi-qubit encoding process and the scalability provided by larger qubit dimensions.

For the SIMO (1×2) configuration shown in Figure 7.30, the use of two receive antennas improves recovery of the transmitted quantum states following measurement, resulting in greater stability even for lower qubit dimensions as channel noise increases. The MISO (2×1) configuration in Figure 7.29 performs approximately 3 dB below the corresponding SIMO configuration because the total transmit power is kept constant across all antenna arrangements. Under equal received-power conditions, the performance difference between MISO and SIMO would be expected to reduce substantially.

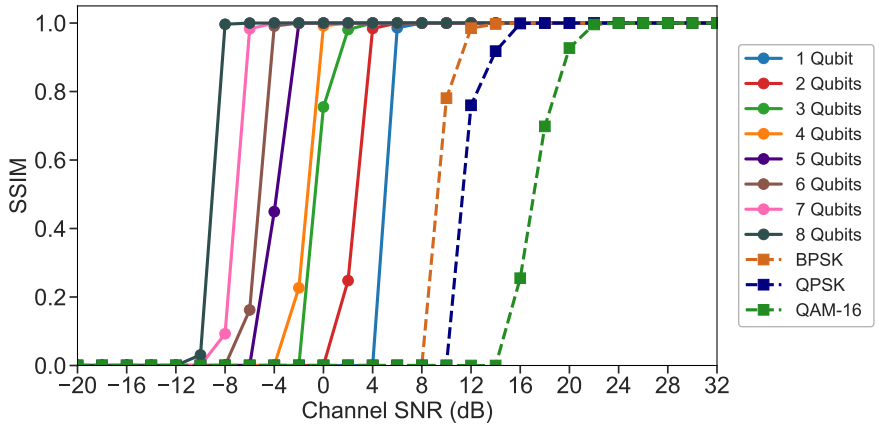
Overall, the JPEG transmission results indicate that the proposed quantum MIMO-OFDM framework is particularly effective under low-SNR and interference-prone communication environments, such as long-range or densely populated wireless channels, whereas the classical transmission schemes remain more suitable for short-range high-SNR scenarios. The obtained results further demonstrate that the proposed quantum framework scales effectively with increasing qubit dimension and benefits significantly from spatial-diversity techniques, particularly under SIMO and MISO configurations, thereby supporting its suitability as an alternative to classical communication approaches under challenging channel conditions.

Performance Comparison of HEIF Image Transmission using Quantum MIMO-OFDM and Classical MIMO-OFDM Systems

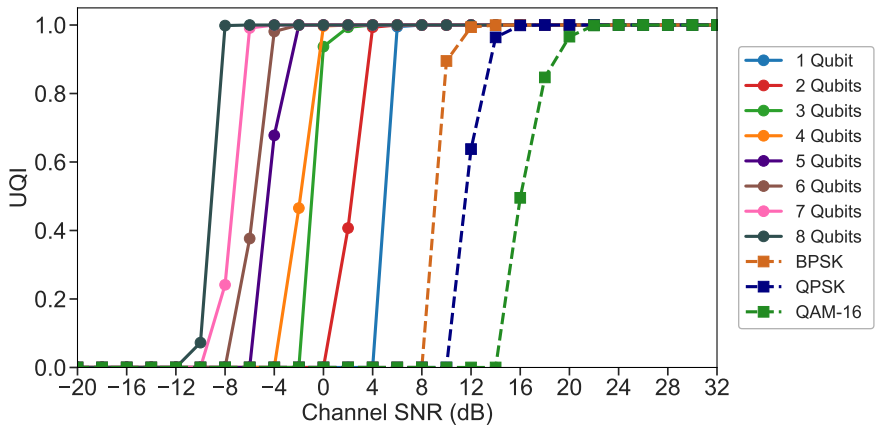
The HEIF transmission results shown in Figures 7.31 to 7.33 demonstrate that the proposed quantum framework consistently outperforms the classical transmission schemes below a given noise threshold across all considered antenna configurations. The classical SISO configuration presented in Figure 7.31 represents the weakest overall case because it lacks both spatial-diversity gain and the additional robustness provided by quantum



(a) PSNR

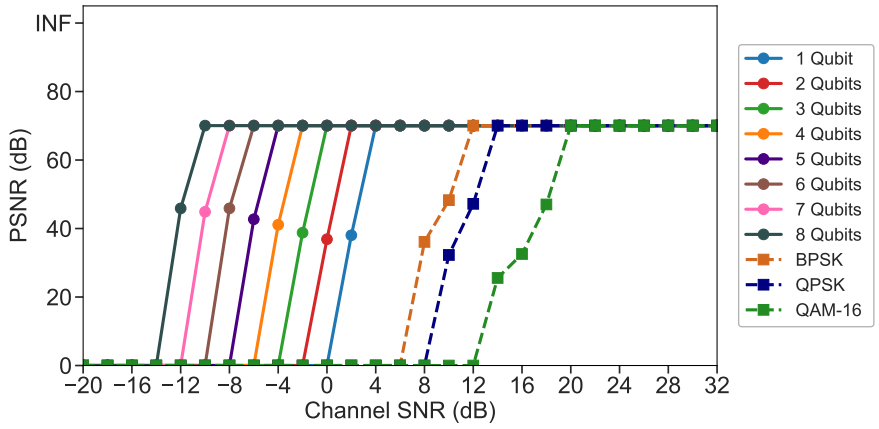


(b) SSIM

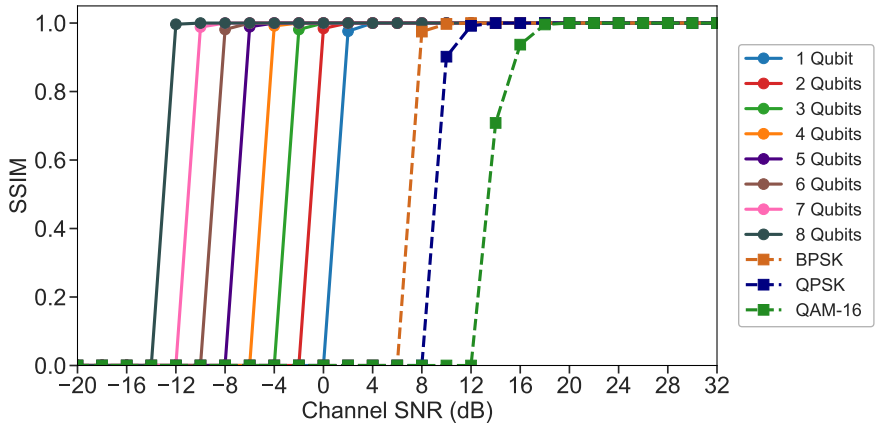


(c) UQI

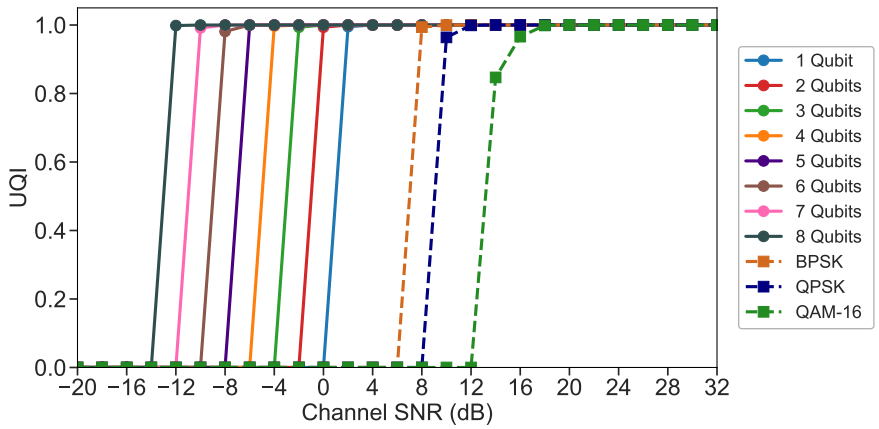
Figure 7.31: PSNR, SSIM, and UQI curves for HEIF image transmission using the proposed quantum MIMO-OFDM and the classical MIMO-OFDM benchmark, 1×1 (SISO).



(a) PSNR

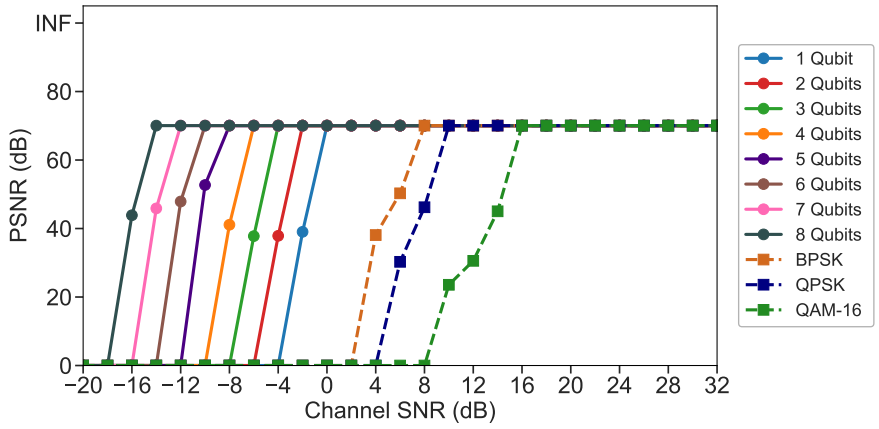


(b) SSIM

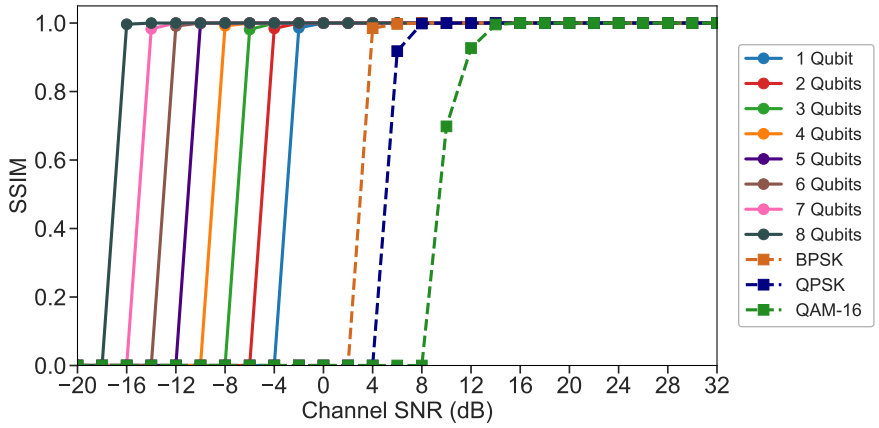


(c) UQI

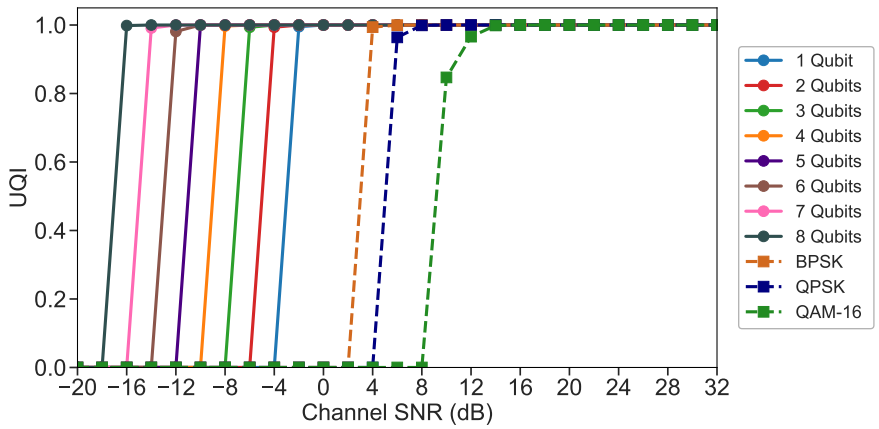
Figure 7.32: PSNR, SSIM, and UQI curves for HEIF image transmission using the proposed quantum MIMO-OFDM and the classical MIMO-OFDM benchmark, 2×1 (MISO).



(a) PSNR



(b) SSIM



(c) UQI

Figure 7.33: PSNR, SSIM, and UQI curves for HEIF image transmission using the proposed quantum MIMO-OFDM and the classical MIMO-OFDM benchmark, 1×2 (SIMO).

encoding. Consequently, this configuration produces the lowest PSNR, SSIM, and UQI performance among all evaluated scenarios.

Introducing spatial diversity through the MISO configuration in Figure 7.32 and the SIMO configuration in Figure 7.33 improves the performance of the classical systems by providing multiple independent transmission paths that reduce the influence of fading and interference. Although reconstruction quality improves noticeably under these diversity configurations, the classical schemes still experience significant degradation under low-SNR conditions.

The proposed quantum framework benefits from the same spatial-diversity mechanisms while additionally exploiting the advantages of multi-qubit encoding within the MIMO-OFDM transmission structure. This combined effect improves both noise resilience and transmission reliability, with the improvement becoming more pronounced as the qubit dimension increases. Larger qubit configurations preserve image information more effectively under noisy channel conditions, and the eight-qubit configuration achieves the highest PSNR, SSIM, and UQI values among all tested systems.

When compared across source-compression formats, HEIF transmission through the proposed quantum framework achieves higher peak reconstruction quality than JPEG under equivalent channel conditions. This improvement arises from the combination of the higher coding efficiency of HEIF together with the robustness provided by the quantum encoding and decoding operations. These two characteristics complement one another and enable reliable high-fidelity image transmission even in challenging noisy environments.

More generally, the interaction between the proposed quantum MIMO-OFDM framework and conventional image-compression formats depends strongly on the underlying compression structure. JPEG employs block-based DCT compression, concentrating most image energy within a limited number of low-frequency coefficients. When mapped into quantum states, this distribution allows the QFT operation to compact and preserve the dominant image information efficiently, resulting in accurate reconstruction quality. HEIF compression, by contrast, employs more advanced predictive and intra-frame coding strategies that distribute image correlations across larger spatial regions and a broader range of frequency components. Consequently, the quantum encoder captures a

richer set of image information within each transmission block, while the QFT maps these correlations into orthogonal frequency-domain quantum subcarriers in a manner that better preserves perceptually important image content.

Mathematical Basis for the 0 dB PAPR Property: Within the proposed quantum MIMO-OFDM framework, the 0 dB PAPR characteristic originates from the quantum-state representation and the unitary nature of the QFT operation rather than from conventional classical waveform superposition principles. Information is encoded within multi-qubit quantum superposition states, while the QFT distributes the corresponding probability amplitudes across the orthogonal quantum subcarriers. Since both the quantum-state evolution and the QFT operation are unitary, the total energy of the transmitted quantum state remains preserved throughout the transmission process. Consequently, the probability amplitudes remain uniformly distributed across the subcarrier structure, avoiding the large instantaneous power fluctuations typically observed in classical OFDM systems. As a result, the instantaneous transmission power remains equal to the average transmission power, leading to a constant PAPR value of 0 dB. The mathematical derivation is presented below.

For an input quantum state $|\psi_{\text{in}}\rangle$ spanning N orthogonal subcarriers, the transmitted QOFDM state $|\rho_{\text{QOFDM}}\rangle$ is generated through the QFT unitary transformation U_{QFT}, as expressed in (7.31). The QFT transformation satisfies the unitary condition shown in (7.32).

$$|\rho_{\text{QOFDM}}\rangle = U_{\text{QFT}}|\psi_{\text{in}}\rangle \tag{7.31}$$

$$U_{\text{QFT}}^{\dagger}U_{\text{QFT}} = I \tag{7.32}$$

The transmitted quantum state remains normalised, ensuring conservation of total probability and total state energy, as given in (7.33).

$$\langle\rho_{\text{QOFDM}}|\rho_{\text{QOFDM}}\rangle = 1 \tag{7.33}$$

The instantaneous quantum-power operator $\hat{P}$ is defined as the projection operator

associated with the transmitted QOFDM state, as expressed in (7.34).

$$\hat{P} = |\rho_{\text{QOFDM}}\rangle\langle\rho_{\text{QOFDM}}| \tag{7.34}$$

The corresponding instantaneous and average powers, denoted by P_{inst} and P_{avg}, are defined in (7.35) and (7.36), respectively. Here, $P_{\text{inst}}(t)$ represents the instantaneous transmitted power at time t, while $E_t[\cdot]$ denotes the temporal averaging operation.

$$P_{\text{inst}} = \langle\rho_{\text{QOFDM}}|\hat{P}|\rho_{\text{QOFDM}}\rangle = 1 \tag{7.35}$$

$$P_{\text{avg}} = E_t[P_{\text{inst}}(t)] = 1 \tag{7.36}$$

Substituting (7.35) and (7.36) into the PAPR definition yields the result shown in (7.37).

$$\text{PAPR} = \frac{P_{\text{peak}}}{P_{\text{avg}}} = 1 \quad \Rightarrow \quad 0 \text{ dB} \tag{7.37}$$

Equation (7.37) therefore confirms that the proposed QOFDM framework maintains a constant 0 dB PAPR independently of the selected qubit dimension.

In addition to the standard image-transmission scenarios, the evaluation further considers high-resolution 4K image transmission in order to verify that the proposed framework maintains effective performance across different image resolutions and source-coding formats. The maximum channel SNR gains achieved by the proposed quantum MIMO-OFDM framework are summarised in Table 7.6. The reported results show a consistent increase in SNR gain as the qubit dimension increases from 1 to 8, independent of the selected image format. These observations demonstrate that the proposed framework scales effectively with qubit dimension while remaining largely insensitive to image resolution and source-coding selection. The framework therefore operates reliably for both compressed image formats, such as JPEG and HEIF, and high-resolution 4K image content. Consequently, the proposed quantum MIMO-OFDM framework represents a promising solution for future multimedia communication applications within next-generation wireless quantum communication networks.

Table 7.6: Highest channel SNR improvements achieved by the proposed multi-qubit quantum MIMO-OFDM framework relative to the classical BPSK-based MIMO-OFDM benchmark for different image formats (dB).

Image Format	Maximum Channel SNR Gains							
	1 Qubit	2 Qubits	3 Qubits	4 Qubits	5 Qubits	6 Qubits	7 Qubits	8 Qubits
JPEG (256×192)	8	10	12	14	16	18	20	22
HEIF (256×192)	8	10	12	14	16	18	20	22
Uncompressed (256×192)	8	10	12	14	16	18	20	22
4K	8	10	12	14	16	18	20	22

Complexity Analysis

The computational complexity of the proposed quantum MIMO-OFDM framework is primarily determined by the QFT operations employed during both transmission and reception. For a k-qubit quantum register, the QFT requires $G_{\mathrm{QFT}}(k) = k(k+1)/2$ quantum gate operations, resulting in quadratic growth with respect to the qubit dimension. The corresponding circuit depth increases approximately linearly according to $D_{\mathrm{QFT}}(k) \approx k$. The resulting gate counts and circuit depths for qubit dimensions ranging from $k = 1$ to $k = 8$ are summarised in Table 7.7. Even for the largest configuration considered ($k = 8$), the QFT requires only 36 quantum gates and a circuit depth of 8 layers, remaining computationally feasible for both classical simulation environments and near-term quantum hardware platforms. The relatively moderate growth in gate count and circuit depth demonstrates that the increased encoding flexibility provided by larger qubit dimensions is achieved with comparatively low computational overhead.

In addition to the quantum-circuit complexity, the practical requirements associated with classical simulation provide further insight into the feasibility of the proposed framework. A quantum state containing k qubits requires 2^k complex probability amplitudes for state-vector representation, causing memory usage to scale according to $O(2^k)$. Furthermore, the computational complexity associated with classical QFT simulation scales approximately as $G_{\mathrm{QFT}}(k) \cdot 2^k$, since each quantum gate operation acts across the complete state vector. Table 7.8 summarises the corresponding state-vector dimensions, memory requirements, floating-point operation counts (FLOPs), and estimated execution times for simulation on a 50 GFLOPS CPU platform. Even for the largest investigated configuration ($k = 8$), the quantum state vector contains only 256

amplitudes, corresponding to approximately 4 KB of memory, while the complete QFT simulation requires fewer than 10^4 FLOPs and achieves sub-microsecond runtime.

Taken together, Tables 7.7 and 7.8 demonstrate that both the quantum-circuit implementation cost and the associated classical-simulation complexity remain computationally manageable across all investigated qubit dimensions. Consequently, the proposed quantum MIMO-OFDM framework achieves a practical balance between computational efficiency and transmission performance throughout the considered $k = 1$ to $k = 8$ operating range.

Table 7.7: QFT gate count and circuit depth as a function of qubit width.

k **(qubits)**	**QFT gates** G_{QFT}	**Circuit depth**
1	1	1
2	3	2
3	6	3
4	10	4
5	15	5
6	21	6
7	28	7
8	36	8

Table 7.8: State-vector size, memory, FLOP count, and estimated CPU runtime for QFT simulation.

k **(qubits)**	**State-vector size** (2^k)	**Memory (KB)**	**Estimated FLOPs**	**Runtime @ 50 GFLOPS**
1	2	0.03	2	4×10^{-11} s
2	4	0.06	12	2.4×10^{-10} s
3	8	0.13	48	9.6×10^{-10} s
4	16	0.25	160	3.2×10^{-9} s
5	32	0.50	480	9.6×10^{-9} s
6	64	1.00	1,344	2.7×10^{-8} s
7	128	2.00	3,584	7.2×10^{-8} s
8	256	4.00	9,216	1.8×10^{-7} s

Scalability

A 2×2 MIMO configuration is adopted within the present framework because it provides a relatively simple structure for analysing the benefits of spatial diversity and evaluating the flexibility of the proposed quantum communication architecture without introducing excessive implementation complexity. Nevertheless, the proposed framework is inherently scalable and can be extended to larger antenna configurations

such as 4×4, 8×8, and higher-dimensional MIMO arrangements as quantum-processing technologies continue to advance. Although increasing the number of antennas and qubits inevitably raises computational and implementation complexity, the modular structure of the proposed architecture enables such expansion without fundamentally altering the underlying transmission framework. This scalability makes the proposed quantum MIMO-OFDM system suitable for future high-throughput quantum communication applications requiring increased transmission capacity and robustness.

Hardware Limitations and Practical Deployment Considerations

The practical implementation of the proposed quantum MIMO-OFDM framework is currently limited by the capabilities of existing quantum-hardware technologies. Large-scale quantum processors capable of executing high-fidelity multi-qubit operations are still under active development, restricting the achievable qubit dimensions, gate fidelities, processing speeds, and coherence durations available for practical deployment. These hardware limitations directly influence the performance of computationally intensive operations such as the QFT, IQFT, and multi-qubit MIMO decoding stages. Furthermore, practical quantum MIMO communication systems require accurate synchronisation and coordinated control across multiple transmit and receive nodes, introducing additional engineering complexity. The exponential growth of the underlying Hilbert space with increasing qubit count and antenna dimension also increases both computational and hardware-management requirements.

Despite these challenges, substantial progress in quantum-hardware technologies, including superconducting-qubit systems, trapped-ion platforms, and photonic quantum processors, indicates that scalable multi-qubit processing is becoming increasingly achievable. Emerging approaches such as fault-tolerant quantum-gate architectures, approximate QFT implementations, and distributed quantum-networking techniques provide promising directions for future realisation. In addition, hybrid classical–quantum communication strategies, such as the polar-coded transmission framework employed in this work, help reduce the processing burden placed on the quantum subsystem while maintaining overall communication reliability.

Although large-scale deployment of the proposed framework is not immediately

feasible with current hardware capabilities, the scalable architecture presented in this work provides a strong foundation for future development as quantum technologies continue to mature. The framework establishes a validated theoretical reference for future experimental prototyping, hardware-in-the-loop testing, and gradual system scaling. In this sense, the proposed framework serves as a bridge between theoretical quantum communication research and future practical deployment.

7.5.3 Section Summary

By unifying the spatial diversity of Sections 7.1–7.2 with the QFT-based multicarrier processing of Sections 7.3–7.4, the resulting quantum MIMO-OFDM framework consistently exceeded the classical MIMO-OFDM benchmark across SISO, MISO, and SIMO configurations and across JPEG and HEIF image inputs, with the eight-qubit configuration again giving the strongest overall performance. Having addressed the physical layer from every angle, the chapter now turns to two higher-layer questions: source layer (Section 7.6) and the content layer (Section 7.7).

7.6 A Quantum Multiple Description Coding Framework for Robust Image Transmission

Publication Notice

The research presented in this section has been published in the following peer-reviewed journal publication:

U. Jayasinghe, P. Samarathunga, P. Cuenca, and A. Fernando, "A quantum-inspired multiple description coding framework for robust image transmission," *IEEE Open Journal of Vehicular Technology*, early access, 2026, doi: 10.1109/OJVT.2026.3711773.

This material is reproduced and adapted under the terms of the IEEE Copyright policy for use in a doctoral thesis. The content has been revised and extended with additional explanations and expanded discussion.

Problem Statement: The frameworks developed so far in this chapter improve transmission robustness either by exploiting spatial diversity (MIMO, Sections 7.1

and 7.2) or by exploiting the frequency dimension of the wireless channel (QOFDM and quantum MIMO-OFDM). In all of these systems, however, the source information is still conveyed as a single bitstream through the wireless channel. Single-stream transmission remains highly sensitive to channel impairments: even a small fraction of bit errors in a compressed image bitstream (JPEG, JPEG2000, or HEIF) can cause severe reconstruction degradation, commonly referred to as the cliff effect. In dynamic wireless environments, where channel conditions vary rapidly due to mobility, noise, and interference, ensuring robust high-fidelity image transmission therefore remains a critical challenge that cannot be fully addressed by physical-layer techniques alone.

Limitations of Existing Work: MDC has long been employed as a source-layer technique in classical communication systems to improve transmission robustness over unreliable networks. However, classical MDC approaches suffer from a trade-off between redundancy and compression efficiency, and their recovery mechanisms often fail to fully exploit deterministic inter-description correlations. On the quantum side, the frameworks developed in earlier sections of this chapter, as well as most quantum communication systems in the literature, predominantly adopt single-stream transmission models. Although they improve representation efficiency through single-qubit encoding, multi-qubit encoding, or frequency-domain processing, they remain vulnerable to channel impairments and offer limited robustness against packet-level loss. To the best of our knowledge, no existing work has integrated quantum-domain operations with a multi-description transmission strategy to jointly exploit superposition-based encoding, structured inter-description correlations, and packet-level recovery for robust image transmission.

Motivation and Proposed Contribution: To address these limitations, this section proposes a Q-MDC framework for robust image transmission over dynamic and error-prone channels. The proposed framework partitions the source image at the pixel level into odd and even-indexed components to generate two primary descriptions, which are independently source-encoded (using JPEG, JPEG2000, HEIF, or uncompressed formats), optionally channel-coded, and mapped into quantum states in the computational basis. A third correlated description is then generated by applying a controlled-NOT

(CNOT) operation between the two primary descriptions, embedding deterministic inter-description redundancy without increasing transmission bandwidth. All three descriptions are transformed into quantum superposition states using a Hadamard-based encoder and transmitted over independent noisy channels. At the receiver, inverse Hadamard operations restore the computational basis representation, and a packet-wise and qubit-wise deterministic recovery mechanism reconstructs corrupted descriptions by exploiting the inter-description dependencies. It is important to note that the proposed framework is quantum-inspired, where Hadamard and CNOT operations are employed as analytical tools to model structured correlations.

The principal contributions of this work can be summarised as follows.

- **A Q-MDC framework for resilient image delivery** that supports multi-description transmission over time-varying and unreliable channels without relying on retransmission.
- **A CNOT-driven correlation mechanism between descriptions** that facilitates deterministic recovery of unavailable information without requiring iterative decoding procedures.
- **A Hadamard-based superposition encoding scheme** designed to increase tolerance to channel impairments and provide a gradual reduction in reconstruction quality as channel conditions deteriorate.
- **A combined packet and bit-level recovery approach** that exploits complementary reconstruction mechanisms to improve image recovery, particularly under moderate and low SNR conditions.
- **A parallel multi-channel transmission architecture** in which independent channel noise realisations provide diversity that can be exploited during the recovery process.
- **A lightweight reliability mechanism as an alternative to conventional error correction** that obtains robustness through structured inter-description redundancy rather than computationally intensive channel-coding schemes.

7.6.1 System Model

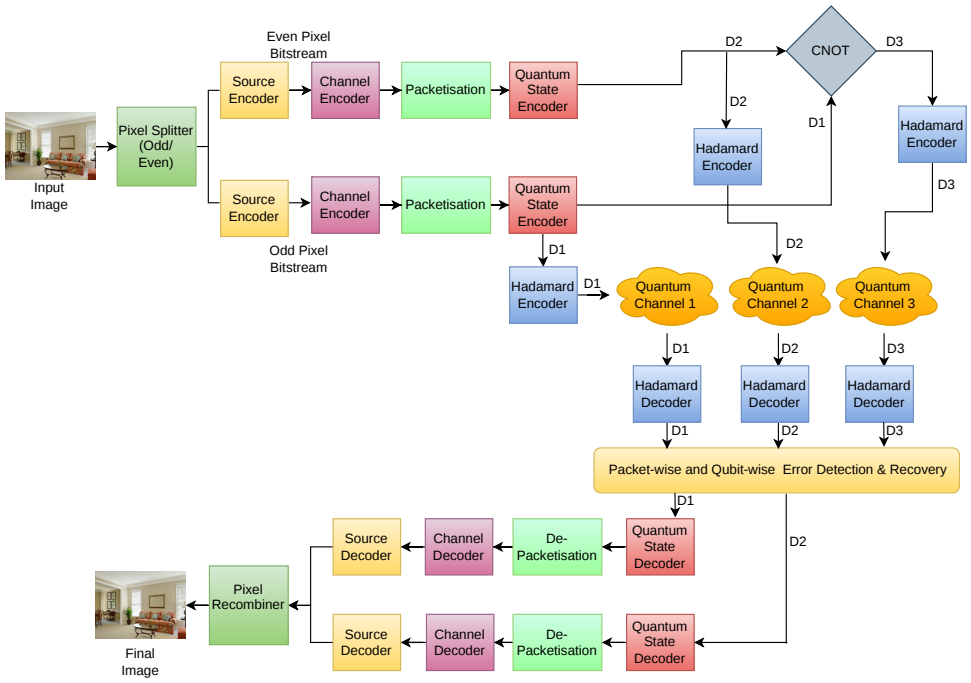


Figure 7.34: System architecture of the proposed Q-MDC framework for image transmission.

As shown in Figure 7.34, the proposed Q-MDC framework takes the input images as the starting point of the transmission process. The selected images represent a broad range of visual properties, covering differences in texture, edge density, contrast, and structural complexity. To facilitate MDC, each input image is spatially divided into two pixel sets. The pixels with odd indices are allocated to Description 1 (D1), whereas those with even indices constitute Description 2 (D2). The two pixel sets are subsequently encoded independently using source coding methods, including JPEG, HEIF, JPEG2000, or uncompressed representation, producing separate binary bitstreams. Depending on the transmission configuration, channel coding may then be applied before the resulting data are represented as quantum states in the computational basis.

Description 3 (D3) is constructed from the quantum representations of D1 and D2 through a CNOT operation. This operation introduces a deterministic relationship between the descriptions and provides additional redundancy without requiring extra transmission bandwidth. Following this process, a Hadamard transformation is applied

to the qubits associated with all three descriptions, converting them into superposition states for transmission through independent noisy channels.

At the receiving side, the received quantum states are first subjected to an inverse Hadamard transformation to recover their computational-basis representations. The resulting descriptions are then examined using a combined packet-wise and qubit-wise error detection and deterministic recovery procedure that exploits the relationships established between D1, D2, and D3. When one of the descriptions is affected by errors while the other two remain valid, the missing information can be deterministically recovered using the corresponding packet-level and qubit-level relationships. After the recovery stage, quantum measurements are performed to obtain the corresponding classical bitstreams, which are subsequently processed through channel and source decoding to obtain the reconstructed image.

The following subsection provides a detailed description of the individual components of the proposed Q-MDC system.

Input Image

The performance of the proposed framework is investigated using an image collection covering different resolutions and visual characteristics. The evaluation comprises 80 images selected from the Microsoft COCO dataset [197], with the images resized to 256×192 and 640×480, along with 40 native 4K images obtained from a Kaggle dataset [219]. The selected datasets contain diverse scene content and variations in texture, edges, and structural information, allowing the proposed approach to be examined across images with different levels of visual complexity. As the proposed framework is independent of image resolution, images with arbitrary dimensions and diverse visual content can be processed without modifying the underlying transmission architecture.

Pixel Splitter, Source Encoder, and Channel Encoder

The spatial decomposition of the input image separates the pixels into two descriptions, with the odd-indexed pixels assigned to D_1 and the even-indexed pixels assigned to D_2. This arrangement allows both descriptions to retain representative spatial and

structural information from the original image. Each description is subsequently encoded independently using JPEG, JPEG2000, HEIF, or an uncompressed representation, resulting in a corresponding binary bitstream. Consistent with the channel-coding configuration adopted in previous sections of this chapter, rate-1/2 polar codes [210] are used for channel encoding. This coding rate introduces redundancy while preserving spectral efficiency and is required to maintain equal bandwidth among the transmitted descriptions. An uncoded configuration is additionally included for benchmarking purposes. Following channel encoding, the resulting bitstreams are divided into fixed-length packets to support packet-level transmission and recovery. Packet lengths of 100, 500, and 1000 bits are considered to investigate the relationship between recovery performance and computational overhead.

Quantum State Encoding and CNOT-Based Correlated Description

Once packetisation has been completed, the bitstreams associated with D_1 and D_2 are separately represented as quantum states using computational-basis encoding. Under this representation, each classical bit is mapped to a corresponding qubit, such that the logical values 0 and 1 are represented by the basis states $|0\rangle$ and $|1\rangle$, respectively, with matrix forms as defined in (7.1)–(7.2) of Section 7.1.

The correlated description D_3 is subsequently obtained through a CNOT operation applied between D_1 and D_2. In this operation, the qubits belonging to D_1 serve as control qubits, whereas those associated with D_2 serve as target qubits. When the control qubit is in the state $|0\rangle$, the target state remains unchanged; when the control qubit is in the state $|1\rangle$, the target state is inverted, as defined in (7.38) and (7.39).

$$|0\rangle |x\rangle \rightarrow |0\rangle |x\rangle \tag{7.38}$$

$$|1\rangle |x\rangle \rightarrow |1\rangle |x \oplus 1\rangle \tag{7.39}$$

Consequently, D_3 represents a deterministic relationship between the two original descriptions and introduces structured redundancy that can subsequently be exploited

during the recovery process.

$$D_2(i) = D_1(i) \oplus D_3(i) \tag{7.40}$$

Hadamard Encoder

Once the three descriptions have been established in the computational basis, a Hadamard transformation is applied independently to each qubit to produce the corresponding superposition states. The transformation follows the procedure described in Section 3.1, Equations (3.1)–(3.5). Through this operation, the basis representation of each qubit is transformed into a superposition of computational-basis states, providing increased resilience to impairments introduced during channel transmission.

Quantum Channel

The three quantum descriptions, D1, D2, and D3, are conveyed through separate quantum channels that are assumed to be statistically independent within the proposed Q-MDC framework. Each transmission path incorporates a composite set of quantum noise processes, namely bit-flip, phase-flip, depolarising, amplitude damping, and phase damping [127]. The corresponding noise processes are represented through Kraus operators, resulting in a completely positive trace-preserving (CPTP) channel representation. This provides the physical framework for modelling quantum-state evolution in the presence of noise, as discussed in Section 3.1. Rather than restricting the analysis to an ideal quantum channel, the use of several CPTP noise processes enables the proposed framework to account for different forms of decoherence and channel degradation. Consequently, the transmission performance of the Q-MDC system can be examined across a broader range of noisy operating conditions. The use of independent composite noise processes for the three descriptions also introduces channel diversity into the transmission system. If one description undergoes substantial degradation, the information available from the other descriptions can still be exploited by the deterministic reconstruction mechanism to recover the affected data. It should also be noted that the reported results assume idealised quantum operations. Therefore, the findings represent system-level performance insights rather than a direct demonstration

of a practical quantum hardware implementation, which is appropriate for the early-stage communication research considered in this work. For the proposed Q-MDC configuration, D1, D2, and D3 are transmitted through independent quantum channels having different SNR conditions. This setup represents a heterogeneous channel environment in which the three descriptions are exposed to different degrees of degradation. The SNR associated with D1 varies from 30 dB to -5 dB, while D2 covers the range from 25 dB to -10 dB and D3 operates between 35 dB and 0 dB. Each range is evaluated at 1 dB intervals, allowing the behaviour of the system to be examined progressively from favourable channel conditions to severe degradation.

Because the transmission paths are independent, the noise processes affecting the individual descriptions are statistically uncorrelated. This independence is important for the proposed packet-wise and qubit-wise deterministic recovery mechanism, since it improves the probability that one or more descriptions remain sufficiently reliable to support recovery when another description experiences substantial corruption.

For comparison across the different transmission paths, an overall SNR measure is obtained by combining the contributions of the three channels. The signal powers associated with the independent descriptions are combined according to (7.41).

$$\mathrm{SNR}_{\mathrm{combined}} = 10 \log_{10} \left(\frac{1}{3} \sum_{i=1}^{3} 10^{\mathrm{SNR}_i/10} \right) \tag{7.41}$$

Here, SNR_i represents the SNR in dB corresponding to the i-th transmission channel. The expression therefore calculates the mean channel SNR after converting the individual values into the linear power domain. This provides a common SNR measure for comparison with single-channel transmission systems under the assumption that the descriptions have equal bandwidth and contribute equally to the overall transmission.

Hadamard Decoder

At the receiving end, the Hadamard operation is performed on the transmitted states to transform the superposition representations into the computational basis. Because the Hadamard operator is both unitary and self-inverse ($H^{-1} = H$), the resulting state $|\psi'\rangle$ can be expressed as $|\psi'\rangle = H\,|\psi\rangle$, where $|\psi\rangle$ represents the received quantum state.

Packet-Wise Error Detection and Deterministic Recovery

Following Hadamard decoding, the computational-basis states associated with D1, D2, and D3 can be affected by errors introduced independently across the transmission channels. A combined packet-wise and qubit-wise detection and deterministic recovery procedure is therefore applied using the predefined relationships among the three descriptions.

At the packet level, each received packet is examined to determine whether its states conform to the expected representation. A packet is identified as erroneous when at least one of its states is affected by an error. The corresponding error indicators for D1, D2, and D3 are represented by e_1, e_2, and e_3, respectively, as defined in (7.42).

$$e_k = \begin{cases} 1, & \text{if packet contains errors} \\ 0, & \text{otherwise} \end{cases}, \quad k \in \{1, 2, 3\} \tag{7.42}$$

The deterministic relationships established among the descriptions are subsequently used to perform recovery. Since D1 and D2 represent the original information-bearing descriptions, the recovery procedure reconstructs an affected primary description by exploiting D3. When one description is corrupted and the remaining two descriptions are available, the corresponding description can be obtained using the relationships given in (7.43).

$$D1 = D2 \oplus D3, \quad D2 = D1 \oplus D3 \tag{7.43}$$

When both D1 and D2 are identified as corrupted at the packet level, complete packet recovery cannot be guaranteed. Nevertheless, individual qubit positions can still be examined independently. If two corresponding qubits are correctly received, the missing qubit can be determined from the remaining two according to (7.44).

$$D2(i) = D1(i) \oplus D3(i) \tag{7.44}$$

The same principle can be applied to reconstruct D1 from D2 and D3 using the relationship in (7.44). Consequently, information within an otherwise corrupted packet can be recovered at individual qubit positions. Because D3 serves as an auxiliary

description providing redundancy, it does not need to be reconstructed for the final image generation.

The proposed recovery process therefore combines packet-level error identification through (7.42) with qubit-level reconstruction based on (7.43) and (7.44). This multi-level recovery mechanism makes use of the available redundancy between descriptions. In addition, the statistical independence of the transmission channels increases the likelihood that two descriptions remain sufficiently reliable at a particular bit position, allowing the corresponding information to be reconstructed.

Quantum State Decoding, Source Decoding, and Image Reconstruction

Following the recovery stage, the quantum states are measured in the computational basis to obtain the corresponding classical bits. The projective measurement operators $M_0 = |0\rangle\langle 0|$ and $M_1 = |1\rangle\langle 1|$, defined in Section 7.1, are used for this purpose. The recovered packets belonging to D_1 and D_2 are subsequently combined to form continuous bitstreams. Where channel coding is employed, polar decoding is performed to eliminate the introduced redundancy and mitigate remaining transmission errors. The resulting bitstreams are then processed using the corresponding source decoder, namely JPEG, JPEG2000, HEIF, or the uncompressed representation. Finally, the reconstructed image is obtained by interleaving the odd- and even-indexed pixel components associated with the two primary descriptions.

Benchmark Systems and Simulation Setup

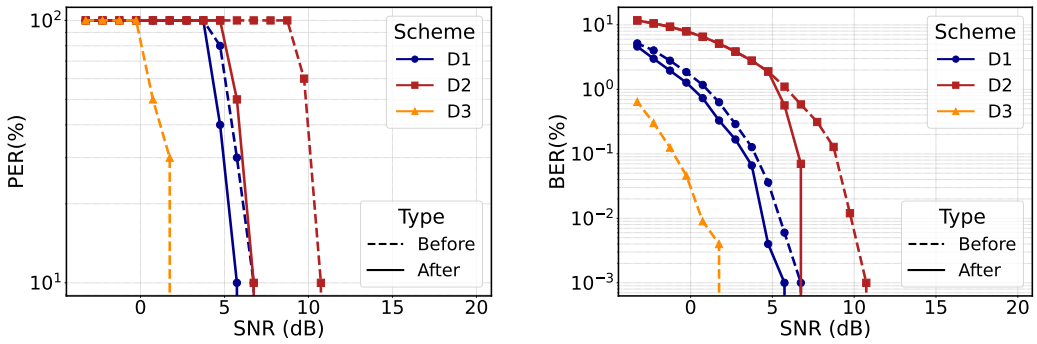
The proposed framework is assessed against three reference configurations: quantum single-stream (Q-Single), classical single-stream (C-Single), and classical MDC (C-MDC). All systems are evaluated under equivalent transmission conditions and bandwidth constraints. In the Q-Single configuration, the bitstreams corresponding to $\{D_1, D_2, D_3\}$ are combined and transmitted through a single channel while retaining the quantum processing operations of the proposed system. The C-Single configuration employs BPSK transmission over an AWGN channel. When channel coding is enabled, a rate-$2/3$ polar code is adopted to ensure that the overall bandwidth corresponds to that of the Q-MDC configuration. For C-MDC, the same general MDC structure is retained, but

the third description is produced using a bitwise XOR operation ($D_3 = D_1 \oplus D_2$) rather than a CNOT operation. The packet-wise and qubit-wise recovery procedures are then implemented in the classical domain. The evaluation considers 80 images from the Microsoft COCO dataset [197], resized to 256×192 and 640×480, together with 40 4K images from a Kaggle dataset [219]. The reported performance values are obtained by averaging the results across the considered packet sizes, image samples, and 1000 independent trials.

7.6.2 Results

This section evaluates the proposed Q-MDC framework under different channel conditions using BER, PER, PSNR, SSIM, and UQI as functions of the combined SNR. Both uncoded and channel-coded configurations are considered.

Packet Error Rate (PER) and Bit Error Rate (BER) Analysis



(a) PER (b) BER

Figure 7.35: PER and BER comparison for the Q-MDC system before and after applying the proposed recovery mechanism.

Figure 7.35a shows different PER characteristics for D1, D2, and D3 due to their different channel conditions. D3 achieves the lowest PER over most of the SNR range, followed by D1, while D2 degrades more rapidly at lower SNR. Packet recovery provides a clear improvement for D2 by using D1 and D3 to reconstruct corrupted packets. The improvement for D1 is smaller because its recovery requires both D2 and D3 to be correctly received. At very low SNR, the PER of all descriptions approaches

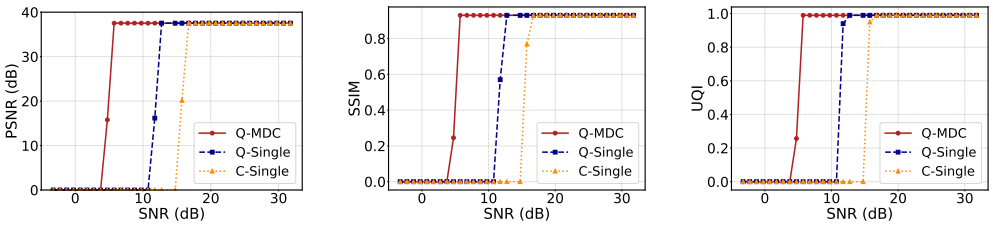
100% because of severe channel noise. These results demonstrate the benefit of inter-description redundancy for packet recovery. Figure 7.35b presents the BER results. D2 is the most sensitive to channel degradation, whereas D1 and D3 show greater resilience. The recovery mechanism reduces the BER of D2 by exploiting information from the other descriptions. Improvement for D1 is more limited because its reconstruction depends on D2 and D3. Since D3 provides redundancy, it is not required for final image reconstruction.

Comparative Analysis of Reconstructed Image Quality under Uncoded Q-MDC and Single-Stream Transmission

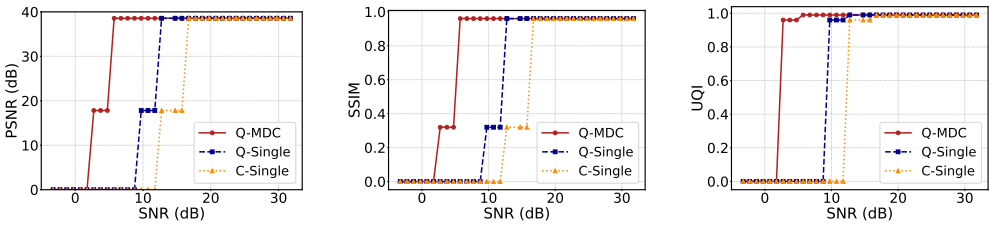
The uncoded systems are evaluated using PSNR, SSIM, and UQI for JPEG, JPEG2000, and HEIF. Figure 7.36 shows that the schemes perform similarly at high SNR, while the advantage of Q-MDC becomes clearer as SNR decreases. Q-MDC maintains the highest reconstruction quality down to approximately 5 dB, compared with approximately 12 dB for Q-Single and 16 dB for C-Single. At lower SNR, Q-MDC can still preserve partial image information and important structural features, whereas single-stream systems experience greater degradation from bitstream corruption. This improvement results from distributing the source information across correlated descriptions under equal bandwidth constraints. The additional description provides redundancy that enables corrupted information to be recovered and produces a more gradual reduction in image quality.

Similar trends are obtained for JPEG, JPEG2000, and HEIF, indicating that the Q-MDC advantage is not strongly dependent on the source encoder. Since no channel coding is used, the observed differences arise from the transmission and recovery mechanisms. When all three descriptions are received, Q-MDC provides complete reconstruction with high PSNR, SSIM, and UQI. With only one description, complete recovery is not possible, but partial reconstruction and basic structural information can still be retained.

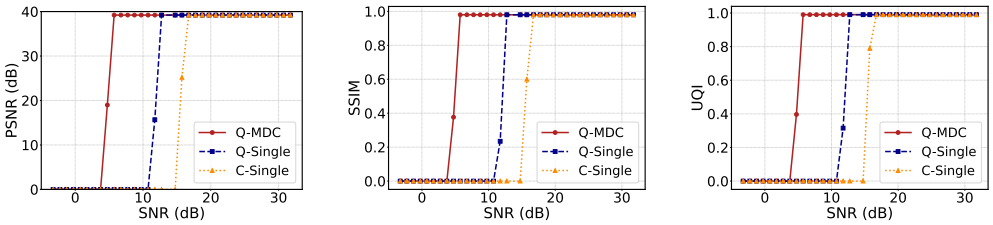
Figure 7.37 presents the results for uncompressed image transmission. At high SNR, all schemes approach near-perfect reconstruction, while the differences become more evident as SNR decreases.



(a) JPEG-PSNR (b) JPEG-SSIM (c) JPEG-UQI

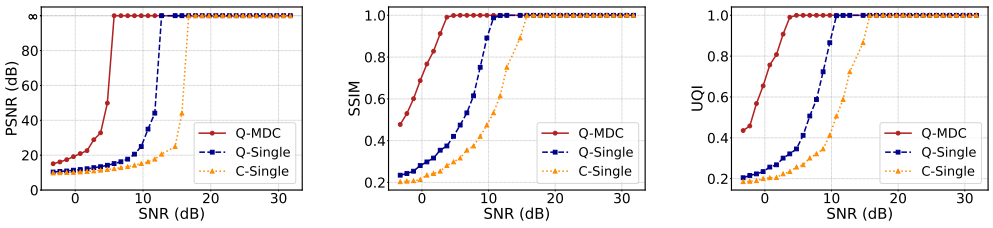


(d) JPEG2000-PSNR (e) JPEG2000-SSIM (f) JPEG2000-UQI



(g) HEIF-PSNR (h) HEIF-SSIM (i) HEIF-UQI

Figure 7.36: PSNR, SSIM, and UQI comparison for JPEG, JPEG2000, and HEIF images transmitted using uncoded Q-MDC and single-stream configurations over different SNR conditions.

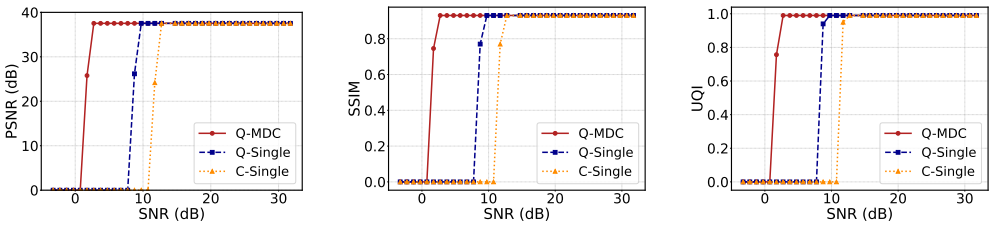


(a) PSNR (b) SSIM (c) UQI

Figure 7.37: PSNR, SSIM, and UQI comparison for uncompressed images transmitted using uncoded Q-MDC and single-stream configurations under different SNR conditions.

Q-MDC maintains better reconstruction quality under noisy conditions, demonstrating that its robustness is not restricted to a particular source encoding method. Since these experiments are uncoded, the improvement is attributed to quantum encoding, inter-description redundancy, and deterministic recovery, supporting Q-MDC as a robust and low-complexity transmission approach.

Comparative Analysis of Reconstructed Image Quality under Channel-Coded Q-MDC and Single-Stream Transmission



(a) JPEG-PSNR (b) JPEG-SSIM (c) JPEG-UQI

Figure 7.38: PSNR, SSIM, and UQI comparison for JPEG images transmitted using channel-coded Q-MDC and single-stream configurations under different SNR conditions.

Figure 7.38 shows the reconstruction performance when channel coding is introduced into the transmission process. The additional coding stage reduces the number of bit errors reaching the image reconstruction stage and consequently allows the PSNR, SSIM, and UQI performance to remain stable at lower SNR values. The improvement is especially important for single-stream transmission, where accumulated bit errors can otherwise lead to severe reconstruction degradation.

Q-MDC benefits from channel coding in a complementary manner. The framework already provides redundancy through D1, D2, and D3, together with packet-level and qubit-level recovery. Channel coding provides an additional layer of protection by addressing residual bit errors before the reconstruction stage. The combination therefore extends the range of channel conditions over which reliable image reconstruction can be achieved. The proposed structure does not depend exclusively on channel coding for its recovery capability. D1 and D2 contain the primary image information, while D3 provides additional redundancy through $D3 = D1 \oplus D2$. When the required descriptions are available, the complete image can be reconstructed with high PSNR, SSIM, and

UQI. If only one description survives the transmission process, complete recovery is not possible because the correlation information required for reconstruction is unavailable. However, the surviving description can still provide partial image information and preserve coarse structural characteristics.

Therefore, the channel-coded results demonstrate the complementary roles of conventional channel coding and the proposed Q-MDC mechanism. Channel coding reduces bit-level errors, whereas the multi-description structure provides additional information for packet and qubit-level recovery. Their combination improves the reliability of image transmission over a wider range of SNR conditions.

Performance Advantages and Quantum-Domain Insights

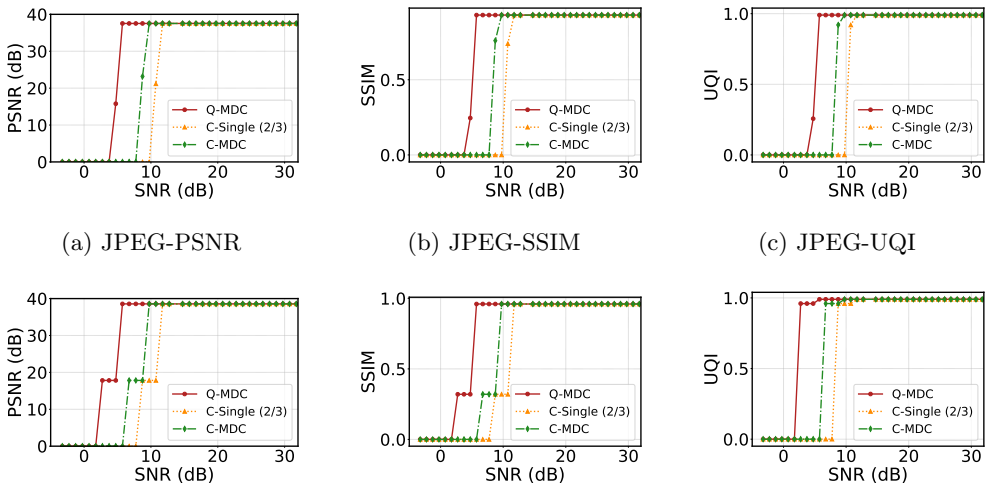
The proposed Q-MDC framework improves transmission reliability by combining correlated descriptions, independent channels, and deterministic recovery under equal bandwidth constraints. The distributed image representation enables partial recovery when some descriptions are corrupted, resulting in more gradual quality degradation.

D3 provides additional redundancy, particularly at low SNR where primary descriptions are more likely to be affected. The Hadamard transformation introduces superposition-based representation, while the CNOT operation establishes deterministic relationships that support direct recovery.

The independent channels further provide transmission diversity, allowing reliable information from different descriptions to contribute to reconstruction. Overall, the combination of quantum encoding, inter-description redundancy, and deterministic recovery improves robustness against channel errors while maintaining low computational complexity.

Comparison of Q-MDC with Classical MDC and Channel-Coded Single-Stream Transmission

The proposed uncoded Q-MDC configuration is further compared with two reference approaches: classical MDC and channel-coded single-stream transmission. All three systems are evaluated under the same transmission conditions and equal bandwidth constraints. Since Q-MDC transmits three descriptions ($D1$, $D2$, and $D3$), its total



(a) JPEG-PSNR (b) JPEG-SSIM (c) JPEG-UQI

(d) JPEG2000-PSNR (e) JPEG2000-SSIM (f) JPEG2000-UQI

Figure 7.39: Comparison of reconstructed PSNR, SSIM, and UQI for JPEG and JPEG2000 images using Q-MDC, classical MDC, and channel-coded single-stream transmission under equal bandwidth constraints and varying SNR conditions.

bandwidth usage is three times that of an individual description. To establish a fair comparison, the classical single-stream $(D1, D2)$ configuration employs a rate-2/3 polar code, whereas the classical MDC configuration consists of two primary descriptions and a third redundant description obtained through a bitwise XOR operation $(D3 = D1 \oplus D2)$. Packet-wise and bit-wise recovery procedures equivalent to those used in the Q-MDC system are also implemented for the classical configuration.

Figure 7.39 shows the resulting PSNR, SSIM, and UQI performance. Across the investigated SNR range, Q-MDC provides higher reconstruction quality than both classical MDC (C-MDC) and channel-coded single-stream transmission (C-Single (2/3)). The Q-MDC system maintains high-quality reconstruction at SNR values of approximately 5 dB, whereas classical MDC reaches comparable performance at approximately 9 dB and the single-stream configuration requires still higher SNR values. This represents an effective SNR improvement of approximately 4 dB. The same general behaviour is obtained for the different source encoding formats considered, indicating that the improvement is not tied to a specific source encoder.

Although the classical single-stream configuration incorporates channel coding, residual errors can still propagate through the reconstructed bitstream because of

the probabilistic nature of its decoding process. Classical MDC provides additional robustness by distributing the information among several descriptions, but its XOR-based redundancy offers more limited recovery capability when the channel becomes severely degraded. The structured correlation used by Q-MDC provides a more direct mechanism for reconstructing unavailable information.

The resulting improvement is therefore associated with the combined use of quantum-domain transformations and multi-description transmission. The CNOT operation establishes deterministic correlations that support direct recovery, while the Hadamard transformation represents the information in superposition states and contributes to improved tolerance against channel noise. Consequently, at low SNR values, Q-MDC can retain partial image quality while the classical alternatives experience substantially faster degradation caused by bitstream errors.

Although the redundant description in the proposed framework is produced through a CNOT operation, its resulting relationship is not equivalent to a conventional bit-level redundancy mechanism because the descriptions undergo transform-domain processing before transmission. In classical MDC, redundancy is generated directly from binary information, leaving the transmitted data in a discrete bit representation. Channel errors can therefore directly alter individual bits and propagate through subsequent reconstruction operations, potentially producing abrupt quality degradation.

In Q-MDC, each encoded description undergoes a Hadamard transformation before being transmitted. This operation acts as a structured orthogonal transformation that distributes the encoded information among different components. Consequently, the influence of a local channel disturbance is distributed within the transformed representation rather than being restricted to a single original bit. This behaviour contributes to more gradual degradation and greater tolerance to localised or burst-like errors.

The resulting performance improvement is therefore produced by the combined influence of transform-domain spreading and structured inter-description correlation. The Hadamard operation distributes the encoded information across multiple components, while the CNOT-based relationship establishes deterministic and position-aligned dependencies between the descriptions. These characteristics allow corrupted informa-

tion to be recovered efficiently. Unlike classical MDC, where redundancy is primarily established through direct bit-level relationships, Q-MDC combines transform-domain diversity with structured redundancy to improve resilience against channel degradation.

Evaluation of Quantum Correlation Strategies for Multi-Description Generation

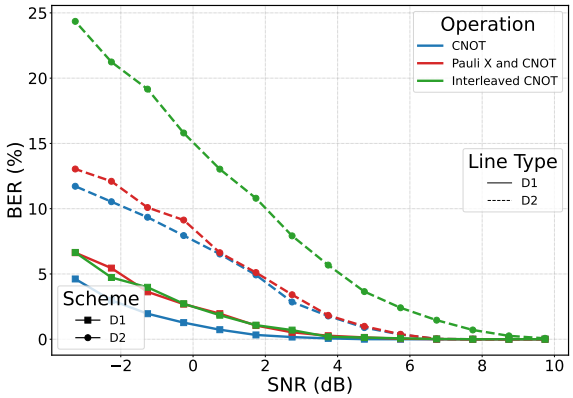


Figure 7.40: BER comparison of alternative correlated-description generation approaches, namely CNOT, Pauli-X with CNOT, and interleaved CNOT, for D1 and D2 over different SNR levels.

Figure 7.40 compares three quantum-based approaches for constructing correlated descriptions: standard CNOT, Pauli-X combined with CNOT, and interleaved CNOT. Under the standard CNOT configuration, the relationship $D3 = D1 \oplus D2$ is maintained, providing a direct correlation between the descriptions and supporting deterministic recovery. In the Pauli-X + CNOT configuration, the second description is first modified according to $D2' = \overline{D2}$, which changes the resulting correlation structure. The interleaved CNOT approach introduces an index mismatch through $D3(i) = D1(i) \oplus D2(\pi(i))$, where $\pi(i)$ represents a permutation function that changes the ordering of the indices of $D2$. The results indicate that standard CNOT produces the lowest BER throughout the investigated SNR range. The Pauli-X + CNOT configuration results in a moderate increase in BER, whereas the interleaved CNOT configuration produces the highest BER. These observations demonstrate that direct, structured, and position-preserving relationships between descriptions are important for achieving reliable transmission and deterministic recovery.

Computational Complexity

The computational cost of the proposed Q-MDC framework is considered for single-qubit encoding ($k = 1$), in which every classical bit is represented by one qubit. Let b represent the total number of bits contained in the input bitstream. Under this configuration, the number of transmitted qubits is therefore $q = b$. At the transmitter, the generation of the bitstream, qubit preparation, Hadamard transformation, and CNOT-based correlation are performed on a per-qubit basis. These operations collectively require $\mathcal{O}(b)$ computational complexity. At the receiving side, inverse Hadamard operations, quantum measurement, error identification, and deterministic CNOT-based recovery are likewise performed for individual qubits, resulting in $\mathcal{O}(b)$ complexity. Thus, the complete Q-MDC processing chain maintains an overall linear complexity of $\mathcal{O}(b)$. Alternative correlation approaches, including Pauli-X with CNOT and interleaving, introduce additional processing operations, but their asymptotic complexity remains unchanged.

Basic operations in classical transmission systems can also be implemented with $\mathcal{O}(b)$ complexity. However, more advanced error-correction techniques, such as polar codes, require successive cancellation or iterative decoding procedures and can therefore involve higher computational costs, such as $\mathcal{O}(b \log b)$. The proposed Q-MDC framework consequently combines improved transmission reliability with linear computational complexity, supporting its suitability for applications requiring efficient processing.

7.6.3 Section Summary

Moving beyond the physical-layer techniques presented in the preceding sections, this section demonstrated that integrating the proposed quantum communication framework with the source-layer technique of MDC significantly improves transmission robustness. By introducing deterministic inter-description redundancy through a CNOT-based correlation mechanism, the proposed Q-MDC framework achieved lower BER and higher reconstruction quality than both classical MDC and channel-coded single-stream transmission while maintaining low computational complexity. Specifically, the proposed framework provided channel SNR gains of up to 4 dB over classical MDC and up to 7 dB over channel-coded single-stream transmission under equivalent bandwidth

constraints. These results confirm that source-layer redundancy can effectively complement physical-layer robustness, thereby providing enhanced reliability for image transmission over noisy communication channels. The following section investigates semantic communication, shifting the focus from bit-level protection to content-layer robustness by prioritising the transmission of semantically important information for high-quality image reconstruction.

7.7 Quantum Communication for Semantic Communication-Based Image Transmission

Publication Notice

The research presented in this section has been published in the following peer-reviewed journal publication:

U. Jayasinghe, P. Samarathunga, N. Pollwaththage, T. Fernando, and A. Fernando, "Quantum communication for semantic communication based image transmission," *IEEE Transactions on Vehicular Technology*, early access, 2026, doi: 10.1109/TVT.2026.3663843.

This material is reproduced and adapted under the terms of the IEEE Copyright policy for use in a doctoral thesis. The content has been revised and extended with additional explanations and expanded discussion.

Problem Statement: The preceding sections demonstrated the integration of the proposed quantum communication framework across multiple layers of modern multimedia communication systems. At the physical layer, MIMO, QOFDM, and MIMO-QOFDM were employed to improve transmission robustness through spatial diversity, multicarrier processing, and their combined operation. At the source layer, Section 7.6 showed that embedding structured redundancy directly into the transmitted descriptions using Q-MDC effectively mitigates packet losses and transmission errors. Together, these approaches enhance communication reliability by protecting the transmitted bitstream without questioning whether every transmitted bit is equally important to the receiving application. This final section shifts the focus to the content layer by integrating the proposed quantum communication framework with semantic communication, where the objective is to preserve and transmit semantically meaningful information rather than the complete image bitstream. Conventional image communication systems are designed to transmit complete image bitstreams while preserving pixel-level accuracy. However, many modern intelligent applications, including autonomous vehicles, smart surveillance, remote sensing, and real-time decision-making systems, do not necessarily require exact pixel reconstruction. Instead, these systems primarily rely on the preserva-

tion of semantic information such as objects, structures, and contextual content within the image. Transmitting the entire image bitstream therefore introduces significant transmission overhead, particularly under bandwidth-constrained and noisy wireless environments. Semantic communication has emerged as a promising solution to this problem by transmitting compact semantic representations instead of complete raw image data. By focusing on semantically important features, semantic communication can significantly reduce bandwidth requirements while still preserving information necessary for machine interpretation and intelligent decision-making. However, reliable transmission of semantic representations remains a major challenge in practical wireless environments. Channel noise, fading, interference, and transmission errors can distort the transmitted semantic latent representations, leading to loss of contextual information and degradation in reconstructed image quality. Therefore, developing robust semantic communication frameworks capable of preserving semantic information under adverse channel conditions remains an important research challenge.

Limitations of Existing Work: Existing semantic communication frameworks are primarily developed using conventional classical communication architectures. Although these methods reduce transmission overhead through semantic feature compression, their performance remains highly sensitive to channel impairments such as noise, fading, and interference. Most existing approaches focus mainly on deep learning-based semantic encoding and decoding while relying on conventional transmission mechanisms that provide limited robustness in highly noisy communication environments. At the same time, existing quantum communication research has largely focused on conventional image or bitstream transmission rather than semantic latent representation transmission. Furthermore, many existing studies do not integrate semantic feature extraction, channel coding, and quantum-domain transmission within a unified end-to-end framework. Consequently, there remains a lack of robust communication frameworks that jointly combine semantic communication, channel coding, and quantum-inspired transmission techniques for reliable semantic image transmission over noisy communication channels.

Motivation and Proposed Contribution: Motivated by these limitations, this work proposes a quantum semantic communication framework for robust image transmission

under noisy communication conditions. The main objective of the proposed framework is to improve transmission robustness while preserving semantically important image information using compact latent representations instead of complete image bitstreams. Within the proposed framework, semantic features are first extracted from input images and represented as compact latent vectors. These latent vectors are then converted into classical bitstreams and protected using polar channel coding to improve robustness against transmission errors. The encoded bitstreams are subsequently mapped into quantum-inspired superposition states using Hadamard-based quantum encoding and transmitted through noisy quantum communication channels. At the receiver, inverse quantum operations and polar channel decoding are performed to recover the transmitted latent representations. Finally, semantic decoders reconstruct the transmitted images while preserving important structural and contextual information. Unlike conventional semantic communication systems that rely entirely on classical transmission mechanisms, the proposed framework integrates semantic feature extraction, polar channel coding, and quantum communication within a unified end-to-end transmission model. The framework is evaluated using objective image quality metrics including PSNR, SSIM, and UQI, together with CNN-based image classification analysis to assess semantic preservation and machine interpretability. By combining semantic communication with quantum transmission techniques, the proposed system aims to improve transmission reliability, semantic preservation capability, and reconstructed image quality under noisy and bandwidth-constrained communication environments.

7.7.1 System Model

In this study, an end-to-end quantum communication system is proposed for image transmission based on semantic communication, as shown in Figure 7.41. The process begins with the selection of images, which are then semantically encoded. The resulting feature vector information is subsequently converted into a bitstream and channel encoded using polar codes. After channel encoding, the bitstream is converted into qubit superposition states using a quantum encoder. This step is crucial because it takes advantage of the quantum superposition to enhance error resilience and enable high-quality image transmission. The qubit superposition states are then transmitted

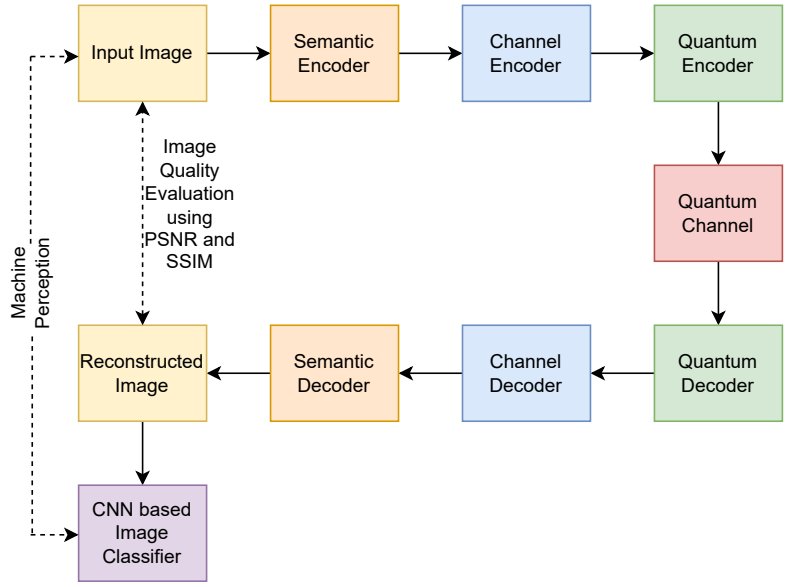


Figure 7.41: Proposed end-to-end quantum communication system for semantic communication based image transmission.

over a quantum channel, where they may encounter noise. In the receiver, the process begins with the application of measurement operators in the quantum decoder. These operators extract the classical information from the received qubit superposition states, converting them back into classical bits. The classical bitstream is then subjected to channel decoding using the polar decoder, which corrects any errors that may have occurred during transmission. Finally, the reconstructed classical information relevant to the latent vector is processed through a semantic decoder. This decoder interprets the semantic data and reconstructs the final image, prioritising its meaningful content.

A detailed description of each block in the proposed method is provided below.

Information Source

To evaluate the proposed framework, two widely used benchmark image datasets, CIFAR-10 [221] and MNIST [220], are employed. CIFAR-10 consists of 60,000 colour images of size $32 \times 32 \times 3$, equally distributed across 10 object classes, with 50,000 images allocated for training and 10,000 for testing. MNIST contains 70,000 greyscale handwritten digit images of size $28 \times 28 \times 1$, comprising 60,000 training samples and

10,000 testing samples. Although the proposed framework is compatible with any image dataset, CIFAR-10 and MNIST are selected because they provide a suitable balance between computational complexity and data diversity, making them well suited for training and evaluating the semantic encoder.

Semantic Encoder and Decoder

Before designing the semantic encoder and decoder, a mathematical framework is established to define the transformation of an input image into a latent representation and its reconstruction. The encoding process is described in (7.45).

$$h = f(W_{\text{enc}} \cdot X + b_{\text{enc}}) \tag{7.45}$$

In this framework, the input image is denoted as $X \in \mathbb{R}^{m \times n \times c}$, where m and n represent the image's height and width, and c is the number of colour channels. The encoder operates with a weight matrix $W_{\text{enc}} \in \mathbb{R}^{p \times mnc}$, where p is the reduced dimension relative to the input size mnc. Additionally, a bias vector $b_{\text{enc}} \in \mathbb{R}^{p \times 1}$ is used. The output of the encoder is a latent representation vector $h \in \mathbb{R}^{p \times 1}$, which captures the essential features of the input image. The activation function $f(\cdot)$ is applied to introduce non-linearity into the encoding process. This formulation guides the semantic encoder in generating a compact yet information-preserving image representation.

The decoding process, which reconstructs the image from its latent representation, is mathematically represented in (7.46).

$$\hat{X} = f(W_{\text{dec}} \cdot h + b_{\text{dec}}) \tag{7.46}$$

Here, $\hat{X}$ is the semantically reconstructed version of the original image X. The decoding process is carried out by applying the decoder's weight matrix W_{dec} and bias matrix b_{dec} to the latent representation h, followed by an activation function.

The relationship between the original image X and the semantically decoded image $\hat{X}$ can be further described by (7.47), where n_{sem} represents the semantic noise introduced during the encoding-decoding process. Due to semantic noise, the decoded image quality is lower than that of the original image even in the absence of channel noise.

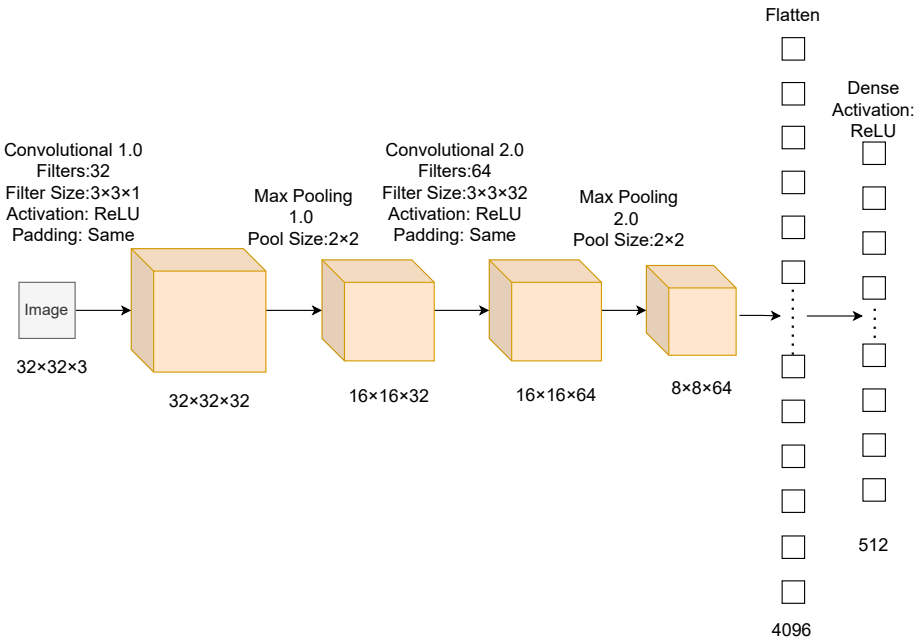


Figure 7.42: Proposed semantic encoder.

$$\hat{X} = X + n_{\text{sem}} \tag{7.47}$$

The proposed architecture of the semantic encoder, as depicted in Figure 7.42, is implemented within an autoencoder framework. The initial layer consists of a convolutional layer with 32 filters, each having a kernel size of 3×3, which processes a single input channel. The sequence of convolutional layers, max-pooling layers, activation functions, and dense layers have been carefully designed to optimise performance while minimising resource consumption. To preserve the spatial dimensions of the input, padding is set to "same" and a stride of 1 is used during the convolution operation.

Following the first convolutional layer, a max-pooling layer with a pool size of 2×2 is applied, effectively reducing the spatial dimensions of the feature maps by half in both height and width. This marks the initial stage of the convolutional process. In the subsequent convolutional layer, 64 filters, each with dimensions of 3×3, are utilised, processing inputs with 32 channels. The increased number of filters enhances the model's ability to extract higher-level features from the input data. As the network progresses deeper, the features learned become increasingly complex, enabling the detection of

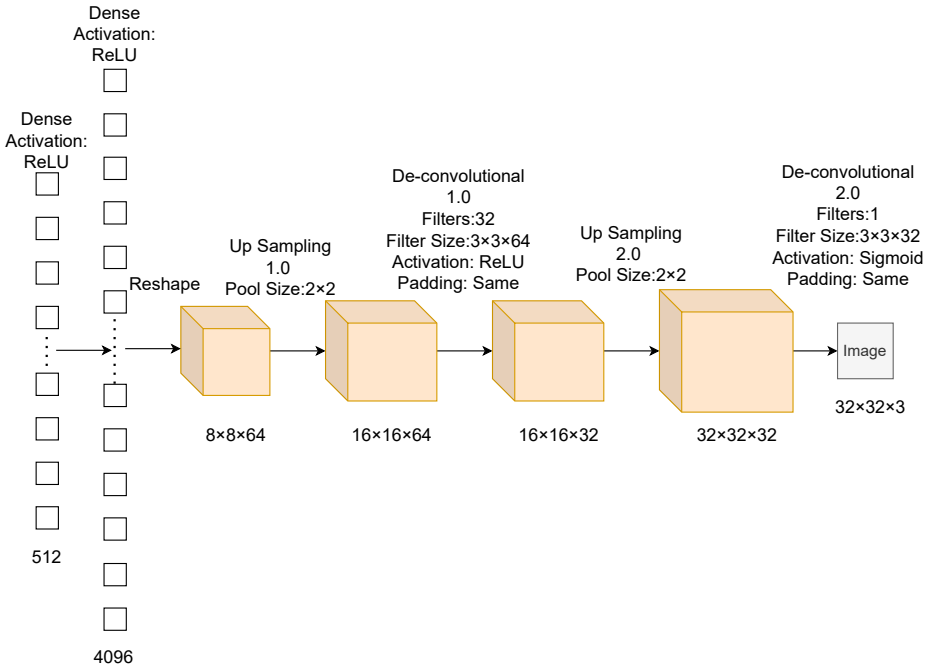


Figure 7.43: Proposed semantic decoder.

intricate patterns within the data. A stride of 1 is applied in both convolutional layers, with all spatial downsampling performed exclusively by the max-pooling layer.

A second max-pooling operation follows this layer, further reducing the feature maps to a size of 8×8 with 64 channels. The resulting output is then flattened into a one-dimensional array with dimensions $4{,}096 \times 1$, which serves as input to the fully connected layers. The architecture concludes with a dense layer, functioning as the bottleneck (latent vector) of the autoencoder. This layer employs the ReLU activation function to produce the final encoded representation with dimensions 512×1. The entire model is implemented using the Keras library in Python.

The decoder component of the autoencoder is schematically represented in Figure 7.43. Initially, a dense layer transforms the 512×1 latent vector into a $4,096 \times 1$ representation, using the ReLU activation function. This vector is then reshaped into a three-dimensional tensor of size 8×8 with 64 channels. To reconstruct the original single-channel image, the tensor is processed through a sequence of two deconvolution layers interleaved with up-sampling operations. The decoder concludes with a sigmoid-activated layer to generate the output image. The full autoencoder is constructed by

linking the encoder and decoder sequentially. For all experiments, training is carried out for 100 epochs with a batch size of 12, employing the Adam optimiser with a learning rate of 0.001, and using binary cross-entropy as the loss function to ensure stable learning. This consistent setup guarantees uniform evaluation across different experiments.

Channel Encoder and Decoder

In this work, polar codes [210] are utilised for channel coding, specifically employing a code rate of 1/2.

Quantum Encoder and Decoder

In this section, the same quantum encoder and decoder described in Section 3.1 are employed. As their architectures remain unchanged, the corresponding descriptions are not repeated here.

Quantum Channel

To emulate practical quantum-channel behaviour, our experiments incorporate standard quantum noise models, including bit-flip, phase-flip, depolarising, amplitude-damping, and phase-damping noise [127]. System performance is assessed across SNR levels by randomly adjusting the noise-type probabilities, enabling evaluation under diverse channel conditions as detailed in Section 3.1.

Convolutional Neural Network (CNN) for Machine Based Perception

Due to the absence of a standard machine-oriented image quality metric, a separate CNN is used to evaluate classification accuracy, reflecting the machine's ability to interpret and utilise the transmitted semantic information. The structure of the proposed CNN classification model, as illustrated in Figure 7.44, is employed to evaluate the received images. The model accepts input images with dimensions of $28 \times 28 \times 1$ and processes them using two convolutional layers, each with a kernel size of 3×3 and ReLU activation. These layers are followed by two max-pooling layers, each with a pool size of 2×2, to down-sample the feature maps. The network also includes three dense layers with

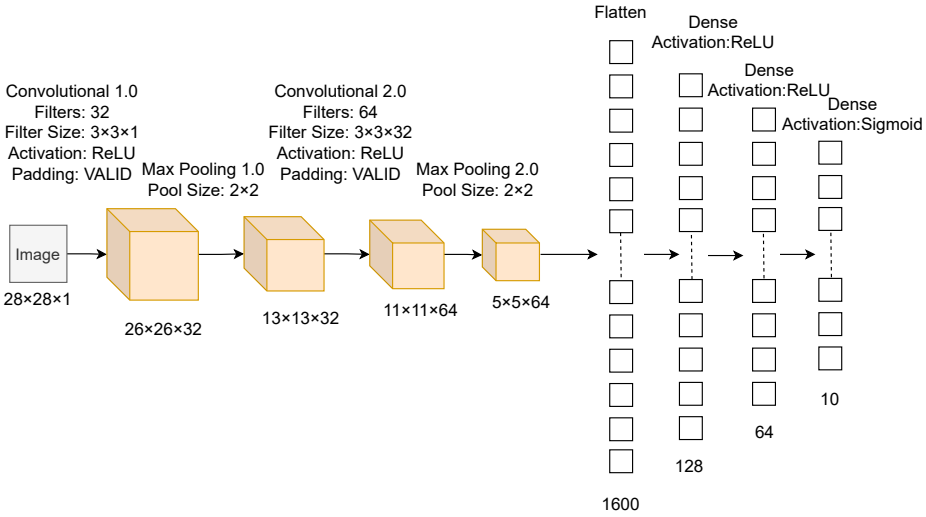


Figure 7.44: Proposed CNN for machine-based perception.

ReLU activation, culminating in a final dense layer with a sigmoid activation function for classification tasks.

Once the images are reconstructed after transmission, they are fed into the CNN model for classification, as depicted in Figure 7.44. This process evaluates whether the reconstructed images retain sufficient quality and features for successful classification or fail to provide accurate results.

To assess the effectiveness of the proposed quantum communication system for semantic image transmission, a comparative analysis is carried out against three baseline systems, ensuring consistent bandwidth usage across all configurations.

- A semantic communication-based classical communication system using the same rate channel code with BPSK modulation (C-SEMANTIC).
- A quantum communication system for compressed image transmission with JPEG compression to match the bitrate to the semantically encoded latent vector and same rate channel code (Q-JPEG).
- A classical communication system for compressed image transmission, using JPEG compression to match the bitrate to the semantically encoded latent vector, with the same rate channel code and BPSK modulation (C-JPEG).

The performance of all four systems is evaluated using PSNR, SSIM and UQI to provide quantitative image quality comparisons. Additionally, CNN-based analysis demonstrates the proposed system's ability to preserve semantically important features, ensuring high interpretability and utility for AI-driven tasks. Furthermore, the simulation is entirely based on a mathematical modelling framework implemented in Python 3 to emulate encoding, decoding, and channel noise. This approach provides an efficient and rigorous evaluation of the Q-SEMANTIC system. Quantum simulators are not used in this research due to their high computational complexity and incompatibility with our end-to-end Q-SEMANTIC system. Instead, a mathematical modelling framework is employed, which is sufficient for evaluation as it accurately captures the effects of quantum noise and encoding on system performance.

7.7.2 Results

In this section, we present a comprehensive analysis of the proposed quantum communication system for semantic communication-based image transmission (Q-SEMANTIC). To benchmark its performance, we compare it with three systems: the semantic communication-based classical communication system (C-SEMANTIC), the quantum communication system for compressed image transmission (Q-JPEG), and the classical communication system for compressed image transmission (C-JPEG). The analysis is organised into the following subtopics.

C-JPEG vs. Q-JPEG

The comparison of image quality in terms of PSNR demonstrates the superior performance of the Q-JPEG system over the C-JPEG system, as illustrated in Figure 7.45a-Figure 7.45c. As shown in Figure 7.45a, Q-JPEG achieves a maximum PSNR of 24.4 dB, with noticeable gain in the channel SNR range of 10.5 dB to 8 dB. In contrast, the performance of C-JPEG is capped at a PSNR of approximately 0 dB for channel SNR values below 9 dB. This improvement is attributed to the quantum communication framework, which utilises quantum superposition to enhance error resilience, especially in highly noisy environments. The peak value of 24.4 dB is due to the effect of quantisation noise, which arises because the JPEG-compressed bitstream is matched

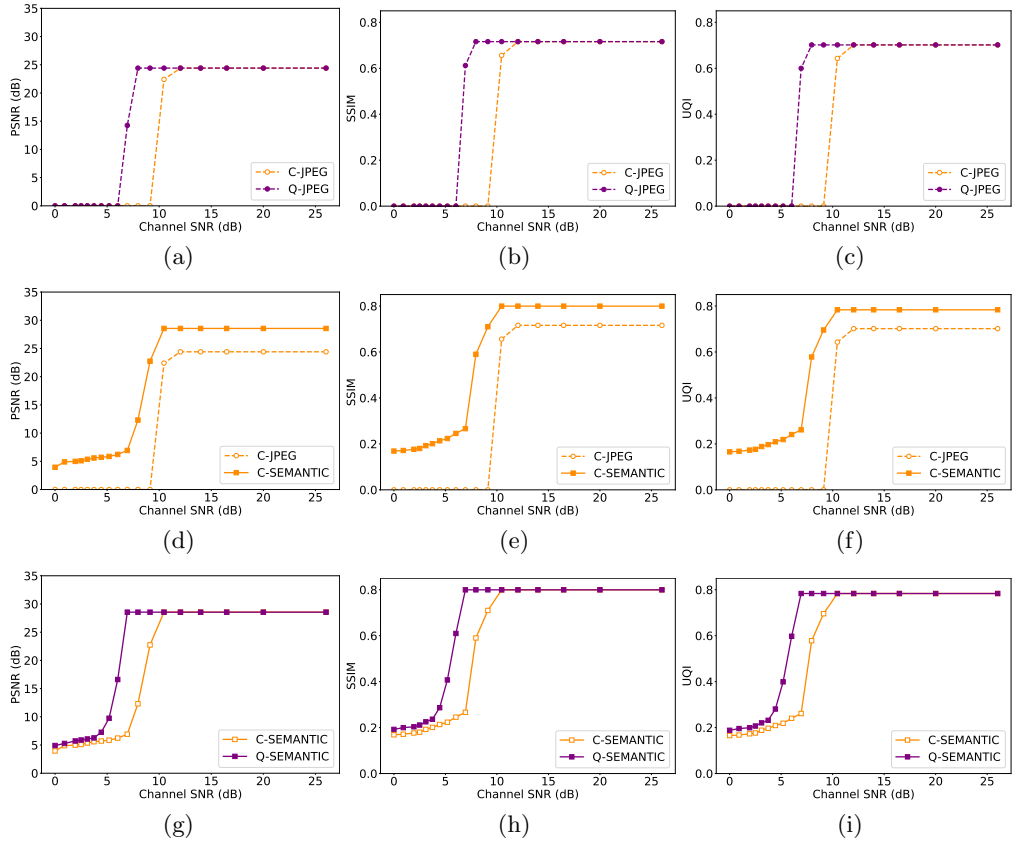


Figure 7.45: Comparison of different communication schemes under varying channel SNR levels. Columns represent performance evaluation metrics (PSNR, SSIM, UQI), and rows represent comparisons: (Row 1) Q-JPEG vs. C-JPEG, (Row 2) C-SEMANTIC vs. C-JPEG, (Row 3) Q-SEMANTIC vs. C-SEMANTIC.

in bandwidth to the semantic-encoded bitstream. These results demonstrate that even with JPEG compression, Q-JPEG delivers superior performance compared with classical communication methods.

As shown in Figure 7.45b, Q-JPEG demonstrates superior SSIM performance compared with the C-JPEG system. This performance difference highlights the enhanced noise-handling capabilities of quantum communication, enabling Q-JPEG to better preserve structural integrity in images than its classical counterpart. The UQI results, shown in Figure 7.45c, further validate this observation. UQI measures overall image quality by jointly considering correlation loss, luminance distortion, and contrast distortion, providing a comprehensive assessment of how well the reconstructed image maintains fidelity to the original.

C-JPEG vs. C-SEMANTIC

According to Figure 7.45d, the C-JPEG system exhibits significantly lower PSNR values at all channel SNR levels, with a maximum PSNR of 24.4 dB. In particular, below 9 dB channel SNR, the PSNR of the C-JPEG system remains close to 0 dB, indicating severe degradation in image quality. In contrast, the C-SEMANTIC system achieves a peak PSNR of 28.55 dB up to 9 dB channel SNR, with a gradual decrease to 4 dB at 0 dB channel SNR. Although the C-JPEG system maintains a PSNR of 0 dB from 9 dB to 0 dB channel SNR, the C-SEMANTIC system outperforms it by maintaining higher PSNR values throughout. The maximum PSNR of 28.55 dB is constrained by semantic noise introduced during lossy encoding, which prevents the reconstructed image from achieving the quality of the original. The additional advantage of semantic communication lies in its ability to extract and transmit the essential meaning of the image, enabling a more efficient transmission. This approach ensures superior image quality, even under challenging conditions, further highlighting the robustness and reliability of the C-SEMANTIC system compared with C-JPEG methods. The SSIM (Figure 7.45e) and UQI (Figure 7.45f) results further confirm that C-SEMANTIC substantially outperforms C-JPEG in preserving image content and structural similarity under noisy conditions. The near-zero PSNR, SSIM, and UQI values for C-JPEG at SNRs below 9 dB occur because JPEG's compressed bitstream is highly fragile, small bit errors caused by channel noise can corrupt entire blocks, leading to catastrophic decoding failure. In contrast, semantic encoding with error correction distributes essential information redundantly, allowing meaningful image reconstruction even when some bits are corrupted.

C-SEMANTIC vs. Q-SEMANTIC

The Q-SEMANTIC system consistently outperforms the C-SEMANTIC system at every SNR level. As shown in Figure 7.45g, while Q-SEMANTIC achieves a steady PSNR of 28.55 dB up to 7 dB channel SNR, C-SEMANTIC experiences significant degradation in PSNR starting from 9 dB channel SNR. Between 9 dB and 7 dB channel SNR, C-SEMANTIC's performance is noticeably lower than that of Q-SEMANTIC, which maintains a constant maximum PSNR of 28.55 dB throughout this channel SNR range.

Additionally, the Q-SEMANTIC system consistently achieves the highest SSIM and UQI values across all tested SNR levels, as shown in Figure7.45h and Figure 7.45i, further supporting the results of the PSNR analysis. This superior performance highlights the advantages of integrating semantic communication with quantum communication. The quantum framework enhances the noise resilience of semantic communication and significantly improves image transmission quality under challenging conditions, making Q-SEMANTIC the optimal choice for reliable image transmission in noisy environments. Furthermore, we perform paired t-tests on PSNR, SSIM, and UQI across all test images to statistically assess whether the observed differences between Q-SEMANTIC and C-SEMANTIC are significant. The paired t-test assesses whether the mean difference between paired measurements for the same images is significantly different from zero. In low-SNR conditions (below 9 dB), Q-SEMANTIC outperforms C-SEMANTIC with $p \leq 0.001$, where p is the probability that the observed difference occurs by chance under the null hypothesis of no true performance gain. Across most SNR levels, Q-SEMANTIC maintains a measurable advantage, confirming its approximately 3 dB operational gain and demonstrating robust semantic transmission.

When comparing all systems, it is evident that semantic communication systems consistently outperform classical compressed image transmission. Additionally, all quantum communication systems surpass their classical counterparts at low SNR levels, demonstrating enhanced noise resilience and suitability for high-quality image transmission. In conclusion, by combining all its advantageous features, we can deduce that the Q-SEMANTIC system outperforms all other systems, leveraging the combined benefits of quantum communication and semantic communication. In highly noisy environments, compressed images experience significant degradation, rendering them difficult to decode as recognisable images, which impacts the Q-JPEG system's performance. However, semantic communication systems do not face this decoding issue.

Additionally, CNN-based image classifiers show varying performance in interpreting transmitted images under different channel SNRs, as shown in Figure 7.46. In this context, "Classified" indicates that the classifier achieves at least 90% accuracy, representing a practically reliable level of semantic recognition. Significant differences are observed across transmission techniques, including Q-SEMANTIC, C-SEMANTIC, Q-JPEG,

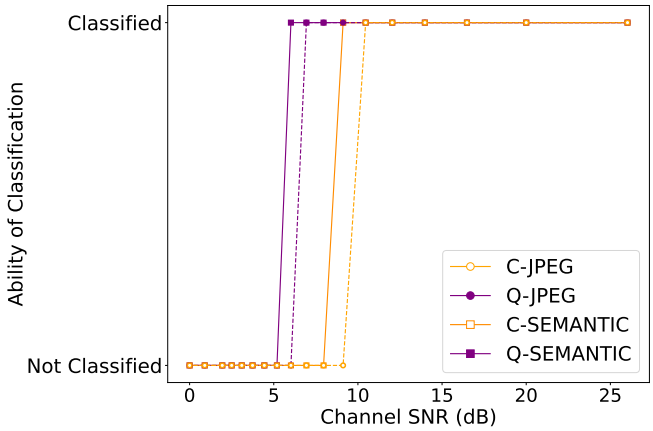


Figure 7.46: Ability of image classification using CNN model.

and C-JPEG. Q-SEMANTIC demonstrates exceptional robustness, maintaining reliable classification above 90% accuracy at SNRs as low as 6 dB. C-SEMANTIC struggles below 9 dB, while C-JPEG requires approximately 10.5 dB to reach the same threshold. Q-JPEG outperforms C-SEMANTIC, achieving classification above 90% down to 7 dB. Using the 90% threshold allows for clear comparison of the operational limits and noise resilience of each method, reflecting their practical reliability in maintaining semantic information under channel noise.

Notably, the 3 dB performance advantage of Q-SEMANTIC over C-SEMANTIC arises from the combined benefits of quantum-domain encoding, polar-coded error correction, and semantic feature preservation. Q-SEMANTIC maps the polar-coded classical bitstream into quantum superposition states, distributing information across multiple basis states and providing intrinsic robustness to channel noise. Superposition allows error smoothing, interference exploitation, and reduced redundancy requirements, enabling reliable retention of semantic features even at lower SNRs. While both methods use polar codes, the integration with quantum encoding in Q-SEMANTIC amplifies error correction effectiveness, lowering the bit error rate and preserving critical latent features. These factors collectively shift the classification reliability threshold from 9 dB in C-SEMANTIC to 6 dB in Q-SEMANTIC, demonstrating the observed 3 dB gain under noisy channel conditions.

Therefore, these findings highlight Q-SEMANTIC system's potential in demanding applications. Its robust performance makes it particularly well-suited for applications,

where accurate and reliable image interpretation is essential. Furthermore, the computational complexity and latency of the C-SEMANTIC system for information transmission is lower than that of the C-JPEG system. However, the Q-SEMANTIC system exhibits even lower computational complexity and latency than all other systems, particularly in comparison to the Q-JPEG and C-SEMANTIC systems with the advantage of combined quantum and semantic properties. The proposed Q-SEMANTIC system leverages semantic compression and single-qubit encoding, the lowest-complexity quantum-domain encoding, to achieve lower resource usage, reduced latency, and higher reconstruction quality compared with classical semantic communication methods. Semantic compression reduces the transmitted bitstream size, while single-qubit encoding with quantum superposition efficiently preserves semantic information under noisy channels with minimal computational overhead. Combined with polar-coded error correction, this approach ensures high semantic fidelity even at low SNRs. Furthermore, even QEC are not employed in this study due to the additional complexity associated with existing methods. Therefore, Q-SEMANTIC enhances energy efficiency by reducing unnecessary retransmissions and processing in scenarios with degraded image quality. This dual benefit of improved performance and sustainability underscores its value in real-world vehicular communication networks.

Moreover, the proposed framework is highly scalable, allowing future enhancements such as replacing single-qubit encoding with multi-qubit encoding, integrating adaptive quantum-channel strategies, or adopting hybrid quantum-classical processing techniques. This ensures highly robust, efficient, and accurate image reconstruction and semantic analysis, addressing the demanding performance requirements of next-generation communication systems. The simulation-based evaluation further demonstrates the effectiveness of the Q-SEMANTIC framework under diverse channel conditions and noise levels, confirming its theoretical advantages. These results not only validate the framework's potential for practical deployment but also provide a solid foundation for extending it to real-world applications in autonomous driving, intelligent transportation systems, and advanced vehicular networks.

7.7.3 Section Summary

This section demonstrated that integrating the proposed quantum communication framework with semantic communication provides an effective approach to achieving content-layer robustness for image transmission over noisy channels. Unlike the physical-layer and source-layer techniques presented earlier in this chapter, semantic communication improves robustness by prioritising the transmission of semantically meaningful information rather than preserving every transmitted bit. The proposed Q-SEMANTIC framework achieved the best overall performance, attaining a PSNR of up to 28.55 dB, an SSIM of up to 0.7996, and a UQI of up to 0.7836, outperforming both the classical semantic communication system (C-SEMANTIC) and conventional compressed image transmission systems (Q-JPEG and C-JPEG). Furthermore, CNN-based image classification confirmed that the Q-SEMANTIC framework more effectively preserved semantic information, demonstrating superior machine perception and robustness under channel impairments. These results highlight the potential of quantum semantic communication for reliable, high-quality, and content-aware image transmission.

7.8 Chapter Summary

This chapter addressed the integration of quantum-domain encoding with established multimedia transmission architectures, extending the standalone quantum frameworks of Chapters 3–6 into practical wireless communication settings. Seven integrated frameworks were developed, each targeting a distinct research question regarding the interaction between quantum signal representations and classical communication mechanisms such as MIMO, OFDM, MDC, and semantic communication.

Sections 7.1 and 7.2 investigated the integration of quantum superposition-based encoding with MIMO transmit and receive diversity for image and video transmission, respectively. The quantum MIMO image transmission framework achieved PSNR values of up to 58.27 dB for JPEG and 64.72 dB for HEIF, with SSIM reaching 0.9999 across SISO, MISO, and SIMO configurations over Rayleigh fading channels, outperforming conventional classical MIMO systems. The extension to video transmission delivered up to 39.12 dB PSNR, 0.9471 SSIM, and 92.47 VMAF, further demonstrating that

spatial diversity gains and quantum encoding jointly preserve both spatial fidelity and temporal consistency under fading conditions more effectively than classical transmission approaches.

Sections 7.3 and 7.4 developed QOFDM frameworks that integrated multi-qubit encoding with QFT-based orthogonal subcarrier generation for image and video transmission. The QOFDM image framework demonstrated the scalability of qubit-based encoding, with the eight-qubit configuration providing the highest noise resilience. The video extension, combining VVC compression with multi-qubit encoding, achieved PSNR up to 47.60 dB, SSIM up to 0.9987, and VMAF up to 96.40, with the highest-qubit configuration providing approximately 22 dB SNR gain over classical baselines under urban Rayleigh fading.

Section 7.5 unified the spatial and frequency domain advantages into a complete end-to-end quantum MIMO-OFDM framework. The eight-qubit configuration surpassed all other quantum and classical systems across diversity schemes, achieving PSNR values of up to 58.48 dB for JPEG, 70.04 dB for HEIF, and nearly ideal reconstruction for uncompressed images even at very low SNR levels, thereby confirming the benefits of jointly exploiting spatial diversity and multicarrier processing in the quantum domain.

Section 7.6 introduced a Q-MDC framework that moved beyond physical-layer enhancements by embedding deterministic inter-description redundancy through a CNOT-based correlation mechanism between Hadamard-encoded descriptions. The hybrid packet-level and qubit-level recovery strategy achieved channel SNR gains of up to 4 dB over classical MDC and up to 7 dB over channel-coded classical single-stream transmission under equivalent bandwidth constraints, while maintaining low computational complexity.

Finally, Section 7.7 presented a quantum semantic communication framework that combined deep learning-based semantic feature extraction, polar channel coding, and Hadamard-based quantum encoding within a unified end-to-end model. The proposed Q-SEMANTIC framework achieved PSNR up to 28.55 dB, SSIM up to 0.7996, and UQI up to 0.7836, maintaining reliable CNN-based classification ($\geq 90\%$ accuracy) at SNRs as low as 6 dB, compared with 9 dB for its classical counterpart, representing a 3 dB operational gain confirmed by paired t-tests ($p \leq 0.001$).

Collectively, these seven frameworks demonstrated that the benefits of quantum-domain encoding established in Chapters 3–6 extend coherently to integrated communication architectures. Combining quantum encoding with spatial diversity, multicarrier processing, multi-description coding, and semantic transmission consistently yielded measurable improvements in robustness, reconstruction fidelity, and bandwidth efficiency over equivalent classical systems under identical channel and bandwidth conditions, establishing a coherent pathway toward practical quantum-assisted multimedia communication systems.

It should be noted that the performance improvements reported throughout this chapter are achieved entirely by the proposed end-to-end quantum communication frameworks. Across Sections 7.1–7.7, the reported results are obtained by integrating the proposed quantum communication framework with established multimedia communication technologies, including quantum MIMO image transmission, quantum MIMO video transmission, QOFDM image transmission, QOFDM video transmission, quantum MIMO-OFDM image transmission, Q-MDC, and semantic communication. No receiver-side image restoration or enhancement techniques are employed in any of these frameworks. Consequently, the reported compression, transmission, and reconstruction performance directly reflects the effectiveness of the proposed quantum communication framework and its integration with these multimedia communication systems.

Chapter 8

Conclusions and Future Work

This thesis presented a comprehensive investigation into quantum communication frameworks for high-fidelity image and video transmission over noisy and bandwidth-constrained communication channels. Beginning from fundamental superposition-based quantum encoding principles and progressively advancing toward integrated communication architectures, the research addressed key challenges associated with transmission robustness, reconstruction fidelity, compression efficiency, scalability, and practical deployment for image and video communication systems. Through a sequence of progressively enhanced frameworks, the thesis demonstrated that quantum communication can provide substantial and consistent performance advantages over conventional classical communication approaches. The principal contributions and findings of each chapter are summarised below.

8.1 Summary of Contributions

Chapter 3 established the foundational quantum communication framework for image and video transmission. The chapter first demonstrated that superposition-based quantum encoding via the Hadamard transform provided inherently superior noise resilience compared to classical BPSK transmission, as information distributed across probability amplitudes was less vulnerable to channel noise than deterministic binary symbol levels. Building upon this foundation, a three-qubit QEC code was introduced, achieving PSNR values of up to 64.5 dB for HEIF and 58.3 dB for JPEG with SSIM exceeding 0.999,

significantly outperforming rate-1/3 polar codes under identical bandwidth constraints. The chapter subsequently proposed an adaptive QEC framework that dynamically selected among three, five, seven, and nine-qubit codes based on real-time channel conditions. The framework achieved PSNR values of up to 40.51 dB, SSIM values of up to 0.9730, and UQI values of up to 0.9998 for JPEG-compressed images, and PSNR values of up to 45.44 dB, SSIM values of up to 0.9889, and UQI values of up to 0.9999 for HEIF-compressed images, while maintaining a balance between error resilience and computational complexity compared to fixed-qubit and classical polar-coded systems. The framework was further extended to video transmission, where the highest-qubit QEC system consistently achieved the highest reconstruction fidelity across varying GOP sizes, frame rates, and resolutions, confirming its scalability to temporally correlated image and video content. The QEC maintained reliable reconstruction at SNR values as low as -10 dB, while the gate complexity scaled linearly with the number of physical qubits, resulting in low processing latency.

Chapter 4 introduced a multi-qubit encoding strategy that exploited higher dimensional Hilbert space representations to enhance transmission robustness without requiring ancilla qubits. By increasing the qubit group size from $k = 1$ to $k = 8$, the system achieved SNR gains of up to 15 dB for JPEG and 17 dB for HEIF relative to single-qubit encoding when combined with polar channel coding. An adaptive variable-qubit encoding framework was further developed for video transmission, achieving a consistent $\sim$20 dB SNR gain across all tested resolutions, frame rates, and GOP sizes, establishing a scalable and ancilla-free multi-qubit quantum image and video communication framework. Both gate complexity and processing latency scaled linearly with k, keeping the overall computational and timing overhead well within real-time transmission requirements.

Chapter 5 advanced the framework into the frequency domain through QFT-based processing. The frequency-domain multi-qubit encoding system outperformed the time-domain multi-qubit system, achieving an additional 4 dB channel SNR gain, particularly for eight-qubit configurations. This improvement is attributed to the dual amplitude–phase encoding capability provided by the QFT. The chapter also presented a unified QFT-based compression and transmission architecture, where image and video

information was directly embedded into quantum frequency components, achieving symbol-level compression ratios of up to 256:1 for the eight-qubit configuration. To address the trade-off between compression efficiency and noise robustness at higher qubit dimensions, semantic-aware restoration frameworks were introduced. A DDPM-based reconstruction achieved SSIM values of approximately 0.9996 under low-SNR conditions for images, while a U-Net-based refinement framework achieved PSNR values up to 48.36 dB, SSIM up to 0.9921, and VMAF scores up to 92.22 for video transmission, providing a practical pathway for high-fidelity transmission over severely degraded channels. The QFT introduced quadratic gate complexity, $O(k^2)$, with linear circuit depth, $O(k)$, resulting in low processing times for all qubit configurations up to $k = 8$.

Chapter 6 introduced COUS encoding as a novel quantum encoding technique that jointly exploited amplitude and phase diversity within multi-qubit states. The single-qubit COUS configuration surpassed the QFT-based frequency-domain framework by approximately 4 dB in channel SNR, while higher-qubit configurations achieved channel SNR gains of up to 23 dB compared to 19 dB for Hadamard-based encoding. Critically, these performance improvements were achieved without increasing circuit depth and while maintaining linear gate complexity $O(k)$ with respect to the number of qubits. The framework avoided the transform-domain processing overhead of QFT-based systems, with runtime analysis confirming practical feasibility across all evaluated configurations and making the framework particularly suitable for near-term NISQ device implementation.

Chapter 7 investigated the integration of the developed quantum communication frameworks with established wireless communication architectures for practical deployment. Combining quantum superposition encoding with MIMO spatial diversity techniques significantly improved image and video transmission under Rayleigh fading conditions, achieving PSNR values of up to 58.27 dB for JPEG images and 64.72 dB for HEIF images, with corresponding SSIM values of up to 0.9994 and 0.9999, respectively, across various SNR levels and image quantisation parameters (QP25 and QP100), outperforming conventional classical MIMO systems. For video transmission, the proposed system achieved PSNR values of up to 39.12 dB, SSIM values of up to 0.9471, and VMAF scores of up to 92.47 across SISO, MISO, and SIMO configurations,

consistently demonstrating robustness across different GOP sizes, resolutions, and frame rates. A QOFDM framework was developed for multicarrier transmission, where the eight-qubit configuration achieved approximately 22 dB SNR gains over classical OFDM under urban Rayleigh fading. A hybrid quantum MIMO-OFDM architecture further combined these advantages, achieving peak performance metrics such as PSNR values of up to 58.48 dB, SSIM values of up to 0.9993, and UQI values of up to 0.9999 for JPEG images; PSNR values of up to 70.04 dB, SSIM values of up to 0.9998, and UQI values of up to 0.9999 for HEIF images; and near-ideal reconstruction performance for uncompressed images, with infinite PSNR, SSIM of 1, and UQI of 1 at very low SNR levels. The chapter also introduced a Q-MDC framework that achieved an effective SNR gain of approximately 4 dB over classical MDC and up to 7 dB over classical single-stream transmission while maintaining linear computational complexity. Finally, a quantum semantic communication (Q-SEMANTIC) framework was proposed, achieving PSNR values of up to 28.55 dB and SSIM up to 0.7996 with CNN-based classification reliability maintained at SNRs as low as 6 dB, representing a 3 dB improvement over classical semantic communication. Despite the architectural integration, the overall gate complexity and end-to-end latency remained dominated by classical post-processing operations, with quantum encoding and decoding contributing only minimal overhead per transmitted symbol.

8.2 Overall Conclusion

The central research question posed in Chapter 1 asked how quantum communication techniques can be designed and integrated with classical communication pipelines to improve reliability, reduce complexity, enhance adaptability, and preserve reconstruction quality in image and video transmission over noisy and bandwidth-constrained channels. The combined evidence of Chapters 3–7 answers this question affirmatively and consistently. The frameworks developed span single-qubit Hadamard encoding and adaptive QEC, multi-qubit and QFT-based frequency-domain encoding, novel COUS representations, and fully integrated MIMO, OFDM, MIMO-OFDM, MDC, and semantic communication architectures. Across all of them, quantum state representations delivered substantial and repeatable gains in reconstruction fidelity and noise robustness

over their classical counterparts, while incurring only linear or, at most, quadratic gate complexity for the qubit dimensions relevant to near-term hardware.

This consistency supports a single overarching conclusion: the advantage of quantum communication for visual data delivery is structural rather than incidental. Distributing each unit of information across a high-dimensional probabilistic state space, and exploiting both amplitude and phase degrees of freedom, transforms the localised vulnerabilities of classical binary modulation into globally robust representations. Equally important, these gains were shown to compound with, rather than replace, established classical wireless infrastructure, which makes quantum-enhanced multimedia communication an incrementally deployable enhancement rather than a wholesale alternative.

Viewed against the aim and objectives defined in Chapter 1, the research aim has been met in full, and each objective has been addressed by one or more chapters. The single-qubit end-to-end framework of Chapter 3 delivers a reliable quantum image and video transmission pipeline together with the integration of quantum and classical error correction (Objectives 1 and 2). The multi-qubit encoding strategy of Chapter 4 provides efficient and scalable representation, analyses the advantages of different quantum encoding techniques, and introduces adaptive encoding (Objectives 3, 4, and 6). The quantum frequency-domain techniques of Chapter 5, together with the DDPM and U-Net-based restoration, address the analysis of quantum encoding techniques, quantum-domain signal processing for reconstruction-quality enhancement, and the evaluation of adaptive encoding and alternative state representations (Objectives 4, 5, and 6). The novel COUS encoding of Chapter 6 improves noise resilience and computational efficiency while extending the comparative analysis of encoding techniques, the signal-processing study, and the assessment of state representations (Objectives 3, 4, 5, and 6). Finally, the integration of these techniques with MIMO, OFDM, MIMO-OFDM, MDC, and semantic communication systems in Chapter 7 satisfies the objectives of efficient and scalable transmission, encoding analysis, quantum-domain signal processing, and integration with existing transmission frameworks (Objectives 3, 4, 5, and 7). Taken together, these outcomes confirm that the proposed framework achieves reliable, scalable, adaptable, and high-fidelity image and video transmission under noisy and dynamically varying channel conditions, as the aim of this thesis required.

Collectively, the proposed frameworks establish a new paradigm for image and video transmission based on quantum communication principles. Rather than incrementally improving individual components of conventional communication systems, this research demonstrates that quantum state representations can be systematically integrated with established multimedia transmission techniques to overcome several fundamental limitations of classical communication, including limited robustness to channel impairments, restricted information representation, and reduced adaptability under dynamic transmission conditions. The resulting frameworks combine the advantages of quantum information processing with mature communication technologies, providing a unified approach for reliable, scalable, and high-fidelity multimedia transmission across a wide range of image and video communication scenarios.

In addition, the image and video datasets used throughout this thesis were selected to provide a representative range of multimedia characteristics encountered in practical communication systems. For image transmission, multiple images were employed throughout the experimental evaluation, with the exact number depending on the specific study, to capture diverse spatial characteristics, including variations in texture, edge density, contrast, structural complexity, and visual content. For video transmission, three representative video sequences exhibiting low, medium, and high-motion characteristics were selected to encompass diverse levels of spatial information (SI), temporal information (TI), and scene dynamics. Although only three video sequences were considered, each was evaluated at multiple spatial resolutions and frame rates, thereby representing a wide range of practical multimedia transmission scenarios. These variations ensure that the proposed quantum communication frameworks are evaluated under diverse multimedia conditions rather than being optimised for a particular image, video sequence, resolution, or frame rate.

Furthermore, the proposed methodologies are inherently content-independent, as they operate on the compressed multimedia bitstream and its corresponding quantum representation rather than on the semantic or visual characteristics of the input data. Consequently, the proposed frameworks are applicable to arbitrary image and video content irrespective of scene complexity, texture, object composition, or spatial resolution. Therefore, the selected image and video datasets provide representative test cases for

evaluating the proposed communication systems while demonstrating their general applicability to a broad range of multimedia content.

To further improve the reliability of the evaluation, extensive Monte Carlo transmission trials were performed for every experimental configuration by generating multiple independent channel realisations for each image, video sequence, channel condition, and SNR value. The reported performance metrics therefore represent averages over numerous independent transmission trials, reducing the influence of individual noise realisations and content-specific characteristics. Consequently, the experimental results provide statistically robust performance estimates and increase confidence that the proposed quantum communication frameworks generalise beyond the specific images and video sequences evaluated in this thesis.

It should also be emphasised that the contributions presented in this thesis are established through rigorous end-to-end simulation-based evaluation. This methodology represents the standard and widely accepted first step in the development of emerging quantum communication systems, as current quantum hardware remains constrained by limited qubit counts, finite coherence times, imperfect gate fidelities, and restricted quantum memory resources, preventing the implementation of large-scale multimedia communication frameworks. Consequently, the proposed systems should be regarded as theoretical and simulation-validated communication architectures that establish their fundamental feasibility and performance characteristics. As quantum hardware continues to mature, these frameworks provide a strong foundation for future experimental validation and practical deployment of quantum-enhanced image and video communication systems.

8.3 Key Scientific Insights

Beyond the per-chapter contributions summarised above, several cross-cutting scientific insights emerged from this thesis. These insights extend beyond any single framework and collectively illuminate why quantum communication offers fundamental advantages for visual content delivery over noisy channels.

Insight 1: Information Distribution Across Probabilistic State Spaces is the Source of Quantum Advantage

A central insight that emerged across all chapters is that the principal advantage of quantum communication arises not solely from quantum superposition as an abstract phenomenon, but from the ability of quantum state representations to distribute information across high-dimensional probabilistic state spaces. Whereas classical binary modulation encodes information into discrete symbol levels that are vulnerable to noise-induced threshold crossings, quantum encoding spreads each information unit across multiple probability amplitudes. This distribution fundamentally alters the geometry of the symbol constellation, transforming localised vulnerabilities into globally robust representations. The progressive gains observed from single-qubit Hadamard encoding (Chapter 3) through eight-qubit multi-qubit configurations (Chapter 4) confirm that the advantage scales with the dimensionality of the available state space, rather than being a fixed property of any single encoding scheme.

Insight 2: Joint Amplitude–Phase Encoding Outperforms Amplitude-Only Encoding Under Realistic Noise

A second insight, established quantitatively in Chapters 5 and 6, is that encoding schemes which exploit both amplitude and phase components of quantum states deliver consistent gains over those that exploit amplitude alone. Hadamard encoding produces real-valued superposition states confined to a single axis of the Bloch sphere, leaving them susceptible to specific noise processes such as amplitude damping. QFT and COUS encoding, in contrast, distribute information across orthogonal quadratures, effectively doubling the dimensionality of the noise space the channel must corrupt to cause an error. This geometric argument explains why COUS encoding achieved 23 dB SNR gains versus 19 dB for Hadamard encoding at the eight-qubit configuration, and why this advantage persists across diverse channel conditions. The insight has implications beyond this thesis: it suggests that future quantum communication systems should be designed to exploit the full complex state space rather than restricting themselves to real-valued subspaces.

Insight 3: Quantum Advantage Compounds with, Rather Than Replaces, Classical Communication Infrastructure

A third insight, demonstrated in Chapter 7, is that quantum encoding integrates synergistically with established classical wireless architectures rather than competing with them. The hybrid quantum MIMO, OFDM, and MIMO-OFDM framework achieved higher reconstruction quality combining quantum-domain noise resilience with spatial and frequency diversity. Similarly, Q-MDC and Q-SEMANTIC frameworks demonstrated that quantum encoding strengthens, rather than supplants, classical multiple-description and semantic communication paradigms. This compositional property is critical for practical deployment, as it implies that quantum-enhanced communication does not require wholesale replacement of existing infrastructure but can be introduced incrementally as a complementary processing layer.

Insight 4: Robustness Gains Are Achievable Without Prohibitive Complexity

A persistent concern with quantum communication systems is that performance gains may come at the cost of exponential complexity. The results across this thesis demonstrate that this trade-off is not fundamental. The Hadamard and COUS multi-qubit encoding frameworks maintained linear gate complexity $O(k)$ with linear circuit depth, while even the QFT-based framework with quadratic gate complexity $O(k^2)$ retained linear circuit depth and low latency for $k \leq 8$. Across all developed frameworks, quantum processing contributed low computational overhead per symbol, with end-to-end latency dominated by classical operations such as compression and channel coding. This finding establishes that quantum communication gains are not inherently traded against real-time deployability for the qubit dimensions relevant to current and near-term hardware.

Insight 5: The Compression–Robustness Trade-off Can Be Resolved through Semantic Restoration

A final insight emerged from Chapter 5, where higher-qubit QFT-based compression introduced a tension between compression efficiency (up to 256:1 at $k = 8$) and

reconstruction fidelity at low SNR. The integration of DDPM and U-Net-based semantic restoration demonstrated that this trade-off is not absolute. By relocating part of the reconstruction burden from the transmission channel to the receiver, semantic-aware processing recovered fidelity even when the raw signal was severely degraded. This insight reframes the design space of quantum communication: aggressive compression and transmission strategies become viable when paired with intelligent receiver-side reconstruction, suggesting that the boundary between source coding, channel coding, and reconstruction is more fluid in quantum-enhanced systems than in classical ones.

8.4 Limitations

Despite the promising performance demonstrated throughout this research, several important limitations should be acknowledged. These limitations span the simulation methodology, the assumed channel and hardware models, the scope of the comparative baselines, and the computational footprint of the proposed receiver-side restoration modules.

Simulation-Based Validation

The proposed frameworks were evaluated through end-to-end simulation, which is the standard first step in the development of large-scale quantum communication systems because current quantum hardware cannot yet support multimedia communication involving thousands to millions of transmitted qubits. As scalable fault-tolerant quantum hardware becomes available, additional impairments, including finite gate fidelities, decoherence, measurement errors, and qubit connectivity constraints, will need to be incorporated. These effects are expected to reduce the absolute performance achieved by the proposed frameworks; however, experimental validation will establish the extent to which the relative advantages observed in simulation are maintained in practical implementations.

Channel and Propagation Assumptions

Channel estimation in the proposed adaptive frameworks, QOFDM, and hybrid MIMO-OFDM architectures was performed assuming perfect CSI to isolate the performance of

the proposed quantum communication techniques. In practical systems, channel estimation errors would introduce additional detection inaccuracies and reduce the achievable BER, PSNR, SSIM, and VMAF. Nevertheless, the proposed quantum frameworks are expected to retain their relative performance advantages, although the absolute reconstruction quality would decrease. Future work should therefore investigate robust channel estimation and imperfect CSI models.

Scalability Beyond Eight Qubits

The proposed multi-qubit frameworks were evaluated for up to eight qubits, balancing computational feasibility with representative quantum encoding dimensions. Future evaluation using larger quantum systems would enable higher information density and potentially improved robustness through higher-dimensional state representations. However, larger qubit dimensions would also increase circuit depth, error accumulation, and hardware resource requirements, requiring more advanced quantum error correction and scalable quantum architectures.

Receiver-Side Computational Overhead

The DDPM and U-Net-based semantic restoration frameworks in Chapter 5 achieved substantial fidelity improvements at low SNR, but at the cost of considerable computational overhead at the receiver. While this overhead is manageable in offline reconstruction settings and on GPU-equipped infrastructure, it may pose challenges for strict real-time deployment on constrained edge devices such as mobile handsets, IoT nodes, or in-vehicle systems. Lightweight restoration architectures or model-compression strategies would be required before these benefits can be realised in latency-sensitive applications.

Overall, these limitations do not affect the validity of the proposed communication principles, which were intentionally evaluated under controlled simulation conditions to establish their theoretical feasibility. Instead, they define the next stages of research required to transition from simulation-based validation towards practical quantum communication systems. As quantum hardware, channel modelling, and large-scale quantum networking technologies continue to mature, addressing these limitations will

enable a more comprehensive assessment of the proposed frameworks under realistic deployment conditions while preserving the fundamental communication architecture developed in this thesis.

8.5 Future Work

While the contributions presented in this thesis advance the state of quantum image and video communication, several important research directions remain open for further investigation. The QEC schemes employed in this thesis, including the three, five, seven, and nine-qubit codes in Chapter 3, were investigated as standalone mechanisms. Future research should explore the integration of low-complexity QEC codes with the multi-qubit encoding frameworks of Chapters 4–6 and the system architectures of Chapter 7. In particular, the development of QEC techniques that are jointly optimised with COUS encoding or QFT-based processing could yield further performance gains while managing the associated implementation overhead. Additionally, the current systems rely on classical polar codes as the primary channel coding mechanism; investigating hybrid quantum-classical error correction strategies that combine the strengths of both domains represents a promising direction for improving overall system reliability.

The Chapter 5 focuses on QFT-based frequency-domain processing because of its natural compatibility with quantum-state representations and efficient quantum circuit implementation, alternative quantum transform-domain techniques also merit investigation. In particular, quantum wavelet transforms offer multiresolution analysis and improved spatial localisation, making them well suited for representing local image and video features. Future research should investigate the integration of quantum wavelet transforms into the proposed multimedia communication frameworks and compare their performance with QFT-based approaches in terms of compression efficiency, reconstruction quality, robustness to channel impairments, computational complexity, and quantum circuit resource requirements. Hybrid frameworks that combine the global frequency representation of the QFT with the localised feature extraction capability of quantum wavelet transforms also represent a promising direction for quantum multimedia communication.

The MIMO and OFDM integration studies presented in Chapter 7 were limited

to antenna configurations of up to 2×2 and assumed perfect CSI. Future research should investigate the proposed quantum communication framework under larger MIMO configurations, imperfect CSI estimation, and more realistic propagation environments, including frequency-selective fading, time-varying channels, and millimetre-wave propagation conditions relevant to 5G and beyond-5G communication systems. Furthermore, extending the quantum MIMO-OFDM framework to multi-user and multi-hop communication scenarios incorporating resource allocation and interference management would enable a more realistic assessment of the proposed framework under practical wireless network conditions. Addressing these assumptions will determine whether the performance gains demonstrated in this thesis can be maintained in realistic deployment scenarios and will provide greater confidence in the practical feasibility of quantum-enhanced multimedia communication systems.

The semantic communication framework introduced in Chapter 7 was limited to image transmission using single-qubit encoding. Future research should extend this framework to video transmission and investigate the effectiveness of multi-qubit semantic encoding for preserving both spatial and temporal semantic information under noisy channel conditions. Furthermore, integrating semantic-aware processing with the DDPM and U-Net-based restoration techniques presented in Chapter 5 could enable jointly optimised systems that preserve both pixel-level fidelity and semantic integrity. These developments would facilitate the deployment of quantum semantic communication in intelligent multimedia applications requiring robust, low-latency, and high-quality image and video transmission.

Although all frameworks presented in this thesis have been validated through comprehensive simulation studies, overcoming the limitations of current quantum hardware remains a critical direction for future research. Present-day quantum processors are constrained by limited qubit counts, short coherence times, imperfect gate fidelities, restricted qubit connectivity, and measurement errors, all of which limit the implementation of large-scale multimedia communication systems. Future research should therefore investigate fault-tolerant quantum computing architectures, scalable quantum memory, improved QEC, and hardware-aware circuit optimisation techniques to mitigate these limitations. As quantum computing and quantum networking technologies continue

to mature, the proposed encoding, transmission, and decoding pipelines should be implemented and evaluated on publicly accessible quantum computing platforms and emerging quantum networking testbeds. Such investigations will enable a comprehensive assessment of their practical performance under realistic hardware and networking conditions and determine how closely the simulation results reported in this thesis can be reproduced in practice. The COUS encoding framework presented in Chapter 6, with its shallow circuit depth and linear gate complexity, is particularly well suited for implementation on near-term NISQ devices and provides a promising starting point for future experimental validation.

The adaptive mechanisms developed in this thesis, including the adaptive QEC selection in Chapter 3 and the adaptive multi-qubit encoding strategy in Chapter 4, relied on predefined threshold-based switching mechanisms with perfect CSI. Future research should investigate machine learning-based channel estimation and adaptive encoding selection to enable more responsive and fine-grained optimisation under dynamically varying channel conditions with imperfect CSI. Such approaches could also be extended to jointly optimise source coding parameters, quantum encoding configurations, channel coding, and diversity schemes within an end-to-end learning framework. This would enable fully intelligent quantum communication systems capable of autonomously adapting to changing network conditions while maximising transmission reliability, efficiency, and reconstruction quality.

Another important direction for future research is the development of hybrid quantum-classical multimedia communication systems for real-time applications. While quantum processing provides significant advantages in information representation and robustness, many practical tasks, including source coding, channel estimation, adaptive resource allocation, semantic analysis, and receiver-side image restoration, are more efficiently performed using classical processors or AI accelerators. Future work should therefore investigate hybrid system architectures that combine quantum communication with classical CPUs, GPUs, and dedicated AI hardware to distribute computational tasks according to their respective strengths. Such architectures would reduce processing latency, improve scalability, and facilitate the deployment of quantum-enhanced multimedia communication systems in real-time applications such as live video streaming,

autonomous vehicles, extended reality (XR), intelligent surveillance, and next-generation wireless networks.

Future research should also investigate the suitability of the reconstructed images and videos for downstream computer vision tasks. Although this thesis primarily evaluates transmission performance using objective quality metrics, future studies should assess the effectiveness of the reconstructed multimedia for applications such as image classification, object detection, semantic segmentation, and visual tracking. Such evaluations would determine whether the proposed quantum communication frameworks preserve not only perceptual quality but also the semantic information required for reliable machine perception, thereby extending their applicability to intelligent multimedia systems, autonomous vehicles, smart surveillance, remote sensing, and other AI-driven applications.

Finally, the Q-MDC framework presented in Chapter 7 demonstrated the feasibility of exploiting quantum-domain correlations for robust image transmission. Future research should extend this framework to video transmission and evaluate its performance in heterogeneous and multi-hop network environments where different transmission paths experience diverse channel conditions. In addition, investigating the integration of the proposed quantum communication framework with emerging wireless technologies such as reconfigurable intelligent surfaces (RIS), non-orthogonal multiple access (NOMA), and integrated sensing and communication (ISAC) would enable a comprehensive assessment of its compatibility with next-generation wireless communication systems. These investigations would broaden the applicability of the proposed framework and support its evolution from simulation-based multimedia communication architectures towards practical quantum-enhanced communication networks.

8.6 Closing Remarks

The work presented in this thesis was motivated by a simple shift in perspective: treating high-fidelity image and video delivery, rather than secure key exchange, as the primary objective of a quantum communication system. Pursuing this objective has demonstrated that the advantages of quantum state representations extend naturally from still images to video and from standalone transmission schemes to fully integrated

wireless communication architectures. More broadly, this research establishes a new paradigm for image and video transmission by demonstrating that quantum communication can serve as a fundamental multimedia communication framework, overcoming several inherent limitations of conventional classical communication systems in terms of robustness, adaptability, and reconstruction quality. Although significant challenges remain before these concepts can be fully realised on large-scale quantum hardware and operational quantum networks, these challenges define the next stage of research in quantum multimedia communication. As quantum computing and quantum networking technologies continue to mature, it is hoped that the frameworks, methodologies, and insights presented in this thesis will provide a solid foundation for researchers and engineers working towards practical quantum-enhanced image and video communication systems.

Appendix A

Analysis of COUS Encoding with Three-Qubit QEC

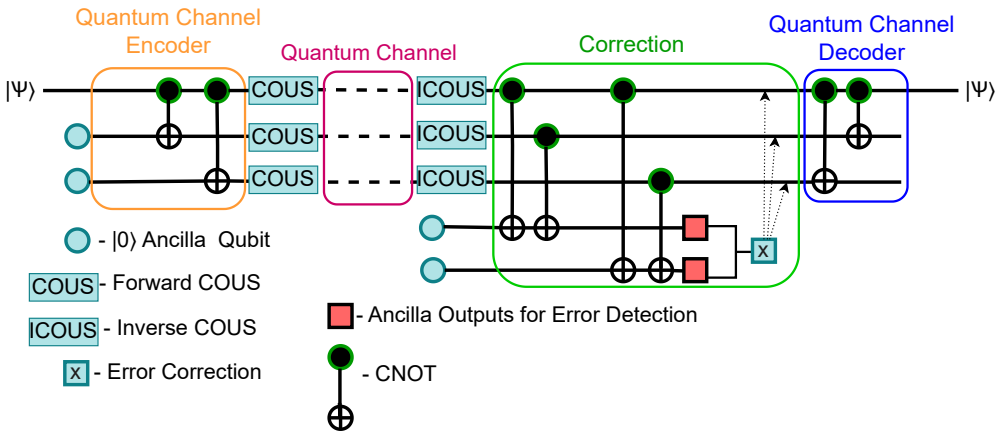
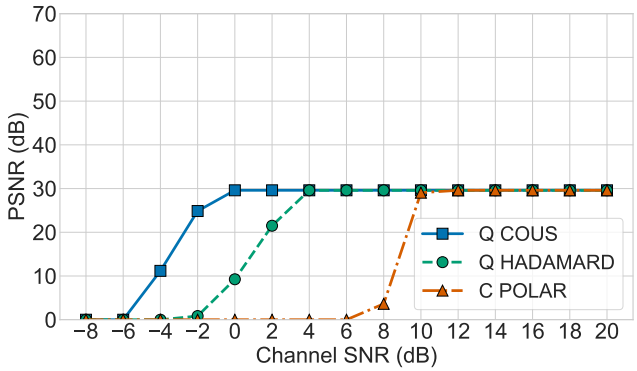
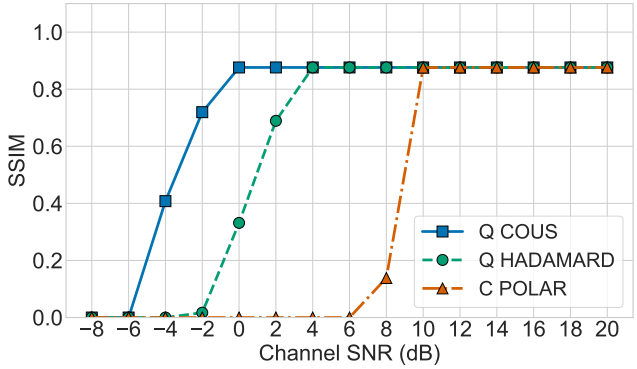


Figure A.1: The proposed COUS encoding based three-qubit QEC scheme.

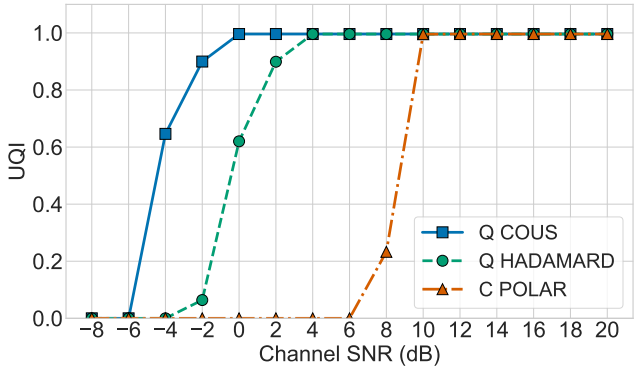
The QEC scheme employed in this analysis is illustrated in Figure A.1. The overall transmission pipeline follows the structure described in Section 3.2, with the only modification being the incorporation of COUS encoding prior to channel transmission and inverse COUS (ICOUS) decoding at the receiver [232]. Additional results for different compression formats and compression levels are presented below.



(a)

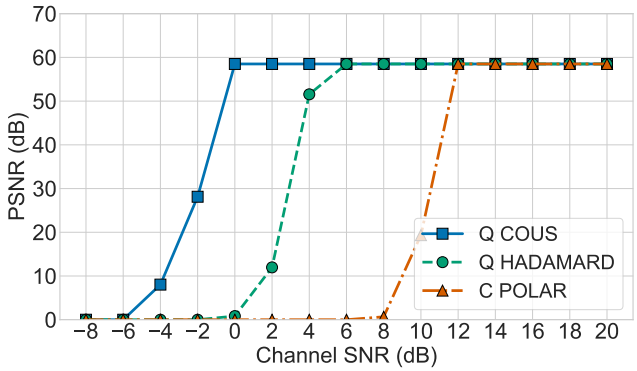


(b)

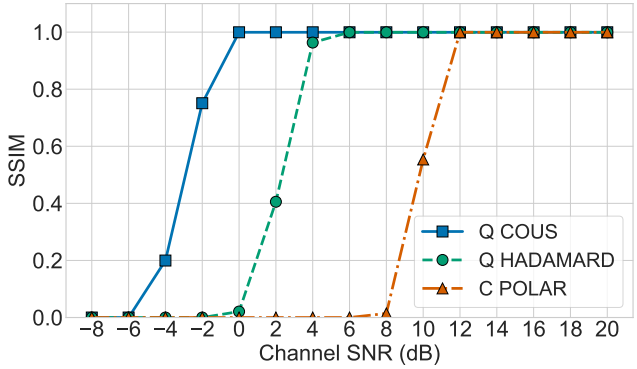


(c)

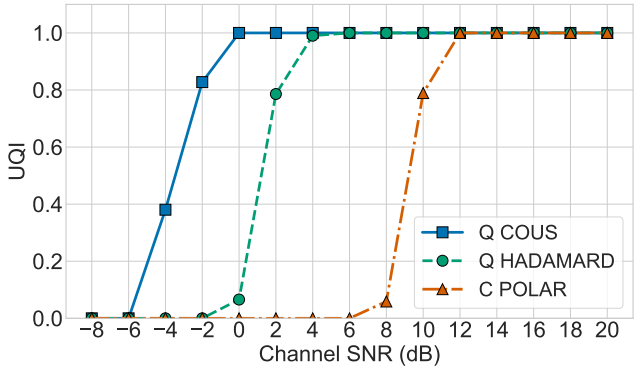
Figure A.2: Performance of JPEG QP=25 compressed image transmission evaluated using (a) PSNR, (b) SSIM, and (c) UQI, under the proposed COUS encoding-based three-qubit QEC system (Q COUS), the conventional Hadamard encoding-based three-qubit QEC system (Q HADAMARD), and the classical polar-coded system (C POLAR).



(a)

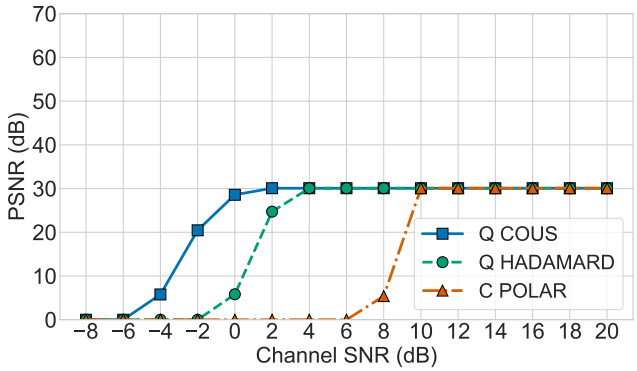


(b)

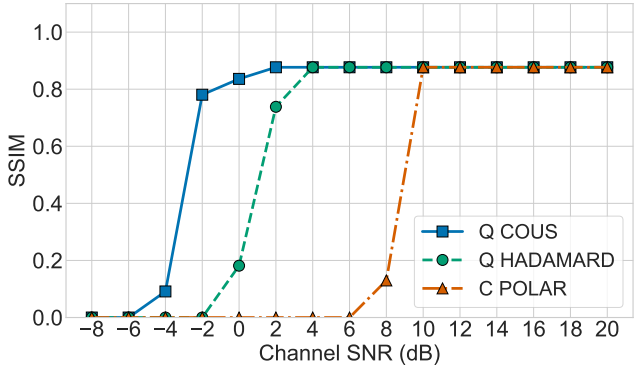


(c)

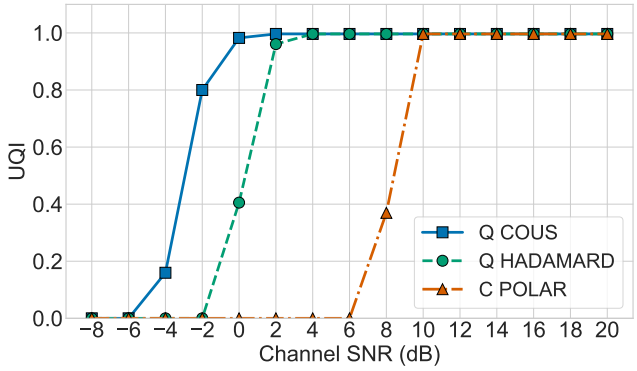
Figure A.3: Performance of JPEG QP=100 compressed image transmission evaluated using (a) PSNR, (b) SSIM, and (c) UQI, under the proposed COUS encoding-based three-qubit QEC system (Q COUS), the conventional Hadamard encoding-based three-qubit QEC system (Q HADAMARD), and the classical polar-coded system (C POLAR).



(a)

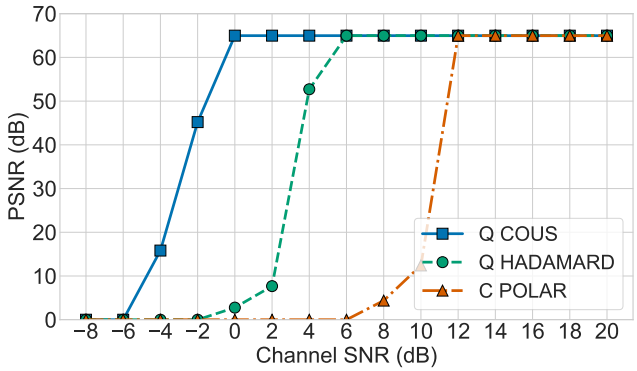


(b)

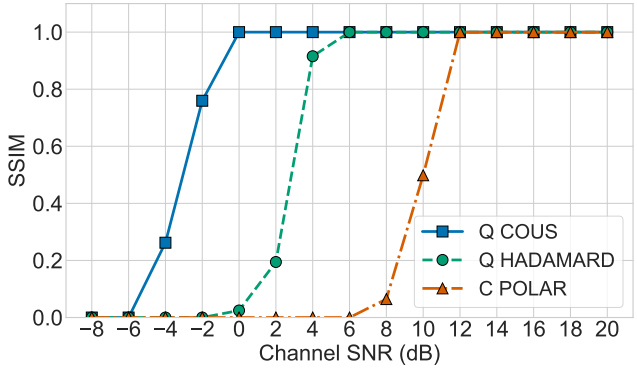


(c)

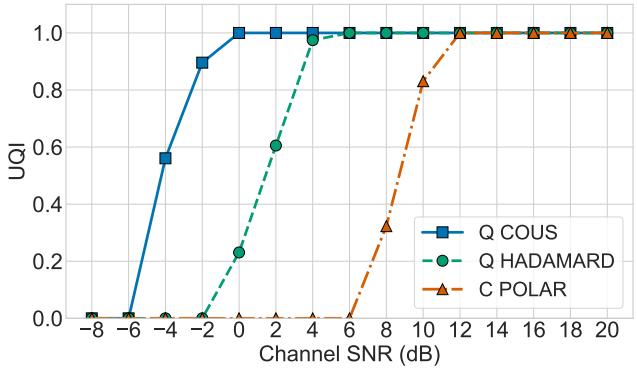
Figure A.4: Performance of HEIF QP=25 compressed image transmission evaluated using (a) PSNR, (b) SSIM, and (c) UQI, under the proposed COUS encoding-based three-qubit QEC system (Q COUS), the conventional Hadamard encoding-based three-qubit QEC system (Q HADAMARD), and the classical polar-coded system (C POLAR).



(a)



(b)



(c)

Figure A.5: Performance of HEIF QP=100 compressed image transmission evaluated using (a) PSNR, (b) SSIM, and (c) UQI, under the proposed COUS encoding-based three-qubit QEC system (Q COUS), the conventional Hadamard encoding-based three-qubit QEC system (Q HADAMARD), and the classical polar-coded system (C POLAR).

Appendix B

Derivation of the COUS Gate Decomposition

The COUS gate G_{COUS} defined in (6.8) can be expressed as a sequence of standard single-qubit gates: $G_{\mathrm{COUS}} = S \cdot H \cdot S$. This appendix derives the decomposition explicitly.

The phase gate S and the Hadamard gate H are defined as in (B.1) and (B.2), respectively.

$$S = \begin{pmatrix} 1 & 0 \\ 0 & i \end{pmatrix} \tag{B.1}$$

$$H = \frac{1}{\sqrt{2}} \begin{pmatrix} 1 & 1 \\ 1 & -1 \end{pmatrix} \tag{B.2}$$

Computing $S \cdot H$ yields the intermediate matrix in (B.3).

$$S \cdot H = \frac{1}{\sqrt{2}} \begin{pmatrix} 1 & 1 \\ i & -i \end{pmatrix} \tag{B.3}$$

Right-multiplying by S gives the final result in (B.4).

$$(S \cdot H) \cdot S = \frac{1}{\sqrt{2}} \begin{pmatrix} 1 & i \\ i & 1 \end{pmatrix} = G_{\mathrm{COUS}} \tag{B.4}$$

This confirms that G_{COUS} admits the decomposition $S \cdot H \cdot S$ using only standard single-qubit gates, which are native to most quantum hardware platforms including superconducting qubits, trapped ions, and photonic systems. The total per-qubit gate count is therefore three, and since these gates are applied sequentially on a single qubit, the per-qubit circuit depth is also three. For a k-qubit COUS encoder, the gates act independently on each qubit, allowing parallel execution across qubits; consequently, the overall circuit depth remains constant ($\mathcal{O}(1)$) with respect to the qubit count k, while the total gate count scales linearly as $3k$.

References

[1] Cisco Systems, "Cisco annual internet report (2018–2023) white paper," Cisco, San Jose, CA, USA, Tech. Rep. C11-741490, 2020. [Online]. Available: https://www.cisco.com/c/en/us/solutions/collateral/executive-perspectives/annual-internet-report/white-paper-c11-741490.html

[2] Ericsson, "Ericsson mobility report," Stockholm, Sweden, Nov. 2023, accessed: 2025-05-20. [Online]. Available: https://www.ericsson.com/en/reports-and-papers/mobility-report

[3] N. Batra and B. Singh, "A study of automatic modulation classification for rayleigh fading channel," in *2021 IEEE Bombay Section Signature Conference (IBSSC)*, 2021, pp. 1–4.

[4] B. Fong, G. Hong, and A. Fong, "Constrained error propagation for efficient image transmission over noisy channels," *IEEE Transactions on Consumer Electronics*, vol. 48, no. 1, pp. 49–55, 2002.

[5] B. Tahir, S. Schwarz, and M. Rupp, "Ber comparison between convolutional, turbo, ldpc, and polar codes," in *2017 24th International Conference on Telecommunications (ICT)*, 2017, pp. 1–7.

[6] A. C. Vaz, C. G. Nayak, D. Nayak, and N. T. Hegde, "Performance analysis of forward error correcting codes in a visible light communication system," in *Proceedings of the 2021 IEEE International Conference on Electronics, Computing and Communication Technologies (CONECCT)*, 2021, pp. 1–5.

[7] M. Zhang, "Major automatic repeat request protocols generalization and future develop direction," in *2013 6th International Conference on Information Man-*

agement, Innovation Management and Industrial Engineering, vol. 2, 2013, pp. 5–8.

[8] Z. Jiawei, D. Mengxue, L. Jianyu, Y. Yahong, and X. Duo, "Improved automatic repeat request (arq) - retransmission using index coding," in *2025 IEEE 12th Joint International Information Technology and Artificial Intelligence Conference (ITAIC)*, vol. 12, 2025, pp. 619–623.

[9] Y. Wang, W. Liu, and L. Fang, "Adaptive modulation and coding technology in 5g system," in *2020 International Wireless Communications and Mobile Computing (IWCMC)*, 2020, pp. 159–164.

[10] H. Gu, N. Guo, T. Xue, and Q. Zhang, "Adaptive modulation and coding techniques based on reinforcement learning," in *Proceedings of the 16th International Conference on Wireless Communications and Signal Processing (WCSP)*, Hefei, China, 2024, pp. 863–868.

[11] G. Wallace, "The jpeg still picture compression standard," *IEEE Transactions on Consumer Electronics*, vol. 38, no. 1, pp. xviii–xxxiv, 1992.

[12] M. M. Hannuksela, J. Lainema, and V. K. Malamal Vadakital, "The high efficiency image file format standard [standards in a nutshell]," *IEEE Signal Processing Magazine*, vol. 32, no. 4, pp. 150–156, 2015.

[13] G. J. Sullivan, J.-R. Ohm, W.-J. Han, and T. Wiegand, "Overview of the high efficiency video coding (hevc) standard," *IEEE Transactions on Circuits and Systems for Video Technology*, vol. 22, no. 12, pp. 1649–1668, 2012.

[14] B. Bross, Y.-K. Wang, Y. Ye, S. Liu, J. Chen, G. J. Sullivan, and J.-R. Ohm, "Overview of the versatile video coding (vvc) standard and its applications," *IEEE Transactions on Circuits and Systems for Video Technology*, vol. 31, no. 10, pp. 3736–3764, 2021.

[15] P. Rosedale, "Virtual reality: The next disruptor: A new kind of world wide communication," *IEEE Consum. Electron. Mag.*, vol. 6, no. 1, pp. 48–50, Jan. 2017.

[16] D. Jo and G. J. Kim, "Ariot: scalable augmented reality framework for interacting with internet of things appliances everywhere," *IEEE Trans. on Consum. Electron.*, vol. 62, no. 3, p. 334–340, Aug. 2016. [Online]. Available: https://doi.org/10.1109/TCE.2016.7613201

[17] R. Albert, A. Patney, D. Luebke, and J. Kim, "Latency requirements for foveated rendering in virtual reality," *ACM Transactions on Applied Perception*, vol. 14, no. 4, pp. 1–13, 2017.

[18] G. Arun and V. Mishra, "A review on quantum computing and communication," in *2014 2nd International Conference on Emerging Technology Trends in Electronics, Communication and Networking*, Surat, India, 2014, pp. 1–5.

[19] L. E. Ballentine, *Quantum Mechanics: A Modern Development*, 2nd ed. Singapore: World Scientific Publishing Company, 2014.

[20] I. B. Djordjevic, *Quantum Communication, Quantum Networks, and Quantum Sensing.* Tucson, AZ, United States: Academic Press, 2022.

[21] G. T. Sridhar, A. P, and N. Tabassum, "A review on quantum communication and computing," in *2023 2nd International Conference on Applied Artificial Intelligence and Computing (ICAAIC)*, Salem, India, 2023, pp. 1592–1596.

[22] M. A. Shafique, A. Munir, and I. Latif, "Quantum computing: Circuits, algorithms, and applications," *IEEE Access*, vol. 12, pp. 22 296–22 314, 2024.

[23] A. I. Nurhadi and N. R. Syambas, "Quantum key distribution (qkd) protocols: A survey," in *2018 4th International Conference on Wireless and Telematics (ICWT)*, 2018, pp. 1–5. [Online]. Available: https://doi.org/10.1109/ICWT.2018.8527822

[24] T. Miyadera and H. Imai, "No-cloning theorem on quantum logics," *Journal of Mathematical Physics*, vol. 50, no. 10, p. 102107, October 2009. [Online]. Available: https://doi.org/10.1063/1.3245811

[25] N. Ul Ain, M. Waqar, A. Bilal, A. Kim, H. Ali, U. Ullah Tariq, and M. Shahroz Nadeem, "A novel approach based on quantum key distribution

using bb84 and e91 protocol for resilient encryption and eavesdropper detection," *IEEE Access*, vol. 13, pp. 32 819–32 833, 2025.

[26] M. F. Zulfa and K. Anwar, "Development of quantum key distribution (qkd) with e91 protocol for future secure quantum networks," in *Journal of Physics: Conference Series*, vol. 2980. IOP Publishing, 2025, p. 012038.

[27] M. Mehic, L. Michalek, E. Dervisevic, P. Burdiak, M. Plakalovic, J. Rozhon, N. Mahovac, F. Richter, E. Kaljic, F. Lauterbach, P. Njemcevic, A. Maric, M. Hamza, P. Fazio, and M. Voznak, "Quantum cryptography in 5g networks: A comprehensive overview," *IEEE Communications Surveys & Tutorials*, vol. 26, no. 1, pp. 302–346, 2024.

[28] P. Q. Le, F. Dong, and K. Hirota, "A flexible representation of quantum images for polynomial preparation, image compression, and processing operations," *Quantum Information Processing*, vol. 10, no. 1, pp. 63–84, 2011.

[29] S. Valsalam and T. Thomas, "Cnn with neqr encoding for quantum-classical hybrid image compression," in *ICT for Intelligent Systems*, ser. Lecture Notes in Networks and Systems, J. Choudrie, P. N. Mahalle, T. Perumal, and A. Joshi, Eds. Singapore: Springer, 2026, vol. 1507. [Online]. Available: https://doi.org/10.1007/978-981-96-8750-3_43

[30] G. Beach, C. Lomont, and C. Cohen, "Quantum image processing (quip)," in *32nd Applied Imagery Pattern Recognition Workshop, 2003. Proceedings.*, 2003, pp. 39–44.

[31] M. Pivoluska and M. Plesch, "Implementation of quantum compression on ibm quantum computers," *Scientific Reports*, vol. 12, no. 1, p. 5841, 2022. [Online]. Available: https://doi.org/10.1038/s41598-022-09881-8

[32] Y. Qiu, T. Li, J. Cui, Y. Wang, K. Zhang, and Y. Su, "Quantum watermarking scheme based on DNA encoding and quantum error correction," *Journal of King Saud University - Computer and Information Sciences*, vol. 38, no. 8, pp. 1–20, 2026, article no. 8.

[33] A.Arulmurugan, M. S. K, and P. Mahesh, "Encryption and decryption in quantum cryptography," in *2025 3rd International Conference on Self Sustainable Artificial Intelligence Systems (ICSSAS)*, 2025, pp. 1348–1353.

[34] A. Kwasinski and V. Chande, "Source coding and signal compression," in *Joint Source-Channel Coding*, A. Kwasinski and V. Chande, Eds. Wiley, 2022, ch. 2. [Online]. Available: https://doi.org/10.1002/9781118693803.ch2

[35] N. Ahamed, N. B, and S. R, "Classification of channel encoders using convolutional neural network," in *2024 16th International Conference on COMmunication Systems & NETworkS (COMSNETS)*, 2024, pp. 590–593.

[36] A. Viterbi, "Convolutional codes and their performance in communication systems," *IEEE Transactions on Communication Technology*, vol. 19, no. 5, pp. 751–772, 1971.

[37] C. Berrou, R. Pyndiah, P. Adde, C. Douillard, and R. Le Bidan, "An overview of turbo codes and their applications," in *The European Conference on Wireless Technology, 2005.*, 2005, pp. 1–9.

[38] R. Gallager, "Low-density parity-check codes," *IRE Transactions on Information Theory*, vol. 8, no. 1, pp. 21–28, 1962.

[39] E. Arikan, "Systematic polar coding," *IEEE Communications Letters*, vol. 15, no. 8, pp. 860–862, 2011.

[40] E. Krouk and S. Semenov, *Modulation and Coding Techniques in Wireless Communications*. Wiley, 2011. [Online]. Available: https://books.google.co.uk/books?id=q3HREAAAQBAJ

[41] R. Karnani and P. Singh, "An improved performance and efficiency of the system by using bpsk modulation for wireless communication," in *2023 IEEE 4th Annual Flagship India Council International Subsections Conference (INDISCON)*, 2023, pp. 1–6.

[42] T. D. Memon, W. Ghangro, B. Chowdhry, and A. A. shaikh, "Quadrature phase shift keying modulator & demodulator for wireless modem," in *2009 2nd*

International Conference on Computer, Control and Communication, 2009, pp. 1–6.

[43] O. Solomentsev, M. Zaliskyi, R. Odarchenko, and S. Gnatyuk, "Research of energy characteristics of qam modulation techniques for modern broadband radio systems," in *2016 International Conference on Electronics and Information Technology (EIT)*, 2016, pp. 1–6.

[44] C. Yu, C.-H. Sung, C.-H. Kuo, M.-H. Yen, and S.-J. Chen, "Design and implementation of a low-power ofdm receiver for wireless communications," *IEEE Transactions on Consumer Electronics*, vol. 58, no. 3, pp. 739–745, 2012.

[45] Y. Hou and T. Hase, "New flexible ofdm structure for consumer electronics communication systems," *IEEE Transactions on Consumer Electronics*, vol. 55, no. 1, pp. 191–198, 2009.

[46] Shekhar, A. Singhal, R. Sharma, and P. Singh, "Study of analysis of multiple input and multiple outputs (mimo) technology in wireless communication," in *2016 International Conference on Micro-Electronics and Telecommunication Engineering (ICMETE)*, Ghaziabad, India, 2016, pp. 658–662.

[47] L. C. Png, L. Xiao, K. S. Yeo, T. S. Wong, and Y. L. Guan, "Mimo-diversity switching techniques for digital transmission in visible light communication," in *2013 IEEE Symposium on Computers and Communications (ISCC)*. Split: IEEE, Jul. 2013, pp. 000 576–000 582.

[48] H. Harkat, P. Monteiro, A. Gameiro, F. Guiomar, and H. Farhana Thariq Ahmed, "A survey on MIMO-OFDM systems: Review of recent trends," *Signals*, vol. 3, no. 2, pp. 359–395, 2022.

[49] W.-W. Hu, "A low-complexity mimo-ofdm transmission scheme for optical wireless communications," *IEEE Access*, vol. 13, pp. 94 777–94 784, 2025.

[50] V. Goyal, "Multiple description coding: compression meets the network," *IEEE Signal Processing Magazine*, vol. 18, no. 5, pp. 74–93, 2001.

[51] N. K. Ibrahim, A. Sali, H. A. Karim, A. F. Ramli, N. S. Ibrahim, and D. Grace, "Multiple description coding for enhancing outage and video performance over relay-assisted cognitive radio networks," *IEEE Access*, vol. 10, pp. 11 750–11 762, 2022.

[52] X. Luo, H.-H. Chen, and Q. Guo, "Semantic communications: Overview, open issues, and future research directions," *IEEE Wireless Communications*, vol. 29, no. 1, pp. 210–219, 2022.

[53] G. Xin, P. Fan, and K. B. Letaief, "Semantic communication: A survey of its theoretical development," *Entropy*, vol. 26, no. 2, p. 102, 2024. [Online]. Available: https://doi.org/10.3390/e26020102

[54] C. Shannon and W. Weaver, *The Mathematical Theory of Communication*. Champaign, IL, USA: University of Illinois Press, 1949.

[55] J. Balsa, T. Domínguez-Bolaño, Ó. Fresnedo, J. A. García-Naya, and L. Castedo, "Transmission of still images using low-complexity analog joint source-channel coding," *Sensors*, vol. 19, no. 13, p. 2932, 2019. [Online]. Available: https://doi.org/10.3390/s19132932

[56] J. G. Proakis and M. Salehi, *Digital Communications*, 5th ed. New York, NY, USA: McGraw-Hill, 2008.

[57] A. Goldsmith, *Wireless Communications*. Cambridge, U.K.: Cambridge University Press, 2005.

[58] J. Hagenauer and T. Stockhammer, "Channel coding and transmission aspects for wireless multimedia," *Proceedings of the IEEE*, vol. 87, no. 10, pp. 1764–1777, 1999.

[59] M. Simon and M. Alouini, "A unified approach to the performance analysis of digital communication over generalized fading channels," *Proceedings of the IEEE*, vol. 86, no. 9, pp. 1860–1877, 1998.

[60] A. S. M. M. Jameel, A. Malhotra, A. E. Gamal, and S. Hamidi-Rad, "Deep ofdm channel estimation: Capturing frequency recurrence," *IEEE Communications Letters*, vol. 28, no. 3, pp. 562–566, 2024.

[61] K. Wang, "Design and performance analysis of ofdm systems in 5g networks," in *2024 IEEE 2nd International Conference on Sensors, Electronics and Computer Engineering (ICSECE)*, 2024, pp. 1840–1844.

[62] L. P. Qian, C. Wang, Q. Wang, M. Wu, Y. Wu, and X. Yang, "Ofdm receiver design with learning-driven automatic modulation recognition," *IEEE Transactions on Cognitive Communications and Networking*, vol. 10, no. 2, pp. 429–441, 2024.

[63] Y. Huang, K. Yan, C. Cao, L. Yuan, Y. Fang, A. Nayak, and W. Gong, "Efficient covert communication with ambient ofdm wifi backscatter," *IEEE Journal on Selected Areas in Communications*, vol. 44, pp. 1665–1674, 2026.

[64] M. F. A. Ghani, N. M. A. Latiff, S. K. S. Yusof, R. A. Rashid, N. N. N. A. Malik, and K. M. Yusof, "Video transmission based on orthogonal frequency division multiplexing (ofdm) utilizing television white space," in *2017 IEEE 13th Malaysia International Conference on Communications (MICC)*, 2017, pp. 152–157.

[65] H. Wu, Y. Shao, K. Mikolajczyk, and D. Gündüz, "Channel-adaptive wireless image transmission with ofdm," *IEEE Wireless Communications Letters*, vol. 11, no. 11, pp. 2400–2404, 2022.

[66] S. P. Paul and D. Vetrithangam, "A thorough assessment on orthogonal frequency division multiplexing (ofdm) based wireless communication: Challenges and interpretation," in *2023 International Conference on Sustainable Computing and Smart Systems (ICSCSS)*, 2023, pp. 1145–1151.

[67] V. K. Sachan, A. Gupta, and A. Kumar, "Performance analysis of mimo space diversity technique for wireless communications," in *2008 Fourth International Conference on Wireless Communication and Sensor Networks*. Indore, India: IEEE, Dec. 2008, pp. 153–156.

[68] O. Elijah, S. K. Abdul Rahim, W. K. New, C. Y. Leow, K. Cumanan, and T. Kim Geok, "Intelligent massive mimo systems for beyond 5g networks: An overview and future trends," *IEEE Access*, vol. 10, pp. 102 532–102 563, 2022.

[69] L. Mohandas and V. Bhaskar, "Performance analysis of mimo transmission modes in an lte system," in *IET Chennai Fourth International Conference on Sustainable Energy and Intelligent Systems (SEISCON 2013)*, 2013, pp. 548–553.

[70] S. K. Mahto, A. K. Singh, R. Sinha, M. Alibakhshikenari, S. Khan, and G. Pau, "High isolated four element mimo antenna for ism/lte/5g (sub-6ghz) applications," *IEEE Access*, vol. 11, pp. 82 946–82 959, 2023.

[71] C. Pan, S. Chen, W. Wu, J. Qian, and L. Wang, "Research on space-time block code technology in mimo system," in *2021 7th International Conference on Computer and Communications (ICCC)*, 2021, pp. 1875–1879.

[72] S. Alamouti, "A simple transmit diversity technique for wireless communications," *IEEE Journal on Selected Areas in Communications*, vol. 16, no. 8, pp. 1451–1458, 1998.

[73] A. Krishnamoorthy and R. Schober, "Downlink massive mu-mimo with successively-regularized zero forcing precoding," *IEEE Wireless Communications Letters*, vol. 12, no. 1, pp. 114–118, 2023.

[74] M. Bashar, P. Xiao, R. Tafazolli, K. Cumanan, A. G. Burr, and E. Björnson, "Limited-fronthaul cell-free massive mimo with local mmse receiver under rician fading and phase shifts," *IEEE Wireless Communications Letters*, vol. 10, no. 9, pp. 1934–1938, 2021.

[75] P. Patil, M. R. Patil, S. Itraj, and U. L. Bomble, "A review on mimo ofdm technology basics and more," in *2017 International Conference on Current Trends in Computer, Electrical, Electronics and Communication (CTCEEC)*, 2017, pp. 119–124.

[76] Y. Li, J. Winters, and N. Sollenberger, "Mimo-ofdm for wireless communications: signal detection with enhanced channel estimation," *IEEE Transactions on Communications*, vol. 50, no. 9, pp. 1471–1477, 2002.

[77] M. Yazgan, H. Arslan, and S. Vakalis, "Mimo-ofdm imaging using shared time and bandwidth," *IEEE Open Journal of the Communications Society*, vol. 6, pp. 4885–4893, 2025.

[78] M. J. Zakavi, S. A. Nezamalhosseini, and L. R. Chen, "Multiuser massive mimo-ofdm for visible light communication systems," *IEEE Access*, vol. 11, pp. 2259–2273, 2023.

[79] Z. Z. Abdulhameed and S. J. Mohammed, "Performance lte downlink based on mimo-ofdm," in *2024 3rd International Conference on Advances in Engineering Science and Technology (AEST)*, 2024, pp. 142–147.

[80] Z. S. Hammed, S. Y. Ameen, and S. R. M. Zeebaree, "Massive mimo-ofdm performance enhancement on 5g," in *2021 International Conference on Software, Telecommunications and Computer Networks (SoftCOM)*, 2021, pp. 1–6.

[81] B. Li, C. Ju, H. Yang, and G. Liu, "Adaptive coded modulation based on ldpc codes," in *2015 10th International Conference on Communications and Networking in China (ChinaCom)*, 2015, pp. 648–651.

[82] K. M. S. Soyjaudah and B. Rajkumarsingh, "Adaptive coding and modulation using reed solomon codes for rayleigh fading channels," in *EUROCON 2001. International Conference on Trends in Communications, Technical Program, Proceedings (Cat. No.01EX439)*, vol. 1, 2001, pp. 50–53.

[83] E. Armanious, D. D. Falconer, and H. Yanikomeroglu, "Adaptive modulation, adaptive coding, and power control for fixed cellular broadband wireless systems: some new insights," in *2003 IEEE Wireless Communications and Networking, WCNC 2003*, vol. 1, 2003, pp. 238–242.

[84] L. Muchen, X. Jin, and S. Goto, "Adaptive coding based on a new slice type in surveillance systems," in *2011 IEEE 7th International Colloquium on Signal Processing and its Applications*, 2011, pp. 151–154.

[85] M. Kazemi, S. Shirmohammadi, and K. H. Sadeghi, "A review of multiple description coding techniques for error-resilient video delivery," *Multimedia Systems*, vol. 20, no. 3, pp. 283–309, 2014.

[86] X. Hu, Y. Pan, Y. Wang, L. Zhang, and S. Shirmohammadi, "Multiple description coding for best-effort delivery of light field video using gnn-based compression," *IEEE Transactions on Multimedia*, vol. 25, pp. 690–705, 2023.

[87] D. Gündüz, Z. Qin, I. E. Aguerri, H. S. Dhillon, Z. Yang, A. Yener, K. K. Wong, and C.-B. Chae, "Beyond transmitting bits: Context, semantics, and task-oriented communications," *IEEE Journal on Selected Areas in Communications*, vol. 41, no. 1, pp. 5–41, 2023.

[88] H. Xie, Z. Qin, G. Y. Li, and B.-H. Juang, "Deep learning enabled semantic communication systems," *IEEE Transactions on Signal Processing*, vol. 69, pp. 2663–2678, 2021.

[89] W. Chen, J. Li, M. Fu, P. Zhou, S. Li, C. Zhang, M. Zhang, and D. Wang, "Semantic communication for image transmission in intra-datacenter optical interconnects," in *2023 21st International Conference on Optical Communications and Networks (ICOCN)*, 2023, pp. 1–3.

[90] J. Zhang, Y. Zhang, B. Ji, A. Chen, A. Liu, and H. Xu, "Feature-driven semantic communication for efficient image transmission," *Entropy*, vol. 27, no. 4, p. 369, 2025. [Online]. Available: https://doi.org/10.3390/e27040369

[91] M. U. Lokumarambage, V. S. S. Gowrisetty, H. Rezaei, T. Sivalingam, N. Rajatheva, and A. Fernando, "Wireless end-to-end image transmission system using semantic communications," *IEEE Access*, vol. 11, pp. 37 149–37 163, 2023.

[92] C. Liang, X. Deng, Y. Sun, R. Cheng, L. Xia, D. Niyato, and M. A. Imran, "Vista: Video transmission over a semantic communication approach," in *2023 IEEE International Conference on Communications Workshops (ICC Workshops)*, 2023, pp. 1777–1782.

[93] P. Samarathunga, Y. Ganearachchi, T. Fernando, J. Adhuran, T. Sivalingam, N. Rajatheva, and A. Fernando, "Enhanced semantic communications and vvc-based hybrid video coding system," *IEEE Access*, vol. PP, pp. 1–1, 01 2026.

[94] P. Samarathunga, Y. Ganearachchi, T. Fernando, A. Jayasingam, T. Sivalingam, N. Rajatheva, and A. Fernando, "Context-aware semantic video coding using

pretrained motion-adaptive models and bidirectional prediction," *IEEE Access*, vol. 14, pp. 69 730–69 755, 2026.

[95] P. Samarathunga, N. Pollwaththage, T. Fernando, U. Jayasinghe, N. Ihalagamage, Y. Ganearachchi, and A. Fernando, "Semantic and technical noise modeling in semantic image communication over wireless channels," *IEEE Access*, vol. PP, pp. 1–1, 01 2025.

[96] D. J. Griffiths and D. F. Schroeter, *Introduction to Quantum Mechanics*, 3rd ed. Cambridge: Cambridge University Press, 2018.

[97] J. J. Sakurai and J. Napolitano, *Modern Quantum Mechanics*, 3rd ed. Cambridge: Cambridge University Press, 2020.

[98] S. M. Sze and K. K. Ng, *Physics of Semiconductor Devices*, 3rd ed. John Wiley & Sons, 2007.

[99] J. Preskill, "Quantum computing in the nisq era and beyond," *Quantum*, vol. 2, p. 79, 2018.

[100] W. Wootters and W. Zurek, "A single quantum cannot be cloned," *Nature*, vol. 299, pp. 802–803, 1982.

[101] Q. Inspire, "Qubits - quantum inspire knowledge base," 2024, accessed: October 12, 2024. [Online]. Available: https://www.quantum-inspire.com/kbase/qubits/

[102] C. Hughes, J. Isaacson, A. Perry, R. Sun, and J. Turner, "Introduction to superposition," in *Quantum Computing for the Quantum Curious*. Cham: Springer, 2021.

[103] J. Malhotra, O. Chavan, and P. Thakur, "Grover algorithm: Enhancing the search mechanism," in *2025 4th OPJU International Technology Conference (OTCON) on Smart Computing for Innovation and Advancement in Industry 5.0*, 2025, pp. 1–8.

[104] S. Mishra, O. Agarwal, and S. K. Patel, "Quantum decryption using shor's algorithm," in *2024 IEEE Pune Section International Conference (PuneCon)*, 2024, pp. 1–6.

[105] L. Gouba, "Role of qubits in quantum entanglement and quantum teleportation," *Mathematics*, vol. 13, no. 17, p. 2857, 2025.

[106] N. Zou, "Quantum entanglement and its application in quantum communication," *Journal of Physics: Conference Series*, vol. 1827, p. 012120, 2021, paper • Open Access.

[107] D. R. Bes, *Quantum Mechanics: A Modern and Concise Introductory Course*. Berlin, Heidelberg: Springer Berlin Heidelberg, 2012. [Online]. Available: https://doi.org/10.1007/978-3-642-20556-9

[108] S. Sarkar, "Quantum logic gates: A detailed theoretical study of the hadamard gate," *International Research Journal of Modernization in Engineering Technology and Science*, vol. 2, pp. 884–892, May 2020.

[109] A. Sharma and M. J. Nene, "Quantum information transmission using cnot gate," in *Recent Trends in Intensive Computing*, ser. Advances in Parallel Computing. IOS Press, 2026.

[110] ShareTechnote, "Quantum computing - pauli-x,y,z," https://www.sharetechnote.com/html/QC/QuantumComputing_Gate_X.html, accessed: 2024-10-12.

[111] McKinsey and Company, "What is quantum computing?" *McKinsey Explainers*, 2023, accessed: 12-October-2024. [Online]. Available: https://www.mckinsey.com/featured-insights/mckinsey-explainers/what-is-quantum-computing

[112] J. Chen, "Review on quantum communication and quantum computation," *Journal of Physics: Conference Series*, vol. 1865, no. 2, p. 022008, April 2021. [Online]. Available: https://dx.doi.org/10.1088/1742-6596/1865/2/022008

[113] P. Krantz, M. Kjaergaard, F. Yan, T. P. Orlando, S. Gustavsson, and W. D. Oliver, "A quantum engineer's guide to superconducting qubits," *Applied Physics Reviews*, vol. 6, no. 2, p. 021318, 6 2019. [Online]. Available: https://doi.org/10.1063/1.5089550

[114] C. D. Bruzewicz, J. Chiaverini, R. McConnell, and J. M. Sage, "Trapped-ion quantum computing: Progress and challenges," *Applied Physics Reviews*, vol. 6, no. 2, p. 021314, 2019.

[115] S. Slussarenko and G. J. Pryde, "Photonic quantum information processing: A concise review," *Applied Physics Reviews*, vol. 6, no. 4, p. 041303, 12 2019. [Online]. Available: https://doi.org/10.1063/1.5115814

[116] S. Sunami, S. Tamiya, R. Inoue, H. Yamasaki, and A. Goban, "Scalable networking of neutral-atom qubits: Nanofiber-based approach for multiprocessor fault-tolerant quantum computers," *PRX Quantum*, vol. 6, p. 010101, Feb 2025. [Online]. Available: https://link.aps.org/doi/10.1103/PRXQuantum.6.010101

[117] G. Burkard, T. D. Ladd, A. Pan, J. M. Nichol, and J. R. Petta, "Semiconductor spin qubits," *Rev. Mod. Phys.*, vol. 95, p. 025003, Jun 2023. [Online]. Available: https://link.aps.org/doi/10.1103/RevModPhys.95.025003

[118] Qiskit contributors, "Qiskit: An open-source framework for quantum computing," 2023.

[119] K. Bharti, A. Cervera-Lierta, T. H. Kyaw, T. Haug, S. Alperin-Lea, A. Anand, M. Degroote, H. Heimonen, J. S. Kottmann, T. Menke, W.-K. Mok, S. Sim, L.-C. Kwek, and A. Aspuru-Guzik, "Noisy intermediate-scale quantum algorithms," *Rev. Mod. Phys.*, vol. 94, p. 015004, Feb 2022. [Online]. Available: https://link.aps.org/doi/10.1103/RevModPhys.94.015004

[120] B. M. Terhal, "Quantum error correction for quantum memories," *Rev. Mod. Phys.*, vol. 87, pp. 307–346, Apr 2015. [Online]. Available: https://link.aps.org/doi/10.1103/RevModPhys.87.307

[121] T. Janani and M. Brindha, "A secure medical image transmission scheme aided by quantum representation," *Journal of Information Security and Applications*, vol. 59, p. 102832, Jun. 2021.

[122] S. Johnson, J. Rarity, and M. Padgett, "Transmission of quantum-secured images," *Scientific Reports*, vol. 14, no. 1, p. 11579, May 2024.

[123] S. V. Bezzateev, S. G. Fomicheva, and G. A. Zhemelev, "Quantum control mechanisms of superdense coding," in *2022 Wave Electronics and its Application in Information and Telecommunication Systems (WECONF)*, 2022, pp. 1–7.

[124] J. M. Lukens, N. A. Peters, and B. Qi, "Hybrid classical–quantum communication networks," *Progress in Quantum Electronics*, vol. 103, p. 100586, 2025.

[125] A. Peruzzo, J. McClean, P. Shadbolt, M.-H. Yung, X.-Q. Zhou, P. J. Love, A. Aspuru-Guzik, and J. L. O'Brien, "A variational eigenvalue solver on a photonic quantum processor," *Nature Communications*, vol. 5, p. 4213, 2014.

[126] M. Cerezo, A. Arrasmith, R. Babbush, S. C. Benjamin, S. Endo, K. Fujii, J. R. McClean, K. Mitarai, X. Yuan, L. Cincio, and P. J. Coles, "Variational quantum algorithms," *Nature Reviews Physics*, vol. 3, no. 9, pp. 625–644, 2021.

[127] M. A. Nielsen and I. L. Chuang, *Quantum Computation and Quantum Information: 10th Anniversary Edition*. Cambridge University Press, 2010.

[128] V. S. Thakur, A. Kumar, J. Das, K. Dev, and M. Magarini, "Quantum error correction codes in consumer technology: Modeling and analysis," *IEEE Transactions on Consumer Electronics*, vol. 70, no. 4, pp. 7102–7111, 2024.

[129] J. Roffe, "Quantum error correction: an introductory guide," *Contemporary Physics*, vol. 60, pp. 226–245, 2019.

[130] M. Gong, X. Yuan, S. Wang, Y. Wu, Y. Zhao, C. Zha, S. Li, Z. Zhang, Q. Zhao, Y. Liu, F. Liang, J. Lin, Y. Xu, H. Deng, H. Rong, H. Lu, S. C. Benjamin, C.-Z. Peng, X. Ma, Y.-A. Chen, X. Zhu, and J.-W. Pan, "Experimental exploration of five-qubit quantum error-correcting code with superconducting qubits," *National Science Review*, vol. 9, no. 1, p. nwab011, 01 2021.

[131] P. W. Shor, "Scheme for reducing decoherence in quantum computer memory," *Phys. Rev. A*, vol. 52, pp. R2493–R2496, Oct 1995.

[132] A. M. Steane, "Simple quantum error-correcting codes," *Phys. Rev. A*, vol. 54, pp. 4741–4751, Dec 1996.

[133] K. R. Colladay and E. J. Mueller, "Rewiring stabilizer codes," *New Journal of Physics*, vol. 20, p. 083030, 2018.

[134] Z. Zhou, A. Ji, and Y. Ding, "Surface code error correction with crosstalk noise," in *2025 IEEE International Conference on Quantum Computing and Engineering (QCE)*, vol. 01, 2025, pp. 627–636.

[135] T. Coopmans, R. Knegjens, A. Dahlberg, D. Maier, L. Nijsten, J. de Oliveira Filho, M. Papendrecht, J. Rabbie, F. Rozpedek, M. Skrzypczyk, L. Wubben, W. de Jong, D. Podareanu, A. Torres-Knoop, D. Elkouss, and S. Wehner, "NetSquid: A NETwork simulator for QUantum information using discrete events," *Communications Physics*, vol. 4, no. 1, p. 164, 2021.

[136] X. Wu, A. Kolar, J. Chung, D. Jin, T. Zhong, R. Kettimuthu, and M. Suchara, "Sequence: A customizable discrete-event simulator of quantum networks," *Quantum Science and Technology*, vol. 6, no. 4, p. 045027, sep 2021.

[137] R. Satoh, M. Hajdušek, N. Benchasattabuse, S. Nagayama, K. Teramoto, T. Matsuo, S. A. Metwalli, P. Pathumsoot, T. Satoh, S. Suzuki, and R. V. Meter, "Quisp: a quantum internet simulation package," in *2022 IEEE International Conference on Quantum Computing and Engineering (QCE)*, 2022, pp. 353–364.

[138] A. Dahlberg and S. Wehner, "Simulaqron—a simulator for developing quantum internet software," *Quantum Science and Technology*, vol. 4, no. 1, p. 015001, jan 2019.

[139] S. Diadamo, J. Nötzel, B. Zanger, and M. M. Beşe, "Qunetsim: A software framework for quantum networks," *IEEE Transactions on Quantum Engineering*, vol. 2, pp. 1–12, 2021.

[140] C. Developers, "Cirq," Jun. 2026. [Online]. Available: https://doi.org/10.5281/zenodo.21080138

[141] E. Osaba, E. Villar-Rodriguez, and I. Oregi, "A systematic literature review of quantum computing for routing problems," *IEEE Access*, vol. 10, pp. 55 805–55 817, 2022.

[142] Google, "Google willow quantum chip," 2025, accessed: 2025-02-02. [Online]. Available: https://blog.google/technology/research/google-willow-quantum-chip/

[143] T. Barros, P. Álvarez, B. Vidal, and M. Solar, "A review on quantum fourier transform," *Quantum Information Processing*, vol. 25, p. 41, 2026.

[144] F. Montalfu, S. Al Abdul Wahid, F. Mohammadi, and A. Asad, "Simulation of quantum discrete cosine transform for grayscale image compression using qiskit," *IEEE Access*, vol. 13, pp. 199 064–199 073, 2025.

[145] H.-S. Li, P. Fan, H. Peng, S. Song, and G.-L. Long, "Multilevel 2-d quantum wavelet transforms," *IEEE Transactions on Cybernetics*, vol. 52, no. 8, pp. 8467–8480, 2022.

[146] A. Mahmoud As'Ad Alnaser, H. M. S. Hatamleh, N. A. Almolhis, S. Duraibi, and Y. Alqahtani, "Secure quantum communication with multi-users in quantum networks," *IEEE Open Journal of the Communications Society*, vol. 6, pp. 2397–2419, 2025.

[147] P.-Y. Kong, "Uav-assisted quantum key distribution for secure communications with resource limited devices," *IEEE Transactions on Vehicular Technology*, vol. 73, no. 8, pp. 11 923–11 933, 2024.

[148] A. S. Cacciapuoti, M. Caleffi, R. Van Meter, and L. Hanzo, "When entanglement meets classical communications: Quantum teleportation for the quantum internet," *IEEE Transactions on Communications*, vol. 68, no. 6, pp. 3808–3833, 2020.

[149] B. Narottama and S. Y. Shin, "Federated quantum neural network with quantum teleportation for resource optimization in future wireless communication," *IEEE Transactions on Vehicular Technology*, vol. 72, no. 11, pp. 14 717–14 733, 2023.

[150] Z. Qu, X. Fu, L. Sun, and G. Muhammad, "Qdicp: A quantum blockchain model for copyright protection of digital images in consumer electronics," *IEEE Transactions on Consumer Electronics*, vol. 71, no. 2, pp. 5189–5200, 2025.

[151] Y. Hariprasad, S. Iyengar, and N. K. Chaudhary, "Securing the future: Advanced encryption for quantum-safe video transmission," *IEEE Transactions on Consumer Electronics*, vol. 71, no. 1, pp. 140–153, 2025.

[152] A. Feix, M. Araújo, and Č. Brukner, "Quantum superposition of the order of parties as a communication resource," *Phys. Rev. A*, vol. 92, p. 052326, Nov 2015. [Online]. Available: https://link.aps.org/doi/10.1103/PhysRevA.92.052326

[153] P. A. Guérin, A. Feix, M. Araújo, and Č. Brukner, "Exponential communication complexity advantage from quantum superposition of the direction of communication," *Physical Review Letters*, vol. 117, no. 10, p. 100502, 2016. [Online]. Available: https://doi.org/10.1103/PhysRevLett.117.100502

[154] F. Del Santo and B. Dakić, "Coherence equality and communication in a quantum superposition," *Phys. Rev. Lett.*, vol. 124, p. 190501, May 2020. [Online]. Available: https://link.aps.org/doi/10.1103/PhysRevLett.124.190501

[155] S. Salek, D. Ebler, and G. Chiribella, "Quantum communication in a superposition of causal orders," *arXiv preprint arXiv:1809.06655*, 2018. [Online]. Available: https://doi.org/10.48550/arXiv.1809.06655

[156] K. Goswami, Y. Cao, G. A. Paz-Silva, J. Romero, and A. G. White, "Increasing communication capacity via superposition of order," *Phys. Rev. Res.*, vol. 2, p. 033292, Aug 2020. [Online]. Available: https://link.aps.org/doi/10.1103/PhysRevResearch.2.033292

[157] S. S. Zhou, T. Loke, J. A. Izaac *et al.*, "Quantum fourier transform in computational basis," *Quantum Information Processing*, vol. 16, p. 82, 2017.

[158] T. K. Patel, D. Knutson, G. Uehara, F. Marfai, C. Jazwin, J. Larson, and A. Spanias, "Image analysis-synthesis using the quantum fourier transform," in *2025 IEEE International Symposium on Circuits and Systems (ISCAS)*, 2025, pp. 1–5.

[159] S. Chakraborty, S. H. Shaikh, A. Chakrabarti, and et al., "An image denoising technique using quantum wavelet transform," *International Journal*

of Theoretical Physics, vol. 59, pp. 3348–3371, 2020. [Online]. Available: https://doi.org/10.1007/s10773-020-04590-2

[160] A. Fijany and C. P. Williams, "Quantum wavelet transforms: Fast algorithms and complete circuits," in *Quantum Computing and Quantum Communications*, ser. Lecture Notes in Computer Science, C. P. Williams, Ed., vol. 1509. Berlin, Heidelberg: Springer, 1999, pp. 10–33.

[161] G. Wang, W. Zhao, P. Zou *et al.*, "Quantum image edge detection based on haar wavelet transform," *Quantum Information Processing*, vol. 23, p. 302, 2024.

[162] M. Reed, L. DiCarlo, S. Nigg, L. Sun, L. Frunzio, S. Girvin, and R. Schoelkopf, "Realization of three-qubit quantum error correction with superconducting circuits," *Nature*, vol. 482, pp. 382–5, 02 2012.

[163] C.-P. Yang and J. Gea-Banacloche, "Three-qubit quantum error-correction scheme for collective decoherence," *Phys. Rev. A*, vol. 63, p. 022311, Jan 2001.

[164] D. Ristè, S. Poletto, M. Z. Huang, A. Bruno, V. Vesterinen, O. P. Saira, and L. DiCarlo, "Detecting bit-flip errors in a logical qubit using stabilizer measurements," *Nature Communications*, vol. 6, p. 6983, April 2015.

[165] A. V. Antipov, E. O. Kiktenko, and A. K. Fedorov, "Realizing a class of stabilizer quantum error correction codes using a single ancilla and circular connectivity," *Phys. Rev. A*, vol. 107, p. 032403, Mar 2023.

[166] S. Deb and W. Pan, "Quantum image compression: Fundamentals, algorithms, and advances," *Computers*, vol. 13, no. 8, p. 185, 2024.

[167] A. Tiwari, S. Sakhuja, and Britant, "Benchmarking quantum image representations algorithms for hybrid-quantum applications," in *2025 17th International Conference on COMmunication Systems and NETworks (COMSNETS)*, 2025, pp. 1108–1113.

[168] M. E. Haque, M. Paul, A. Ulhaq, and T. Debnath, "Advanced quantum image representation and compression using a dct-efrqi approach," *Scientific Reports*, vol. 13, no. 1, p. 4129, Mar. 2023.

[169] S. H. R. Devarapalli, H. Jadhav, and J. Dontabhaktuni, "Image compression using quantum wavelet transforms," *Proc. SPIE Int. Soc. Opt. Eng.*, vol. 13391, p. 1339117, 2025.

[170] Y. Ma and N. Zhou, "Quantum color image compression and encryption algorithm based on fibonacci transform," *Quantum Information Processing*, vol. 22, p. 39, 2023.

[171] M. G. Amankwah, D. Camps, E. W. Bethel, R. V. Beeumen, and T. Perciano, "Quantum pixel representations and compression for n-dimensional images," *Scientific Reports*, vol. 12, p. 7712, 2022.

[172] D. T. Mukhamedieva, R. A. Sobirov, N. M. Turgunova, and B. N. Samijonov, "Quantum Fourier transform in image processing," in *Information Technologies and Intelligent Decision Making Systems*, ser. Communications in Computer and Information Science, A. Gibadullin, Ed. Springer, Cham, 2024, vol. 2112, pp. 143–151.

[173] S. R. Majji, A. Chalumuri, and B. S. Manoj, "Quantum approach to image data encoding and compression," *IEEE Sensors Letters*, vol. 7, no. 2, pp. 1–4, 2023.

[174] M. Chehimi, C. Chaccour, C. K. Thomas, and W. Saad, "Quantum semantic communications for resource-efficient quantum networking," *IEEE Communications Letters*, vol. 28, no. 4, pp. 803–807, 2024.

[175] S. M. A. Rizvi, U. Khalid, S. Chatzinotas, T. Q. Duong, and H. Shin, "Controlled quantum semantic communication for industrial cps networks," *IEEE Transactions on Network Science and Engineering*, pp. 1–14, 2025.

[176] N. Nunavath, N. Hello, E. C. Strinati, R. Bassoli, and F. H. P. Fitzek, "Towards quantum semantic communications: A framework for integrating quantum and semantic technologies," in *2024 IEEE Globecom Workshops (GC Wkshps)*, 2024, pp. 1–5.

[177] A. Andreou, C. X. Mavromoustakis, G. Mastorakis, A. Bourdena, and E. K. Markakis, "Quantum computing in semantic communications: Overcoming opti-

mization challenges with high-dimensional hilbert spaces," *IEEE Access*, vol. 13, pp. 157 942–157 964, 2025.

[178] U. Khalid, M. S. Ulum, A. Farooq, T. Q. Duong, O. A. Dobre, and H. Shin, "Quantum semantic communications for metaverse: Principles and challenges," *IEEE Wireless Communications*, vol. 30, no. 4, pp. 26–36, 2023.

[179] B. E. Arfeto, S. Tariq, U. Khalid, T. Q. Duong, and H. Shin, "Gensc-6g: A prototype testbed for integrated generative ai, quantum, and semantic communication," *IEEE Communications Magazine*, vol. 63, no. 10, pp. 28–35, 2025.

[180] S. Tariq, U. Khalid, B. E. Arfeto, T. Q. Duong, and H. Shin, "Integrating sustainable big ai: Quantum anonymous semantic broadcast," *IEEE Wireless Communications*, vol. 31, no. 3, pp. 86–99, 2024.

[181] A. M. Sayeed, "Quantum mimo: A framework for entanglement distribution in spatial multipath channels," in *Quantum 2.0 Conference and Exhibition*. Washington, D.C.: Optica Publishing Group, 2022.

[182] R. Shi, J. Shi, Y. Guo, X. Peng, and M. H. Lee, "Quantum mimo communication scheme based on quantum teleportation with triplet states," *International Journal of Theoretical Physics*, vol. 50, no. 8, pp. 2334–2346, Aug. 2011.

[183] N. K. Kundu, M. R. McKay, A. Conti, R. K. Mallik, and M. Z. Win, "Mimo terahertz quantum key distribution under restricted eavesdropping," *IEEE Transactions on Quantum Engineering*, vol. 4, pp. 1–15, 2023.

[184] X. Y. Yan, N. R. Zhou, L. H. Gong, Y. Q. Wang, and X. J. Wen, "High-dimensional quantum key distribution based on qudits transmission with quantum fourier transform," *Quantum Information Processing*, vol. 18, no. 9, p. 271, 2019.

[185] Z. Cao, C. Zhang, C. He, and M. Zhang, "Quantum teleportation protocol of arbitrary quantum states by using quantum fourier transform," *International Journal of Theoretical Physics*, vol. 59, pp. 3174–3183, 2020.

[186] A. Sabaawi, M. Almasaoodi, and S. Imre, "Exploiting ofdm method for quantum communication," *Quantum Information Processing*, vol. 23, no. 256, 2024.

[187] M. R. Almasaoodi, A. M. A. Sabaawi, and S. Imre, "Quantum ofdm: A novel approach to qubit error minimization," in *2024 14th International Symposium on Communication Systems, Networks and Digital Signal Processing (CSNDSP)*, 2024, pp. 53–58.

[188] A. M. A. Sabaawi, M. R. Almasaoodi, and S. Imre, "Advancing quantum communications: Q-ofdm with quantum fourier transforms for enhanced signal integrity," in *2024 International Conference on Software, Telecommunications and Computer Networks (SoftCOM)*, 2024, pp. 1–6.

[189] B. Mallick, P. Parida, C. Nayak, T. Khalifa, M. Kumar Panda, N. Ali, G. Uttam Patil, and B. Prasad, "Multi-channel multi-protocol quantum key distribution system for secure image transmission in healthcare," *IEEE Access*, vol. 13, pp. 62 476–62 505, 2025.

[190] A. Shafique, S. A. A. Naqvi, A. Raza, M. Ghalaii, P. Papanastasiou, J. McCann, Q. H. Abbasi, and M. A. Imran, "A hybrid encryption framework leveraging quantum and classical cryptography for secure transmission of medical images in iot-based telemedicine networks," *Scientific Reports*, vol. 14, p. 31054, 2024.

[191] F. Rahman, "Quantum image transmission," *Nature Methods*, vol. 23, p. 1286, jul 2026.

[192] U. Jayasinghe, P. Samarathunga, Y. Ganearachchi, T. Fernando, and A. Fernando, "Quantum communications for image transmission over error-prone channels," *Electronics Letters*, vol. 60, no. 15, Aug. 2024.

[193] ——, "Adaptive coding-based quantum communication system for image transmission," *Electronics Letters*, vol. 61, no. 1, p. e70299, 2025.

[194] U. Jayasinghe, P. Samarathunga, T. Fernando, Y. Ganearachchi, and A. Fernando, "Image transmission over quantum communication systems with three-qubit error correction," *Electronics Letters*, vol. 61, no. 1, p. e70205, 2025.

[195] U. Jayasinghe, T. Fernando, and A. Fernando, "Optimizing quantum image transmission through an adaptive quantum error correction framework," in *2026 IEEE International Conference on Consumer Electronics (ICCE)*, 2026, pp. 1–6.

[196] U. Jayasinghe, P. Samarathunga, N. Pollwaththage, Y. Ganearachchi, T. Fernando, and A. Fernando, "Quantum communication for video transmission over error-prone channels," *IEEE Transactions on Consumer Electronics*, vol. 71, no. 1, pp. 1148–1155, 2025.

[197] T.-Y. Lin *et al.*, "Microsoft coco: Common objects in context," in *European Conference on Computer Vision*, 2014, pp. 740–755.

[198] P. E. Frenkel, "Classical simulations of communication channels," *Quantum*, vol. 6, p. 751, Jun. 2022.

[199] M. Chakraborty, A. Mukherjee, A. Nag, and S. Chandra, "Hybrid quantum noise model to compute gaussian quantum channel capacity," *IEEE Access*, vol. 12, pp. 14 671–14 689, 2024.

[200] A. Horé and D. Ziou, "Is there a relationship between peak-signal-to-noise ratio and structural similarity index measure?" *IET Image Processing*, vol. 7, pp. 12–24, 2013.

[201] M. López-Benítez, "Performance analysis of SNR threshold-setting strategies for adaptive modulation and coding under fading channels," *Physical Communication*, vol. 30, pp. 154–166, 10 2018. [Online]. Available: https://doi.org/10.1016/j.phycom.2018.08.009

[202] M. B. Ginting, K. Anwar, and D. Maryopi, "Constructing quantum surface codes for arbitrary surface forms," in *2021 IEEE Symposium On Future Telecommunication Technologies (SOFTT)*, 2021, pp. 75–80.

[203] A. Wieckowski, J. Brandenburg, T. Hinz, C. Bartnik, V. George, G. Hege, C. Helmrich, A. Henkel, C. Lehmann, C. Stoffers, I. Zupancic, B. Bross, and D. Marpe, "Vvenc: An open and optimized vvc encoder implementation," in *2021 IEEE International Conference on Multimedia and Expo Workshops (ICMEW)*. IEEE, 2021, pp. 1–2.

[204] B. Bross, J. Chen, J. R. Ohm, G. J. Sullivan, and Y. K. Wang, "Developments in international video coding standardization after avc, with an overview of versatile video coding (vvc)," *Proc. IEEE*, vol. 109, no. 9, pp. 1463–1493, Sep. 2021.

[205] T. Miroshnichenko, "People playing soccer," [Online]. Available: https://www.pexels.com/video/people-playing-soccer-6077718/.

[206] P. Midtrack, "People enjoying the day in a beach," [Online]. Available: https://www.pexels.com/video/people-enjoying-the-day-in-a-beach-3150419/.

[207] Cup of Couple, "A bowl of avocados and vegetables," [Online]. Available: https://www.pexels.com/video/a-bowl-of-avocados-and-vegetables-7656166/.

[208] International Telecommunication Union (ITU), "Methodologies for the Subjective Assessment of the Quality of Television Pictures," International Telecommunication Union, Geneva, Switzerland, ITU-R Recommendation BT.500, 2022. [Online]. Available: https://www.itu.int/rec/R-REC-BT.500

[209] U. Jayasinghe, N. Kushantha, T. Fernando, and A. Fernando, "A robust multi-qubit quantum communication system for image transmission over error prone channels," *IEEE Transactions on Consumer Electronics*, vol. 71, no. 3, pp. 7551–7558, 2025.

[210] P. Pathak and R. Bhatia, "Performance analysis of polar codes for next generation 5g technology," in *2022 3rd International Conference for Emerging Technology (INCET)*. Belgaum, India: IEEE, May 2022, pp. 1–4.

[211] Z. Wang and A. Bovik, "A universal image quality index," *IEEE Signal Processing Letters*, vol. 9, no. 3, pp. 81–84, 2002.

[212] U. Jayasinghe, T. Fernando, and A. Fernando, "High-fidelity image transmission in quantum communication with frequency domain multi-qubit techniques," *Algorithms*, vol. 18, no. 8, p. 501, 2025.

[213] ——, "A comparative study of quantum haar wavelet and quantum fourier transforms for quantum image transmission," *Information*, vol. 16, no. 11, p. 962, 2025.

[214] ——, "Quantum fourier transform-based adaptive image compression and transmission system," *Electronics Letters*, vol. 61, no. 1, p. e70430, 2025.

[215] U. Jayasinghe and A. Fernando, "Rethinking video transmission: A quantum fourier transform-based approach for error-prone channels," *Electronics*, vol. 15, no. 6, p. 1323, 2026.

[216] R. Wille, A. Lye, and R. Drechsler, "Optimal swap gate insertion for nearest neighbor quantum circuits," in *2014 19th Asia and South Pacific Design Automation Conference (ASP-DAC)*, 2014, pp. 489–494.

[217] V. Dixit and S. Jian, "Quantum fourier transform to estimate drive cycles," *Scientific Reports*, vol. 12, p. 654, 2022.

[218] ImageNet, "Imagenet: A large-scale hierarchical image database," [Online]. Available: https://www.image-net.org/, accessed on Mar. 30, 2025.

[219] Kaggle Contributor, "Images 4k," [Online]. Available: https://www.kaggle.com/datasets/evgeniumakov/images4k, accessed on Mar. 30, 2025.

[220] Keras, "Mnist digits classification dataset," 2024, accessed: 11 May 2025. [Online]. Available: https://keras.io/api/datasets/mnist/

[221] A. Krizhevsky, "Cifar-10 and cifar-100 datasets," https://www.cs.toronto.edu/~kriz/cifar.html, accessed: 10-10-2024.

[222] C. N. Valdebenito Maturana, A. L. Sandoval Orozco, and L. J. García Villalba, "Exploration of metrics and datasets to assess the fidelity of images generated by generative adversarial networks," *Applied Sciences*, vol. 13, no. 19, p. 10637, 2023.

[223] U. Jayasinghe, P. Samarathunga, N. Pollwaththage, T. Fernando, and A. Fernando, "Quantum communication for semantic communication based image transmission," *IEEE Transactions on Vehicular Technology*, 2026, early Access.

[224] U. Jayasinghe and A. Fernando, "Complex-valued unitary superposition–driven multi-qubit encoding for quantum video transmission," *Electronics*, vol. 15, no. 9, p. 1906, 2026. [Online]. Available: https://doi.org/10.3390/electronics15091906

[225] C. Gerry and P. Knight, *Introductory Quantum Optics*. Cambridge University Press, 2004.

[226] U. Jayasinghe, T. Fernando, Y. Ganearachchi, P. Samarathunga, and A. Fernando, "Quantum communication based image transmission with transmit and receive diversity in mimo communication systems," *IEEE Transactions on Consumer Electronics*, vol. 71, no. 2, pp. 2500–2507, 2025.

[227] U. Jayasinghe, P. Samarathunga, T. Fernando, and A. Fernando, "Transmit and receive diversity in mimo quantum communication for high-fidelity video transmission," *Algorithms*, vol. 18, no. 7, p. 436, 2025.

[228] U. Jayasinghe and A. Fernando, "A quantum ofdm framework for high-fidelity image transmission," *IEEE Transactions on Consumer Electronics*, vol. 71, no. 4, pp. 9628–9636, 2025.

[229] ——, "A quantum ofdm framework for next-generation video transmission over noisy channels," *Electronics*, vol. 15, no. 2, p. 284, 2026.

[230] U. Jayasinghe, T. Fernando, and A. Fernando, "A quantum mimo-ofdm framework with transmit and receive diversity for high-fidelity image transmission," *Telecom*, vol. 6, no. 4, p. 96, 2025.

[231] B. Sklar, "Rayleigh fading channels in mobile digital communication systems. i. characterization," *IEEE Communications Magazine*, vol. 35, no. 9, pp. 136–146, 1997.

[232] U. Jayasinghe and A. Fernando, "Complex-valued orthogonal unitary superposition encoding for robust three-qubit quantum-error-correction-based image transmission," *Algorithms*, vol. 19, no. 4, p. 304, 2026.